NASA/TP-20205008233

Demonstration of Multilayer Insulation, Vapor Cooling of Structure, and Mass Gauging for Large-Scale Upper Stages: Structural Heat Intercept, Insulation, and Vibration Evaluation Rig (SHIIVER) Final Report

Wesley L. Johnson
Glenn Research Center, Cleveland, Ohio

Ramaswamy Balasubramaniam
Case Western Reserve University, Cleveland, Ohio

Richard Hibbs
Jacobs Space Exploration Group, Huntsville, Alabama

Gregory A. Zimmerli
Glenn Research Center, Cleveland, Ohio

Marius Asipauskas
Universities Space Research Association, Cleveland, Ohio

Samantha Bittinger, Christopher Dardano, and F. David Koci
Glenn Research Center, Cleveland, Ohio

August 2021

NASA STI Program . . . in Profile

Since its founding, NASA has been dedicated to the advancement of aeronautics and space science. The NASA Scientific and Technical Information (STI) Program plays a key part in helping NASA maintain this important role.

The NASA STI Program operates under the auspices of the Agency Chief Information Officer. It collects, organizes, provides for archiving, and disseminates NASA's STI. The NASA STI Program provides access to the NASA Technical Report Server—Registered (NTRS Reg) and NASA Technical Report Server—Public (NTRS) thus providing one of the largest collections of aeronautical and space science STI in the world. Results are published in both non-NASA channels and by NASA in the NASA STI Report Series, which includes the following report types:

- TECHNICAL PUBLICATION. Reports of completed research or a major significant phase of research that present the results of NASA programs and include extensive data or theoretical analysis. Includes compilations of significant scientific and technical data and information deemed to be of continuing reference value. NASA counter-part of peer-reviewed formal professional papers, but has less stringent limitations on manuscript length and extent of graphic presentations.

- TECHNICAL MEMORANDUM. Scientific and technical findings that are preliminary or of specialized interest, e.g., "quick-release" reports, working papers, and bibliographies that contain minimal annotation. Does not contain extensive analysis.

- CONTRACTOR REPORT. Scientific and technical findings by NASA-sponsored contractors and grantees.

- CONFERENCE PUBLICATION. Collected papers from scientific and technical conferences, symposia, seminars, or other meetings sponsored or co-sponsored by NASA.

- SPECIAL PUBLICATION. Scientific, technical, or historical information from NASA programs, projects, and missions, often concerned with subjects having substantial public interest.

- TECHNICAL TRANSLATION. English-language translations of foreign scientific and technical material pertinent to NASA's mission.

For more information about the NASA STI program, see the following:

- Access the NASA STI program home page at http://www.sti.nasa.gov

- E-mail your question to help@sti.nasa.gov

- Fax your question to the NASA STI Information Desk at 757-864-6500

- Telephone the NASA STI Information Desk at 757-864-9658

- Write to:
  NASA STI Program
  Mail Stop 148
  NASA Langley Research Center
  Hampton, VA 23681-2199

NASA/TP-20205008233

Demonstration of Multilayer Insulation, Vapor Cooling of Structure, and Mass Gauging for Large-Scale Upper Stages: Structural Heat Intercept, Insulation, and Vibration Evaluation Rig (SHIIVER) Final Report

Wesley L. Johnson
Glenn Research Center, Cleveland, Ohio

Ramaswamy Balasubramaniam
Case Western Reserve University, Cleveland, Ohio

Richard Hibbs
Jacobs Space Exploration Group, Huntsville, Alabama

Gregory A. Zimmerli
Glenn Research Center, Cleveland, Ohio

Marius Asipauskas
Universities Space Research Association, Cleveland, Ohio

Samantha Bittinger, Christopher Dardano, and F. David Koci
Glenn Research Center, Cleveland, Ohio

National Aeronautics and
Space Administration

Glenn Research Center
Cleveland, Ohio 44135

August 2021

Acknowledgments

In order to execute on a task with hardware the size of Structural Heat Intercept, Insulation, and Vibration Evaluation Rig (SHIIVER), it takes a multitude of people and groups to make it happen. The results presented herein may be written by a few, but they reflect the work of many. First, the authors would like to acknowledge Joseph Zoeckler and Lauren Ameen who laid the foundation for SHIIVER as product lead engineers the first 4 years. Keith Johnson led the instrumentation and electrical portions of SHIIVER, offering up many excellent ideas and also making sure the instrumentation was just as was needed to make SHIIVER successful. Michael Senchak and Joseph Powell monitored the SHIIVER hardware integration daily and made sure that all the plans were in place well ahead of time and thoroughly thought through before any two pieces of hardware were put together. Mark Springowski installed every piece of instrumentation, ensuring they were correctly located and mounted and carefully wired the system together. Arthur Werkheiser and Michael Reynolds who helped to navigate the SHIIVER test article from the Marshall Space Flight Center including all the foaming and associated work. The SHIIVER engineering team also included Tiodor (Ted) Kovacevich who did much of the structural analysis, Barry Battista who provided much help with the thermal and structural analysis and test plan development, and Andrew Smith who helped both. Jeffrey Oliver who supported initial acoustic test development. Dale Diedrick and Harry Harris who made all of the computer automated drawings (CADs) and drawings for the SHIIVER hardware. Bradley Lerch who performed several series of structural testing on multilayer insulation (MLI) coupons. The MLI design, fabrication, and installation team led by David Oberg, including Brent Anderson, Jim Sokup, David Frank, Ted Nast, and Vinay Mistry. The fabrication and welding team led by Daniel Kocka and Brian Brandenburg who fabricated the Thermal Test Support stand, the aft skirt, and the forward skirt, including fabricating items on rapid timelines after external vendors fell through. The Neil A. Armstrong Test Facility teams at the In-Space Propulsion Facility, led by Nicholas Connelly, Stanley Grisnik, Wesley Sallee, and Kirk Berhent spent much time carefully assembling the hardware and operating the testing. David Linden and Christian Maloney who made sure all of the data made it out the other end of SHIIVER in a usable form. The Reverberant Acoustic Test Facility engineering and technician teams led by Aron Hozman and Stephen West who made sure we got the best acoustic test possible. The Marshall Space Flight Center spray-on foam insulation (SOFI) team, led by Steven Whitfield and Guy McDougal who not only sprayed the SHIIVER tank with SOFI, but also when the SHIIVER team burned through portions of it, patiently taught us how to repair the SOFI to allow SHIIVER to remain on schedule for testing.Finally, Hans Hansen, as project manager who helped pave the way for SHIIVER throughout its life and saw as many of the ups and downs as the rest of us. This effort was funded as a part of the Evolvable Cryogenics project, a part of the Technology Demonstration Mission Program within the NASA Space Technology Mission Directorate.

Level of Review: This material has been technically reviewed by expert reviewer(s).

Available from

NASA STI Program
Mail Stop 148
NASA Langley Research Center
Hampton, VA 23681-2199

National Technical Information Service
5285 Port Royal Road
Springfield, VA 22161
703-605-6000

This report is available in electronic form at http://www.sti.nasa.gov/ and http://ntrs.nasa.gov/

Contents

Demonstration of Multilayer Insulation, Vapor Cooling of Structure, and Mass Gauging for Large-Scale Upper Stages: Structural Heat Intercept, Insulation, and Vibration Evaluation Rig (SHIIVER) Final Report

Wesley L. Johnson
National Aeronautics and Space Administration
Glenn Research Center
Cleveland, Ohio 44135

Ramaswamy Balasubramaniam
Case Western Reserve University
Cleveland, Ohio 44106

Richard Hibbs
Jacobs Space Exploration Group
Huntsville, Alabama 35812

Gregory A. Zimmerli
National Aeronautics and Space Administration
Glenn Research Center
Cleveland, Ohio 44135

Marius Asipauskas
Universities Space Research Association
Cleveland, Ohio 44135

Samantha Bittinger, Christopher Dardano, and F. David Koci
National Aeronautics and Space Administration
Glenn Research Center
Cleveland, Ohio 44135

Summary

Testing was completed on the Structural Heat Intercept, Insulation, and Vibration Evaluation Rig (SHIIVER) between August 2019 and January 2020. SHIIVER was designed to be a testbed for the scaling of cryogenic fluid management technologies as applied to large upper stages and long-duration in-space stages. The hardware consists of a 4-m-diameter stainless steel tank, structural skirts supporting the tank in the aft direction, and an aluminum forward skirt with vapor-cooling channels bolted to it. The initial testing of the SHIIVER hardware was with liquid hydrogen and liquid nitrogen (as a substitute fluid for liquid oxygen and liquid methane) and sought to demonstrate the use of boiloff vapor to intercept heat on a structural skirt, multilayer insulation (MLI) on the tank domes, and the Radio Frequency Mass Gauge (RFMG). Testing was completed in four stages: a baseline thermal vacuum test prior to installation of the MLI, a thermal vacuum test after the MLI installation, a reverberant acoustic test, and a subsequent thermal vacuum test to verify that no damage occurred during the reverberant acoustic testing. Each thermal vacuum test with chamber wall at ambient temperature and vacuum level in the 10^{-6} torr range was conducted continuously between approximately 90 and 25 percent full. Test results showed that the vapor cooling reduced the heat load to the tank by approximately 10 percent, but the boiloff by less than 3 percent at 50 percent full with no MLI on the domes. It reduced the heat load to the tank by approximately 10 percent, but the boiloff was essentially unchanged at 50 percent full with MLI on the domes. The MLI reduced the heat load to the tank by approximately 40 percent at all fill levels, but the boiloff by approximately 25 percent at 90 percent full and 45 percent below 65 percent full. The RFMG performed well over all fill ranges, and several radio frequency tank modes were used to gauge the mass of fluid in the tank. SHIIVER was then exposed to an acoustic environment of 147 dB overall sound pressure

level in a reverberant chamber. The acoustic environment and profile envelopes the upper stage internal acoustic level of several different modern launch vehicles. No structural or thermal performance changes were observed as a result of acoustic testing. Final thermal vacuum testing after the acoustic testing showed no degradation to the MLI due to the acoustic environment as measured via system heat loads.

1.0 Introduction

The Structural Heat Intercept, Insulation, and Vibration Evaluation Rig (SHIIVER) was developed to be a multipurpose, large-scale testbed. It was specifically designed to simulate upper stage rocket tanks, both from a geometry and heat load distribution perspective. While SHIIVER is approximately half the size of the Exploration Upper Stage (EUS) hydrogen tanks, it is nearly full size for the EUS oxygen tanks and the Delta Cryogenic Second Stage (DCSS).

The main technological objectives for this initial SHIIVER testing are (i) to test vapor cooling wherein boiloff vapor is routed through the forward skirt to cool it and intercept a portion of the heat load, (ii) test multilayer insulation (MLI) installed on the domes of a large-scale tank to reduce the heat flux to the tank, (iii) test vapor cooling and MLI in combination, and (iv) demonstrate mass gauging using a Radio Frequency Mass Gauge (RFMG) on a large cryogenic tank.

The current design methodology of rocket upper stages prioritizes structural performance over thermal performance. Due to the duration of the missions that such stages undergo, tanks are typically oversized and tolerate the propellant losses that accompany the poor thermal performance of the stages. Efforts to include MLI on upper stages were previously undertaken by Lockheed Martin Corporation on the Titan IV-based Centaur G-Prime. Using just three layers of MLI on the sidewalls, the Centaur liquid oxygen and liquid hydrogen (LH_2) heat fluxes were cut to nearly half of the baseline heat load using spray-on foam insulation (SOFI) on the tank surface (Ref. 1). While the mass improvements of a vapor-cooled skirt are much less understood, initial modeling indicates that by cooling just the lower 25 percent of the skirt, the heat load through the skirt could be reduced by up to 54 percent.

In order to demonstrate full performance after vibrational loads from launch, as well as the impacts and improvements of the thermal performance of the system, the SHIIVER test article was subjected to a sequence of thermal and vacuum testing, acoustic testing, and another round of thermal and vacuum testing. For comparison to future testing, an initial thermal vacuum baseline test with SOFI as the only insulation on the tank was performed to set a baseline that is similar in configuration to current upper stage designs. The SHIIVER test article demonstration will provide insight into the fabrication costs, installed masses, and associated thermal performance benefits for insulation and vapor-cooling structures. In order for this effort to be successful, the actual fabrication and demonstration must be performed on a fairly large and representative system.

1.1 Background

Following on the success of the Mercury, Gemini, and Apollo programs, NASA pushed onwards towards Mars. This manifested in the Mars Nuclear Vehicle (MNV), which intended to store LH_2 for a 9-month trip to Mars and provide propulsive capability for the astronauts' return (Ref. 2). During the development of the MNV, NASA began the investigation into vehicle thermal design for long-duration missions. While there have been numerous investigations into MLI on a small scale either for basic material characterization or small applications, large demonstrations are much less frequent. Several large-scale testbeds have been developed over the past 50 year to allow for the demonstration of cryogenic fluid management technologies at relevant scales. These tests are summarized in Table 1.

As early as 1967, Lockheed (Refs. 3 and 4), Boeing (Ref. 5), The Goodyear Tire & Rubber Company (Ref. 6), McDonnell Douglas Corporation (Ref. 7), and General Dynamics Corporation (Ref. 8), among others, were studying the design and fabrication of large MLI blankets in addition to in-house NASA efforts at both Lewis Research Center (now Glenn Research Center) and Marshall Space Flight Center (Refs. 9 and 10). Down selection of those efforts led to the testing of systems built by both Lockheed Martin and McDonnell Douglas (Ref. 2). Only the McDonnell Douglas system ever saw flight on a large-scale system; however, it was not cryogenic. The McDonnell Douglas system flew on the forward dome of Skylab to enable thermal control of the habitation model. These results are presented by Daniels et al. in Reference 11.

Following the cancellation of NASA's Mars mission in favor of the Space Transportation System (a.k.a. Space Shuttle), efforts on the maturation of MLI continued along two distinct paths: reusable systems for inside the Space Shuttle payload bay to be used on kick stages to retrieve satellites from geostationary orbit and for other upper stages such as Centaur. General Dynamics demonstrated a reusable system for the Space Shuttle, which was exposed to 100 pressurization cycles with only minor repairs after the 51st cycle (Ref. 12). Similarly, at Lewis Research Center, Sumner did similar testing on a competitive system (Ref. 13). Beech Aircraft Corporation (Beech) did design studies for spherical vacuum-jacketed life support tanks for durations up to 180 days including the Oxygen Thermal Test Article (OTTA) (Ref. 14). The Beech design eventually became the Power Reactant Storage and Distribution (PRSD) system tanks for the Space Shuttle's power and life

support system. Internally, at Lewis Research Center, NASA developed an insulation system upgrade for the Centaur upper stage (Ref. 15). Eventually, a three-layer blanket did fly on the Titan Centaur upper stage, but this was not nearly as thick of a blanket as is needed for long-duration stages (Refs. 1 and 16). For the U.S. Air Force, Ball Aerospace, part of the Ball Corporation, performed a study for large insulation systems after which testing was supposed to occur, however, the project was canceled before testing could commence (Refs. 17 and 18).

In the early 1990s with NASA's renewed interest in Mars and the Space Exploration Initiative (SEI), large-scale demonstrations of insulation became a necessary step once again. Marshall developed the Multipurpose Hydrogen Test Bed (MHTB) as a large-scale demonstration platform. With a 10- by 10-ft tank, the MHTB included at various times insulation demonstrations, thermodynamic vent demonstrations with multiple fluids, and zero boiloff demonstrations (Ref. 19).

While many of these early demonstrations did not use vapor cooling of either the MLI or the structure, small-scale efforts have been done prior. Vapor-cooled shielding in the MLI blanket is discussed as early as the late 1950s based on the work at the National Bureau of Standards (NBS). Vapor cooling is most often used in industry on liquid helium vessels. Cunnington developed an approach for the minimization of structural heat load and MLI separately using the second law of thermodynamics (Ref. 20). Cooling on struts was optimized by Li, Eyssa, and McIntosh for up to six cooling points for helium, essentially expanding on the work of Cunnington and applying it to helium (Ref. 21). Most vapor-cooled shields for small dewars are hung from the tank struts. Thus, the struts are cooled by the vapor-cooled shield as discussed by Hopkins and Payne (Ref. 22). Canavan and Miller developed a methodology to optimize cooling along a structural skirt, but only allowed for conduction down the skirt, not radiation to it (Ref. 23). For large geometries, radiation can become a dominant mode of heat transfer, as is discussed in Section 1.3.

The Beechcraft efforts in developing a 180-day hydrogen system also included a boiler shield and a vapor-cooling shield within the insulation system (Ref. 14). This approach was an extension of their systems design for oxygen and hydrogen tanks that stored reactants for the fuel cells on Gemini, Apollo, and Space Shuttle spacecraft. In the late 1980s, Martin Marrietta developed a 1.07-m- (42-in.-) diameter tank on which they installed a vapor-cooled shield in the middle of the MLI blanket. Cooling was only applied within the blanket (48 layers below and 24 layers on top) and an 18.5 percent decrease in heat leak was noted (Ref. 24).

TABLE 1.—SUMMARY OF LARGE-SCALE TEST GEOMETRIES

Test name	Tank diameter, m	No. MLI[a] layers	MLI[a] thickness, cm	Foam	Cryogenic test fluid	Purge gas
Beech Aircraft Corporation OTTA[b]	2.16	46	Unknown	No	Helium/nitrogen	Vacuum jacketed
NASA Marshall[c]	3.05	45	3.8	3.5 cm	Hydrogen	Nitrogen
NASA Lewis (Sumner)[d]	1.39	30	1.7	No	Hydrogen	Helium
NASA Lewis (Knoll and DeWitt)[e]	2.23	30	1.7	No	Hydrogen	Helium
General Dynamics Corporation[f]	2.21	44	4.0	No	Hydrogen	Helium
McDonnell Douglas Corporation[g]	2.67	70	1.8	No	Hydrogen	Helium
Lockheed Martin Corporation[h]	2.79	105	1.7	No	Hydrogen	Helium

[a]Multilayer insulation (MLI).

[b]Oxygen thermal test article (OTTA). Reference 14.

[c]Reference 19.

[d]Reference 13.

[e]Reference 15.

[f]Reference 12.

[g]Reference 2.

[h]Reference 4.

1.1.1 Testing With Both Liquid Nitrogen and Liquid Hydrogen

While the MHTB has been tested with LH_2, liquid nitrogen (LN_2), and liquid methane over the years, it was only tested with LH_2 before the MLI was damaged (Refs. 19, 25, and 26). There have been few other test articles tested with both LN_2 and LH_2 for comparison of heat loads between the two. Furthermore, the testing of two diverse fluids in the vapor-cooling configuration of SHIIVER should provide an interesting comparison. Due to the approximately 6-to-1 ratio of sensible to latent heat for LH_2, it is often considered an ideal fluid for vapor-cooling applications. On the other hand, this ratio is 1 to 1 for LN_2 so it is usually not considered for vapor cooling. Initial calculations on theoretical limits show that it is quite easy to achieve greater than 75 percent heat load reduction for hydrogen cases; however, estimates for nitrogen (including oxygen and methane) are much lower, less than 20 percent (Ref. 27).

1.2 Technological Objectives

There are four main technological objectives for the current SHIIVER testing: the first concerns vapor cooling, the second is regarding insulation, while the third is a combination of the first two, and the fourth is regarding mass gauging. Each technical objective has its own subset of objectives that are described as follows:

1.2.1 Vapor-Cooling Technological Objectives

The main vapor-cooling objective is to demonstrate vapor cooling of a representative structural system on a representatively scaled LH_2 test hardware. This can be broken down into the following subset of objectives:

1. Cool a skirt structural support using the boiloff vapor from a LH_2 tank.
   - The demonstration of using hydrogen vapor to cool the structure of a tank on the scale of SHIIVER has never been completed before. The demonstration of a known implementation of vapor cooling will greatly increase the data that could be used for design and implementation of flight concepts.
2. Measure the increase in thermal performance of a system when vapor cooling is used on a representative system.
   - Once the vapor-cooling system has been built while focusing on the much larger application, understanding the performance and improvement in performance over the uncooled skirt as a function of both position and fill level is fundamentally required in order to predict the benefits to a mission.
3. Accurately predict the thermal performance change of a system when vapor cooling is used on a representative system.
   - In addition to understanding performance, predicting it and demonstrating the methodology in doing so is necessary to apply these benefits to future missions.
4. Determine the mass savings that vapor cooling can provide on a large upper stage.
   - Once fundamental thermal performance (and improvement in performance) have been determined, mass savings can be determined for future missions.
5. Based on test planning and results, determine areas of the cooling technique that are most sensitive for future study.
   - Whenever something of this scale is performed, unexpected phenomena and results may appear that require further study. The SHIIVER test should recognize and identify these observations for future study.

1.2.2 Insulation Technological Objectives

The main objective here is to demonstrate the insulation of a representatively scaled LH_2 test hardware. This can be broken down into the following subset of objectives:

1. Insulate a representatively scaled LH_2 test apparatus.
   - While tanks have been insulated with MLI and other highly capable insulation materials, they were never performed in a manner addressing the scale of the application in mind. The design, fabrication, and installation of the insulation system must be representative of what is required on the application-scaled tank. For the SHIIVER system, the MLI was designed for an 8.4-m-diameter tank application and then scaled down to the 4-m-diameter SHIIVER test hardware.
2. Measure the thermal performance of the insulation system on the representatively scaled LH_2 test apparatus.
   - Once the insulation system has been built to the appropriately scaled application, understanding the performance and improvement in performance over the state-of-the-art spray-on foam applications is fundamentally needed in order to predict the benefits to a mission.
3. Accurately predict the thermal performance of the insulation system on the representatively scaled LH_2 test apparatus.
   - In addition to understanding the performance, predicting it and demonstrating the methodology in doing so is necessary to apply these benefits to future missions.
4. Determine the mass savings of the insulation system on a large upper stage and its associated cost.

- Once fundamental performance (and improvement in performance) have been determined, mass savings can be determined for future missions.

5. Based on test planning and results, determine areas of the insulation system that are most sensitive for future study.
   - Whenever something of this scale is performed, unexpected phenomena and results may appear that require further study. The SHIIVER test should recognize and identify these observations for future study.

1.2.3 Combined Effect of Multilayer Insulation and Vapor-Cooling Technical Objective

The third technical objective is to understand the combined effects of MLI and vapor cooling in reducing the heat load to the system. Applying MLI to the domes should both reduce the heat load and associated boiloff flow rate out of the SHIIVER tank as well as reduce the exit gas temperature from the vent line (by reducing the heat into the ullage portion of the tank). This should have a significant effect on the skirt, and it may even improve the heat load reduction due to the colder inlet gas temperature.

1.2.4 Mass Gauging Technical Objective

The main objective here is to demonstrate the performance of the RFMG on a representatively scaled upper stage tank. This instrument will be used to measure fluid mass in the tank and infer fluid levels during the test.

1.3 Rationale for Acoustic Testing Details

As noted in Reference 28, MLI has flown numerous times but limited flight- or ground-test structural evaluations have been made of integrated MLI and broad area cooling (BAC) shield systems. As noted by Jones (Ref. 28), high-frequency, acoustically driven launch environments are expected to be the critical environment for the MLI and BAC shield systems. This is due to the large surface areas, relatively large area to weight ratios, and relatively delicate materials that comprise the insulation and BAC shield systems. The risk of acoustic vibration damage increases as the tank size increases.

Subscale testing would be an acceptable method for down-selecting various MLI configurations or materials for a trade study, or for assessing MLI blankets subjected only to high-frequency acoustics (frequencies >50 Hz). However, to fully characterize system-level damping and modal performance of MLI blankets subjected to low-frequency acoustic vibrations (frequency <50 Hz), a full-scale acoustic tank test is needed. A full-scale, filled, and pressurized tank (or an idealized tank assembly) will yield significantly different modal responses than a subscale panel test. While it is possible to adjust panel stiffness to approximate a full-scale tank, subscale tests such as the Reference 28 Cryogenic Propellant Storage and Transfer (CPST) test cannot account for the damping effects over large insulation areas.

Previous acoustic testing of MLI blankets have shown that subscale acoustics do not degrade MLI performance (as long as aluminum foil was not used) (Refs. 29 and 30) but scaling to the full tank size may show excitation at low frequencies.

2.0 Description of Structural Heat Intercept, Insulation, and Vibration Evaluation Rig (SHIIVER) Hardware

2.1 Main Subsystems

SHIIVER consists of three main components: the LH_2 tank, a vapor-cooled forward test skirt, and the aft test skirt. The structural support for the tank is designed in a manner that represents stage heating into the tank using the forward and aft skirts. The cryogenic tank has a diameter of 4 m, and the forward and aft structural skirts are bolted to interface flanges on the tank. The forward skirt is mounted on the top of the tank and is primarily used for introducing representative structure-borne heat loads into the tank and to investigate vapor-cooling-based heat interception. It also contains fluid interface connections between the test tank assembly and the facility vent system. The aft skirt provides structural support for the tank and also contains the fill and drain fluid interface connections to the facility. The bottom of the tank has simulated engine feedline connections to introduce representative fluid penetration heat loads and also provide low point drain capability to the assembly. The top of the tank has representative vent and relief lines in addition to the lines that feed the vapor-cooling channels on the forward skirt.

The SHIIVER, as a test article, was developed to simulate the operation of an upper stage vehicle LH_2 tank in space thermal environments. The fluid penetrations, skirts, and fluid line routing were developed using information provided by the EUS team to be representative, but not duplicative of the EUS while still manufacturable and robust so that the tank could be used multiple times. The test article was designed using industry standard processes and fabricated using commercially available materials to comply with safety and reliability requirements at a lower cost than a prototype flight configuration.

Figure 1 shows a schematic of the SHIIVER test article. The test article has two different support structures, one for the thermal vacuum testing and one for the acoustic vibration testing. These, along with other supporting structures, are described in Section 2.2.

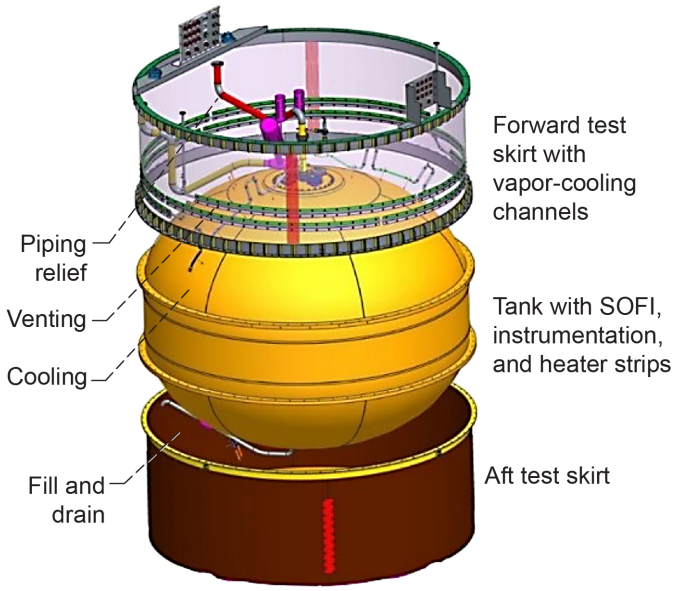

Figure 1.—Structural Heat Intercept, Insulation, and Vibration Evaluation Rig (SHIIVER) test article. Spray-on foam insulation (SOFI).

2.1.1 Tank

The tank is made of 304L stainless steel. The overall geometry is based upon the EUS LH_2 tank, but the vessel is designed as an American Society of Mechanical Engineers (ASME) code vessel with a constant wall thickness of 1.1 cm. The internal tank height and diameter are 3.3 and 4 m, respectively. The top and bottom of the tank has a 61-cm manway opening on each dome and is fitted with manway covers that are 3.8 cm thick with a diameter of 74.6 cm. The manway covers have ports for instrumentation and fluid connections and are sealed using spring-energized C-seals. The manway ports have recesses to allow for the installation of support rings from which internal components can be suspended and supported. The tank also has internal studs that allow for the installation of components along the tank wall. The weight of the tank and the manway covers is 6,778 kg, with the top and bottom covers weighing 176 and 159 kg, respectively. The tank volume is 31.1 m^3. The tank is designed to operate with a differential pressure ranging from vacuum to 738 kPa, and in the temperature range of 20 to 311 K. Figure 2 shows a drawing of the tank.

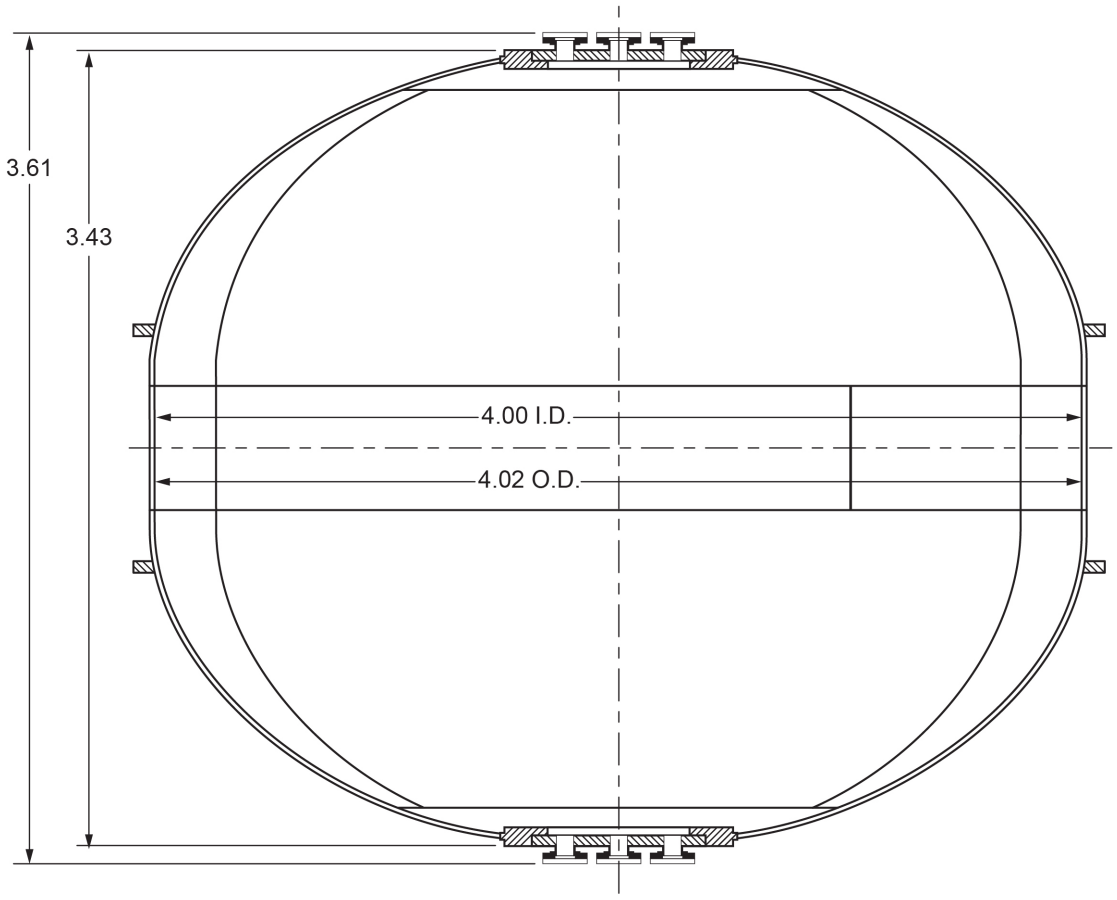

Figure 2.—Tank drawing. Dimensions in meters.

The barrel section of the tank is cylindrical while the top and bottom domes are ellipsoidal in shape with a semimajor to semiminor axis ratio of √2. The forward and aft skirts are bolted to the tank's barrel at the forward and aft girth flange, respectively, using 72 bolts spaced 5° apart. The exterior of the tank is instrumented with diode temperature and heat flux sensors at selected locations (see Section 3.0) prior to the application of insulation (SOFI). Piping support standoffs were also welded to the tank surface prior to SOFI application. The tank was manufactured by Didion's Mechanical in Bellevue, Ohio, and the tank external instrumentation and SOFI application were performed at NASA Marshall Space Flight Center in Huntsville, Alabama.

There are four lifting panels that attach to the tank forward and aft girth flanges to lift it. Trunnions are attached to two of the lifting panels. Tailing and lifting lugs are attached to the other panels. The lifting panel with trunnion assemblies are diametrically opposed around the vertical centerline of the tank cylindrical section. The lifting panel with tailing and lifting lug assemblies are perpendicular to the lifting panel with trunnion assemblies and diametrically opposed. These lifting panels are removed from the tank prior to testing.

2.1.2 Forward Skirt

The forward (upper) test skirt is a straight cylindrical geometry made of aluminum alloy 6061. This gives a thermal behavior similar to the currently planned EUS metallic skirts that intend to use a higher strength aluminum alloy, but at a much lower cost. It has two vapor-cooling channels attached to it. The vapor-cooled skirt interfaces with the SHIIVER tank and is designed to accommodate the difference in thermal contraction between the aluminum skirt and the stainless steel tank flange. The skirt also has fluid connections to the tank vent for cooling along with fluid and instrumentation interface connections between the tank and the test facility. It is insulated on the interior surface by 10 layers of MLI to minimize radiation to the cooling circuit from the inside. The skirt is instrumented with temperature sensors to measure the axial surface temperature profile at multiple circumferential locations, as well as along the cooling loops. In addition, heat flux sensors are present on the outer surface of the skirt to measure the radiation flux at several locations. Accelerometers are attached to the skirt at a few locations to monitor accelerations during assembly, transport, and acoustic vibration testing.

The forward tank skirt is essentially a cylindrical metallic weldment having a nominal wall thickness of 4.76 mm. A circular bolt flange is affixed to the upper and lower edges to facilitate physical attachment to the tank at the lower end; the upper flange is not used but is included in the interest of maintaining a flight-like representation. The inside diameter of the skirt is 4.01 m and the nominal height of the element is 1.52 m. The weight of the skirt is 572 kg. Figure 3 shows a drawing of the SHIIVER forward skirt with vapor-cooling channels attached.

The forward skirt includes a vapor-cooling fluid network. The vapor flow from the tank vent is split in half with two sets of tubing running from the vent along the top of the tank to the bottom of the skirt (approx. 0.18 m above the bottom), with the tubes approximately 10° from being a true 180° apart. The tubing then spirals around the skirt, each spiral going a full 360° before being plumbed back together for venting out of the vacuum chamber. The vapor-cooling tube is attached to the skirt by L-brackets welded to each side of the tube (see Figure 4). The helically coiled channel is secured by bolting the L-brackets to the interior surface of the skirt. There are 8 L-bracket (4 each on top and bottom) sections that are held in place by bolts that are 0.15 m (20 per bracket) apart. The thermal performance of the tank with vapor cooling is assessed by comparing the performance with and without the boiloff vapor going through the cooling loops. Temperature sensors are located along the length of the tubing to help determine the heat transfer and effectiveness of the heat-interception system.

The design of the vapor-cooling coils just described was arrived at after considerable analysis and subscale testing that is documented in References 31 and 32. For the subscale tests, several test articles made from Al 2219 were used, with typical width of 0.61 m and a height of 1.22 m. The test articles are contoured to be an arc of a cylinder of 4-m diameter to represent a portion of the forward skirt. Test Article 1 has two rectangular cooling channels for vapor flow that are welded to the interior

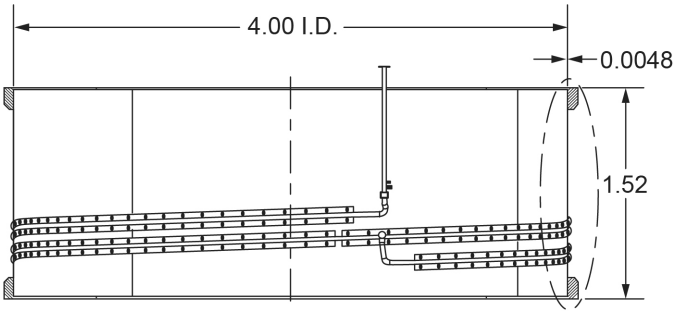

Figure 3.—Forward skirt. Dimensions in meters.

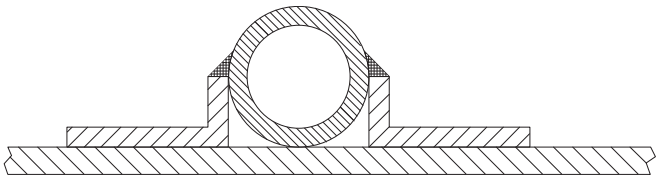

Figure 4.—Attachment of vapor-cooling tube to skirt interior surface.

of the aluminum substrate. Test Article 2 uses high-strength stainless steel bolts to attach the cooling channels to the substrate, along with flexible graphene as a conductive interface material between the channel and the substrate. A third test article, termed the Prototype, uses an aluminum pipe as the cooling channel, that is butt-welded at the end of one leg of an aluminum L-bracket, with the other leg of the bracket welded to the substrate. Thus, in this design, the cooling channel has some standoff distance from the substrate, and the heat flow from the substrate to the cooling channel is by heat conduction via the L-bracket. It is from testing with the Prototype that the final attachment design (shown in Figure 4) evolved. For all test articles, the environmental heat load to the test article, with and without cooling vapor flow, is measured by attaching the article to a flat plate boiloff calorimeter. The first two tests indicated that the method of attachment (welding versus bolting) of the test article to the substrate has little influence on the effectiveness of vapor cooling and, furthermore, vapor cooling can achieve a heat load reduction of 55 to 80 percent of the uncooled value, depending on the test conditions. However, it was observed in the Prototype testing that the heat load reduction was diminished. Though primarily due to reasons of manufacturability, the round tube having two welded conduction paths and shorter L-brackets, as shown in Figure 4, was chosen to be most beneficial to improving heat transfer.

2.1.3 Aft Skirt

The tank is a stamped ASME pressure vessel and is designed for a maximum full tank weight based on the density of liquid oxygen to accommodate possible future testing. It is much heavier than a flight hydrogen tank. The aft skirt requires more strength than a typical flight skirt would provide and is made of stainless steel 304/304L for strength to support the heavy tank. Though thicker than flight, the aft skirt has a similar heat load as an aluminum flight skirt might have.

Figure 5 shows a drawing of the SHIIVER aft test skirt. The aft test skirt has a diameter of 4 m, a thickness of 6.35 mm, a height of 1.56 m, and a mass of 1,395 kg. The skirt interfaces with the tank structural flange and the test support structure. The skirt also contains fluid and instrumentation interface connections between the tank and the facility.

2.2 Subsystems for Handling and Test Support

In addition to the main subsystems described previously, SHIIVER used a number of other subsystems to interface with the various facilities it was tested in and for the purpose of transportation.

2.2.1 Tank-Handling Fixture

The tank-handling fixture is used to install instrumentation and heaters to the tank surface and then to apply and trim SOFI. It is made of various metals including structural carbon steel and some stainless steel and has a mass of 2,631 kg. A schematic of the fixture is shown in Figure 6. Its height, width, and depth are 3.1 by 3.7 by 4.6 m. During initial use for installation of instrumentation, it was determined that the SHIIVER tank was not perfectly round (it was round enough to pass ASME code), but during use, several counterbalances were used to allow for free rotation of the tank. A motor can be attached to the shelf on the right to help control the rotation of the tank.

2.2.2 Thermal Test Support Stand

The thermal test support stand is used to anchor the SHIIVER test article and to provide space under it for assembly and integration in the vacuum chamber during boiloff testing. The support stand is made of stainless steel and is 2.3 m in height, and 4.1 m in diameter. The door openings are 1.5 m in height and about 0.84 m in width (Figure 7). Its mass is nearly 2,077 kg.

The thermal support stand is mounted on an adapter plate that has a thickness of 2.54 cm (1 in.). The adapter plate is attached to the triangular support structure of the vacuum chamber facility that serves as the base of the SHIIVER test article. The three legs of this triangular structure use three support points at the bottom of the vacuum chamber.

2.2.3 Acoustic Test Support Stand

The acoustic test support stand (Figure 8) is used to anchor the SHIIVER test article for testing in the Reverberant Acoustic Test Facility (RATF) chamber. Its dimensions are 4.2 m in diameter and 2.4 m in height and has a mass of 4,273 kg.

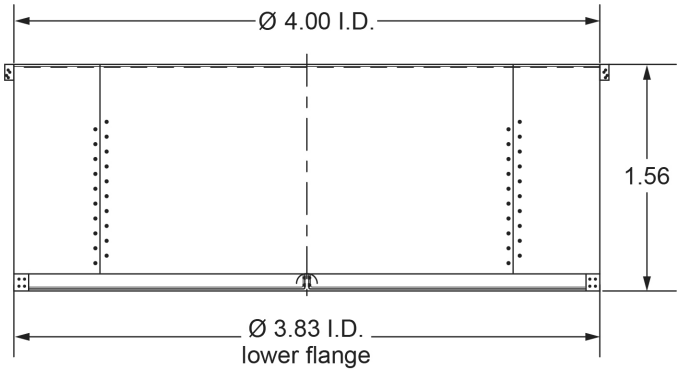

Figure 5.—Aft skirt. Dimensions in meters.

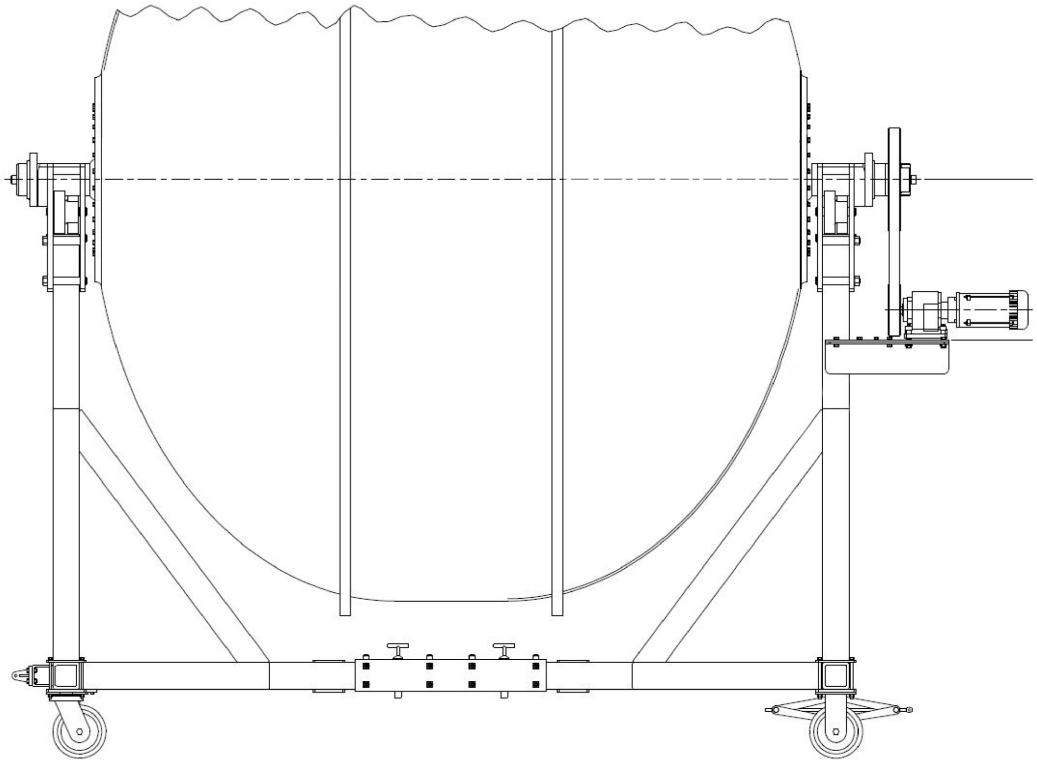

Figure 6.—Tank-handling fixture.

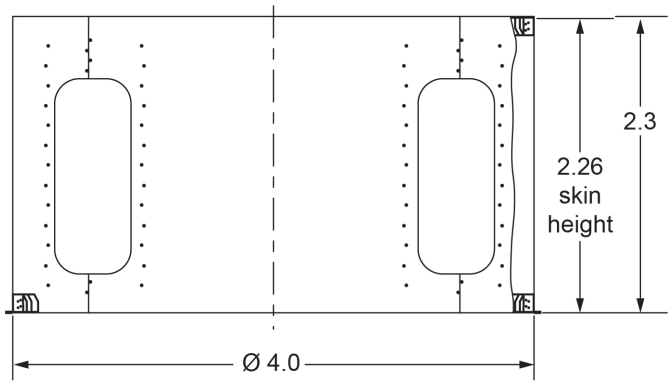

Figure 7.—Thermal test support stand. Dimensions in meters.

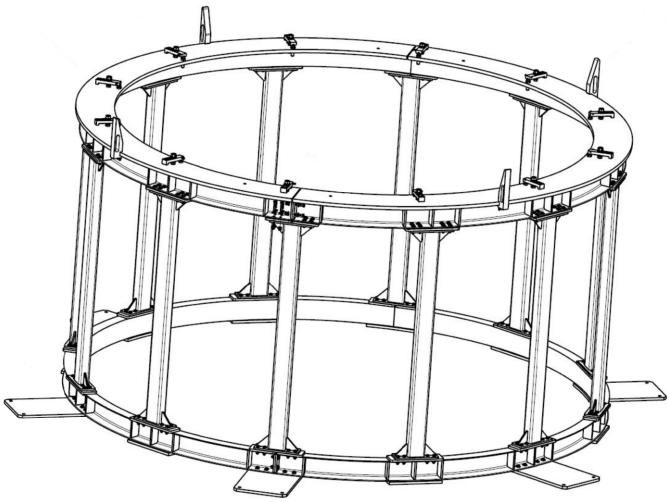

Figure 8.—Acoustic test support stand.

2.3 Detailed Description of Insulation

Two tank insulation configurations were evaluated under the SHIIVER test program: SOFI only and SOFI together with MLI. The SOFI-only test configuration was used as the baseline test configuration (see Section 4.1). The remaining test series (Thermal 1, Acoustic Test, and Thermal 2) were performed in the SOFI plus MLI configuration (see Section 4.2, 4.4, and 4.5, respectively). For all the tests conducted including the baseline tests, MLI was used in the interior of the forward and aft skirts. Details of the insulation configurations are described further in subsequent sections.

2.3.1 Spray-On Foam Insulation

SOFI has been used on launch vehicle cryogenic tanks for more than 50 years for thermal insulation to prevent condensation of air and ice formation on the launch pad, isolate the tank from the environment, and reduce the liquid boiloff for short durations on orbit (Ref. 33). For this reason, the SOFI-only insulation configuration is evaluated as the baseline test condition and is used for comparison to the advanced SOFI plus MLI Thermal 1 and Thermal 2 test configurations.

With respect to order of operations, the SHIIVER tank was first instrumented with heat flux sensors and silicon diodes (SDs) on the outer metallic surface, prior to the application of SOFI. Following instrumentation, the tank was sent to the NASA Marshall Space Flight Center for application of Stepan S-180 polyurethane closed cell SOFI (Stepan Company). The SOFI was sprayed on the tank with the tank mounted on the tank-handling fixture (Figure 6). The SOFI was trimmed after it was cured.

Optical white light scanning was performed before and after the application of SOFI and trimming to determine its local thickness at various locations. The dataset, however, was too large and unwieldy for visualization and analysis. Therefore, a tank model was devised to determine the SOFI thickness. In this model, the forward and aft domes are discretized into 19 axial by 24 circumferential locations (456 locations in each dome). Likewise, the tank barrel is discretized into 17 axial by 24 circumferential locations (408 locations). The optical scans, before and after SOFI installation, are queried to determine the substrate points nearest to the discretized model locations, and the SOFI thickness is calculated as the distance between these points normal to the substrate. The SOFI thickness map thus obtained is shown in Figure 9. The mean SOFI thickness in the forward and aft domes, and the tank barrel are 3.38, 3.19, and 2.38 cm, respectively. Their distribution and standard deviations are shown in Figure 10.

Since the discretization in the SOFI tank model is quite coarse, the thickness obtained was verified in selected regions, specifically over the heat flux sensor regions (each sensor is 20 by 20 cm), by using all points in the optical scans (greater than 10,000 points) over each sensor. The comparison of the two SOFI thickness is very good and is shown in Figure 11, where the nearest point thickness refers to the coarse grid value, and the regional thickness refers to the average over all points on a heat flux sensor. SOFI thickness over all the heat flux sensors is also given in Table 2.

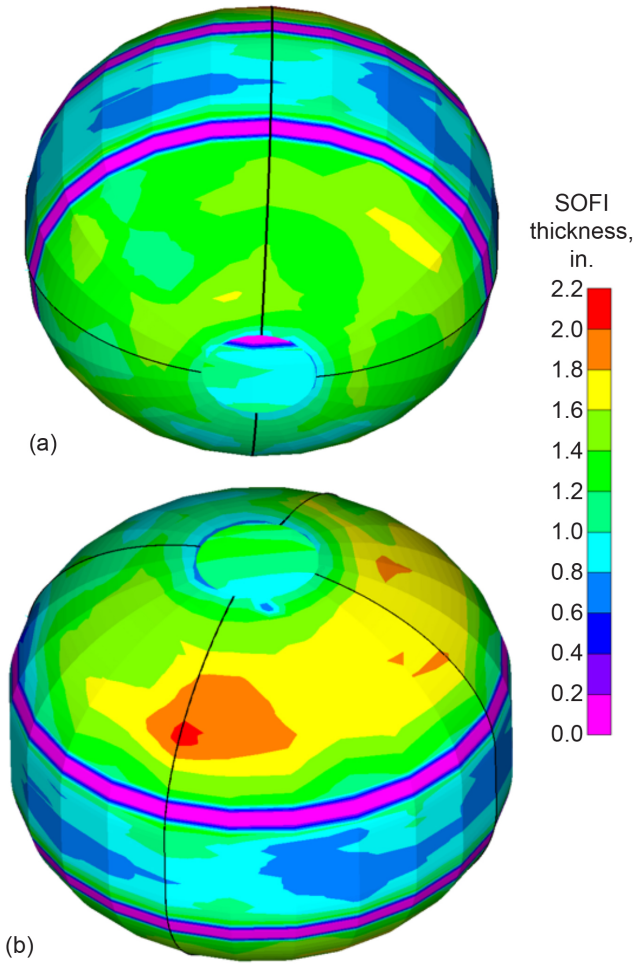

Figure 9.—Spray-on foam insulation thickness.

2.3.2 Multilayer Insulation

MLI blankets are used to significantly reduce the heat load to the tank and its application is one of the main objectives of the SHIIVER project. The blankets are installed on the top and bottom tank domes, in the interior of the forward and aft skirts, and around tank piping. The design, fabrication, and installation of the MLI blankets as well as structural, thermal, and electrostatic testing of coupons of the MLI are discussed in detail in Appendix J. A brief summary of the salient features of the MLI design and installation is described here.

The dome MLI blankets lie on top of the SOFI but are not mechanically attached to it. The blanket design incorporates features such as seams, structure, penetrations, and materials that closely approximate how a system would be installed on a real flight tank but scaled down for the size of the SHIIVER tank. Specifically, the MLI on the dome consists of three subblankets of 10 reflector layers each, where each reflector is made of 0.25-mil-thick polyimide that is double aluminized. The interior and exterior coversheets are double aluminized polyimide sheets that are 1 mil thick, reinforced with a layer of Nomex® (DuPont™), and mitigate the risk of static discharge. Two layers of Dacron® (Invista) netting are used as spacers between each reflector. The nominal layer density of the blankets is 18 layers per centimeter. Nylon tags are used to hold the blankets together (less than 25 per square meter to minimize their thermal penalty). A single seam is used from the edge to the center of the blanket with the seams clocked around the tank to prevent them from stacking up on top of each other. Seams are overlapped with fastener tape attached with pressure-sensitive adhesive and with tags every 0.30 to 0.45 m. The total mass of the dome MLI blanket is 18.5 kg. The MLI on the forward and aft skirts cover the inside of the skirt around the entire circumference with an axial length of approximately 1.2 m. The skirt MLI has 10 layers of polyimide separated by two layers of netting. The MLI design, fabrication, and installation was performed by Aerospace Fabrication & Materials, LLC (AFM) and Lockheed Martin.

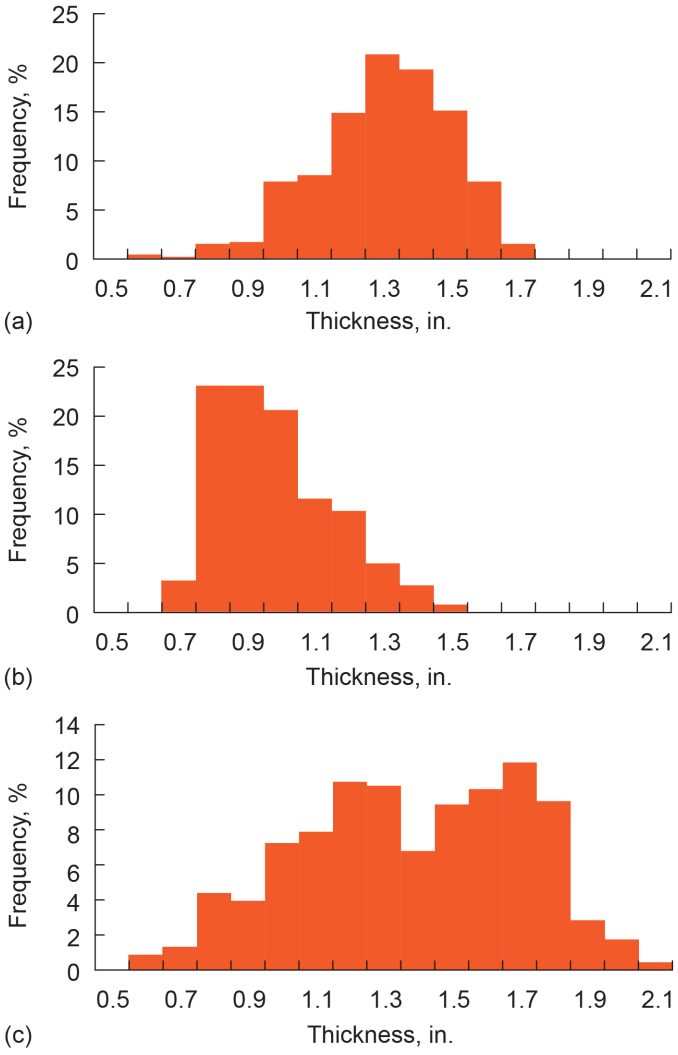

Figure 10.—Spray-on foam insulation thickness distribution. (a) Aft dome. 456 points; 0.538 ≤ Δ*x* ≤ 1.643; mean = 1.254; and standard deviation = 0.195. (b) Barrel. 408 points; 0.612 ≤ Δ*x* ≤ 1.438; mean = 0.936; and standard deviation = 0.173. (c) Forward dome. 456 points; 0.529 ≤ Δ*x* ≤ 2.067; mean = 1.332; and standard deviation = 0.329.

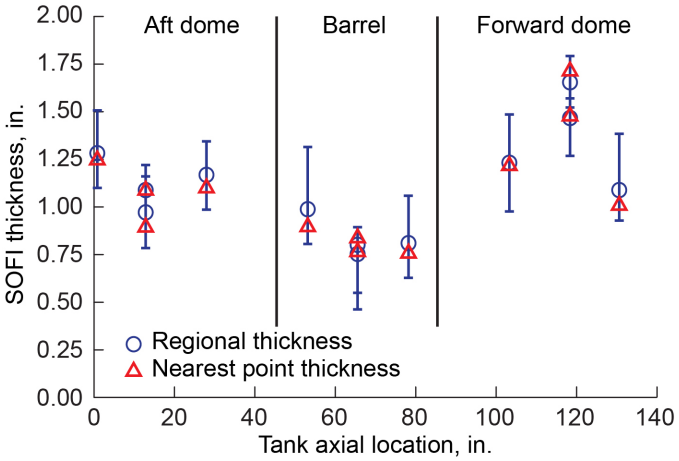

Figure 11.—Spray-on foam insulation thickness comparison.

TABLE 2.—THICKNESS OF SPRAY-ON FOAM INSULATION OVER HEAT FLUX SENSORS (HFS) INSTALLED ON SHIIVER[a] TANK

[Station location from tank bottom. Top tank flange is at 86.625 in.]

Sensor	Station location, in.	Angular location, θ, degree	Mean thickness, in.	Standard deviation of thickness, in.	Points
HFS01	130.57	225	1.085	0.109	32,889
HFS02	118.43	225	1.468	.054	29,633
HFS03	103.31	225	1.237	.115	25,621
HFS04	118.43	45	1.652	.057	50,768
HFS05	12.82	45	.971	.058	33,647
HFS06	27.94	225	1.168	.075	30,335
HFS07	12.82	225	1.087	.059	39,425
HFS08	.69	225	1.285	.093	40,379
HFS09	65.63	45	.804	.079	7,344
HFS10	65.63	225	.752	.060	50,127
HFS11	78.13	135	.810	.072	37,522
HFS12	53.12	315	.984	.093	44,599

[a]Structural Heat Intercept, Insulation, and Vibration Evaluation Rig (SHIIVER).

Figure 12 shows a schematic of the MLI blanket used on the tank domes. Also shown in the figure are the placement of SDs within it for temperature measurement. The diodes are placed on layers 0, 5, 11, and 20, where layer 0 is the layer adjacent to the outer surface of the SOFI. Figure 13 shows pictures of the MLI being installed on the top dome and in the interior of the forward and aft skirts.

A novel method of attaching the dome MLI was designed where the outermost subblanket becomes a harness that is then attached to the skirt. Attachment patches made out of 10-mil plain polyimide (a total of 44 patches) are bonded with an adhesive to the outermost subblanket around the circumference near the base and are sewn together to enhance strength. The patches are attached to the skirt using zip ties. Structural analysis shows that the maximum loads are driven by the depressurization load within the MLI blankets. Using a maximum pressure differential across the MLI during evacuation of approximately 15 torr, the load on the MLI for SHIIVER is 11.6 kN. Analysis also shows that each patch withstands a minimum load of 376 N, and the 44 patches together exceeds the total anticipated load of 11.6 kN with a safety factor of 1.4.

Analysis and historical evidence suggest that the thermal performance of the MLI is such that the effective heat flux through it is around 1.1 W/m^2. This figure includes the basic insulation properties of the stacked MLI subblankets, and heat leaks due to seam overlap and conduction via structural paths and its ties.

2.3.3 Emissivity Measurements

Measurements of the emissivity of various surfaces of the hardware were performed in situ using a Surface Optics Corporation Reflectometer (Model 410-0038). It is a portable device (Ref. 34) that is ASTM E–903 (Ref. 35) compliant and designed to make accurate reflectance and emittance measurements. The instrument is calibrated with a gold coupon, and measures the directional reflectance at two angles of incidence (20° and 60°) in the infrared spectrum wavelength bands 1.5 to 2, 2 to 3.5, 3 to 4, 4 to 5, 5 to 10.5, and 10.5 to 21 μm. The directional total emissivity at the two incidence angles and the hemispherical total emissivity are then calculated from the six spectral values. Several measurements were taken on the surfaces of the SOFI, aft skirt, forward skirt, and the heat flux sensor, with two measurements taken at every location. The average total hemispherical emissivity and the standard deviations of the various surfaces are given in Table 3.

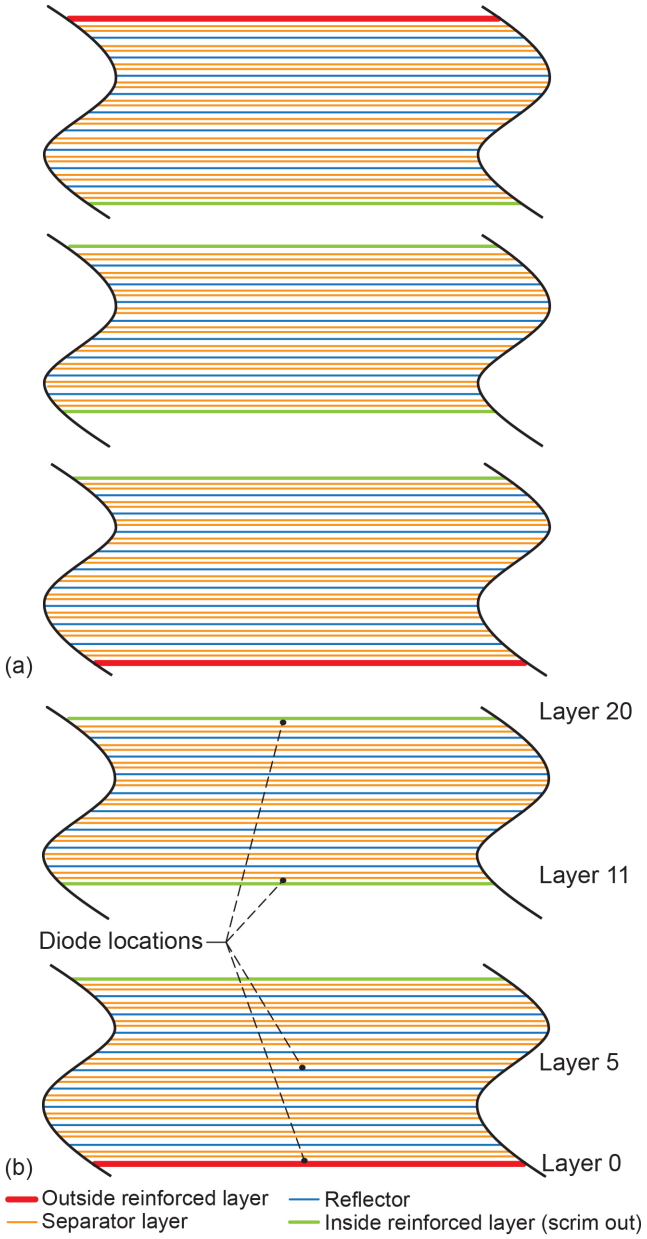

Figure 12.—Multilayer insulation blanket. (a) Layer construction. Outboard subblanket: one 1.0-mil reinforced polyimide (PI), one 0.5-mil reinforced polyethylene terephthalate (PET), nine 0.25-mil PET reflector, and 20 Dacron® B4A (Invista) spacer. Inner subblanket: two 0.5-mil reinforced PET, eight 0.25-mil PET reflector, and 18 B4A spacer. Inboard subblanket: one 10-mil reinforced PET, one 0.5-mil reinforced PET, nine 0.25-mil PET reflector, and 20 B4A spacer. Blanket totals: one 1.0-mil reinforced PET, one 1.0-mil reinforced PI, four 0.5-mil reinforced PET, 26 0.25-mil PET reflector, and 58 B4A spacer. (b) Placement of silicon diodes. Note that (b) does not show outer subblanket, which had no instrumentation.

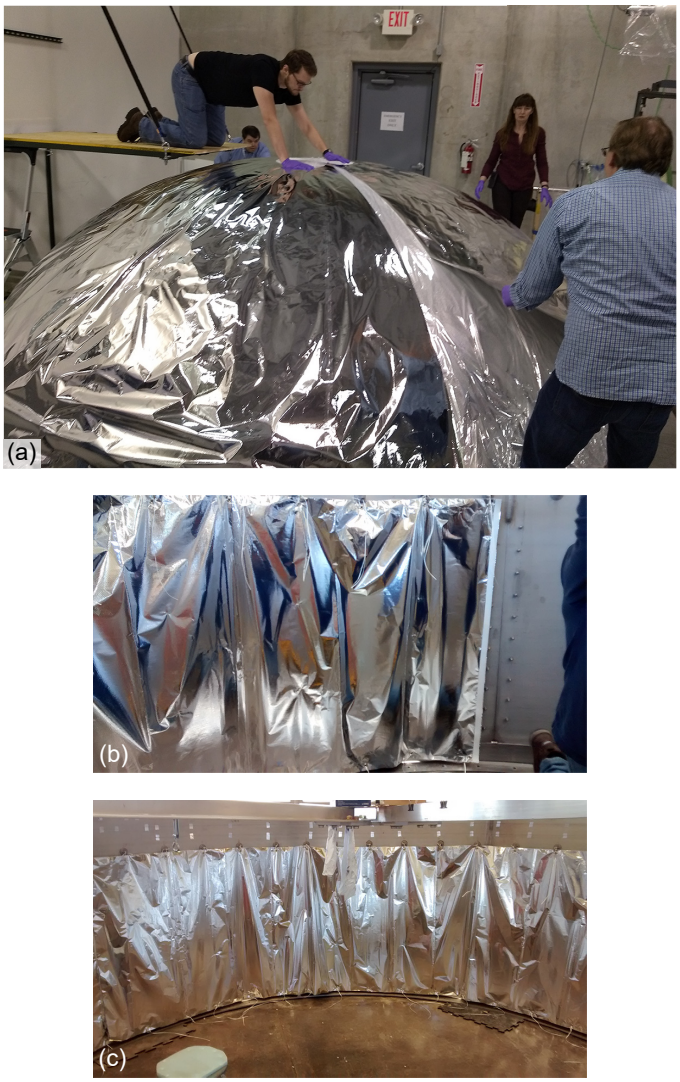

Figure 13.—Installation of multilayer insulation. (a) Dome mold. (b) Interior of forward skirt. (c) Aft skirt.

TABLE 3.—EMISSIVITY OF VARIOUS SURFACES

Surface	Total hemispherical emissivity	
	Mean	Standard deviation
Spray-on foam insulation	0.697	0.009
Tank	.314	.022
Forward skirt	.152	.013
Aft skirt	.349	.032
Heat flux sensor on forward skirt	.119	.023

2.4 Description of Facility

Testing of SHIIVER was performed at Glenn Research Center's Plum Brook Station (PBS)[1] in Sandusky, Ohio. The preacoustic and postacoustic boiloff testing was performed at the In-Space Propulsion Facility (ISPF; formerly B–2 facility), and the acoustic testing was performed in the RATF. A very brief overview of the facilities is provided in the following sections.

2.4.1 In-Space Propulsion Facility

The ISPF test facility was designed in the 1960s to provide a test bed for upper stage vehicles (Ref. 36). It is a high-altitude facility capable of testing full-scale launch vehicles in a simulated space environment. It is NASA's third largest thermal vacuum facility and the largest designed to store and transfer large quantities of LH_2 and liquid oxygen.

The center of the ISPF is a large vertical vacuum chamber consisting of a cylindrical section that is 14 m high and 11.5 m in diameter, topped with a hemispherical head. Figure 14 shows an artist's rendering of the facility. Test articles up to a nominal size of 6.7 m in diameter and 15.8 m in height can be installed into the test chamber via a hinged hatch at the top of the hemispherical dome using a 20-ton overhead crane. Access to the chamber is provided by 1.8-m-diameter circular doors located at the bottom of the chamber and at a height of 12.5 m above the bottom.

The lower end of the chamber has a 3.4-m-diameter by 11.3-m-long exhaust duct sealed with a high-vacuum valve. Vacuum levels as low as 10^{-7} torr are achieved using oil diffusion pumps and a series of mechanical pumps. Numerous high-vacuum penetrations exist at multiple elevations for routing of fluids and electrical power or signals internal to the chamber without compromising the vacuum environment.

The control room for the facility is located in a separate building nearly a quarter mile away. Control, remote video monitoring, and data acquisition (DAQ) is fed from the test facility to the control building via a fiber optic network.

2.4.2 Reverberant Acoustic Test Facility

The RATF (Ref. 37) is a massive reverberant acoustic facility that can achieve an empty-chamber acoustic overall sound pressure level (OASPL) of 163 dB, and capable of a tailored wide range of acoustic spectra in the frequency range from 31.5 Hz up to 10 KHz one-third octave bands (OTOB). The RATF chamber internal dimensions are 11.4 m wide by 14.5 m deep by 17.4 m high. The RATF includes various supporting subsystems including a gaseous nitrogen generation

[1]Plum Brook Station is now known as Neil A. Armstrong Test Facility.

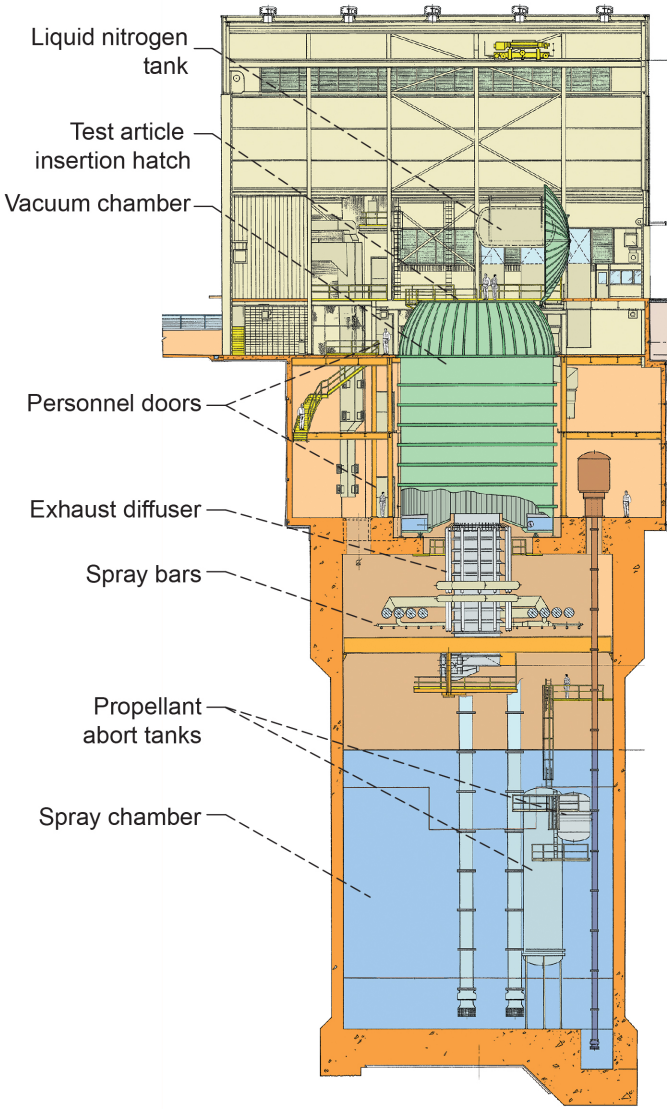

Figure 14.—In-Space Propulsion Facility.

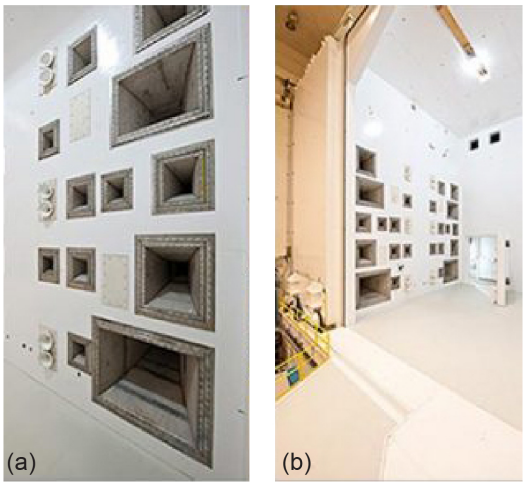

Figure 15.—Reverberant Acoustic Test Facility (RATF). (a) Horn wall. (b) Chamber.

system, horn room with acoustic modulators and horns, acoustic control system, and hydraulic supply system. Test articles are mounted onto elevated customer-provided mounting fixtures for testing using a 30-ton bridge crane. Up to 19 control microphones can be placed around the test article for closed-loop control. There are seven classes of cutoff frequency horns at 25, 35, 50, 80, 100, 160, and 250 Hz. The chamber can be operated as a Class 100,000 clean room if desired. A picture of the RATF facility is shown in Figure 15.

3.0 Description of Instrumentation

SHIIVER is outfitted with various sensors that are used to monitor temperatures within the tank and in the system, tank pressure, and the level of LH_2 in the tank, along with vibrations generated when moving the equipment and during vibroacoustic testing. Table 4 provides a list of the instrumentation used and Table 5 shows their general specifications. Figure 16 shows a schematic of the instrument location on the tank. All of the instrumentation (except for RFMG) and electronics on the test article is connected to three interconnect panels on the SHIIVER test article: two on the forward test skirt top flange and one in the aft test skirt. This type of interface provides a quick, convenient, and centralized location to connect and disconnect the test article instrumentation and electronics to the test facility.

3.1 Silicon Diodes

The primary temperature measuring devices used are SDs manufactured by Scientific Instruments, Inc. (Model 410AA). Both canister- and bobbin-style sensors (Figure 17) are used. The canister style has a diameter of 2.36 mm and a length of 6.35 mm, while the corresponding dimensions of the bobbin style are 9.14 and 3.05 mm. The diodes are four-wire devices that require a 10 μV input and generate a 0 to 2 VDC output based on the measured temperature. The diodes are bonded to the surfaces using epoxy-based adhesives (Scotch-Weld™ 2216 (3M™) or CryoBond™ 621 (Composite Technology Development, Inc.)). The SDs are installed on the exterior of the tank, which includes support structures and piping (listed in Table 6). SDs are also located on the forward and aft skirts (listed in Table 7 and Table 8; see Figure 18 and Figure 19 for diodes on the forward skirt), on the liquid-level-monitoring rake located inside the tank (see Figure 20 and Figure 21) and on the SOFI and MLI (listed in Table 9 to Table 11). The SDs on the tank surface, SOFI, MLI, and the tank internal rake are the canister style (diodes SD1 to SD105, SD150 to SD153, SD158 to SD166), while those on the forward and aft skirts, and other locations on the SHIIVER structure are the bobbin style (diodes SD106 to SD146, SD179 to SD189). The diodes measure temperatures to within ±0.1 K from 1.5 to 25 K, and to within ±0.5 K from 25 to 450 K. The SDs have a phosphor bronze extension wire that minimizes heat load to the sensor.

The fill levels shown in Table 6 and Table 9 are based on sensor station locations at room temperature, and do not account for any shrinkage of the tank at cryogenic temperature.

TABLE 4.—TEST ARTICLE INSTRUMENTATION

Instrument and electronics	Location	Parameter measured
Accelerometer	Forward and aft skirts Forward and aft manways	Vibration
Capacitance probe	Inside tank	Tank-fill level
Flowmeter	Backpressure control cart	Gas flow
Heater strip	Forward and aft tank domes Tank barrel section	Heat
Heat flux sensor	Forward and aft tank domes Tank barrel section Forward skirt above the flange	Heat flux
Microlimit sensor	On fluid valves	Valve travel
Pressure sensor	In-line cooling In-line venting	Tank and coolant loop pressure
Radio Frequency Mass Gauge	Inside tank	Tank-fill level
Silicon diode	Rake inside tank Forward and aft tank domes Tank barrel section Multilayer insulation (MLI) In-line and on line cooling In-line venting On line fill and drain On fluid valves On capacitance probe Cabling bundles	Temperature
Thermocouple	In-line relief MLI	Temperature

TABLE 5.—INSTRUMENTATION AND HEATER GENERAL SPECIFICATIONS

Device	Vendor	Model	Operating range	Sensitivity	Input	Output
Silicon diodes	Scientific Instruments, Inc.	410AA–LP4 410AA–2P4	1.5 to 450 K	±0.1K, 1.5 to 25K ±0.5K, 25K to 450K	10 μA	0 to 2 V
Thermocouples	Omega Engineering, Inc.	Type T	50 to 400 K	±1 K	NA	0 to 1 V
Heat flux sensor	Captec Entreprise	200 by 200 mm	–500 to 500 kW/m²	0 to 624 μV/(W/m²)	NA	0 to 1 V
Accelerometer	PCB Piezotronics, Inc.	356A33	(±10%): 0.3 to 10,000 Hz	10 mV/g at ±500 g pk	2 to 20 mA	0 to 2 V
Capacitance probe and controller	American Magnetics, Inc.	1700	0 to 40 °C	NA	4 to 20 mA	0 to 10 V
Heaters (barrel)	EGC Enterprises, Inc.	Thermafoil PTC Series	0 to 2 kW	Watt density 1.2 W/in²	0 to 120 VAC	250 W/unit
Heaters (domes)	Omega Engineering, Inc.	Kapton KH Series	0 to 1 kW	Watt density 10 W/in²	0 to 120 VAC	640 W/unit
Pressure transducers	Stellar Technology	GT2250	0 to 345 kPa 0 to 50 psia	± 0.20% FSO[a]	4 o 20 mA	0 to 10 V
Flowmeters	Emerson Electric Co.—Micro Motion	CMF–025M CMF–050M CMF–100M CMFS100M	0 to 604 g/s 0 to 1,882 g/s 0 to 7,537 g/s 0 to 7,182 g/s	0.02% FSO[a]	65 mA at resonant frequency	4 to 20 mA
Microlimit switches	Honeywell International, Inc.	EX–AR800	Pretravel 0.219 in.	Differential travel 0.007 in.	120 VAC	15 A 1NC/1NO[b]
Vibration monitoring sensor	Lansmont Corporation	Saver 3X90	0 to 5 kHz	0 to 200 g FSO	9 VDC	0 to 5 g

[a]Full-scale output (FSO).

[b]Normally closed (NC). Normally open (NO).

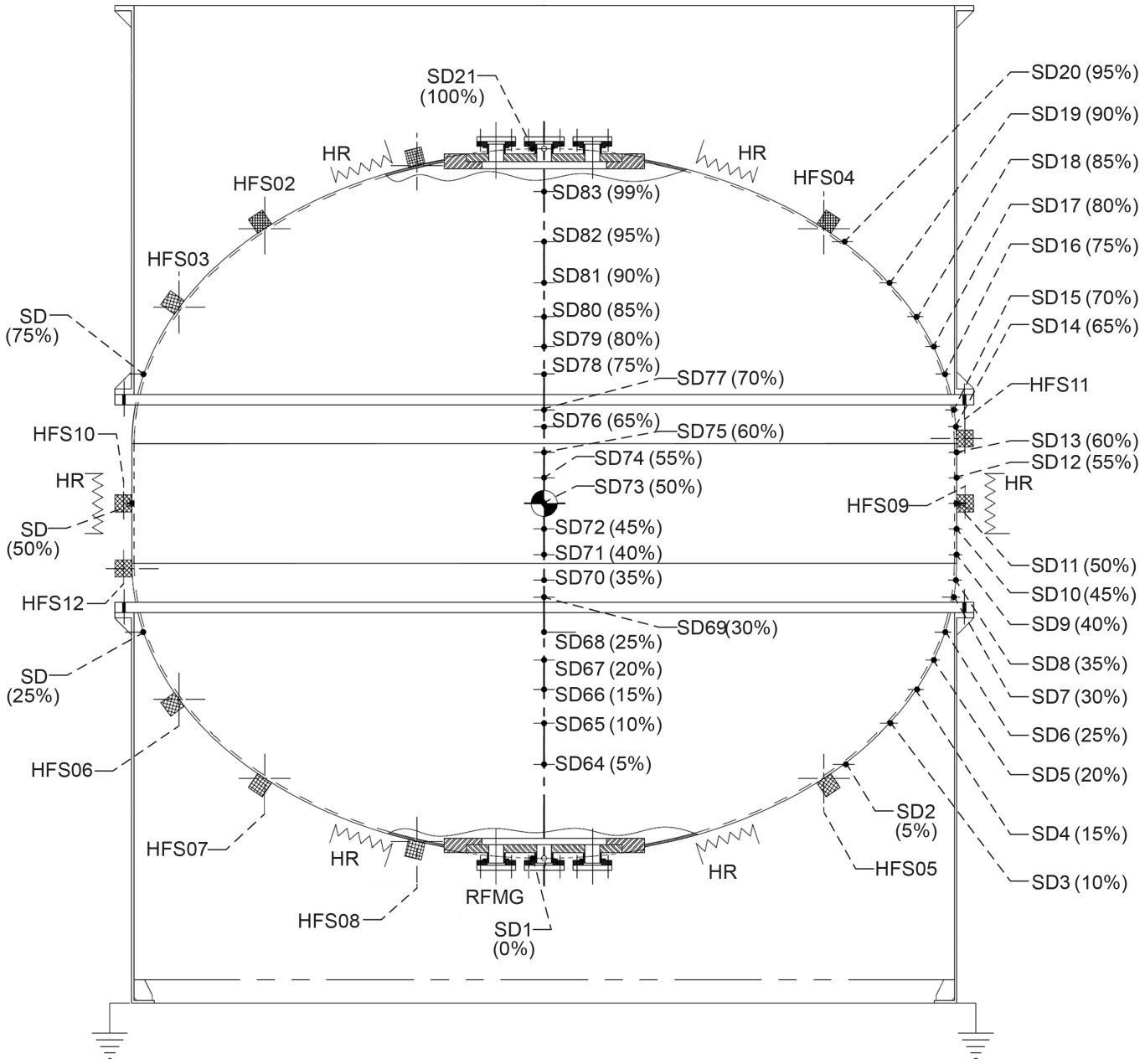

Figure 16.—Tank instrumentation. Heat flux sensor (HFS). Heater (HR). Radio Frequency Mass Gauge (RFMG). Silicon diode (SD).

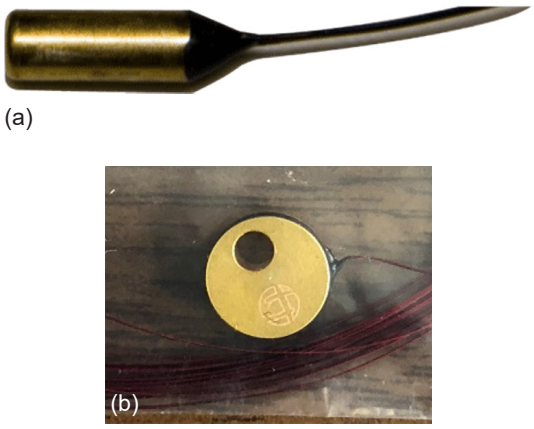

Figure 17.—Silicon diode (Scientific Instruments, Inc., Model 410AA). (a) Canister style. (b) Bobbin style.

TABLE 6.—LOCATION OF SILICON DIODES (SDs) (CANISTER STYLE) ON TANK SURFACE

[Station location from tank bottom. Top tank flange is at 86.625 in.]

Diode	Station location, in.	Angular location, θ, degree	Fill level, percent	Diode	Station location, in.	Angular location, θ, degree	Fill level, percent
SD01	–2.063	0	0	SD16	90.438	45	75
SD02	15.5	45	5	SD17	95.750	45	80
SD03	23.375	45	10	SD18	101.500	45	85
SD04	29.875	45	15	SD19	108.063	45	90
SD05	35.563	45	20	SD20	115.938	45	95
SD06	40.938	45	25	SD21	133.31	0	100
SD07	47.625	45	30	SD22	40.938	135	25
SD08	50.875	45	35	SD23	40.938	225	25
SD09	55.813	45	40	SD24	40.938	315	25
SD10	60.750	45	45	SD25	65.635	135	50
SD11	65.625	45	50	SD26	65.625	225	50
SD12	70.563	45	55	SD27	65.625	315	50
SD13	75.438	45	60	SD28	90.438	135	75
SD14	80.375	45	65	SD29	90.438	225	75
SD15	83.625	45	70	SD30	90.438	315	75

TABLE 7.—LOCATION OF SILICON DIODES (SDs)
(BOBBIN STYLE) ON FORWARD SKIRT

[Station location is from tank bottom flange. Top tank flange is at 86.625 in.]

Diode	Station location, in.	Angular location, θ, degree
SD106	86.625	180
SD107	89.625	180
SD108	92.625	180
SD109	95.625	180
SD110	105.625	180
SD111	111.625	180
SD112	117.625	180
SD113	123.625	180
SD114	146.625	180
SD115	86.625	120
SD116	94.625	120
SD117	102.625	120
SD118	115.625	120
SD119	146.625	120
SD120	86.625	40
SD121	99.625	40
SD122	107.625	40
SD123	120.625	40
SD124	146.625	40
SD125	86.625	360
SD126	89.625	360
SD127	92.625	360
SD128	95.625	360
SD129	99.625	360

Diode	Station location, in.	Angular location, θ, degree
SD130	105.625	360
SD131	111.625	360
SD132	146.625	360
SD133	86.625	300
SD134	90.625	300
SD135	94.625	300
SD136	98.625	300
SD137	102.625	300
SD138	106.625	300
SD139	110.625	300
SD140	146.625	300
SD141	86.625	230
SD142	92.625	230
SD143	98.625	230
SD144	105.625	230
SD145	107.625	230
SD146	120.625	230
SD179	146.625	230
SD185	94.625	182
SD186	115.625	182
SD187	95.625	302
SD188	95.625	232
SD189	115.625	232

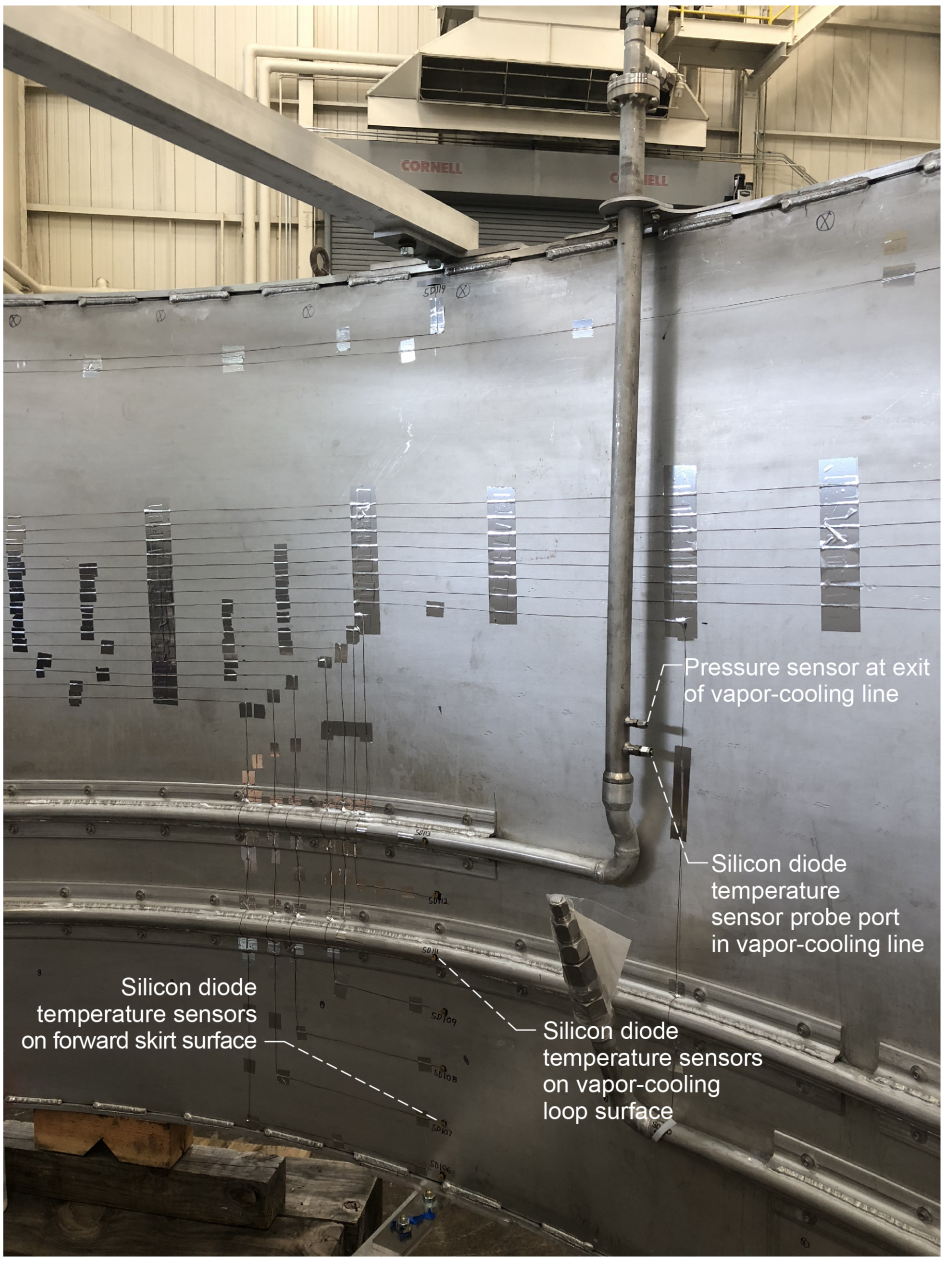

Figure 18.—Forward skirt silicon diode installed.

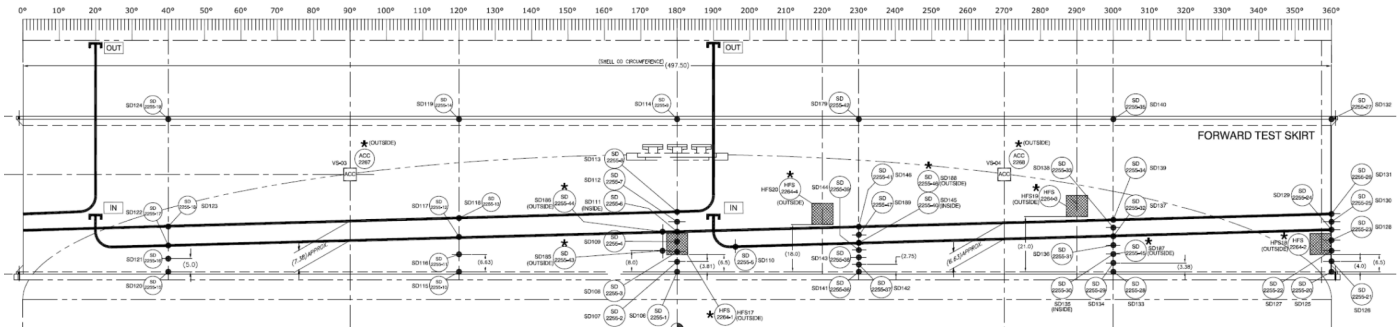

Figure 19.—Forward skirt sensor locations (for a clearer view of temperature sensor locations, see Figures 231 to 233).

TABLE 8.—LOCATION OF SILICON DIODES (SDs) (BOBBIN STYLE) ON AFT SKIRT

[Station location is from the tank bottom. The bottom tank flange is at 44.625 in.]

Diode	Station location, in.	Angular location, θ, degree
SD180	38.625	180
SD181	41.625	180
SD182	44.625	180
SD183	41.625	300
SD184	44.625	300

TABLE 9.—LOCATION OF SILICON DIODES (SDs) (CANISTER STYLE) ON SPRAY-ON FOAM INSULATION

[Station location is from the tank bottom. Measurements are taken from lip of top manway (SD31 and SD32) and bottom manway (SD37 and SD38). SD33 to SD36 are on barrel section.]

Diode	Station location, in.	Angular location, θ, degree	Fill level, percent
SD31	10.29	225	3
SD32	10.29	45	3
SD33	64.50	45	50
SD34	64.50	135	50
SD35	64.50	225	50
SD36	64.50	315	50
SD37	118.00	45	97
SD38	118.00	225	97

TABLE 10.—FORWARD DOME LOCATION OF SILICON DIODES (SDs) (CANISTER STYLE) AND THERMOCOUPLES (TCs) TYPE T ON MULTILAYER INSULATION (MLI)

Location	Stack 1	Stack 2	Stack 3
Spray-on foam insulation	SD37	SD38	----------
Sublayer 0	SD44	SD48	SD47
Sublayer 5	SD45	SD42	SD43
Sublayer 11	SD46	SD39	SD40
Sublayer 20	SD150	SD41	SD151
MLI surface	TC–2	TC–3	TC–4

TABLE 11.—AFT DOME LOCATION OF SILICON DIODES (SDs) (CANISTER STYLE) AND THERMOCOUPLES (TCs) TYPE T ON MULTILAYER INSULATION (MLI)

Location	Stack 1	Stack 2	Stack 3
Spray-on foam insulation	SD31	SD32	---------
Sublayer 0	SD54	SD55	SD152
Sublayer 5	SD58	SD57	SD153
Sublayer 11	SD50	SD52	SD56
Sublayer 20	SD51	SD53	SD49
MLI surface	TC–5	TC–6	TC–7

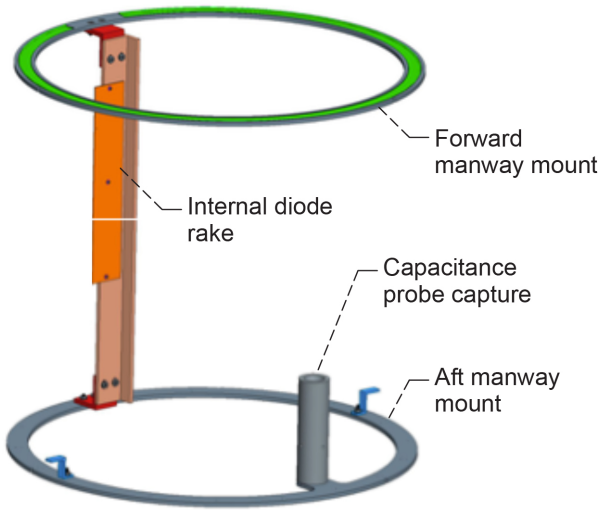

Figure 20.—Diode rake mounting.

3.2 Diode Rake

The diode rake runs longitudinally 3.31 m through the height of the tank and is mounted on rings attached to the forward and aft manway covers in the tank (see Figure 20). The rake has 20 SDs along its length for fluid temperature monitoring (Figure 21). In Figure 21, the diode locations on the rake and the corresponding fill levels are rounded to the nearest ±0.5 percent due to uncertainty, which takes into account the shrinkage of the tank and the rake at cryogenic temperature. Wet and dry temperature transitions of the diodes are also used to gauge the tank-fill level. Traditionally, wet and dry indications of the diodes are accomplished by overpowering the sensors and monitoring their temperatures subsequently. The dry diodes have a much greater rate of temperature increase than ones that are wet. This method was not employed here. Instead, it was found during boiloff testing that a similar rate of temperature

change naturally occurred when the liquid-vapor interface crossed a particular diode—the diode would exhibit a steep change from a liquid-like rate of temperature increase to a gas-like behavior as the interface moved past the diode. The only exception was for diodes in the ullage in the forward dome with MLI when the liquid level was above the forward flange. In this case, such a steep change in the temperature was not detected, and wet and dry diodes could not be discerned. During pressure rise testing as well, there was a dichotomy in the temperature rise behavior of wet and dry diodes.

3.3 Flowmeters

The flowmeters used are the Micro Motions, ELITE family of flow sensors manufactured by Emerson Electric Company. The selected models, CMF025M, CMF050M, and CMF100M are Coriolis devices, which offer a high level of measurement accuracy with a wide operational range (see Table 5). The selected flowmeters offer electronic sensing that allows monitoring and data collection remotely. The flowmeters operate to provide a 4 to 20 mA output. Since their operational ranges are different, the flowmeters are placed in a serial and parallel configuration where flow paths from the tank vent line to the ISPF vent are accomplished by appropriately opening and closing valves in the flow path of the desired selected flowmeter (see Figure 22). Specifically, the flow path is such that the flow rate is measured by FM2, or both FM2 and FM3, or by FM2, FM3, and FM4. When more than one meter is used, the same flow passes through multiple flowmeters. Another flowmeter CMFS100M is installed in the vapor-cooling lines to measure the vapor flow through them.

3.4 Heat Flux Sensors

The heat flux sensors manufactured by Captec Entreprise are used to measure the amount of heat leak that occurs during testing. The sensors are located on the tank's surface and forward skirt. The sensor size is 20.3 by 20.3 cm (see Figure 23). The sensor takes a thermal input and converts it to a voltage. The output from these sensors is typically in μV per W/m², and the measurement range is from –500 to 500 kW/m². Sixteen sensors were installed, four each on the forward dome, aft dome, tank barrel, and forward skirt (see Table 12).

3.5 Heaters

The test tank was equipped with two types of heaters—eight positive temperature coefficient graphite element strip heaters with a maximum power of 375 W each on the tank barrel section, and four heating patches with a maximum power of 640 W each on the top and bottom domes (see Table 13 for heater locations). The dome heaters are foil-etched Kapton® (DuPont™) covered heater elements and are attached to the outside metallic surfaces before SOFI was sprayed on the tank. The top dome heaters were removed, and bottom dome heaters were not used due to installation issues. The heaters were intended to be used to (i) provide heat input to the tank wall during transient tests that mimic tank wall heating during autogenous tank pressurization and (ii) assist with warming up the tank after completion of the tests.

During cold-shock pretesting with LN_2, an overheating anomaly occurred and the top dome heaters and the insulation in the vicinity were damaged and charred. After SOFI repair, it was decided not to use the dome heaters for subsequent tests. Thus, in the science data that is reported herein, none of the heaters were energized. The barrel heaters, however, were successfully used in some instances to aid in posttest warming of the tank.

Device	Location	Fill level, %
SD83	124.9	99.0
SD82	115.3	95.5
SD81	109.5	90.5
SD80	101.1	85.5
SD79	95.4	80.5
SD78	90.1	75.5
SD77	83.4	69.0
SD76	80.1	65.5
SD75	75.4	60.5
SD74	70.5	55.5
SD73	64.6	49.0
SD72	59.8	44.0
SD71	54.9	39.0
SD70	50.0	34.0
SD69	47.4	30.5
SD68	40.3	24.0
SD67	34.9	19.0
SD66	29.2	14.0
SD65	22.7	9.0
SD64	15.0	4.5

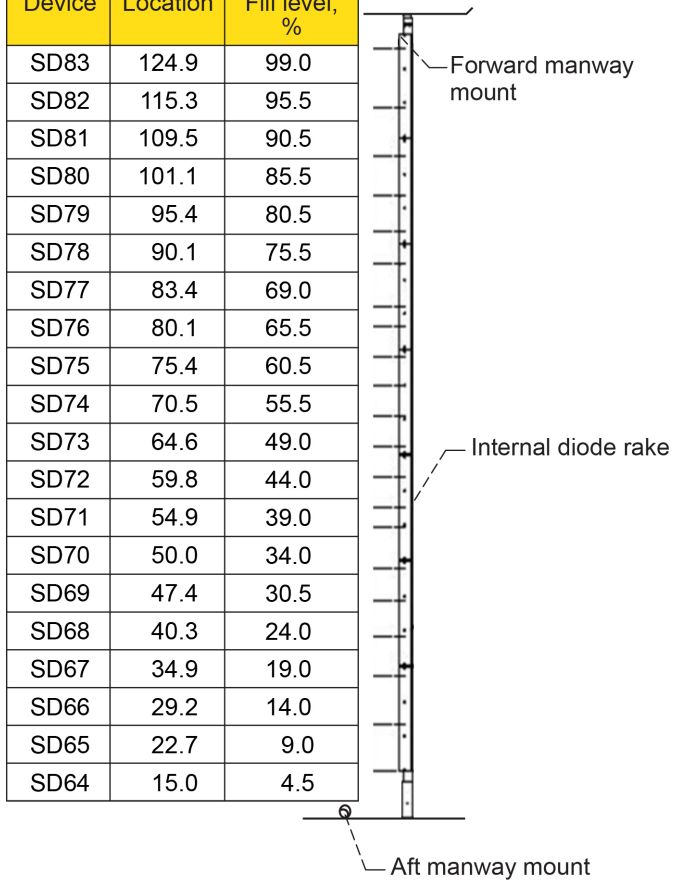

Figure 21.—Diode rake. Silicon diode (SD).

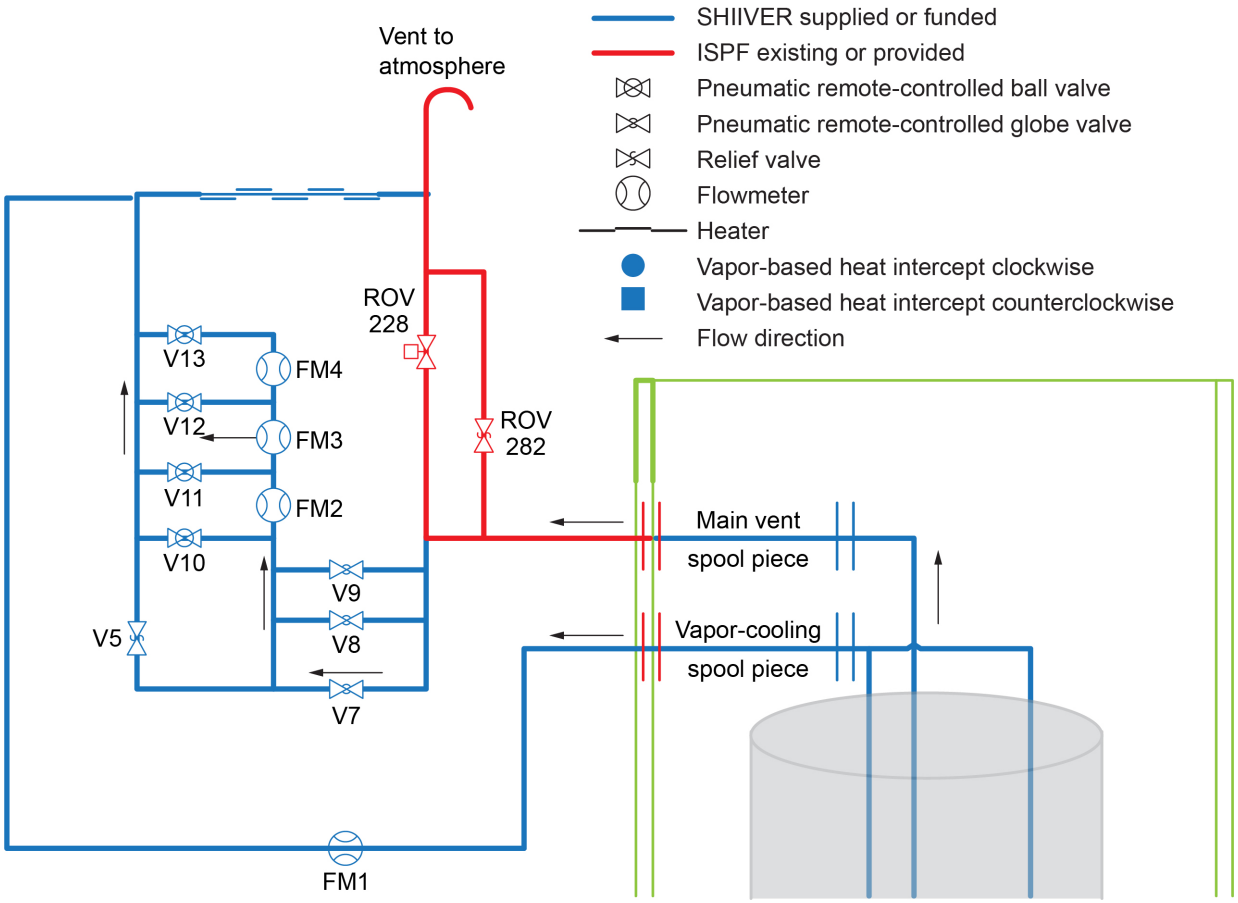

Figure 22.—Flowmeter configuration. Structural Heat Intercept, Insulation, and Vibration Evaluation Rig (SHIIVER). In-Space Propulsion Facility (ISPF).

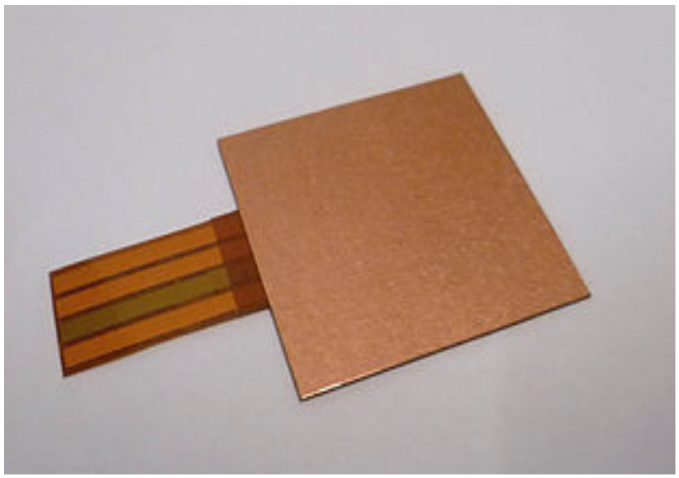

Figure 23.—Heat flux sensor (Captec Entreprise).

TABLE 12.—HEAT FLUX SENSOR (HFS) LOCATIONS

[Station location is from tank bottom.]

Tank position	Heat flux sensor	Station location, in.	Angular location, θ, degree	Fill level, percent
Forward dome	HFS01	124	225	99
	HFS02	118.1	225	97
	HFS03	100.5	225	86
	HFS04	118.1	45	97
Aft dome	HFS05	10.4	45	3
	HFS06	28.1	225	14
	HFS07	10.4	225	3
	HFS08	.5	225	0
Tank barrel	HFS09	64.3	45	50
	HFS10	64.3	225	50
	HFS11	76.3	135	63
	HFS12	52.3	315	37
Forward skirt	HFS17	86	180	73
	HFS18	86	357	73
	HFS19	88.1	290	75
	HFS20	87	220	74

3.6 Pressure Transducers and Pressure Control

The pressure transmitters used on the SHIIVER test article are four GT2250 (Stellar Technology), two-wire absolute transmitters that are used to monitor inlet and outlet tank pressure along with monitoring pressure on the cooling loop assembly. The transmitters have a range of 0 to 345 kPa (50 psia) and operate via a current loop producing a 4 to 20 mA output. The GT2250 is a CSA Group-approved intrinsically safe electronic package designed for hazardous locations.

During boiloff testing without vapor cooling, a pressure control system provided by the ISPF was also used to maintain the tank pressure at a desired constant level, typically 138 kPa (20 psia) via control valves and proportional integral derivative (PID) control loops (see Figure 24). It turned out, however, that tight pressure control was chiefly achievable only when one of the flowmeters (CFM100M (FM2) that has the largest internal opening) present downstream was used. Except for a few cases (where the hydrogen boiloff rate was less than 4 g/s), the other flowmeters imparted too much backpressure to the vent system and effective pressure control could not be achieved at the desired 138-kPa (20-psia) operating point.

TABLE 13.—LOCATION OF HEATERS ON TANK SURFACE

[Station location is from tank bottom flange.]

Device	Station location, in.	Angular location, θ, degree	Removed	Not used	Used
HR01	7.300	45	----	x	----
HR02	7.300	315	----	x	----
HR03	65.625	200	----	----	x
HR04	65.625	157	----	----	x
HR05	65.625	113	----	----	x
HR06	65.625	70	----	----	x
HR07	65.625	20	----	----	x
HR08	65.625	250	----	----	x
HR09	65.625	293	----	----	x
HR10	65.625	337	----	----	x
HR11[a]	123.700	315	x	----	----
HR12[a]	123.700	135	x	----	----
HR13[a]	123.700	45	x	----	----
HR14[a]	7.300	135	----	x	----
HR15[a]	7.300	225	----	x	----
HR16[a]	123.700	225	x	----	----

[a]Heaters on the forward dome (11, 12, 13, and 16) were removed after initial cold shock due to burning through the SOFI caused by poor thermal contact to the tank coupled with poor heat removal in the vapor.

3.7 Radio Frequency Mass Gauge

An RFMG was installed and tested in the SHIIVER tank to test scaling of the technology to larger tank sizes. Because the radio frequency (RF) mode frequencies of a tank decrease as the size of the tank increases, the RFMG antenna size increases in order to have a higher gain at the frequencies of interest. After the SHIIVER tank was built, an RF ping test was conducted at the manufacturing site before any hardware was installed in the tank to verify a good RF mode spectrum using a dipole antenna of appropriate length mounted on a mast. A good RF spectrum was obtained from the ping test, and a loop antenna (approx. 23 in. in length) was subsequently designed and constructed for installation into the SHIIVER tank. Two loop antennas were installed as shown in Figure 25 and were mounted to threaded studs welded to the tank sidewalls. A pair of spaceflight-rated RF coaxial cables were used to connect the antenna assemblies to RF weld passthroughs with grounded shields on a port at the bottom of the tank.

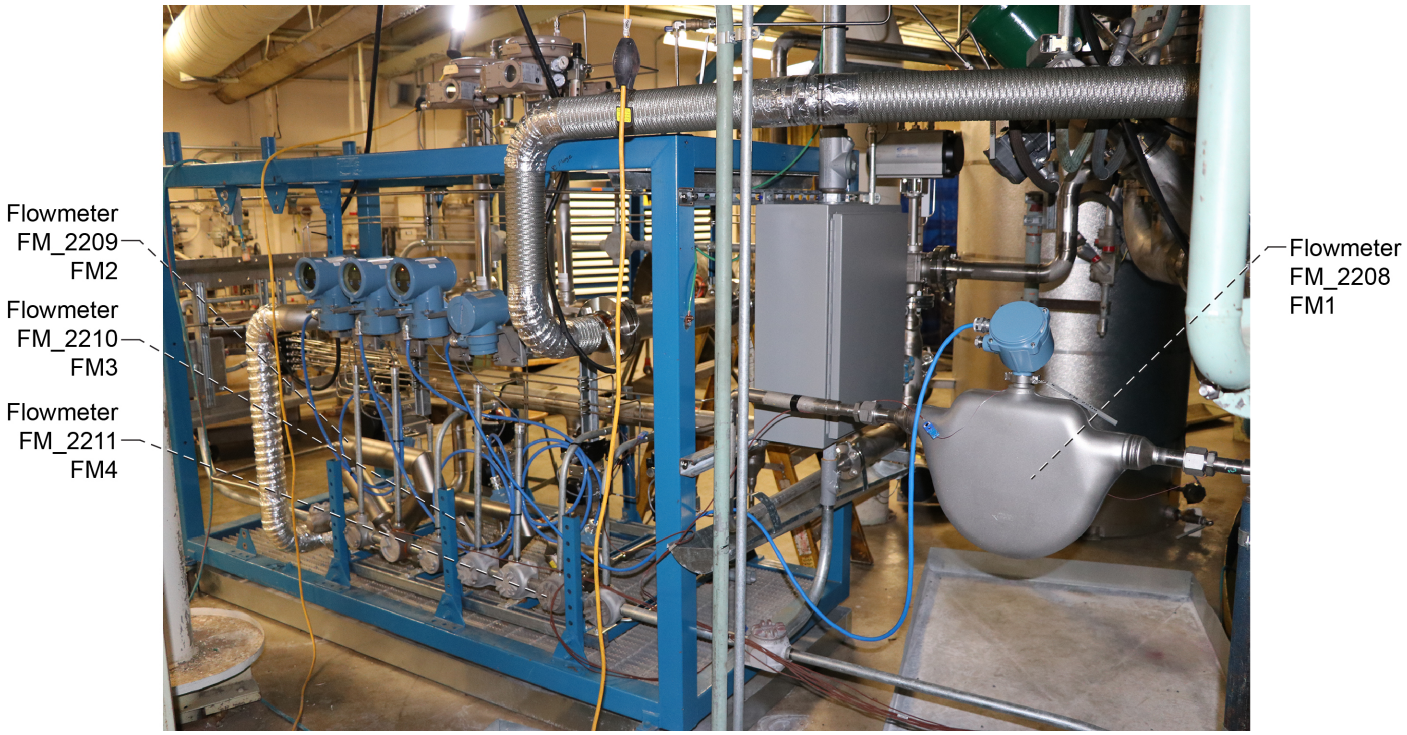

Figure 24.—Backpressure control cart.

The RF signals used to ping the antennas in the tank were generated by a pair of universal serial bus- (USB-) powered vector network analyzers (VNAs). RF cables connected the VNAs to the tank passthroughs, and isolated shield passthroughs were used on the vacuum chamber wall. The VNAs were located in an equipment cabinet just outside the vacuum chamber and were controlled by a laptop in the PBS control room. Firewalls were used to establish a virtual private network (VPN) session between the controlling laptop at PBS and another laptop at a Lewis Field office. The remote operation allowed the RFMG team members to view the data remotely, make changes to DAQ parameters, and set up automated RFMG output plots for viewing from either the control room or the remote office location. The RFMG control software application was a custom-built C++ application.

3.8 Capacitance Probe

The capacitance probe is a 12.7-mm stainless steel tube with a total length of 3.38 m manufactured by American Magnetics Inc. (Model 1700 Liquid Level Controller). A schematic of the capacitance probe is shown in Figure 26. The sensor, which is located inside the tank, is used in conjunction with an oscillator that is outside the tank. The probe measures the LH_2 height within the tank up to 3.3 m. From this measurement, the tank-fill level can be calculated from the known height to volume relationship of the tank. The probe is mounted on a 7-cm-outer-diameter conflat flange and is placed into a port located on the storage tanks top manway cover. When installed, the probe mates with a stabilization capture located on the bottom instrument rake mounting bracket (see Figure 20).

The probe's accuracy is rated to within 0.1 percent of the measured value. The output from the probe is a converted 4- to 20-mA excitation used to reference the hydrogen liquid level. The uniqueness of this device is its length. Generally, capacitance probes are not greater than a few meters in length. The SHIIVER capacitance probe is greater than 3 m in length.

3.9 Accelerometers

To support acoustics testing at the RATF, 12 triaxial accelerometers (PCB Piezotronics, Inc., Model 356A33) were used to monitor the structural response of the test article and measure their movement (see Figure 27). Their placement is listed in Table 14 and are distributed between the tank's manways and support structures. The triaxial devices monitor vibration in the x, y, and z directions and converts that to a voltage, with a sensitivity of 10 mV/g. The frequency range of operation for these devices is from 2 to 7,000 Hz (±5 percent) and output monitoring up to ±500 g. The accelerometers require an excitation from 2 to 20 mA during normal operation. The specifications of the accelerometers and the microphones used in acoustic testing are listed in Table 15.

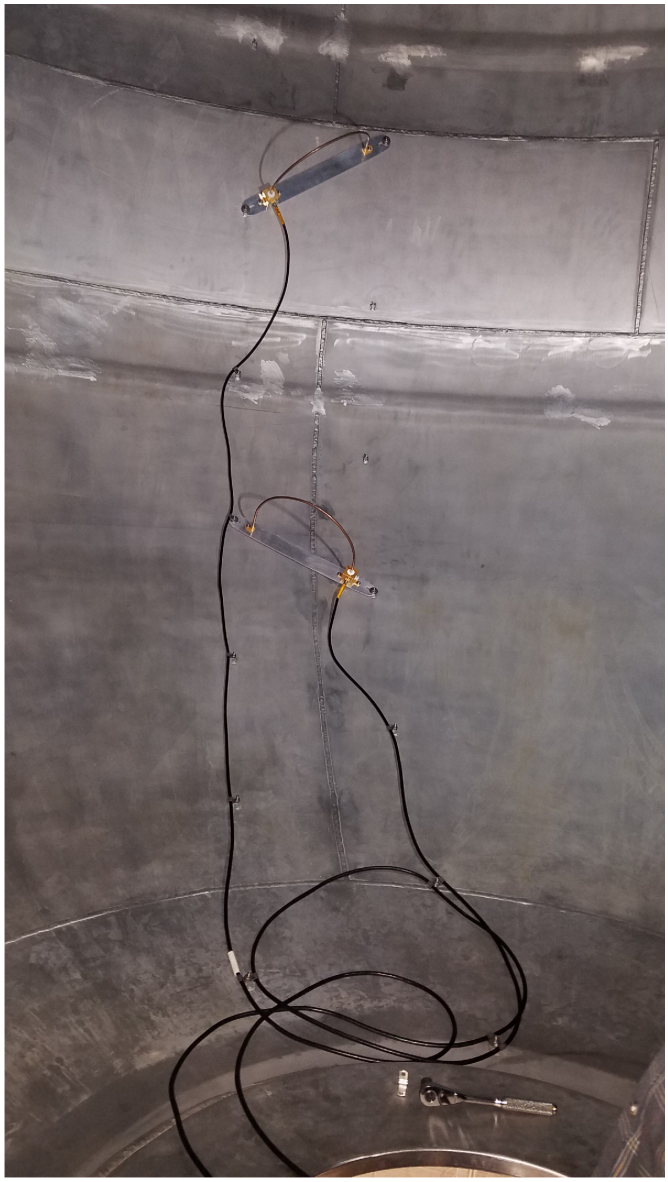

Figure 25.—Radio Frequency Mass Gauge loop antennas installed in Structural Heat Intercept, Insulation, and Vibration Evaluation Rig (SHIIVER) tank.

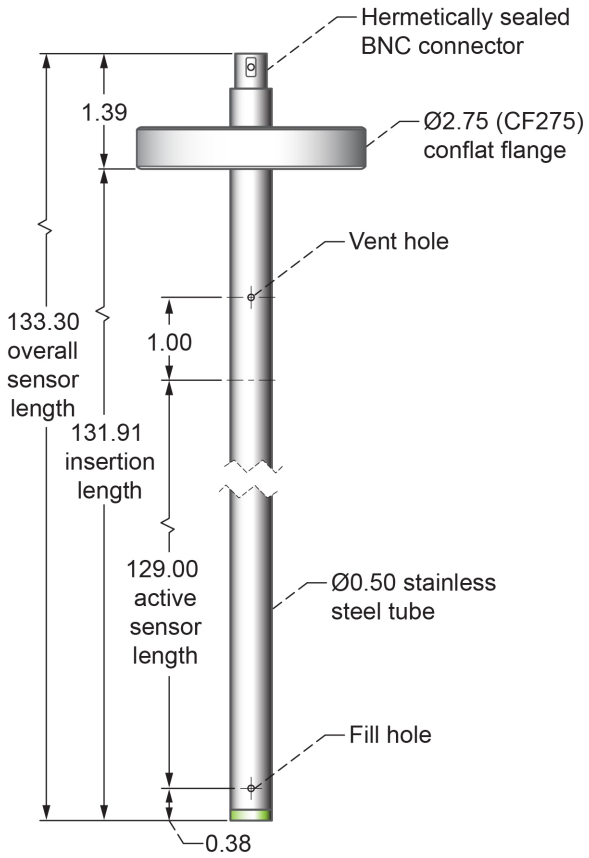

Figure 26.—Capacitance probe. Dimensions in inches. Bayonet nut coupling (BNC).

Figure 27.—Accelerometer model 356A33 (PCB Piezotronics, Inc.).

TABLE 14.—ACCELEROMETER LOCATIONS

Accelerometer	Location
VS01	Aft manway cover
VS02	Fill and drain valve V1
VS03	Fill and drain line free end
VS04	Aft skirt
VS05	Forward manway cover
VS06	Vent valve V2
VS07	Vapor-cooling line
VS08	Vapor cooling valve V5
VS09	Vapor cooling valve V4
VS10	Box beam
VS11	Forward skirt 1
VS12	Forward skirt 2

TABLE 15.—ACCELEROMETER AND MICROPHONE SPECIFICATIONS

Type and location	Range	Number	Nominal sensitivity	Model
Accelerometers (triaxial)	0 to 500 g	12	10 mV/g	PCB 356A33
Control microphones	4 to 70,000 Hz, 30 to 172 dB	8	1.6 mV/Pa	B&K 4938

4.0 Test Results

Testing was split into four separate test windows. Each test lasted a week or more, and there was quite a bit of hardware activity between the tests. The baseline test was performed with SOFI installed on the tank, but prior to installation of the MLI onto the domes. The preacoustic test was performed after the installation of the MLI onto the domes. The baseline and preacoustic tests with LH_2 are comprehensive and included boiloff, pressure rise, and vapor-cooling tests at various fill levels. Acoustic testing was then completed. Finally, postacoustic testing was completed. All the tests were completed with LH_2. In addition, the preacoustic testing was completed using LN_2 as well, to provide data for comparison in case postacoustic testing with LH_2 was not possible. The LN_2 and postacoustic test with LH_2 only included selected tests to judge the thermal performance of the system. The test summary showing what tests were run during each thermal vacuum test is shown in Table 16. Note that throughout this section the capacitance probe response has been adjusted, as shown in Section 5.4, to show the correct fill levels.

4.1 Baseline Test

The baseline test started on Aug. 23, 2019, at approximately 7 a.m. EST. The baseline test consisted of three main test runs: (1) boiloff, (2) vapor cooling, and (3) helium pressurization. The baseline test series was completed on Aug. 29, 2019, at approximately 8 a.m. EST, with a total test duration of nearly 145 h. A brief summary of baseline test events follows, then more details are provided in Sections 4.1.1 to 4.1.4.

1. Boiloff testing: To start boiloff testing, the SHIIVER tank was filled with LH_2, allowed to sit for approximately 5 h, and then topped off with LH_2 to a fill level more than 90 percent. With the tank chilled in, boiloff testing commenced, with the vapor routed through the main vent line, until the fill level reached approximately 70 percent (just below the forward flange). The 70-percent fill level was confirmed by diode SD77 transitioning from wet to dry. Next, a self-pressurization test was performed from approximately 138 kPa (20 psia) to 276 kPa (40 psia). Venting the tank pressure back to 138 kPa (20 psia), boiloff testing continued to less than 25 percent (just below the aft flange), as determined by diode SD68 transitioning from wet to dry.
2. Vapor-cooling testing: To begin the vapor-cooling portion of testing, the SHIIVER tank was topped off and the vapor-cooling loops were opened as a second vent line. After a few hours chilldown and another topoff, the boiloff gas was routed through the vapor-cooling circuit and allowed to boiloff to approximately 70 percent. At this point, a pressure rise test was attempted from just

under 138 kPa (20 psia) to 276 kPa (40 psia). During this pressure rise test, a fault occurred, and the vent valve opened unintentionally; this was quickly remedied but disturbed the pressure rise test. After remedying the fault noted previously, the tank was vented back down and boiloff testing with the vapor routed through the vapor-cooling network continued until 50 percent was reached. The 50-percent fill level was verified by SD73 transitioning from wet to dry. At 50 percent full, a pressure rise test was repeated from less than 138 kPa (20 psia) to 276 kPa (40 psia). The vapor-cooling test was then continued to a fill level less than 25 percent.

3. Final test run: The SHIIVER tank was refilled to approximately 75 percent full and allowed to boiloff to 70 percent, with the vapor routed through the vapor-cooling network. At 70 percent, a pressure rise test was repeated, to make up for the anomaly experienced during the previous test run. Following a successful pressure rise test, vapor-cooling boiloff testing continued to the 50-percent fill level. As a final test series, a helium pressurization test was run. The goal was to determine the energy put into the system by a helium pressurization event compared to that of a self-pressurization event. After the helium pressurization event was completed, the tank was vented back to atmospheric pressure, the baseline test was complete, and the tank was drained.

During testing, the vacuum pressure was maintained well below 1×10^{-4} torr as required for SOFI insulation. Since the ion gauge (IG) was calibrated in air (the residual gas analyzer (RGA) indicated a majority of helium and hydrogen in the vacuum chamber during this testing), its results are probably off by a factor of 2 to 3. As a result, the IG data shown in Figure 28 is for reference only and provides an indication of where leakage occurred. The large spikes shown in this figure are indicators of when leakage occurred, which was usually triggered by the opening of the SHIIVER fill valve. This leak was noted and fixed prior to the preacoustic thermal testing, as it would have been inappropriate to test MLI at these vacuum levels. The cold wall temperatures during the duration of the baseline test are shown in Figure 29. While the temperatures were stable throughout the testing, they did oscillate with the day and night cycle during a 24-h period. The temperatures generally stayed between 286 and 292 K (55 to 65 °F). It should be noted that all listed times during the baseline testing are referenced to noon EST on Aug. 23, 2019.

TABLE 16.—STRUCTURAL HEAT INTERCEPT, INSULATION, AND VIBRATION EVALUATION RIG (SHIIVER) AS RUN THERMAL VACUUM TEST MATRIX

Test	Description	Fill level(s), percent	Baseline LH_2[a]	Preacoustic LH_2[a]	Preacoustic LN_2[b]	Postacoustic LH_2[a]
1	Pressure rise test[c]	70	X	X	----	X[d]
		50	----	X	----	----
		25	----	X[d]	----	----
2	Boiloff test	90 to 70	X	X	X	X
		65 to 25	X	X	----	X
3	Vapor-cooling test	90 to 25	X	X	X[e]	----
4	Transient test with vapor cooling	70	X	X	----	----
5	Transient test without vapor cooling	70	X	X	----	----
		50	----	X	----	----
6	Cyclical pressure rise test	50	----	X	----	----
7	Helium pressurization test	50	X	----	----	----

[a]Liquid hydrogen (LH_2).

[b]Liquid nitrogen (LN_2).

[c]Pressure rise tests were generally conducted during both the boiloff and vapor-cooling tests.

[d]This pressure rise test was only conducted during boiloff testing.

[e]Vapor-cooling testing with LN_2 had two drains interspersed between the data. Testing was done between approximately 90 to 80, 50 to 45, and 25 to 24 percent fill.

During baseline testing, a few issues were encountered, namely the largest flowmeter on the vent line and the flowmeter on the vapor-cooling line did not operate correctly. These events are described more thoroughly in the later sections. It should also be noted that the capacitance probe was maxed out at approximately 92 percent full during the entire test series.

4.1.1 Boiloff Testing

During the boiloff testing to a fill level of 70 percent, the largest flowmeter (FM2) in the backpressure control system did not provide readouts at all. As such, the SHIIVER team was forced to use the medium flowmeter (FM3). The restriction through the medium flowmeter would not let the appropriate mass flow through in order to maintain the tank at 138 kPa (20 psia). This was unfortunate as the main parameter for the determination of system performance was originally going to be the boiloff flow rate. However, due to this event, heat load or equivalent boiloff flow rate needed to be calculated and is addressed in Section 5.0. As such, the pressure was allowed to rise during the boiloff testing as required (see Figure 30) and reached a peak of approximately 240 kPa (35 psia). The result of that was that the boiloff flow was also a function of time (see Figure 31) and the bulk liquid temperature rose (see Figure 32). It is easy to see where the diodes transition from wet (immersed in liquid) to dry (in vapor) in Figure 32.

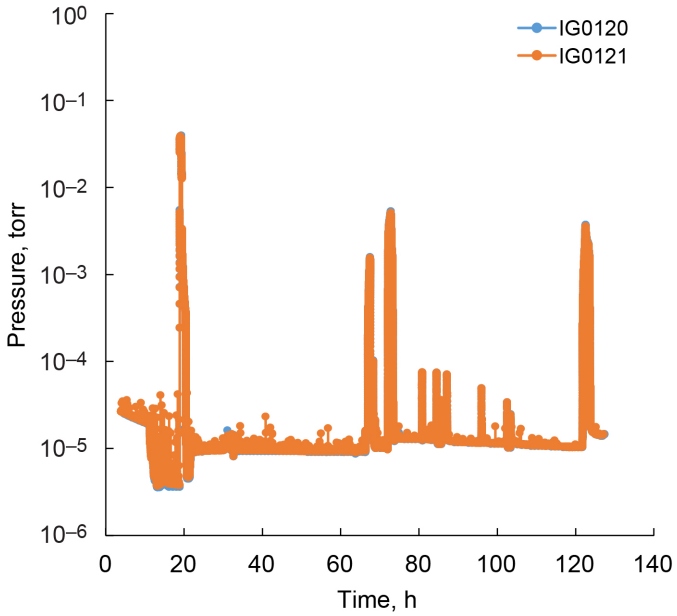

Figure 28.—Vacuum pressure for duration of baseline testing. Times are referenced to noon EST on Aug. 23, 2019.

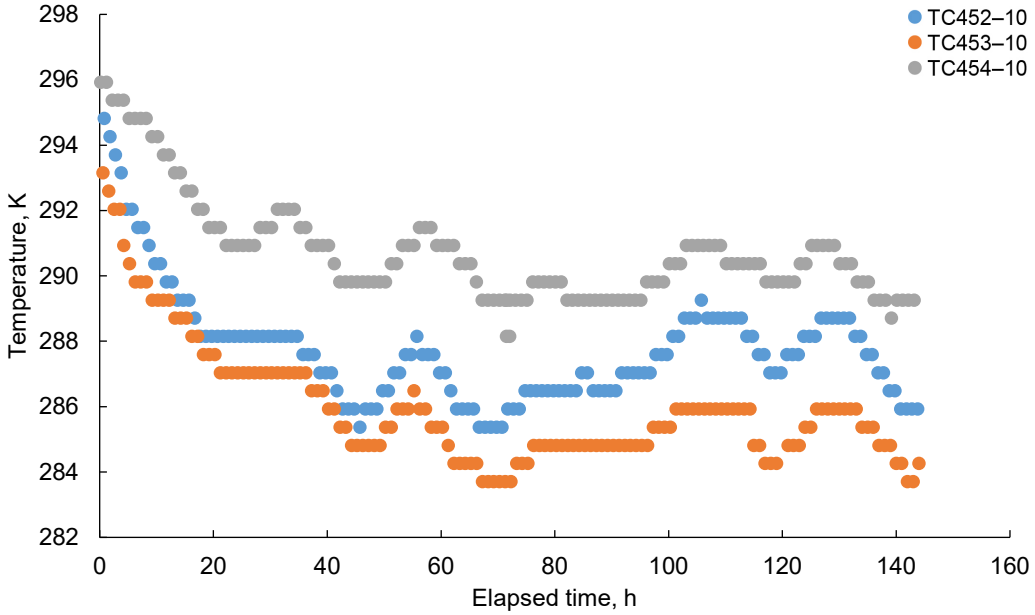

Figure 29.—Vacuum chamber wall temperatures during baseline testing. Times are referenced to noon EST on Aug. 23, 2019.

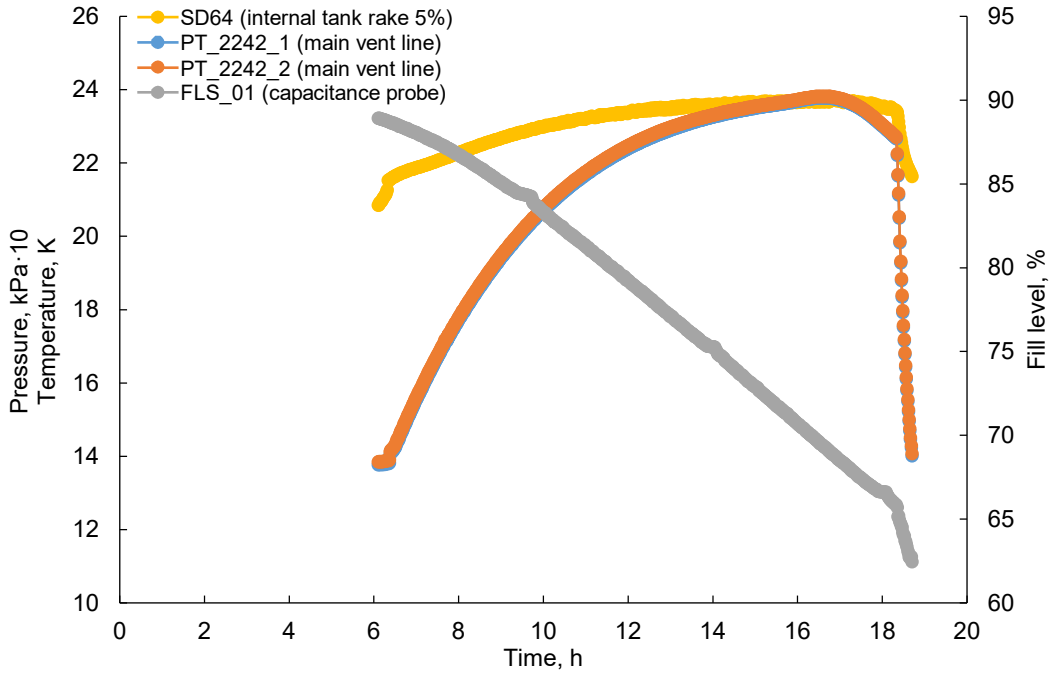

Figure 30.—Tank pressure, bulk liquid temperature, and capacitance probe reading during initial boiloff testing.[2]

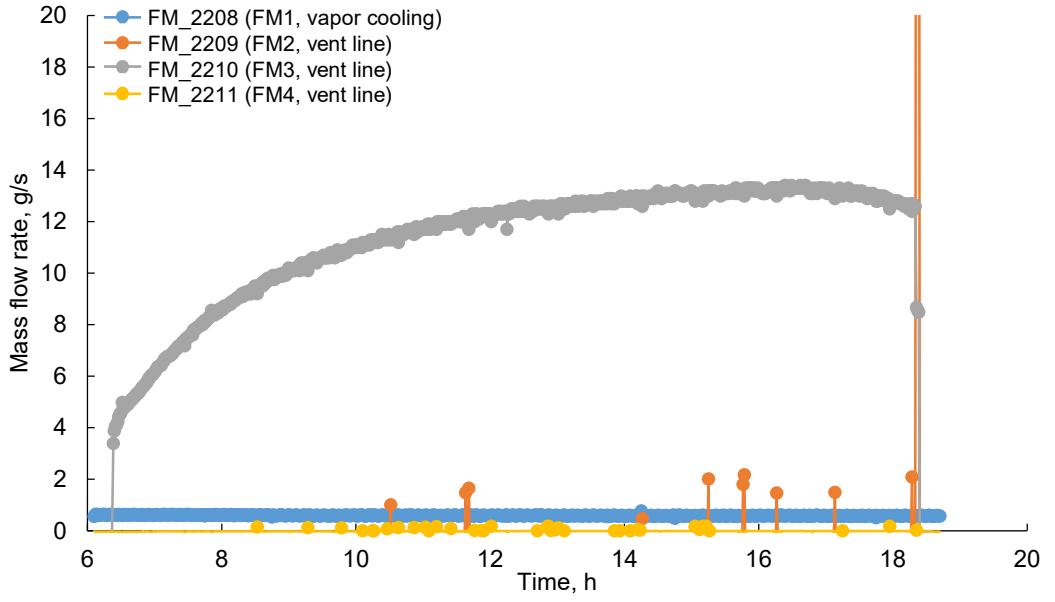

Figure 31.—Flowmeter readout during initial boiloff testing.

[2]The left side y-axis units used for pressure and temperature enable both to be plotted on the same scale. What is plotted for the pressure is the value in kPa divided by 10. Formally, the pressure unit is 10·kPa, but there is no name for it in International System of Units (SI) units according to National Institute of Standards and Technology (NIST) SP 811, 2008.

During the boiloff test to 25 percent fill, similar flow issues were encountered; however, the pressure did not rise nearly as high as in the first test, rising only to 183.4 kPa (26.6 psia). Pressure slowly came back down as the flow decreased. After the liquid level passed the aft flange, the tank could finally be controlled to 138 kPa (20 psia); this transition across the flange is observed between 47 and 50 h (see Figure 33 and Figure 34). The bulk liquid temperatures follow the saturation pressure and very little stratification, if any, is observed in the tank (see Figure 35). The ullage however is seen to stratify significantly with the top of the tank attaining over 130 K by the end of the test as seen in Figure 35.

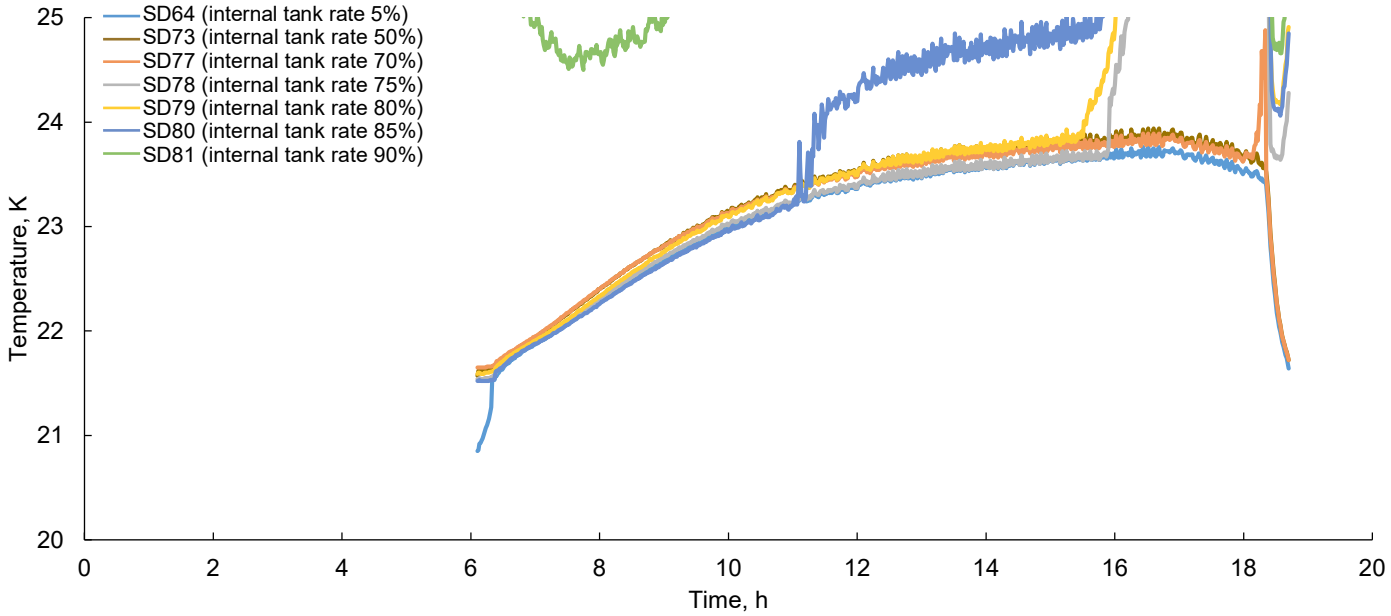

Figure 32.—Liquid temperatures during initial boiloff testing. SD80 (dark blue), SD79 (yellow), SD78 (gray), and SD77 (orange) transition from liquid to vapor.

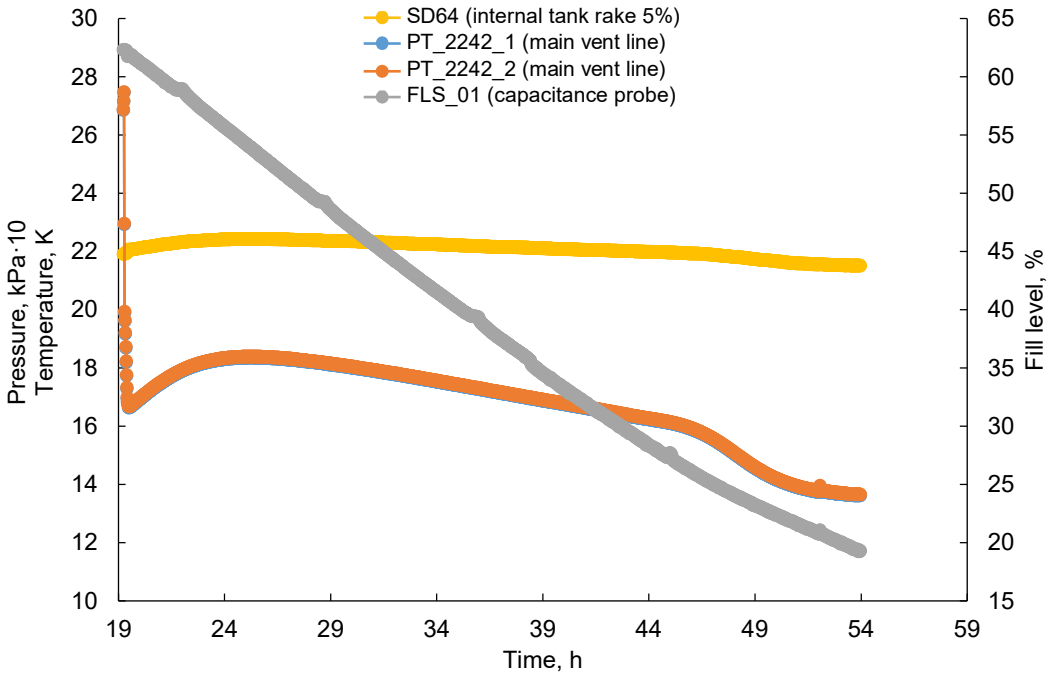

Figure 33.—Tank pressure, bulk fluid temperature, and capacitance probe reading during boiloff to 25 percent fill testing.

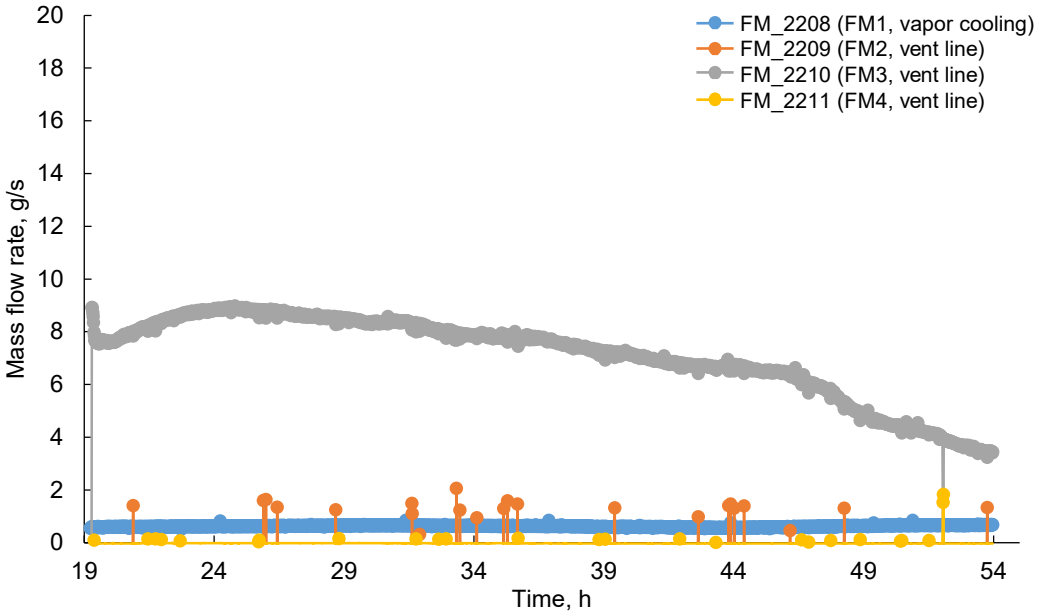

Figure 34.—Flowmeter readout during boiloff to 25 percent fill testing.

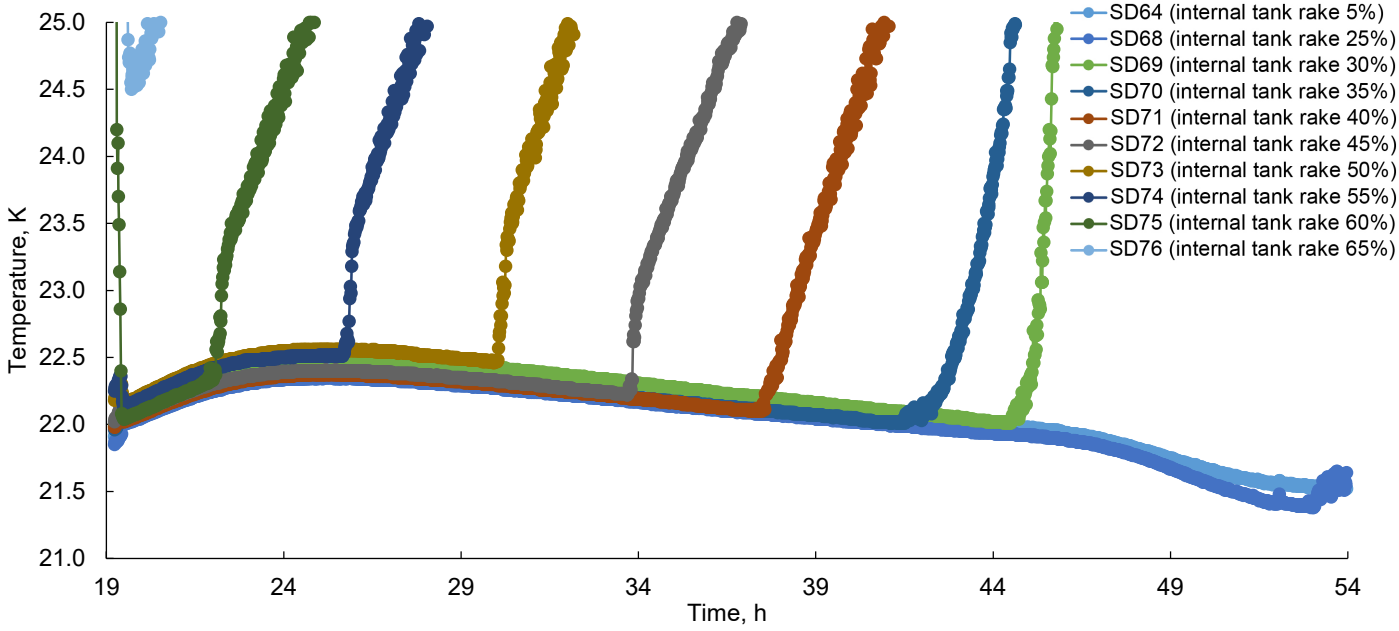

Figure 35.—Liquid temperatures as function of time while boiling off to 25 percent fill.

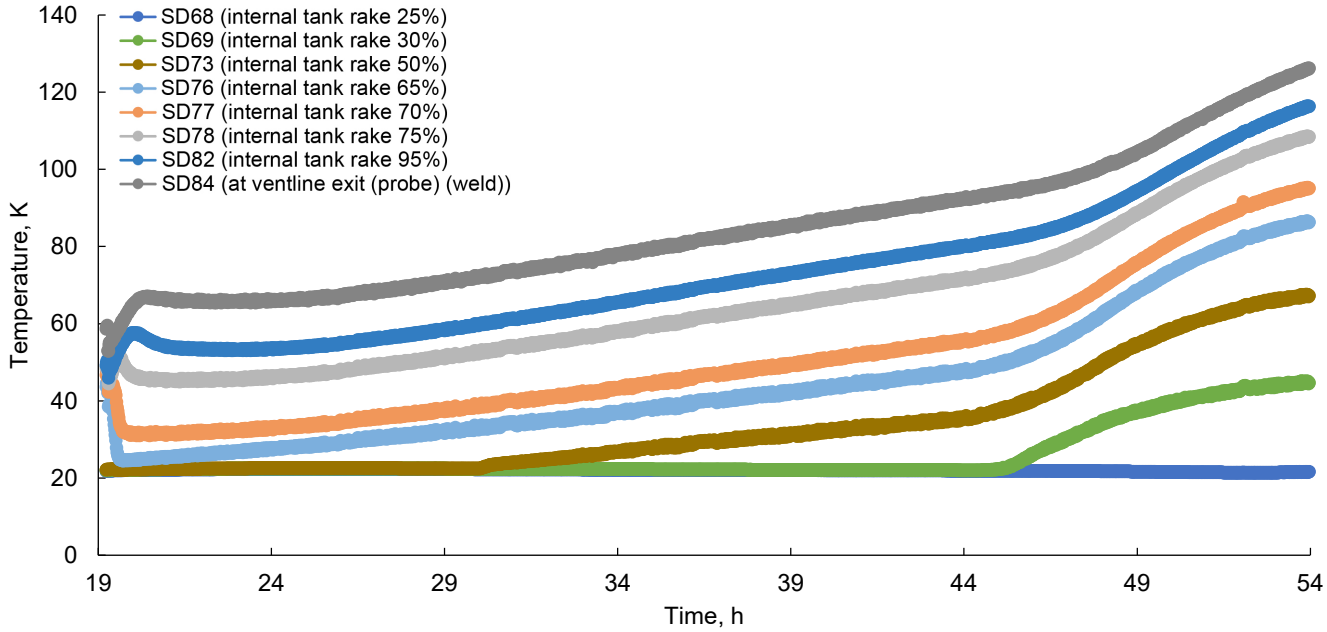

Figure 36.—Vapor temperatures as function of time during boiloff testing to 25 percent fill (25 percent achieved at ~47 h). Notice stratification in temperature across different tank levels.

4.1.2 Vapor-Cooling Testing

Vapor-cooling tests were run from 90 to 25 percent fill levels with brief stops for pressure rise tests at 70 and 50 percent. The vapor-cooling flowmeter did not work for any of the testing, and multiple different methods (differential of capacitance probe, diode transitions, and RFMG) had to be used to back out the flow rates through the cooling channels on the skirt. Figure 37 to Figure 48 show the temperature and pressure data at the different fill levels. No difference was seen in the temperatures in the two cooling loops to indicate imbalance of the flows through these loops. There are several pressure spikes in the data where attempts were made to use the vent line flowmeters to measure the vapor-cooling rate by flowing the boiloff through the vent line for a few minutes (see, e.g., just after hour 70 in Figure 37). However, this did not work so it was not attempted any further during the vapor-cooling tests. The pressure was fairly constant at approximately 117 kPa (17 psia) at high and medium fill levels (see Figure 37 and Figure 41), dropping off to 103 kPa (15 psia) by the end of the low fill level (as seen in Figure 45). The liquid temperatures (Figure 38, Figure 42, and Figure 46) remained isothermal at all fill levels and show transitions of various diodes from liquid to vapor. The vapor temperatures (Figure 39, Figure 43, and Figure 47) show that the vapor is stratified, and its temperature rises as the fill level decreases. The vapor-cooling loop temperatures for high fill (Figure 40) shows that the vapor is cold, and its temperature is relatively constant during the test, while for medium fill (Figure 44), the vapor warms up. For low fill, Figure 48 shows that the vapor is considerably warm and likely much less effective in intercepting heat from the forward skirt.

After the initial vapor-cooling testing, the SHIIVER tank was refilled to approximately 75 percent full to repeat the vapor-cooling pressure rise test, transient test, and testing down to approximately 50 percent full (see Figure 49 to Figure 56). The test data was not much different than the first time, but during this test window a clean pressure rise test was run. The system did reestablish stable boundary conditions for the pressure rise test as seen in Figure 49 to Figure 52.

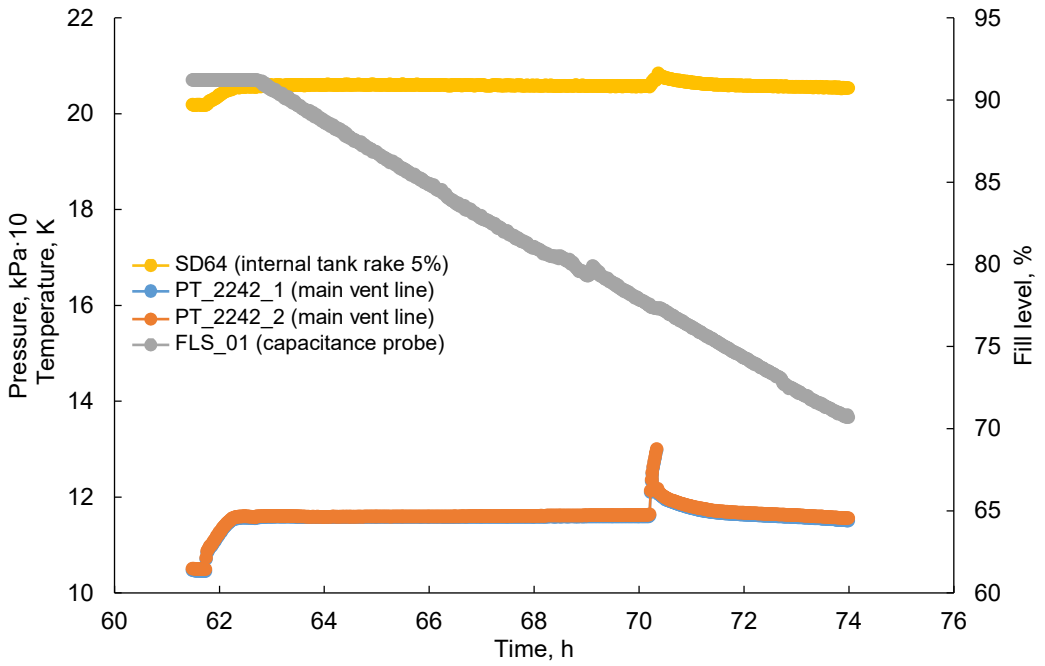

Figure 37.—Vapor cooling, liquid temperature, and pressure as function of time, 90 to 70 percent. Spikes correspond to efforts to measure boiloff.

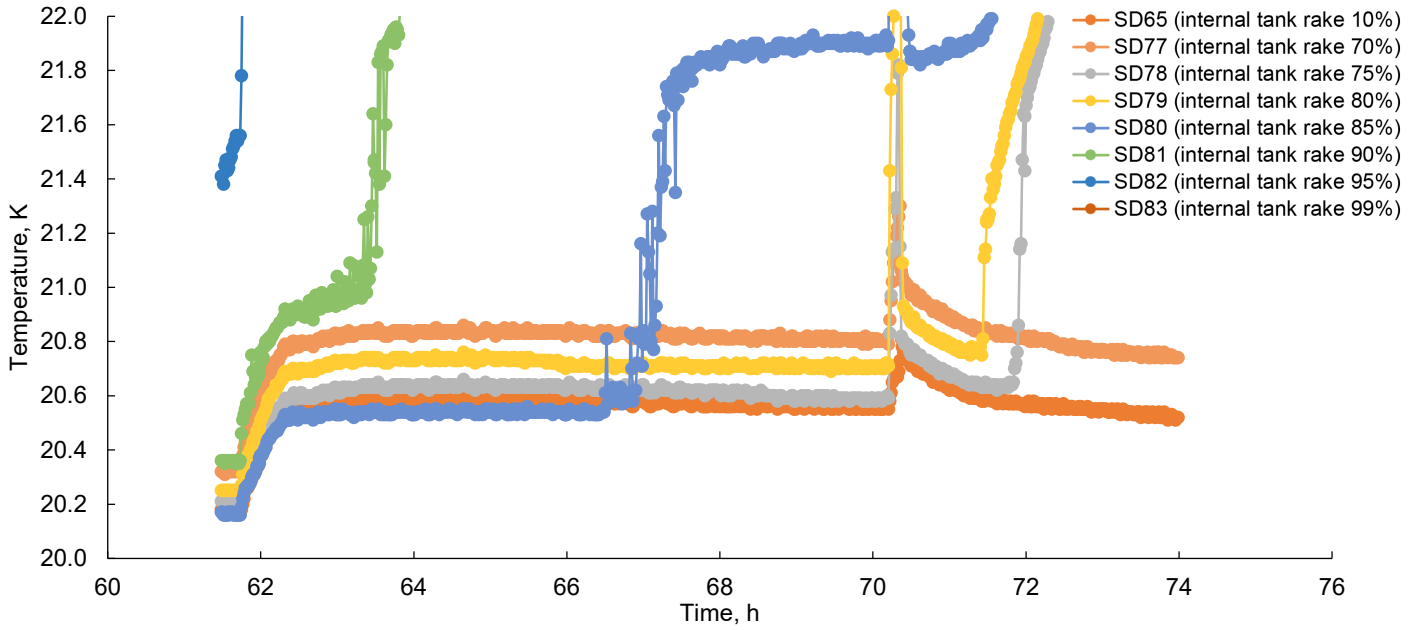

Figure 38.—Liquid temperatures during high-fill vapor-cooling test.

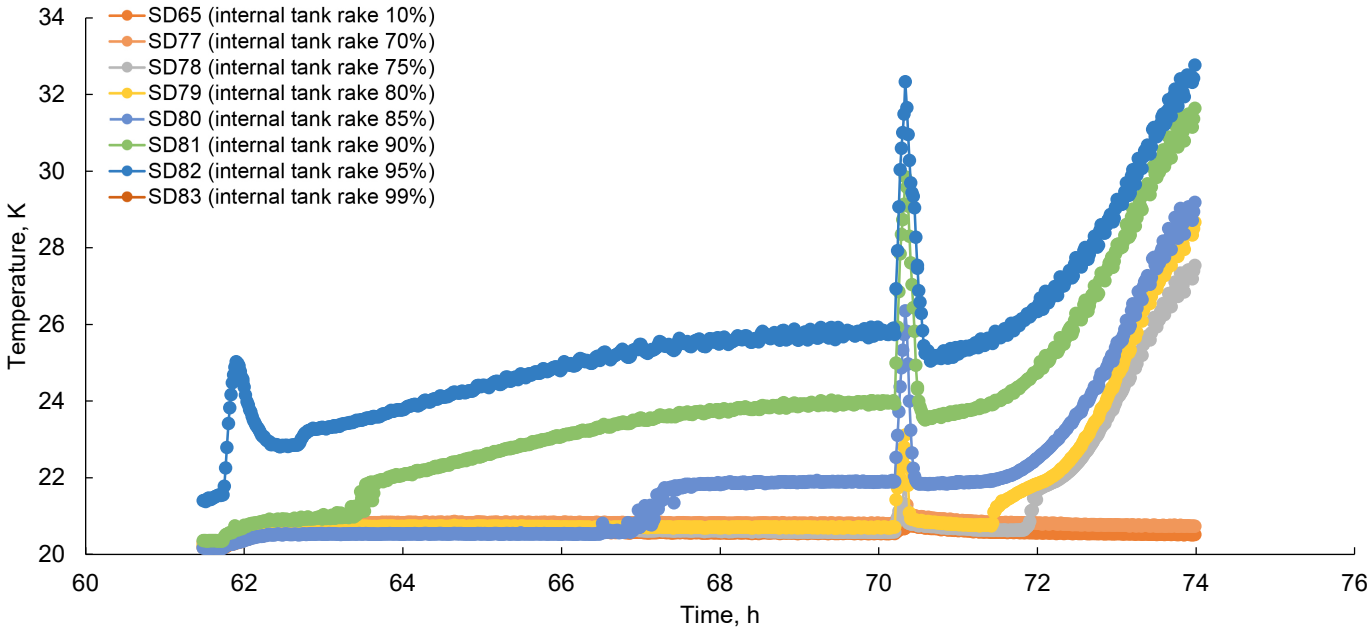

Figure 39.—Vapor temperatures during high-fill vapor-cooling test.

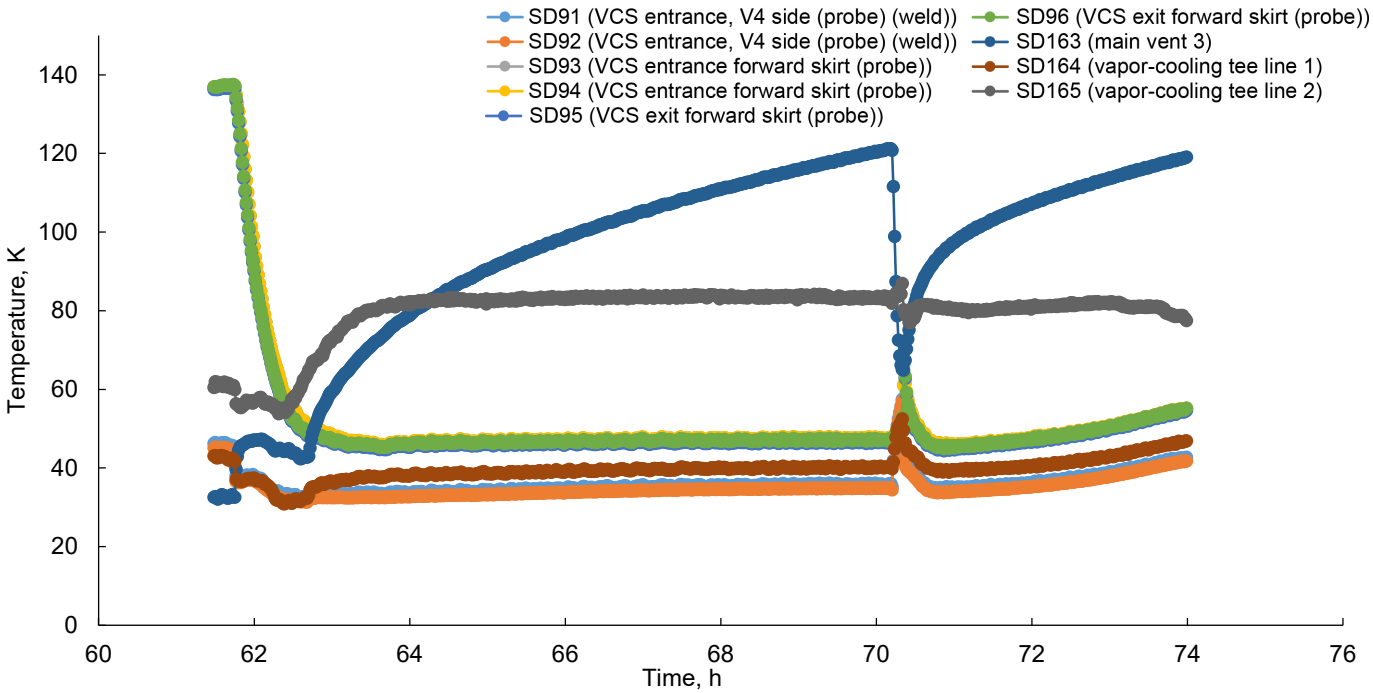

Figure 40.—Vapor-cooling loop temperatures during high-fill vapor-cooling test. Vapor-cooling system (VCS).

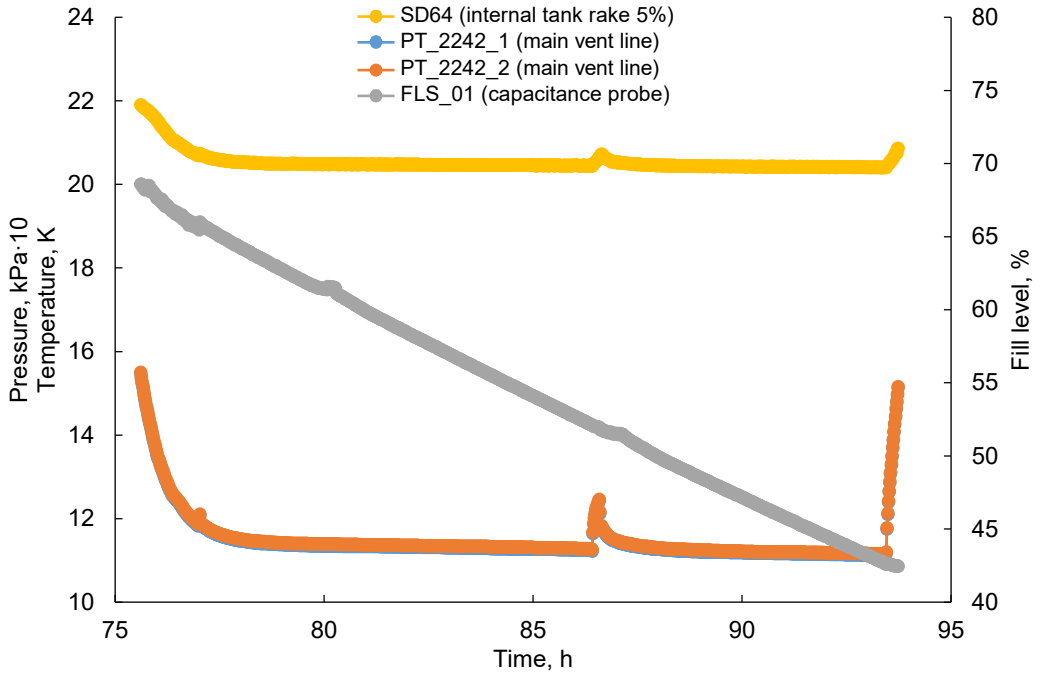

Figure 41.—Pressure and bulk fluid temperature during vapor-cooling testing from 70 to 50 percent full.

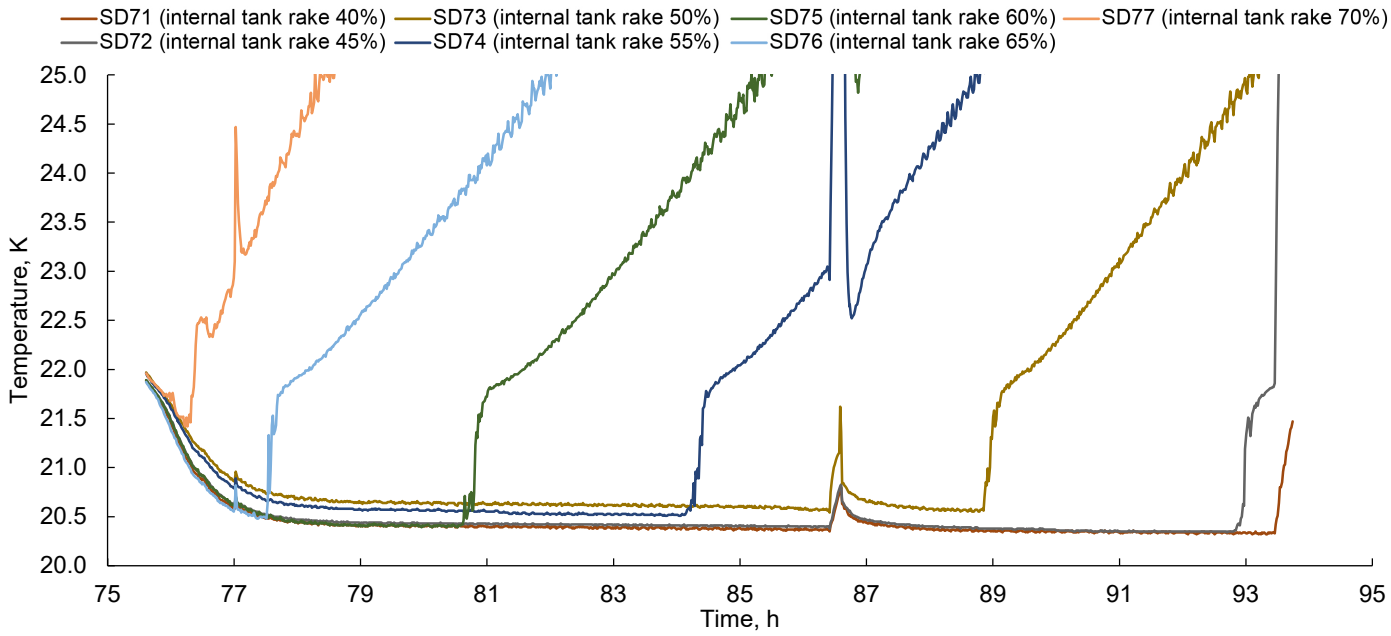

Figure 42.—Liquid temperatures as function of time during medium-fill vapor-cooling testing.

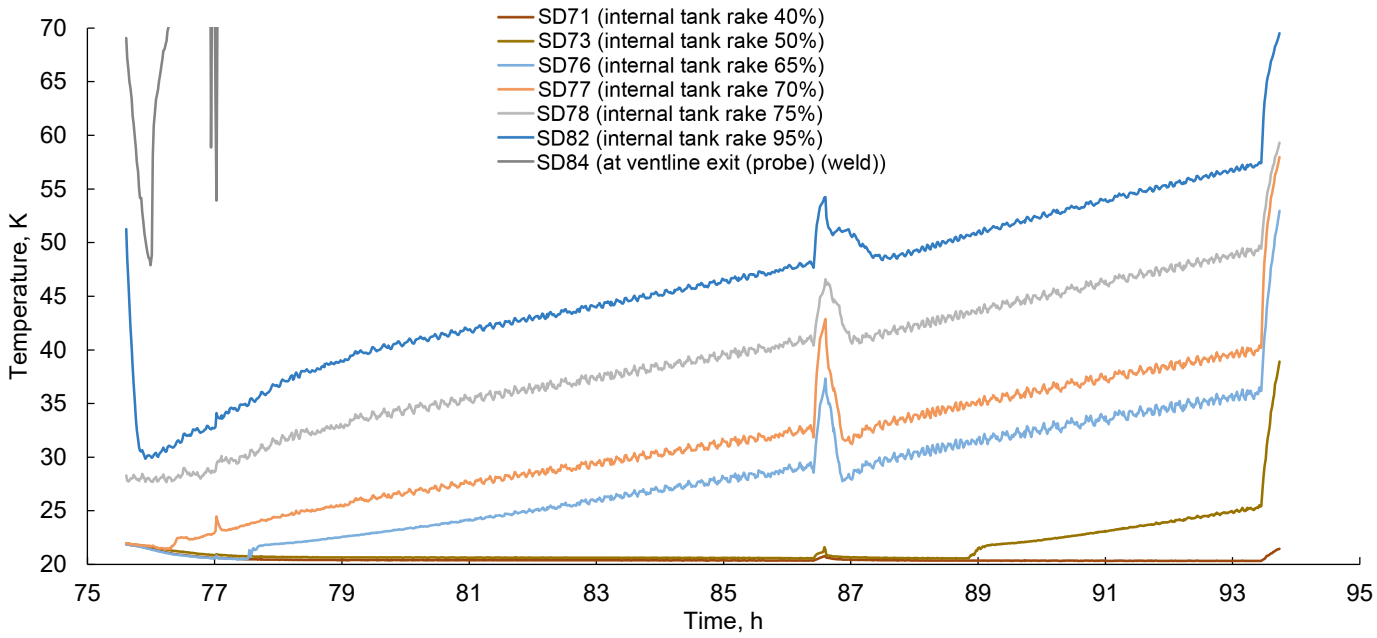

Figure 43.—Vapor temperatures as function of time during medium-fill vapor-cooling testing.

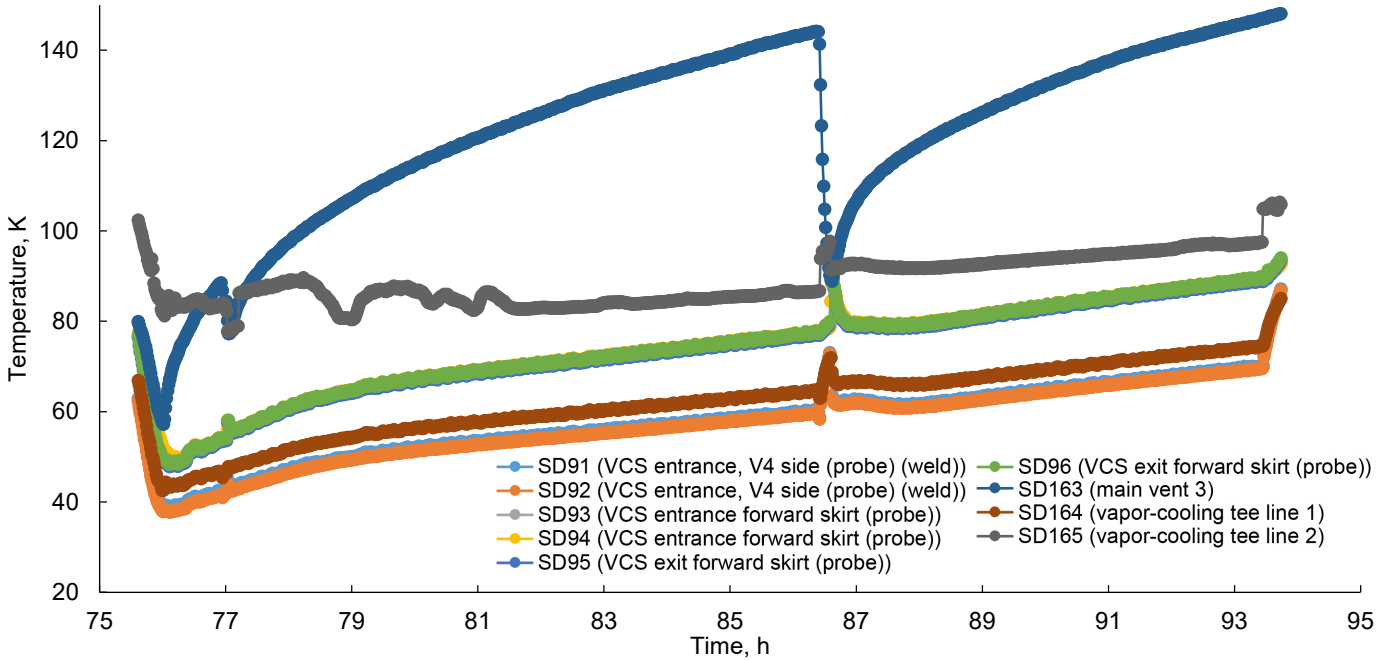

Figure 44.—Vapor-cooling loop temperatures during medium-fill vapor-cooling test. Vapor-cooling system (VCS).

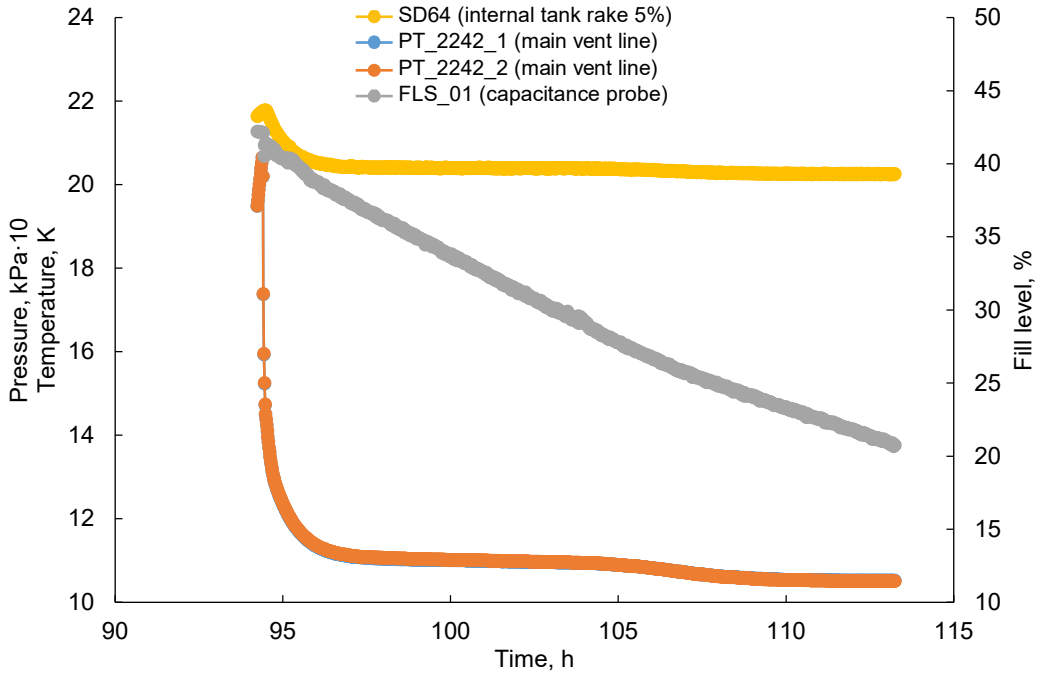

Figure 45.—Pressure and bulk fluid temperature during low-fill vapor-cooling testing.

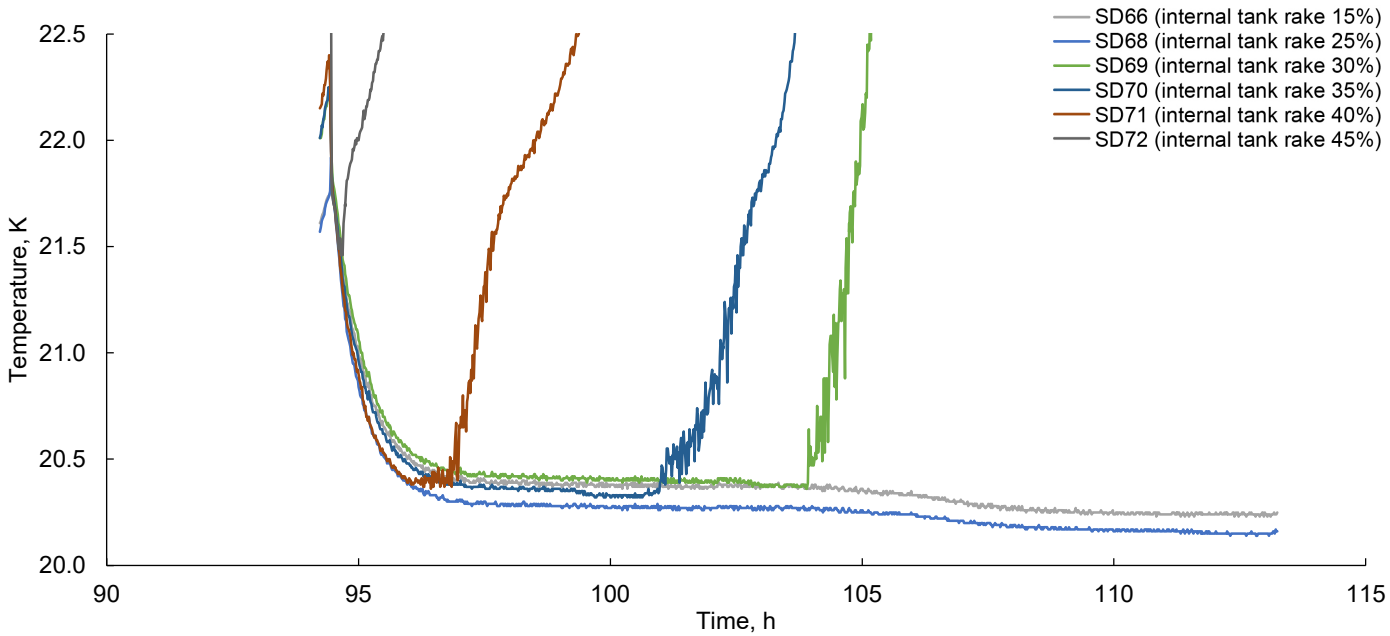

Figure 46.—Liquid temperatures during low-fill vapor-cooling test.

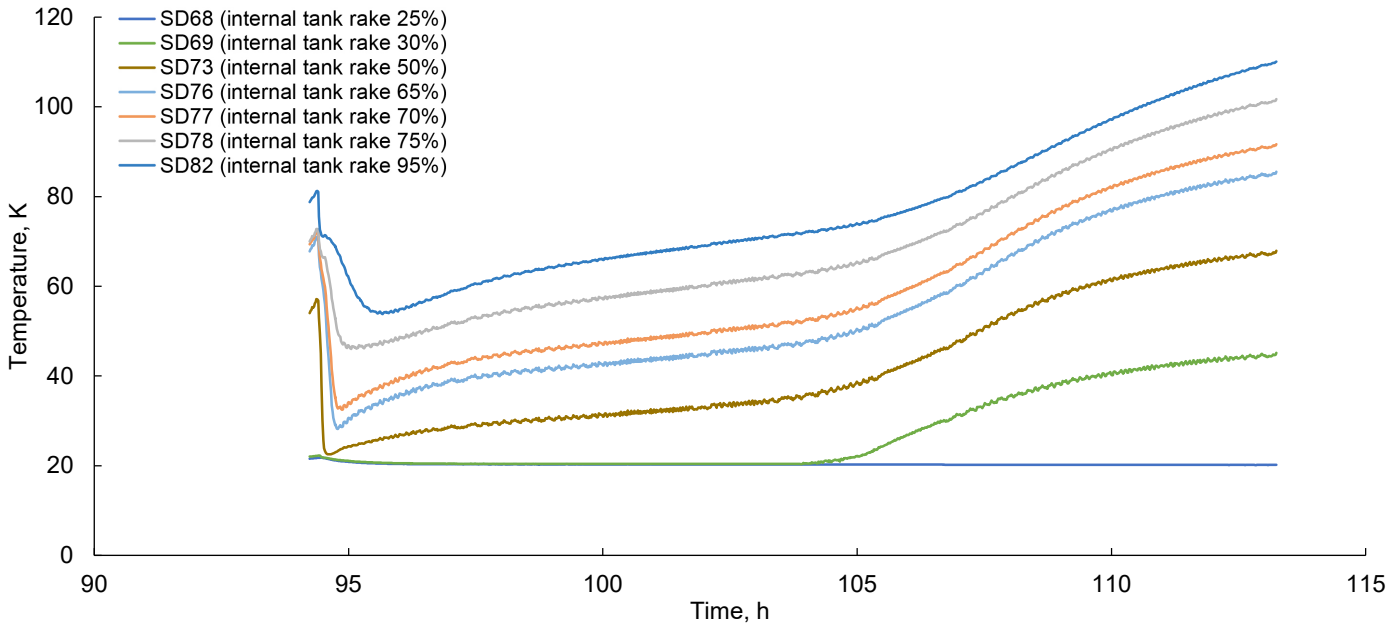

Figure 47.—Vapor temperatures during low-fill vapor-cooling test.

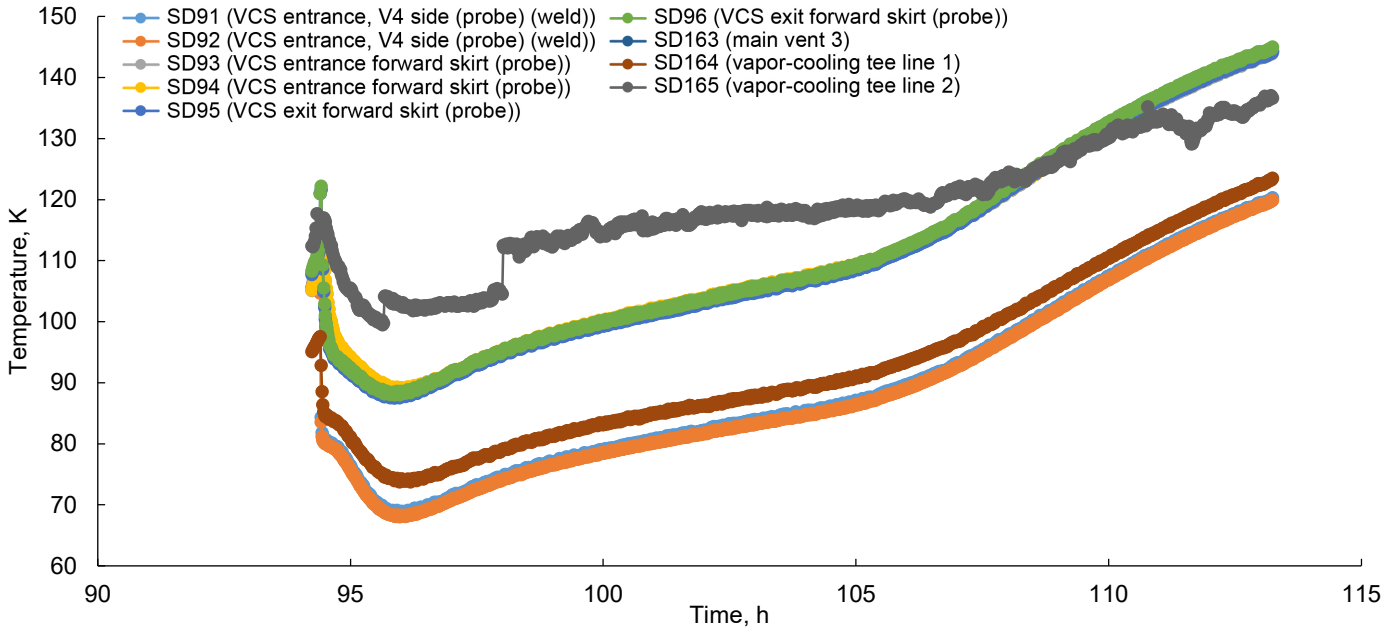

Figure 48.—Vapor-cooling loop temperatures during low-fill vapor-cooling test. Vapor-cooling system (VCS).

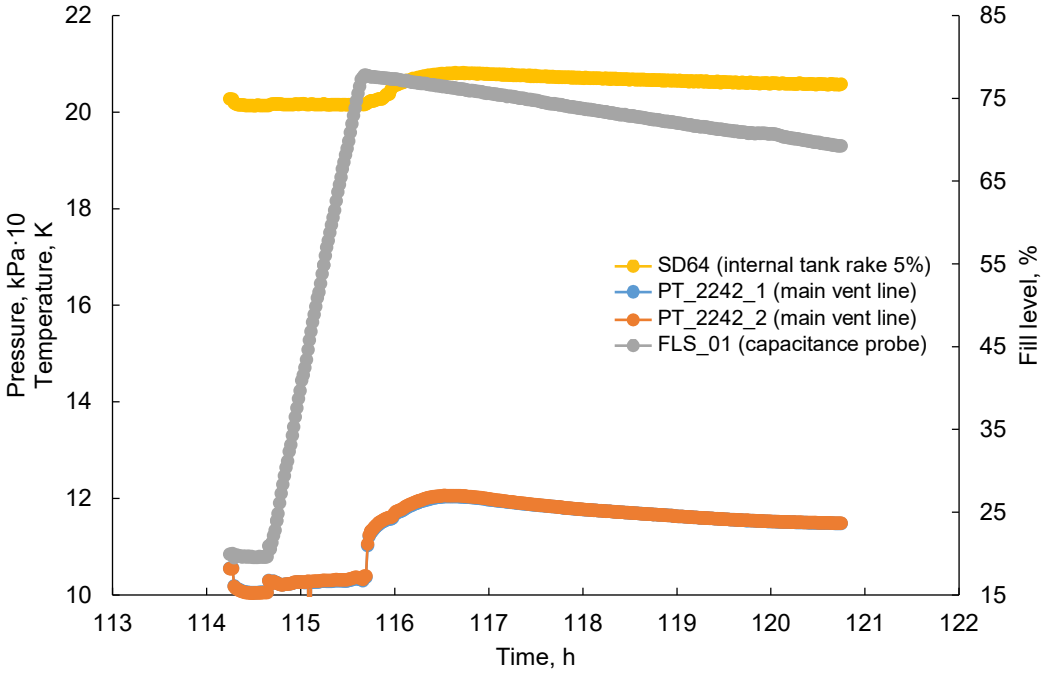

Figure 49.—Pressure and bulk fluid temperature during second vapor-cooling testing from 75 to 70 percent.

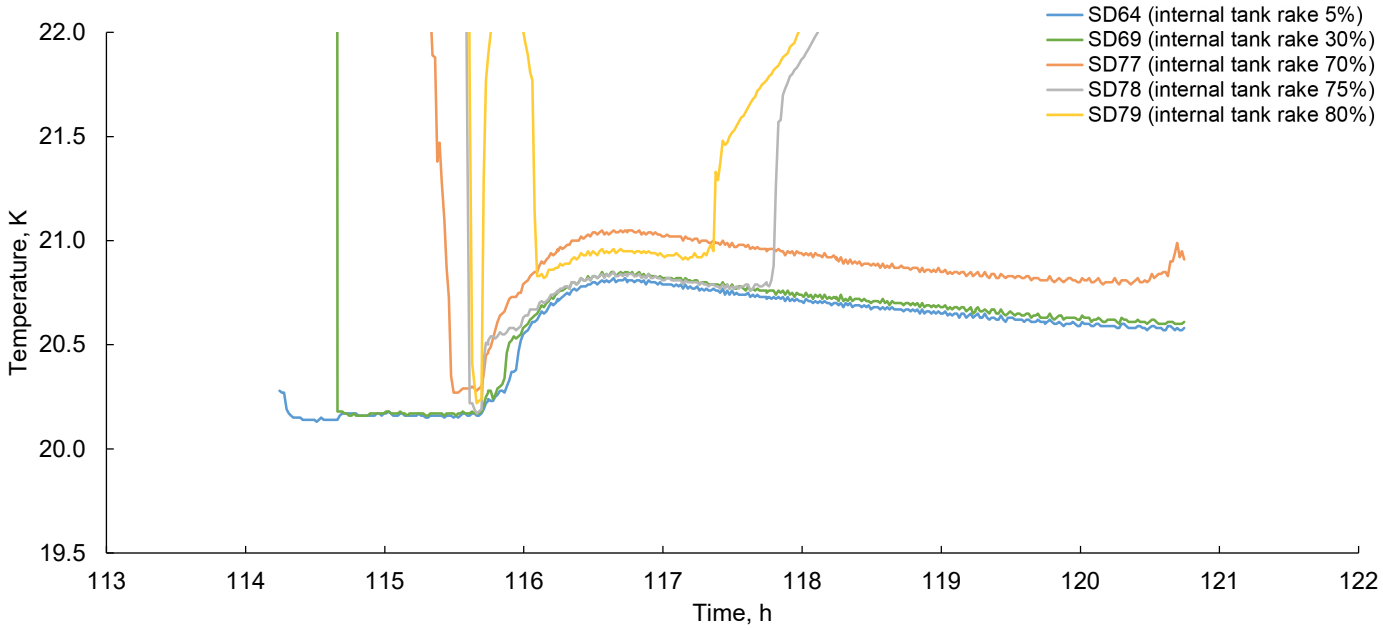

Figure 50.—Liquid temperatures during second high-fill vapor-cooling test.

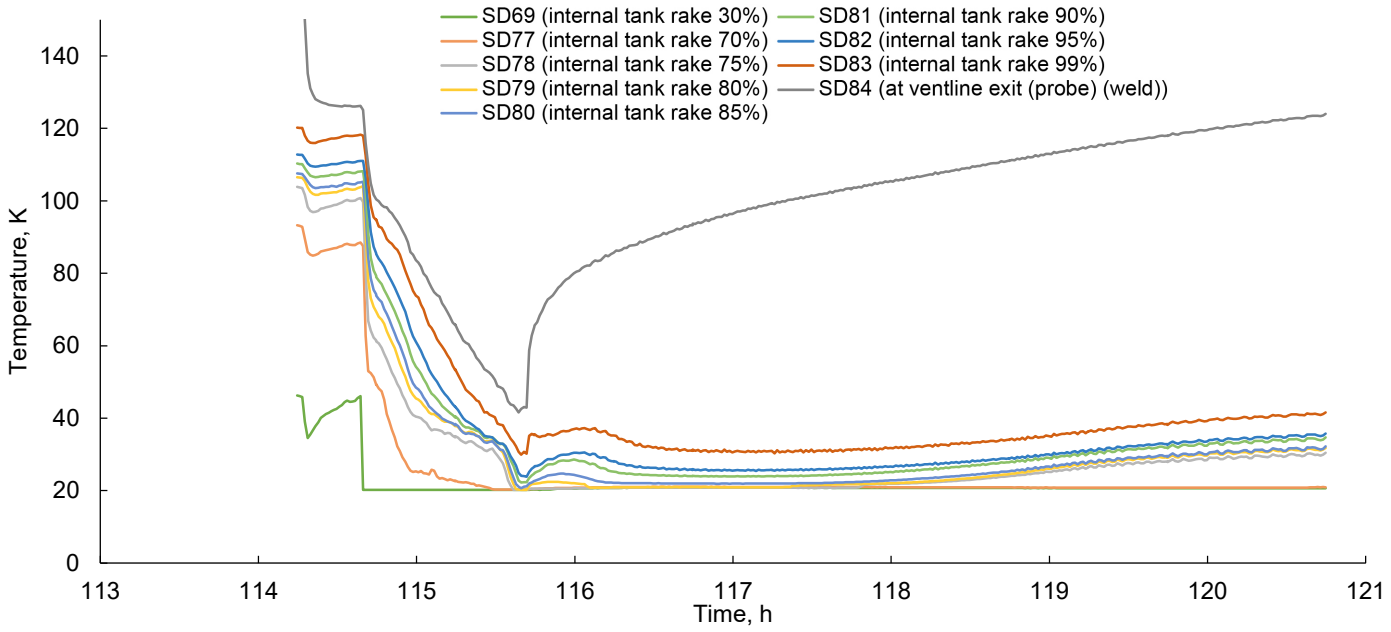

Figure 51.—Vapor temperatures during second high-fill vapor-cooling test.

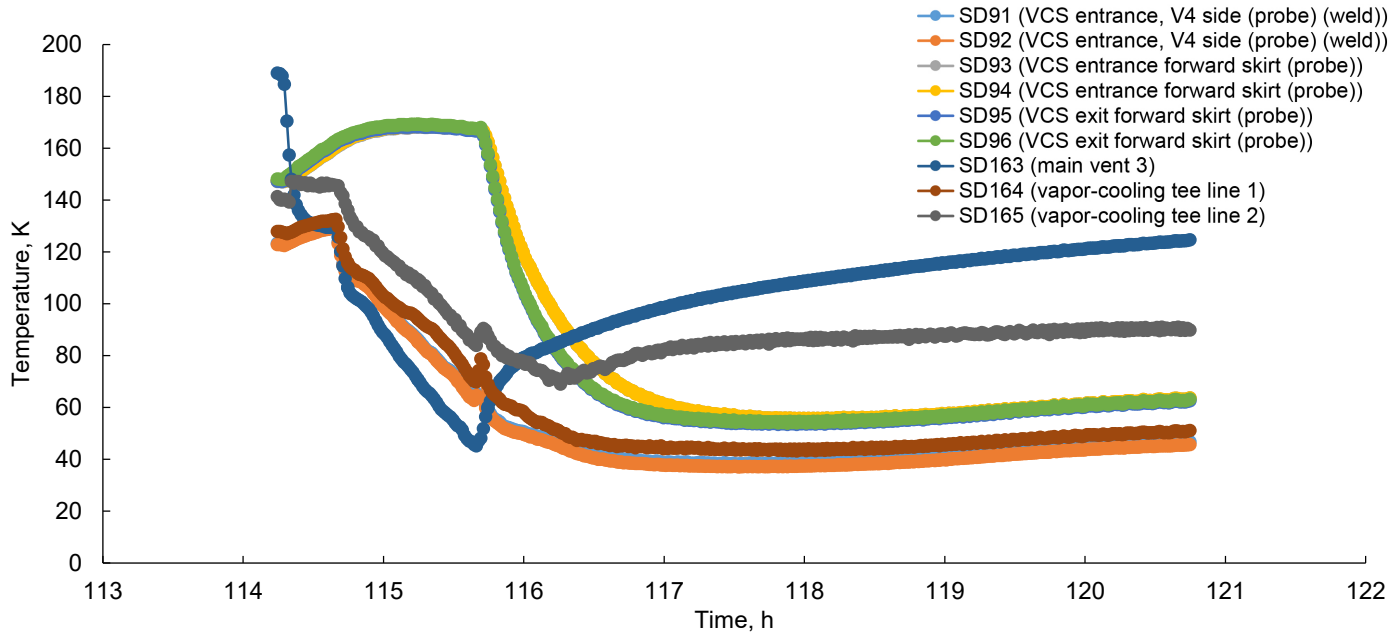

Figure 52.—Vapor-cooling loop temperatures during second high-fill vapor-cooling test. Vapor-cooling system (VCS).

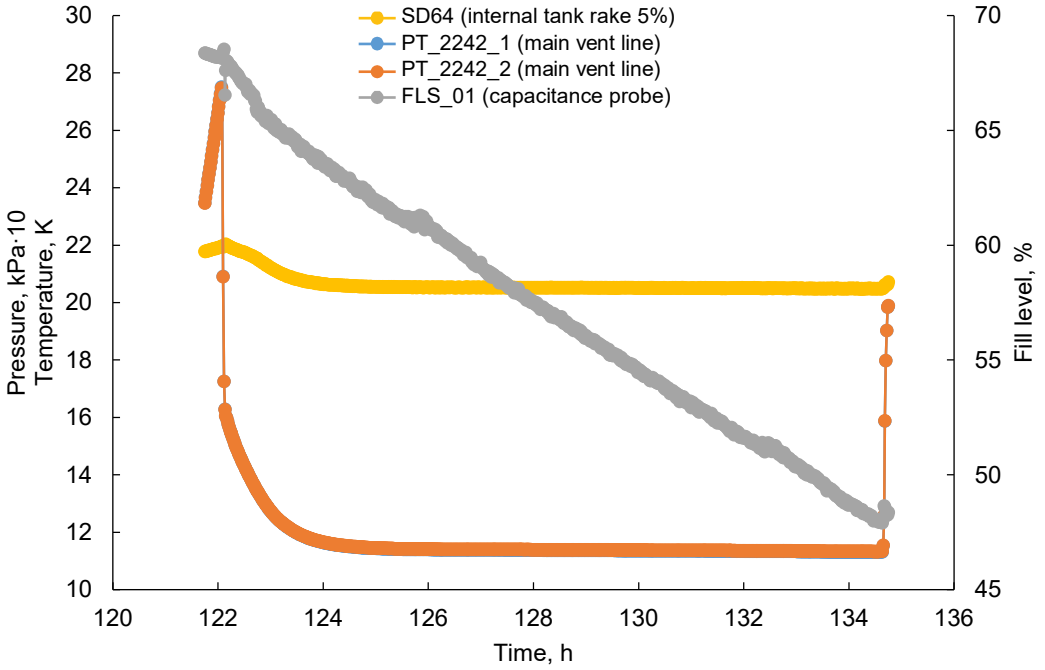

Figure 53.—Pressure and bulk fluid temperature during second vapor-cooling testing from 70 to 50 percent.

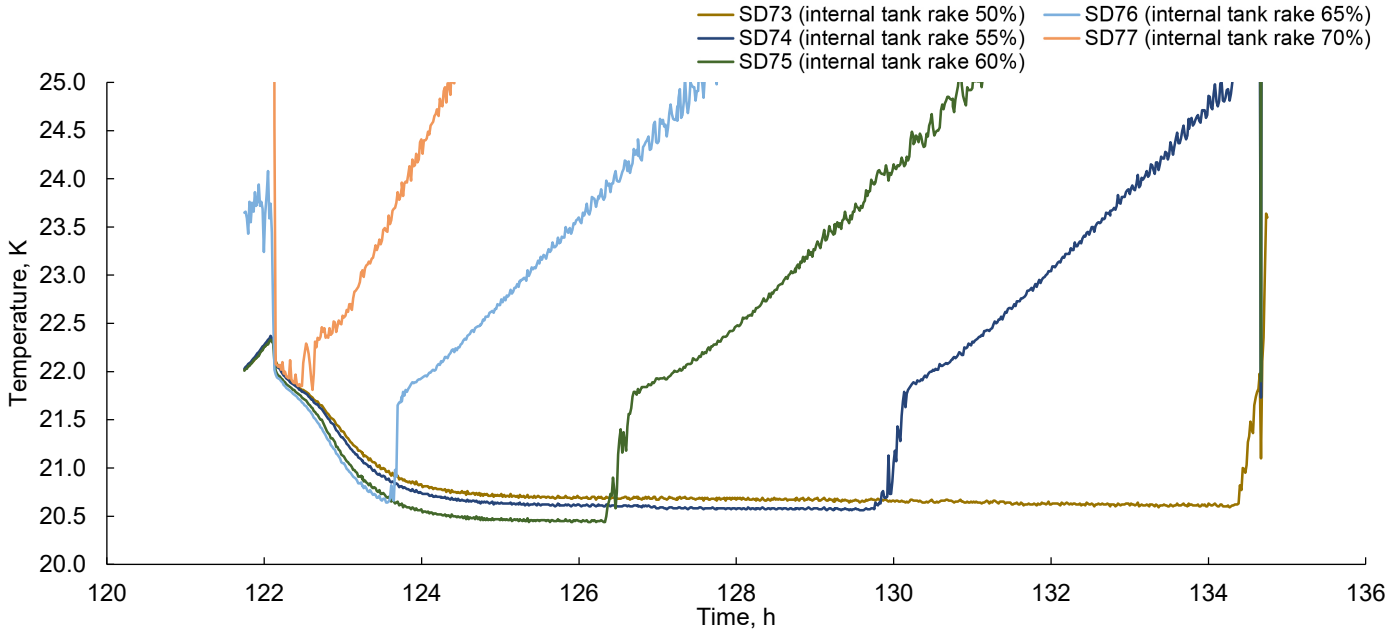

Figure 54.—Liquid temperatures during second medium-fill vapor-cooling test.

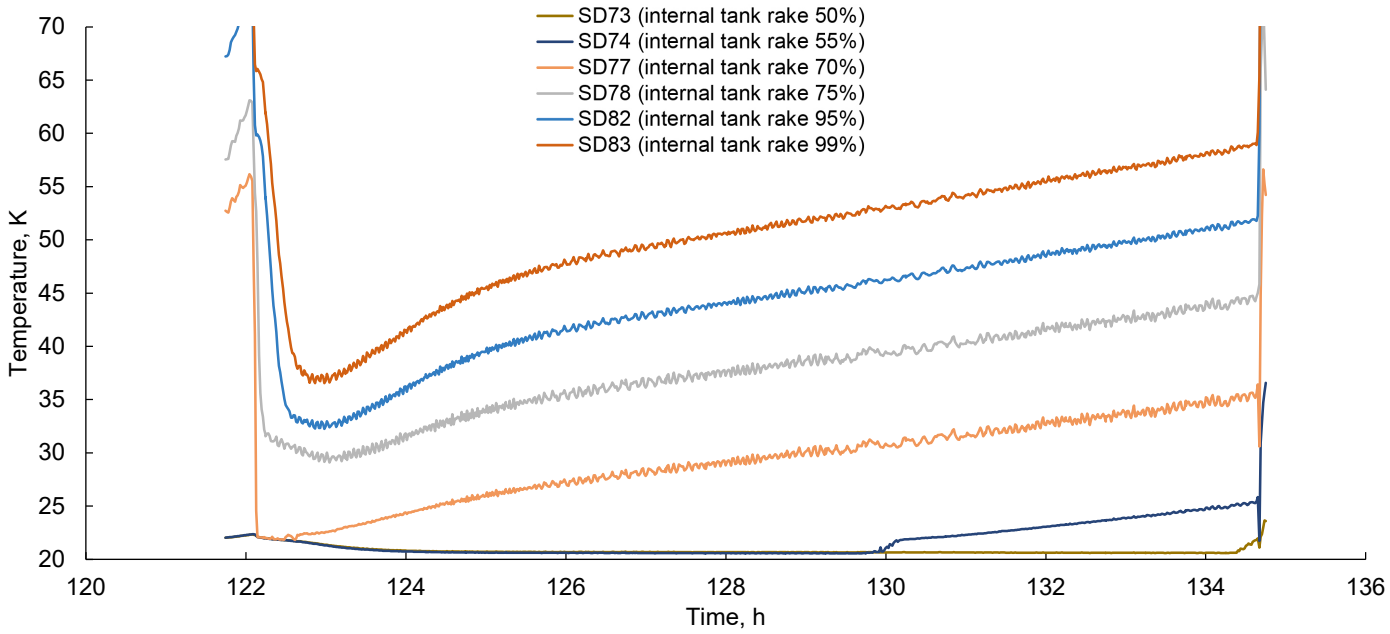

Figure 55.—Vapor temperatures during second medium-fill vapor-cooling test.

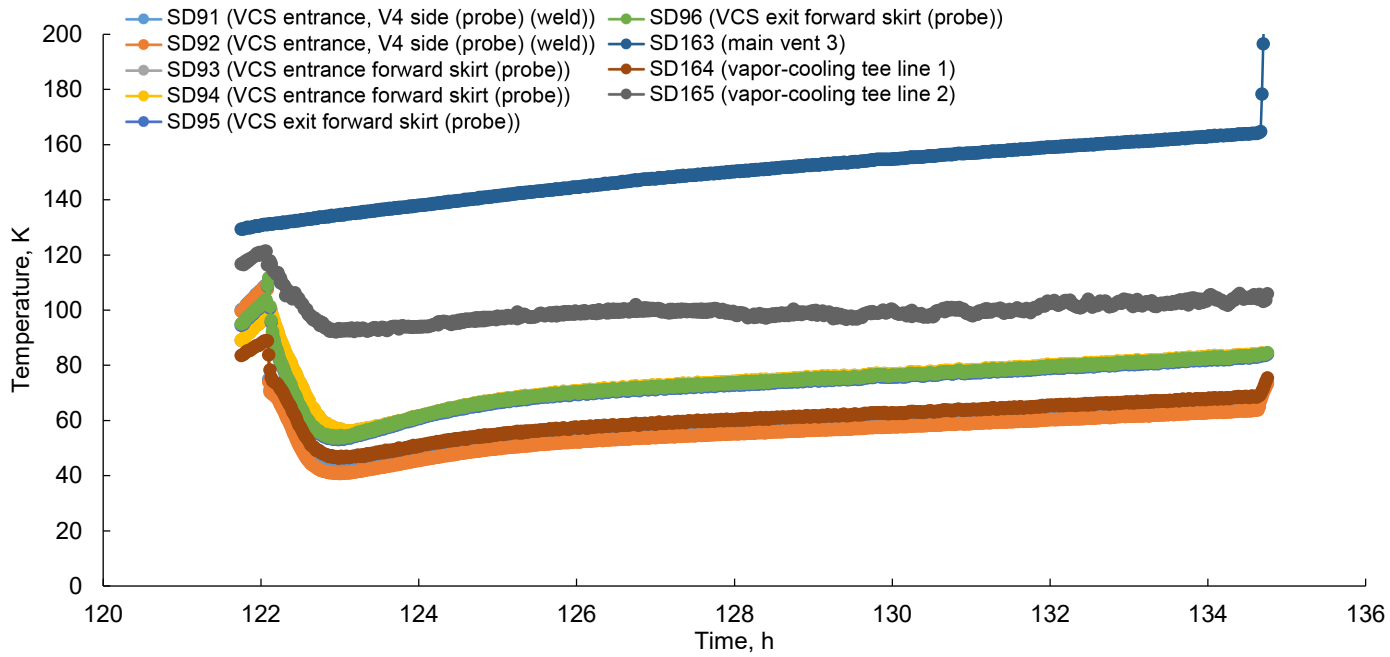

Figure 56.—Vapor-cooling loop temperatures during second medium-fill vapor-cooling test. Vapor-cooling system (VCS).

4.1.3 Pressure Rise Testing

Pressure rise testing was conducted at approximately 70 percent fill for both the boiloff and vapor-cooling testing. Figure 57 shows the results of the pressure rise test conducted in between boiloff testing, while Figure 58 displays the fluid temperatures for that same pressure test. Figure 59 shows pressure rise during an initial attempt of a pressure rise test in between vapor-cooling tests. A pressure sensor anomaly occurred during the test, briefly opening the vent line. This was corrected and the test was able to proceed. However, this caused the team to repeat the test (see Figure 60 to Figure 62). A pressure rise test was also completed at 50 percent full during the vapor-cooling testing as shown in Figure 63. Table 17 shows the pressure rise rates for each of the pressure rise tests. It can be clearly seen that the pressure rises more slowly in vapor-cooling tests than the boiloff tests. This can be explained by the skirt temperatures. Figure 64 shows that the skirt temperatures do not vary with time during boiloff testing and the skirt is at steady state. Figure 65 shows the skirt temperatures for vapor-cooling testing. The vapor cooling reduces the temperatures in the skirt, and it is initially quite cold. The skirt absorbs the heat coming in during the pressure rise testing and warms up, thereby significantly decreasing the heat load to the tank and the pressure rise rate. The pressure rise rates of the two repeated vapor-cooling tests were essentially the same.

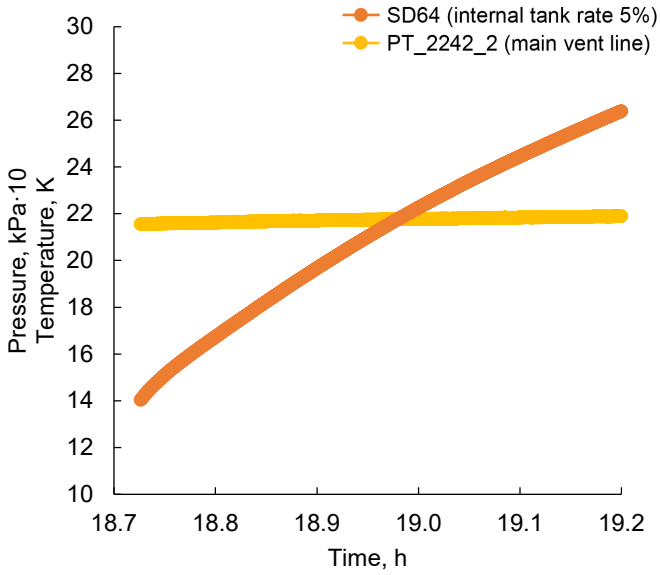

Figure 57.—Pressure and bulk liquid temperature during baseline pressure rise test.

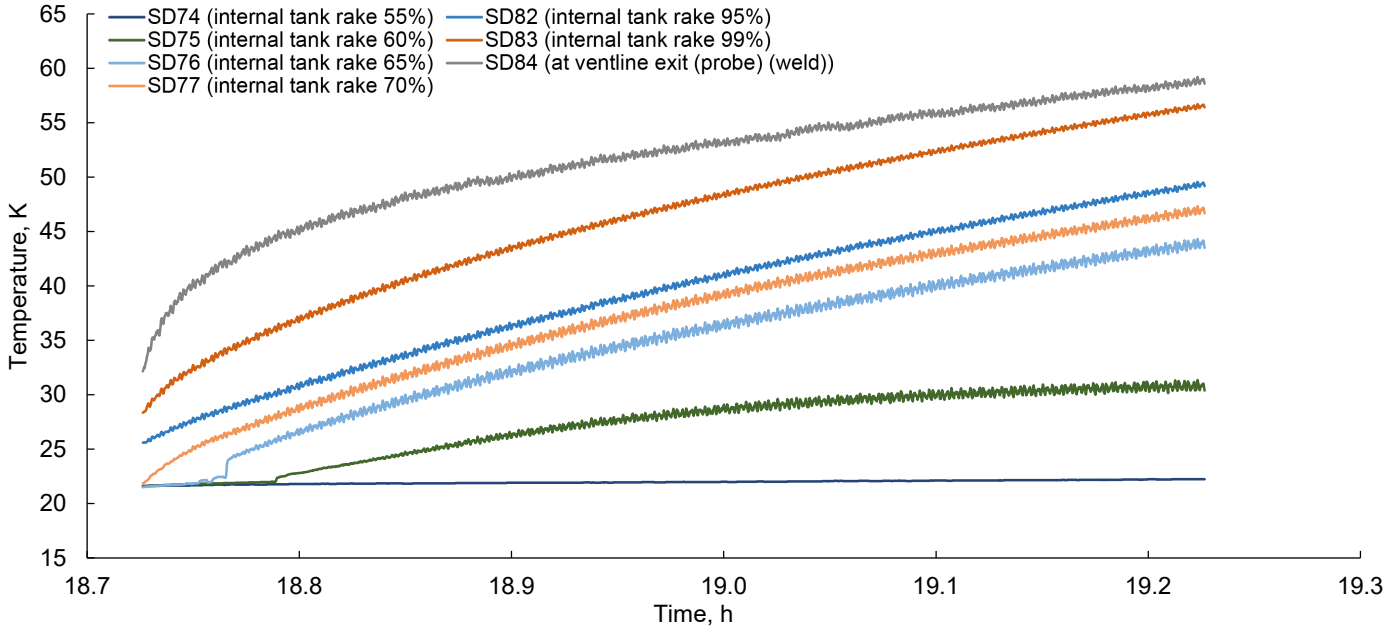

Figure 58.—Liquid and vapor temperatures during baseline pressure rise test.

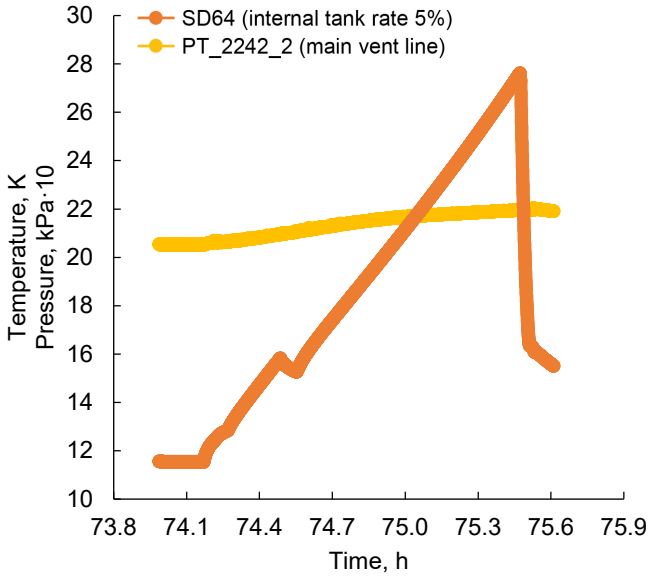

Figure 59.—Initial pressure rise test in between vapor-cooling tests. Pressure sensor anomaly at 74.5 h briefly caused vent valve to open disturbing test.

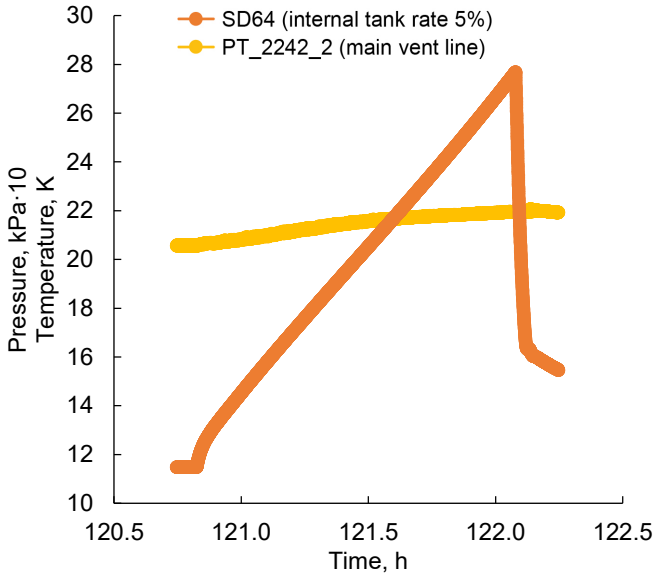

Figure 60.—Second (repeat) pressure rise test in between vapor-cooling tests at approximately 70 percent full.

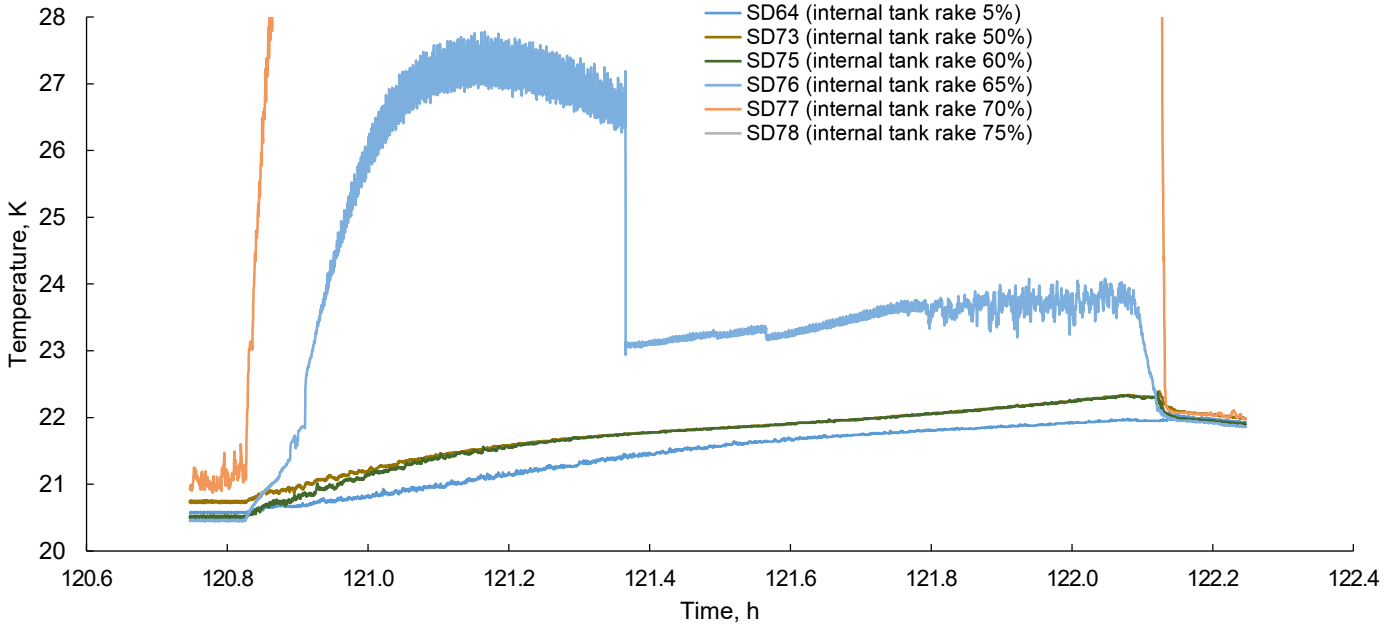

Figure 61.—Liquid temperatures during pressure rise testing between two vapor-cooling tests.

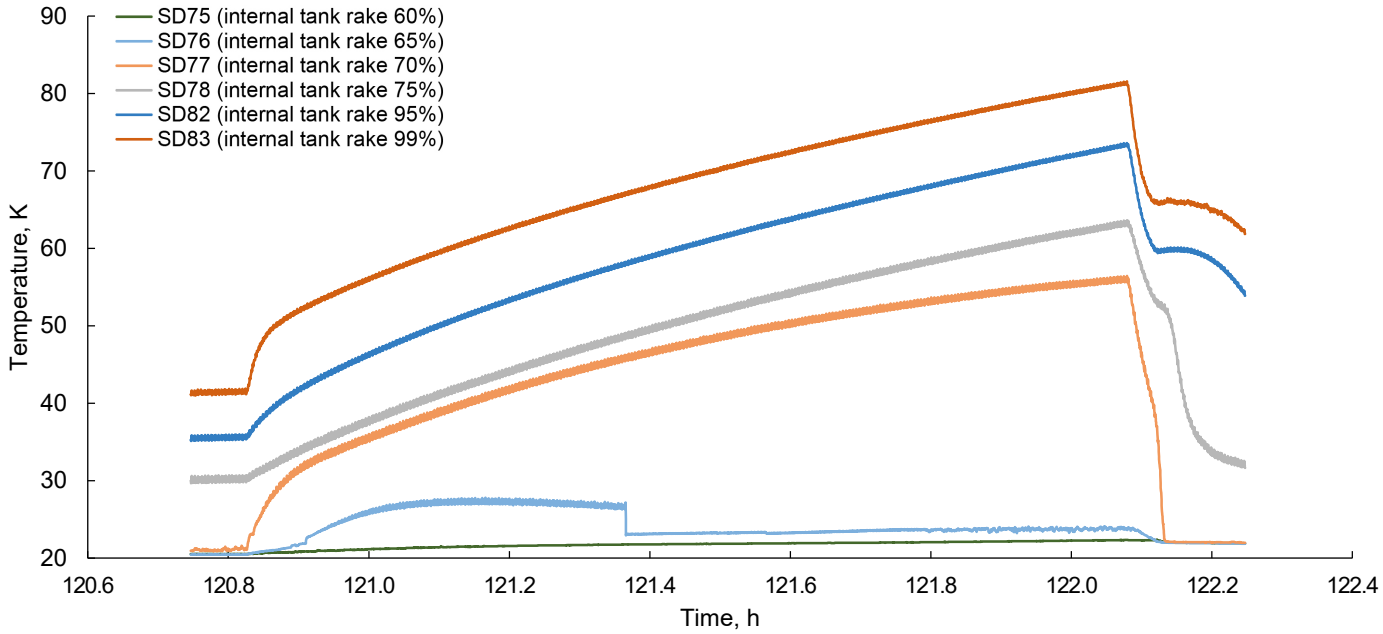

Figure 62.—Vapor temperatures during pressure rise testing between vapor-cooling tests.

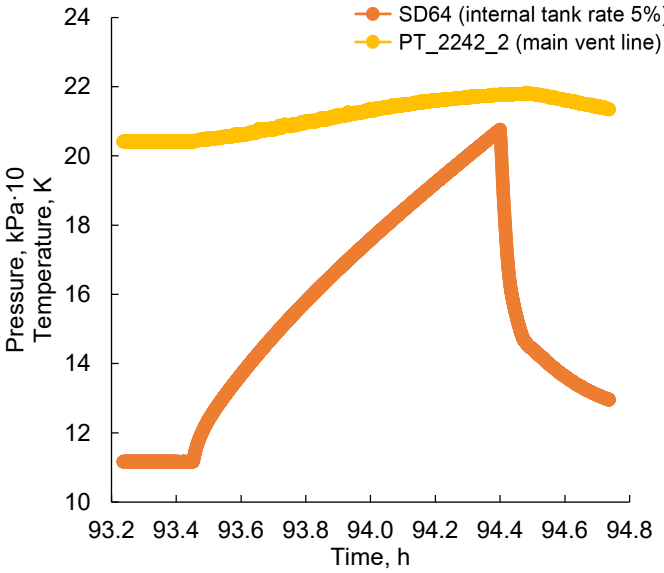

Figure 63.—Pressure rise test at 50 percent fill in between vapor-cooling tests.

TABLE 17.—RESULTS FROM PRESSURE RISE TESTS

Pressure rise test	Start time, h	End time, h	Start pressure, kPa	End pressure, kPa	Duration, h	dP,[a] kPa	dP/dt,[b] kPa/h
Boiloff	18.73	19.26	139.7	274.4	0.53	134.7	254.2
Vapor cooling	74.56	75.47	154.3	276.1	.91	121.7	133.8
Vapor cooling 2	120.83	122.08	114.9	274.9	1.25	160.0	128.0
Vapor cooling 50	93.45	94.4	111.5	207.3	.95	95.8	100.9

[a]Differential pressure (dP).

[b]Differential time (dt).

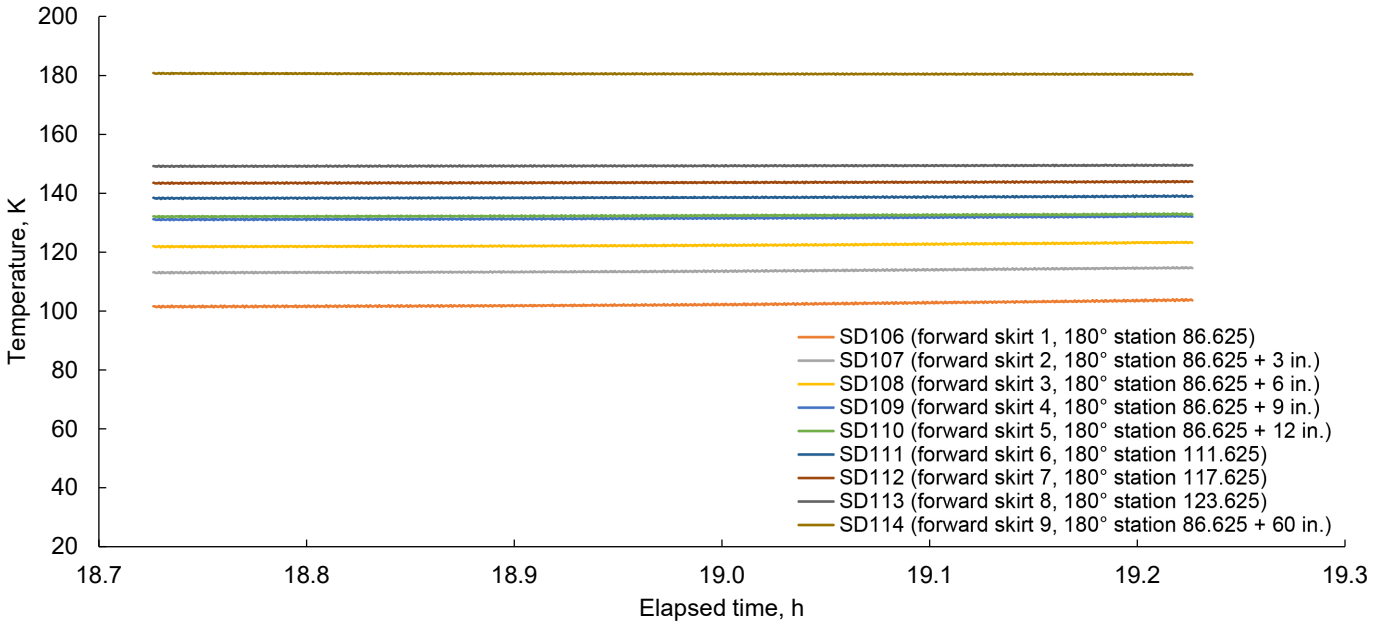

Figure 64.—Skirt temperatures at 180° location during pressure rise test in between boiloff tests.

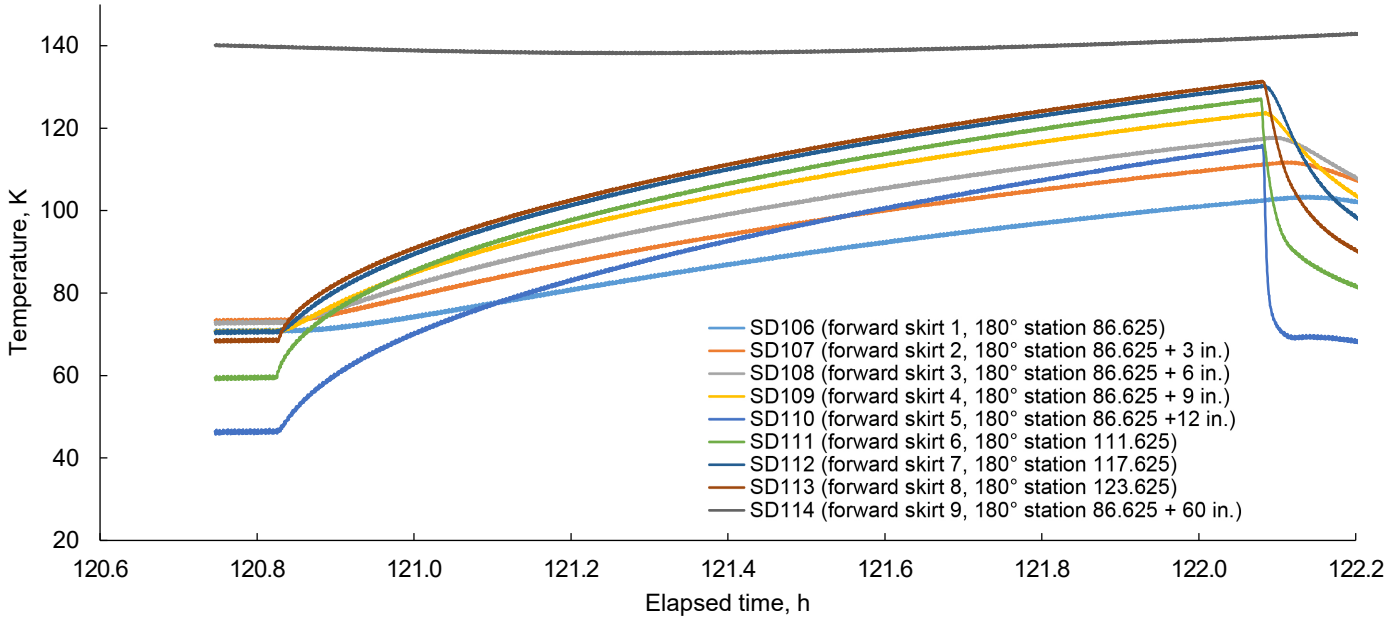

Figure 65.—Skirt temperatures at 180° location during pressure rise test in between vapor-cooling tests.

4.1.4 Posttest Inspection Results

After testing was completed, the test team reentered the vacuum chamber and inspected the test article. No damage was observed on any lines or instrumentation. The MLI was then installed on the domes for the next test. Prior to starting the next test, the flowmeters were all serviced by the vendor to address the performance issues experienced in baseline testing.

4.2 Preacoustic Test—Liquid Hydrogen

The preacoustic LH_2 test started on Sept. 23, 2019, at approximately 7 a.m. EST and consisted of two main test runs: (1) boiloff and (2) vapor-cooling. The preacoustic LH_2 test series was completed on Oct. 1, 2019, at approximately 5:30 p.m. EST, with a total test duration of over 200 h. A brief summary of the preacoustic test events is given below while more details are provided in Sections 4.2.1 to 4.2.4.

1. Boiloff testing: To start, the SHIIVER tank was filled with LH_2 and allowed to sit for approximately 8 h before being topped off with LH_2 at a fill level greater than 90 percent. With the tank chilled in, it was then allowed to boiloff, with the vent flow routed through the main vent line until the tank reached approximately 70 percent fill. At this point, a self-pressurization test was performed from approximately 138 kPa (20 psia) to 276 kPa (40 psia). Following the self-pressurization test, the pressure vented to 138 kPa (20 psia) and boiloff testing continued to approximately 50 percent fill. Next, all the tank valves were closed again, and a second self-pressurization test was performed from 138 kPa (20 psia) to 276 kPa (40 psia). The pressure was returned to 138 kPa (20 psia) and boiloff testing continued to less than 25 percent fill. A third self-pressurization test was completed at approximately 25 percent, after which the pressure was allowed to return to 138 kPa (20 psia) and run for a few hours prior to refilling the tank for the next test series.
2. Vapor-cooling testing: At this point, the SHIIVER tank was topped off again and the vapor-cooling loops opened as a second vent line. After a 6-h chilldown period and another topoff, all the boiloff gas was routed through the vapor-cooling circuit and the liquid allowed to boiloff to approximately 70 percent fill. Next, a pressure rise test was performed from just under 138 kPa (20 psia) to 276 kPa (40 psia). The tank was vented to 138 kPa (20 psia) and boiloff testing with the vapor routed through the vapor-cooling network continued until 50 percent was reached. At 50 percent full, a cyclical pressure rise test was completed consisting of three self-pressurization tests from approximately 117 kPa (17 psia) to 172 kPa (25 psia) followed by depressurization back to 117 kPa (17 psia). The vapor-cooling test was then continued until the fill level was less than 25 percent.

During the testing, vacuum pressure was maintained in the 10^{-6} torr range as seen in Figure 66. While there were a few excursions due to opening various valves, the nominal pressure was 3.3×10^{-5} torr. As stated above, the IG data is for reference only as it was calibrated in air. The vacuum pressure was lower due to repairs done on the valves to reduce the leakage at the actuators. The spikes in pressure (nonsingle point) are indicative of valve position changes within the chamber. The cold wall temperature was consistently in the range of 291 K (65 °F) to 294 K (70 °F) as shown in Figure 67.

As mentioned before, prior to the preacoustic LH_2 testing, the flowmeters were all serviced by the vendor to attempt to solve the issues with their readings. This appeared to correct the vapor-cooling flowmeter; however, the large flowmeter on the vent line, while reading, was inconsistent (reading high) when the flow was going through multiple flowmeters. Additionally, all flowmeters had relatively high (~0.5 to 2 g/s) flow cutoff rates,[3] which was realized when the liquid-vapor interface crossed the aft flange.

All times during the preacoustic LH_2 testing are referenced to 7:14:23 a.m. EST on Sept. 23, 2019.

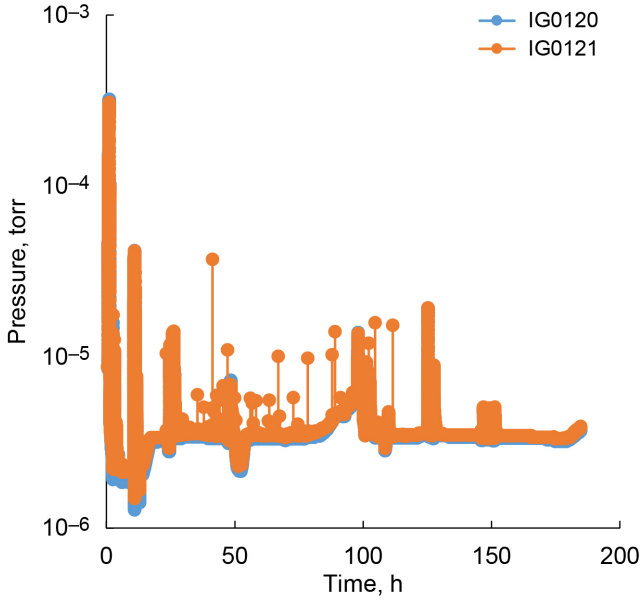

Figure 66.—Vacuum pressure for liquid hydrogen preacoustic testing.

[3]The flow rate at which the flowmeter stopped reading.

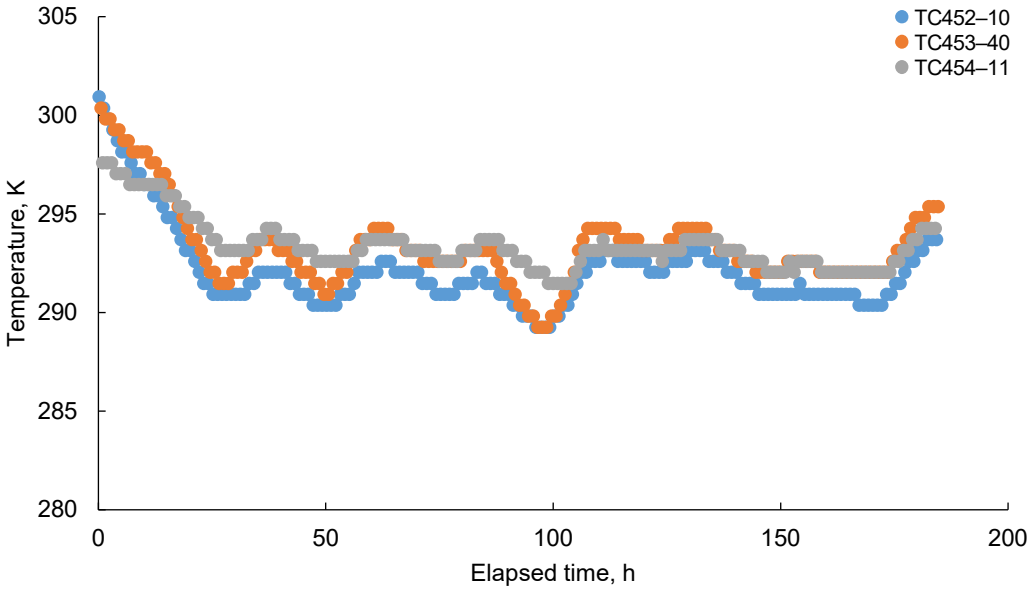

Figure 67.—Cold wall temperatures for liquid hydrogen preacoustic test.

4.2.1 Boiloff Testing

During the boiloff testing, all flowmeters worked and registered values. However, it was noticed that the largest flowmeter, FM2, read with a slight offset from the one used during the baseline test, FM3. As such, both flowmeters were used during the initial testing window at high fill levels. The pressure rise due to lack of pressure control was similar to the baseline test, but the magnitude was less due to the lower heat load going into the system (see Figure 68 to Figure 70). The peak pressure was 200 kPa (29 psia). During the testing, it became obvious that there was very little (if any) stratification in the ullage. Additionally, it was not easy to determine when diodes in the rake transitioned from wet to dry (see Figure 70) while the liquid level was above the forward flange. The capacitance probe was set assuming 92 percent was the maximum fill level observed (the 0 to 10 V signal was multiplied by 0.92 in the data system).

Once the liquid level dropped below the forward flange, the behavior of the system changed. For the first half of the testing, the pressure was controlled to 138 kPa (20 psia) with the boiloff flow going through FM2 only (see Figure 71 and Figure 72). At 39 h, FM3 was opened up to the flow, and the difference between the two flowmeters was evident (Figure 69). At this point, due to the flow constriction by FM2, the pressure began to rise slightly and reached 147.5 kPa (21.4 psia) before starting to decrease again. In addition, with the large amounts of heat coming into the ullage from both the forward skirt and the barrel (that has SOFI only), the distinct signature of the diodes going from wet to dry reappeared (see Figure 73) and the ullage stratified (see Figure 74). However, in the ullage, the temperatures in the forward dome remained similar, showing little to no stratification in the forward dome itself. Similarly, the forward dome temperatures (see Figure 75) show that SD15 (just below the forward flange), SD16, SD17, and SD21 (top manway) are all essentially on top of each other (SD15 is slightly lower than the others) and have similar, if not lower, temperatures than the diodes in the ullage. This indicates that very little energy flows through the MLI, and furthermore, the forward dome may be receiving heat from the ullage.

After the 50 percent pressure rise test, the boiloff test data to 25 percent is summarized in Figure 76. The pressure was controlled to 138 kPa (20 psia) for the majority of the test after slowly recovering from the pressure rise test. The flowmeter data is shown in Figure 77, and during the entirety of the test, flow is through both FM2 and FM3. The flow was directed through FM4 once FM3 reached its low-flow cut off at 0.75 g/s. However, FM4 also had a low-flow cut off in that range, and therefore, did not provide improvement in measurement. Beyond 65 h, the FM2 data is also in the noise of that flowmeter and is not trustworthy. Figure 78 shows the ullage temperatures during this test. The change in slopes in temperature rise rates just after 75 h is due to the aft skirt flange transitioning from liquid to vapor in contact with it. Figure 79 shows that the liquid temperature is maintained fairly constant and the sharp transitions from wet to dry in the diodes remains. Figure 80 shows the tank wall temperatures. Of interest is where SD15 clearly becomes warmer than SD16, SD17, and SD21 indicating that once the liquid level went below the aft flange, the hottest part of the tank is at the forward flange and heat flows from the forward flange to the top of the tank. Data from the heat flux sensors and MLI temperatures as well as global heat flow information presented in Section 5.0 concur with this assessment.

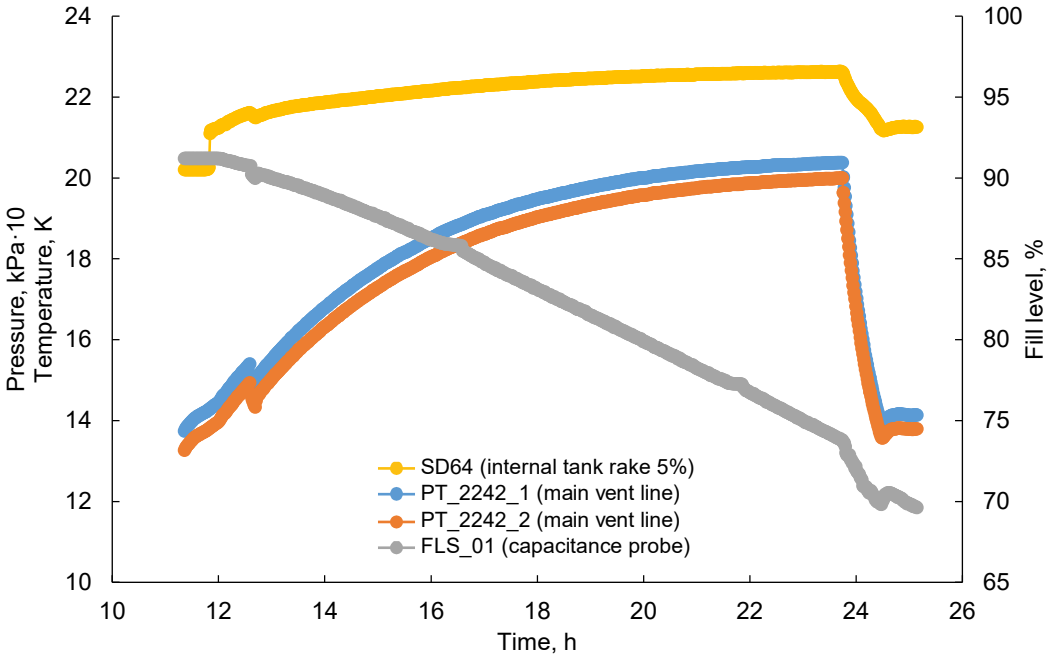

Figure 68.—Tank pressure, liquid bulk temperatures, and fill level for high-fill boiloff test.

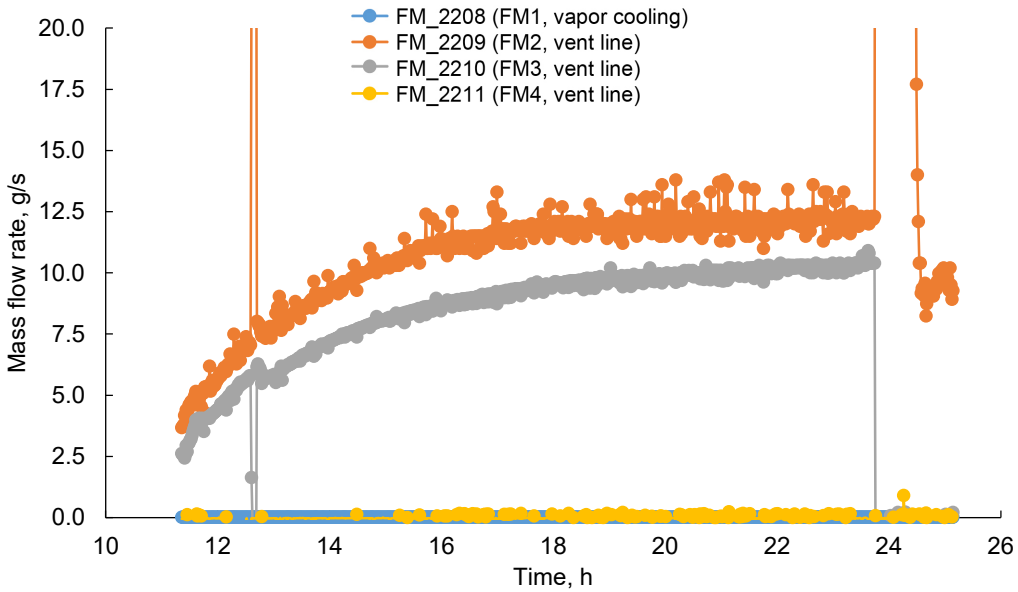

Figure 69.—Boiloff flow rates for high-fill preacoustic liquid hydrogen testing.

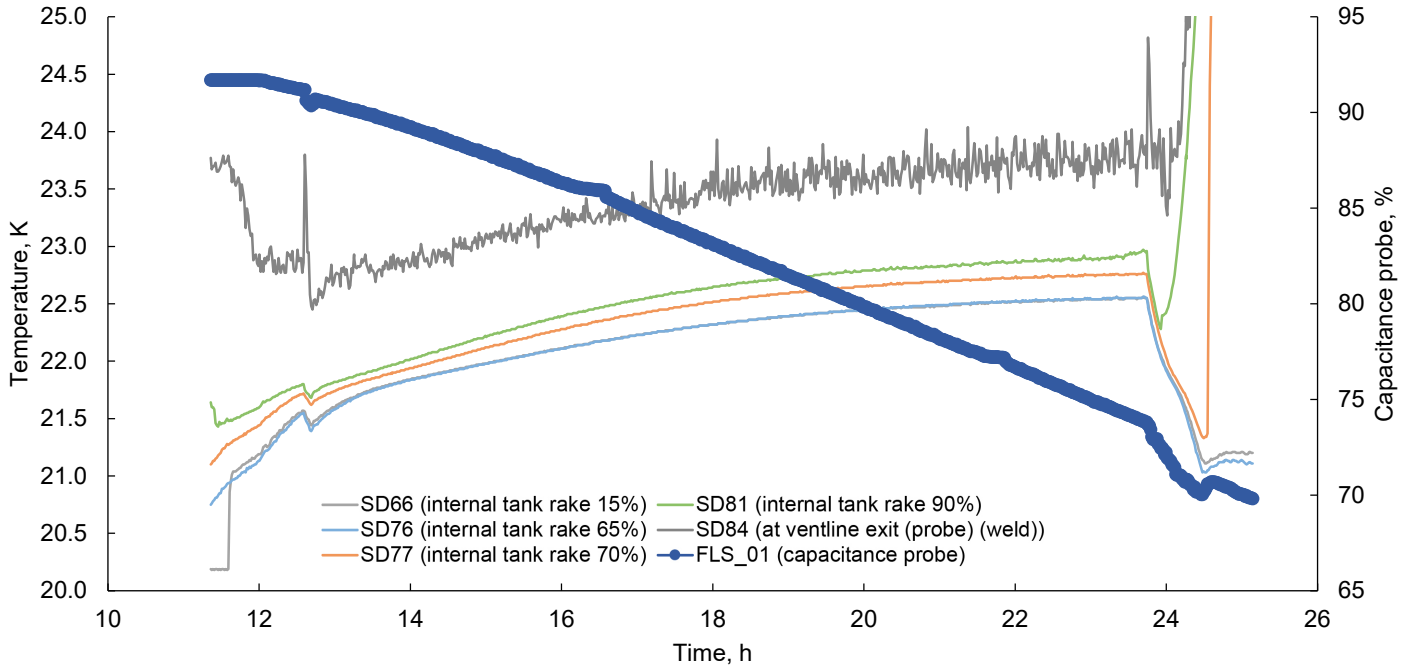

Figure 70.—Fluid temperatures during preacoustic liquid hydrogen testing.

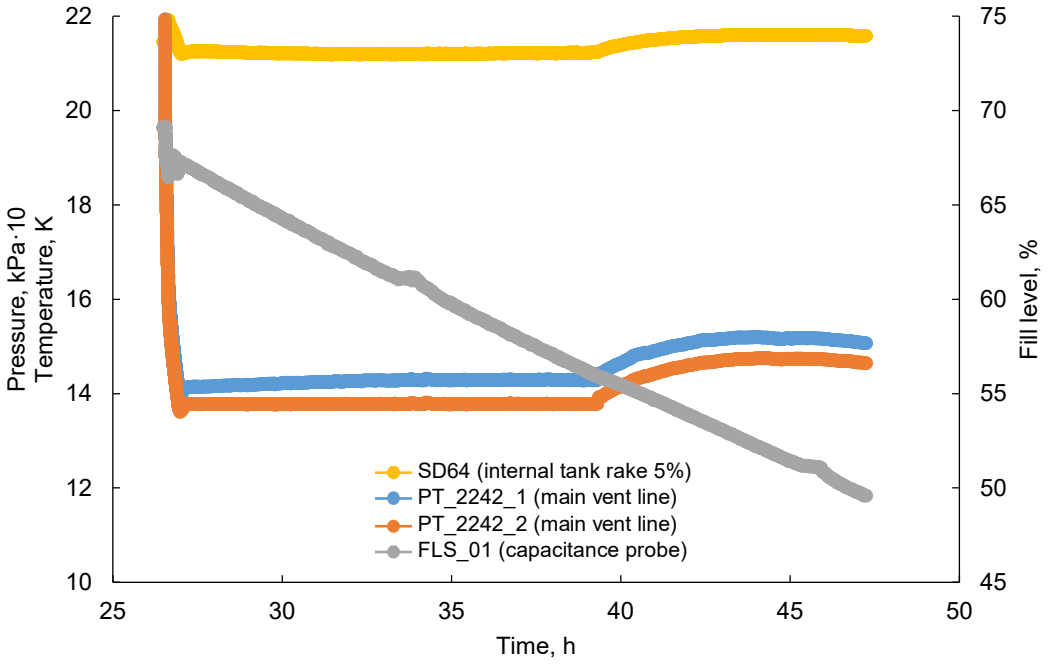

Figure 71.—Tank pressure, liquid temperature, and fill level for preacoustic liquid hydrogen testing between 70 and 50 percent full.

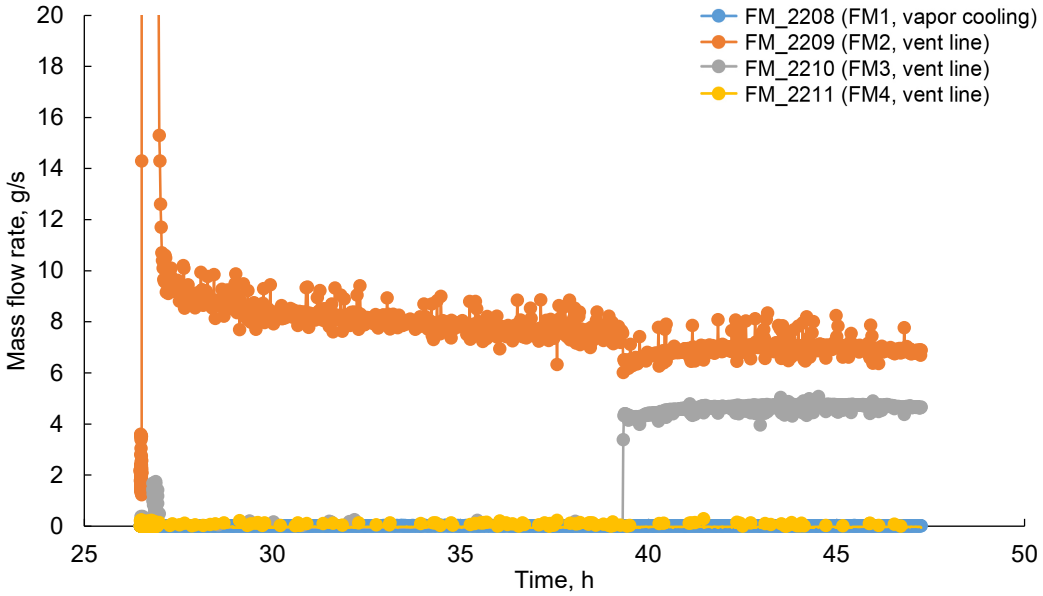

Figure 72.—Flowmeter data from preacoustic testing with liquid hydrogen between 70 and 50 percent.

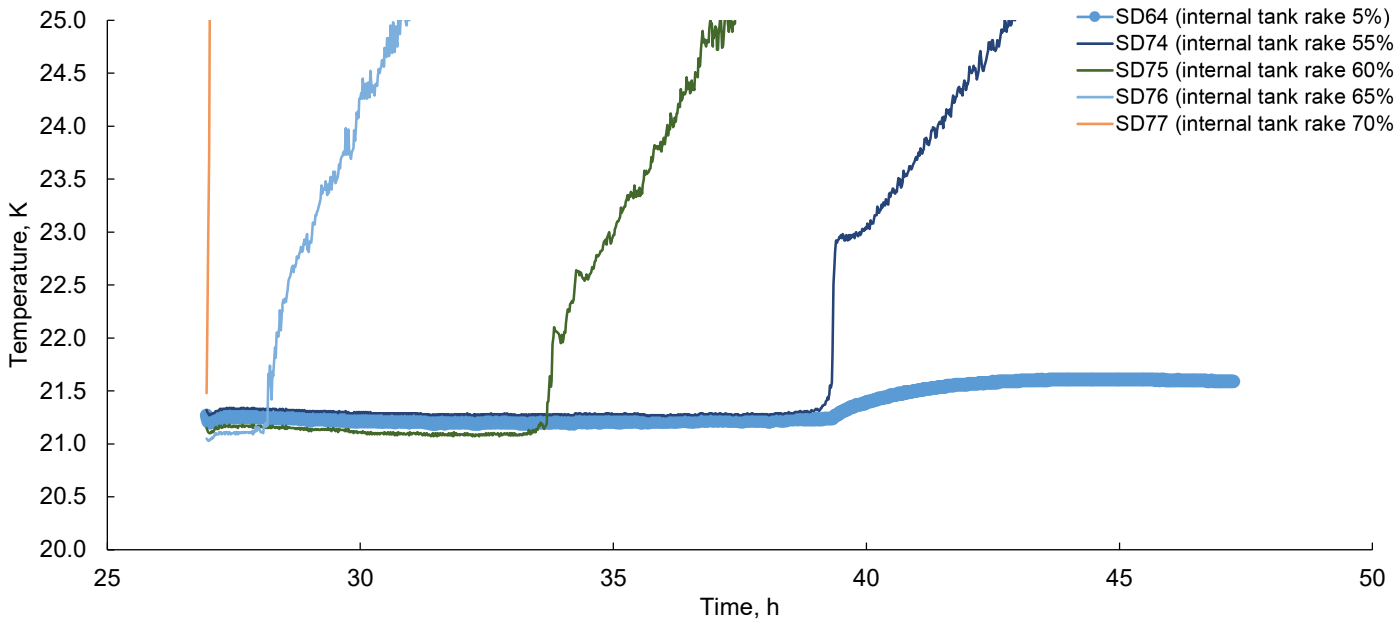

Figure 73.—Liquid temperature data from preacoustic liquid hydrogen testing between 70 and 50 percent full.

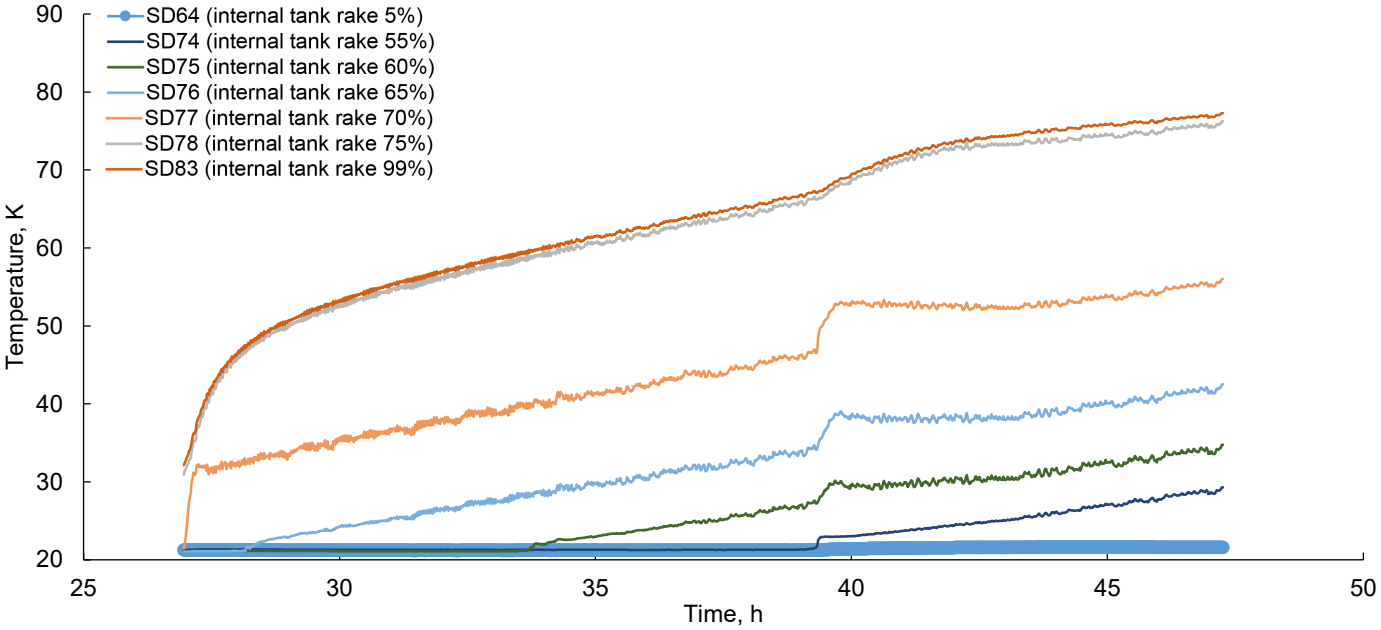

Figure 74.—Ullage temperature data from preacoustic liquid hydrogen testing between 70 and 50 percent full.

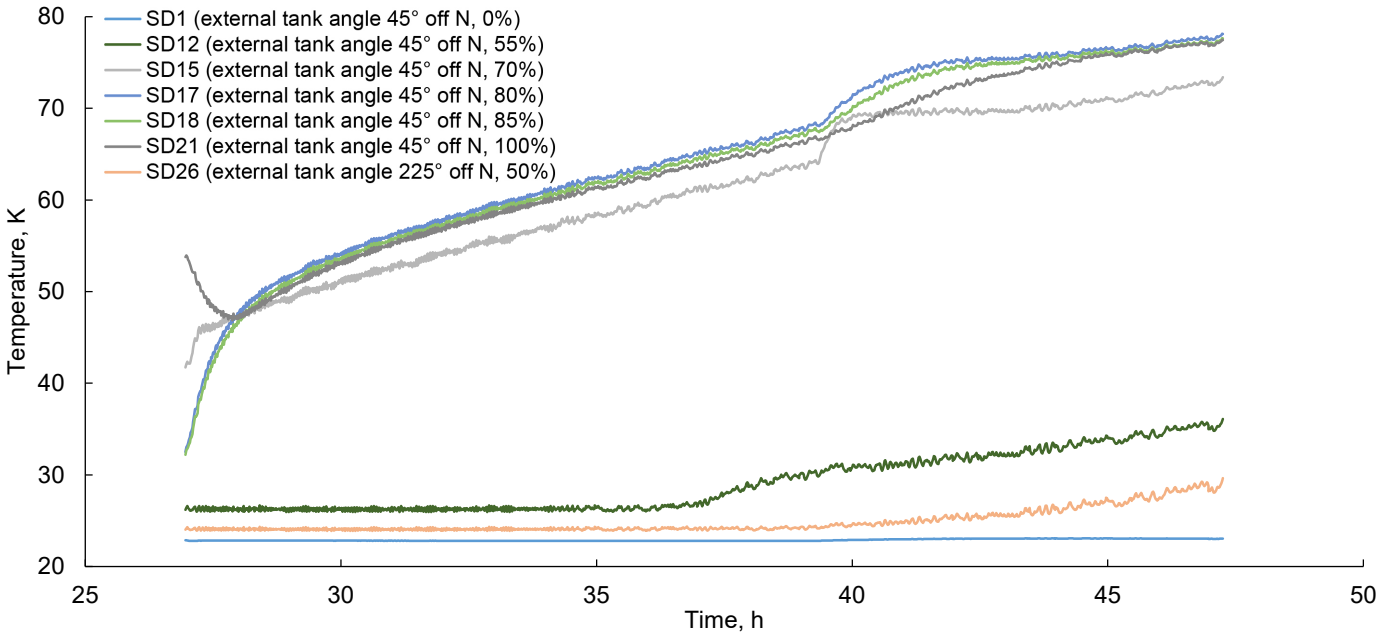

Figure 75.—Tank wall temperature data from preacoustic liquid hydrogen testing between 70 and 50 percent full.

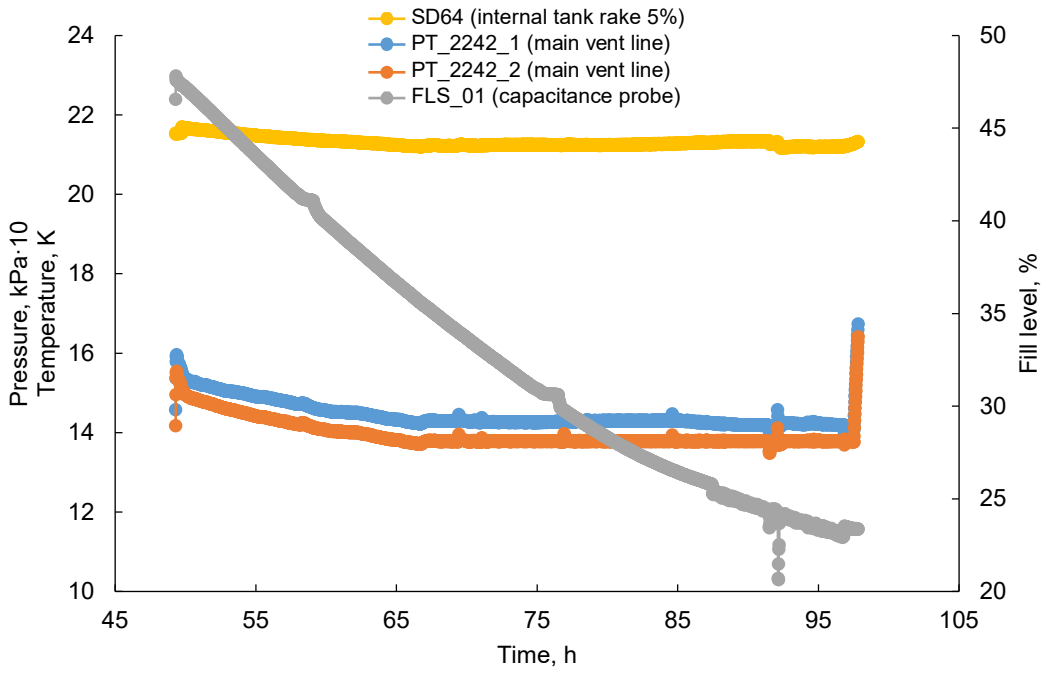

Figure 76.—Tank pressure, liquid temperature, and fill level for preacoustic liquid hydrogen testing between 50 and 25 percent full.

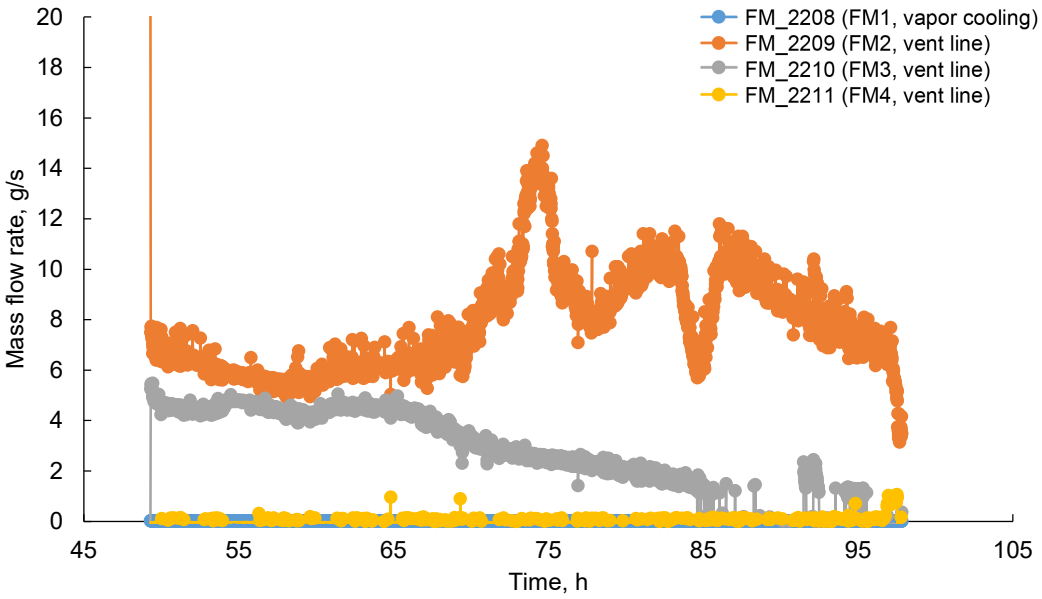

Figure 77.—Flowmeter data from preacoustic testing with liquid hydrogen between 50 and 25 percent full.

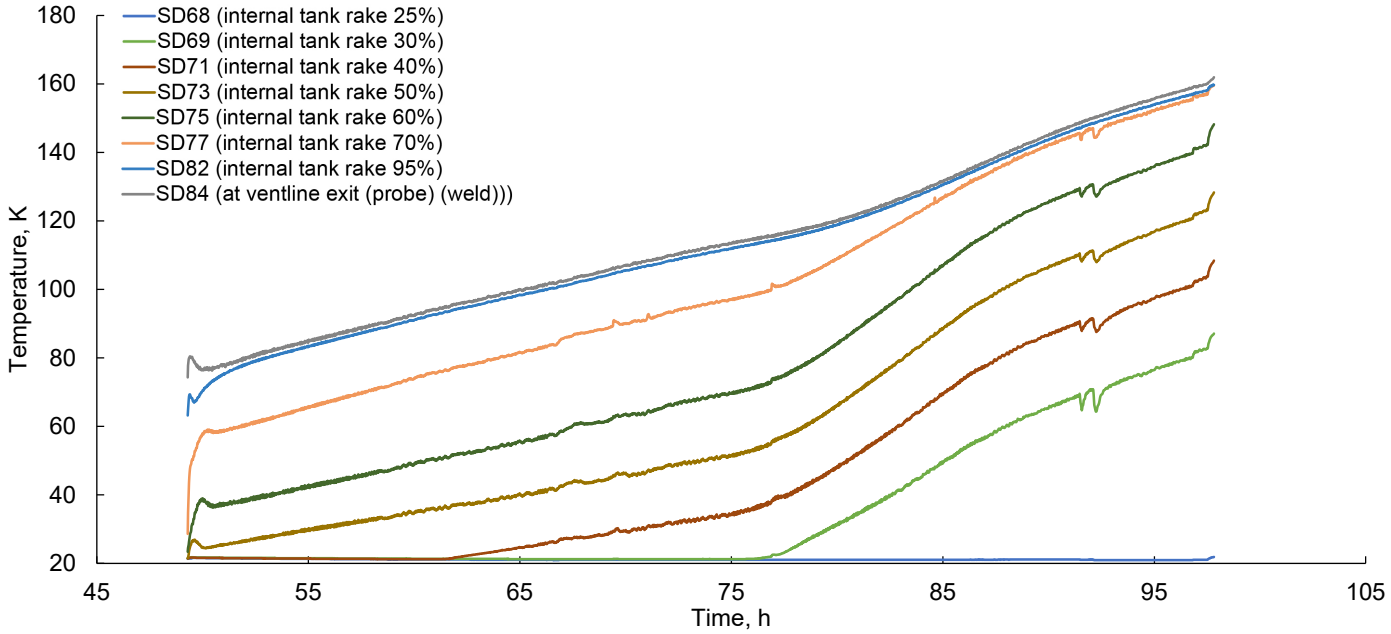

Figure 78.—Hydrogen ullage temperature data from preacoustic testing between 50 and 25 percent full.

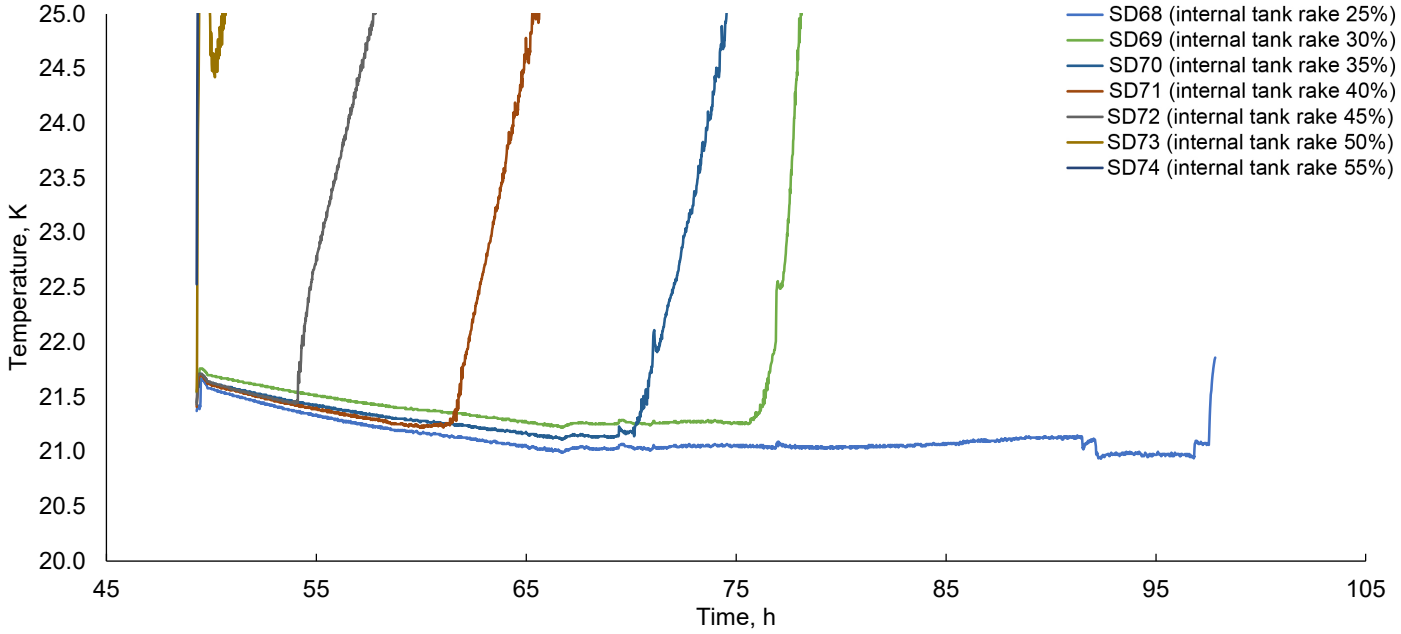

Figure 79.—Liquid temperature data from preacoustic testing with liquid hydrogen between 50 and 25 percent full.

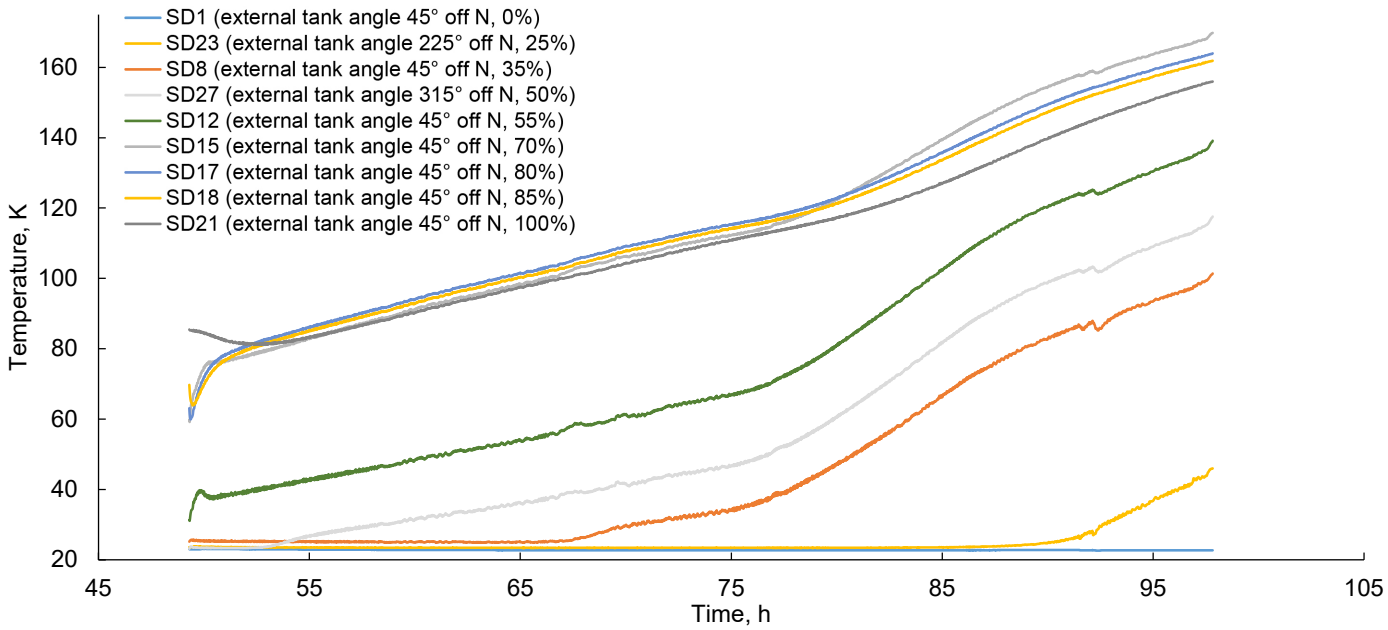

Figure 80.—Tank temperature data from preacoustic testing with liquid hydrogen between 50 and 25 percent full.

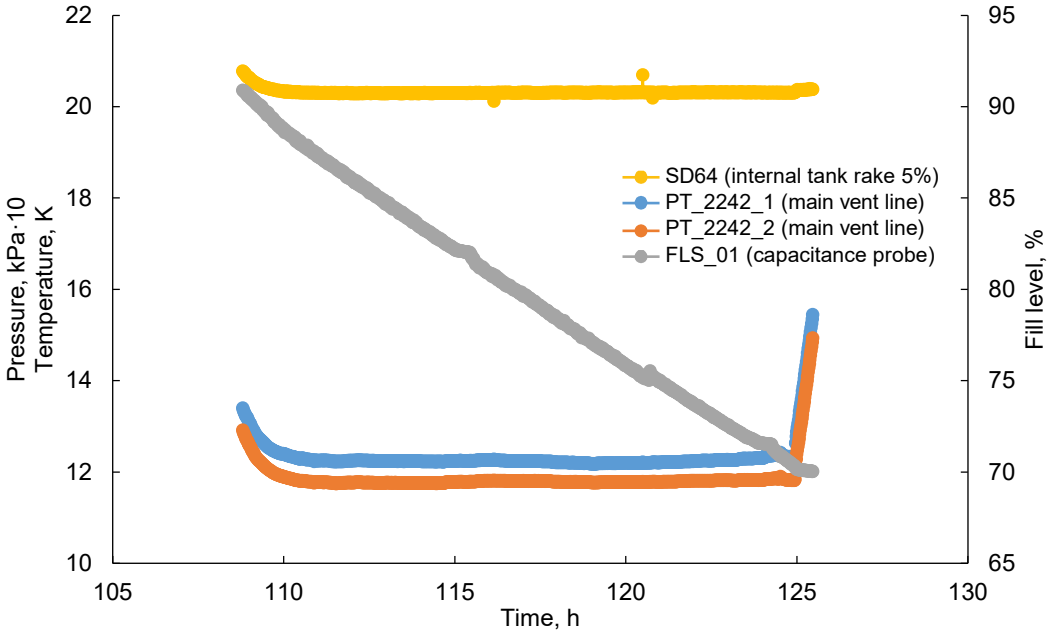

Figure 81.—System pressure and fill level during vapor-cooling test between 90 to 70 percent fill.

4.2.2 Vapor-Cooling Testing

Vapor-cooling testing occurred from approximately 90 to 25 percent fill. The vapor-cooling system had no backpressure control but was instead directly connected to the test facility vent. However, the pressure was nearly constant during testing (see Figure 81). During the initial test period, the vapor-cooling flowmeter, FM1, did not work well as seen in Figure 82. Similar to the boiloff testing, there was essentially no stratification while the liquid vapor interface was in the forward dome (see Figure 83). It should be noted that the forward dome temperatures are slightly colder than those in the boiloff testing. Once the liquid-vapor interface approached the forward flange, the temperatures in the ullage began to show stratification.

During the testing from 70 to 50 percent fill, the pressure remained relatively constant albeit with a slow downward drift as shown in Figure 84. The flowmeter, FM1, finally started working after the initial pressure rise test, as seen in Figure 85, and was relatively constant. As seen in the boiloff test, once the liquid-vapor interface went below the forward flange, the vapor started to stratify (see Figure 86), and there was still minimal temperature gradient across the forward dome. Vapor temperatures were still slightly colder than boiloff testing (see Figure 87).

Figure 88 shows the system pressure during vapor-cooling testing between 50 and 25 percent fill. The pressure remained fairly steady while gradually decreasing. The flowmeter data, shown in Figure 89, confirms that the meter behaved as expected with the exception of the 2 g/s low-flow cutoff encountered at 180 h as the liquid-vapor interface dipped into the aft dome. Fluid temperatures from the same period are shown in Figure 90.

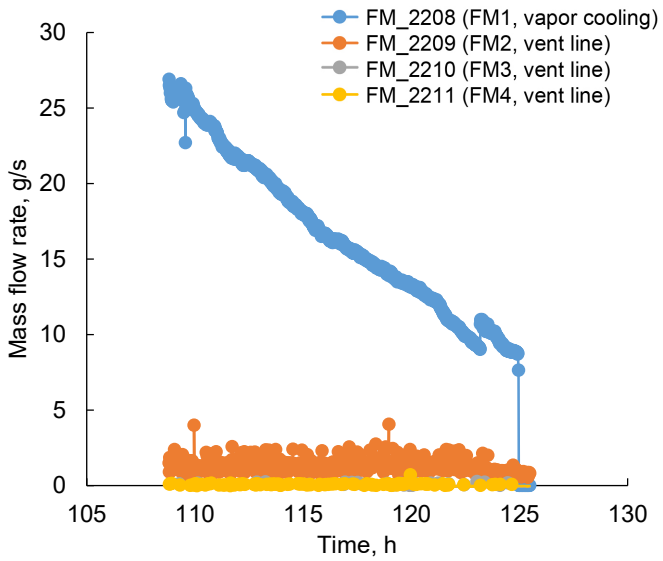

Figure 82.—Flowmeter data during vapor-cooling test between 90 to 70 percent fill.

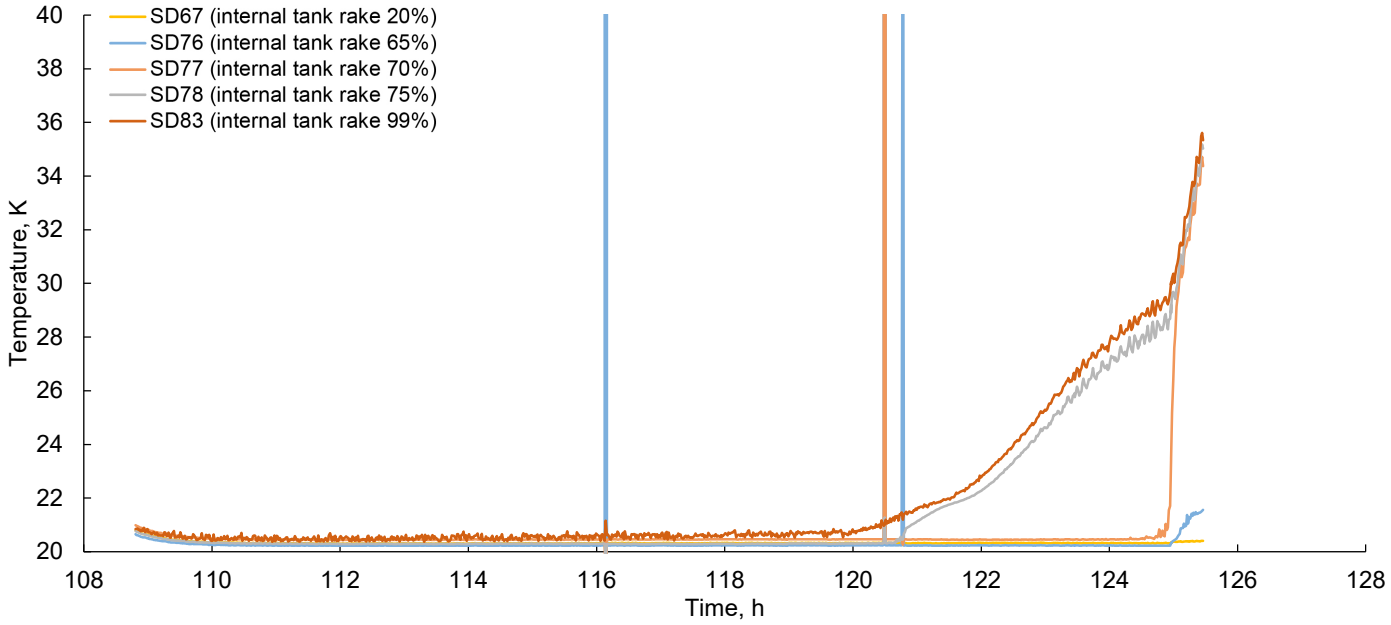

Figure 83.—Fluid temperature data during vapor-cooling test between 90 to 70 percent fill.

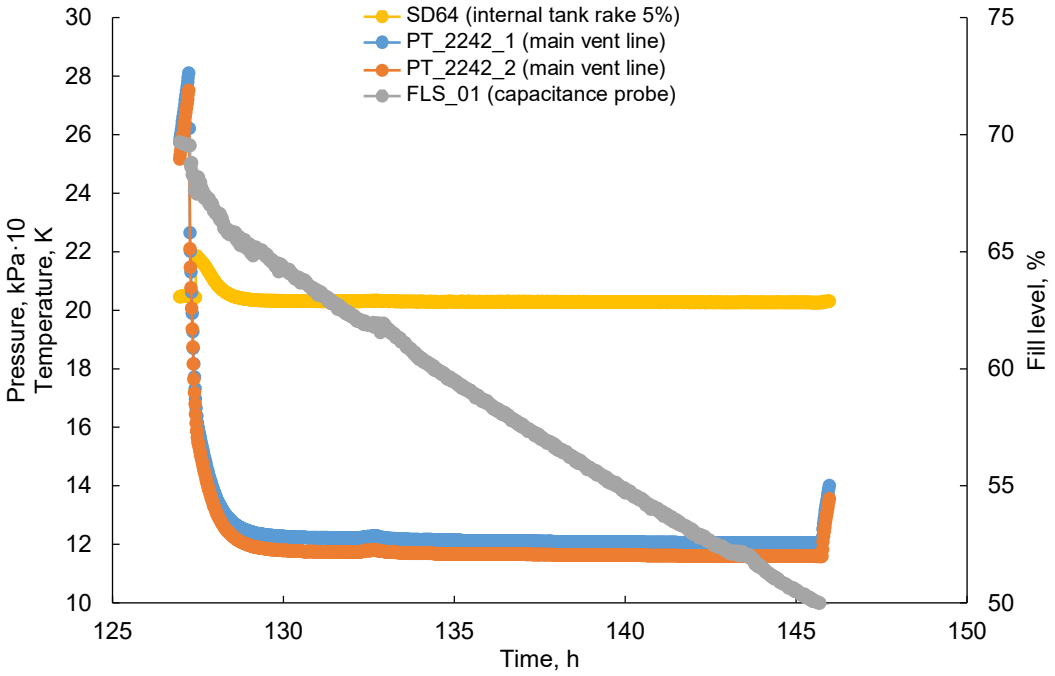

Figure 84.—System pressure and fill level during vapor-cooling test between 70 to 50 percent fill.

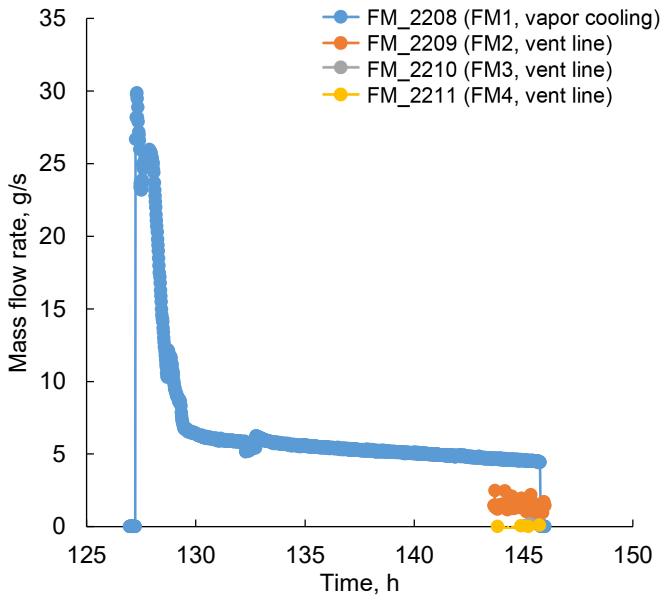

Figure 85.—Flowmeter data during vapor-cooling test between 70 to 50 percent fill.

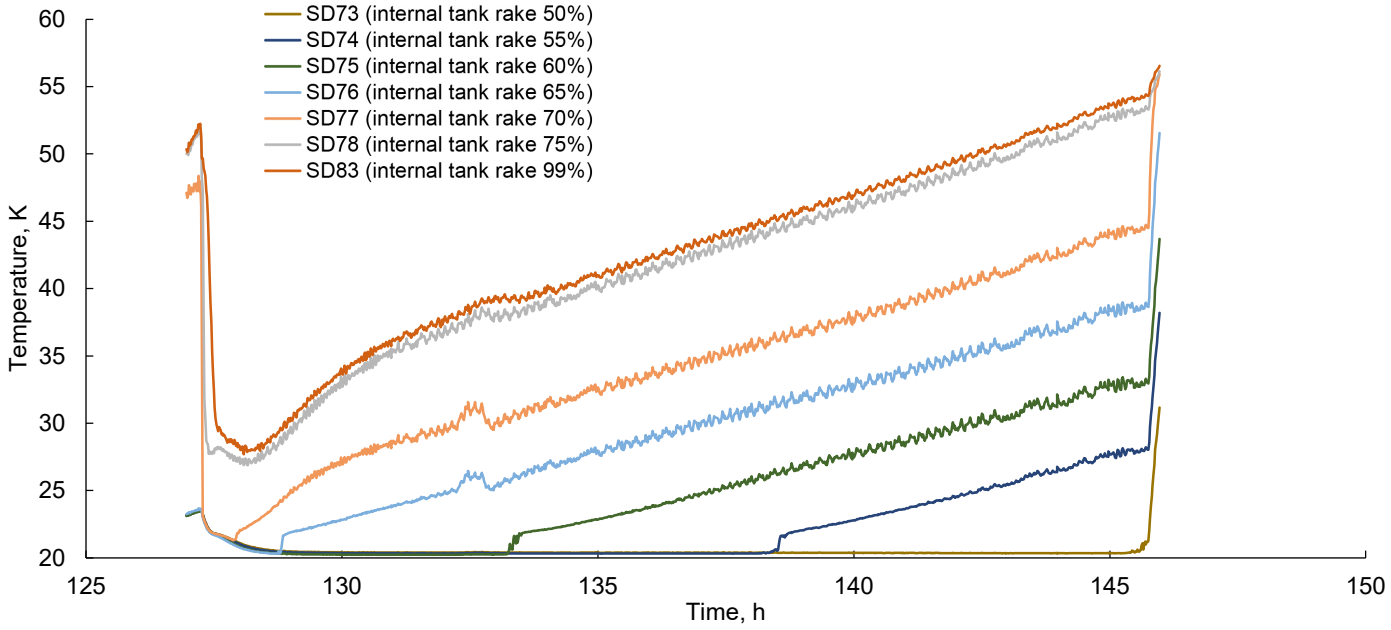

Figure 86.—Fluid temperature during vapor-cooling test between 70 to 50 percent fill.

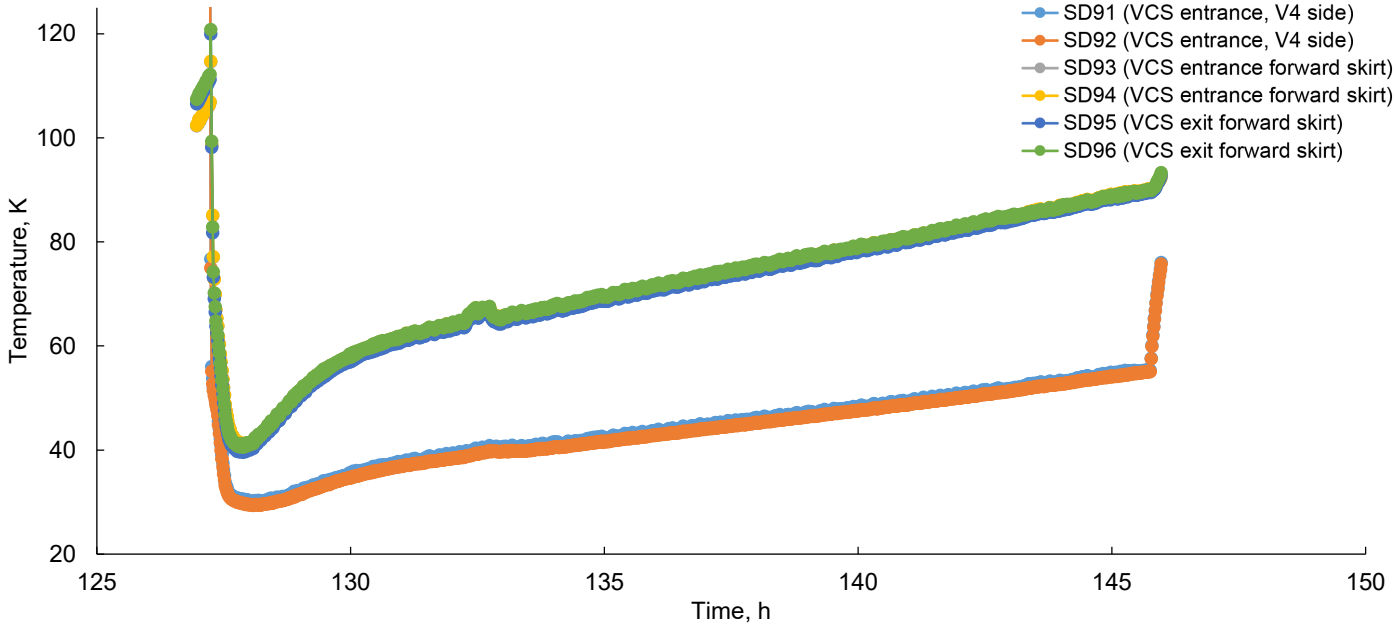

Figure 87.—Vapor-cooling inlet and outlet temperatures as function of time. Vapor-cooling system (VCS).

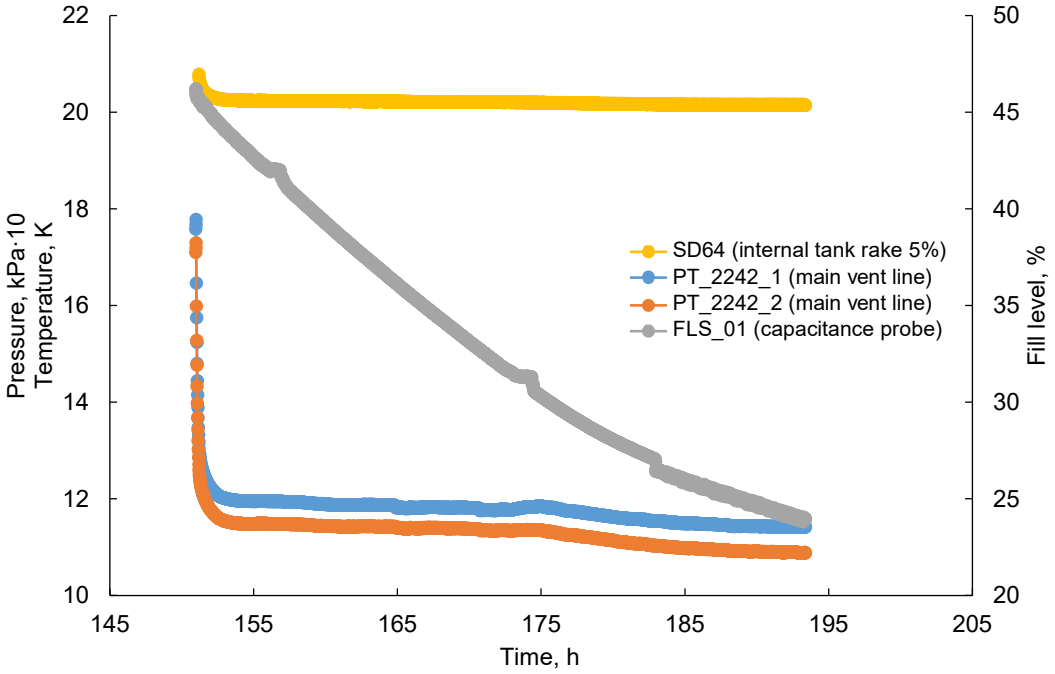

Figure 88.—System pressure and fill level during vapor-cooling test between 50 to 25 percent fill.

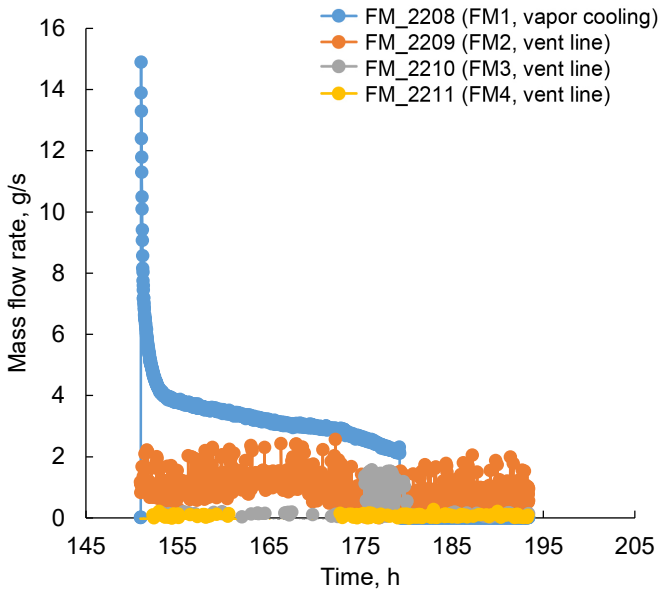

Figure 89.—Flowmeter data during vapor-cooling test between 50 to 25 percent fill. FM_2208 had 2 g/s minimum flow cutoff.

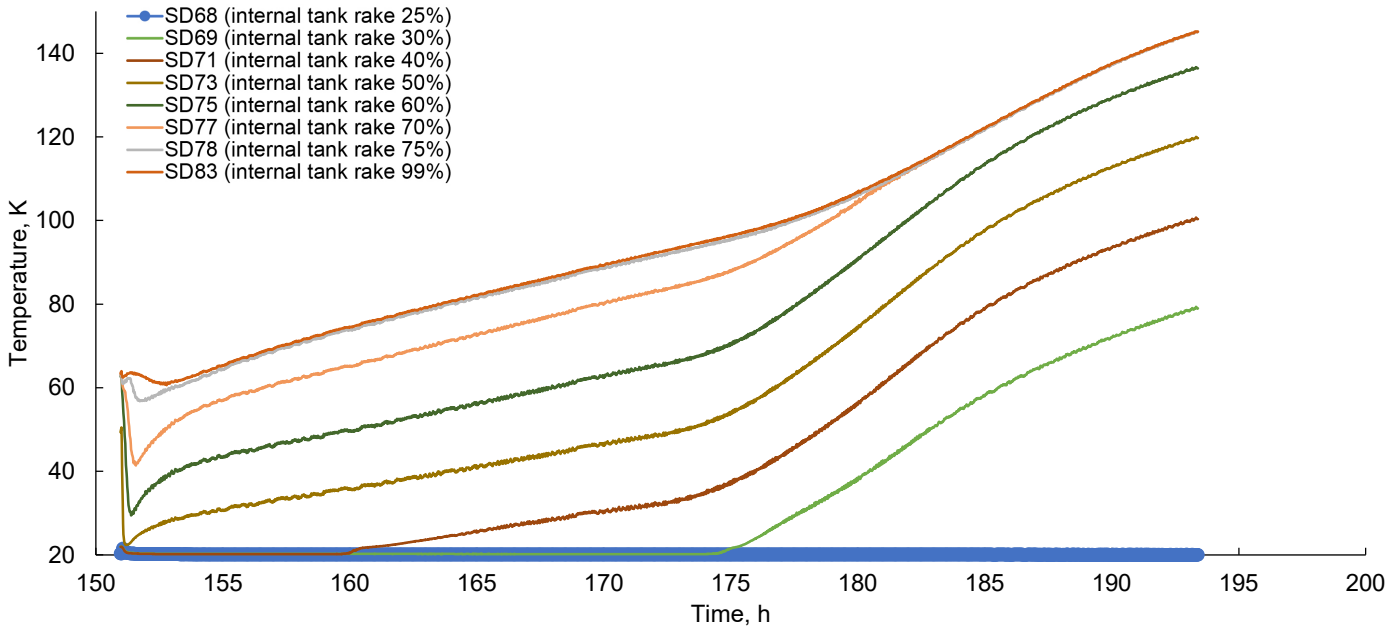

Figure 90.—Fluid temperature during vapor-cooling test between 50 to 25 percent fill.

4.2.3 Pressure Rise Tests

Pressure rise testing was completed at three fill levels (70 percent (Figure 91), 50 percent (Figure 92 and Figure 93), and 25 percent (Figure 94)) during boiloff testing and at a single fill level (70 percent (Figure 95 to Figure 97)) during vapor-cooling testing. Additionally, a cyclical vapor-cooling test was run at 50 percent full (see Figure 98 to Figure 100) to determine how a system might respond to cyclical input with vapor cooling as could be supplied by a bang-bang pressure control system. Generally, the pressure rise tests were relatively straightforward. One interesting observation in the fluid temperatures is that due to the relatively low heat flow into the bottom dome with the MLI, the fluid was heavily stratified during pressure rise testing. The fluid above the aft flange readily warmed up with the pressure, staying saturated while there was no method to translate that heat into the bottom dome due to buoyancy forces. Then during the venting process, the ensuing flow in the vapor likely induces mixing in the liquid and the warm fluid gradually made its way down into the bottom dome (see Figure 93 and Figure 96). Pressure rise rates are listed in Table 18.

The behavior of the forward skirt temperatures after the vapor-cooling application is interesting. The skirt temperatures start out much lower than in the boiloff cases, and then increase as the pressure rises, whereas during the boiloff tests the skirt temperature stays the same. This should have the effect of lowering the pressure rise rate as less energy is getting into the ullage.

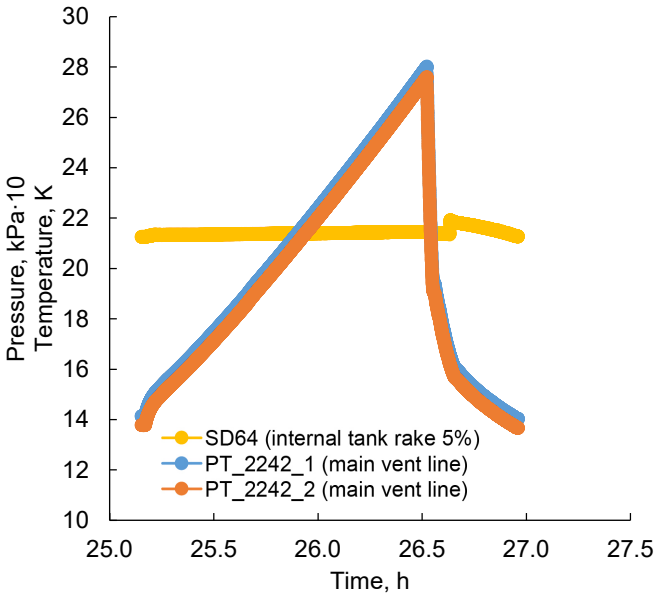

Figure 91.—Pressure rise test at 70 percent fill during boiloff testing.

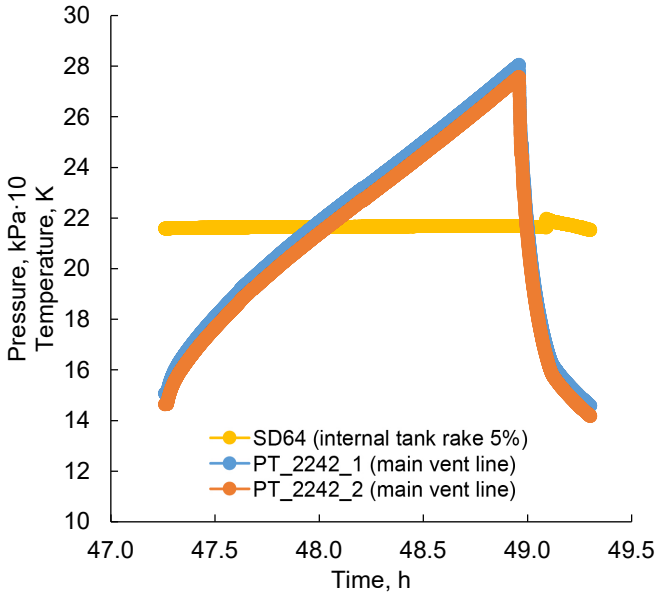

Figure 92.—Pressure rise test at 50 percent fill during boiloff testing.

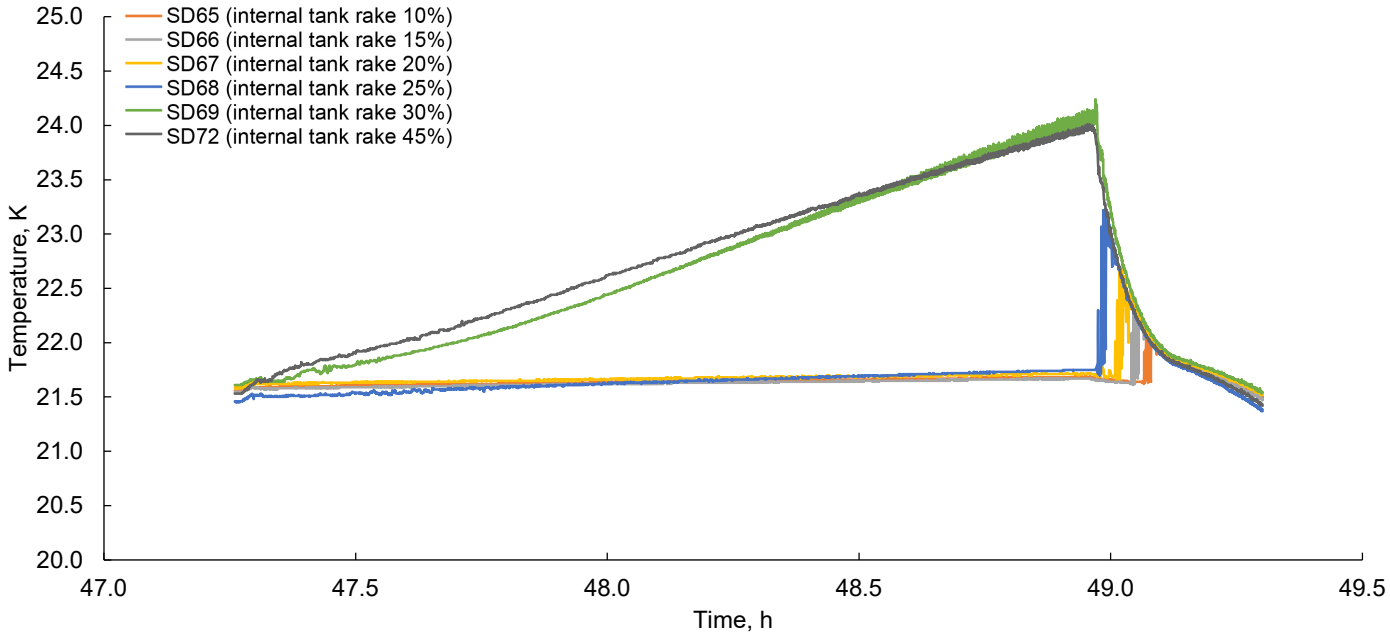

Figure 93.—Liquid temperatures during pressure rise test at 50 percent fill during boiloff testing.

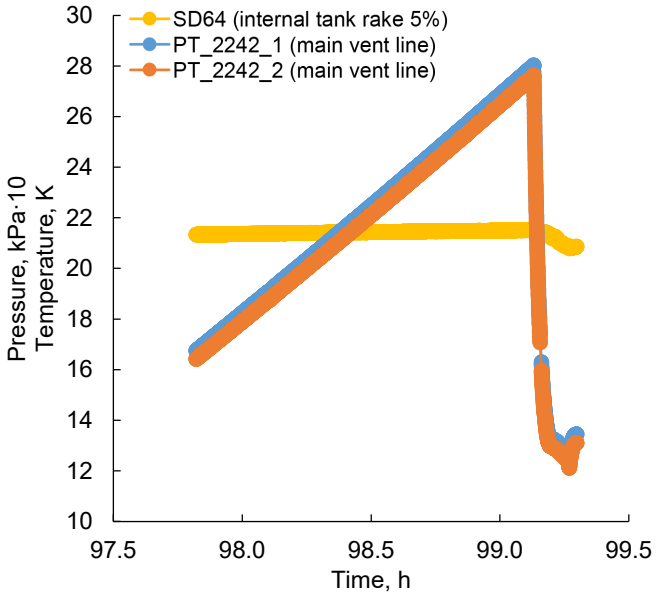

Figure 94.—Pressure rise test at 25 percent fill during boiloff testing.

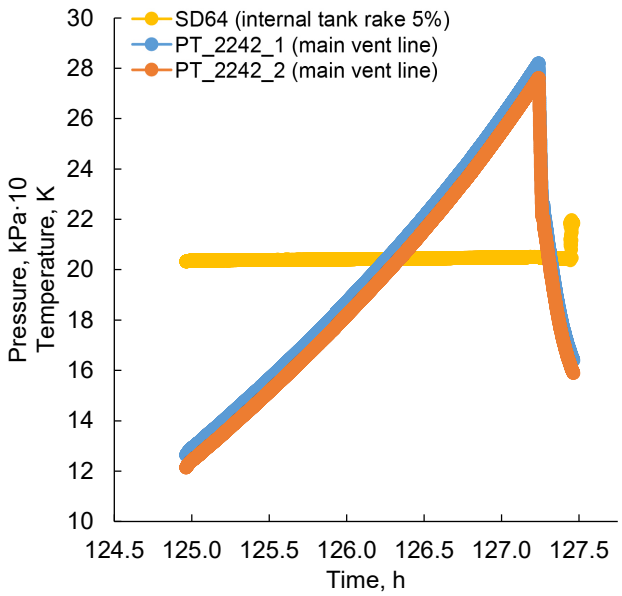

Figure 95.—Pressure rise test at approximately 70 percent fill during vapor-cooling testing.

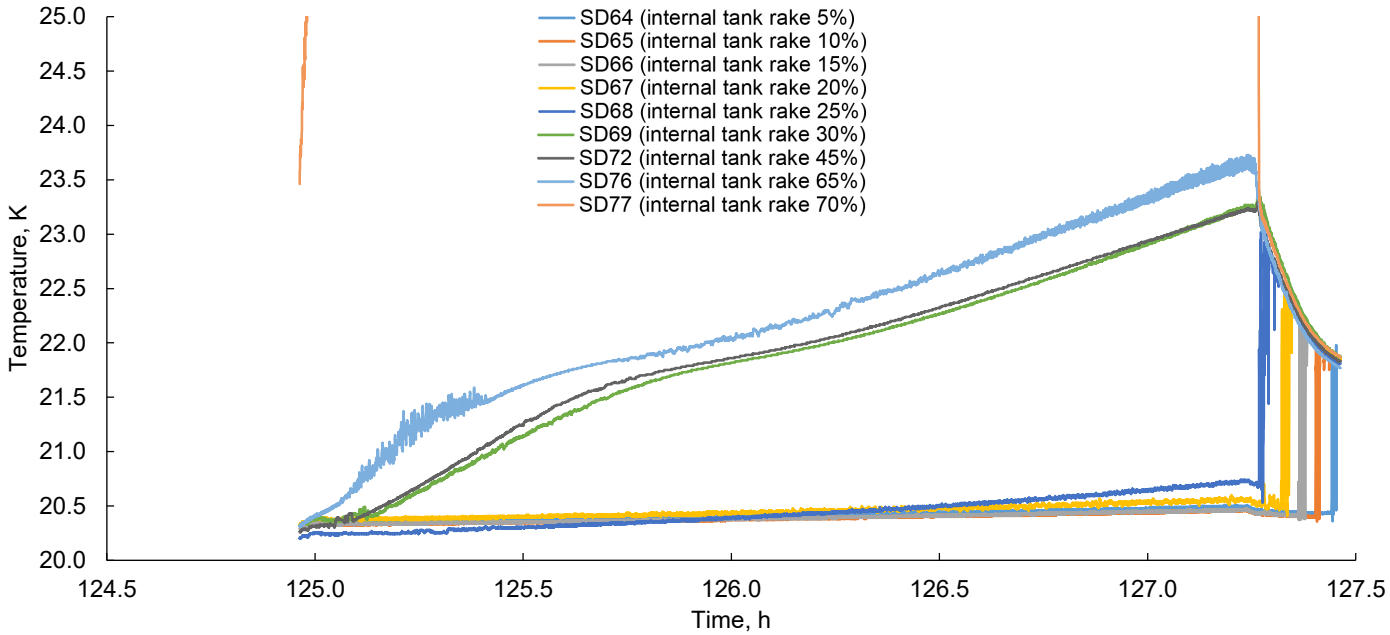

Figure 96.—Liquid temperatures during pressure rise test at 70 percent fill during vapor-cooling testing.

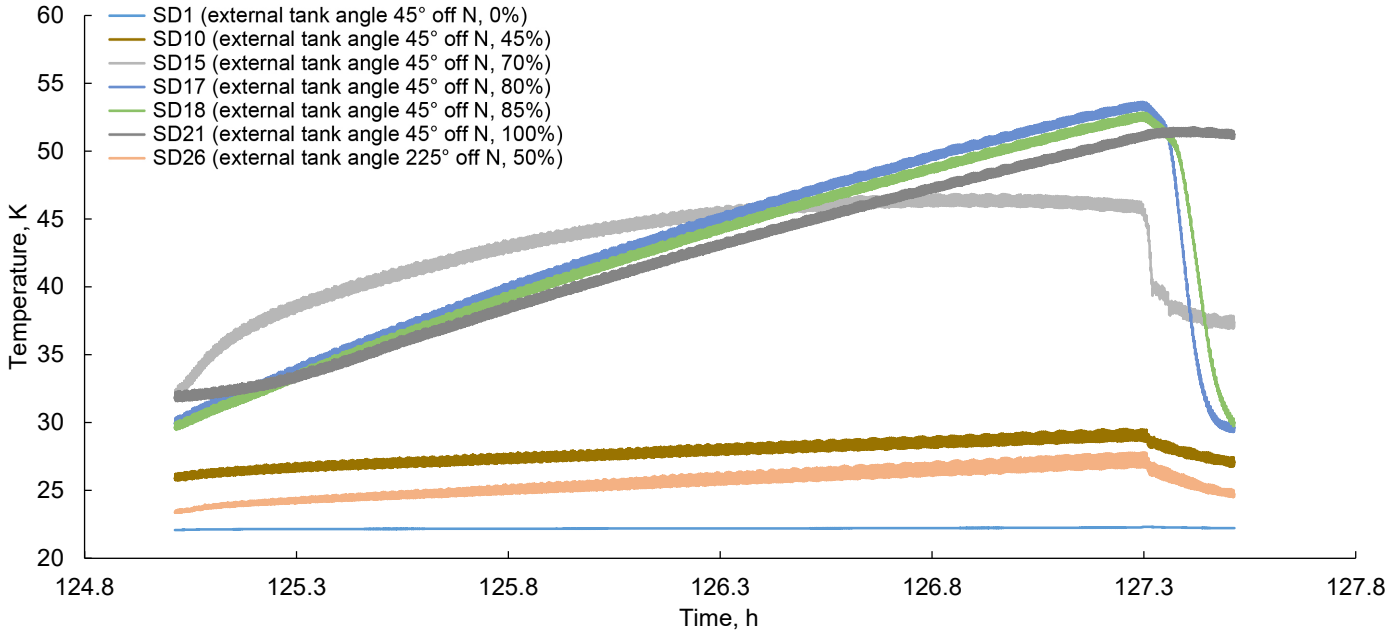

Figure 97.—Tank wall temperatures during pressure rise test at 70 percent fill during vapor-cooling testing.

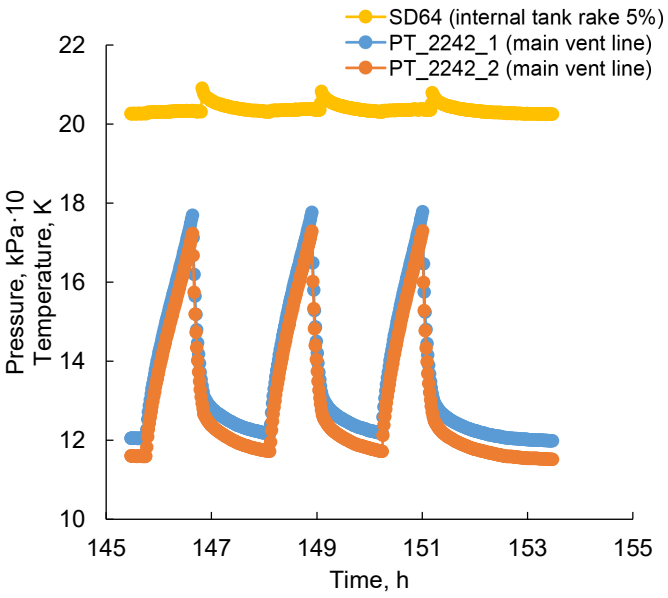

Figure 98.—Cyclical pressure rise test at 50 percent fill during vapor-cooling testing.

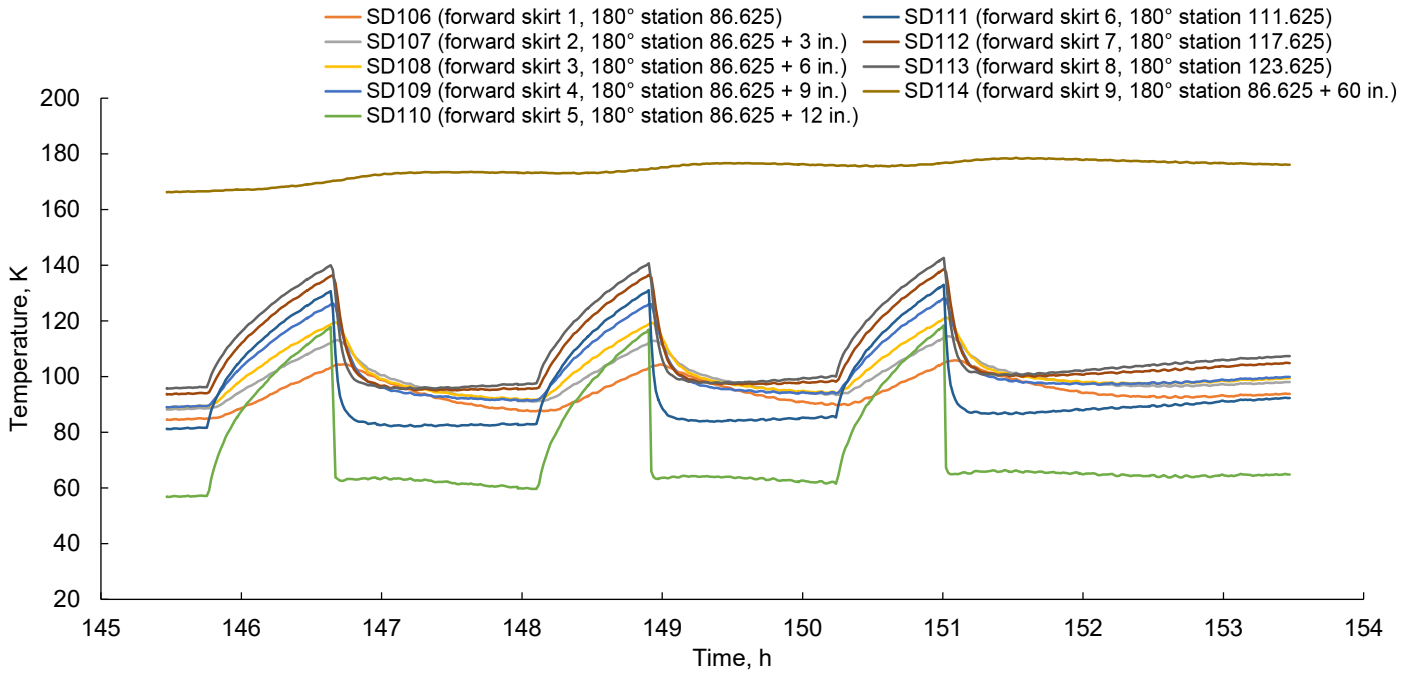

Figure 99.—System temperature responses to cyclical vapor-cooling testing at 50 percent fill.

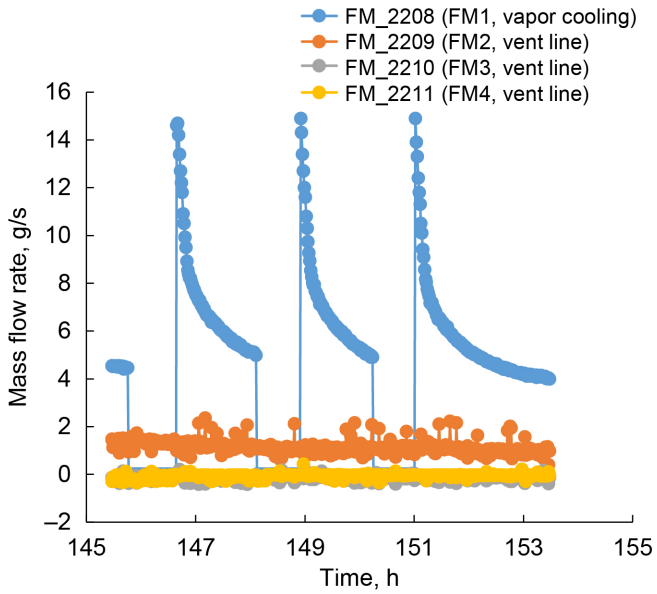

Figure 100.—Flowmeter data during cyclical vapor-cooling testing at 50 percent fill.

TABLE 18.—TEST DATA AND CALCULATED PRESSURE RISE RATES FROM PRESSURE RISE TESTING

Pressure rise test	Start time, h	End time, h	Start pressure, kPa	End pressure, kPa	Duration, h	dP,[a] kPa	dP/dt,[b] kPa/h
Boiloff MLI[c] 70	25.17	26.52	137.7	275.9	1.35	138.2	102.38
Boiloff MLI 50	47.27	48.96	146.4	275.7	1.69	129.3	76.52
Boiloff MLI 25	97.82	99.13	164.0	276.1	1.31	112.1	85.57
VC[d] MLI 70	124.96	127.24	121.3	275.9	2.276	154.7	67.96
Thermal 2 boiloff 70	42.01	43.433	138.1	276.1	1.425	138.0	96.85
VC MLI 50 cycle 1	145.75	146.64	115.9	172.2	.89	56.3	63.25
VC MLI 50 cycle 2	148.1	148.9	117.1	172.7	.8	55.7	69.59
VC MLI 50 cycle 3	150.24	151.01	117.1	172.9	.77	55.8	72.48

[a]Differential pressure (dP).

[b]Differential time (dt).

[c]Multilayer insulation (MLI).

[d]Vapor cooling (VC).

4.2.4 Posttest Inspection Results

After testing was completed, the test team moved directly into LN_2 testing. The tank was purged with inert gasses but was not allowed to fully warm up so that vacuum was not broken.

4.3 Preacoustic Test—Liquid Nitrogen

The preacoustic LN_2 test started on Oct. 2, 2019, at approximately 8 p.m. EST and ran for nearly 230 h, completing on Oct. 12, 2019, at approximately 9:30 a.m. EST. The preacoustic LN_2 test consisted of two main test runs: (1) boiloff and (2) vapor-cooling. This test run was an abbreviated version of the preacoustic LH_2 test run performed previously. The main objective of this test run was to get LN_2 boiloff data at high fill levels to evaluate for degradation in the postacoustic test, in the event that LH_2 was not available for the postacoustic test. A brief summary of the preacoustic test events is provided here. A more detailed discussion is provided in Sections 4.3.1 and 4.3.2.

1. Boiloff testing: First the SHIIVER tank was filled with LN_2 and then allowed to sit for approximately 10 h. Subsequently, the tank was topped off with LN_2 to a fill level more than 90 percent. The tank was then allowed to boiloff with the vapor routed through the main vent line until the tank reached approximately 70 percent fill.
2. Vapor-cooling testing: To begin vapor-cooling testing, the SHIIVER tank was topped off, and the vapor-cooling loops opened as a second vent line. After a 4-h chilldown period and another topoff, the entire boiloff gas was routed through the vapor-cooling circuit for approximately 35 h. At this point, due to limitations in the amount of nitrogen the test facility could drain into the dump tank, it was decided to perform a step drain. The tank was drained from approximately 80 to 50 percent. At this fill level, boiloff testing with the vapor routed through the vapor-cooling network continued for approximately 40 h. The tank was then drained to approximately 25 percent and allowed to boiloff for another 20 h. Finally, the last portion of the LN_2 was drained from the tank and the testing completed.

All drain data was captured but is not presented here. It may be useful for future analysis efforts and has been archived with all the other SHIIVER data.

During the testing, vacuum pressure was maintained in the 10^{-6} torr range as seen in Figure 101. While there were a few excursions due to opening various valves, the nominal pressure was 5.1×10^{-6} torr. The IG data is for reference only as it was calibrated in air. The vacuum pressure was lower due to repairs done on the valves to reduce the leakage at the actuators. The cold wall temperature was consistently in the range of 286 K (55 °F) to 291 K (65 °F) as shown in Figure 102.

All times during the preacoustic LN_2 testing are referenced to noon EST on Oct. 2, 2019.

4.3.1 Boiloff Testing

Boiloff testing was completed with LN_2 from 90 to approximately 70 percent (see Figure 103). The tank pressure was controlled to 138 kPa (20 psia) throughout the test, while FM2 was used to measure the flow (see Figure 104). For nitrogen flows, FM2 and FM3 lined up much better than those with hydrogen when comparing Figure 104 and Figure 72. The fluid temperatures were much noisier during nitrogen testing as in general, the SDs are much less accurate at these elevated temperatures (see Figure 105). It should be noted that the running average on the SD77 shows a much smoother temperature profile. As in the hydrogen preacoustic testing, no stratification was seen in the ullage until the liquid-vapor interface began to interact with the forward flange.

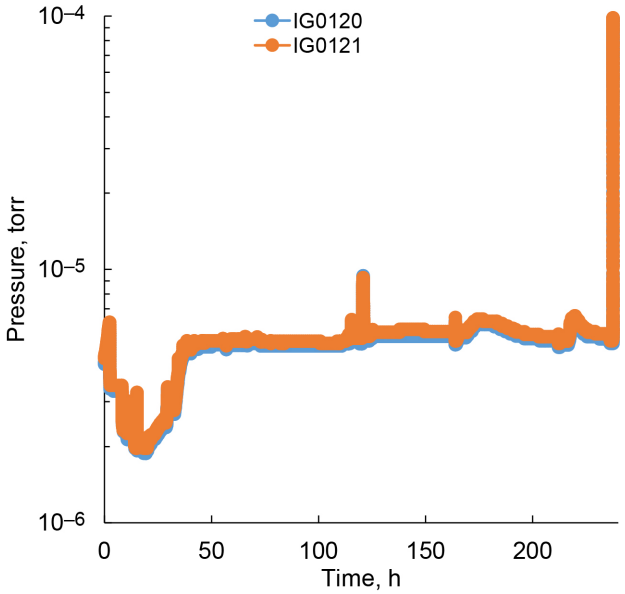

Figure 101.—Vacuum pressure for liquid nitrogen preacoustic testing.

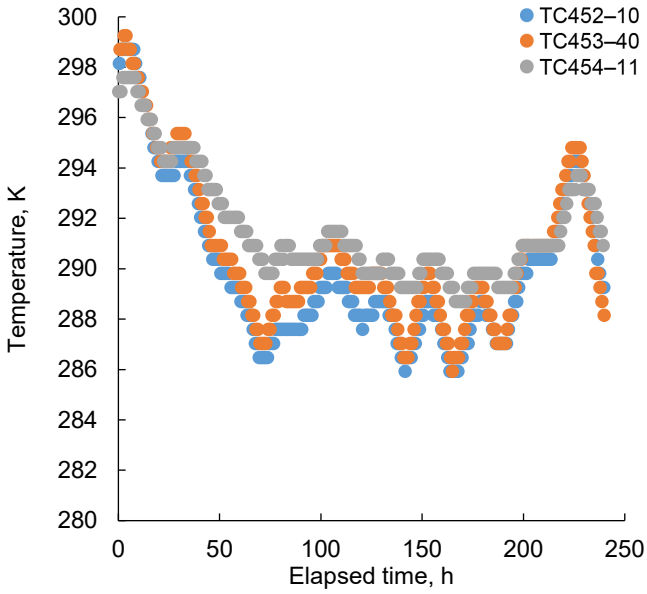

Figure 102.—Cold wall temperatures for liquid nitrogen preacoustic test.

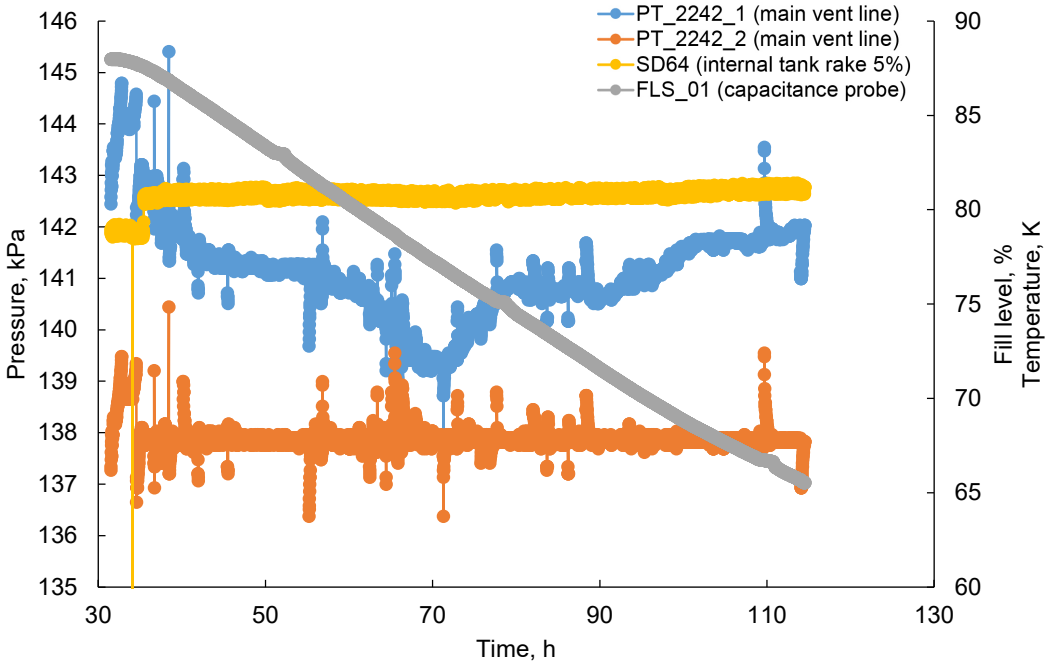

Figure 103.—Liquid temperature, tank pressure, and fill level during liquid nitrogen boiloff testing.

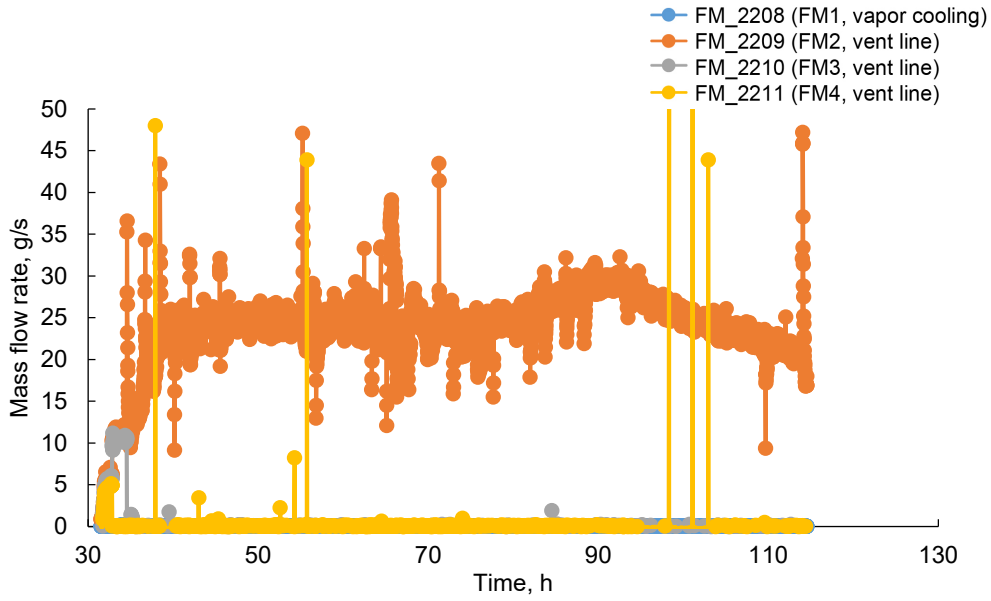

Figure 104.—Boiloff flowmeter data during liquid nitrogen boiloff testing.

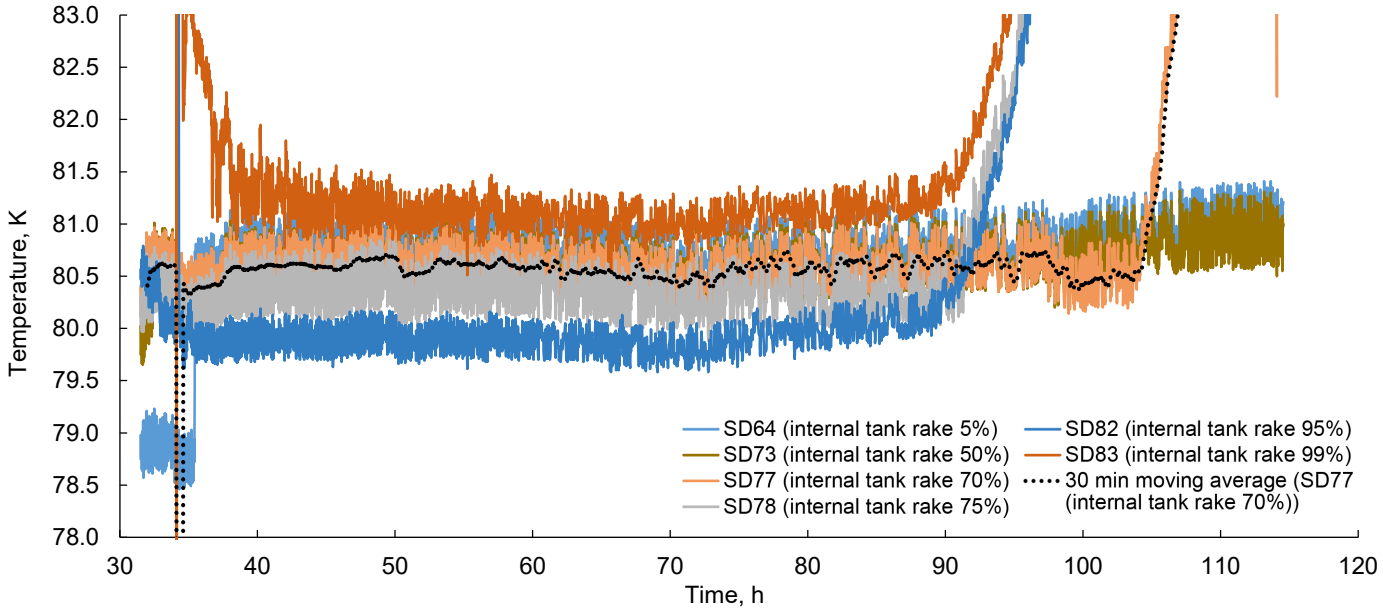

Figure 105.—Fluid temperatures during liquid nitrogen boiloff testing. Black line is running 30-min average of SD77.

4.3.2 Vapor-Cooling Testing

Three LN_2 vapor-cooling tests were run at fill levels of approximately 90, 50, and 25 percent. Data for each of these fill levels are shown in Figure 106 to Figure 117. In between each test, drains were completed to expedite testing and also expedite emptying the nitrogen from the tank. During LN_2 testing, all of the same stratification (or lack thereof) trends observed in the LH_2 testing were also observed. As seen in Figure 108, the tank forward manway took almost 20 h to cool back down after the initial boiloff test. Boiloff rates significantly reduced with fill level (from 10 percent volumetric change in 35 h at the high fill level to approximately 5 percent change over 40 h at about half full to approximately 1 percent change over 20 h at the lowest fill level). During the drain, SD15 was seen to be warmer than the rest of the dome, indicating that the forward skirt was driving heat into the upper dome. The first two tests clearly achieved a steady-state period in the test while the lowest fill level probably did not due to a limited duration of testing.

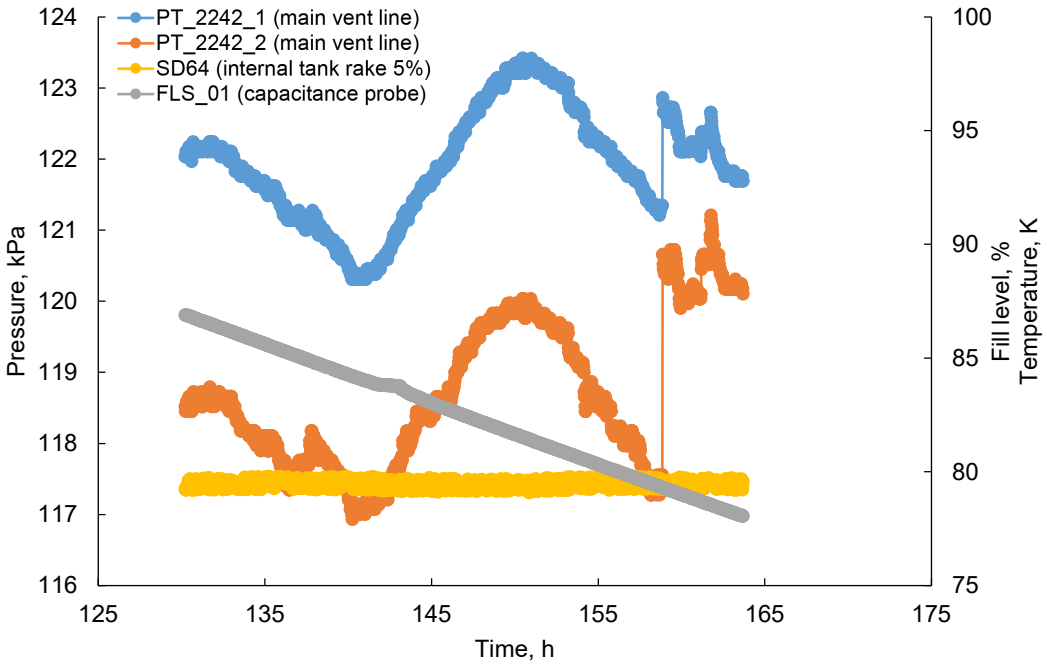

Figure 106.—Tank pressure, liquid temperature, and fill level for liquid nitrogen vapor-cooling testing between 90 and 80 percent fill.

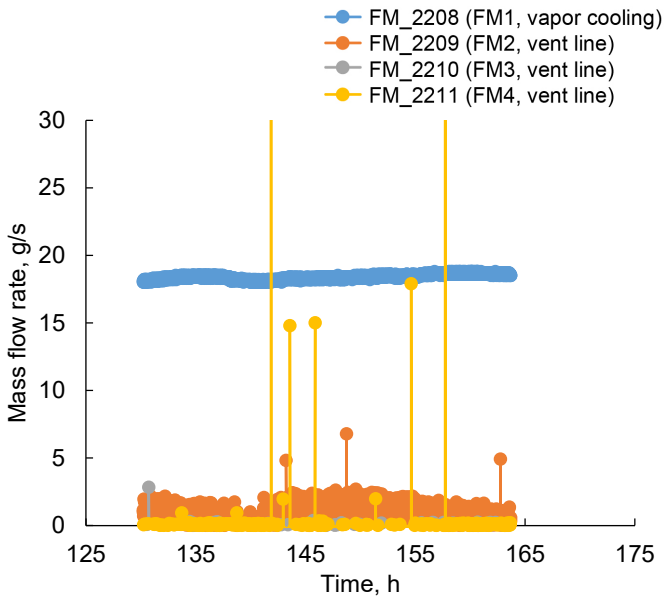

Figure 107.—Vapor-cooling flow rate for liquid nitrogen high-fill vapor-cooling test.

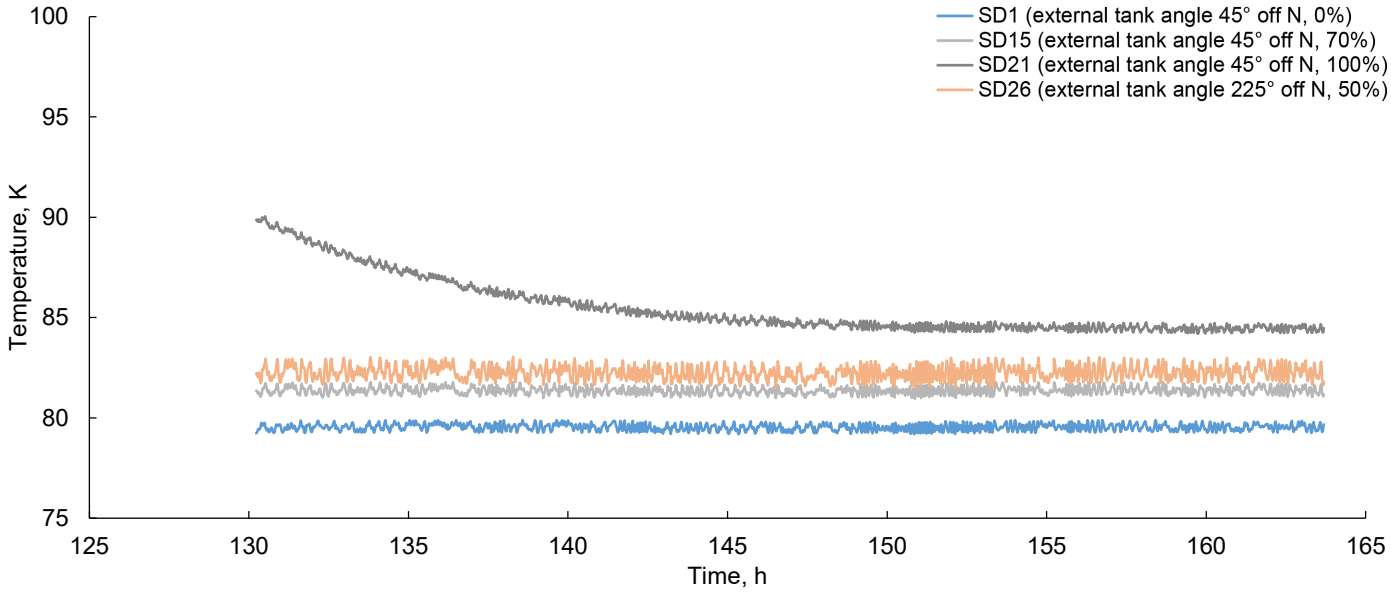

Figure 108.—Tank wall temperatures during liquid nitrogen high-fill vapor-cooling testing.

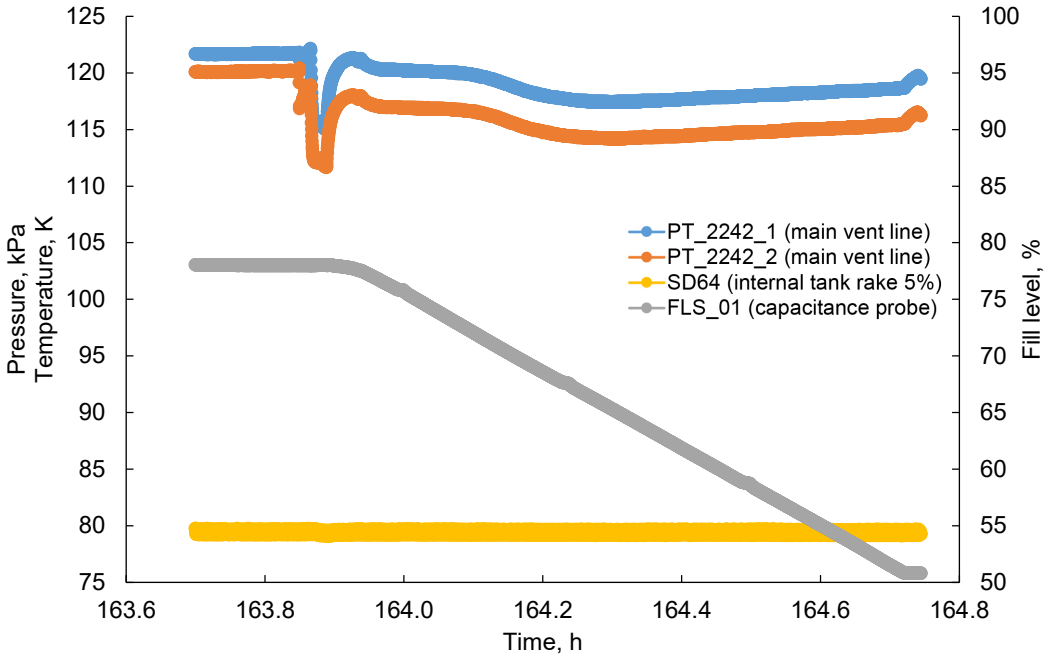

Figure 109.—Tank drain from approximately 80 percent fill liquid nitrogen to approximately 50 percent fill.

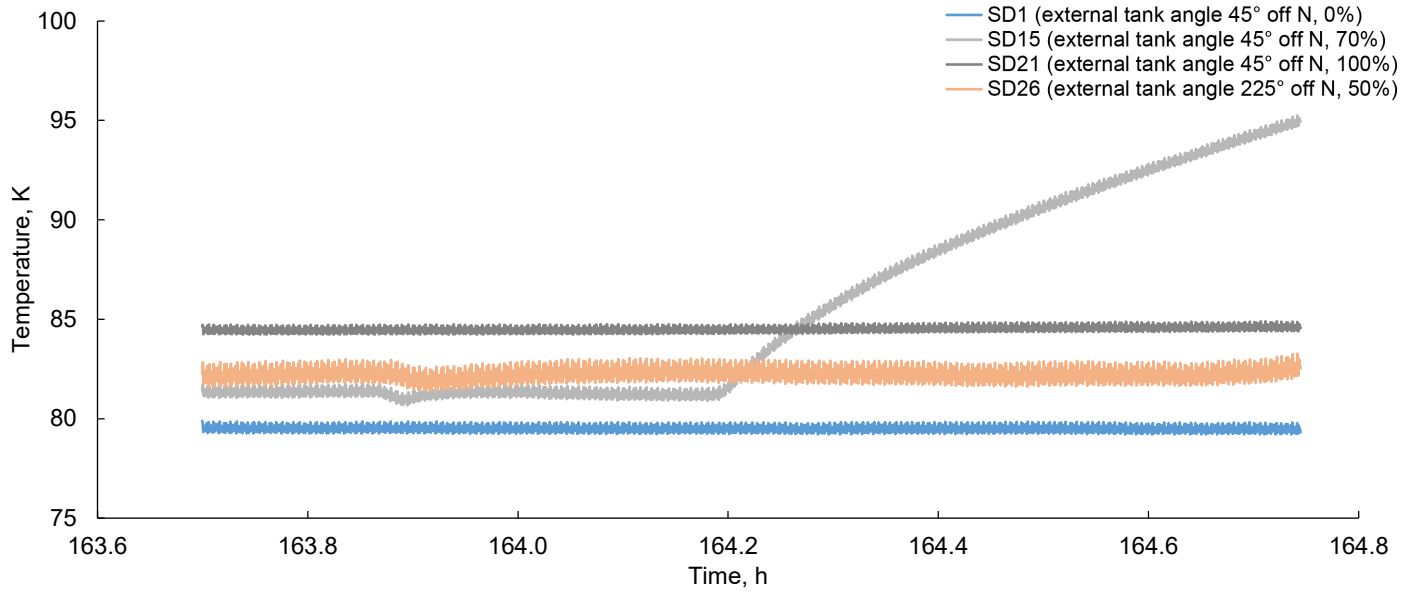

Figure 110.—Tank temperatures during drain. SD15 near the forward skirt flange warms up first.

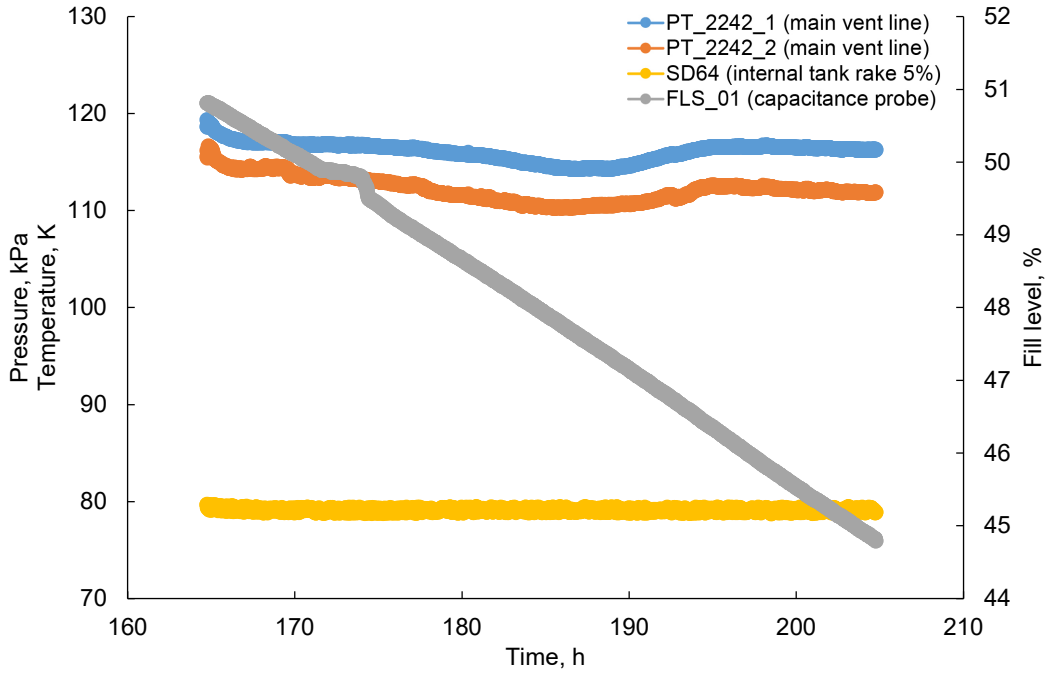

Figure 111.—Liquid nitrogen vapor cooling at approximately 50 percent fill.

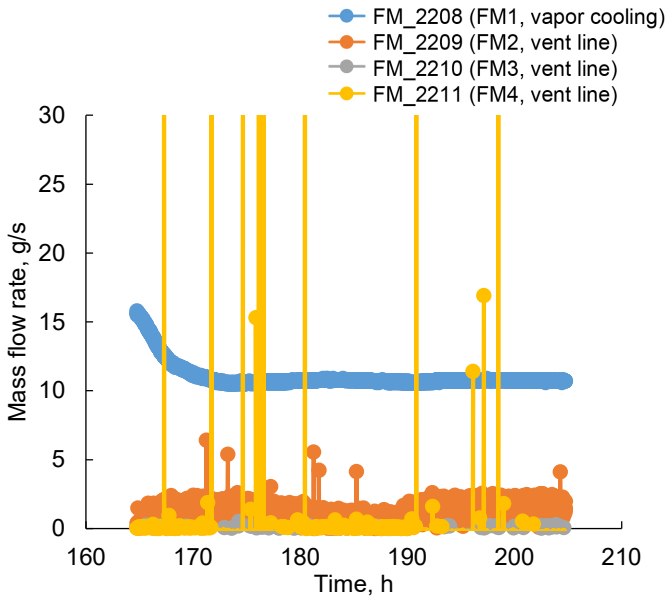

Figure 112.—Vapor-cooling flow rate of nitrogen at 50 percent fill.

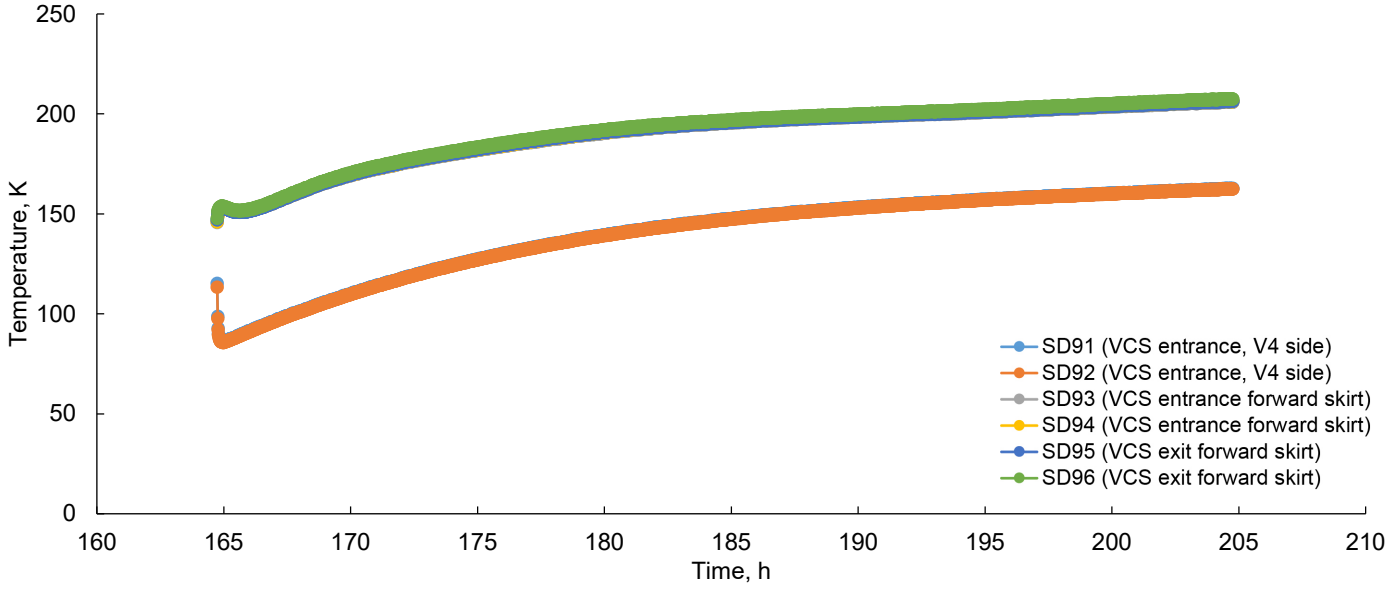

Figure 113.—Vapor-cooling inlet and outlet temperatures during liquid nitrogen vapor cooling at 50 percent. Vapor-cooling system (VCS).

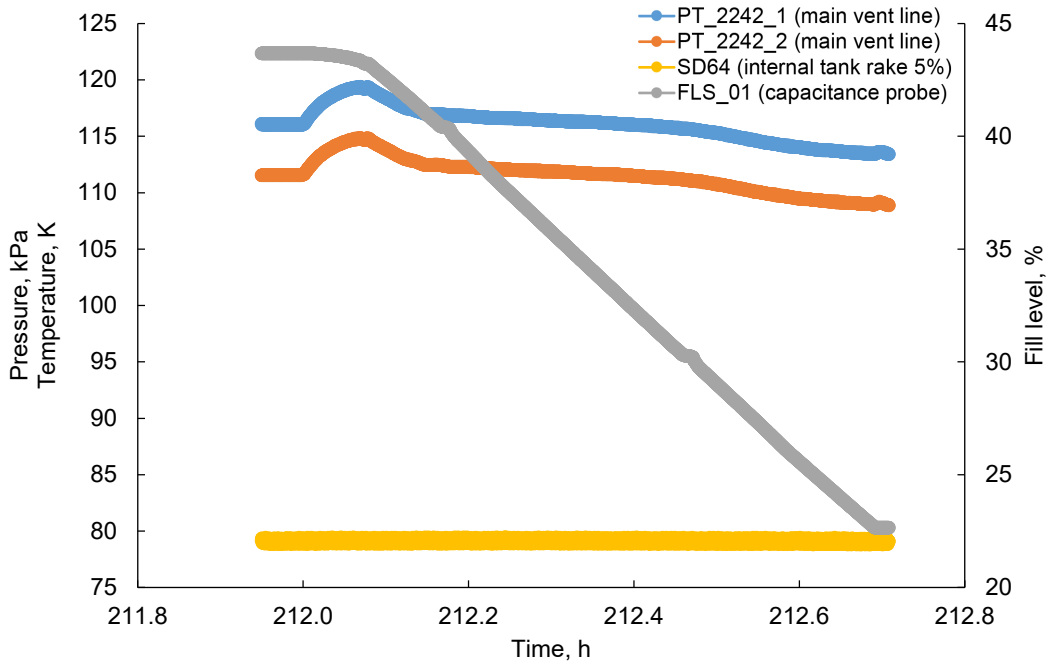

Figure 114.—Liquid nitrogen drain from 50 to 25 percent fill.

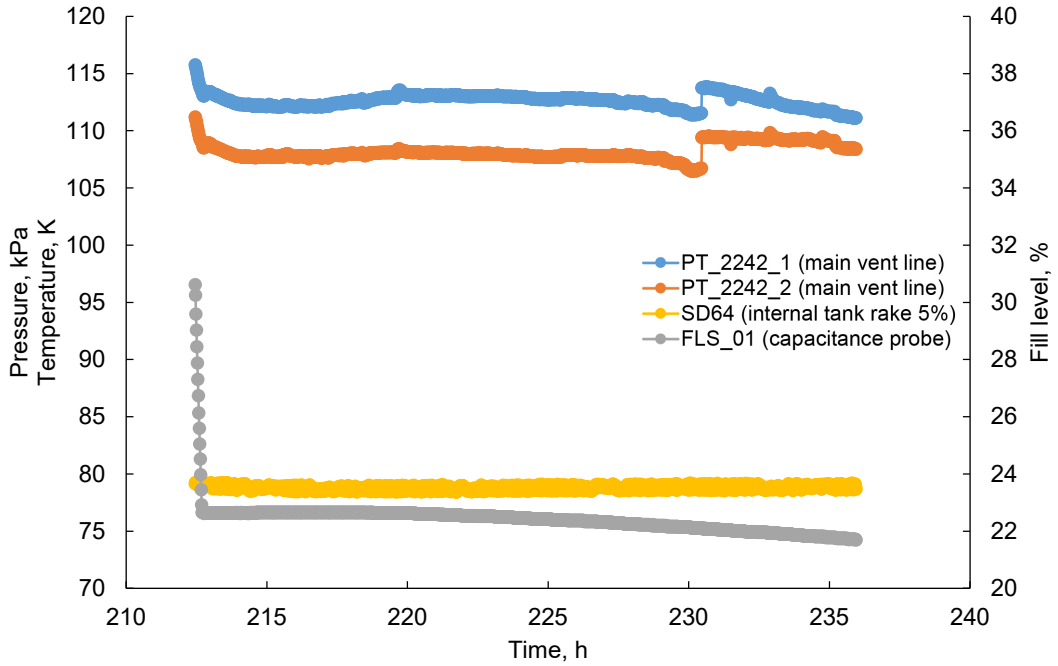

Figure 115.—Liquid nitrogen vapor-cooling testing at approximately 25 percent fill.

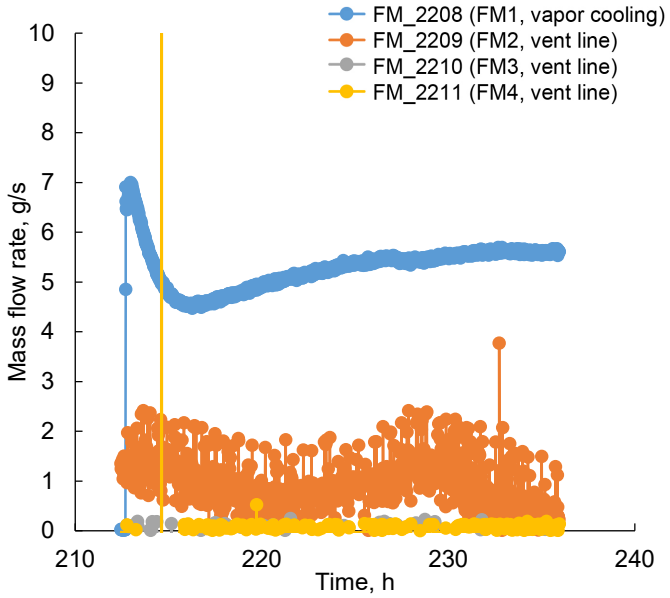

Figure 116.—Liquid nitrogen vapor-cooling flow at approximately 25 percent fill. It is unclear that system came to steady state.

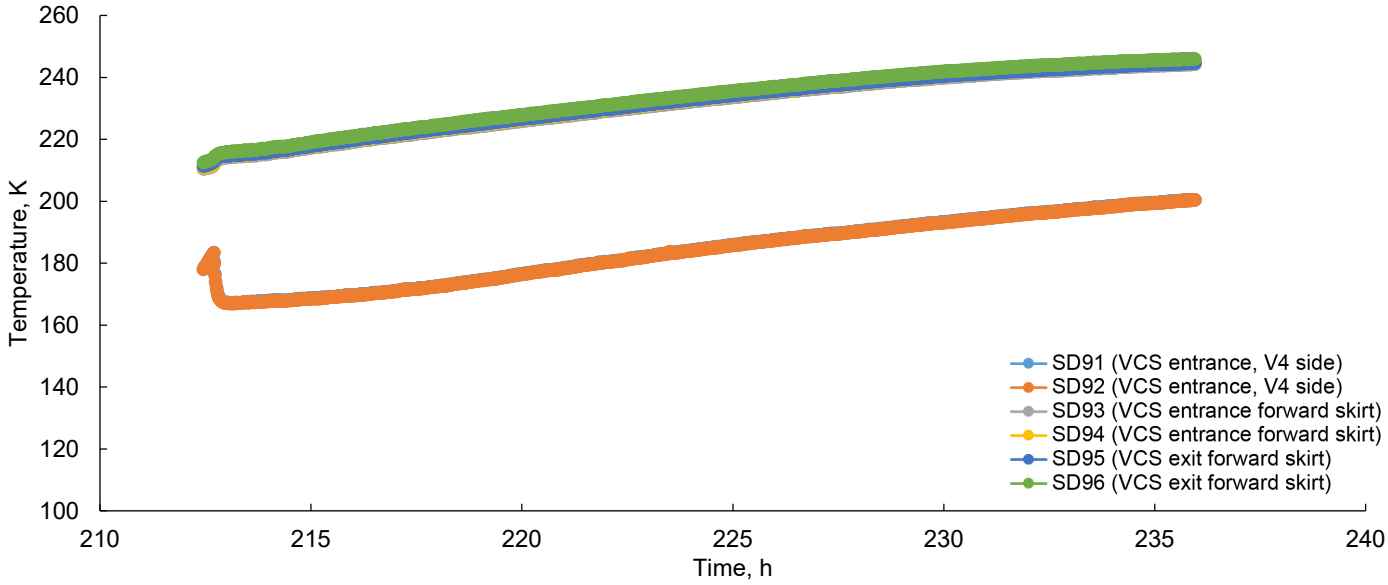

Figure 117.—Vapor-cooling inlet and outlet temperatures during liquid nitrogen vapor cooling at 25 percent. Vapor-cooling system (VCS).

4.4 Acoustic Test

All acoustic testing was performed at RATF. The SHIIVER test hardware was installed on an 8-ft-tall support structure to raise the hardware off the floor and appropriately position the hardware inside the reverberant acoustic chamber. Eight microphones were placed around the test hardware (Figure 118; see specifications in Section 3.9, Table 15). The microphones provide both reverberant acoustic test data and feedback for closed-loop control of the test.

4.4.1 Empty Chamber Testing

Prior to the installation of the test article, "empty chamber" tests were completed with only the test stand in place to set the facility horns to the correct mix and create the desired spectrum (see Section 2.4.2). The results from empty chamber testing are shown in Figure 119. The predicted achievable spectrum is shown in blue. RATF only has active control from the 31.5 to 1,250 Hz OTOB. Frequencies lower than 31.5 Hz cannot be met in this chamber. Levels at frequencies higher than 1,250 Hz are a function of horn spillover and cannot be controlled. These limitations are typical of most reverberant chambers. To mitigate this risk of high frequency under test, SHIIVER will have a +3 dB protoqual test. In a +3 dB test, the high frequencies were expected to come into the desired test tolerance band. This would enable demonstrating that the MLI could survive the appropriate levels at all frequencies.

4.4.2 Structural Heat Intercept, Insulation, and Vibration Evaluation Rig (SHIIVER) Acoustic Testing

The control average sound pressure level in the chamber was slightly out of tolerance for the first two tests (–6 dB (138 dB) and –3 dB (141 dB)). This was expected as it is difficult for the chamber to remain in tolerance at such low levels because the chamber is still in its nonlinear regime. As such, the controls on the chamber inputs are not capable of being tuned at such a low frequency. This was not of concern because the sole function of the low-level tests is to collect data to predict structural response in the high-level tests. To mitigate risk for the higher level tests, the test engineers swapped low-frequency modulators before the full-level test.

Figure 120 shows the chamber control average sound pressure level in the two most important tests: full level (144 dB) and protoqual (+3 dB, 147 dB), compared to the desired spectrum. Between these two tests, all frequencies from 31.5 to 10,000 Hz were tested within tolerance.

During the full-level test, VS11Y (see Table 14) briefly experienced a saturated peak. The time history section of interest is plotted in Figure 121. The peak appeared before the full-level section of the test, and the accelerometer recovered to nominal behavior within 10 s. The cross-axes (x and z) on the accelerometer do not exhibit any effect from this artifact. The character of the time history indicates an electrical rather than mechanical issue. This accelerometer is mounted on the forward skirt. A duplicate accelerometer was mounted to the forward skirt (VS12Y) that compares well to VS11Y in the full-level section. Considering this, the test team decided to leave the accelerometer as is for subsequent tests. The artifact never reappeared.

Figure 118.—Structural Heat Intercept, Insulation, and Vibration Evaluation Rig (SHIIVER) in Reverberant Acoustic Test Facility (RATF). Microphones are located on tripods.

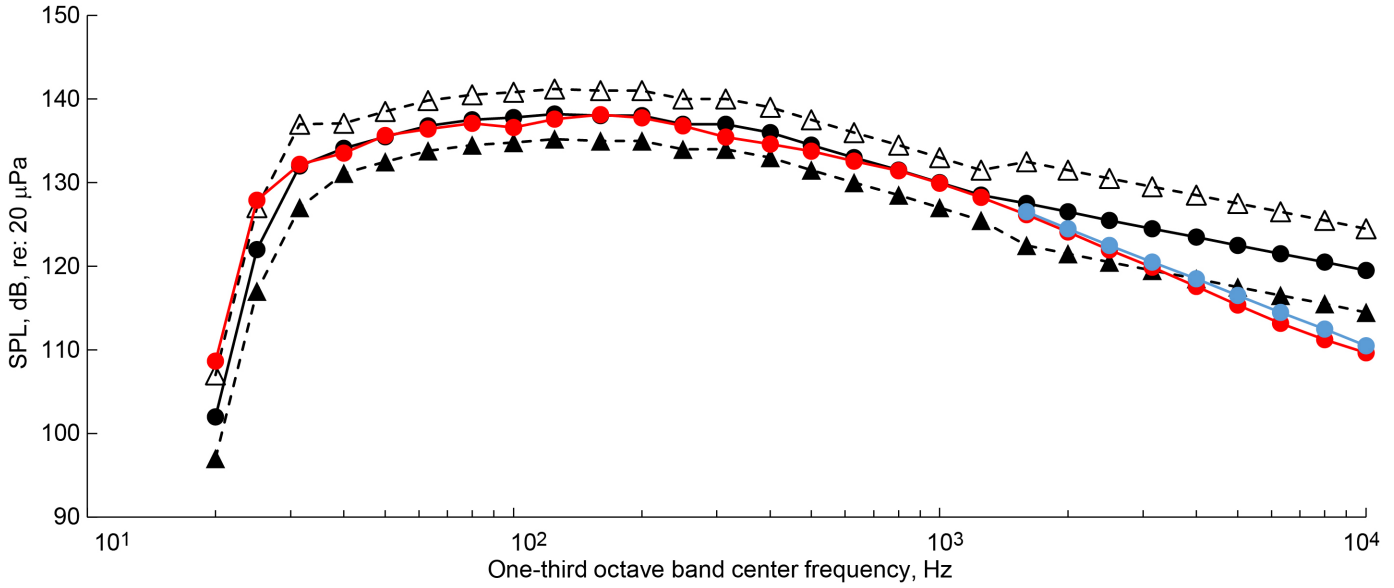

SHIIVER, empty chamber target spectrum "full level" (accounting for 4 dB SHIIVER absorption), 148.32 dB OASPL (20 to 10,000 Hz OTOB's)
Upper SPL test tolerance
Lower SPL test tolerance
CM average, AC0543, SHIIVER, empty chamber target spectrum, "full level" (accounting for 4 dB SHIIVER absorption), 147.8 dB OASPL (20 to 10,000 Hz OTOB's), 30 s test,last 10 s linear average, 08Aug2019.
Proposed SHIIVER spectrum (post empty chamber results), "full level" (accounting for 4 dB absorption), 148.2 dB OASPL (20 to 10,000 Hz OTOB's)

Figure 119.—Empty chamber test results. Sound pressure level (SPL). Overall sound pressure level (OASPL). One-third octave band (OTOB). Structural Heat Intercept, Insulation, and Vibration Evaluation Rig (SHIIVER).

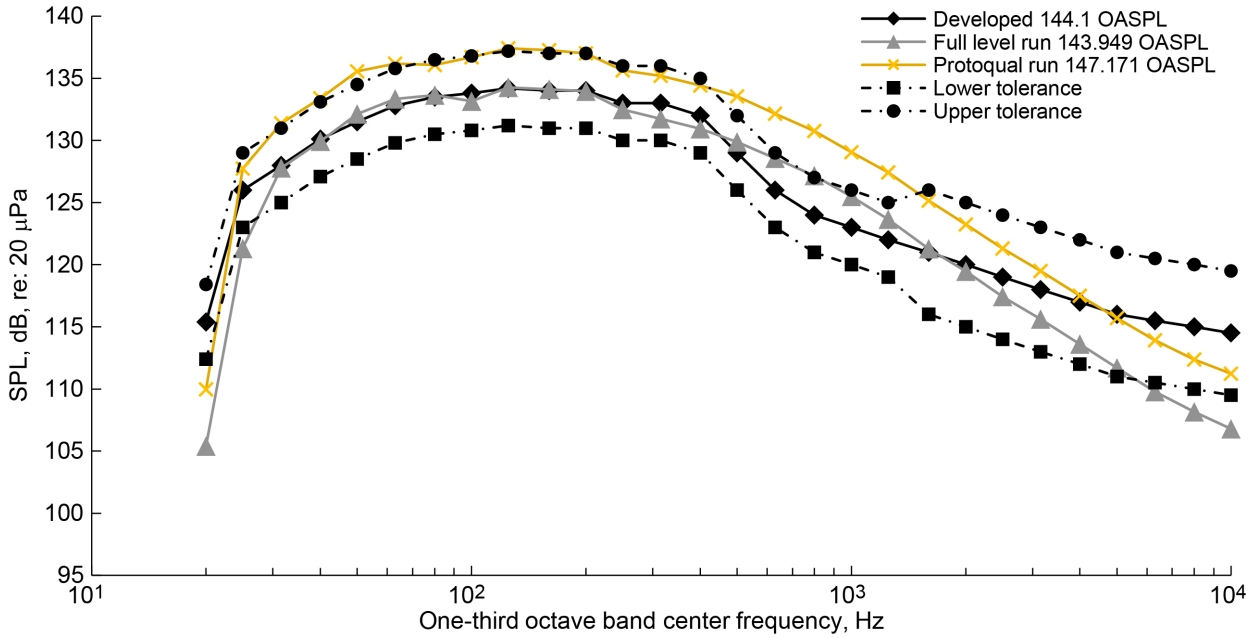

Figure 120.—As-tested chamber control averages. Sound pressure level (SPL). Overall sound pressure level (OASPL).

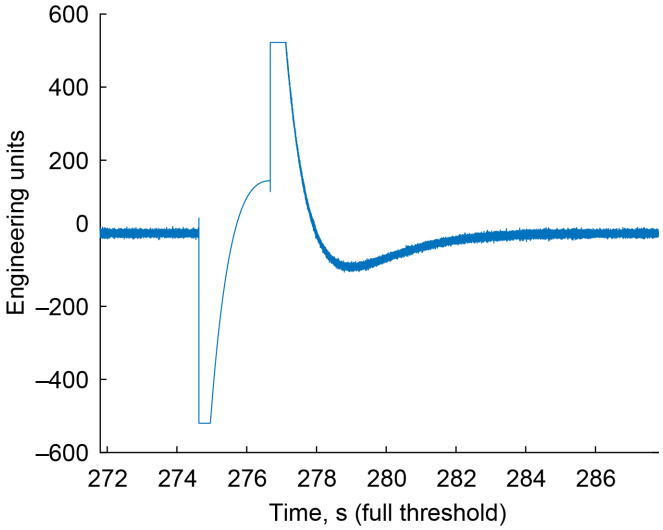

Figure 121.—Accelerometer VS01Y transient artifact during full-level test.

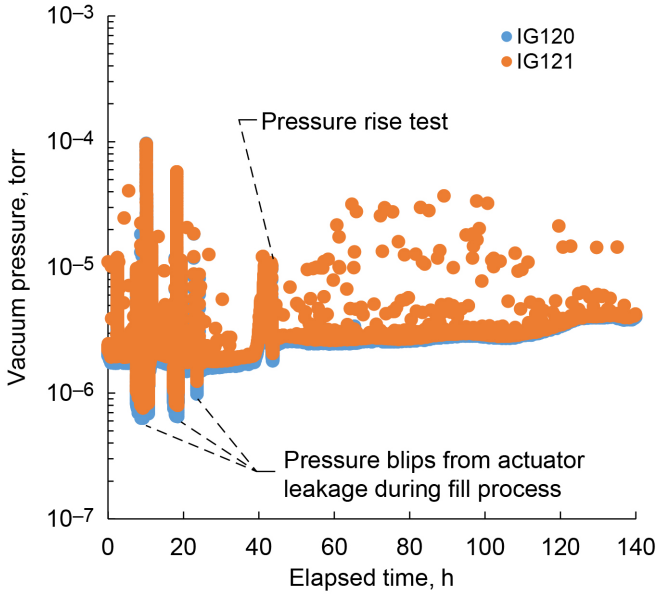

Figure 122.—Vacuum pressure during postacoustic testing.

4.5 Postacoustic Test

After the acoustic testing was completed, the SHIIVER test article was transported back to the ISPF and reinstalled into the vacuum chamber. As there was no concern with the vapor-cooling hardware surviving the acoustic testing, no postacoustic vapor-cooling tests were performed. The postacoustic LH_2 test started on Jan. 20, 2020, at approximately 8 a.m. EST and ran for about 148 h, completing on Jan. 26, 2020, at around noon EST. A brief summary of the postacoustic test events is provided in the following information. A more detailed discussion is provided in Sections 4.5.1 and 4.5.4.

The SHIIVER tank was then filled with LH_2, allowed to sit for approximately 12 h, and then partially topped off. Initially, issues with the ISPF hydrogen transfer system prevented a full topoff, so the transfer was terminated. After troubleshooting, approximately 8 h later a second topoff was successful in getting the fill level above 90 percent. This allowed for an almost 24-h chill in time for SHIIVER, which was very beneficial for the data at high fill levels. The SHIIVER was then allowed to boiloff with the vapor leaving via the main vent system down to approximately 70 percent fill. At this point, a self-pressurization test was run from approximately 138 kPa (20 psia) to 276 kPa (40 psia). The tank was vented back down to 138 kPa (20 psia) and was allowed to boiloff further to less than 25 percent fill. At this point, the test was determined to be complete.

During testing, the vacuum pressure was maintained in the 10^{-6} torr range as required for excellent MLI performance. The IG data shown in Figure 122 is for reference only and was calibrated in air (the RGA indicated a majority of nitrogen and oxygen with a bit of water in the chamber during this test, so the value is probably accurate). It was noticed during the pressure rise that there was a small leak of hydrogen into the chamber. After the pressure rise test, it was noticed that the vent system was subatmospheric and leaking nitrogen purge gas into the vacuum chamber (see Figure 123). However, this was at a low enough rate to not affect the vacuum pressure. The cold wall temperature was significantly colder than previous testing (the postacoustic test was conducted in January whereas the other tests were in August, September, and October). The temperature started off as low as 272 K (30 °F) and over the duration rose to as high as 279 K (43 °F) as shown in Figure 124.

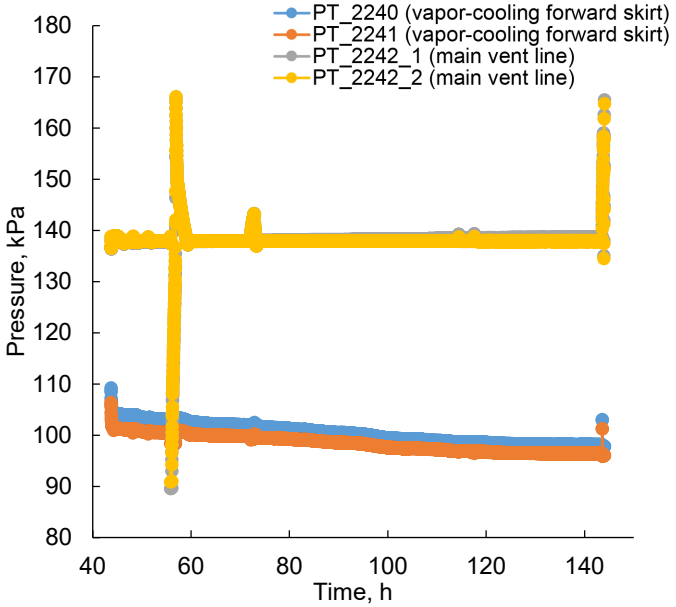

Figure 123.—Vent line pressure going below atmospheric pressure as indicated by vapor-cooling-line pressure transducers.

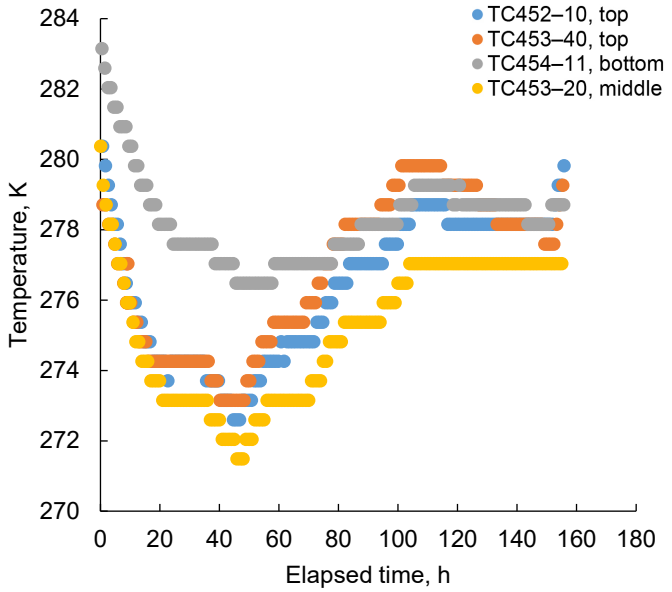

Figure 124.—Cold wall temperature data for postacoustic test.

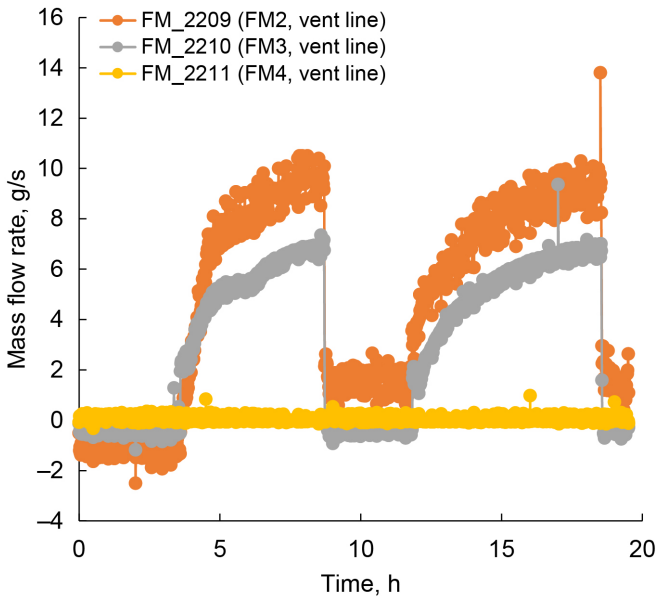

Figure 125.—Flowmeter data during chilldown.

During postacoustic testing, several issues were encountered. The main issue was regarding the capacitance probe. After the nitrogen testing, it had to be reset for hydrogen. In preparation for testing, the empty range was set. As the tank was filled, however, communication with the probe's transmission box was lost, preventing the full level from being set. As such, this was one of the items that needed troubleshooting during the time between the two topoff attempts mentioned earlier. The capacitance probe was finally reset, and a maximum fill command was successfully issued, at a fill level of 78.2 percent (on the RFMG); therefore, the capacitance probe data must be viewed through that lens for use in the postacoustic testing.

All times during the postacoustic testing are referenced to noon EST on Jan. 20, 2020.

4.5.1 Flowmeter Correlation During Chilldown of Hardware

Previous test experience showed that FM2 and FM3 were offset when reading the same flow rate. This observation, combined with the desire to maintain constant 138 kPa via pressure control, led to the use of the chilldown duration to gather data comparing the two flowmeters to allow for corroboration of data using just FM2 during actual testing. The two comparison runs are shown in Figure 125. The comparison with least-squares curve fitting during the second comparison run is shown in Figure 126.

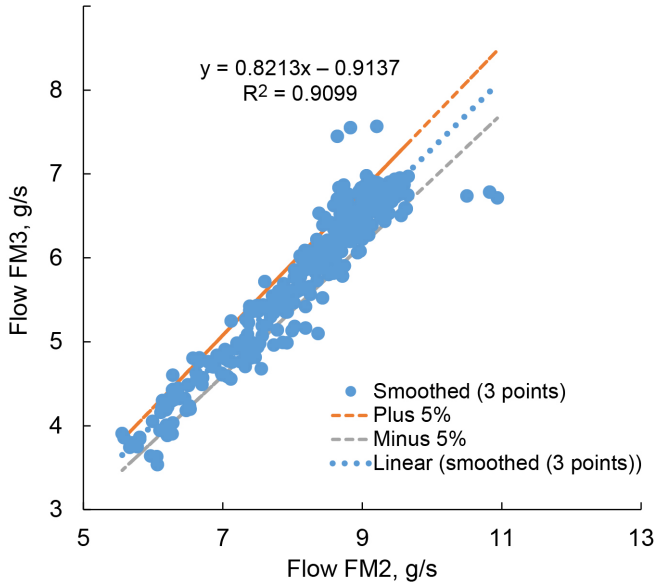

Figure 126.—Flowmeters FM2 and FM3 compared to each other.

4.5.2 Boiloff Testing

During the boiloff testing, FM2 was used to allow the pressure to be controlled at 138 kPa (20 psia). This was highly successful with the tank being controlled within approximately ±0.01 psia. Figure 127 shows the tank pressure and bulk liquid temperature during this time period, and additionally shows the capacitance probe coming back online (reads close to 92 percent fill at that point though in reality the tank is at approx. 78 percent fill). The liquid temperatures were very flat and, as with the preacoustic testing, no stratification was seen in the ullage until the liquid level went below the forward flange (as seen in Figure 128) at which point multiple temperatures, now in the ullage, warmed up rapidly. The flow was steady, but noisier than in previous testing (see Figure 129). The boiloff testing after the self-pressurization

test was also fairly quiet (see Figure 130). The liquid (Figure 131) and vapor (Figure 132) temperatures are shown with the stratification following the same trends as the preacoustic test: there are no temperature dispersions within the forward dome; significant stratification occurs in the barrel with much of the temperature changes driven by the heat coming from the two skirts. Figure 133 shows the tank wall temperatures, which are consistent with the fluid temperatures. The flowmeter data is shown in Figure 134, with both FM2 and FM3 in use the whole time and FM4 being used once the flow went below approximately 1.9 g/s. There are two blips in the data, one being caused by a pressure transducer (PT) anomaly causing loss of backpressure control at approximately 56 h and the second at approximately 73 h, during an early attempt to open up the flow to FM4 before the flow was low enough to maintain 138 kPa in the tank.

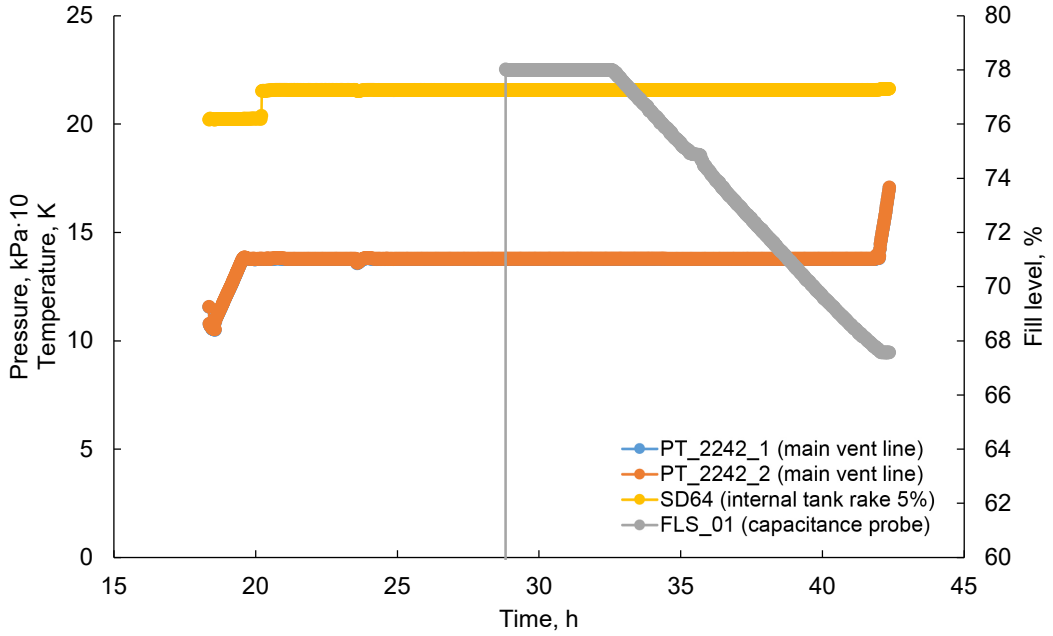

Figure 127.—Tank pressure, liquid temperature, and fill level of postacoustic testing.

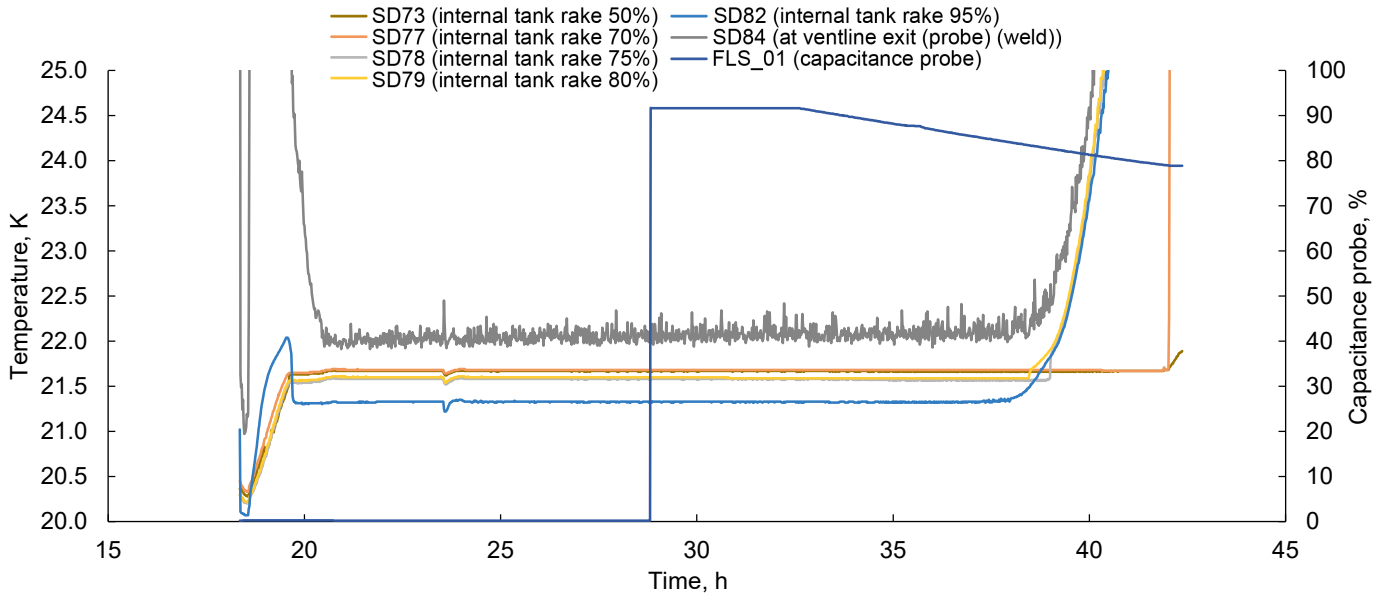

Figure 128.—Liquid temperatures during postacoustic high-fill boiloff testing.

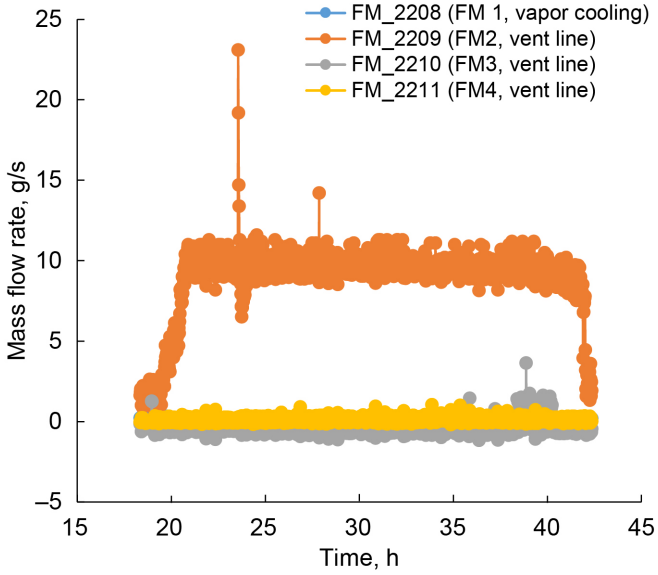

Figure 129.—Flowmeter data during postacoustic testing.

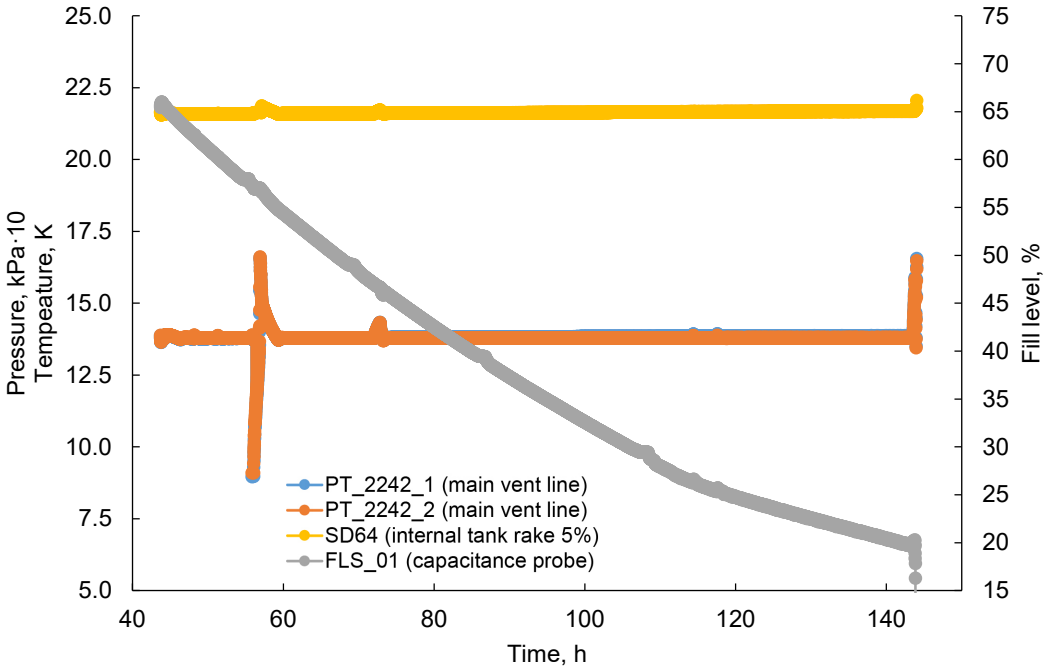

Figure 130.—Tank pressure, bulk liquid temperature, and fill level during boiloff to 25 percent fill.

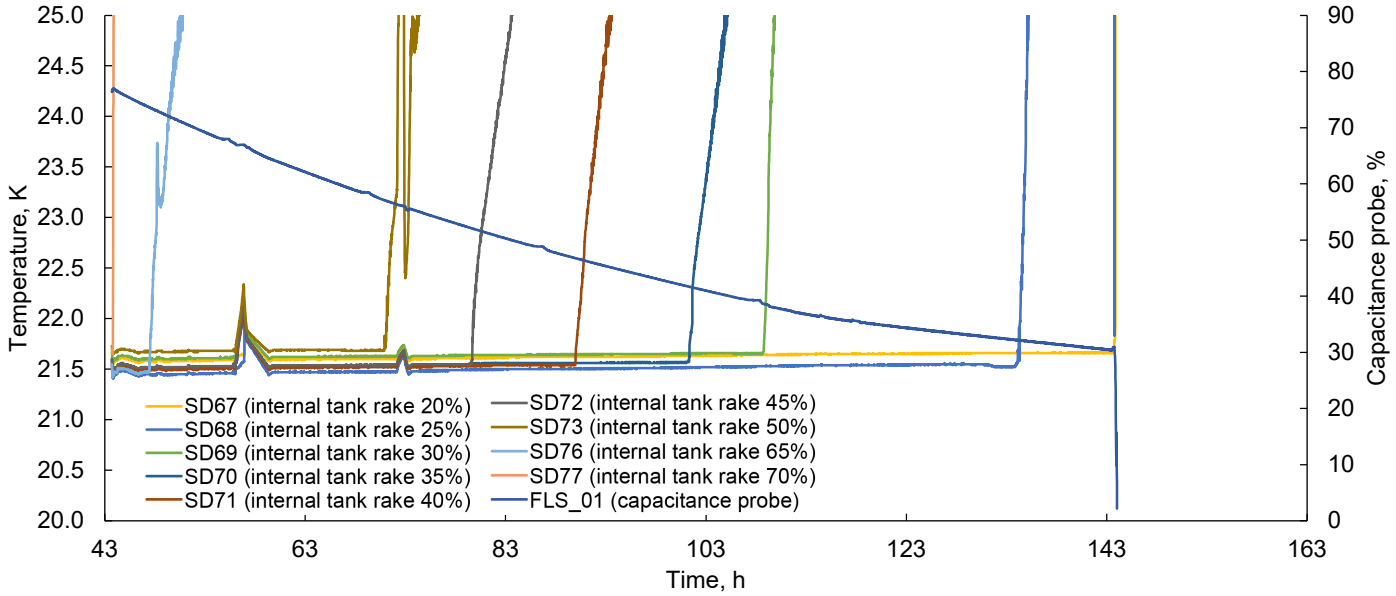

Figure 131.—Liquid temperatures during postacoustic boiloff testing down to 25 percent fill.

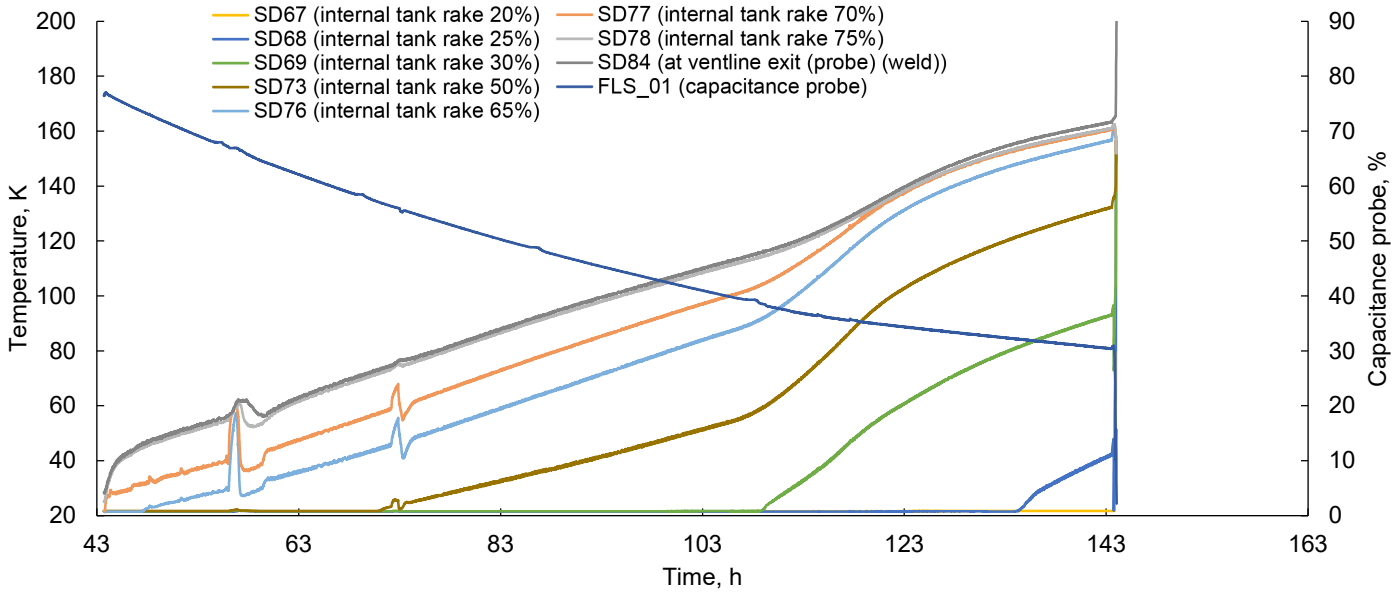

Figure 132.—Ullage temperature during postacoustic testing down to 25 percent fill.

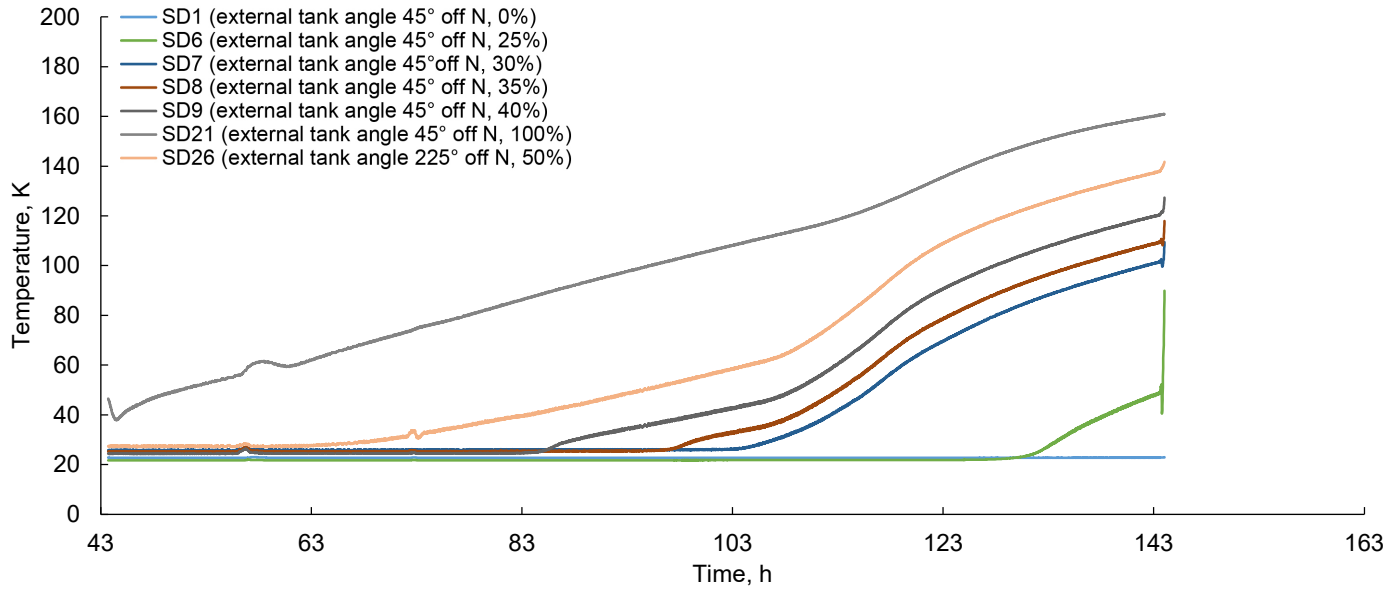

Figure 133.—Tank wall temperatures during postacoustic testing.

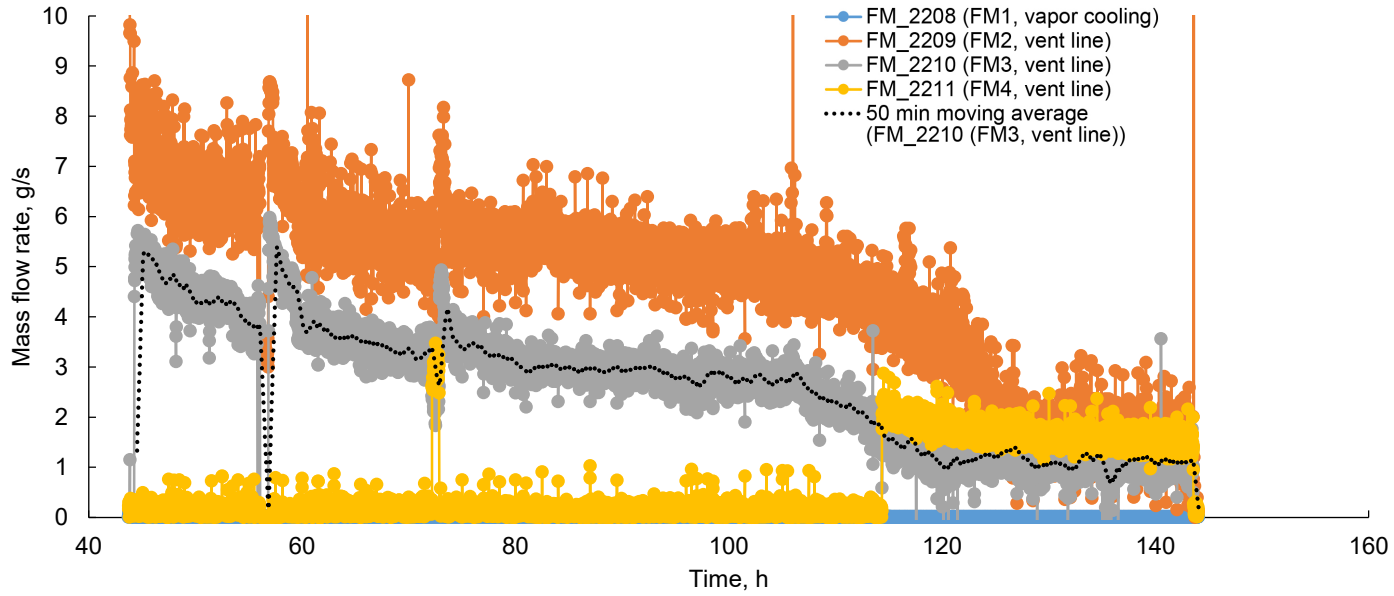

Figure 134.—Flowmeter data during boiloff testing below 70 percent fill. The 50 min moving average on FM3 dampens out much of the noise on the meter.

4.5.3 Self-Pressurization Testing

A single self-pressurization test was completed at approximately 70 percent fill. The main purpose was to run a self-pressurization test after a relatively clean boiloff testing with well-defined and clean initial conditions. The testing went smoothly and the pressure rise was steady (see Figure 135). As seen during preacoustic testing, the liquid temperatures split in two with the liquid above the aft flange warming up with the rising saturation temperature and the liquid below the flange staying relatively cold (see Figure 136). Also, as in previous testing, during depressurization, the two liquid zones progressively remixed, probably due to fluid dynamics during depressurization. The ullage temperatures, as seen in Figure 137, are similarly stratified by groups between the vent line temperatures, the forward dome temperatures, and SD77, which is nominally at 70 percent fill, just below the forward flange. The tank wall and system temperatures responded very similarly as in preacoustic testing.

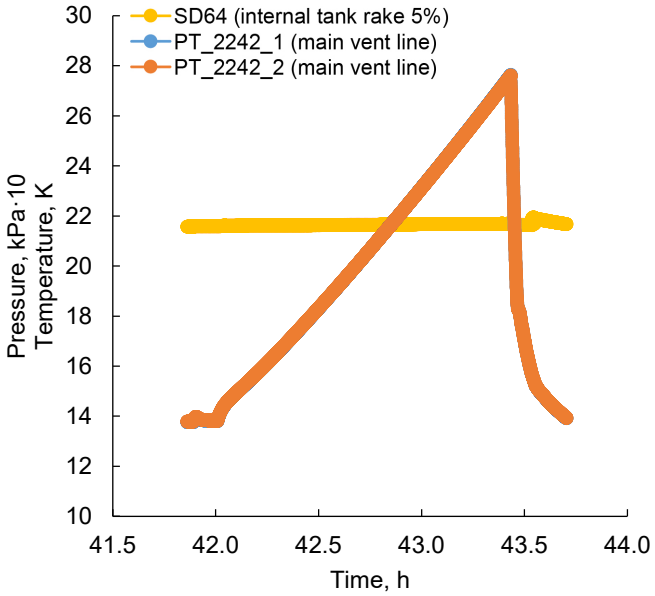

Figure 135.—Pressure and bulk fluid temperature for postacoustic testing self-pressurization.

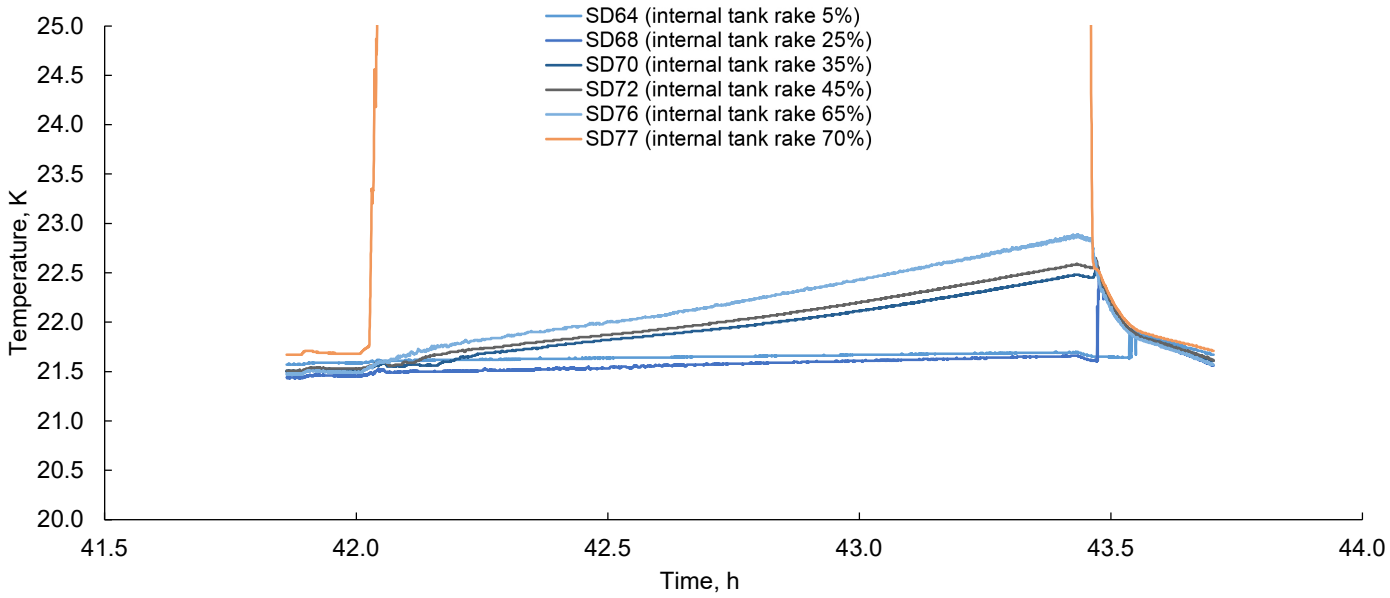

Figure 136.—Liquid temperature during postacoustic self-pressurization testing.

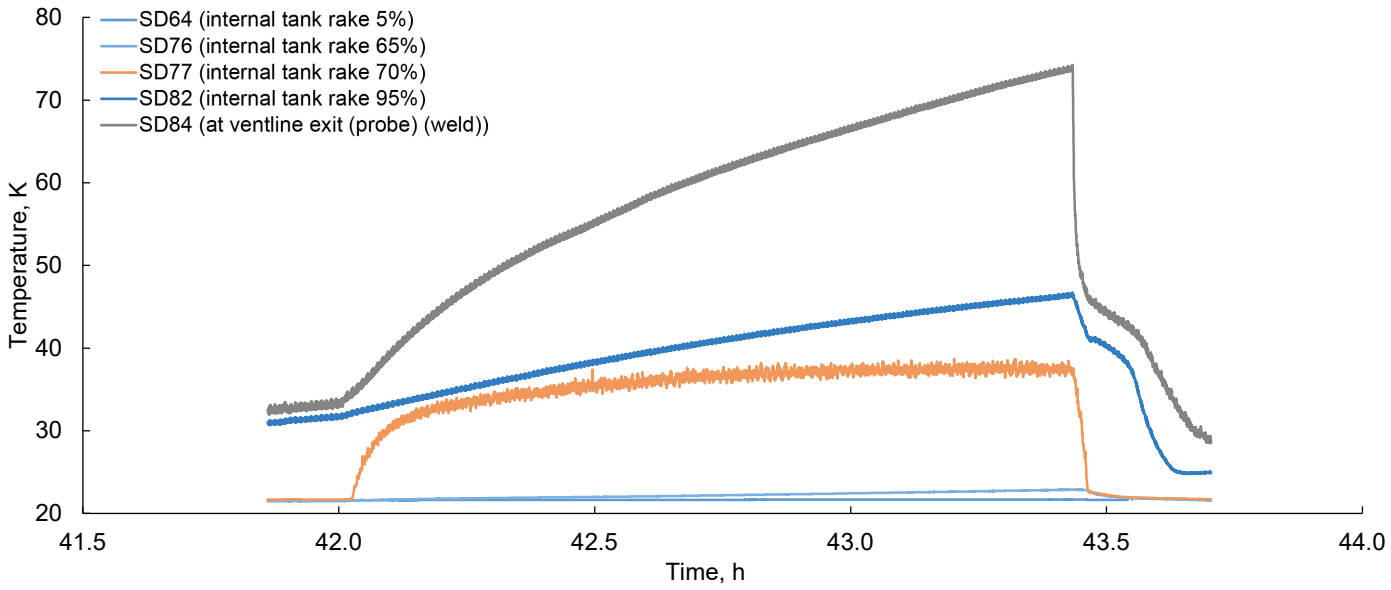

Figure 137.—Ullage temperatures during postacoustic self-pressurization testing.

4.5.4 Fill and Drain

Fill and drain data were captured during the testing and, while not reported here, have been archived and could be used for future analysis.

5.0 Test Data Analysis

5.1 Test Anomalies

Test anomalies are defined as the inability to achieve key test parameters defined in the SHIIVER test plan. General parameter anomalies were observed with tank pressure (Section 5.1.1) and vacuum chamber pressure (Section 5.1.2). In addition, a vapor-cooling parameter anomaly was observed with vapor flow rate (Section 5.1.3). All anomalies were evaluated to estimate experimental error and define techniques for data processing to mitigate error introduced by these anomalies.

5.1.1 Tank Pressure Anomaly

During steady-state boiloff tests, the tank pressure is to be controlled to 137.9 ± 0.07 kPa without vapor cooling to ensure the tank reaches a steady-state condition. Since the tank pressure was not controlled during vapor-cooling tests, variation in tank pressure due to vent system pressure drop is not considered anomalous.

The tank pressure during baseline and preacoustic LH_2 boiloff tests, as shown in Figure 138, could not be controlled within the specified tolerance because of a high-pressure drop in the vent system. This high vent system pressure drop was caused by the medium-capacity mass flowmeter, which was used because the high-capacity flowmeter was nonoperational. The tank pressure during the baseline boiloff test was outside the required range for more than 99 percent of the test duration. Tank pressure during the preacoustic LH_2 boiloff test was lower than that during the baseline test because of reduced boiloff rate and was outside the required range for 57 percent of the test duration.

The tank pressure during preacoustic LN_2 and postacoustic LH_2 boiloff tests are shown in Figure 139. The tank pressure during the preacoustic LN_2 boiloff test was outside the required range due to pressure control system error for 23 percent of the test duration. Most of the tank pressure variation during the postacoustic LH_2 boiloff test was caused by a single low-pressure event, potentially caused by vent line leakage into the vacuum chamber, which caused the pressure control system to over correct. The tank pressure measured by both PTs was below atmospheric pressure for approximately 20 min. This low pressure measurement and the pressure control system response resulted in tank pressure outside the required range for 12 percent of the duration of the postacoustic LH_2 test.

The effects of unsteady tank pressure were considered in processing heat load and boiloff rate results. The heat load to the fluid and boiloff rate were calculated using unsteady forms of energy, excluding kinetic and potential energy contributions, and mass conservation as shown in Equations (1) and (2) (Ref. 38).

$$\dot{Q} = \dot{m}_{v,\text{measured}} h_{\text{vent}} + \frac{\Delta\left(m_v h_v + m_L h_L\right)}{\Delta t} \tag{1}$$

$$\dot{m}_v = \dot{m}_{v,\text{measured}} + \frac{\Delta m_v}{\Delta t} \tag{2}$$

where heat load $\dot{Q}$ is in watts, measured vent flow rate $\dot{m}_{v,\text{measured}}$ is in g/s, calculated boiloff rate $\dot{m}_v$ is in g/s, calculated enthalpy of vent gas h_{vent}, tank bulk vapor h_v, and tank bulk liquid h_L are in J/g, time rate of change $\Delta(\ )/\Delta t$ is per second, and calculated mass of vapor m_v and liquid in tank m_L are in gram.

The primary tank PT indicated erratic behavior approximately 20 min into the vapor-cooling pressure rise test at the 70-percent fill level, as shown in Figure 140. During a 23-s period, beginning approximately 20 min after the start of the pressure rise test, the primary PT (PT_2242_1) indicated between –1,025 and 9,928 kPa while the secondary PT (PT_2242_2) indicated between 157.2 and 157.4 kPa. Once the primary PT output exceeded 344.7 kPa, the pressure control system automatically commanded the vent valve to open; thereby, decreasing tank pressure to 152.4 kPa before the vent valve was closed to resume the pressure rise test. The vapor-cooling pressure rise test at 70 percent fill level was repeated because of this anomaly.

5.1.2 Vacuum Chamber Pressure Anomaly

The maximum allowable vacuum chamber pressure is defined as 1×10^{-5} torr to ensure heat transfer to the SHIIVER tank accurately simulates a space environment. Vacuum chamber pressure anomalies were observed during all LH_2 tests. During the preacoustic LN_2 tests, the chamber pressure was observed to be less than the maximum allowable value due to decreased test article leakage.

The vacuum chamber pressure exceeded the maximum allowable value during baseline and vapor-cooling tests, as

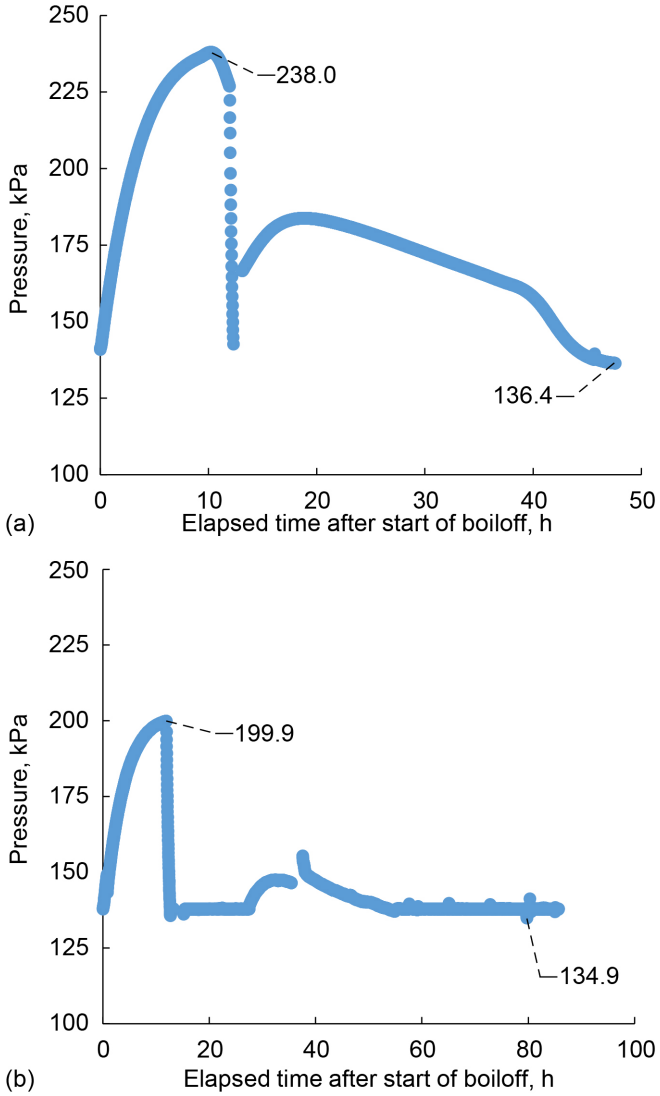

Figure 138.—Tank pressure during (a) baseline and (b) preacoustic liquid hydrogen boiloff tests.

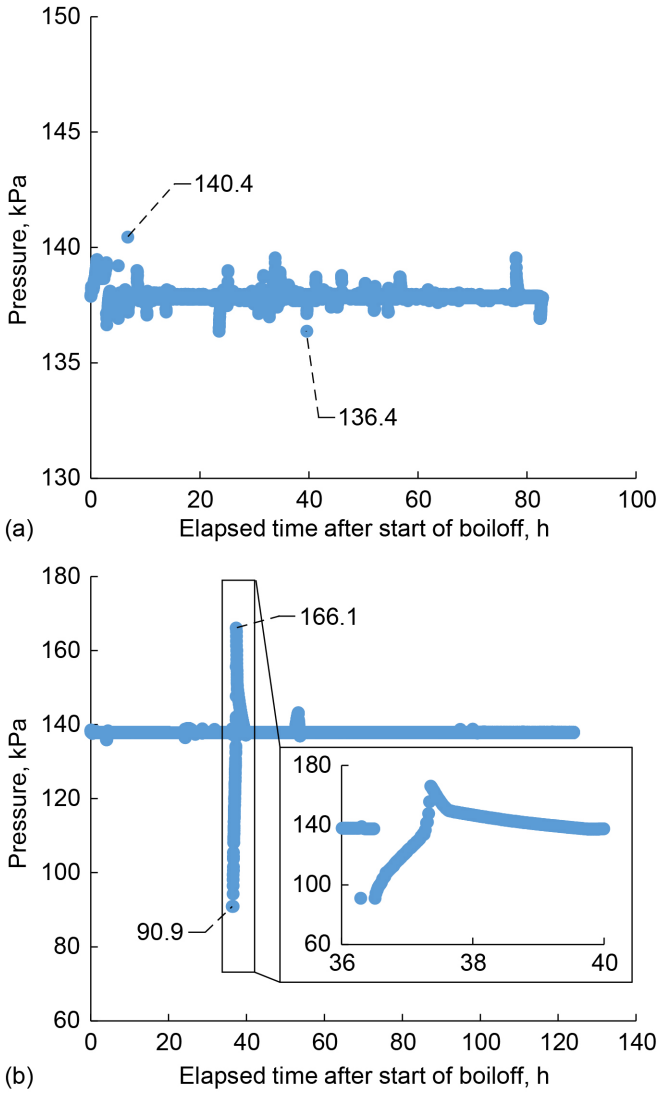

Figure 139.—Tank pressure during (a) preacoustic liquid nitrogen and (b) postacoustic liquid hydrogen boiloff tests.

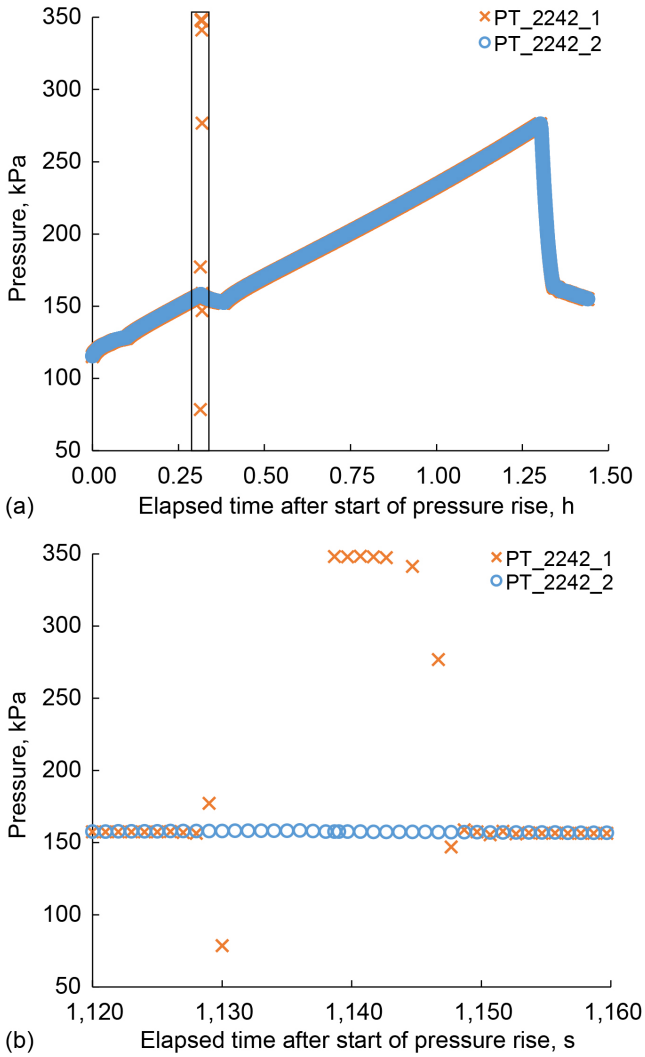

Figure 140.—Tank pressure anomaly during 70 percent fill vapor-cooling pressure rise test. (a) Test time from 0 to 1.5 h. (b) Subset of test time indicated by box in (a).

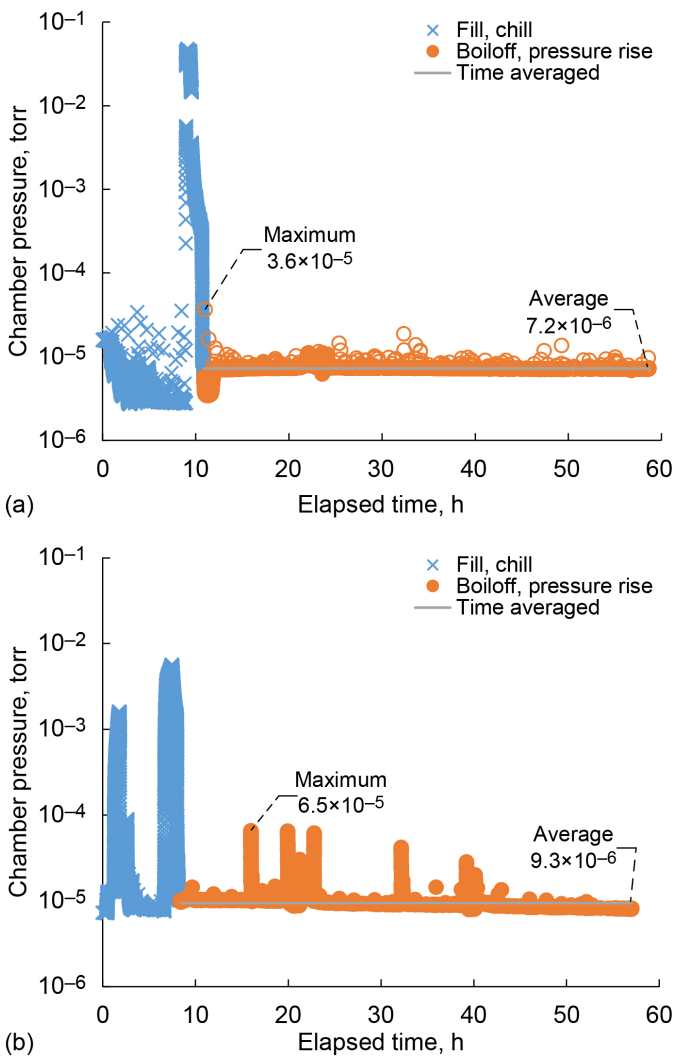

Figure 141.—Chamber pressure during (a) baseline and (b) vapor-cooling tests.

shown in Figure 141. Excessive leakage from the fill and drain valve actuator caused high chamber pressure during fill and chill. Nominal leakage from the test article during boiloff and pressure rise caused instantaneous chamber pressure to exceed the maximum allowable value, but time-averaged chamber pressure was lower than the maximum allowable.

The heat transfer error introduced by high chamber pressure was estimated as the difference in the conduction heat flux at the measured chamber pressure and the maximum allowable chamber pressure divided by the total heat flux (conduction and radiation) at the maximum allowable chamber pressure:

$$\varepsilon = \frac{q_{cond}l_{p\text{chamber}} - q_{cond}l_{p\text{max-allow}}}{q_{cond}l_{p\,\text{max}-\text{allow}} + q_{\text{radiation}}} \tag{3}$$

where heat transfer error ε is dimensionless, conduction heat flux at measured chamber pressure $q_{cond}l_{p\text{chamber}}$ and maximum allowable chamber pressure $q_{cond}l_{p\text{max-allow}}$ are in W/m², and radiation heat flux $q_{\text{radiation}}$ is in W/m².

The conduction heat flux through the SOFI was found to be independent of pressure for pressures less than 1×10^{-3} torr (Ref. 33). Error is caused only by heat transfer from the chamber wall to the SOFI surface because SOFI conductance is independent of pressure at the levels of the observed pressure anomaly. The conduction heat flux $q_{\text{conduction}}$ and $q_{\text{radiation}}$ from the chamber wall to the SOFI surface are estimated using the expressions in Equations (4) and (5), respectively (Refs. 39 and 40).

$$q_{\text{conduction}} = \frac{F_g p}{2}\frac{\gamma+1}{\gamma-1}\left[\frac{a_s a_c}{a_c + \left(\frac{d_s}{d_c}\right)^2 (1-a_s a_c)}\right] \sqrt{\frac{R_u F_e}{2\pi M_W \frac{T_{\text{chamber}} + T_{SOFI}}{2}}} \left(T_{\text{chamber}} - T_{SOFI}\right) \quad (4)$$

$$q_{\text{radiation}} = \sigma \frac{\varepsilon_s \varepsilon_{\text{chamber}}}{\varepsilon_{\text{chamber}} + \left(\frac{d_s}{d_c}\right)^2 (1-\varepsilon_s \varepsilon_{\text{chamber}})} \left(T_{\text{chamber}}^4 - T_{SOFI}^4\right) \quad (5)$$

where $q_{\text{conduction}}$ is in W/m^2, IG factor F_g is dimensionless, vacuum chamber pressure p is in pascal, specific heat ratio γ is dimensionless, accommodation coefficient at SOFI surface a_s and vacuum chamber wall a_c (0.85 assumed) are dimensionless, diameter of SOFI surface d_s and vacuum chamber d_c are in meters, universal gas constant R_u is in J/mol·K, energy conversion factor F_e is 1 J/g = 1,000 m^2/s^2, molecular mass of air in the vacuum chamber M_w is in g/mol, temperatures of the vacuum chamber wall T_c (290 K assumed) and SOFI surface T_s (250 K assumed) are in Kelvin, Stefan-Boltzmann constant σ is 5.6704×10^{-8} W/m^{2}K^4, and emissivity of SOFI surface ε_s (0.90 assumed) and vacuum chamber wall $\varepsilon_{\text{chamber}}$ (0.9 assumed) are dimensionless.

The IG factor is defined as the inverse of the IG sensitivity to residual gas species in the vacuum chamber relative to air. The vacuum chamber RGA indicated a mixture of hydrogen, helium, water, and air. The IG factor was conservatively calculated assuming an average of hydrogen and helium IG sensitivities (Ref. 41), as shown in Equation (6).

$$F_g = \frac{1}{\frac{S_{H_2} + S_{He}}{2}} = \frac{1}{\frac{0.46 + 0.18}{2}} = 3.125 \quad (6)$$

The estimated heat transfer error during baseline and vapor-cooling tests is shown in Figure 142. This error is highest during fill and chill due to elevated vacuum chamber pressure, but tank heat loads during this time do not adversely affect the accuracy of results during steady-state boiloff or transient pressure rise testing. The maximum instantaneous heat transfer error during boiloff and pressure rise testing was 0.3 percent for baseline and 0.7 percent for vapor cooling; time-averaged heat transfer error

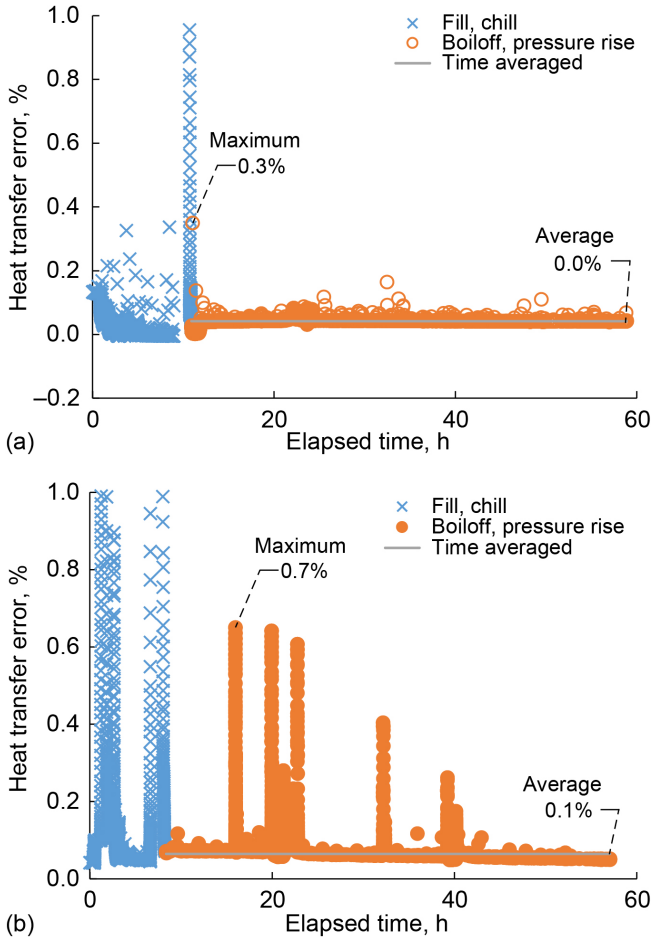

Figure 142.—Estimated heat transfer error during (a) baseline and (b) vapor-cooling tests.

was approximately zero for baseline and 0.1 percent for vapor cooling. These results demonstrate the vacuum chamber pressure anomaly did not adversely affect results of steady-state boiloff and transient pressure rise during the baseline and vapor-cooling tests.

The vacuum chamber pressure exceeded the maximum allowable value during the preacoustic LH_2, preacoustic LH_2 vapor-cooling, and postacoustic LH_2 tests, as shown in Figure 143. The fill and drain valve actuator was replaced after completion of baseline and vapor-cooling tests, which resulted in significantly lower vacuum chamber pressure. Nominal leakage from the test article during preacoustic and postacoustic LH_2 boiloff and pressure rise caused instantaneous chamber pressure to exceed the maximum allowable value, but time-averaged chamber pressure was lower than the maximum allowable. Nominal leakage from the test article during preacoustic LN_2 boiloff did exceed the maximum vacuum chamber pressure requirement.

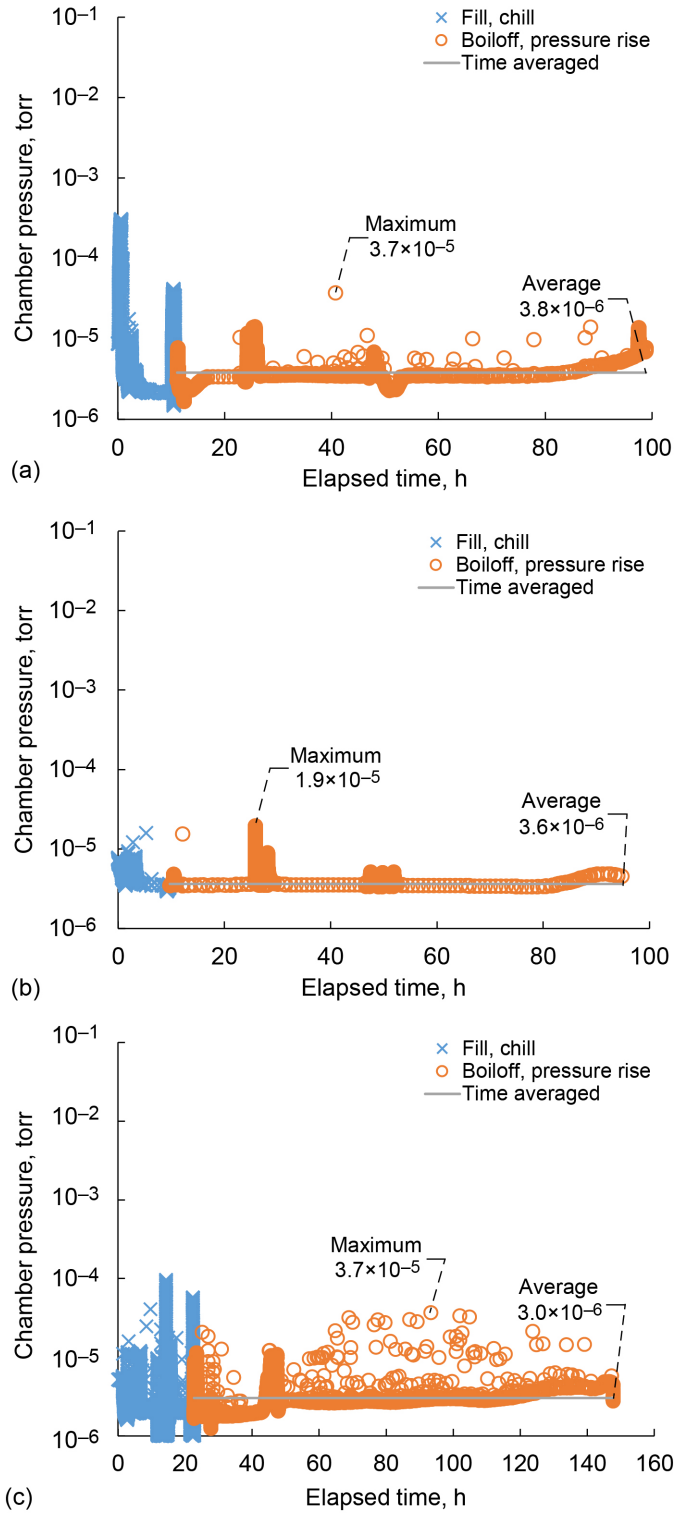

Figure 143.—Chamber pressure during preacoustic and postacoustic liquid hydrogen tests. (a) Preacoustic. (b) Preacoustic vapor cooling. (c) Postacoustic.

From the previous calculations, it was shown that the heat transfer error due to SOFI conductance is negligible for pressures less than 1×10^{-3} torr (Ref. 33). This error for the barrel section of the tank without MLI was estimated using the same method that was used for the baseline and vapor-cooling tests. The heat transfer error for the dome sections of the tank with MLI were estimated as the ratio of heat flux through MLI at measured chamber pressure to that at maximum allowable chamber pressure. The total heat transfer error for the tank was calculated as a surface area weighted average of the barrel (29 percent surface area) and dome (71 percent surface area) errors, as shown in Equation (7).

$$\varepsilon = \frac{A_{SOFI}}{A_{SOFI}+A_{MLI}}\frac{q_{\text{conduction}}p_{\text{chamber}} - q_{\text{conduction}}p_{\text{max-allow}}}{q_{\text{conduction}}p_{\text{max-allow}} + q_{\text{radiation}}} + \frac{A_{MLI}}{A_{SOFI}+A_{MLI}}\frac{q_{\text{gas}}p_{\text{chamber}} - q_{\text{gas}}p_{\text{max-allow}}}{q_{\text{gas}}p_{\text{max-allow}} + q_{MLI}} \tag{7}$$

where surface area of SOFI A_{SOFI} and MLI A_{MLI} are in m², interstitial gas conduction heat flux at measured chamber $q_{\text{gas}}p_{\text{chamber}}$ and maximum allowable chamber pressure $q_{\text{gas}}p_{\text{max-allow}}$ are in W/m², and MLI heat flux q_{MLI} is in W/m².

The interstitial gas conduction q_{gas} and effective q_{MLI} are calculated from the empirical expressions in Equations (8) and (9), respectively, (Ref. 42). The same IG factor defined to account for hydrogen and helium in the vacuum chamber was assumed to apply to q_{gas} (Ref. 41).

$$q_{\text{gas}} = \frac{C_g F_g p}{N_s}\left(T^{0.52}_{\text{chamber}} - T^{0.52}_{SOFI}\right) \tag{8}$$

$$q_{MLI} = \frac{C_s\left[0.017 + 7.0\times10^{-6}\left(800 - \frac{T_{\text{chamber}}+T_{SOFI}}{2}\right)+ 0.0228\ln\left(\frac{T_{\text{chamber}}+T_{SOFI}}{2}\right)\right]\bar{N}^{2.63}}{N_s}\left(T_{\text{chamber}} - T_{SOFI}\right)\ldots + \frac{C_r\varepsilon_{TR}}{N_s}\left(T^{4.67}_{\text{chamber}} - T^{4.67}_{SOFI}\right) \tag{9}$$

where empirical constants C_g (14,600), C_s (2.4×10^{-4}), and C_r (5.39×10^{-10}) are dimensionless, F_g is dimensionless, p is in torr, N_s is the number of MLI layers, temperatures of the vacuum chamber wall T_{chamber} (290 preacoustic and 275 postacoustic assumed) and SOFI surface T_{SOFI} (50 assumed) are in Kelvin, MLI density $\bar{N}$ is in layers per centimeter, and effective transmission of MLI layers ε_{TR} is dimensionless.

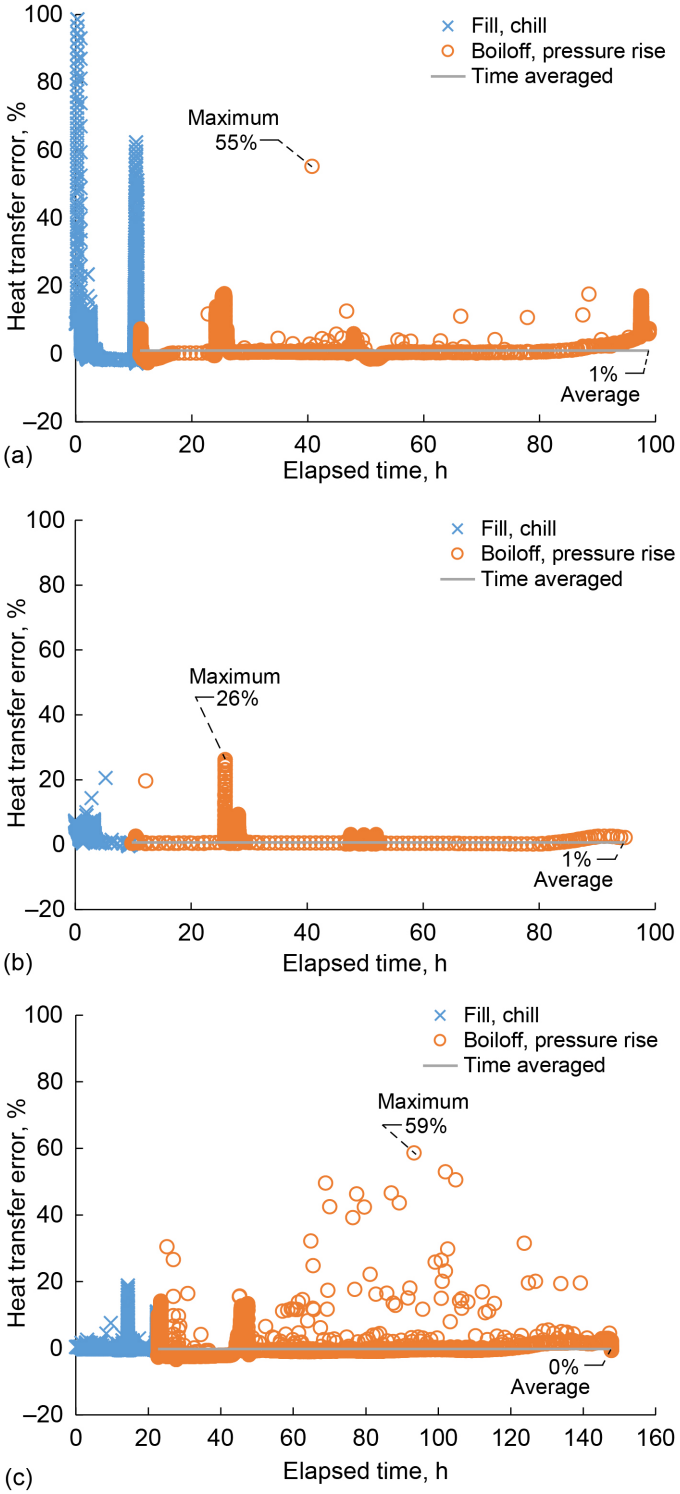

Figure 144.—Estimated heat transfer error during preacoustic and postacoustic liquid hydrogen testing. (a) Preacoustic. (b) Preacoustic vapor cooling. (c) Postacoustic.

The estimated heat transfer error during preacoustic and postacoustic LH_2 tests is shown in Figure 144. This error is highest during fill and chill due to elevated vacuum chamber pressure, but tank heat loads during this time do not adversely affect accuracy of results during steady-state boiloff or transient pressure rise testing. Maximum instantaneous heat transfer error during boiloff and pressure rise testing was 55 percent for preacoustic LH_2, 26 percent for preacoustic LH_2 vapor cooling, and 59 percent for postacoustic LH_2; the time-averaged heat transfer error was 1 percent or less because average chamber pressure was lower than the maximum allowable. These results demonstrate that the vacuum chamber pressure anomaly did not adversely affect results of steady-state boiloff and transient pressure rise during the preacoustic and postacoustic tests. Furthermore, no evidence of increased heat flux during times of elevated chamber pressure was seen in the heat flux sensor output (Section 5.10).

5.1.3 Vapor-Cooling Flow Rate Measurement Anomaly

Measuring the vapor flow rate is required in order to determine the heat absorbed by the vapor-cooling system. A single, high-capacity flowmeter was installed in the vapor-cooling vent system and was nonoperational during 95 percent of the baseline vapor-cooling test duration, as shown in Figure 145. After completion of the vapor-cooling test, the flowmeter was repaired and operated successfully during preacoustic and postacoustic vapor-cooling tests. Additional information about calculating flow rate from measured liquid level and propellant mass is provided in Section 5.4.

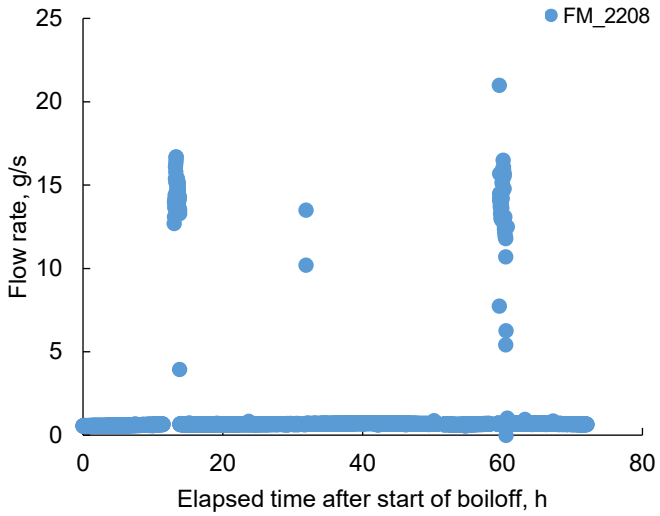

Figure 145.—Measured flow rate during vapor-cooling test.

5.2 Quasi-Steady-State Results

The quasi-steady-state results consist of calculated heat load during boiloff and vapor-cooling portions of the test. The heat load was calculated using two independent methods: heat transfer to the exterior surface of the tank and heat absorbed by the fluid inside the tank. The heat transfer to the exterior surface of the tank was determined from measured tank wall heat flux, calculated SOFI conduction heat flux, and calculated SOFI surface radiation heat flux. The heat transfer to the fluid inside the tank was calculated from measured tank pressure (and associated change in liquid enthalpy), vented vapor temperature, and vent flow rate.

5.2.1 Tank Acreage Heat Load Calculation Method

The heat loads to the acreage areas of the tank (i.e., forward and aft domes and barrel) were calculated as the product of surface area and heat flux. The acreage regions of the tank were exposed to vapor and/or liquid, depending on the instantaneous liquid level, during boiloff tests. The instantaneous liquid level was determined by correlating the capacitance probe output to the wet and dry transition of the fluid temperature sensors that were installed on an internal support rake in approximately 5-percent-fill-level increments (see Figure 21). The capacitance probe was calibrated and correlated three times during testing: before the LH_2 baseline, vapor-cooling, and preacoustic tests; before the LN_2 preacoustic tests; and during the initial LH_2 postacoustic test. These calibrations were required because of the change in dielectric properties of LH_2 and LN_2. The liquid level correlations for the three different capacitance probe calibrations are shown in Figure 146. The symbols in the figure represent the wet and dry transition of fluid temperature sensors. The wet and dry transition was observed during LH_2 baseline testing at 14 temperature sensor locations between 95 and 30 percent fill levels. The transition was also observed during LN_2 preacoustic testing at four locations between 75 and 25 percent fill levels. In addition, the transition was observed during LH_2 postacoustic testing at 11 locations between 70 and 25 percent fill levels.

The tank surface area was calculated from tank dimensions that were modified for cryogenic temperature as a function of liquid height. Surface area correlations were defined for aft dome, barrel, and forward dome regions of the tank as a function of liquid level, as shown in Figure 147.

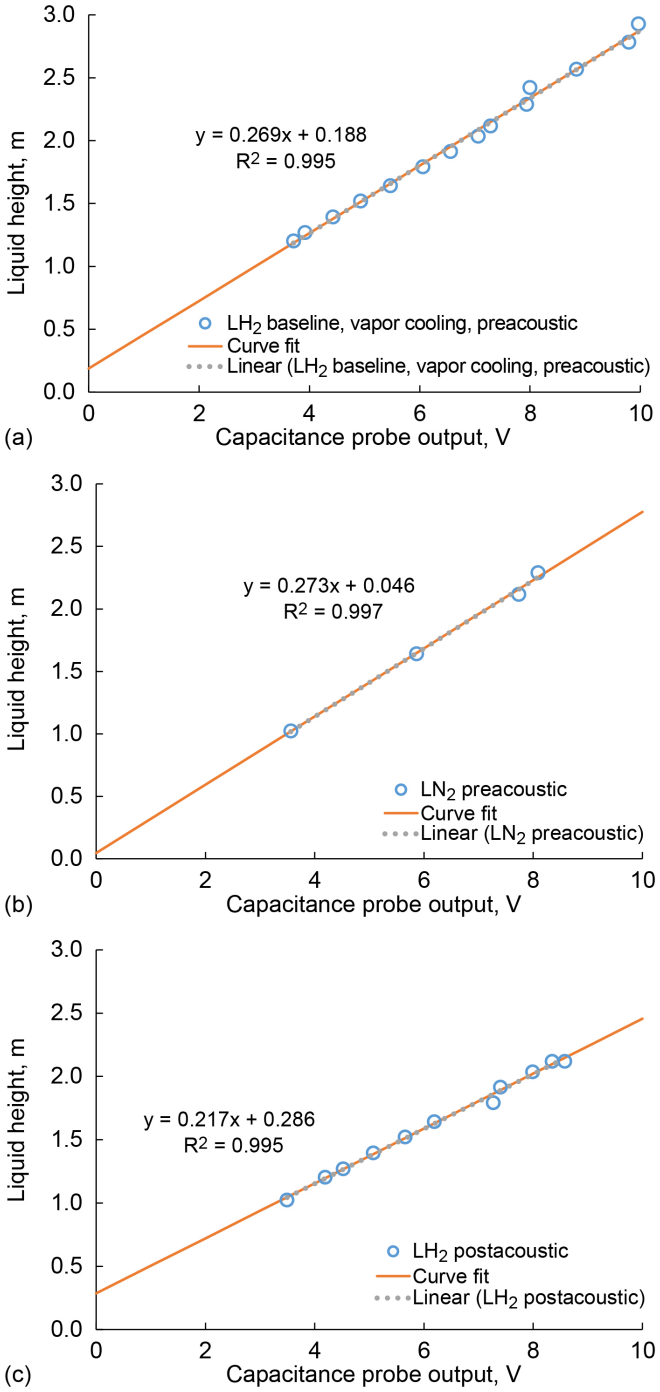

Figure 146.—Liquid level correlation to capacitance probe output. Symbols represent wet and dry transition of fluid temperature sensors. (a) Liquid hydrogen (LH_2) baseline, vapor cooling, and preacoustic. (b) Liquid nitrogen (LN_2) preacoustic. (c) LH_2 postacoustic.

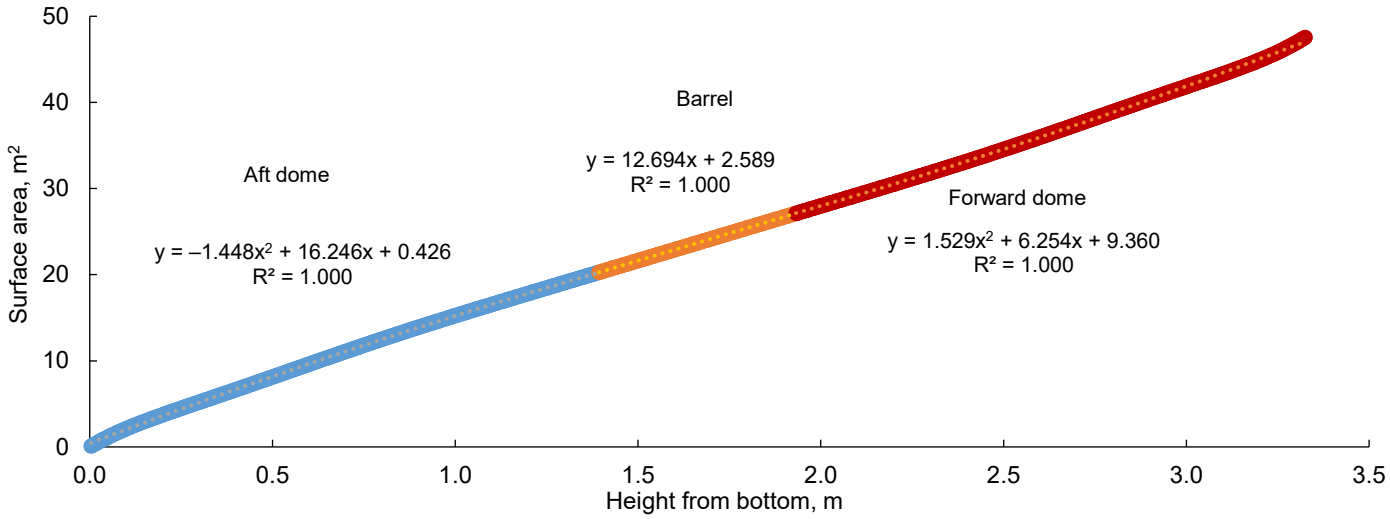

Figure 147.—Tank surface area correlation to liquid level.

5.2.1.1 Forward and Aft Dome Heat Flux Calculation and Verification

Three different methods are used to determine the heat loads coming into the tank in the forward and aft domes: heat flux sensors mounted on the tank surface (under the SOFI), conduction through the SOFI based on SDs mounted on the tank surface and SOFI surface, and radiation from the chamber wall to the outer surface (be it MLI or SOFI).

The forward and aft dome heat flux was measured by heat flux sensors installed at four locations on each dome. The heat flux calculated from measured sensor output voltage and vendor specified sensitivity is discussed in Section 5.10. Significant variation in measured heat flux was observed during baseline and vapor-cooling tests and is largely attributed to uncertainty in voltage measurement when the DAQ system gain was defined too low. For this reason, the maximum measured heat flux of the four sensors on each dome was used to define heat flux during baseline and vapor-cooling tests. Variation among sensor measurements was much less during preacoustic and postacoustic tests so the average heat flux from the four sensors on each dome was used to define heat flux for these tests.

Heat flux by conduction through the SOFI was calculated as a function of measured tank wall and SOFI surface temperatures using the expression in Equation (10).

$$q_{\text{conduction}} = k_{SOFI} \frac{T_{SOFI} - T_{subs}}{\Delta x_{SOFI}} \tag{10}$$

where thermal conductivity of SOFI $k_{SOFI} = 0.011 + 6.231\times10^{-5}$ $[(T_{surf} + T_{subs})/2]$ (Ref. 43), temperatures of SOFI surface T_{SOFI} and tank substrate T_{subs} are in Kelvin, and the local thickness of SOFI at the temperature measurement location Δx_{SOFI} is in Kelvin (see Section 2.3.1).

Heat flux by radiation to the SOFI surface was calculated as a function of measured SOFI surface and vacuum chamber wall temperature during baseline and vapor-cooling tests and MLI interior surface temperature during preacoustic and postacoustic tests. During baseline and vapor-cooling tests, the forward dome experiences radiation from the vacuum chamber wall and the aft dome experiences radiation from the thermal support structure, which are assumed to have the same temperature, but different surface emissivity. During preacoustic and postacoustic tests, both domes experience radiation from the interior surface of the MLI blanket. Radiation heat flux was calculated using Equation (11). The emissivity of the SOFI ε_{SOFI} is 0.9 (Ref. 44), the vacuum chamber wall is 0.9 (Ref. 45), the stainless steel thermal support structure is 0.349 (Section 2.3.3), and the MLI interior surface is 0.035 (Ref. 42). Radiation view factors between the forward dome and the chamber wall and between the aft dome and the tank support structure were assumed to be unity.

$$q_{\text{radiation}} = \frac{\sigma}{\frac{1}{\varepsilon_{SOFI}} + \frac{1}{\varepsilon_{surf}} - 1}\left(T_{surf}^4 - T_{SOFI}^4\right) \tag{11}$$

where ε_{SOFI} and vacuum chamber wall, support structure, or MLI ε_{surf} are dimensionless and the temperatures of SOFI T_{SOFI} and vacuum chamber wall, support structure, or MLI T_{surf} are in Kelvin.

A comparison of measured and calculated heat flux for the forward and aft domes during baseline LH_2 testing is shown in Figure 148. The aft dome heat flux was found to be

about 50 percent lower than the forward dome heat flux due to differences in emissivity of the vacuum chamber wall and support structure. The calculated $q_{conduction}$ is significantly higher than the measured and calculated $q_{radiation}$ so the average dome heat flux was defined as the average of the measured and calculated $q_{radiation}$ values. The root-sum-square average dispersion of measured and calculated heat flux during baseline tests was 7 percent for the forward dome and 12 percent for the aft dome.

A comparison of measured and calculated heat flux for the forward and aft domes during LH_2 vapor-cooling testing is shown in Figure 149. Note that there were two tests between the fill levels of approximately 80 and 50 percent. Differences between forward and aft dome heat flux and among calculated conduction, calculated radiation, and measured heat flux are all similar to those observed during baseline testing and the average dome heat flux was defined as the average of the measured and calculated $q_{radiation}$ values. The root-sum-square average dispersion of measured and calculated heat flux during vapor-cooling tests was 8 percent for the forward dome and 16 percent for the aft dome.

A comparison of measured and calculated heat flux for the forward and aft domes during preacoustic LH_2 testing is shown in Figure 150. Forward and aft dome heat flux was similar during preacoustic testing because both domes were covered by MLI, which decreased sensitivity to the emissivity of the environment surface. The forward dome demonstrated a measured heat flux less than zero at lower fill levels, which indicates heat flow from the fluid to the tank wall. Heat flux to the forward dome is low because of the MLI so heat flux from the barrel heats vapor that then warms the forward dome. This behavior was not observed in the calculated $q_{radiation}$, which indicates the SOFI and MLI temperatures were not at steady state on the forward dome. The calculated $q_{conduction}$ is more

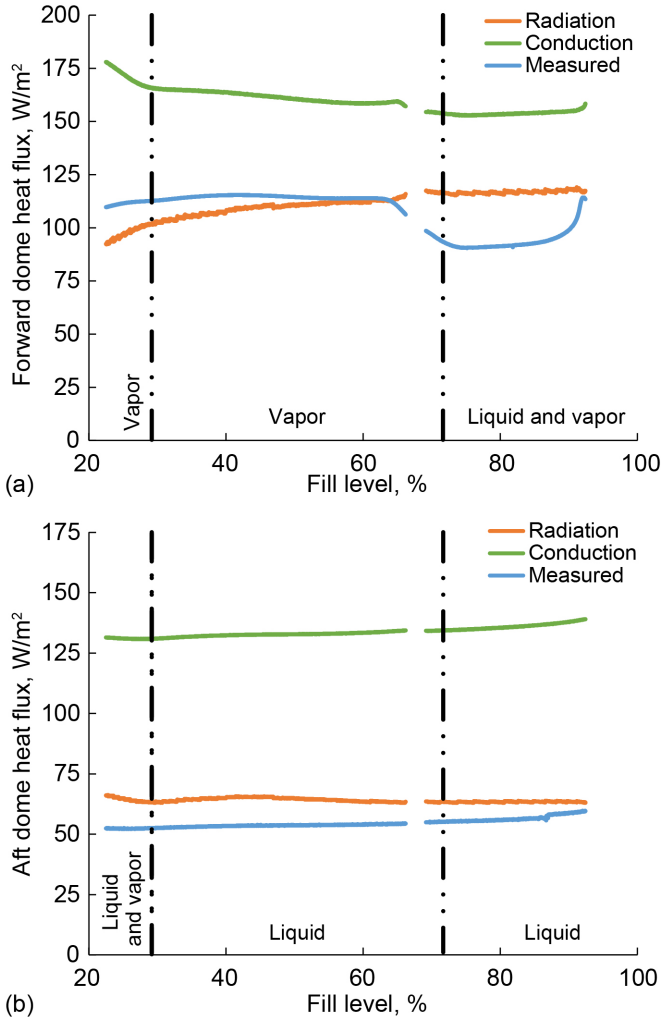

Figure 148.—Baseline liquid hydrogen test heat flux. (a) Forward dome. (b) Aft dome.

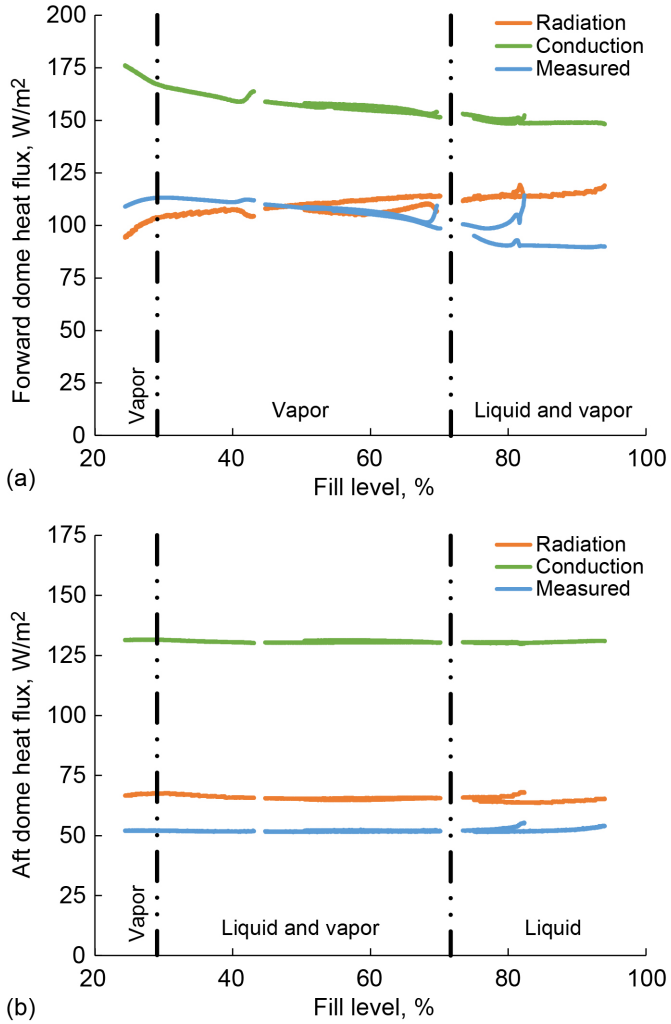

Figure 149.—Baseline liquid hydrogen vapor-cooling test heat flux. (a) Forward dome. (b) Aft dome.

than an order of magnitude higher than the measured and calculated $q_{radiation}$ so the average dome heat flux was defined as the average of the measured and calculated $q_{radiation}$ values. The root-sum-square average dispersion of measured and calculated heat flux during preacoustic LH_2 tests was 31 percent for the aft dome and could not be defined accurately for the forward dome because of the difference in heat flow direction.

A comparison of measured and calculated heat flux for the forward and aft domes during preacoustic LH_2 testing with vapor cooling is shown in Figure 151. Differences between forward and aft dome heat flux and among calculated conduction, calculated radiation, and measured heat flux are all similar to those observed during preacoustic LH_2 testing and the average dome heat flux was defined as the average of the measured and calculated $q_{radiation}$ values. The forward dome also demonstrated measured heat flow from the fluid to the tank wall at low fill levels that was not observed in the calculated $q_{radiation}$. The root-sum-square average dispersion of measured and calculated heat flux during preacoustic LH_2 tests with vapor cooling was 23 percent for the aft dome.

A comparison of measured and calculated heat flux for the forward and aft domes during preacoustic LN_2 testing is shown in Figure 152. Differences between forward and aft dome heat flux and among calculated conduction, calculated radiation, and measured heat flux are all similar to those observed during preacoustic LH_2 testing and the average dome heat flux was defined as the average of the measured and calculated $q_{radiation}$ values. The root-sum-square average dispersion of measured and calculated heat flux during preacoustic LN_2 tests was 36 percent for the aft dome.

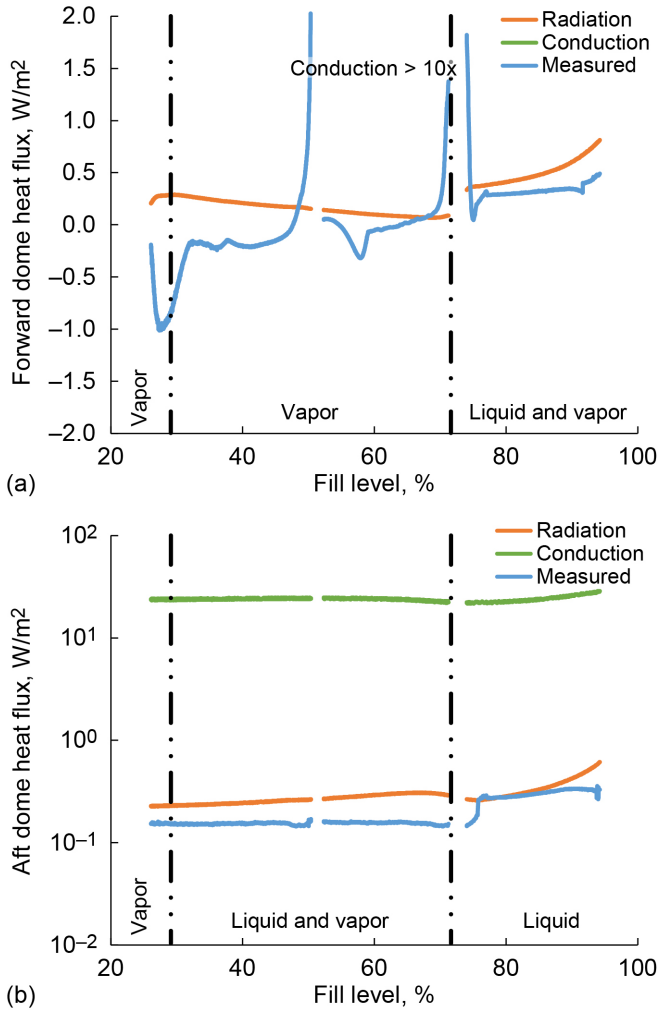

Figure 150.—Preacoustic liquid hydrogen test heat flux. (a) Forward dome. (b) Aft dome.

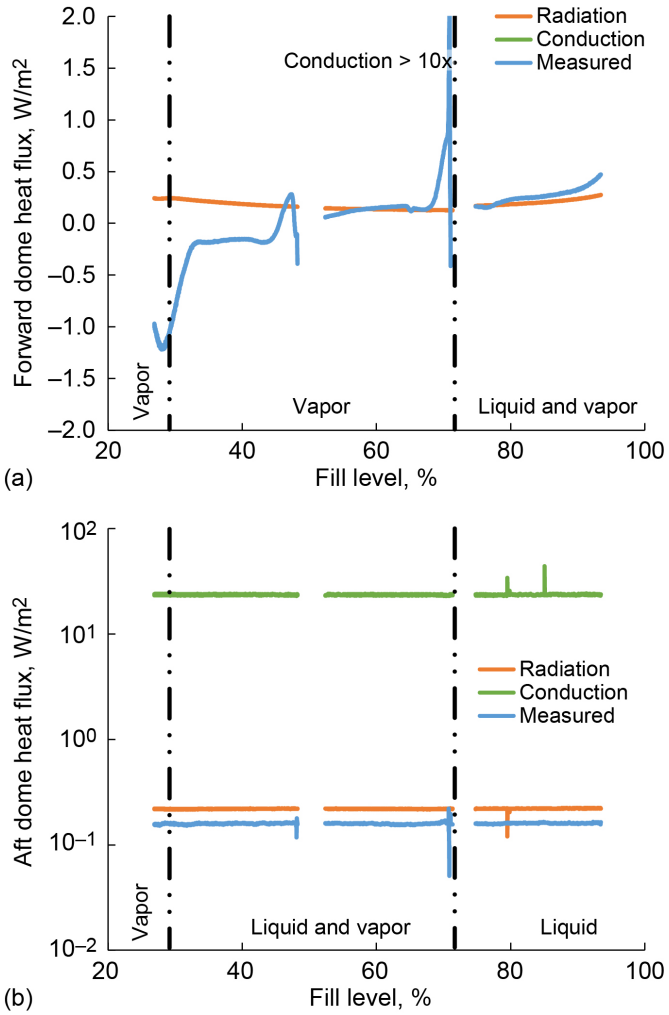

Figure 151.—Preacoustic liquid hydrogen vapor-cooling test heat flux. (a) Forward dome. (b) Aft dome.

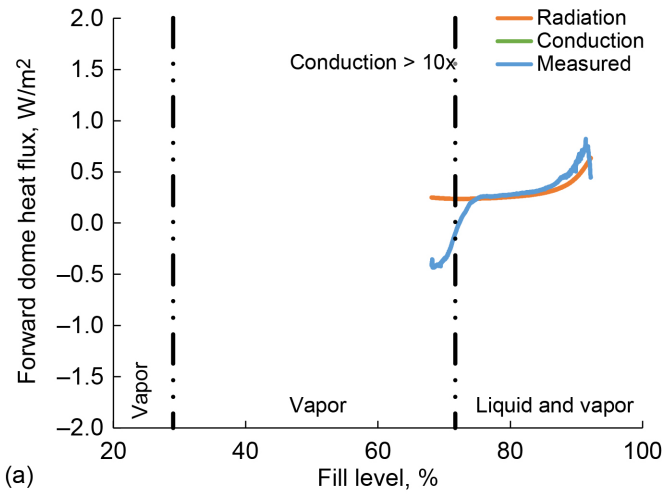

Figure 152.—Preacoustic liquid nitrogen test heat flux. (a) Forward dome. (b) Aft dome.

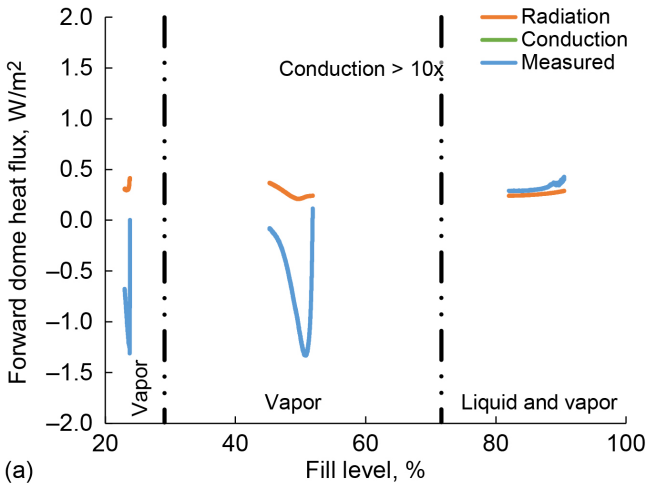

Figure 153.—Preacoustic liquid nitrogen vapor-cooling test heat flux. (a) Forward dome. (b) Aft dome.

A comparison of measured and calculated heat flux for the forward and aft domes during preacoustic LN_2 testing with vapor cooling is shown in Figure 153. Differences between forward and aft dome heat flux and among calculated conduction, calculated radiation, and measured heat flux are all similar to those observed during preacoustic LH_2 and LN_2 testing and the average dome heat flux was defined as the average of the measured and calculated $q_{radiation}$ values. Preacoustic LN_2 vapor-cooling tests at moderate and low fill levels were performed after draining fluid from the tank so steady-state thermal conditions were not achieved. The root-sum-square average dispersion of measured and calculated heat flux during preacoustic LN_2 tests with vapor cooling was 41 percent for the aft dome.

A comparison of measured and calculated heat flux for the forward and aft domes during postacoustic LH_2 testing is shown in Figure 154. Differences between forward and aft dome heat flux and among calculated conduction, calculated radiation, and measured heat flux are all similar to those observed during preacoustic LH_2 and LN_2 testing and the average dome heat flux was defined as the average of the measured and calculated $q_{radiation}$ values. The root-sum-square average dispersion of measured and calculated heat flux during postacoustic LH_2 tests was 69 percent for the aft dome and was influenced by lower heat flux caused by lower vacuum chamber wall temperature.

5.2.1.2 Barrel Heat Flux Calculation and Verification

Barrel heat flux was calculated in the same three manners as the dome heat flux.

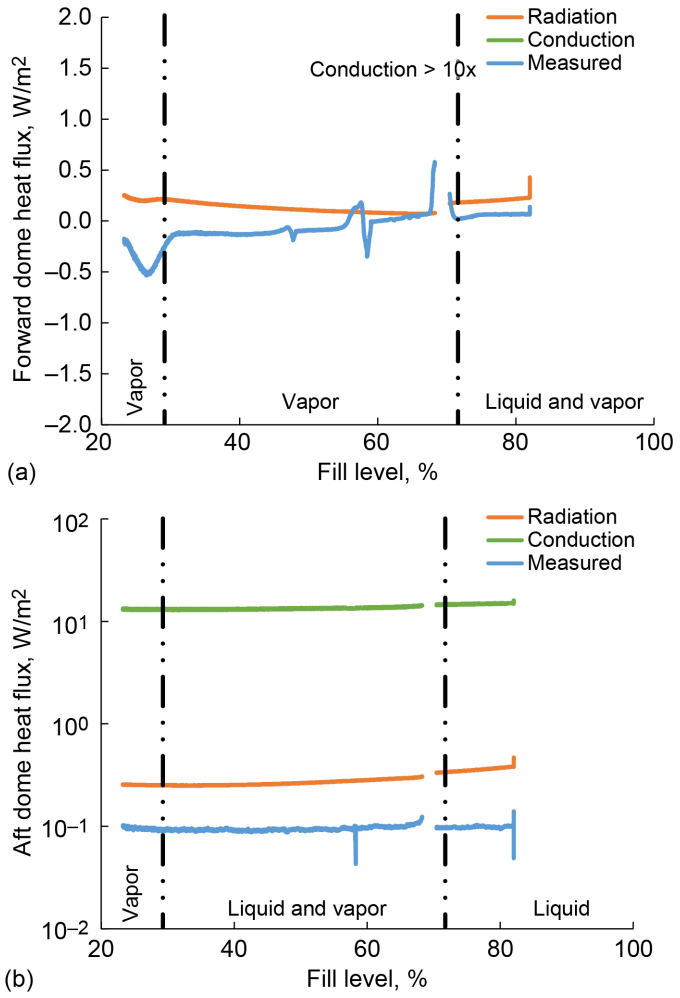

Figure 154.—Postacoustic liquid hydrogen test heat flux. (a) Forward dome. (b) Aft dome.

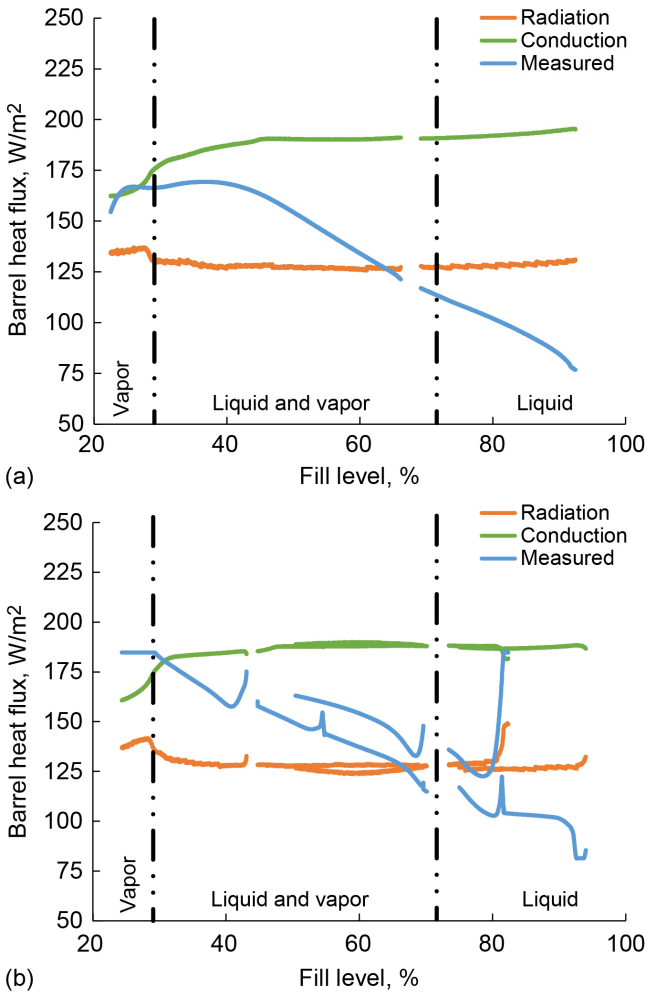

Figure 155.—Baseline boiloff and vapor-cooling liquid hydrogen barrel heat flux. (a) Baseline. (b) Vapor cooling.

The barrel heat flux was measured by heat flux sensors installed at four locations. The calculation of the heat flux from measured sensor output voltage and vendor specified sensitivity is discussed in Section 5.10. Significant variation in measured heat flux was observed during baseline and vapor-cooling tests and is largely attributed to uncertainty in voltage measurement when the DAQ system gain was defined too low. For this reason, the maximum measured heat flux of the four sensors was used to define heat flux during baseline and vapor-cooling tests.

The barrel heat flux by conduction through the SOFI was calculated as a function of measured tank wall and SOFI surface temperature using the expression presented previously for the forward and aft domes. Heat flux by radiation to the SOFI surface was calculated as a function of measured SOFI surface and vacuum chamber wall temperature using the expression surface was calculated as a function of measured SOFI surface and vacuum chamber wall temperature using the expression presented previously for the forward and aft domes.

Comparisons of measured and calculated heat flux for the barrel during baseline boiloff and vapor-cooling LH_2 tests are shown in Figure 155. The average heat flux was defined as the average of measured and both calculated values because the results demonstrate no single outlier. The root-sum-square average dispersion of measured and calculated heat flux was 32 percent for the baseline tests and 30 percent for the vapor-cooling tests.

Comparisons of measured and calculated heat flux for the barrel during preacoustic boiloff and preacoustic vapor-cooling LH_2 tests are shown in Figure 156. The average barrel heat flux was defined as the average of measured and both calculated values because the results demonstrate no single outlier. The root-sum-square average dispersion of measured and calculated heat flux was 29 percent for the preacoustic tests and 38 percent for the preacoustic vapor-cooling tests.

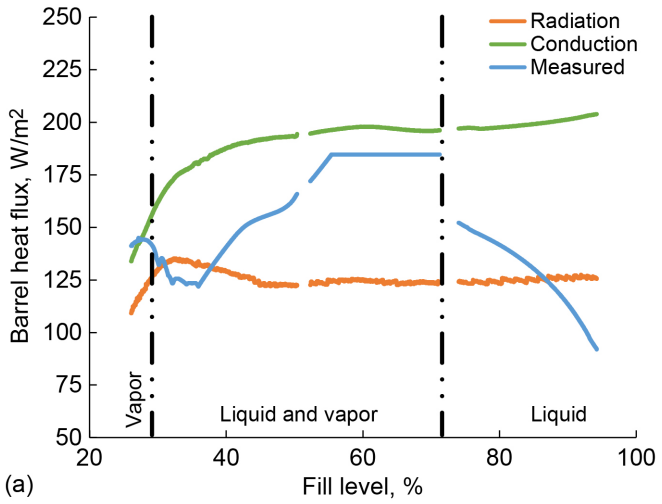

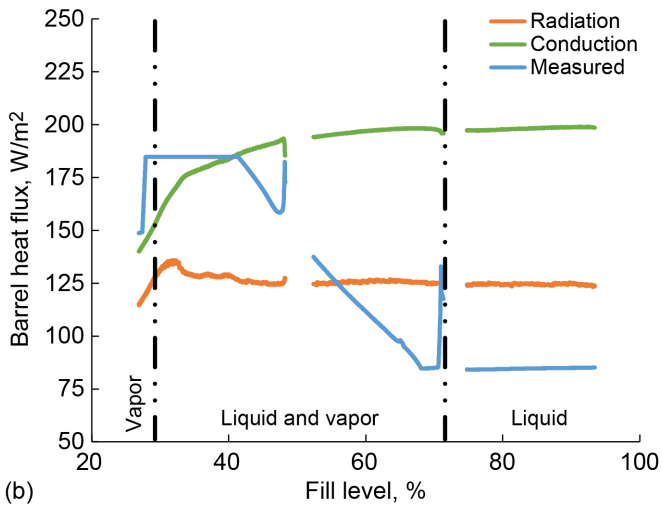

Figure 156.—Preacoustic boiloff and vapor-cooling liquid hydrogen barrel heat flux. (a) Preacoustic. (b) Preacoustic vapor cooling.

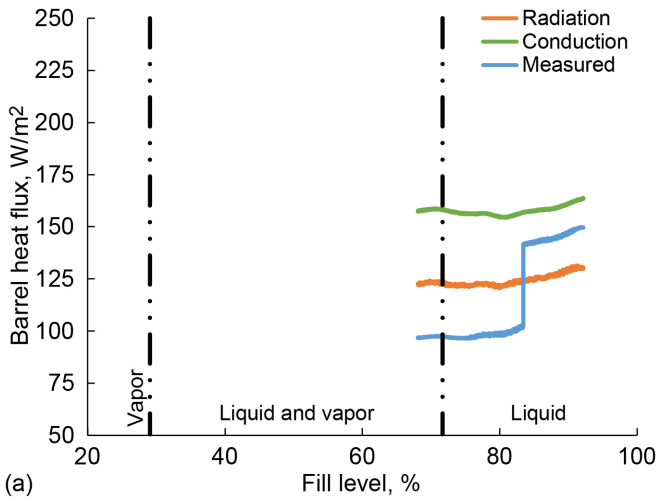

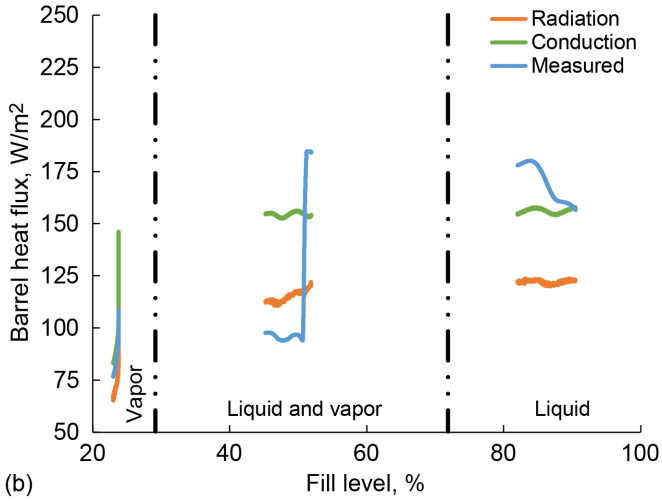

Figure 157.—Preacoustic boiloff and vapor-cooling liquid nitrogen barrel heat flux. (a) Preacoustic. (b) Preacoustic vapor cooling.

Comparisons of measured and calculated heat flux for the barrel during preacoustic boiloff and vapor-cooling LN_2 tests are shown in Figure 157. The average barrel heat flux was defined as the average of measured and both calculated values because the results demonstrate no single outlier. The root-sum-square average dispersion of measured and calculated heat flux was 27 percent for the preacoustic tests and 26 percent for the preacoustic vapor-cooling tests.

A comparison of measured and calculated heat flux for the barrel during postacoustic LH_2 tests are shown in Figure 158. The average barrel heat flux was defined as the average of measured and both calculated values because the results demonstrate no single outlier. The root-sum-square average dispersion of measured and calculated heat flux was 37 percent.

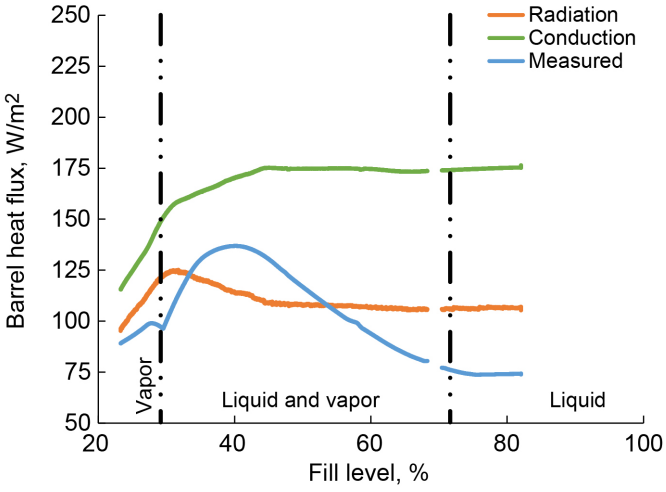

Figure 158.—Postacoustic liquid hydrogen barrel heat flux.

5.2.1.3 Forward and Aft Skirt Heat Flux Calculation and Verification

The forward and aft skirt heat loads were calculated by conduction through the structure along a 76-mm length adjacent to the flange interface with the tank wall using measured temperatures at these two locations as shown in Equation (12).

$$\dot{Q}_{cond} = k_{\text{skirt}} \frac{T_{\text{wall}} - T_{\text{flange}}}{\left(\frac{L}{A}\right)_{eff}} \tag{12}$$

where conduction heat load $\dot{Q}_{cond}$ is in watts, skirt material thermal conductivity k_{skirt} is in W/m·K, the skirt wall T_{wall} and flange T_{flange} temperatures are in Kelvin, and the effective ratio of conduction length of cross-sectional area $(L/A)_{eff}$ is per meter.

The thermal conductivity was defined as a polynomial curve fit of published data. Thermal conductivity of the 6061–T6 aluminum forward skirt was defined from (Ref. 46) and thermal conductivity of the 304L corrosion resistant steel aft skirt was defined from (Ref. 47). Temperature dependent thermal conductivity of both materials are shown in Figure 159 along with the polynomial curve fits used to calculate $\dot{Q}_{cond}$. The effective ratio of conduction length to cross-section area was calculated from design dimensions as 1.281/m for the forward skirt and 0.395/m for the aft skirt.

The forward and aft skirt heat loads were also calculated using an infinite length radiating fin idealization (Ref. 48). The exact solution for the infinite length fin was applied to reflect a width equal to the circumference of the skirt, a thickness equal to the skirt skin thickness, and an assumed end temperature in equilibrium with the chamber wall. This method assumes an adiabatic interior surface of the skirts, which are insulated with MLI. The thermal conductivity of the skirt materials was calculated at the average temperature (measured flange interface and measured chamber wall) using the polynomial curve fits shown in Figure 159. The emissivity of the forward skirt was measured to be 0.152 and that of the aft skirt was measured to be 0.349 (Section 2.3.3).

$$\dot{Q}_{\text{fin}} = 2k_{\text{skirt}} tw \sqrt{\frac{\sigma \varepsilon_{sksurf}}{5k_{\text{skirt}} t}\left(T_{\text{chamber}}^5 - T_{\text{flange}}^5\right)} \tag{13}$$

where radiation heat load estimate for an infinite length fin $\dot{Q}_{\text{fin}}$ is in watts, skirt thickness t is in meters, fin width w (defined as skirt circumference) is in meters, emissivity of the skirt surface ε_{sksurf} is dimensionless, and the temperatures of the vacuum chamber wall T_{chamber} and flange T_{flange} are in Kelvin.

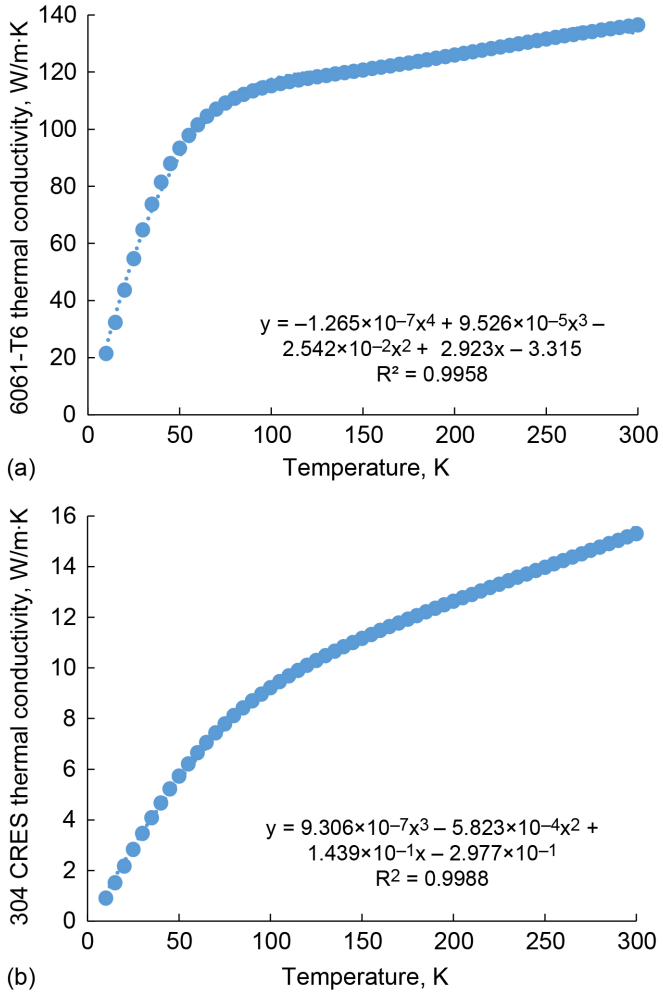

Figure 159.—Thermal conductivity. (a) 6061–T6 aluminum. (b) 304L corrosion resistant steel (CRES).

The forward skirt heat load during boiloff tests without vapor cooling was also estimated from radiation heat transfer exchange with the vacuum chamber wall. This method also assumes an adiabatic interior surface of the skirts, which are insulated with MLI. The total radiation heat load was calculated as the sum of heat loads to each of seven locations along the length of the forward skirt at which skin temperatures were measured, as shown in Equation (14).

$$\dot{Q}_{rad} = \sum_{i=1}^{7} \sigma \frac{\pi D L_i}{\frac{1}{\varepsilon_{\text{skirt}}} + \frac{1}{\varepsilon_{\text{chamber}}} - 1}\left(T_{\text{chamber}}^4 - T_i^4\right) \tag{14}$$

where the forward skirt radiation heat load $\dot{Q}_{rad}$ is in watts, the diameter of the forward skirt D is in meters, the length of the forward skirt segment between temperature measurement locations L_i is in meters, the emissivity of the forward skirt $\varepsilon_{\text{skirt}}$

is 0.152 (see Section 2.3.3) and dimensionless, the emissivity of the vacuum chamber wall $\varepsilon_{chamber}$ is 0.9 (Ref. 45) and dimensionless, and the temperature of the forward skirt segment T_i is in Kelvin.

A comparison of forward and aft skirt heat loads during baseline LH_2 tests is shown in Figure 160. Heat loads calculated by the different methods were found to have an average root-sum-square error of 24 percent for the forward skirt and 13 percent for the aft skirt.

A comparison of aft skirt heat loads during LH_2 vapor-cooling tests is shown in Figure 161. The heat loads to the forward skirt can be accurately calculated only by conduction for tests with vapor cooling because of heat removal to the boiloff vapor. Heat loads calculated by the different methods were found to have an average root-sum-square error of 22 percent.

A comparison of forward and aft skirt heat loads during preacoustic LH_2 tests is shown in Figure 162. Heat loads calculated by the different methods were found to have an

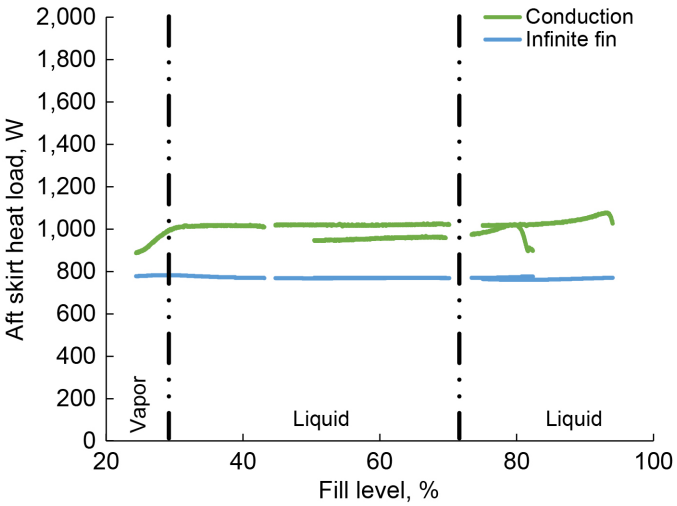

Figure 161.—Liquid hydrogen vapor-cooling aft skirt heat load.

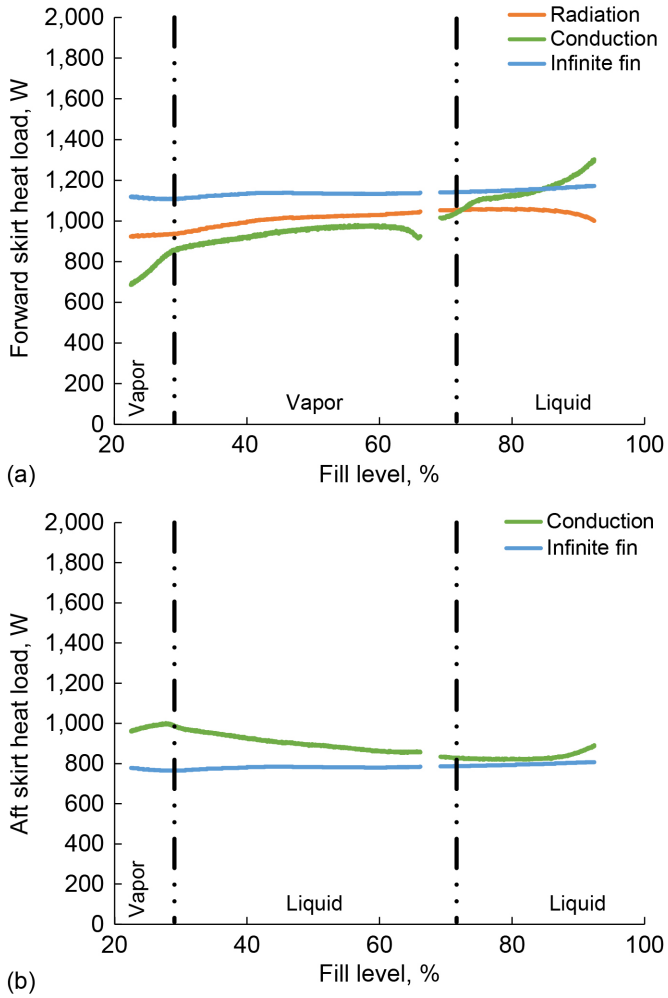

Figure 160.—Baseline liquid hydrogen heat load. (a) Forward skirt. (b) Aft skirt.

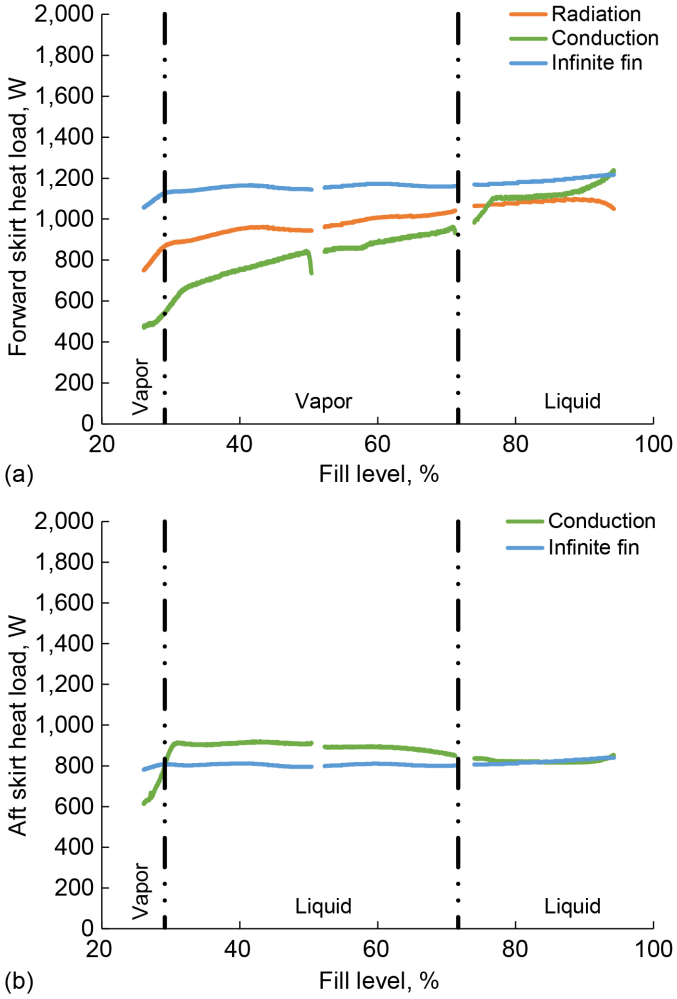

Figure 162.—Preacoustic liquid hydrogen heat load. (a) Forward skirt. (b) Aft skirt.

average root-sum-square error of 60 percent for the forward skirt and 10 percent for the aft skirt.

A comparison of aft skirt heat loads during LH_2 vapor-cooling tests is shown in Figure 163. Heat loads to the forward skirt can be accurately calculated only by conduction for tests with vapor cooling because of heat removal to the boiloff vapor. Heat loads calculated by the different methods were found to have an average root-sum-square error of 11 percent.

A comparison of forward and aft skirt heat loads during preacoustic LN_2 tests is shown in Figure 164. Heat loads calculated by the different methods were found to have an average root-sum-square error of 30 percent for the forward skirt and 11 percent for the aft skirt.

A comparison of aft skirt heat loads during LN_2 vapor-cooling tests is shown in Figure 165. Heat loads to the forward skirt can be accurately calculated only by conduction for tests with vapor cooling because of heat removal to the boiloff vapor. Heat loads calculated by the different methods were found to have an average root-sum-square error of 34 percent.

A comparison of forward and aft skirt heat loads during postacoustic LH_2 tests is shown in Figure 166. Heat loads calculated by the different methods were found to have an average root-sum-square error of 49 percent for the forward skirt and 20 percent for the aft skirt.

Forward and aft skirt heat load was calculated by conduction for all tests because it is the only method that is accurate during vapor cooling. These heat loads were defined as a heat flux to the tank wall that is assumed to be uniformly distributed over the 51-mm flange thickness. This method enables calculation of tank heat load as a function of instantaneous liquid level and proportions skirt heat load to liquid and vapor as the liquid level changes along the flange thickness.

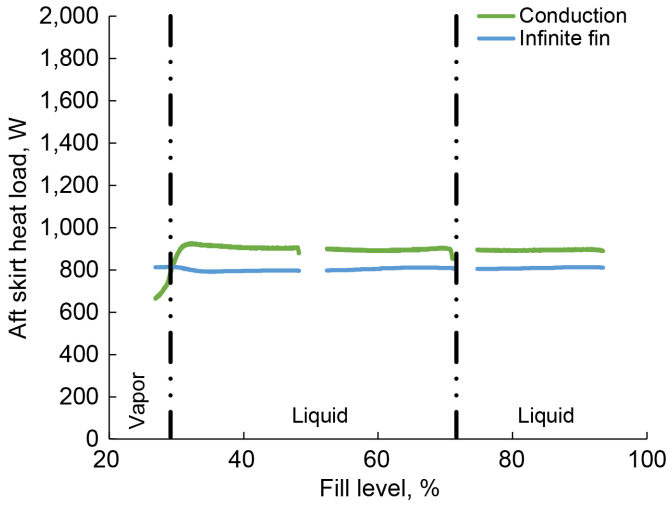

Figure 163.—Preacoustic liquid hydrogen vapor-cooling aft skirt heat load.

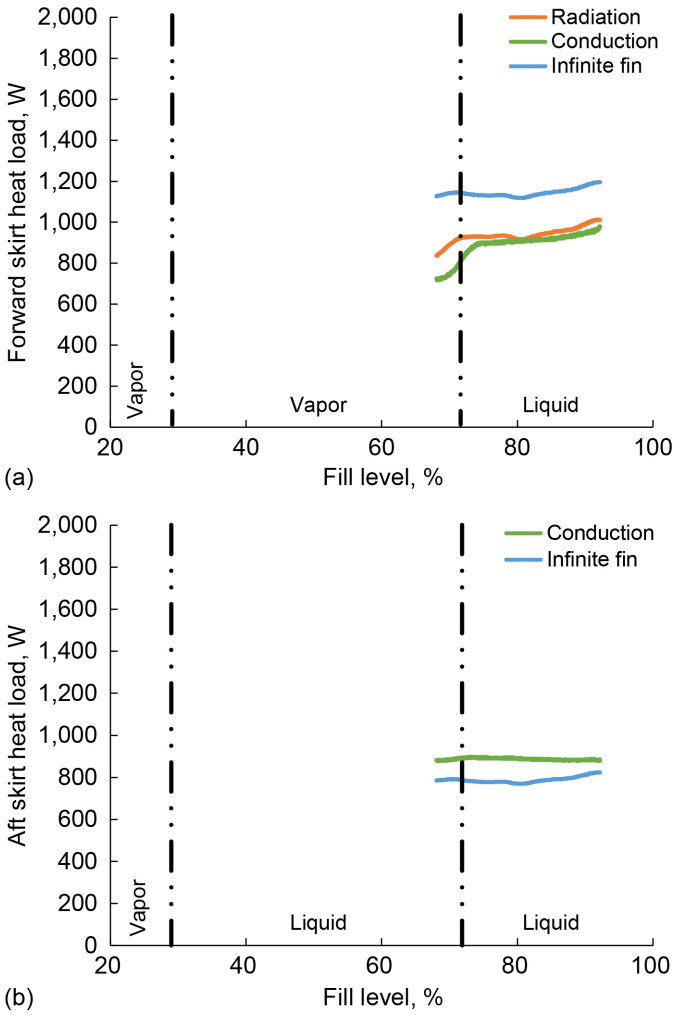

Figure 164.—Preacoustic liquid nitrogen heat load. (a) Forward skirt. (b) Aft skirt.

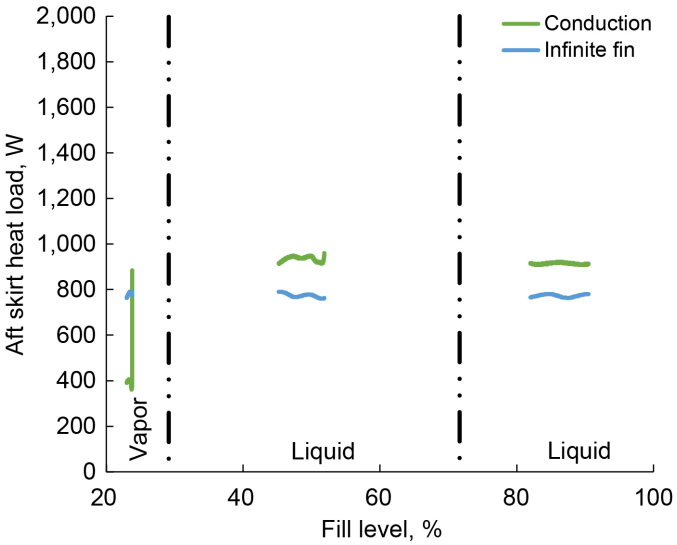

Figure 165.—Preacoustic liquid nitrogen vapor-cooling aft skirt heat load.

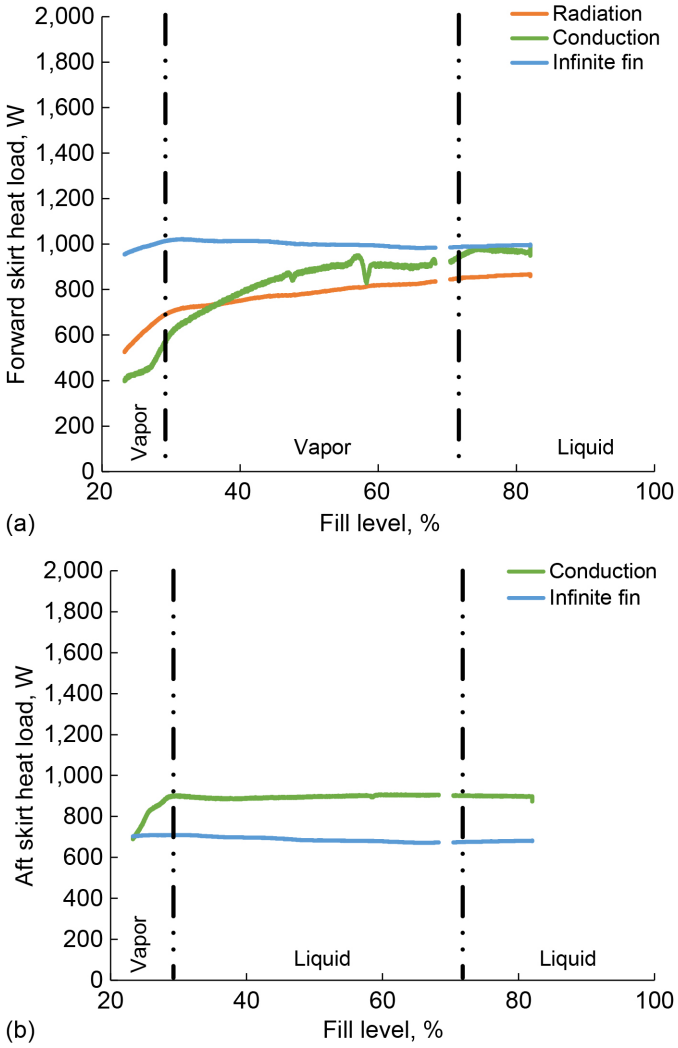

Figure 166.—Postacoustic liquid hydrogen heat load. (a) Forward skirt. (b) Aft skirt.

5.2.2 Dome Cover and Manway Heat Load Calculation Method

The heat loads to the forward and aft dome covers and manways were calculated as the product of surface area and heat flux. The forward and aft dome covers and manways were exposed to vapor and liquid, respectively, during all boiloff tests. The covers and manways have a surface area of 0.842 m² and were not insulated with SOFI. The heat flux during baseline and vapor-cooling tests was calculated from the expression below for radiation with an assumed view factor of unity. The cover emissivity was assumed to be the same as that of the tank, which was measured to be 0.314 (Section 2.3.3). The forward dome cover experiences radiation heat transfer with the vacuum chamber wall having an emissivity of 0.9 (Ref. 45). The aft dome cover experiences radiation heat transfer with the thermal support structure having an emissivity of 0.349 (Section 2.3.3). The thermal support structure is assumed to be in thermal equilibrium with the vacuum chamber wall. Heat flux during preacoustic and postacoustic MLI tests was assumed to be 1.1 W/m² based on analytically predicted MLI performance (Ref. 42).

$$q_{\text{cover}} = \sigma \frac{1}{\frac{1}{\varepsilon_{\text{cover}}} + \frac{1}{\varepsilon_{env}} - 1} \left(T_{\text{chamber}}^4 - T_{\text{cover}}^4 \right) \tag{15}$$

where the cover and manway heat flux q_{cover} is in W/m², the emissivities of the cover $\varepsilon_{\text{cover}}$ and environment surface ε_{env} are dimensionless, and the temperature of the cover T_{cover} is in Kelvin.

5.2.3 Fluid Interface Heat Load Calculation Method

The fluid interface heat loads were calculated by conduction heat transfer between two locations on each propellant line at which temperatures were measured. Fluid interface geometry used for heat load calculations is shown in Table 19. The length defined in the table represents the distance between the two locations on the line at which temperature was measured. The fluid interfaces are insulated with MLI to minimize heat transfer from the vacuum chamber.

TABLE 19.—FLUID INTERFACE GEOMETRY FOR HEAT LOAD CALCULATIONS

Interface	Location	Outer diameter, mm	Wall thickness, mm	Length, mm	Area or length, m
Fill and drain	Aft cover	48.3	2.8	102	0.0039
Vent and relief	Forward cover	88.9	3.0	38.1	.0216
Vapor cooling	Forward cover	26.7	2.1	76.2	.0021

The conduction heat load is calculated for each interface as shown in Equation (16). All fluid lines are made from 304L corrosion resistant steel with temperature dependent thermal conductivity evaluated at the average measured line temperature using the curve fit shown in Figure 159.

$$\dot{Q}_{cond} = k_{\text{line}} \frac{A}{L}\left(T_2 - T_1\right) \tag{16}$$

where line material thermal conductivity k_{line} is in W/m·K, cross-sectional area per unit length of the interface A/L from Table 15 is in meters, and the measured fluid line temperatures T_1 and T_2 are in Kelvin.

The average total fluid interface heat load to the tank is summarized in Table 20 for all tests. These fluid interface heat loads were defined as a heat flux to the tank covers that is assumed to be uniformly distributed over the 0.842 m² cover surface area.

5.2.4 Electrical Interface Heat Load Calculation Method

The electrical interfaces to the propellant consist of lead wires for the temperature sensors installed on the internal rake and on the tank wall, the heat flux sensors installed on the tank wall, heaters installed on the tank wall, and the coaxial cables for the RFMG antenna installed inside the tank. A total of 50 temperature sensors are installed in and on the tank wall and each sensor has four 36-AWG (0.13-mm-diameter) lead wires. A total of 12 heat flux sensors and 16 heaters are installed on the tank wall and each has two 22-AWG (0.64-mm-diameter) lead wires. Two coaxial cables interface with the tank and have a cross-sectional area equal to that of a 22-AWG lead wire. The quantity of sensors, heaters, and coaxial cables at each electrical interface to the tank is shown in Table 21. The heat load for a single lead wire was calculated using an infinite length radiating fin idealization (Ref. 48). The exact solution for the infinite length fin was expressed as a function of conductor diameter, as shown in Equation (17). The thermal conductivity of the copper lead wire conductor was assumed to be 450 W/m·K at an assumed average temperature of 160 K. An effective emissivity of 0.9 was assumed to represent the combined contributions of the vacuum chamber wall and lead wire insulation. The minimum temperature of the conductor was assumed to be the same as that of the tank interface.

$$\dot{Q}_{\text{wire}} = 2k_{\text{wire}} \frac{\pi d^2}{4} \sqrt{\frac{\sigma \varepsilon_{\text{wire}}}{5k_{\text{wire}} \frac{d}{2}}\left(T_{\text{chamber}}^5 - T_{\text{interface}}^5\right)} \tag{17}$$

where radiation heat load estimated for a single lead wire $\dot{Q}_{\text{wire}}$ is in watts, the wire material thermal conductivity k_{wire} is in W/m·K, the wire diameter d is in meters, the effective emissivity of the wire insulation and chamber wall $\varepsilon_{\text{wire}}$ is dimensionless, and the temperature of the wire interface $T_{\text{interface}}$ is in Kelvin.

The total heat load at each interface is calculated from the wire heat load and quantity at each interface, as shown in Equation (18), with the quantity of electrical interfaces defined in Table 17.

$$\begin{aligned}\dot{Q}_{\text{interface}} = {} & 4\dot{Q}_{\text{temperaturesensor}} N_{\text{temperaturesensor}} \\ & + 2\dot{Q}_{\text{heatfluxsensor}} N_{\text{heatfluxsensor}} \\ & + 2\dot{Q}_{\text{heater}} N_{\text{heater}} + \dot{Q}_{\text{coaxial}} N_{\text{coaxial}}\end{aligned} \tag{18}$$

where radiation heat load at each interface $\dot{Q}_{\text{interface}}$ is in watts, heat load for a single temperature sensor conductor $\dot{Q}_{\text{temperaturesensor}}$ is in watts, the quantity of temperature sensors at the interface is $N_{\text{temperaturesensor}}$, the heat load for a single heat flux sensor conductor $\dot{Q}_{\text{heatfluxsensor}}$ is in watts, the quantity of heat flux sensors is $N_{\text{heatfluxsensor}}$, the heat load for a single heater conductor $\dot{Q}_{\text{heater}}$ is in watts, the quantity of heaters at the interface is N_{heater}, the heat load for a single coaxial cable conductor $\dot{Q}_{\text{coaxial}}$ is in watts, and the quantity of coaxial cables at the interface is N_{coaxial}.

TABLE 20.—AVERAGE TOTAL FLUID INTERFACE HEAT LOAD, W

Baseline liquid hydrogen (LH_2)	2.5
LH_2 vapor cooling	–.2
Preacoustic LH_2	9.8
Preacoustic LH_2 vapor cooling	2.6
Preacoustic liquid nitrogen (LN_2)	7.9
Preacoustic LN_2 vapor cooling	2.5
Postacoustic LH_2	9.4

TABLE 21.—ELECTRICAL INTERFACES FOR HEAT LOAD CALCULATIONS

Interface location	Temperature sensor quantity	Heat flux sensor quantity	Heater quantity	Coaxial cable quantity
Aft cover	9	4	4	2
Aft flange	6	2	4	0
Forward flange	6	2	4	0
Forward cover	29	4	4	0

The average total electrical interface heat load to the tank is summarized in Table 22 for all tests. These electrical interface heat loads were defined as a heat flux to the tank covers and flanges that are assumed to be uniformly distributed over the surface area at each interface, which enables calculation of electrical interface heat loads to liquid and vapor as a function of liquid level.

The SD temperature sensors are supplied with 10-mA current and dissipate heat proportional to output voltage. This heat dissipation is a function of sensor temperature and is shown in Figure 167 (Ref. 49). Since only 50 temperature sensors are installed in and on the tank, the total dissipation is much less than 1 W and was not considered as an electrical interface heat load.

5.2.5 Regional Heat Loads

The regional heat loads to the aft dome, aft skirt, barrel, forward skirt, and forward dome of the tank were calculated for all tests. The aft dome heat load includes contributions from the fill and drain line fluid interface, the electrical cable interface, the cover, and the dome acreage. The aft skirt heat load includes contributions from the skirt and electrical interface heat load. The barrel heat load reflects only the barrel acreage. The forward skirt heat load includes contributions from the skirt and electrical interface. The forward dome heat load includes contributions from the vent and vapor-cooling-line fluid interfaces, the electrical cable interface, the cover, and the dome acreage.

A comparison of aft dome heat load is shown in Figure 168 for all LH_2 and LN_2 tests. Similar heat loads were observed at all fill levels during the baseline LH_2 and LH_2 vapor-cooling tests, which demonstrates vapor cooling had little effect on aft dome heat load as expected. Heat loads during preacoustic and postacoustic tests, with and without vapor cooling, were negligible because of the MLI installed over the SOFI.

A comparison of aft skirt heat load is shown in Figure 169 for all LH_2 and LN_2 tests. Similar heat loads were observed at all fill levels at and above the aft flange during all LH_2 and LN_2

TABLE 22.—AVERAGE TOTAL ELECTRICAL INTERFACE HEAT LOAD, W

Baseline liquid hydrogen (LH_2)	8.3
LH_2 vapor cooling	8.1
Preacoustic LH_2	8.6
Preacoustic LH_2 vapor cooling	8.5
Preacoustic liquid nitrogen (LN_2)	8.3
Preacoustic LN_2 vapor cooling	8.1
Postacoustic LH_2	7.4

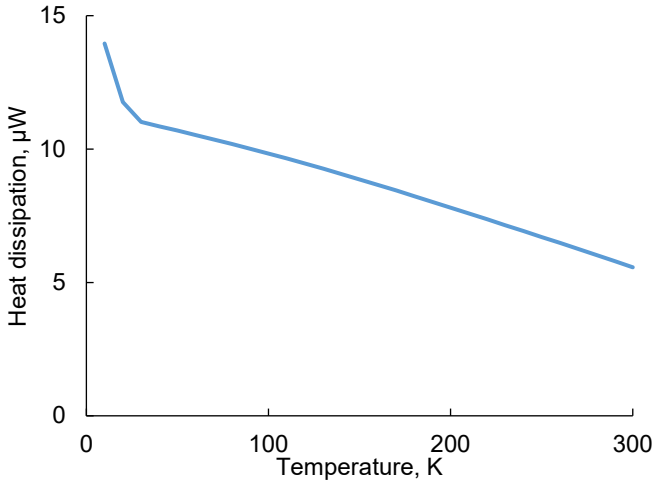

Figure 167.—Silicone diode temperature sensor heat dissipation.

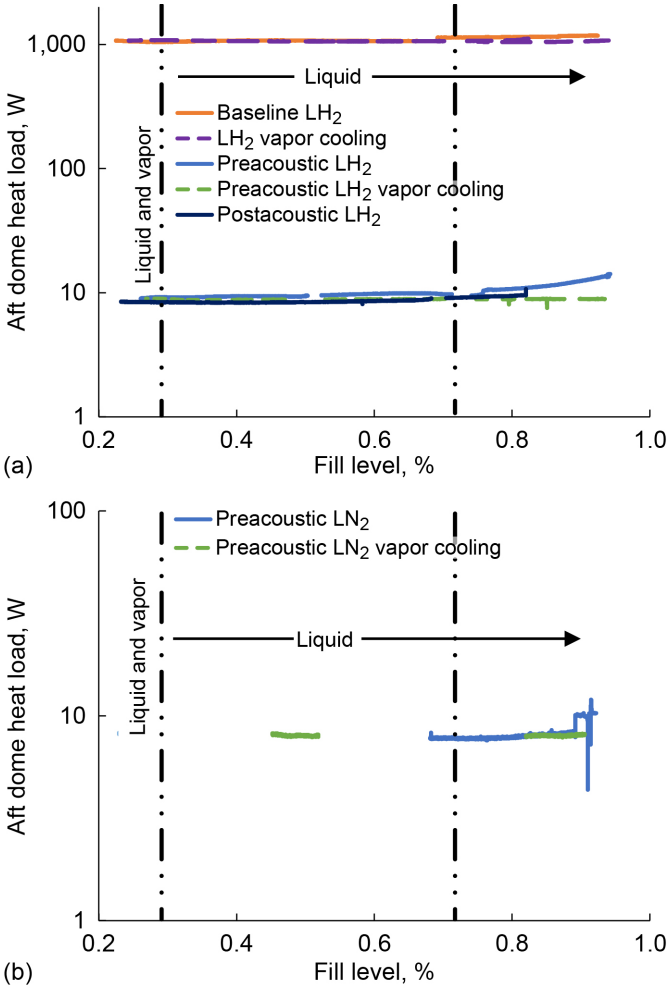

Figure 168.—Comparison of aft dome heat load. (a) Liquid hydrogen (LH_2) tests. (b) Liquid nitrogen (LN_2) tests.

tests, which demonstrates vapor cooling and MLI installation on the domes had little effect on aft skirt heat load as expected. Aft skirt heat loads at fill levels below the aft flange demonstrate installation of MLI on the domes decreases aft skirt heat load by as much as 40 percent.

A comparison of barrel heat load is shown in Figure 170 for all LH_2 and LN_2 tests. Similar heat loads were observed at all fill levels during all LH_2 and LN_2 tests, which demonstrates vapor cooling and MLI installation on the domes had little effect on barrel heat load as expected. Barrel heat load during postacoustic LH_2 tests is lower than during preacoustic LH_2 tests because of the lower vacuum chamber wall temperature.

A comparison of forward skirt heat load is shown in Figure 171 for all LH_2 and LN_2 tests. Similar heat loads were observed at all fill levels during LH_2 and LN_2 tests without vapor cooling, which demonstrates MLI installation on the domes had little effect on forward skirt heat load. Vapor cooling significantly decreases forward skirt heat load at higher fill levels, the reduction decreases with fill level through the barrel section of the tank, and the reduction is negligible at lower fill levels below the aft flange.

A comparison of forward dome heat load is shown in Figure 172 for all LH_2 and LN_2 tests. Vapor cooling was observed to decrease forward dome heat load by as much as 25 percent at fill levels above the forward flange but has little effect on forward dome heat load at lower fill levels. Installing MLI on the domes significantly decreases forward dome heat load, as was observed for the aft dome.

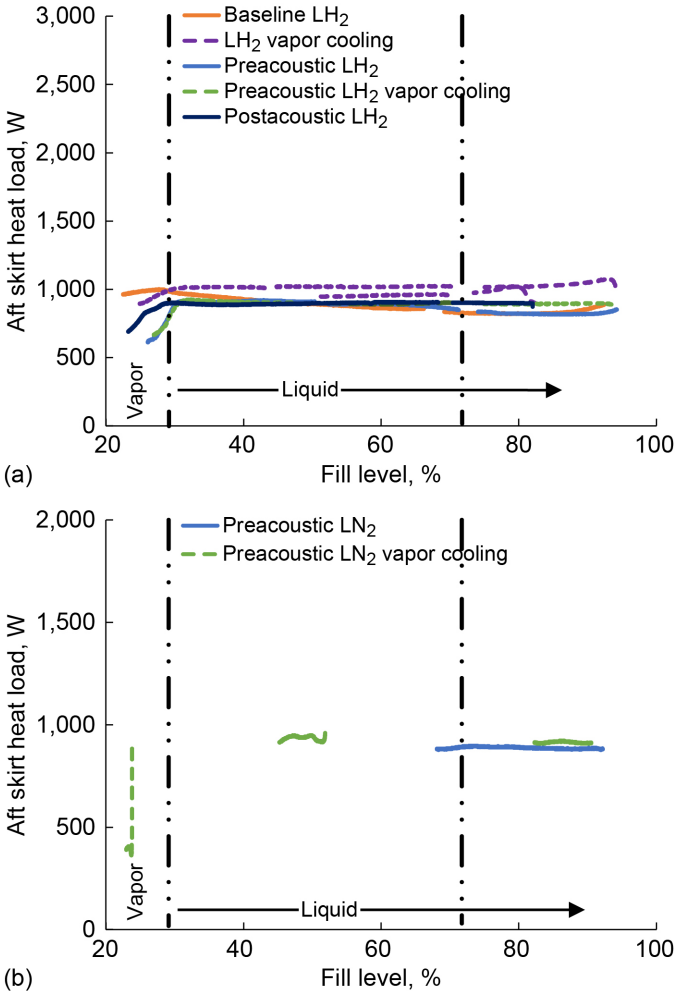

Figure 169.—Comparison of aft skirt heat load. (a) Liquid hydrogen (LH_2) tests. (b) Liquid nitrogen (LN_2) tests.

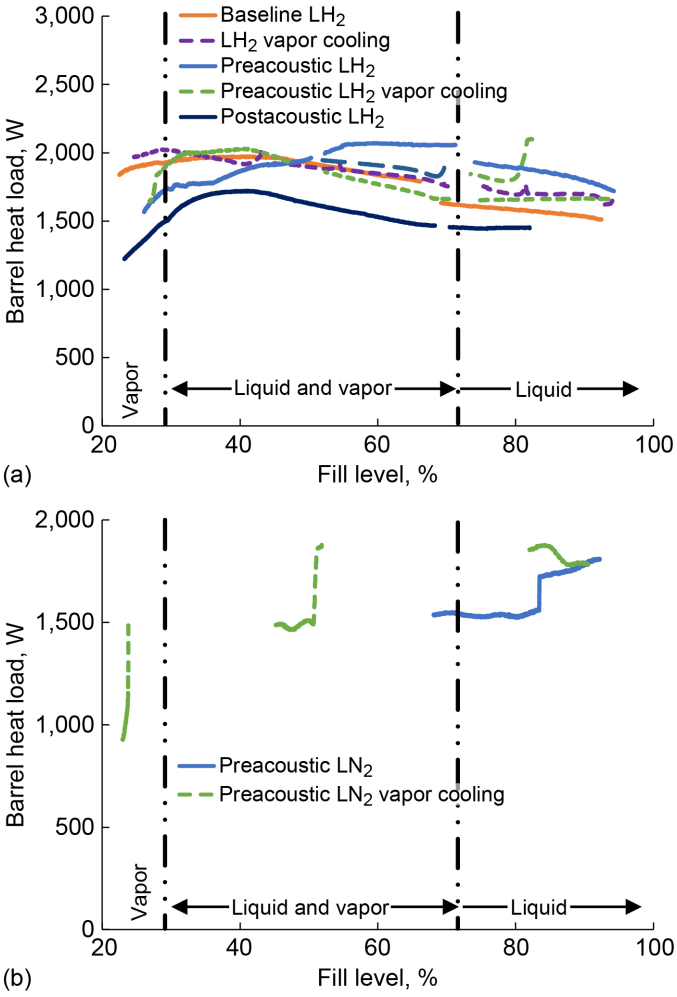

Figure 170.—Comparison of barrel heat load. (a) Liquid hydrogen (LH_2) tests. (b) Liquid nitrogen (LN_2) tests.

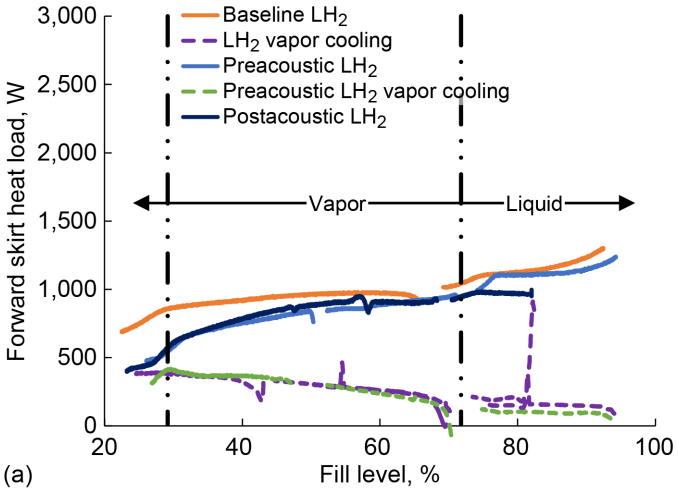

Figure 171.—Comparison of forward skirt heat load. (a) Liquid hydrogen (LH_2) tests. (b) Liquid nitrogen (LN_2) tests.

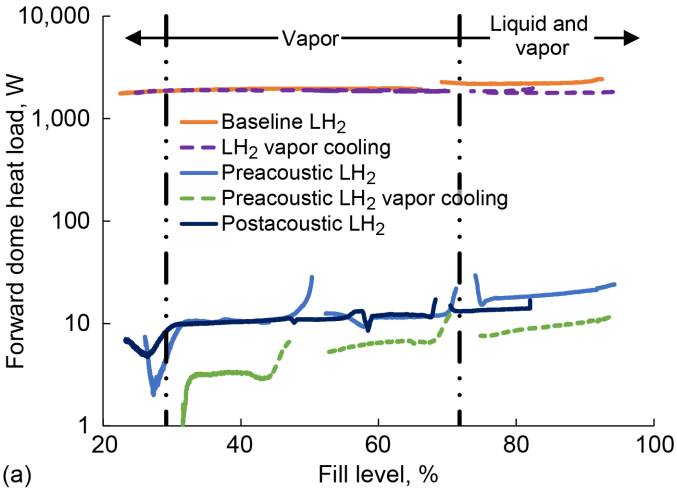

Figure 172.—Comparison of forward dome heat load. (a) Liquid hydrogen (LH_2) tests. (b) Liquid nitrogen (LN_2) tests.

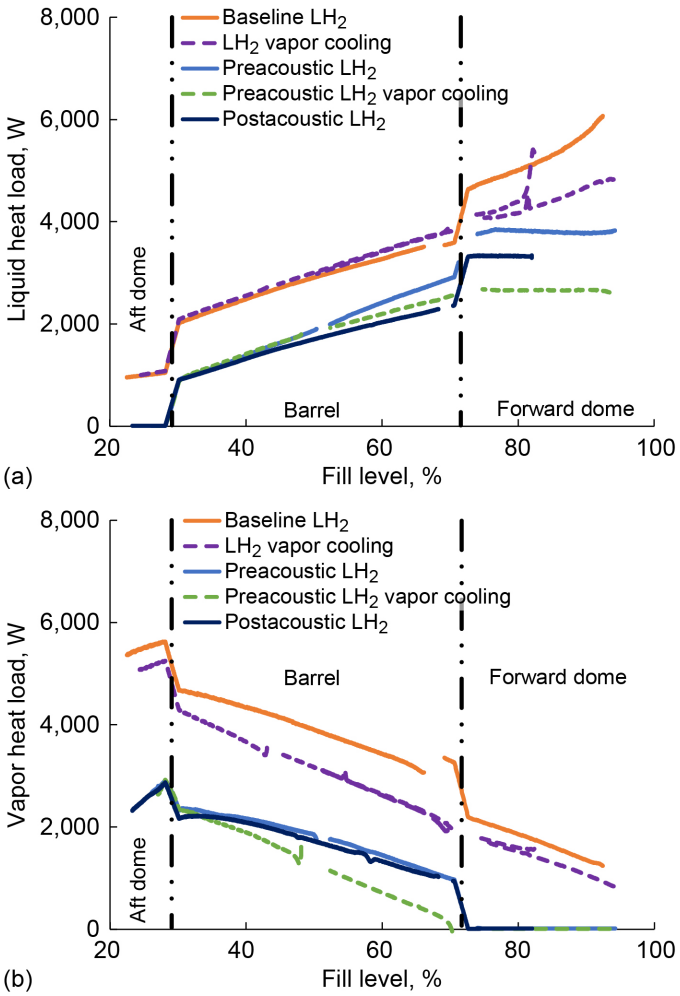

Figure 173.—Comparison of liquid hydrogen (LH_2) fluid region heat loads. (a) Liquid. (b) Vapor.

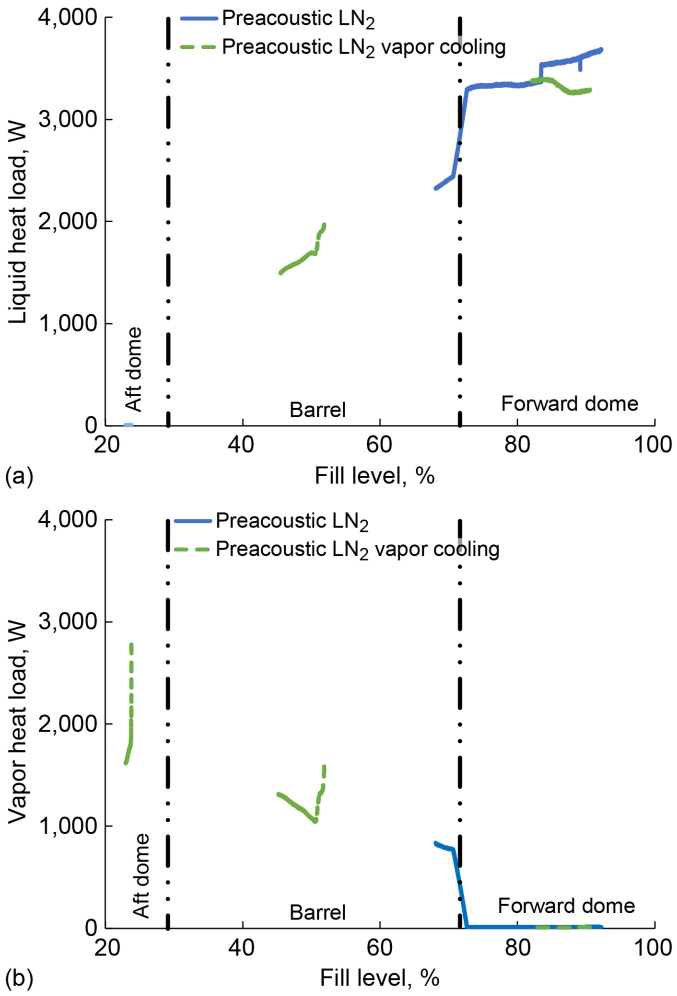

Figure 174.—Comparison of liquid nitrogen (LN_2) fluid region heat loads. (a) Liquid. (b) Vapor.

A comparison of fluid region heat loads is shown in Figure 173 for all LH_2 tests. Heat loads to the liquid region of the tank decrease while heat loads to the vapor region of the tank increase with decreasing fill level. Vapor cooling is observed to minimize heat load from the forward skirt, which is demonstrated by the vapor-cooling heat load profiles showing no abrupt change as liquid level decreases below the forward flange. Installing MLI on the domes decreases fluid heat loads at all fill levels, resulting in negligible heat load to vapor at high fill levels and negligible heat load to liquid at low fill levels.

A comparison of fluid region heat loads is shown in Figure 174 for all LN_2 tests. Similar trends are observed for LN_2 tests that were observed for LH_2 tests, but detailed comparisons cannot be made because of the limited range of fill levels tested.

5.2.6 Total Heat Loads

Total tank heat load is shown in Figure 175 for all LH_2 and LN_2 tests. Vapor cooling is observed to significantly decrease total heat load at higher fill levels but provides little reduction to total heat load at lower fill levels. Installing MLI on the domes significantly decreases total heat load at all fill levels. Total heat load during postacoustic LH_2 tests was observed to be lower than during preacoustic LH_2 tests because of the lower vacuum chamber wall temperature.

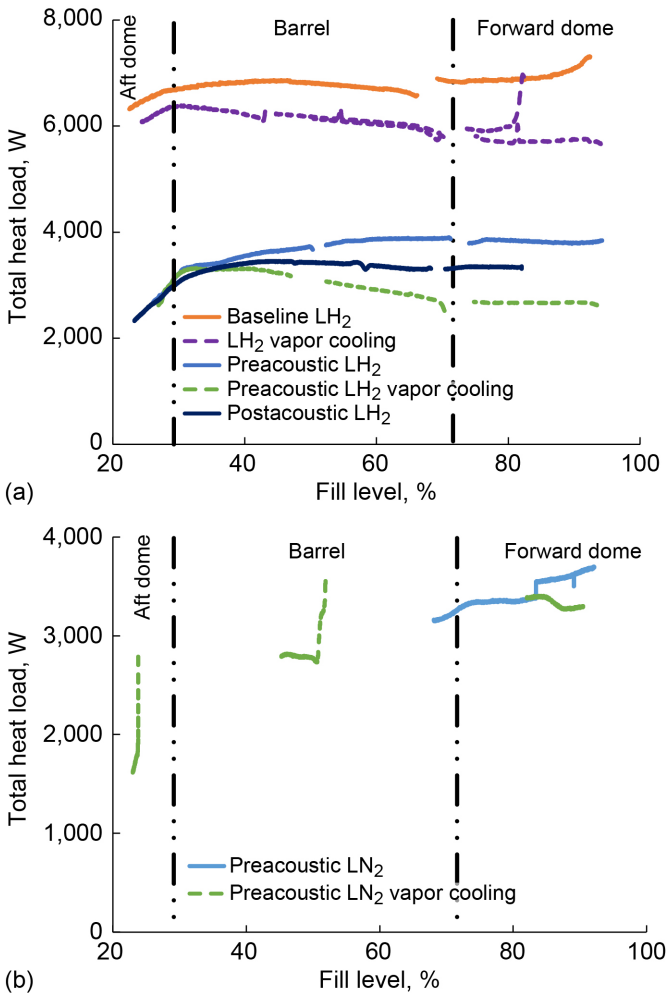

Figure 175.—Comparison of total tank heat loads. Liquid hydrogen (LH_2) tests. (b) Liquid nitrogen (LN_2) tests.

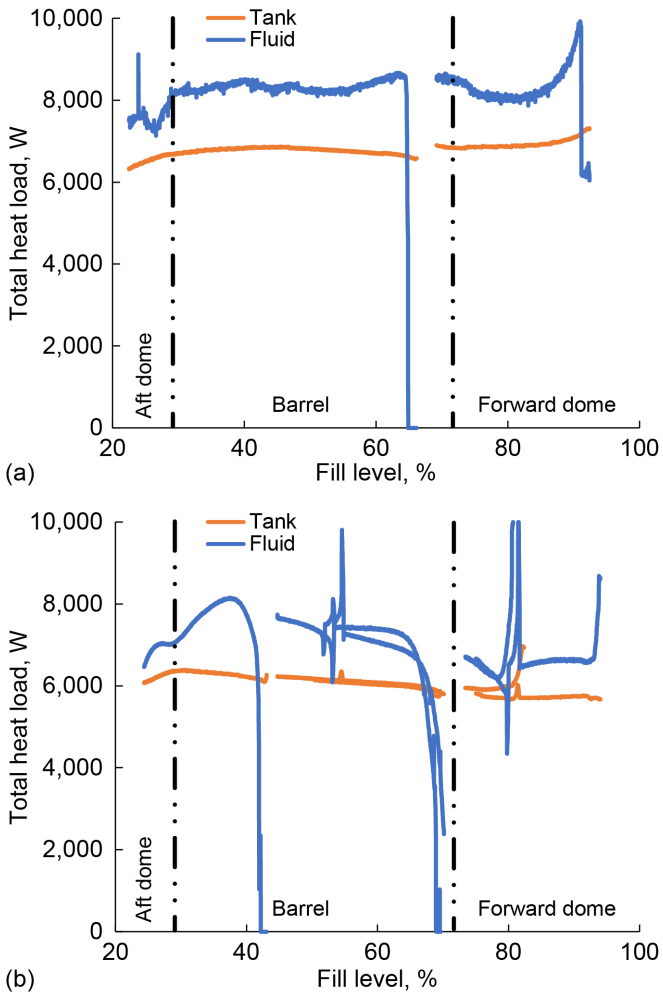

Figure 176.—Comparison of baseline and vapor-cooling liquid hydrogen heat loads. (a) Baseline. (b) Vapor cooling.

5.2.7 Total Heat Load Verification

The total heat loads presented previously reflect measured and calculated heat flux to acreage regions of the tank, calculated heat loads from the skirts and fluid interfaces, and estimated heat loads from the electrical interfaces. Heat loads to the fluid were also calculated from fluid temperature, pressure, and vent flow rate measurement, as described in Section 5.1, and used to verify the calculated heat loads to the tank.

A comparison of heat loads to the tank and to the fluid is shown in Figure 176 for baseline LH_2 and LH_2 vapor-cooling tests. Heat load to the fluid is generally higher for both baseline and vapor-cooling tests. The average difference between heat loads to the tank and to the fluid were 18 percent for both the baseline and vapor-cooling LH_2 tests.

A comparison of heat loads to the tank and to the fluid is shown in Figure 177 for preacoustic LH_2 and preacoustic LH_2 vapor-cooling tests. Heat load to the fluid is generally higher for both preacoustic and preacoustic vapor-cooling tests. The average differences between heat loads to the tank and to the fluid were 24 percent for the preacoustic LH_2 tests and 21 percent for the preacoustic LH_2 vapor-cooling tests.

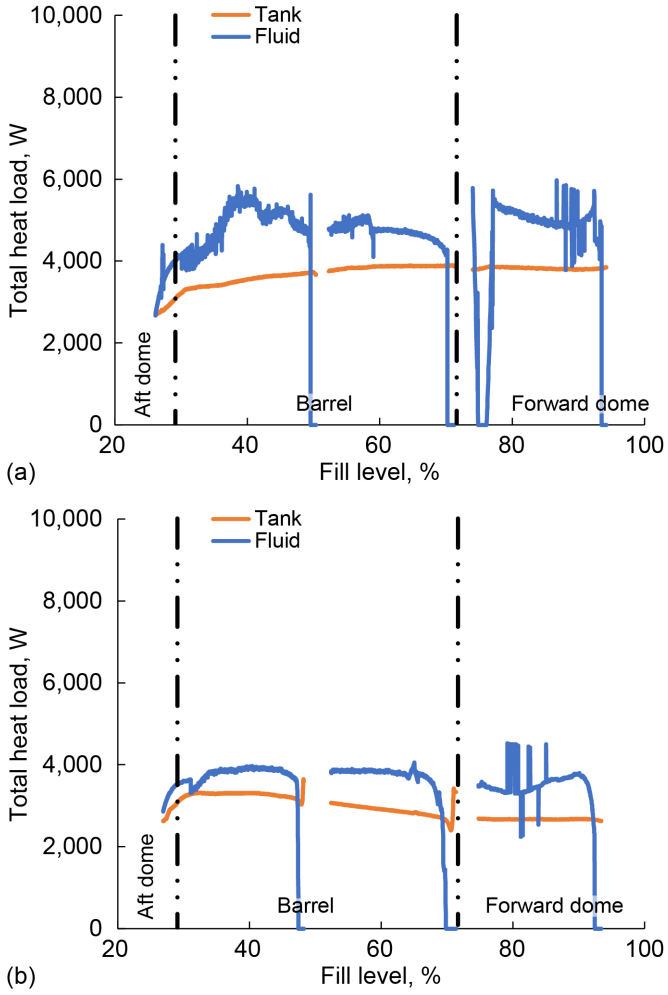

Figure 177.—Comparison of preacoustic and preacoustic vapor-cooling liquid hydrogen heat loads. (a) Preacoustic tests. (b) Preacoustic vapor-cooling tests.

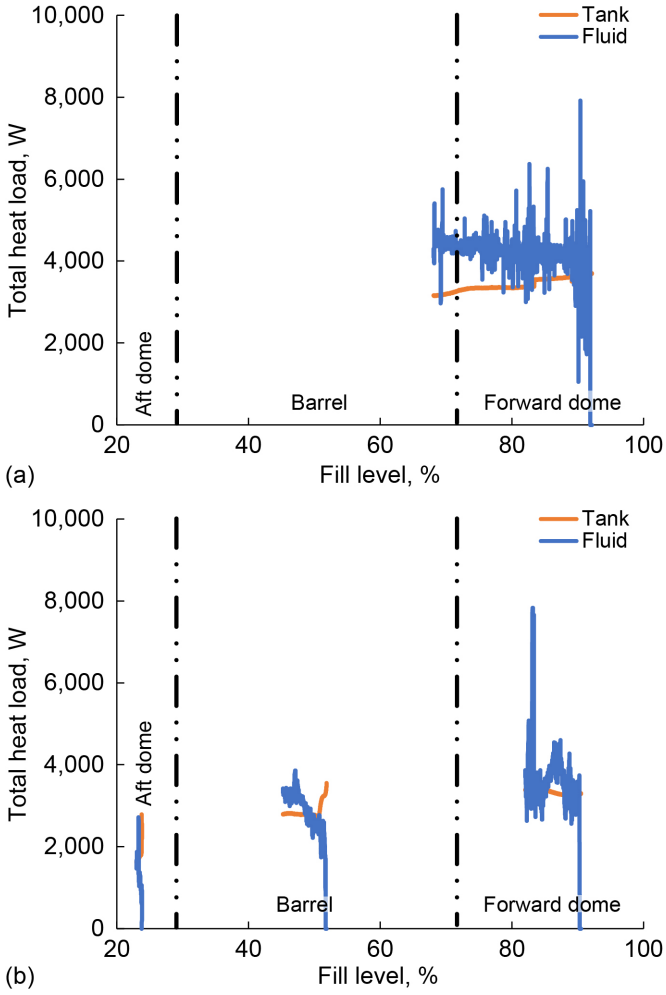

Figure 178.—Comparison of preacoustic and preacoustic vapor-cooling liquid nitrogen heat loads. (a) Preacoustic tests. (b) Preacoustic vapor-cooling tests.

A comparison of heat loads to the tank and to the fluid is shown in Figure 178 for preacoustic LN_2 and preacoustic LN_2 vapor-cooling tests. The heat load is much noisier in the LN_2 test data because the flowmeters were much noisier in response with nitrogen than hydrogen. Heat load to the fluid is generally higher than heat load to the tank for both preacoustic and preacoustic vapor-cooling tests. The average differences between heat loads to the tank and to the fluid were 20 percent for the preacoustic LN_2 tests and 34 percent for the preacoustic LN_2 vapor-cooling tests.

A comparison of heat loads to the tank and to the fluid is shown in Figure 179 for postacoustic LH_2 tests. Heat load to the fluid is generally higher than heat load to the tank, as was previously observed. The average difference between heat loads to the tank and to the fluid was 28 percent.

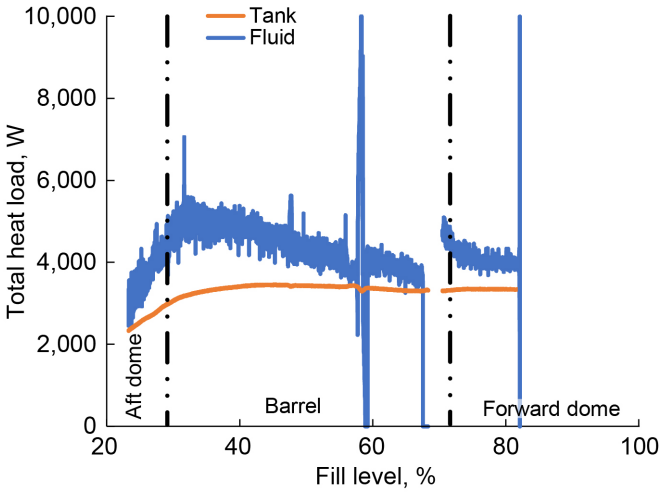

Figure 179.—Comparison of postacoustic liquid hydrogen heat loads.

5.2.8 Fill-Level-Averaged Heat Loads

Calculated heat loads to the tank were averaged over a 5-percent range of fill level to enable comparison of results among the different tests. A comparison of the fill-level-averaged heat loads is shown in Table 23 and graphically in Figure 180 for all tests.

TABLE 23.—FILL-LEVEL-AVERAGED TANK HEAT LOADS

Test	Fill level (±2.5), percent						
	90	80	70	60	50	35	25
	Total average tank heat load, W						
Liquid hydrogen (LH_2) baseline	7,117	6,873	6,854	6,708	6,810	6,784	6,489
LH_2 vapor cooling	5,738	5,925	5,847	6,055	6,151	6,317	6,176
Preacoustic LH_2	3,799	3,844	3,882	3,864	3,731	3,402	2,749
Preacoustic LH_2 vapor cooling	2,671	2,669	2,698	2,915	3,070	3,301	2,666
Preacoustic liquid nitrogen (LN_2)	3,640	3,355	3,212	--------	--------	--------	--------
Preacoustic LN_2 vapor cooling	3,281	--------	--------	--------	2,886	--------	1,873
Postacoustic LH_2	NA	3,329	3,316	3,353	3,426	3,296	2,537

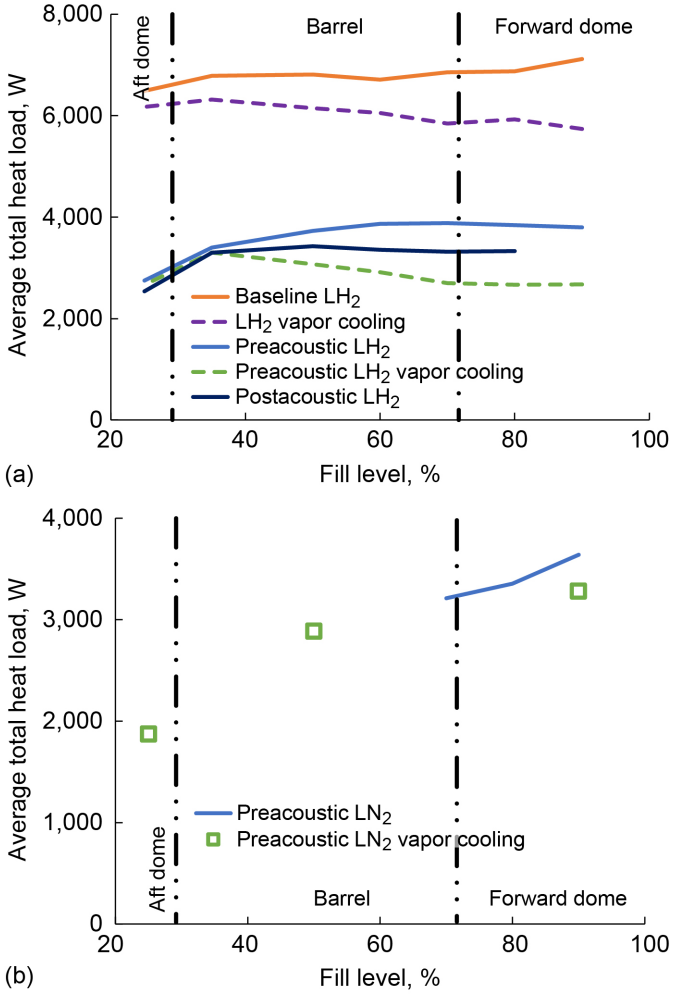

Figure 180.—Comparison of fill-level-averaged tank heat loads. (a) Liquid hydrogen (LH_2) tests. (b) Liquid nitrogen (LN_2) tests.

The reduction in fill-level-averaged heat load is shown in Table 24 and graphically in Figure 181 for all tests. The LH_2 baseline heat loads were used to define the heat load reduction for LH_2 vapor-cooling, preacoustic LH_2, preacoustic LH_2 vapor-cooling, and postacoustic LH_2 tests. The preacoustic LN_2 heat loads were used to define the heat load reduction for preacoustic LN_2 vapor-cooling tests, but a comparison can be made only at the 90-percent fill level.

TABLE 24.—FILL-LEVEL-AVERAGED TANK HEAT LOAD REDUCTION

Test	Fill level (±2.5), percent						
	90	80	70	60	50	35	25
	Total average tank heat load reduction from baseline, percent						
Liquid hydrogen (LH_2) vapor cooling	19	14	15	10	10	7	5
Preacoustic LH_2	47	44	43	42	45	50	58
Preacoustic LH_2 vapor cooling	62	61	61	57	55	51	59
Preacoustic liquid nitrogen vapor cooling	10	------	------	------	------	------	------
Postacoustic LH_2	------	52	52	50	50	51	61

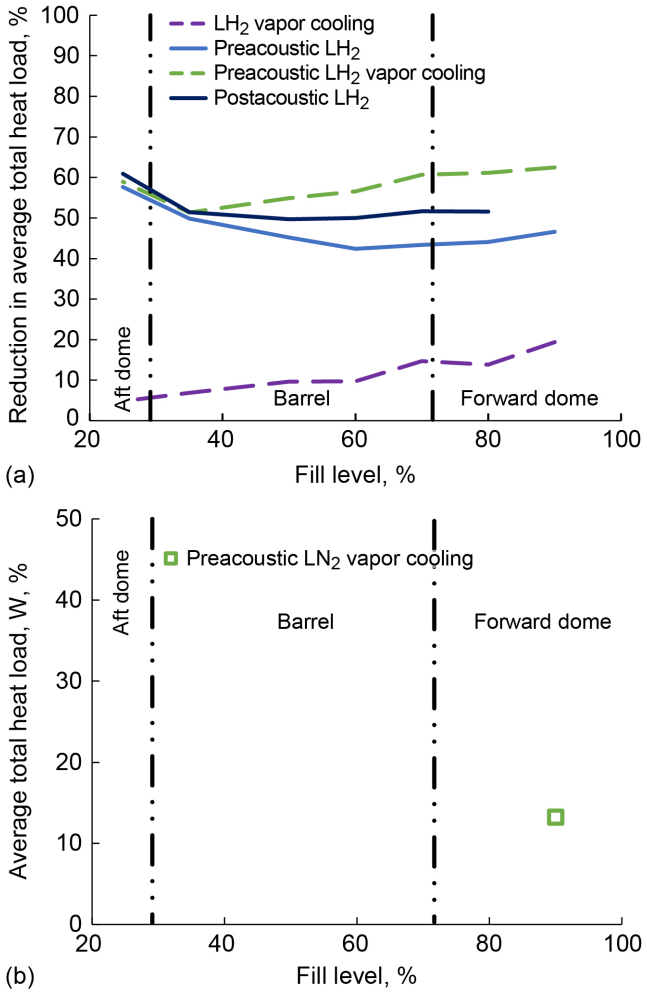

Figure 181.—Comparison of fill-level-averaged heat load reduction.
(a) Reduction in averaged total heat load. Liquid hydrogen (LH_2).
(b) Average total heat load. Liquid nitrogen (LN_2).

TABLE 25.—RELATIVE COMPARISON OF PREACOUSTIC AND POSTACOUSTIC LIQUID HYDROGEN (LH_2) HEAT LOADS

Component	Fill level (±2.5), percent						
	90	80	70	60	50	35	25
	Change in postacoustic LH_2 heat load from preacoustic LH_2 test, percent						
Aft dome	----	–8	–8	–12	–11	–10	–7
Aft skirt	----	8	5	1	0	–2	22
Barrel	----	–23	–29	–26	–17	–6	–19
Forward skirt	----	–13	–1	2	5	1	–11
Forward dome	----	–19	1	7	–23	–4	42
Liquid	----	–13	–13	–16	–11	–2	–8
Vapor	----	–18	–20	–9	–5	–3	–8
Total	----	–13	–15	–13	–8	–3	–8

A relative comparison of preacoustic and postacoustic LH_2 fill-level-averaged heat loads is provided in Table 25 to assess the effect of lower chamber wall temperature during postacoustic testing. Barrel acreage heat load was most sensitive to the decreased vacuum chamber temperature because of the high emissivity of the SOFI surface. Total heat load to the tank during postacoustic tests was 3 to 15 percent lower than during the preacoustic tests.

5.3 Pressurization and Depressurization Testing

Multiple types of pressurization testing occurred during the SHIIVER testing. Most of the tests were self-pressurization tests; however, there was also a single helium pressurization test at the end of the baseline test series and a cyclical pressurization test during the LH_2 vapor-cooling testing with MLI. All pressurization tests were run with LH_2, no pressurization tests were run with LN_2. For self-pressurization during the vapor-cooling testing, the vapor-cooling isolation valves on top of the tank were closed, isolating the entire cooling network from the tank and ceasing vapor flow during those self-pressurization tests.

Depressurization tests occurred after the pressurization tests. The depressurization rate was not controlled, and the system was vented down to the appropriate operating pressure, through a flowmeter. Temperatures and flows were observed and are recorded here.

5.3.1 Self-Pressurization

Pressure rise rates for the different tests are shown in Table 26 using Equation (19). Table 27 shows how those pressure rise rates compare to each other. Generally, there is a short nonlinear portion of the pressurization followed by a long linear pressurization. Both portions of the pressurization test are lumped into the pressure rise calculation:

$$\frac{\mathrm{d}P}{\mathrm{d}t} = \frac{P_{\mathrm{end}} - P_{\mathrm{start}}}{t_{\mathrm{end}} - t_{\mathrm{start}}} \tag{19}$$

where P is the tank pressure at the start and end of the self-pressurization test and t is the time at the start and end of the pressurization test.

During baseline testing, four self-pressurization tests were run, the first at approximately 70 percent fill during boiloff testing and three during vapor-cooling runs, two runs at approximately 70 percent fill and one at 50 percent fill. The first self-pressurization run aborted part way through, and the tank vented to atmosphere before reaching the maximum desired pressure. The second run was performed to achieve a continuously increasing pressure, consistent with the baseline. Interestingly, even though vapor cooling only reduced the total heat load by about 15 percent, it reduced the pressure rise rate by 50 percent; this is because the vapor cooling directly influenced the heat input into the ullage. Since gaseous hydrogen has a much lower specific heat than liquid, putting the additional heat in the ullage causes the gas to warm up faster and the tank pressure rise rate to increase more significantly.

During preacoustic boiloff testing (Thermal 1), self-pressurization runs were performed at approximately 70, 50, and 25 percent fill levels. It is interesting to compare the pressure rise rates between the three tests. With increased ullage space and total heat load unchanged, it is reasonable to expect the pressurization rate to decrease for both 50 and 25 percent fill. However, the pressurization rate increased between 50 and 25 percent. This is due to the aft flange directly heating the ullage

at the 25-percent fill level versus the 50-percent fill level. At 25 percent fill, all of the aft skirt and barrel heating would go directly into the ullage, whereas at 50 percent, most of the heat would go into the liquid. With the greatly reduced heat load of the MLI configuration, the main source of heating into the tank was the barrel section and aft flange. Directing more of the heat into the ullage increases the pressurization rate of the tank due to the smaller thermal capacitance of gas compared to liquid.

During the vapor-cooling test with MLI (Thermal 1), a self-pressurization test was completed at approximately 70 percent full. Eliminating a large portion of the total heat load (~15 percent) and taking even a greater portion of the total heat load out of the ullage with the MLI, the pressure rise rate decreased by 73 percent from the baseline boiloff case, 47 percent from the baseline vapor-cooling case, and 34 percent from the Thermal 1 boiloff case. Once again, the vapor cooling of the forward skirt proved much more beneficial from a pressure-rise-rate-reduction perspective than a total-heat-load-reduction or boiloff-rate-reduction perspective.

During postacoustic thermal testing (Thermal 2), self-pressurization runs were completed at approximately 70 percent full during boiloff testing only. The pressure rise rate was 5 percent less than the preacoustic pressure rise test, with the main difference being a slight reduction of heat load due to lower environmental temperatures.

From these test results, it can be concluded that there are several primary drivers in the pressurization rate. Heat load is certainly very important, but it also matters how the heat load is distributed between the liquid and the ullage. Extra heat into the ullage (compared to in the liquid) increases the pressurization rate. Extra heat into the liquid does not increase the pressurization rate significantly.

TABLE 26.—PRESSURE RISE RATE DATA FROM SELF-PRESSURIZATION TESTS

Test sequence (fill level)	Total heat load,[a] W	Start pressure, kPa	End pressure, kPa	Duration, h	Pressure change, kPa	Average pressure rise rate, kPa/h
Baseline boiloff (70)	7,686	139.7	274.4	0.53	134.7	254.1
Baseline vapor cooling 1 (70)	6,137	154.3	276.1	.91	121.7	133.8
Baseline vapor cooling 2 (70)	6,635	114.9	274.9	1.25	160.0	128.0
Baseline vapor cooling (50)	6,752	111.5	207.3	.95	95.8	100.9
Thermal 1 boiloff (70)	4,145	137.7	275.9	1.35	138.2	102.4
Thermal 1 boiloff (50)	4,253	146.4	275.7	1.69	129.3	76.5
Thermal 1 boiloff (25)	2,963	164.0	276.1	1.31	112.1	85.6
Thermal 1 vapor cooling (70)	3,134	121.3	275.9	2.28	154.7	68.0
Thermal 2 boiloff (70)	3,647	138.1	276.1	1.425	138.0	96.8

[a]Total heat loads are from the average of the conduction and fluid calculated heat flows.

TABLE 27.—RELATIVE CHANGES IN PRESSURE RISE RATES

Test (fill level)	Average pressure rise rate, kPa/h	Decrease in heat load from baseline, percent	Decrease in pressure rise rate from baseline, percent	Decrease in pressure rise rate from other, percent
Baseline vapor cooling (70)	128.0	14	50	----------
Baseline vapor cooling (50)	100.9	12	60	21[a]
Thermal 1 boiloff (70)	102.4	46	49	----------
Thermal 1 boiloff (50)	76.5	45	70	25[b]
Thermal 1 boiloff (25)	85.6	61	66	16[b]
Thermal 1 vapor cooling (70)	68.0	59	73	34[b] (47[a])
Thermal 2 boiloff (70)	96.8	53	62	5[b]

[a]Decrease from baseline 70 percent vapor-cooling case.

[b]Decrease from Thermal 1 70 percent boiloff case.

TABLE 28.—COMPARISON OF PRESSURE RISE RATES TO ISOTHERMAL PRESSURE RISE RATES AT SAME HEAT LOAD

Test (fill level)	Total heat load,[a] W	Average pressure rise rate—Test, kPa/h	Pressure rise rate—Isothermal, kPa/h	Ratio of pressure rise rate test to isothermal case
Baseline boiloff (70)	7,686	254.1	80.5	3.1
Baseline vapor cooling (70)	6,635	128.0	68.1	1.8
Baseline vapor cooling (50)	6,752	100.9	89.3	1.1
Thermal 1 boiloff (70)	4,145	102.4	40.4	2.2
Thermal 1 boiloff (50)	4,253	76.5	51.4	1.3
Thermal 1 boiloff (25)	2,963	85.6	54.4	1.2
Thermal 1 vapor cooling (70)	3,134	68.0	31.1	1.9
Thermal 1 vapor cooling (50)—Cycle 1	3,445	63.2	37.0	1.6
Thermal 2 boiloff (70)	3,647	96.8	37.5	2.4

[a]Total heat loads are from the average of the conduction and fluid calculated heat flows.

5.3.1.1 Comparison of Pressure Rise Rates to Isothermal Case

An isothermal pressure rise model was developed by Van Dresar (Ref. 50) that determines the pressure rise rate of a nonstratified tank. This model is capable of accounting for the thermal mass of the tank wall (for SHIIVER 6,011 kg of stainless steel 304L), along with ullage and liquid thermal mass. The model takes the input total heat load and applies it uniformly through the system keeping everything (ullage, liquid, and tank wall) isothermal. The prediction from this model is the lowest theoretical pressure rise rate that is consistent with the given input conditions.

For purpose of comparison, the total heat load, fill level, initial pressure, and final pressure for each pressure rise test case was input into the isothermal model along with the SHIIVER tank mass and material properties. The calculated isothermal pressure rise rates were calculated and compared to the pressure rise test cases. These comparisons are shown in Table 28. The ratio of pressure rise rate (test) to the isothermal case (theoretical model) gives a qualitative assessment of tank stratification and distribution of heat (ullage versus liquid) during testing.

It is quite clear, given the data, that the forward skirt vapor cooling reduces the ullage stratification during the pressure rise test. For instance, in the baseline test, the pressure rise rate dropped by a factor of two even though the heat load only dropped approximately 10 percent, thus the ratio dropped from 3.1 in the baseline boiloff test to 1.8 in the baseline vapor-cooling test. Adding MLI to the domes only reduced the ratio from 3.1 to 2.2. Similarly, in the preacoustic and postacoustic boiloff tests, the ratio was 2.2 and 2.4, but when the vapor cooling was activated, it dropped to 1.5. The only series that did not follow this trend was the 50 percent test during the preacoustic test series. The reason for the discrepancy was because the pressure rise during the vapor-cooling test was limited to 172 kPa (25 psia), whereas all other pressure rise tests went to 276 kPa (40 psia), so the initial transition period caused the shorter vapor-cooling test to appear higher than it would eventually have flattened out to.

5.3.2 Helium Pressurization

During the baseline testing on the second vapor-cooling run, helium was injected into the tank to raise the pressure to 276 kPa when the tank was at 50 percent fill. This was done mainly to see if there was a difference in how the tank walls responded to warm pressurant gas instead of stratification due to self-pressurization. It was attempted to measure the mass flow rate on FM2 (least restrictive flowmeter) prior to injecting into the tank, but that was not successful as FM2 would still not read that high of a mass flow. However, a model of flow across an orifice was created and it calculated a flow rate of 66 g/s given the assumptions in Table 29. The backpressure range between 110 kPa (16 psia) and 207 kPa (30 psia) does not matter because the flow is choked at the 756 kPa (95 psig) source.

The helium was injected for approximately 250 s to pressurize the tank from 113.3 kPa (16.43 psia) to 193.3 kPa (28.04 psia), at which point injection was stopped to prevent overshoot. The pressure collapsed to 184.5 kPa (26.76 psia) over approximately 30 s and then a second injection began, and the pressure was raised to 207.1 kPa (30.04 psia) over the next 73 s. The pressure collapsed to 191.5 kPa (27.78 psia) over the next 136 s, after which a third injection was completed to raise the pressure back to 207.5 kPa (30.09 psia) over 28 s. Overall, the helium valve was open for 350 s during the multiple pressurization cycles. The vapor-cooling valves were opened a few seconds after the helium and main vent valves were closed and the helium was vented out

of the ullage. The full pressurization event and depressurization is shown in Figure 182. Tank wall temperatures and the warming effect of the helium on them are shown in Figure 183, it is interesting that the rise in wall temperature is very similar to the self-pressurization tests. Figure 184 shows the liquid temperatures during the helium pressurization event and Figure 185 shows the ullage temperatures during the helium pressurization event.

The helium pressurization test showed that the self-pressurization tests and the helium pressurization put approximately the same amount of energy into the tank wall. As such, the self-pressurization tests should be good for estimating transient performances of the MLI in a flight system.

TABLE 29.—ASSUMPTIONS MADE IN CALCULATING HELIUM FLOW RATE

Helium storage pressure, psig	95
Helium storage temperature, K	293
Orifice diameter, in.	0.5
Orifice discharge coefficient	0.9
SHIIVER[a] tank pressure, psia	16/30

[a]Structural Heat Intercept, Insulation, and Vibration Evaluation Rig (SHIIVER).

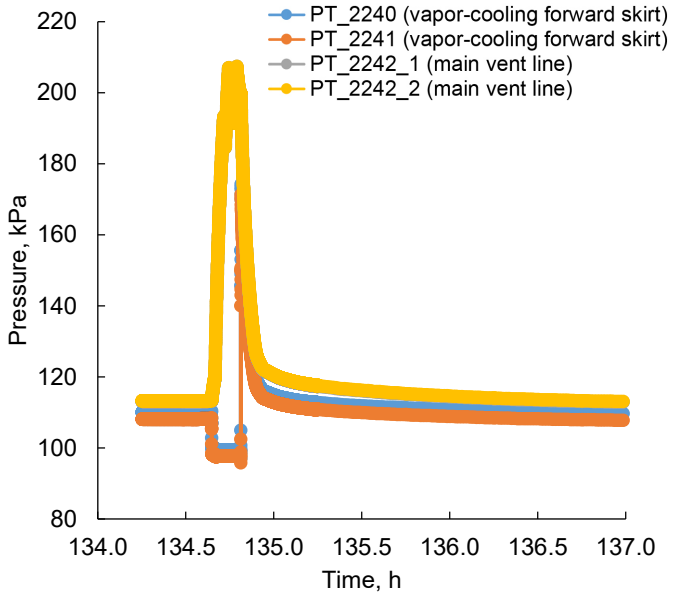

Figure 182.—Pressurization with helium.

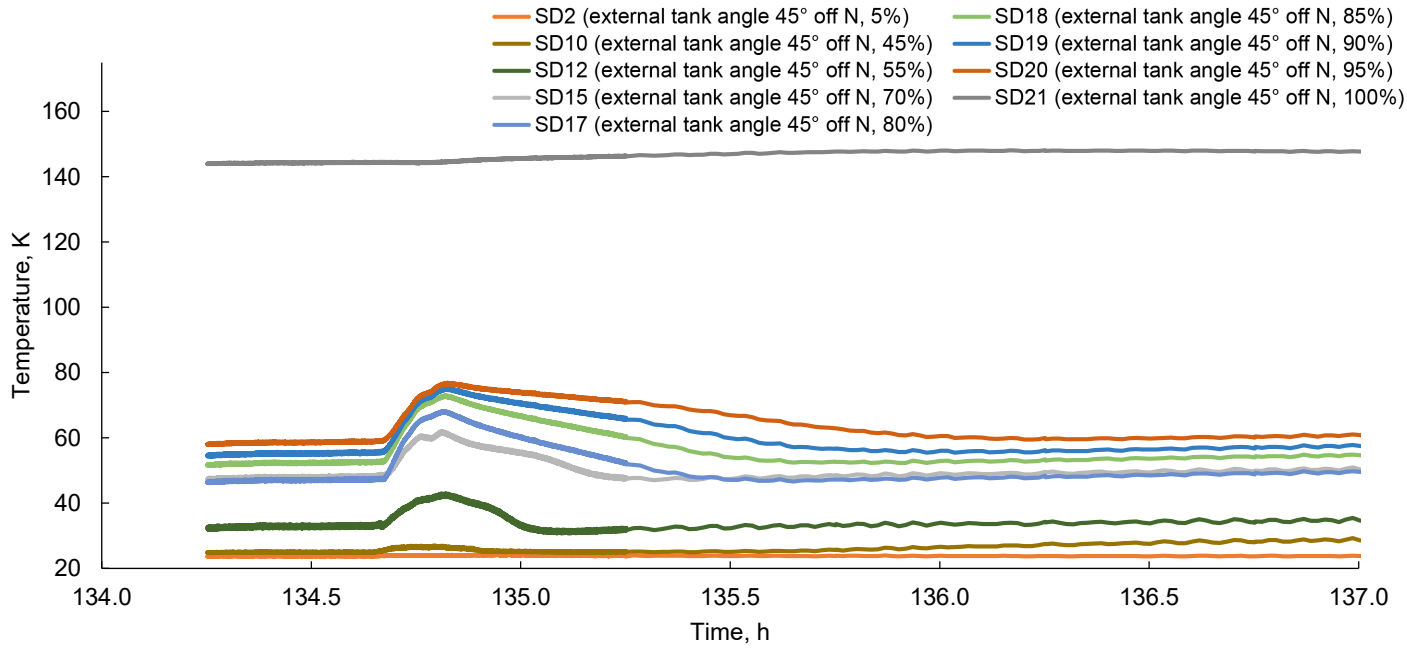

Figure 183.—Tank wall temperatures during helium pressurization test.

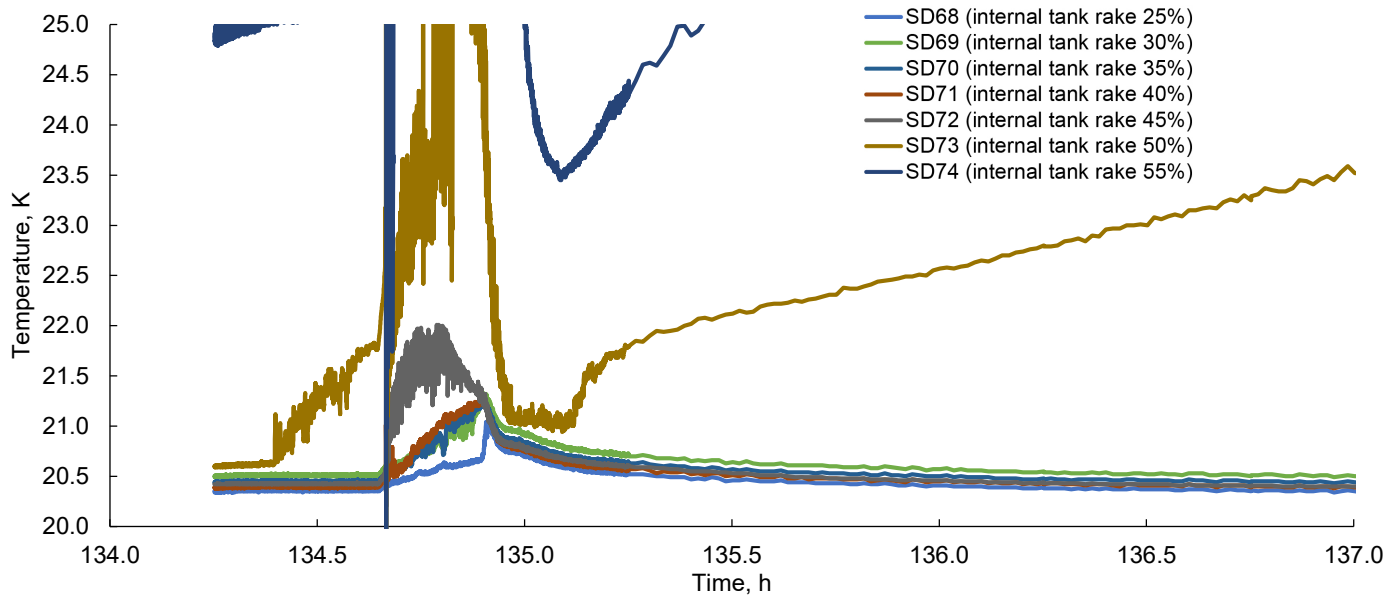

Figure 184.—Liquid hydrogen temperatures during helium pressurization test.

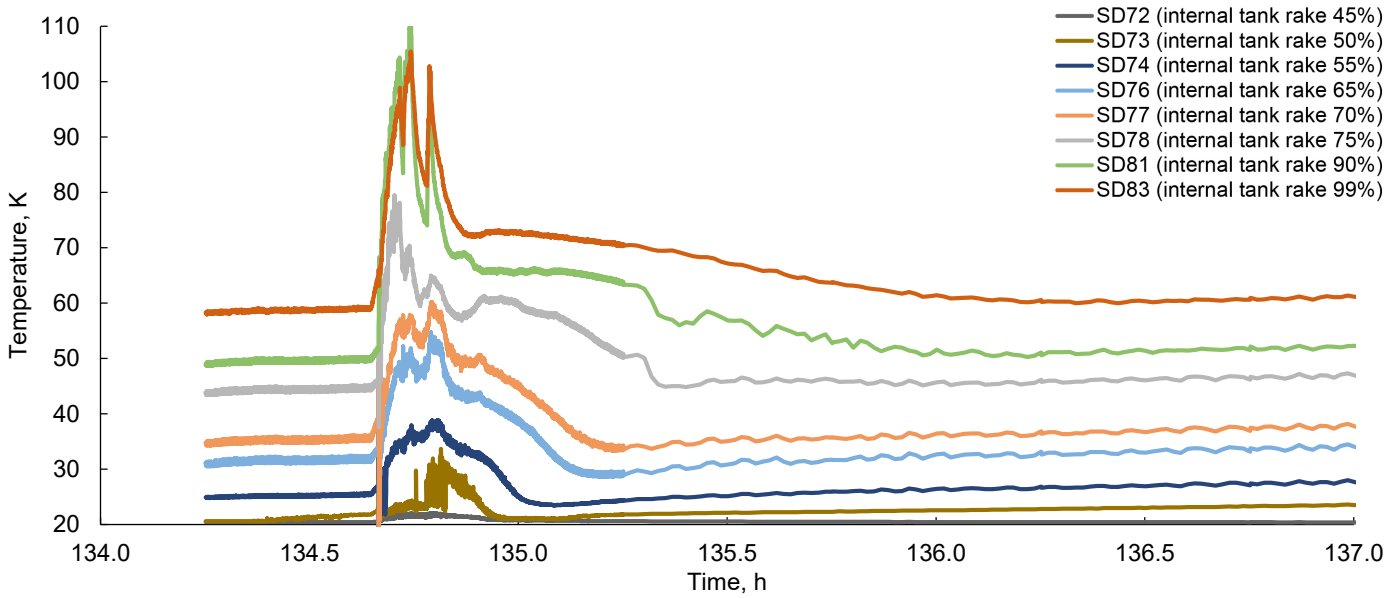

Figure 185.—Ullage temperatures during helium pressurization test.

5.3.3 Cyclical Pressurization

During the preacoustic testing on the vapor-cooling test at 50 percent fill, the pressure was cycled three times between 117 and 172 kPa. This was performed to simulate the use of a bang-bang pressure control system. One such type of pressure control mechanism that is frequently proposed for use on cryogenic systems is known as a thermodynamic vent system (TVS) (Refs. 50 and 51). The data from the cyclic testing is shown in Table 30. Over the three cycles, as the forward skirt has time to warm up between cold hydrogen flows, the pressurization rate increases, approaching the pressurization rate seen on the boiloff test at 50 percent full. Table 31 shows the duty cycle (ratio of time during the cycle that the vapor was flowing through the skirt) of the vapor-cooling loop for all three cycles is approximately 60 percent. Figure 186 shows the pressure rise rate of the cyclical cooling approaching that of the boiloff (no flow through the vapor-cooling circuit on the forward skirt).

TABLE 30.—PRESSURE RISE RATE DATA FROM CYCLICAL PRESSURE RISE DATA

Cycle	Start time, h	End time, h	Start pressure, kPa	End pressure, kPa	Duration, h	Pressure change, kPa	Average pressure rise rate, kPa/h
1	145.75	146.64	115.9	172.2	0.89	56.3	63.2
2	148.10	148.90	117.1	172.7	.80	55.7	69.6
3	150.24	151.01	117.1	172.9	.77	55.8	72.5

TABLE 31.—IMPROVEMENT IN PRESSURE RISE RATES

Cycle	Duration self-pressurization, h	Duration depressurization, h	Duty cycle, percent	Pressurization rate change (previous), percent	Pressurization rate change (boiloff),[a] percent
1	0.89	1.46	62	---	–17
2	.80	1.34	63	10	–9
3	.77	1.18	61	4	–5

[a]See data from “Thermal 1 boiloff (50)” in Table 26.

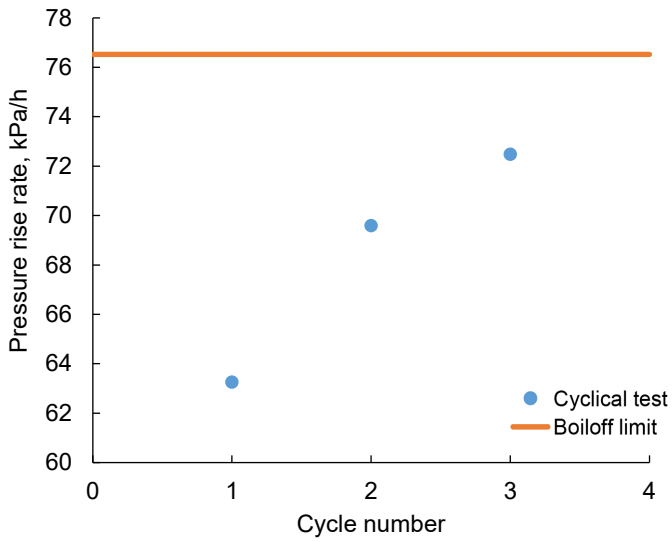

Figure 186.—Cyclic pressure rise rate as function of number of cycles compared to boiloff pressure rise rate.

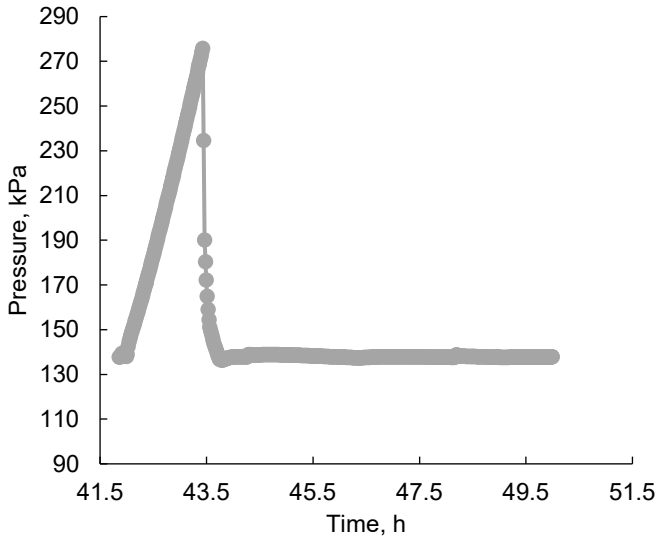

Figure 187.—Tank pressure during pressure rise and depressurization of postacoustic testing.

It would be interesting to see how this changes as a function of both duty cycle and going out beyond three cycles. Typically, a bang-bang pressurization scheme would have much less than 60 percent duty cycle. Based on these results, it is expected that, with reduced duty cycle, the overall vapor-cooling benefit would be reduced. As such, it might be concluded that vapor cooling through a TVS would not provide much reduction in heat load.

5.3.4 Depressurization

Depressurization tests were used as another transient performance test in an attempt to gather transient data on the performance of the different heat-reduction methods. Generally, the tank depressurization rate was limited by the flow resistance of the flowmeter used in the vent line.

Most of the depressurization tests, after the MLI was installed, were very similar. The general overview of the pressurization and depressurization testing, from the postacoustic test temperature perspective, is shown in Figure 187 and Figure 188. After the vent valve, V2, is opened to begin depressurization, the tank pressure and fluid temperatures dropped rapidly, as the warmer ullage was vented. The liquid separated into three main liquid temperature groupings (see Figure 189), the liquid in the bottom dome stayed very close to 20 K, the liquid in the barrel followed the saturation temperature, and a few temperatures right around the flange followed about 0.25 to 0.5 K below the saturation temperature. There is a slope change in the liquid temperatures when all the fluid becomes resaturated. Figure 190 shows the ullage temperature changes during the depressurization and the change in stratification in the ullage portion of the tank. The ullage stratification shows time-dependent cooling as the warm gas, generated during the pressurization testing, is vented and replaced by cold gas recently vaporized from the liquid. Figure 191 shows that during the depressurization, the liquid temperatures converged. Initially, the warmest fluid temperatures dropped, following the liquid saturation curve, while the colder temperatures in the domes rose, likely due to rapid boiling-induced mixing, slowly working its way from the top down in the dome. As shown in Figure 188, before the ullage reached saturated temperatures at 138 kPa (~21 K), the tank started to restratify over time. This is driven by the combination of venting of warm ullage and saturated vapor generated due to the isenthalpic expansion of the liquid.

The tank wall temperatures followed similar trends as the vapor (see Figure 192 and Figure 193), except the vapor was slightly warmer. In Figure 192, the tank wall (SD18) cooled down rapidly during depressurization; however, the tank manway (SD21) took much longer to cooldown. SD15 provided a much more interesting temperature response due to the combination of heat loads coming into it. SD1, SD7, and SD12 track close to liquid temperatures with slight offsets being on the other side of the tank wall in the barrel.

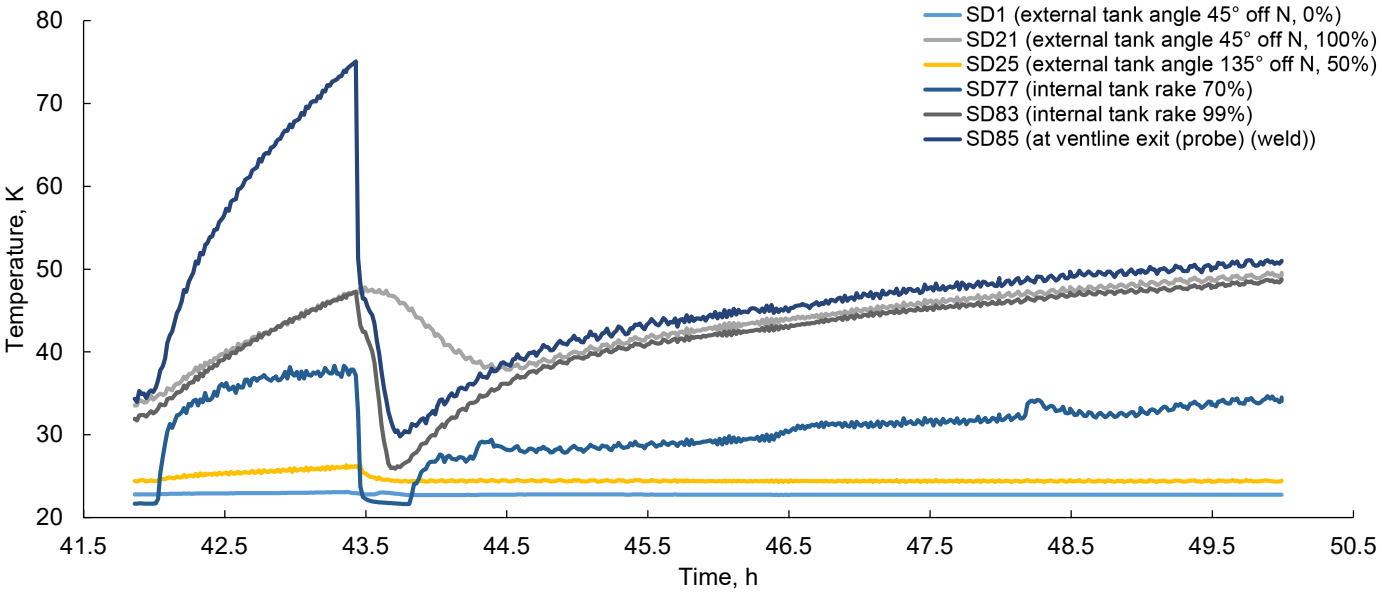

Figure 188.—Tank and fluid temperatures during pressurization and depressurization at approximately 70 percent full during postacoustic testing.

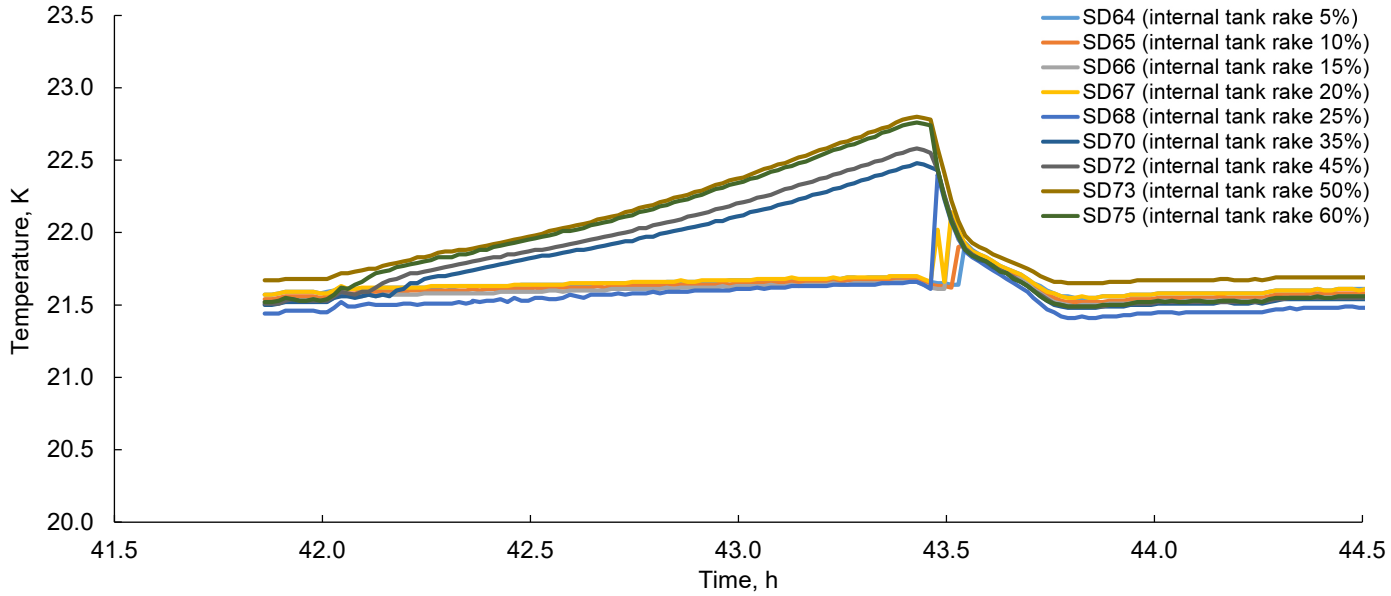

Figure 189.—Hydrogen temperatures during postacoustic thermal test pressurization and depressurization testing. Three distinct groupings correlate with fill levels.

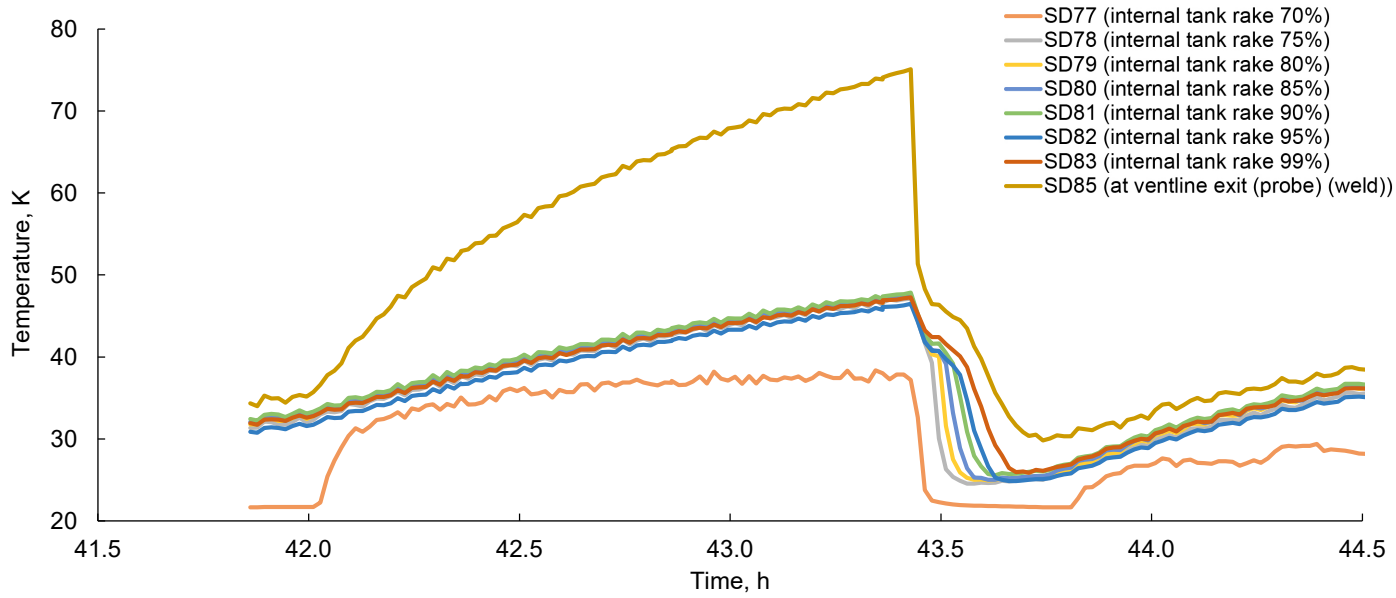

Figure 190.—Ullage temperatures during postacoustic thermal test depressurization.

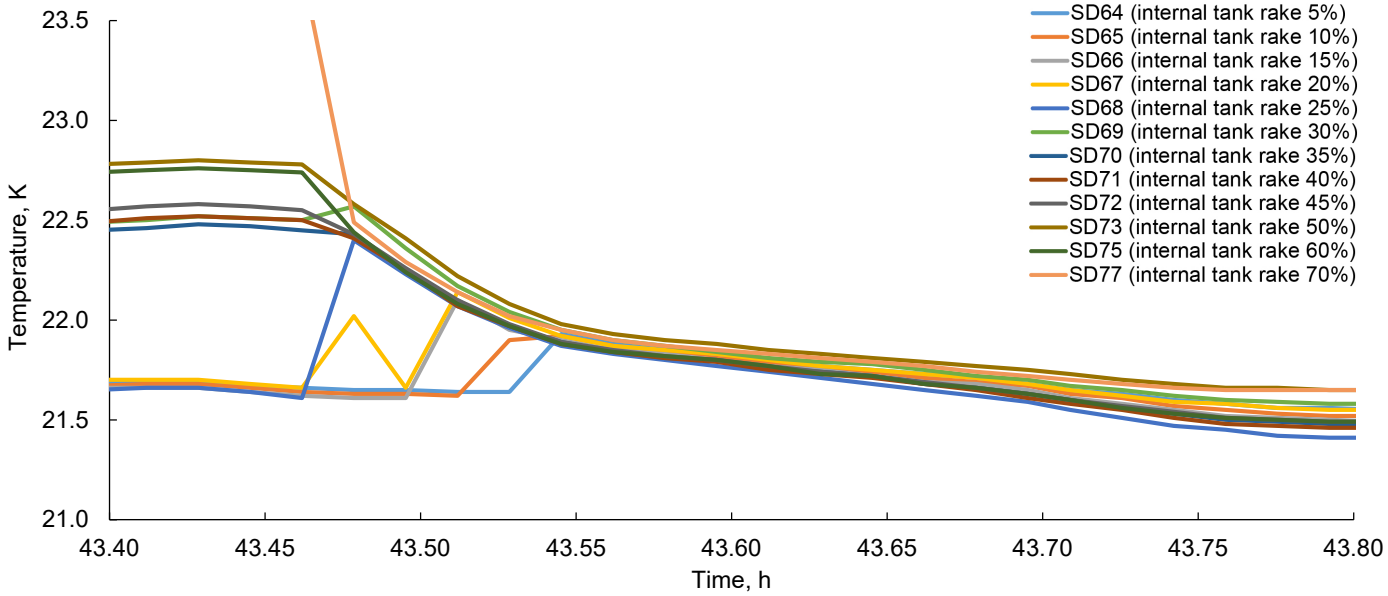

Figure 191.—Hydrogen temperatures during postacoustic thermal test depressurization testing.

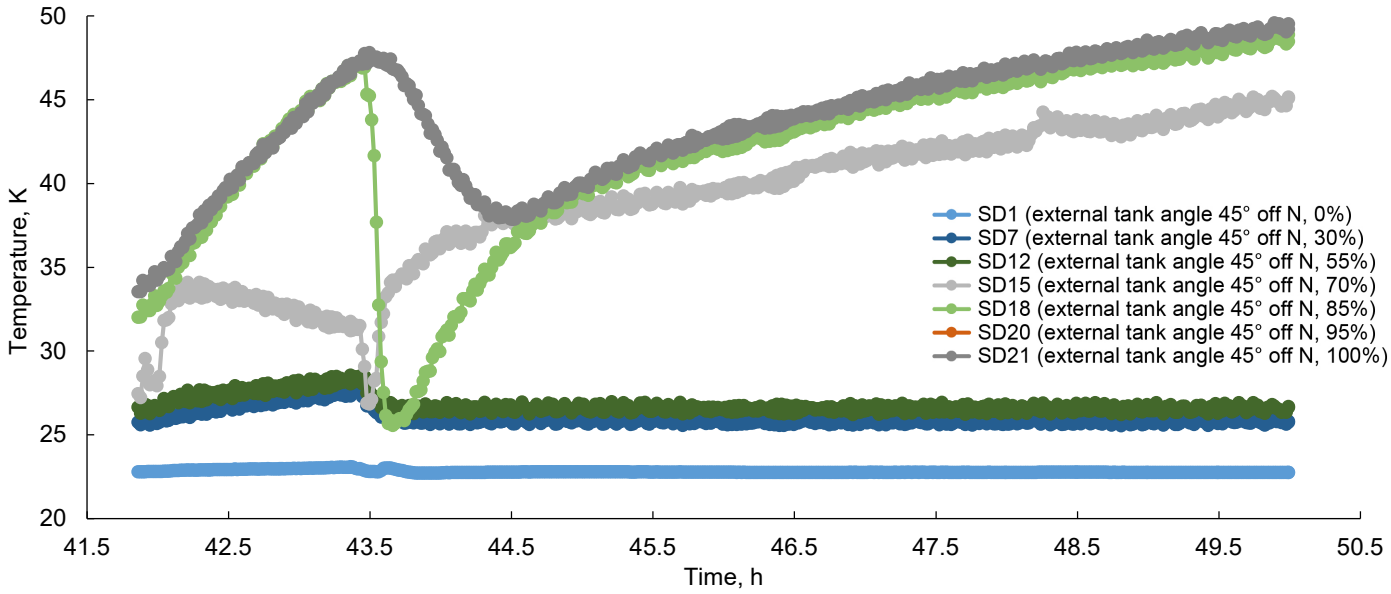

Figure 192.—Hydrogen tank wall temperatures during postacoustic thermal test pressurization and depressurization testing.

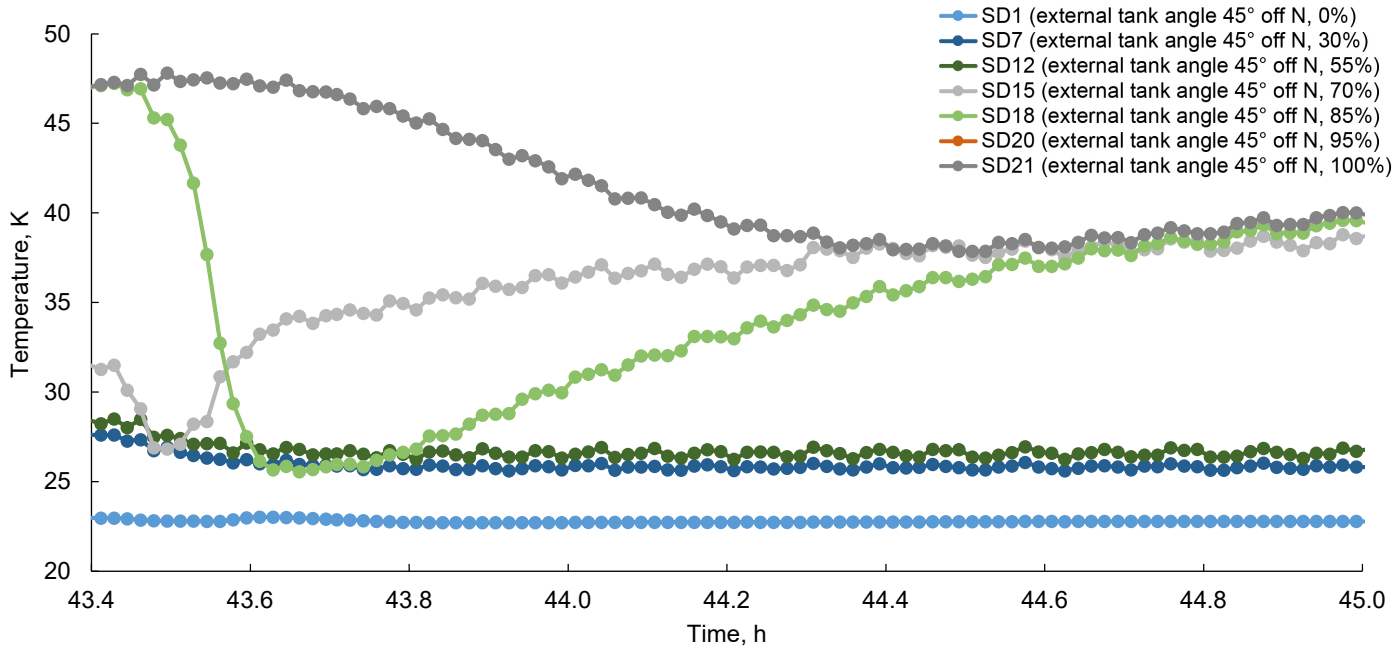

Figure 193.—Hydrogen tank wall temperatures during postacoustic thermal test depressurization testing.

Due to the higher heat loads coming into the tank and more even distribution of the heating, the depressurization during the baseline test was much less eventful. The depressurization itself was much quicker (over just a few minutes) as shown in Figure 194. The liquid temperatures responded in a similarly mundane manner (Figure 195), though there is a slight separation between the temperatures in the aft dome and the other temperatures and a much smaller mixing event during the depressurization. However, in the ullage temperatures, Figure 196, and tank wall temperatures, Figure 197, there is a bit of a warming hump in the ullage portion of the tank that lasts for about an hour after the depressurization.

During vapor-cooling testing, the depressurization took much longer (see Figure 198). The liquid was fully uniform for the whole pressurization and depressurization periods (see Figure 199), and both the fluid temperatures and the tank wall temperatures showed a much longer cooldown period during the depressurization before bouncing back and the tank started pressurizing again (see Figure 200).

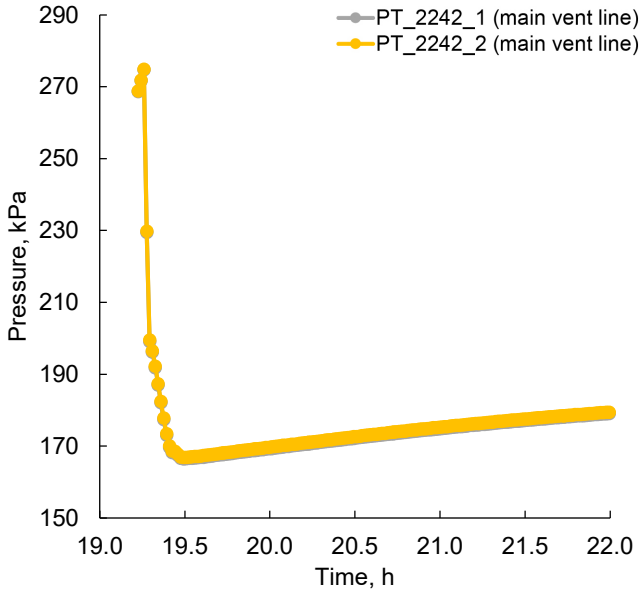

Figure 194.—Tank pressure during depressurization of baseline boiloff test.

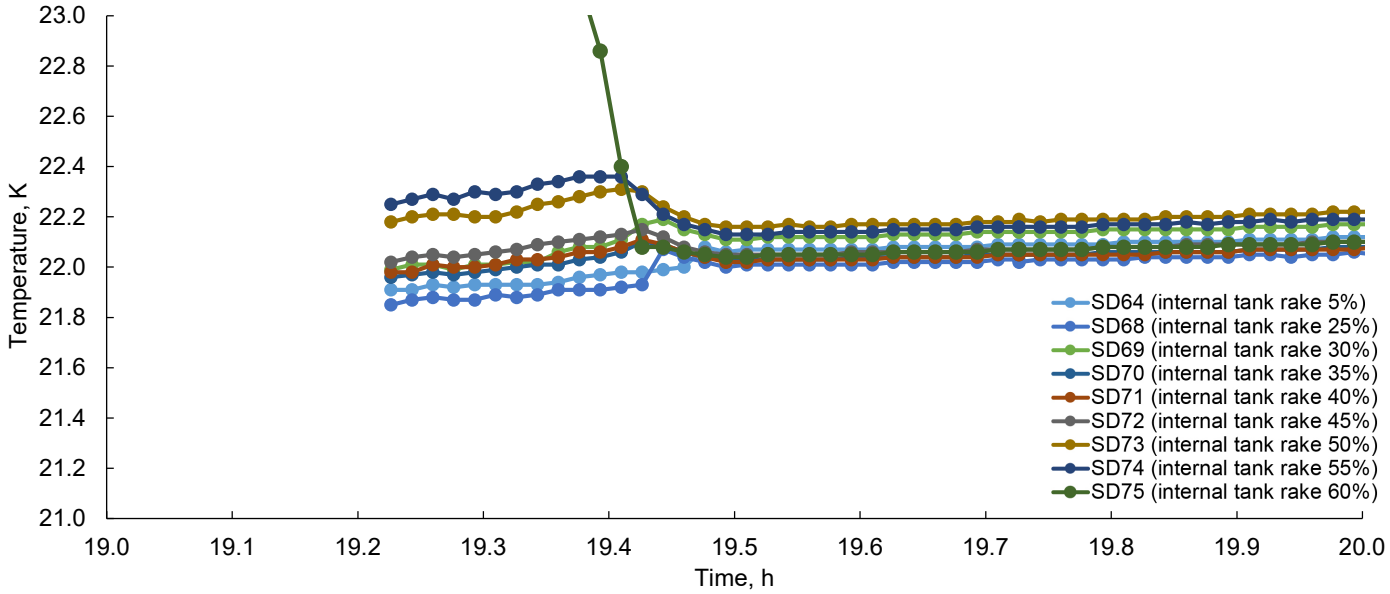

Figure 195.—Liquid temperatures during depressurization test of baseline boiloff.

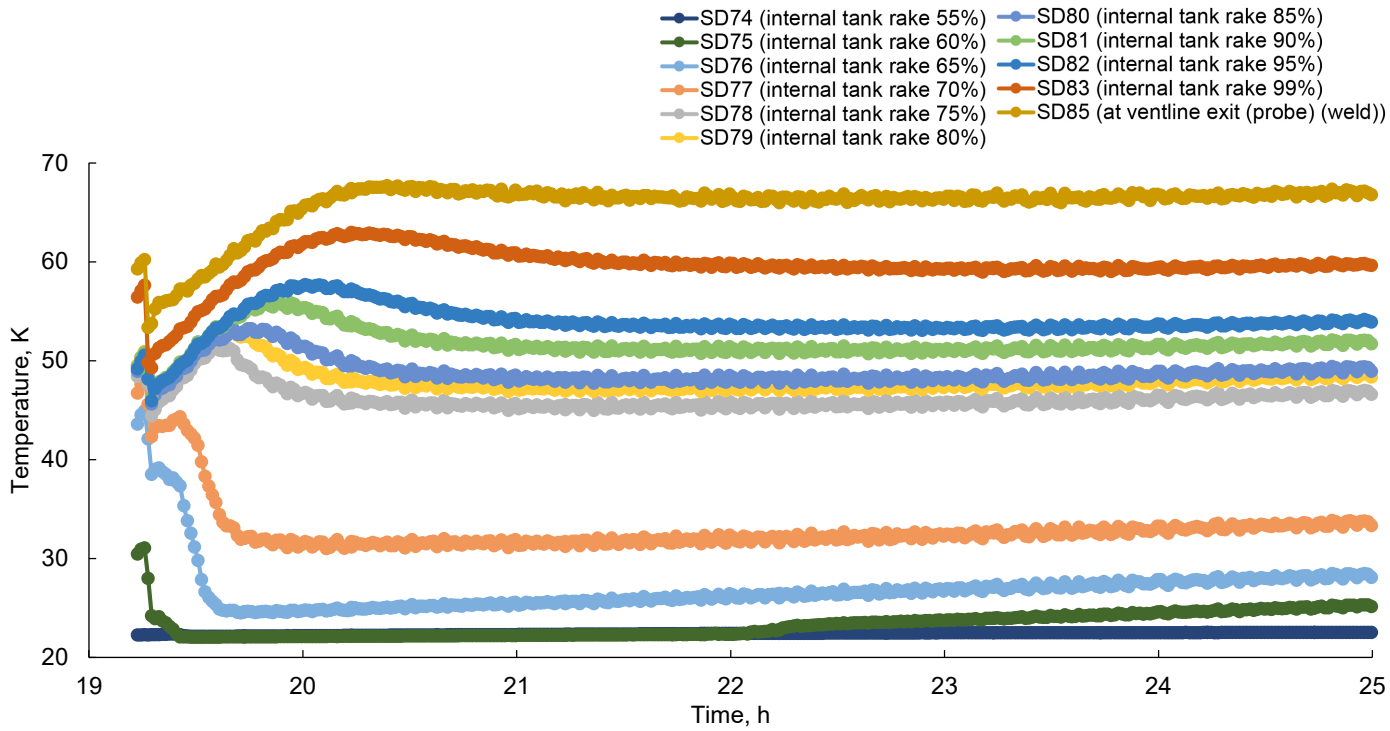

Figure 196.—Fluid temperatures during depressurization test of baseline boiloff.

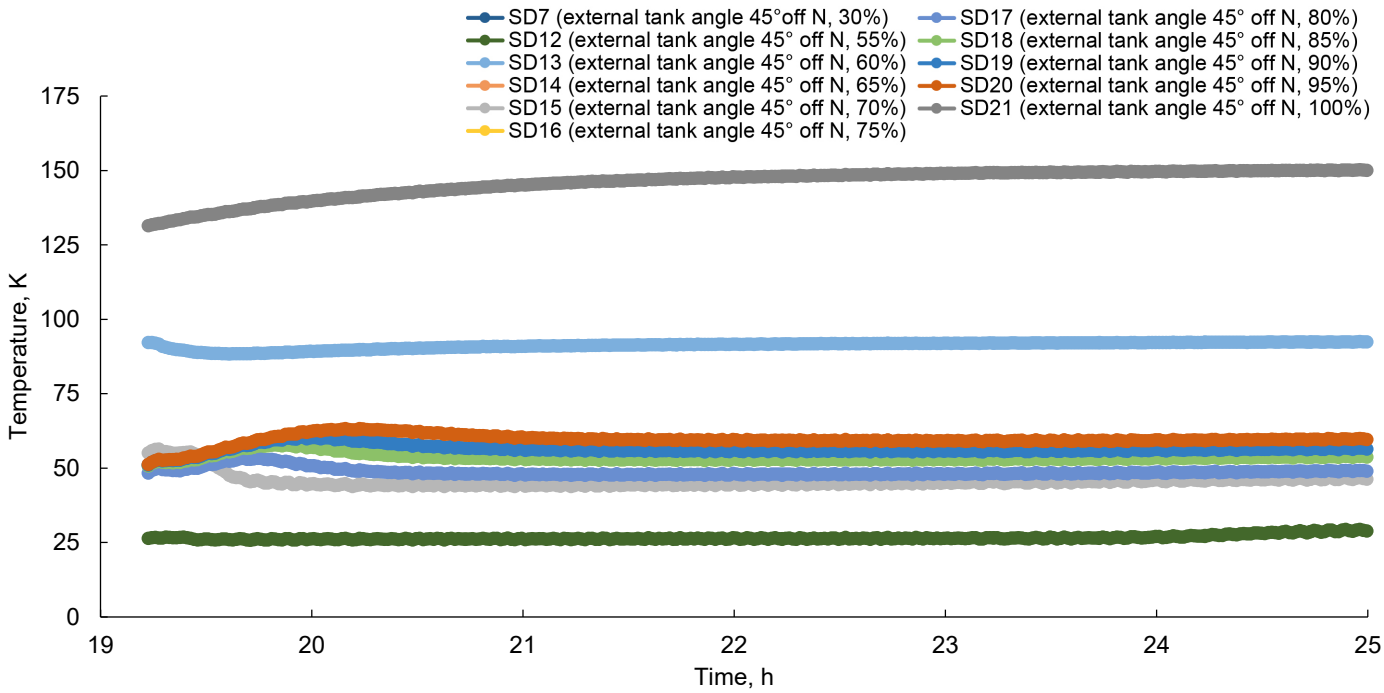

Figure 197.—Tank wall temperatures during depressurization test of baseline boiloff.

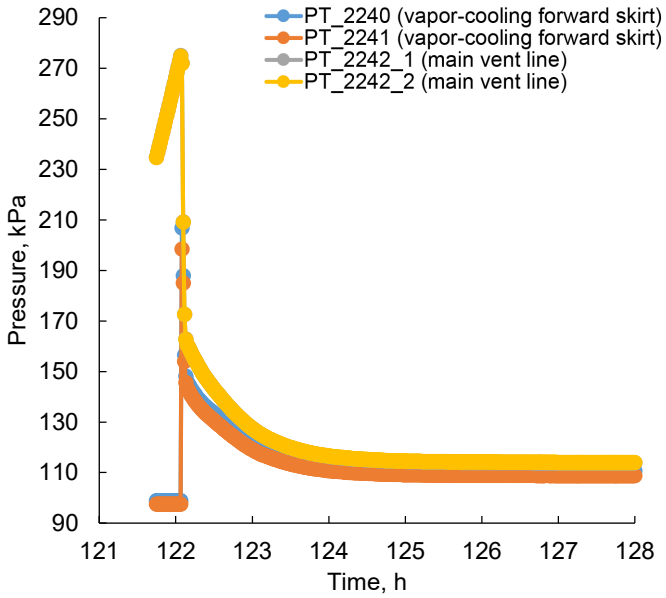

Figure 198.—Baseline vapor-cooling pressures during depressurization.

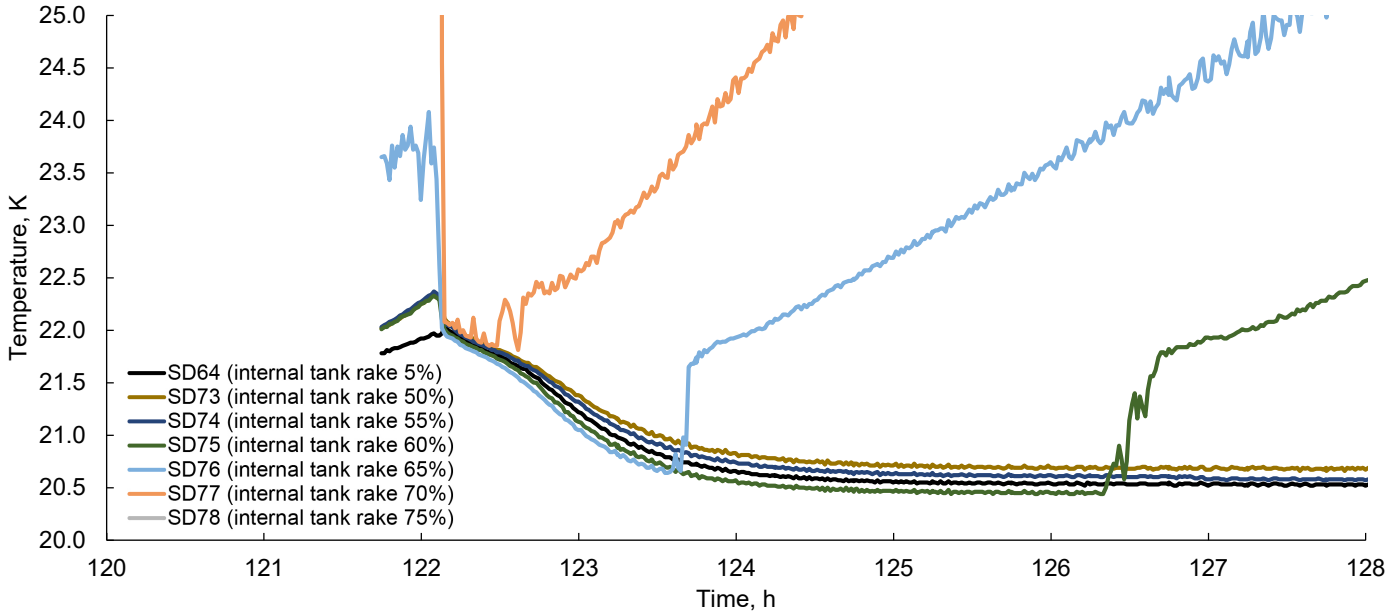

Figure 199.—Internal fluid temperatures during baseline vapor-cooling depressurization event.

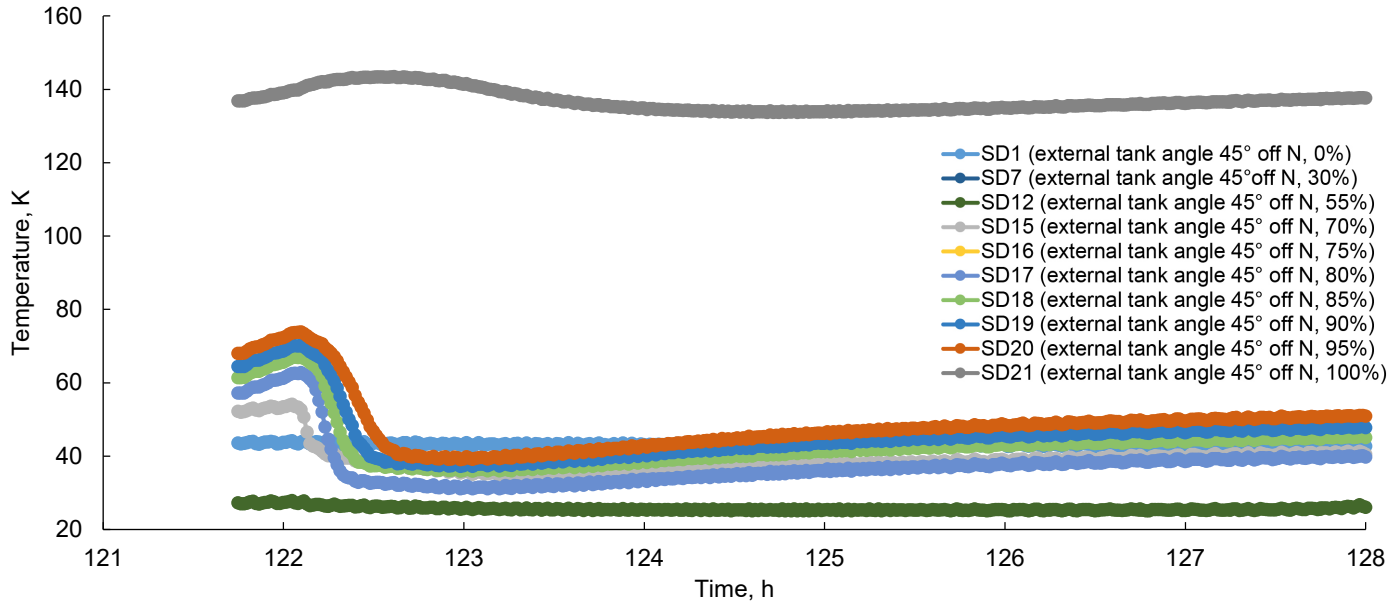

Figure 200.—Tank wall temperatures during baseline vapor-cooling depressurization testing. SD1 and SD21 are on the uninsulated manways.

5.4 Comparison of Boiloff Flow Data

The boiloff flow rate is obtained from the flowmeter measurements. The flowmeter configuration is shown in Figure 22. Without vapor cooling the relevant flowmeters are FM2, FM3, and FM4. Depending on the vent flow path chosen by the positions of the appropriate valves, the boiloff flow rate is measured by FM2 alone, both FM2 and FM3, or by all three flowmeters in the main vent line. In the latter two instances, the same flow rate passes through multiple flowmeters, as they are in series. When vapor cooling on the forward skirt is used, the flow is measured by FM1, and no flow is passed through FM2, FM3, and FM4.

For a significant part of the baseline test, only FM3 was operational. In particular, FM1 did not register any flow for the tests with vapor cooling. Therefore, there was a need to obtain the boiloff flow rate by other means. Since the capacitance probe as well as RFMG measures the amount of fluid in the tank, the rate of change of fluid mass from these measurements must provide the boiloff flow rate. Also, the wet and dry transitions of the diodes inferred from the internal rake temperature measurements provide a means to obtain the average flow rate between the transitions at neighboring diodes.

In what follows, the theoretical basis for the determination of the flow rate from the capacitance probe measurements is first explored. The comparison of the boiloff flow rate for the baseline, preacoustic, and postacoustic tests is then discussed.

5.4.1 Capacitance Probe Analysis

5.4.1.1 Empirical Correlation for Boiloff Flow Rate

The capacitance probe measures the height of the liquid within the probe in the tank. The liquid height measured is related to the liquid volume in the tank from the known tank geometry. Thus indirectly, the capacitance probe reading is a measure of the tank liquid volume (or mass). Let V_{cap} denote the voltage measured by the probe. Thus $V_{cap} \sim \phi \sim M_{H_2}$, where ϕ and M_{H_2} are the fill level and hydrogen mass in the tank, respectively. Therefore, the rate of change of these quantities are also related, that is, $\mathrm{d}V_{cap}/\mathrm{d}t \sim \mathrm{d}M_{H_2}/\mathrm{d}t \sim \dot{m}_{\mathrm{boiloff}}$. The boiloff flow rate $\dot{m}_{\mathrm{boiloff}}$ was correlated to the V_{cap} reading by the following empirical formula.

$$\dot{m}_{\mathrm{boiloff}} = -S\left[1+f(\phi)\right]\frac{\mathrm{d}V_{cap}}{\mathrm{d}t} \qquad (20)$$

where $\dot{m}_{\mathrm{boiloff}}$ is in g/s, V_{cap} is in volts, elapsed time t is in hours, S is a scale factor (that also accounts for conversion of units), and $f(\phi)$ is a correction factor that depends on the fill level. The actual expression used is

$$\dot{m}_{\mathrm{boiloff}} = -50\left\{1+\frac{1}{150}\left[100-10V_{cap}(t)\right]\right\}\frac{\mathrm{d}V_{cap}}{\mathrm{d}t} \qquad (21)$$

This expression was obtained by trial and error by visually fitting Equation (20) with the flowmeter data for the baseline boiloff tests. In order to use this formula, the following data processing steps were applied: (i) the V_{cap} data that was acquired every second was averaged for a minute, (ii) $V_{cap}(t)$ was further smoothened using a moving average over 30 points to obtain $V_{cap,\mathrm{smooth}}(t_{\mathrm{smooth}})$, and (iii) this data was then used in Equation (21) to obtain $\dot{m}_{\mathrm{boiloff}}$.

The boiloff flow rate obtained from Equation (21) and the data from the flowmeter FM3 are shown in Figure 201. The comparison is reasonably good, lending confidence to the fit that was obtained visually. Time in this figure as well as all figures in this section denote elapsed time in hours. The calendar date and time for the time origin t = 0 for each test series is given in Table 32. The capacitance-probe-based flow rate, however, shows some degree of scatter. Furthermore, this empirically calculated flow rate exhibits several spikes that are not physical, where the calculated flow rate deviates

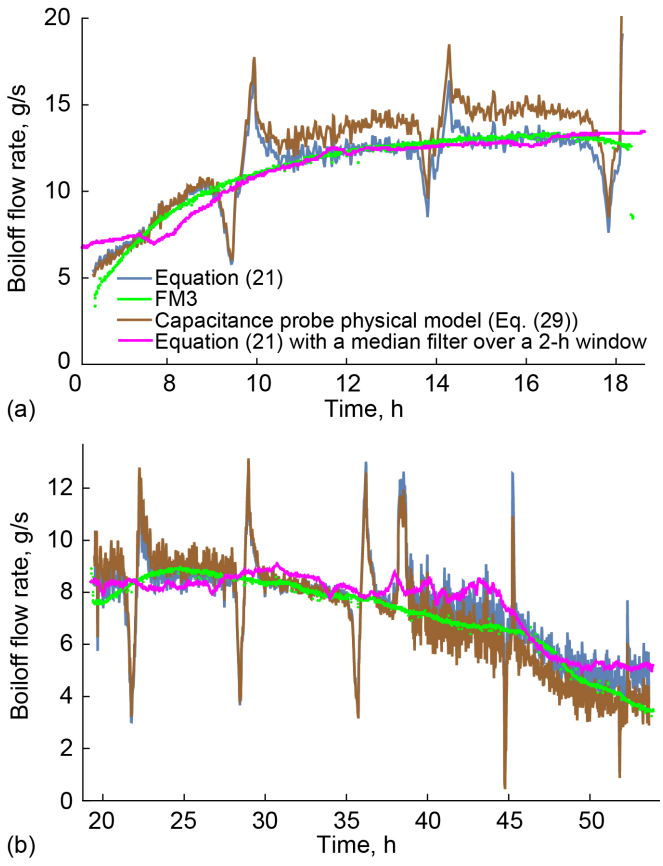

Figure 201.—Calibration and comparison of boiloff flow rate from capacitance probe voltage for baseline boiloff test. (a) Up to 18 h. (b) Beyond 20 h.

TABLE 32.—CAPACITANCE PROBE MAXIMUM CALIBRATION PARAMETERS

Test	Reference for time origin $t = 0$	Maximum calibration fill level, percent	Capacitance probe maximum calibration voltage, V	C_1	Capacitance probe maximum calibration active length, in.
Baseline	8/23/2019, noon EST	90.5	9.9612	–413.7	105.6
Preacoustic hydrogen (H_2)	9/23/2019, 7:14:23 a.m. EST	90.5	9.9665	–414.6	105.6
Preacoustic nitrogen (N_2)	10/2/2019, noon EST	87.5 (69.0[a])	7.7634[a]	–4,442.8[a]	101.6
Postacoustic H_2	1/20/2020, noon EST	78.0	9.9635	–356.9	90.8

[a]Data (for N_2) is not at maximum calibration but is a reference point to determine C_1.

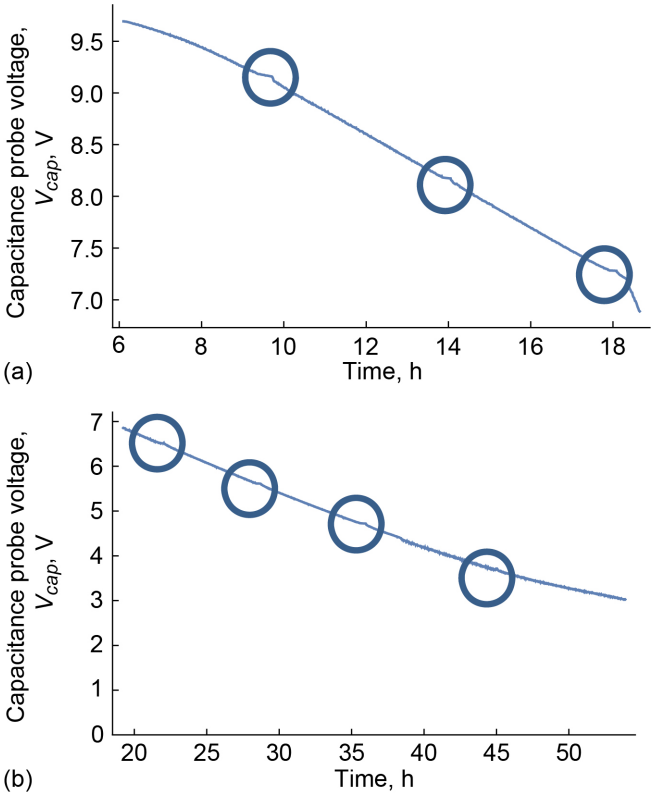

Figure 202.—Capacitance probe voltage corresponding to data in Figure 201. (a) Up to 18 h. (b) Beyond 20 h.

significantly from the flowmeter data. This behavior can be traced to the changes in slope in the capacitance probe voltage (see circled regions in Figure 202). It is speculated that the capacitance probe might contain spacers within it for structural support, and the altered behavior of the probe occurs when the liquid interface moves past the spacers. When a median filter over a 2-h window is applied to the capacitance probe boiloff flow rate calculated from Equation (21) (with V_{cap} data averaged for a minute and without any data smoothing), the spikes in the flow rate are eliminated, as shown by the magenta curve in Figure 201. Systematic application of the median filter, or other means to eliminate the spikes, such as using a polynomial fit for the capacitance probe voltage and calculating the time derivative from the fit, are not discussed further in this report, and is left to be pursued in the future.

By integrating Equation (21), a fill-level fraction ϕ based on mass of fluid in the tank can be obtained as

$$\phi = \frac{1}{M_l}\left[C_1 + 3.6\left(50V_{cap} + \frac{100}{3}V_{cap} - \frac{5}{3}V_{cap}^2\right)\right] \qquad (22)$$

where M_l is the liquid mass of the tank fully filled, and C_1 is an integration constant that is to be determined. In this section, we treat the mass-based fill level and the commonly used volume-based fill level as being the same (the two are related by $\phi_{mass} = (\rho_l/\rho_{l_i})\phi_{vol} + (\rho_v/\rho_{l_i})(1 - \phi_{vol})$, where ρ_l and ρ_v are the liquid and vapor density, and ρ_{l_i} is the initial liquid density when the tank was filled, and differ by a few percent for the various SHIIVER test conditions). C_1 is obtained when the fill level is known at some capacitance probe voltage (such as knowing these values at a given time). During the first fill of the tank with LH_2 in the baseline test, a maximum calibration command was sent to the capacitance probe when the rake diode SD81 was observed to transition to reading cold LH_2 temperature. The corresponding ϕ and V_{cap} values are used to determine C_1. Equations (21) and (22) were only used at subsequent times after the maximum calibration command was issued, so that the capacitance probe calibration is unaltered. Note that after issuing the maximum calibration command, the capacitance probe is only sensitive to lower liquid heights and fill levels. It does not sense higher liquid heights and fill levels; in such instances its voltage output remains constant at the value it had when the maximum command was issued. For the preacoustic test with LH_2 performed almost a month later, a new maximum calibration command was not issued, and the previous maximum voltage from the capacitance probe was found to be valid with very little error (0.05 percent of the full-scale value, which is approximately 10 V). For the preacoustic test with LN_2, and again for the postacoustic test with LH_2, new maximum calibration commands were issued because of the liquid change.

Note that Equations (21) and (22) pertain to LH_2. For tests with LN_2, Equation (21) needs to be modified to take into account the higher density of LN_2. With ρ_{ratio} denoting the ratio of LN_2 to LH_2, the $\dot{m}_{boiloff}$ and the ϕ can be calculated as

$$\dot{m}_{boiloff} = -50\rho_{ratio}\left\{1+\frac{1}{150}\left[100-10V_{cap}(t)\right]\right\}\frac{dV_{cap}}{dt} \quad (23)$$

$$\phi = \frac{1}{M_l}\left[C_1 + 3.6\rho_{ratio}\left(50V_{cap}+\frac{100}{3}V_{cap}-\frac{5}{3}V_{cap}^2\right)\right] \quad (24)$$

with C_1 determined appropriately from the LN_2 test conditions. Note that the dielectric constant for LN_2 is also very different from that of LH_2. However, this change is accommodated by the calibration procedure for the capacitance probe and the issuance of the maximum calibration command and does not affect the boiloff rate and fill-level expressions given previously.

For the postacoustic LH_2 tests, the capacitance probe did not work initially due to issues communicating with it remotely from the control room. It started to work after an onsite physical reset and a maximum calibration command issued at the fill level at that time (~78 percent). Hence a fill-level ratio (ϕ_{ratio} = 78/90.5) needs to be incorporated in Equations (21) and (22) for the postacoustic test.

$$\dot{m}_{boiloff} = -50\phi_{ratio}\left\{1+\frac{1}{150}\left[100-10V_{cap}(t)\right]\right\}\frac{dV_{cap}}{dt} \quad (25)$$

$$\phi = \frac{1}{M_l}\left[C_1 + 3.6\phi_{ratio}\left(50V_{cap}+\frac{100}{3}V_{cap}-\frac{5}{3}V_{cap}^2\right)\right] \quad (26)$$

The values for C_1 for all the tests conducted along with the associated fill levels and capacitance probe voltages when the maximum calibration command was issued are summarized in Table 32.

5.4.1.2 Physical Model for the Capacitance Probe

In the physical model, the boiloff flow rate can be obtained as

$$\dot{m}_{boiloff} = -\frac{dM_{H_2}}{dt} = -(\rho_l-\rho_v)V_{tank}\frac{d\phi}{dt} \quad (27)$$

where V_{tank} is the SHIIVER tank volume.

It is assumed that the liquid and vapor density are constant in Equation (27). This equation can also be used to calculate the $\dot{m}_{boiloff}$ from the fluid mass M_{H_2} in the tank measured by RFMG. The ϕ can be related to the liquid level from the known tank height to volume relationship given in Equation (28) and is shown in Figure 203. This relationship is based on the RFMG model, accounting for the shrinkage of the tank at cryogenic temperature.

$$\phi = \frac{1}{V_{tank}}\sum_{i=0}^{10} a_i h^i \quad (28)$$

where a_0 = 0.004313685, a_1 = 0.415495996, a_2 = 12.64099669, a_3 = –18.97029258, a_4 = 31.00067342, a_5 = –30.00629244, a_6 = 16.42370017, a_7 = –5.090779682, a_8 = 0.836222529, a_9 = –0.057180538, a_{10} = 0.000122776, and h is the liquid height in meters. The capacitance probe measures an active liquid height above a distance h_0 from the bottom of the tank. Thus, it measures a height $x = h - h_0$ (h_0 = 3.81 cm (1.5 in.) is the gap between the capacitance probe and the bottom of the tank), and is related to the measured voltage via $x = (L/10)V_{cap}$, where L is the active length of the capacitance probe when the maximum calibration command was issued ($V_{cap} \approx 10$ V at maximum calibration; see Table 32 for values of L). Thus, the $\dot{m}_{boiloff}$ from the physical model is

$$\dot{m}_{boiloff} = -\left[\frac{(\rho_l-\rho_v)V_{tank}L}{36}\right]\frac{d\phi}{dh}\frac{dV_{cap}}{dt}; \quad h = x + h_0 \quad (29)$$

The units for the quantities in Equation (29) are $\dot{m}_{boiloff}$ in g/s; $(\rho_l - \rho_v)V_{tank}$ in kg; L, x, and h_0 in meters; V_{cap} in volts; and t in hour. The $\dot{m}_{boiloff}$ calculated from the physical model is compared with that from the flowmeter FM3 and the empirical model (Eq. (21)) in Figure 201. The trends are all the same; however, in general, the physical model deviates more from the flowmeter data than the empirical model does. One

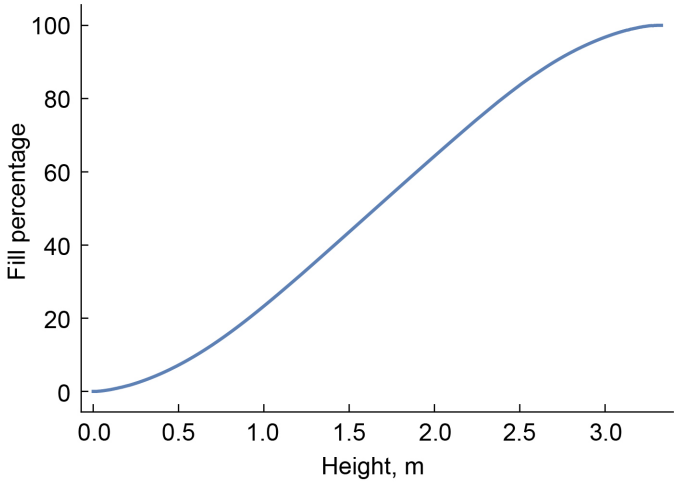

Figure 203.—Fill level versus tank liquid height (from Eq. (28)).

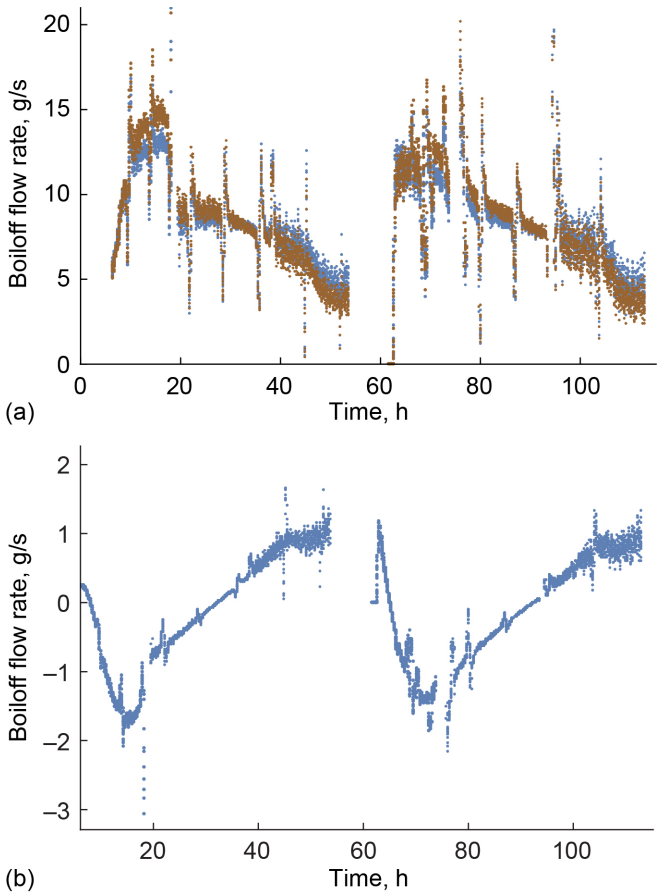

Figure 204.—Comparison of boiloff flow rate for baseline tests. (a) Capacitance probe empirical correlation (blue) and physical model (brown). (b) Deviation of physical model from capacitance probe correlation.

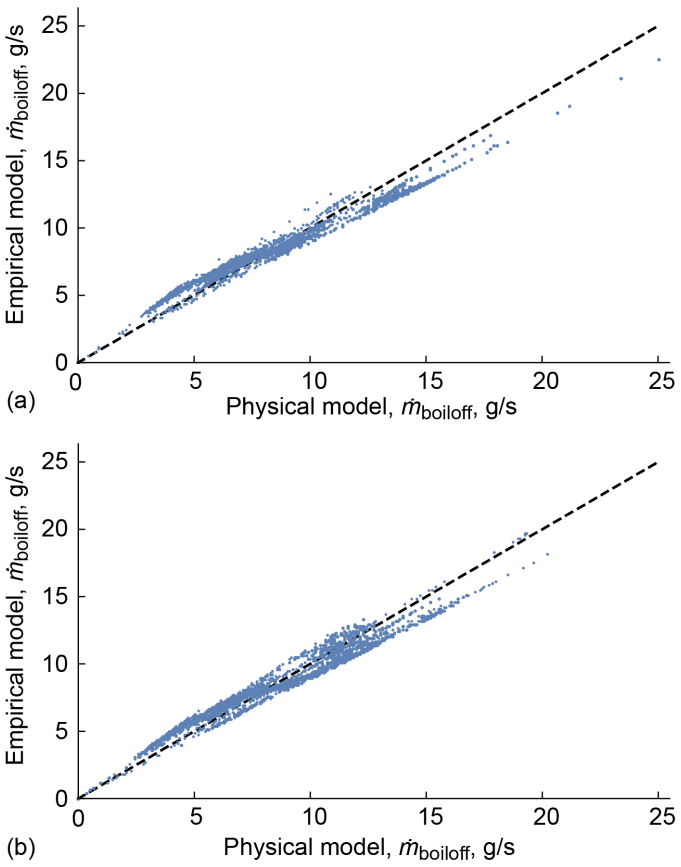

Figure 205.—Parity plot of capacitance probe empirical correlation (y-axis) and physical model (x-axis) for baseline tests. Boiloff flow rate ($\dot{m}_{boiloff}$). (a) Boiloff tests. (b) Vapor-cooling tests.

reason is that the liquid and vapor density in Equation (29) are taken to be constant (values during initial fill), while they do change during the SHIIVER tests. Another reason might be that though shrinkage of the tank at cryogenic temperature is taken into account via a model in Figure 203, the actual height to volume relationship of the tank is different from the model. Also, the empirical model is a fit to the flowmeter data and is anticipated to match. The comparison of the flow rate from the capacitance probe correlation and physical model for all the baseline tests is shown in Figure 204, and a parity plot is shown in Figure 205. Similar behavior was observed for the preacoustic and postacoustic tests; however, in the rest of this report capacitance probe flow rate results are shown only from the empirical correlation.

5.4.1.3 Comparison of Capacitance Probe Voltage and Liquid Height

In Section 5.2 (Figure 146), a correlation was provided for the liquid height in the tank determined from the inferred wet and dry diode transitions to the voltage output from the capacitance probe, for the baseline and preacoustic LH_2, preacoustic LN_2, and the postacoustic LH_2 tests. In Figure 206, those correlations are compared to the height determined from (i) the capacitance probe empirical correlation for the fill level (Eq. (22)) and (ii) the fill level from the capacitance probe physical model $h = (L/10)V_{cap} + h_0$ (see paragraph following Eq. (28)). In general, the comparison is quite good with a maximum deviation of approximately 10 to 15 cm for the capacitance probe correlation. The physical model has a slightly larger deviation.

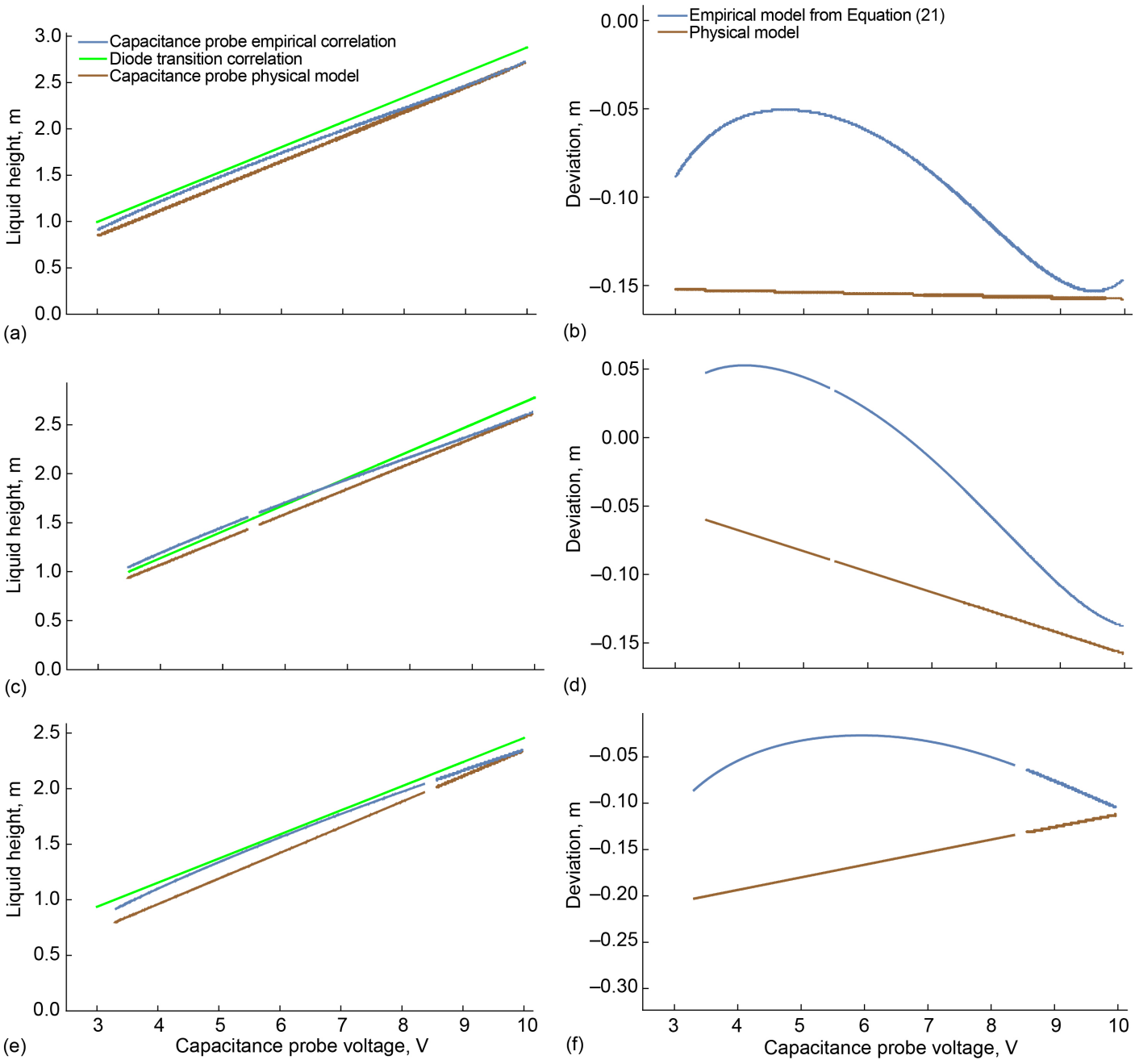

Figure 206.—Comparison of liquid height in tank versus capacitance probe voltage. Baseline and preacoustic liquid hydrogen (LH_2) tests: (a) liquid height and (b) deviation. Preacoustic liquid nitrogen test: (c) liquid height and (d) deviation. Postacoustic LH_2 test: (e) liquid height and (f) deviation.

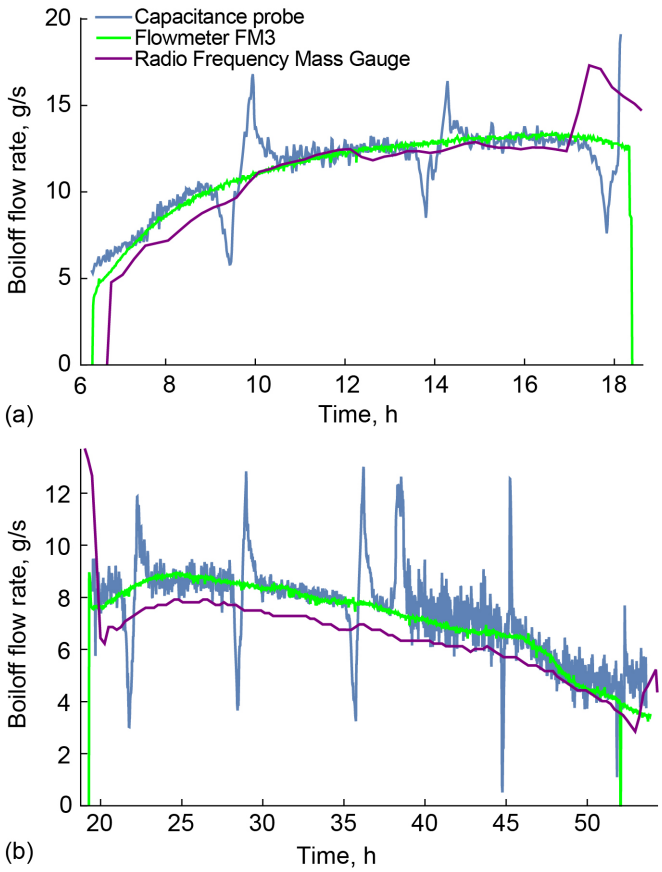

Figure 207.—Boiloff flow rate for baseline boiloff tests. (a) High fill (95 to 70 percent). (b) Medium and low fill (70 to 25 percent).

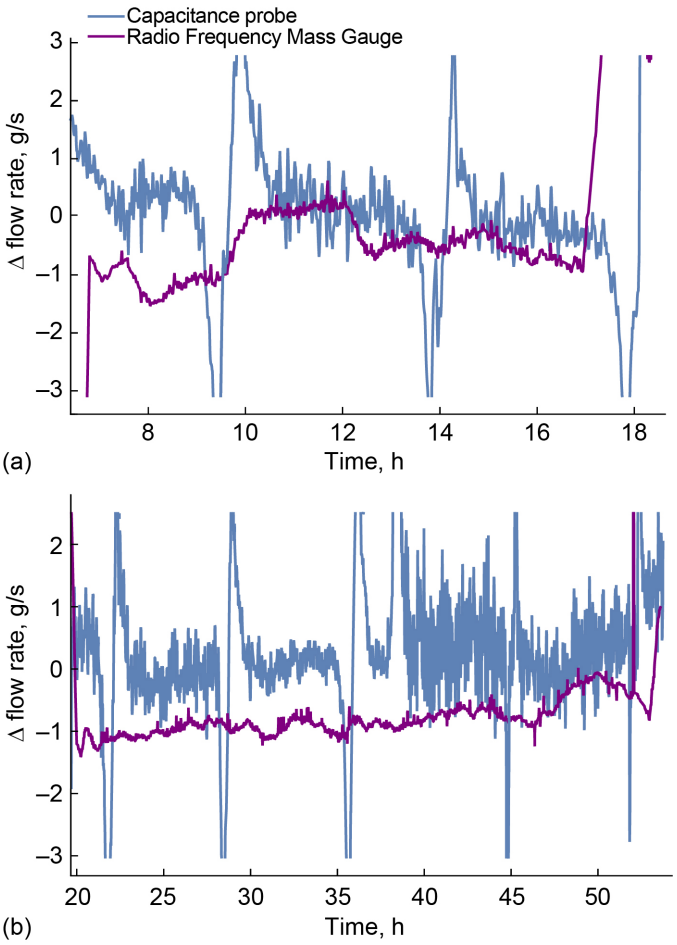

Figure 208.—Deviations from flowmeter data for baseline boiloff tests. (a) Up to 18 h. (b) Beyond 20 h.

5.4.2 Baseline Test Flow Rate and Fill-Level Data

5.4.2.1 Flow Rate Data

The boiloff flow rates from the baseline test are shown in Figure 207. For high-, medium-, and low-fill conditions in the tank, flow rates obtained from the empirically fitted capacitance probe data, flowmeter, and RFMG are shown. Flow rates were obtained from the RFMG tank fluid mass measurements using Equation (27) and smoothed by using a moving average over 10 points (approximately 50 min). The trends in the data from all these measurements are the same. The deviations of the capacitance probe and RFMG-derived flow rates from the flowmeter are shown in Figure 208, and the deviations are typically less than 1 g/s.

Figure 209 shows similar flow rates for the baseline vapor-cooling tests. In addition, the flow rate inferred from the rake SD transitions are shown by orange dashed lines. These flow rates are calculated by using the known fill-level difference of successive diodes, and the elapsed time for the liquid interface to traverse these diodes. Note that flowmeter FM1 was not operational during these tests, except for a very brief time around 76 h; curiously, the capacitance probe data is consistent with the data from FM1 during this short time. Figure 210 shows the deviation of the flow rate between the capacitance probe and RFMG data. The deviations fluctuate due to the scatter and spike behavior in the flow rate calculated from the capacitance flow and is about 1 g/s on average.

In general, the boiloff flow rate is expected to be higher for high fill levels where the heat load is also high, and monotonically decreases as the liquid boils off and the fill level decreases. This expectation, however, is not borne out in the boiloff data in Figure 207 between the times of 6 and 16 h. This is because the tank pressure could not be maintained constant and was rising during this time period (see Figure 66). Therefore, the heat load into the liquid region within the tank is absorbed by the liquid to increase its enthalpy, as the saturation temperature rises with the rising pressure, and the boiloff rate is reduced. Transients in the boiloff rate also exist immediately following a pressure rise test. As an example, in Figure 209 for medium fill level, the boiloff flow rate is large after the tank is vented following the pressure rise test.

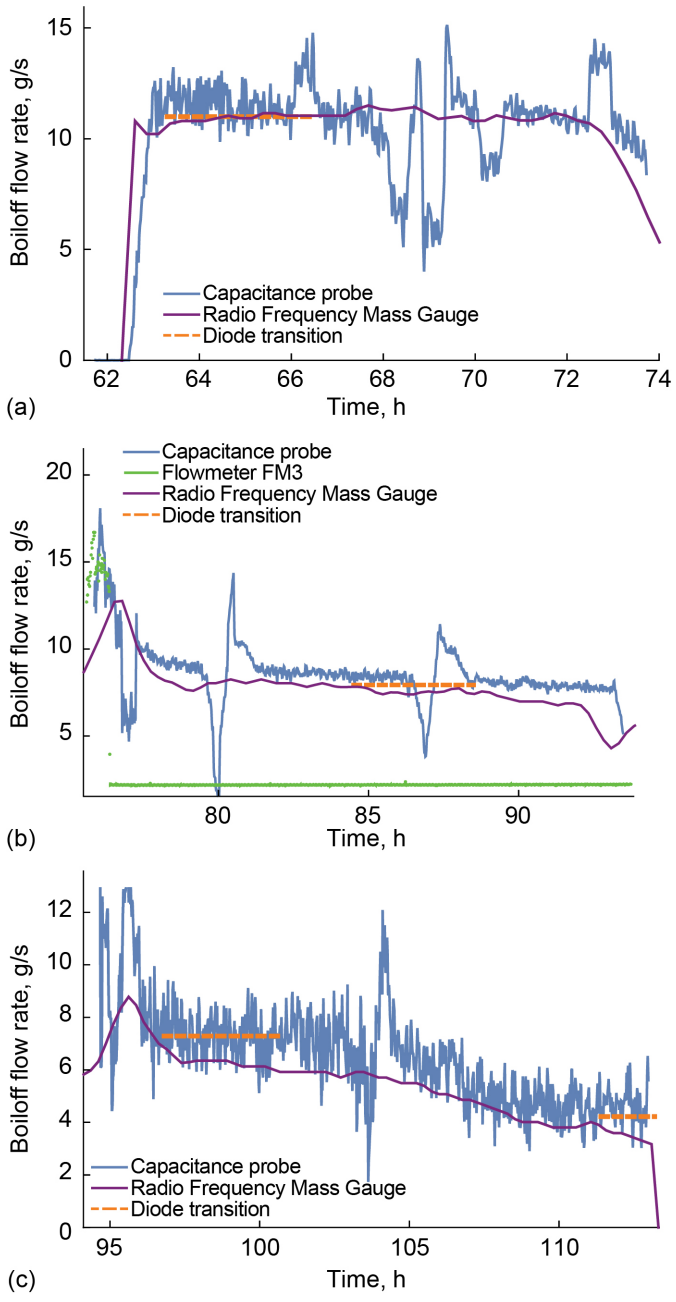

Figure 209.—Boiloff flow rate for baseline vapor-cooling tests. (a) High fill (95 to 70 percent). (b) Medium fill (70 to 50 percent). (c) Low fill (50 to 25 percent).

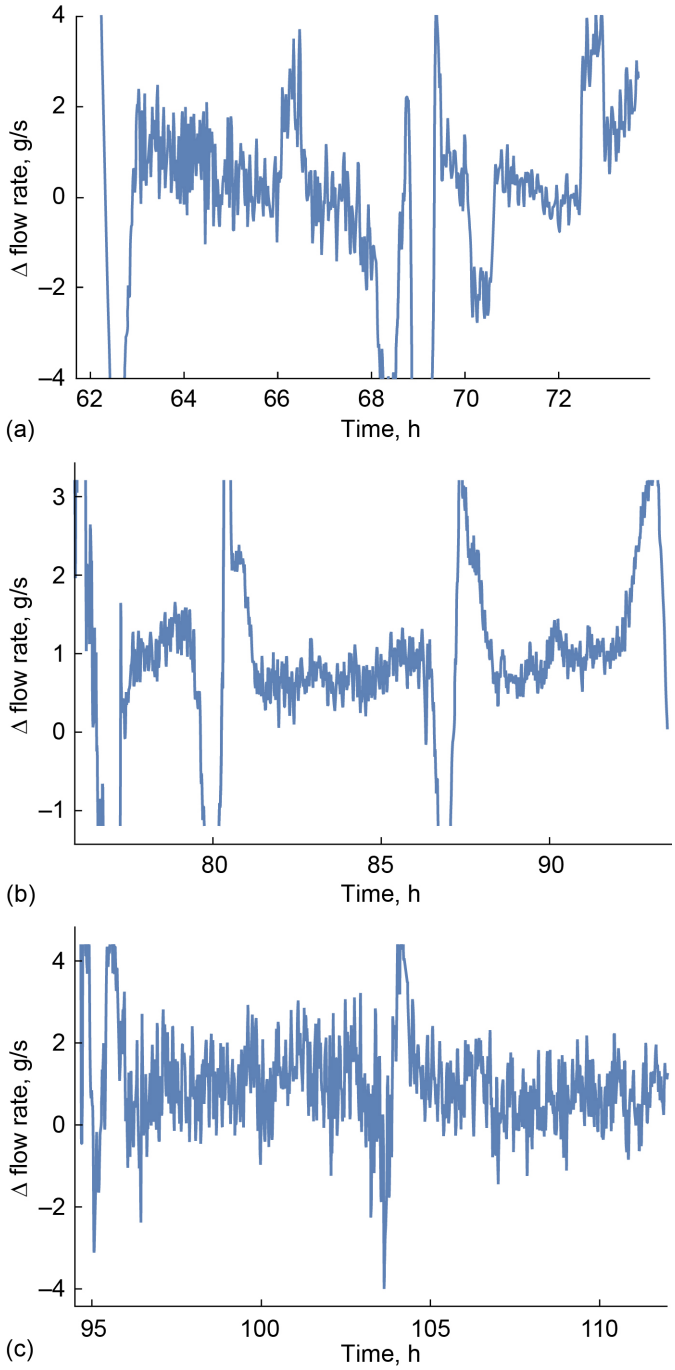

Figure 210.—Deviations between capacitance probe and Radio Frequency Mass Gauge flow rates. (a) High fill (95 to 70 percent). (b) Medium fill (70 to 50 percent). (c) Low fill (50 to 25 percent).

5.4.2.2 Fill-Level Data

The fill level calculated from the RFMG data, capacitance probe empirical correlation, physical model, and the inferred rake diode transitions are shown in Figure 211. While there is general agreement among all these calculated fill levels, the deviation is as high as 4 percent, as shown in Figure 212.

The RFMG measurement and its accuracies are addressed in Section 5.5. It is not easy to quantify the errors in the fill level obtained from the capacitance probe. As operated, the capacitance probe did not have an intrinsic means of anchoring the liquid height in the tank (and thus the fill level) to its measured voltage. Rather, a reference height or fill level must be provided at a measured voltage (such as after the maximum calibration command was issued). This reference fill level is given in Table 32 and uses the transition of rake diode SD81 to read cold LH_2 temperature during the initial fill of the SHIIVER tank during the baseline test. This also coincides with the time when the maximum calibration command was issued. As mentioned before, the capacitance probe without any recalibration was used for the preacoustic LH_2 test. Since the wet and dry point-sense mode of the rake diodes did not work, it is not known where precisely the liquid interface was relative to the location of SD81 (it is moot whether the precise liquid interface location can be determined even if the point-sense mode worked). Thus, there is an uncertainty in the reference fill level used to anchor the relationship between the capacitance probe's measured voltage and the calculated fill level. Note that the point-sense mode is when the diodes are intentionally overpowered and their subsequent response is monitored; rapid temperature rise indicates that the diode is surrounded by gas, whereas a gradual, if any, rise in the temperature indicates that the diode is wet. The reference fill level for the preacoustic LN_2 test was similarly obtained by using an inferred wet and dry transition of SD77 during boiloff testing for that test. Hence, similar questions of uncertainty remain regarding the precise location of the liquid interface for the LN_2 test as well.

The uncertainty affects the value of the constant C_1 shown in Table 32, and thus the fill level calculated by using empirical capacitance probe correlation (Eqs. (22), (24), and (26)). Note that C_1 does not appear in the expressions for the boiloff flow rate (Eqs. (21), (23), and (25)); therefore, the uncertainty in these flow rates only depends on the goodness of the empirical fits with the data from flowmeter FM3 (it is assumed that FM3 is accurate). For the capacitance probe physical model, the reference fill level affects the active length L of the capacitance probe when the maximum calibration command was issued and affects both the flow rate and fill levels calculated. Also, the capacitance probe physical model assumes constant liquid and vapor density during tests. The initial tank fill was at atmospheric pressure (LH_2 density = 70.8 kg/m^3), but the tank

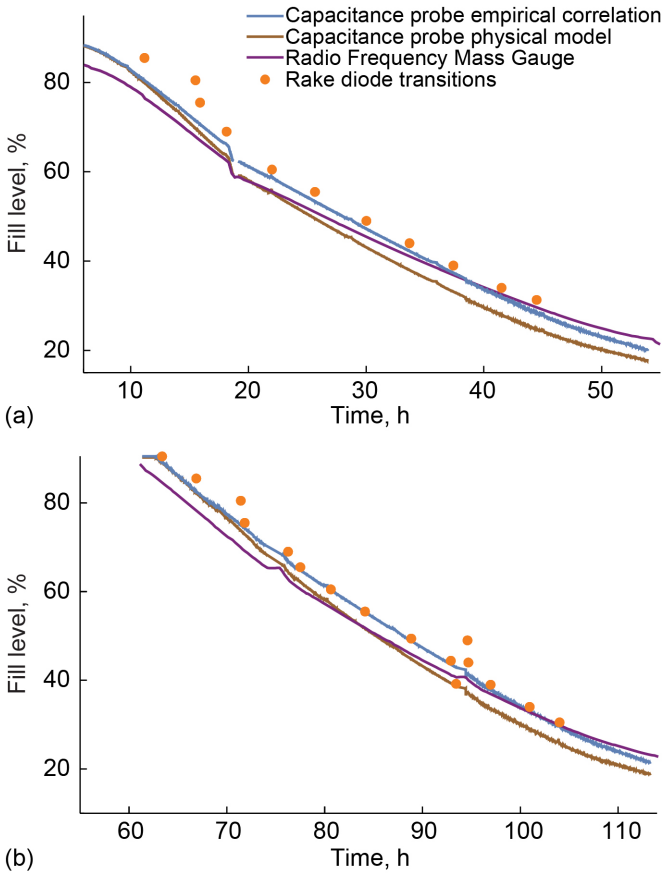

Figure 211.—Fill level for baseline test. (a) Boiloff tests. (b) Vapor-cooling tests.

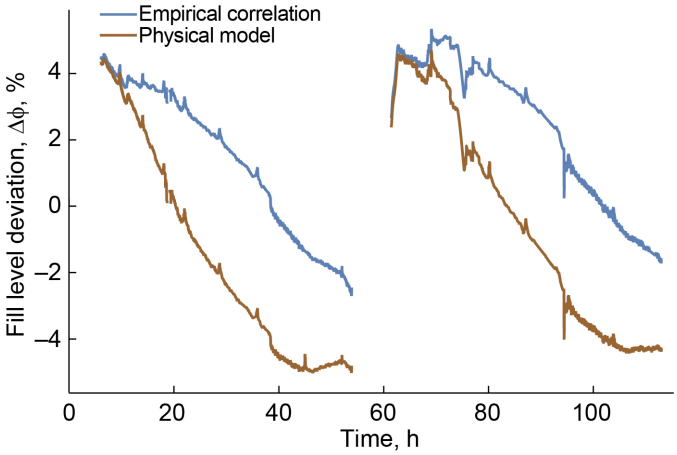

Figure 212.—Fill-level deviations from Radio Frequency Mass Gauge measurements for baseline test.

pressure was briefly as high as 234 kPa for the baseline boiloff test (LH_2 density = 66.8 kg/m^3). For most of the boiloff tests, the pressure was between 117 and 172 kPa (LH_2 density between 70.2 and 68.5 kg/m^3). Another point to note is that no distinction is made between a mass-based fill level and a volume-based fill level in the capacitance probe analyses. Between atmospheric pressure and 172 kPa, the liquid density change is 3.25 percent. Other errors will compound with this value, and it is conceivable that the deviations shown in Figure 212 are reflective of the uncertainty in the fill level obtained from the analysis of the capacitance probe measurements.

5.4.3 Thermal 1 Liquid Hydrogen Test Flow Rate Data

5.4.3.1 Flow Rate Data

The boiloff flow rates for the preacoustic test with LH_2 are shown in Figure 213. For high-, medium-, and low-fill conditions in the tank, flow rates obtained from the capacitance probe, flowmeters FM2 and FM3, and RFMG are shown. The trends in the data from all these measurements are the same. FM2, however, reads a higher flow rate than FM3 for all tests. The capacitance probe and RFMG data are consistent with FM3 but not FM2. For low-fill conditions, FM3 does not register a reading when the flow rate falls below its low cutoff (~2 g/s). The deviations of the capacitance probe and RFMG-derived flow rates from flowmeter FM3 are shown in Figure 214. While the deviations are typically less than 1 g/s, there are several spikes where the deviation is as large as 3 g/s.

The corresponding flow rates and deviations for the preacoustic vapor-cooling tests are shown in Figure 215 and Figure 216. It should be noted that flowmeter FM1 performance was erratic throughout this test sequence. As shown in Figure 213, flowmeter FM1 reads significantly higher than other measures during the high-fill test. The capacitance probe and RFMG flow rates are consistent confirming that FM1 is the anomalous reading. Between the high- and medium-fill tests, a pressure rise test was performed, following which FM1 returned to reporting flow rates consistent with the capacitance probe and RFMG data. FM1 also displays a low cutoff below 2 g/s. As before, the deviations in the flow rates are typically below 1 g/s.

5.4.3.2 Fill-Level Data

The fill level calculated from the capacitance probe empirical correlation, physical model, RFMG data, and the rake diode transitions are shown in Figure 217. While the trends are the same and the agreement is good, the maximum deviation is as high as 4 percent as shown in Figure 218, similar to the baseline tests. Comments previously made regarding the fill-level uncertainties for the capacitance probe in the baseline tests apply here as well. Note that for fill levels greater than ~70 percent, diode transitions to demarcate liquid and vapor are not evident.

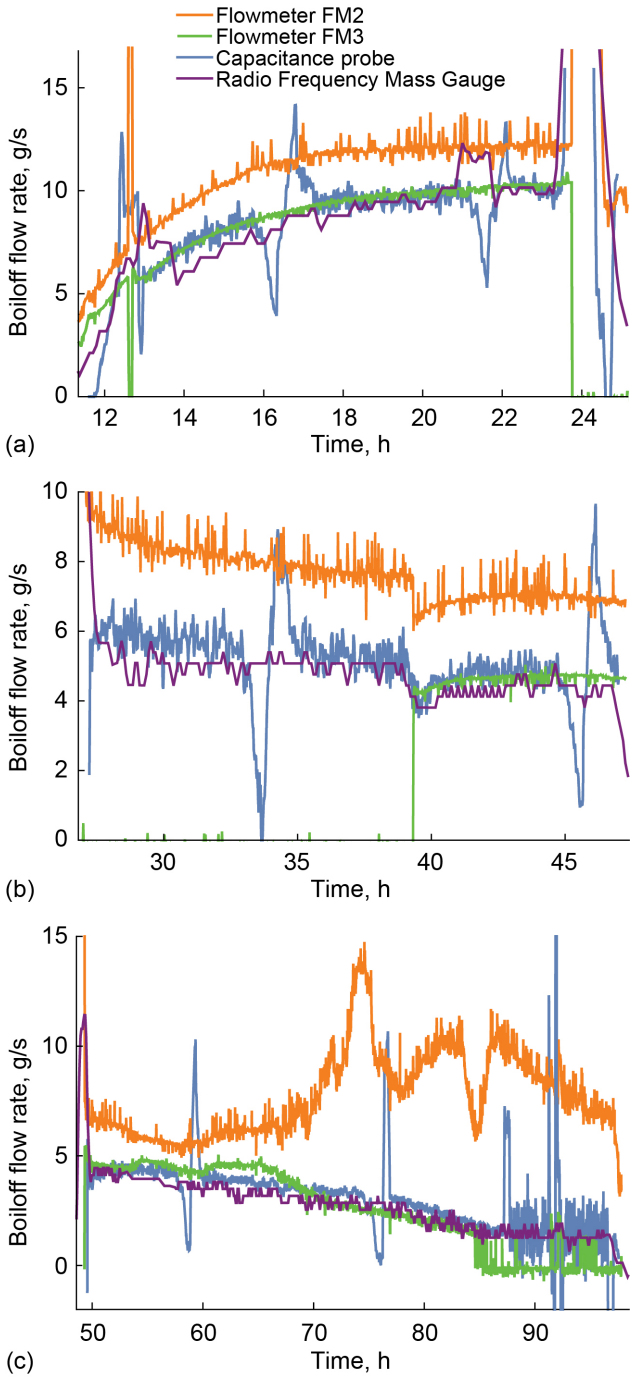

Figure 213.—Boiloff flow rate for preacoustic liquid hydrogen boiloff tests. (a) High fill (90 to 70 percent). (b) Medium fill (70 to 50 percent). (c) Low fill (50 to 25 percent).

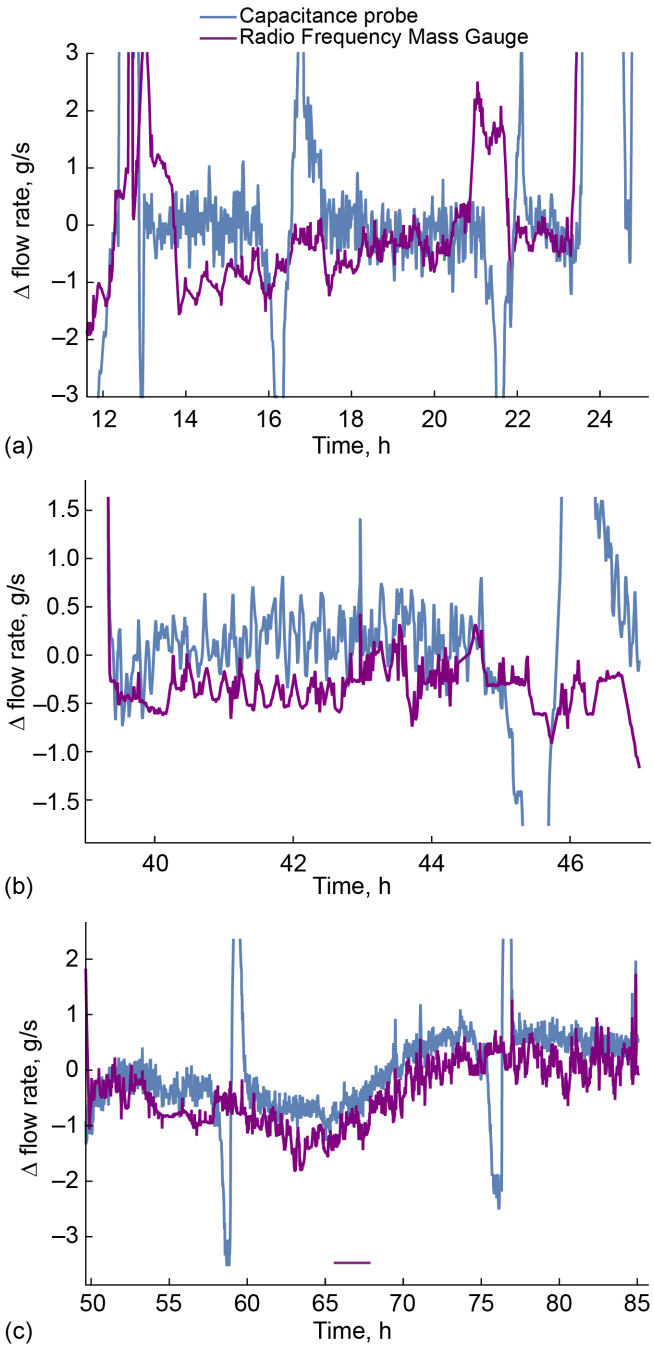

Figure 214.—Deviations from flowmeter FM3 data for preacoustic liquid hydrogen boiloff tests. (a) High fill (90 to 70 percent). (b) Medium fill (70 to 50 percent). (c) Low fill (50 to 25 percent).

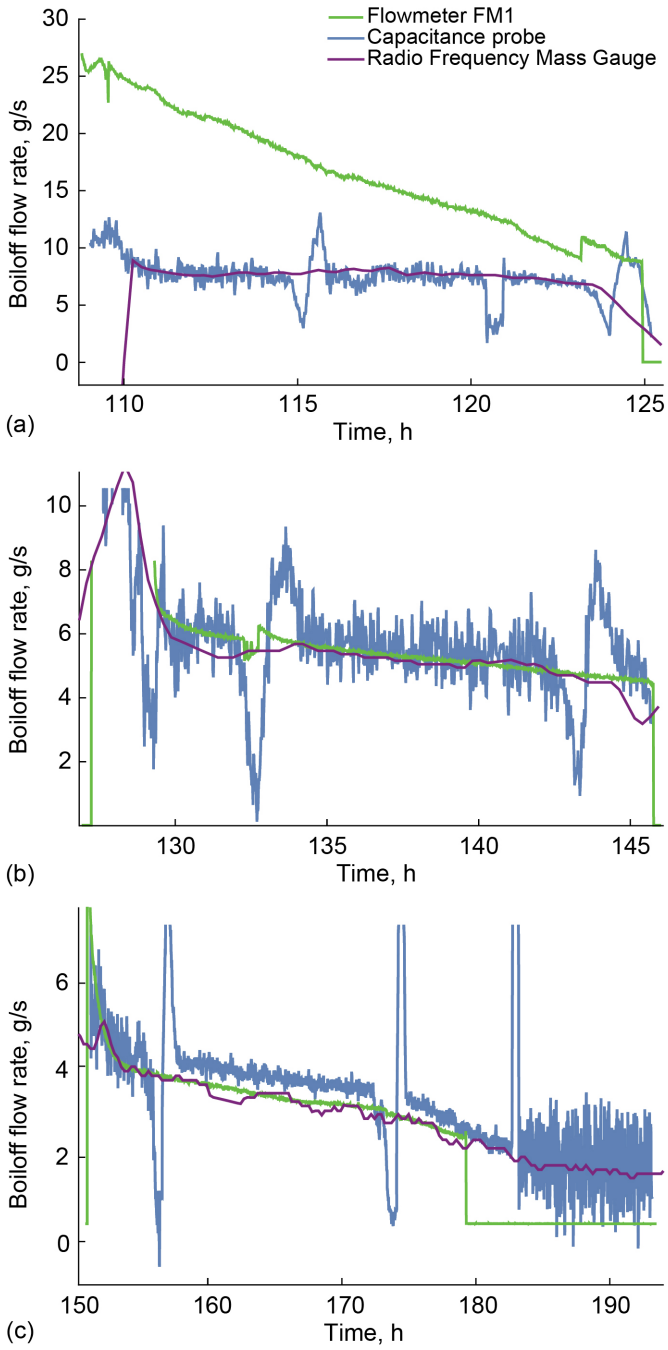

Figure 215.—Boiloff flow rate for preacoustic liquid hydrogen vapor-cooling tests. (a) High fill (95 to 70 percent). (b) Medium fill (70 to 50 percent). (c) Low fill (50 to 25 percent).

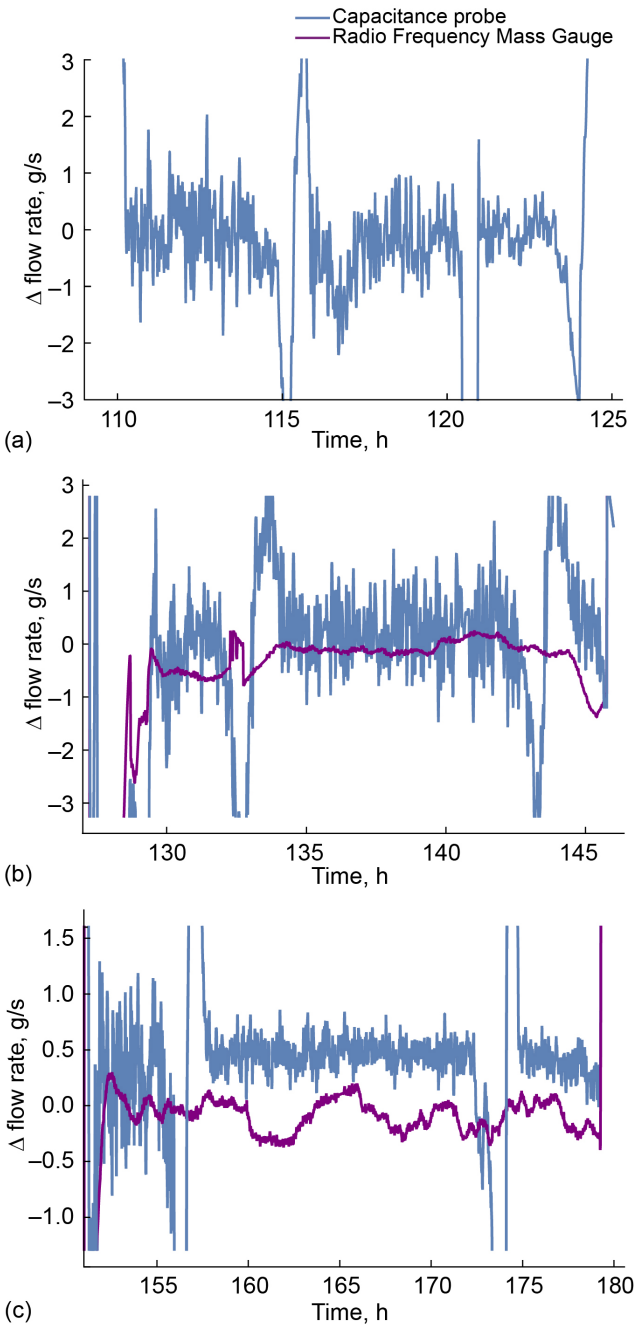

Figure 216.—Flow rate deviations. (a) High fill (95 to 70 percent). (b) Medium fill (70 to 50 percent). (c) Low fill (50 to 25 percent). For high fill, deviation is between capacitance probe and Radio Frequency Mass Gauge (RFMG). For medium and low fill, deviation is from flowmeter FM1.

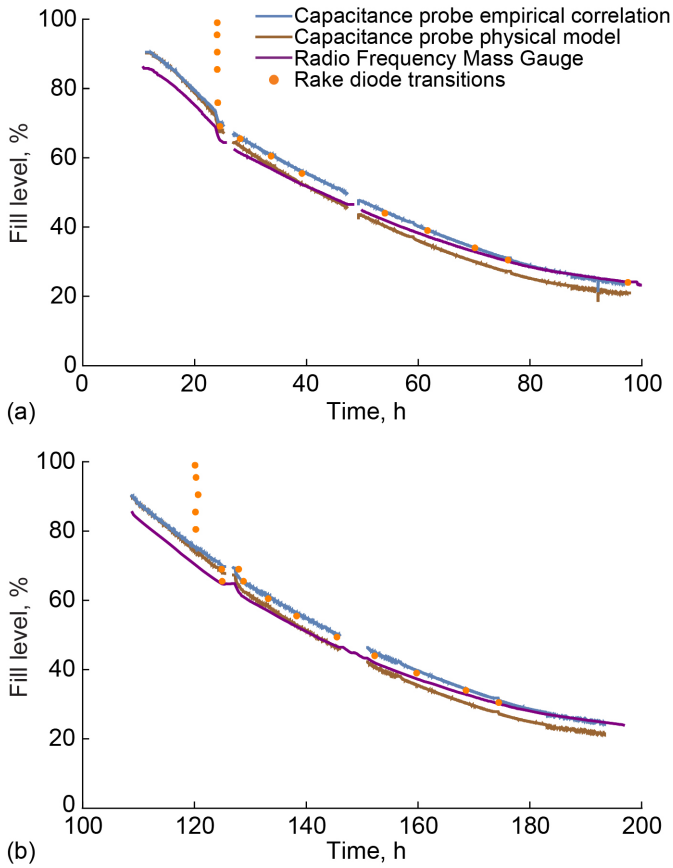

Figure 217.—Fill level for preacoustic liquid hydrogen test. (a) Boiloff tests. (b) Vapor-cooling tests.

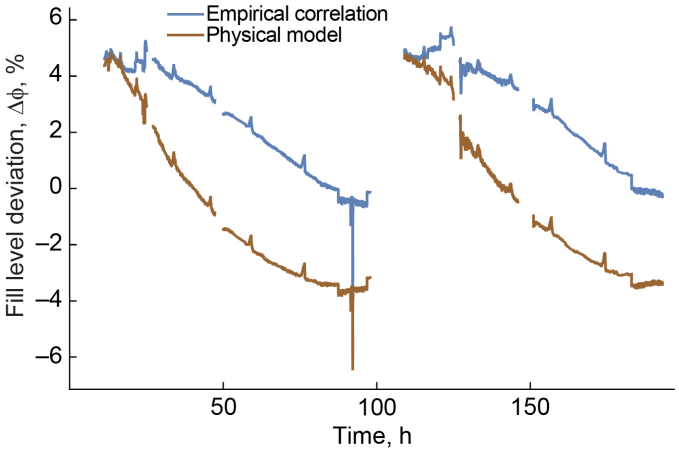

Figure 218.—Fill-level deviations from Radio Frequency Mass Gauge measurements for preacoustic liquid hydrogen test.

5.4.4 Thermal 1 Liquid Nitrogen Test Flow Rate Data

5.4.4.1 Flow Rate Data

The flow rates for the preacoustic test with LN_2 are shown in Figure 219. The boiloff flow rates for a high fill (approximately 87.5 to 70 percent during the course of the test) are shown in Figure 219(a). For most of the test FM2 was used; early on, both FM2 and FM3 were briefly operational and show agreement in the measured flow rate. From approximately 40 to 70 h, the RFMG, diode transition, and FM2 flow rates are in good agreement, while the flow rate from the capacitance probe

is a bit lower. Beyond this time period (70 to 120 h), the flow rate from RFMG, capacitance probe, and diode transition are in good agreement, while FM2 read higher. The reasons for variation in flow measurement agreement is unknown.

The remaining plots in Figure 219 show the flow rates for the vapor-cooling tests (note that the green curve now displays FM1 readings). All flow rate measurements are in reasonable agreement for the vapor-cooling tests, except for the low-fill case. The capacitance probe data was extremely scattered for this case and is likely unreliable; what is shown is a moving average over an 8-h period.

5.4.4.2 Fill-Level Data

The fill-level data for the entire preacoustic LN_2 tests, from the capacitance probe empirical correlation, physical model, RFMG, and diode transitions, are shown in Figure 220(a). As in the preacoustic LH_2 test, the diode transition data did not clearly demarcate liquid and gas when the liquid interface is in the upper dome of the tank (fill level approx. greater than 70 percent). The two sharp drops in the fill level at approximately 160 and 210 h correspond to tank draining. To speed up the test, the tank level was reduced to the desired fill level by draining the tank. Curiously, the diode transitions, capacitance probe data, and RFMG are all able to accurately follow the tank drain at approximately 210 h. Figure 220(b) shows the deviations in the fill level from that measured by RFMG, and the typical deviation is approximately 2 percent. The tank pressure control during the LN_2 test was very good (see Section 4.3). Therefore, the liquid temperature and density was constant, leading to fewer deviations in the calculated fill levels.

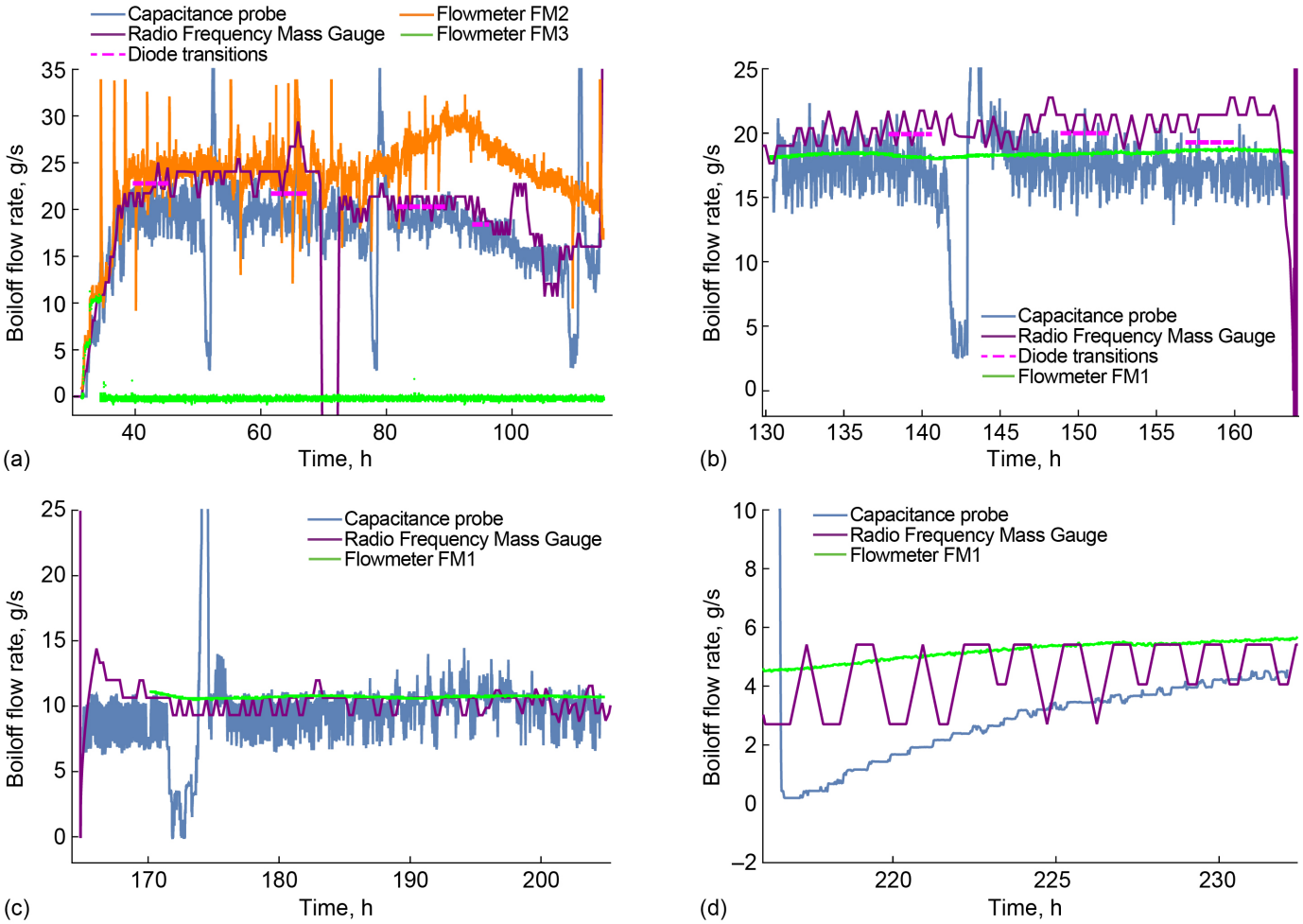

Figure 219.—Boiloff flow rate for preacoustic liquid nitrogen tests. (a) High-fill-level boiloff. (b) High-fill-level vapor cooling. (c) Medium-fill-level vapor cooling. (d) Low-fill-level vapor cooling.

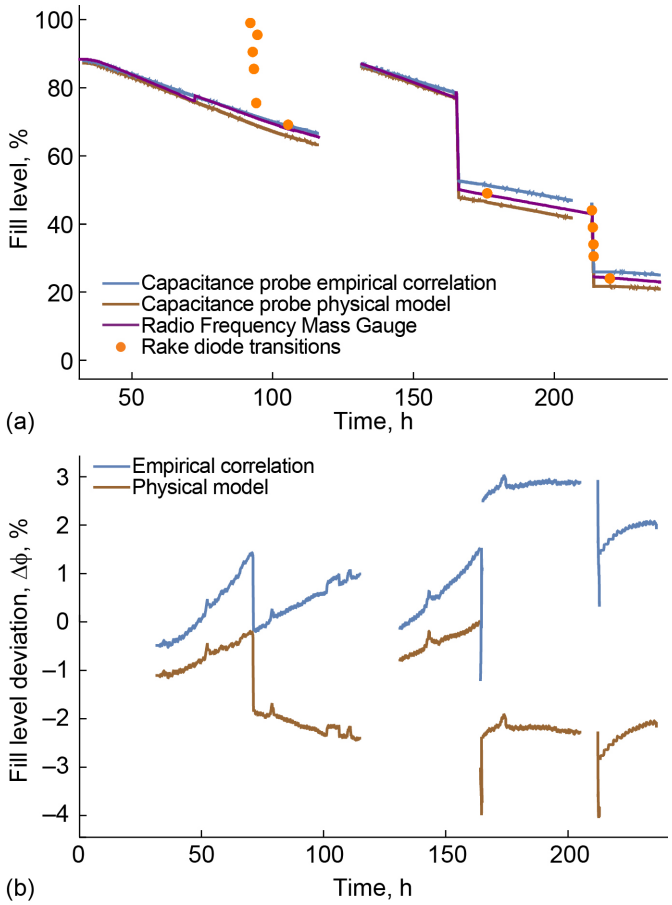

Figure 220.—Fill level for the preacoustic liquid nitrogen test. (a) Fill level. (b) Fill-level deviations from Radio Frequency Mass Gauge measurements.

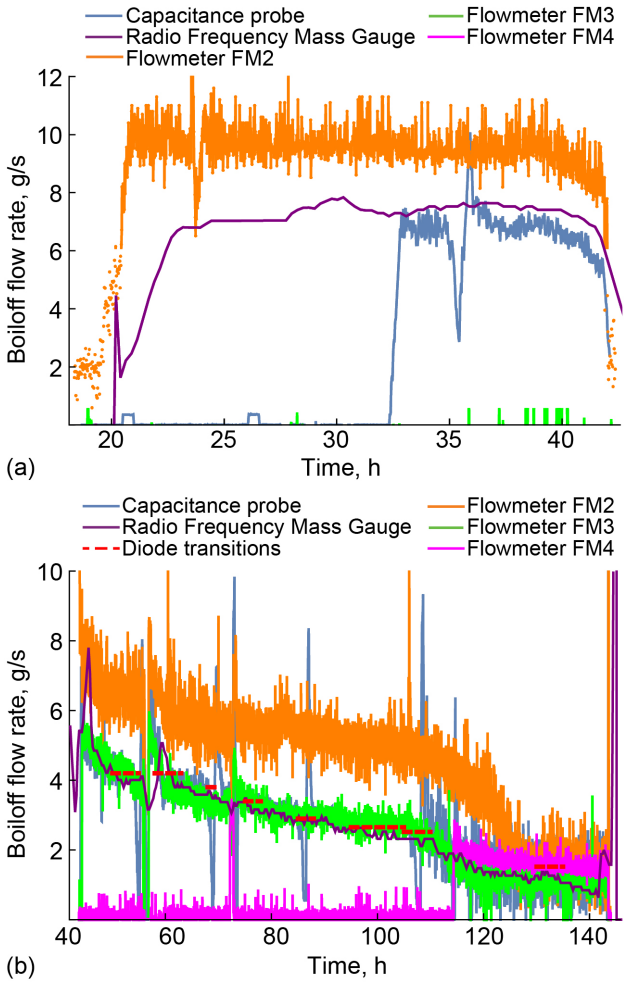

Figure 221.—Boiloff flow rate for postacoustic liquid hydrogen boiloff tests. (a) Fill level (95 to 70 percent). (b) Fill level (70 to 25 percent).

5.4.5 Thermal 2 Liquid Hydrogen Test Flow Rate Data

5.4.5.1 Flow Rate Data

In the postacoustic test with LH_2, no vapor-cooling tests were performed. The flow rates for the boiloff tests are shown in Figure 221. The capacitance probe was not operational until approximately 32 h into the test. Figure 221(a) shows the flow rate for high fill level (95 to 70 percent) and Figure 221(b) shows the flow rate for medium to low fill level. For high fill, only flowmeter FM2 was used, while for medium and low fill, FM2 and FM3 were primarily used, with FM4 used towards the end. In comparison with previous tests, there is more noise evident in the flowmeter readings, likely due to altered meter settings. The flow rate from the capacitance probe correlation is consistent with FM3 and FM4. As before, FM2 reads a higher flow rate. The flow rate deviations are shown in Figure 222, and the typical deviation is less than 1g/s.

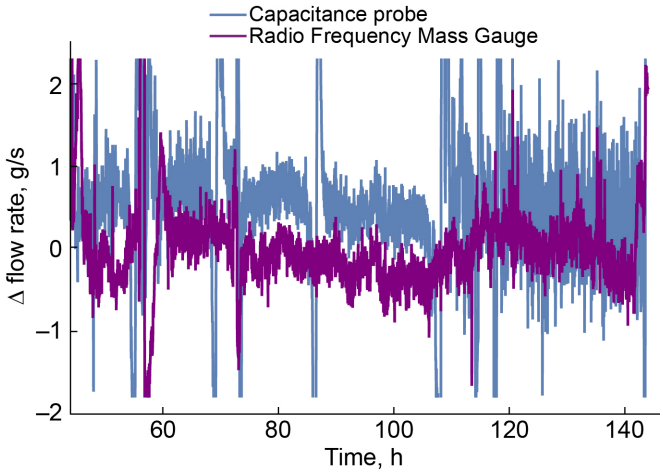

Figure 222.—Deviations from flowmeter FM3 data for postacoustic liquid hydrogen boiloff tests.

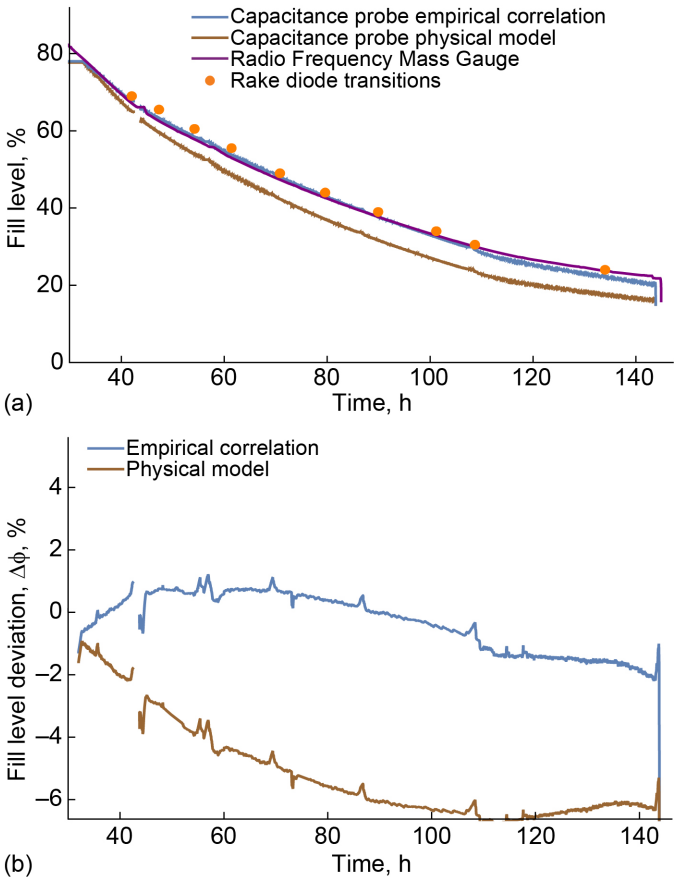

Figure 223.—Fill level for the postacoustic liquid hydrogen test. (a) Fill level. (b) Fill-level deviations from Radio Frequency Mass Gauge measurements.

5.4.5.2 Fill-Level Data

The fill-level data for the postacoustic test is shown in Figure 223. The capacitance probe correlation and diode transition data are consistent with RFMG measurements, with a typical deviation of 1 percent. The tank pressure control during the postacoustic LH_2 test was also very good (see Section 4.5). Thus, the liquid temperature and density was constant, which may explain the lower fill-level deviation of the capacitance probe correlation. The physical model, however, gives a lower fill level with a maximum deviation in excess of 6 percent.

5.4.6 Flow Rate Comparison

In order to compare the flow rate among the various tests, the flow rate for the boiloff tests (red) and vapor-cooling tests (blue) is plotted against the fill level in Figure 224. Wherever possible, the flow rate from flowmeter FM3 is used for the boiloff tests and that from FM1 is used for the vapor-cooling tests; when the data is not available or not reliable, the capacitance probe flow rate correlation is used. The fill level is obtained from the capacitance probe correlations (Eqs. (22), (24), and (26)).

Several trends are evident in Figure 224: (i) the boiloff flow rate decreases as the fill level decreases. (ii) The mass flow rate is higher for the LN_2 test than the LH_2 tests; however, because the density of LN_2 is more than a factor of 10 greater than that of LH_2, the volumetric flow rate of LN_2 is comparatively low, and the LN_2 tests take longer to complete. Therefore, LN_2 boiloff data was only measured at selected fill levels, with the tank drained between fill levels. (iii) Among the LH_2 tests, the flow rate is higher for the baseline test (no MLI) than that of the preacoustic and postacoustic tests, which include MLI. This is a consequence of improved insulative performance of MLI versus the baseline condition. (iv) The postacoustic LH_2 test has a smaller flow rate than the preacoustic LH_2 test. This is likely due to the decrease in the vacuum chamber wall temperature for the postacoustic LH_2 test, which was conducted months later during winter. (v) For the LH_2 vapor-cooling tests, the boiloff flow rate is reduced, as compared to no vapor cooling, for fill levels larger than approximately 70 percent. At fill levels lower than approximately 60 percent, the performance benefit of vapor cooling was negligible. For the LN_2 tests, there is a slight, but not clearly distinct, reduction in the flow rates with vapor cooling. (vi) For both baseline and preacoustic LH_2 test, the boiloff tests at high fill level were not at a quasi-steady state, and strong transient effects existed. As discussed before, this was due to nonconstant tank pressure (tank pressure was rising).

Table 33 shows the average boiloff flow rates at various fill levels (averaged over a ±2.5-percent-fill-level interval). To take into account the enthalpy change of the liquid in the tank due to changing pressure, equivalent boiloff flow rates are calculated and are shown in Table 34. The equivalent boiloff rate is defined in reference to the measured boiloff rate from the flowmeters ($\dot{m}_{v,\text{measured}}$) and total heat load ($\dot{Q}_f$) as

$$\dot{m}_{v,\text{equivalent}}\left(h_{\text{vent}}-h_L\right)\equiv \dot{m}_{v,\text{measured}}h_{\text{vent}}+\frac{\Delta\left(m_v h_v+m_L h_L\right)}{\Delta t}=\dot{Q}_f \tag{30}$$

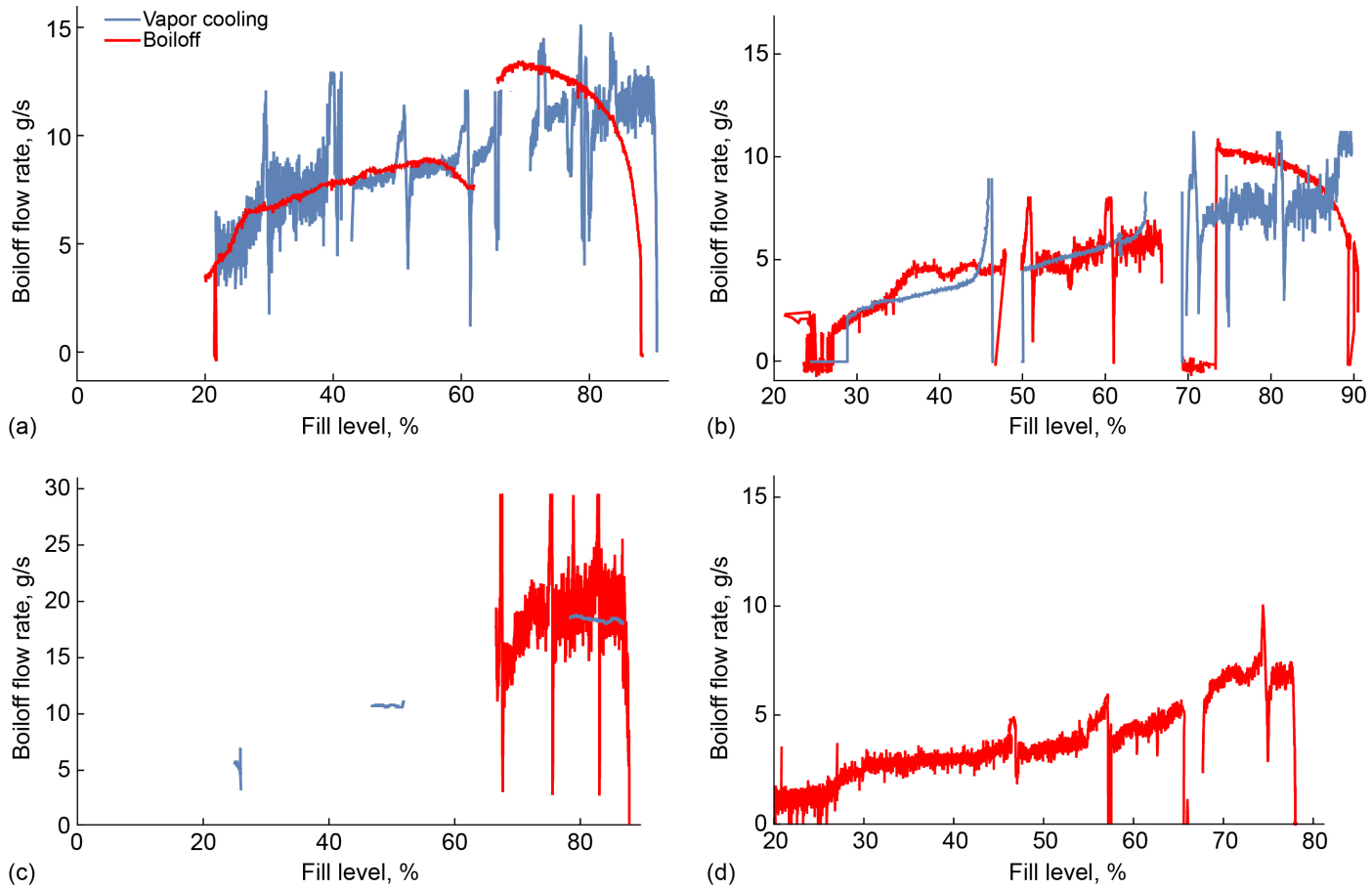

Figure 224.—Boiloff flow rate versus fill level for all tests. (a) Baseline tests. (b) Preacoustic liquid hydrogen (LH_2) tests. (c) Preacoustic liquid nitrogen tests. (d) Postacoustic LH_2 tests.

TABLE 33.—FILL-LEVEL-AVERAGED BOILOFF FLOW RATES

Test	Fill level (±2.5), percent						
	90	80	70	60	50	35	25
	Average boiloff flow rate, g/s						
Liquid hydrogen (LH_2) baseline	8.3	12.8	13	8.7	8.4	7.0	4.3
LH_2 vapor cooling	11.1	10.4	9.4	8.7	8.2	7.3	4.6
Preacoustic LH_2	8.4	10.2	5.2	4.1	4.6	3.0	1.5
Preacoustic LH_2 vapor cooling	5.7	5.6	4.7	5.3	4.5	2.9	1.5
Preacoustic liquid nitrogen (LN_2)	20.5	21.8	20.4	-----	-----	-----	-----
Preacoustic LN_2 vapor cooling	18.3	18.6	-----	-----	10.7	-----	4.6
Postacoustic LH_2	-----	8.9	5.5	3.8	3.3	2.8	1.6

TABLE 34.—FILL-LEVEL-AVERAGED EQUIVALENT BOILOFF FLOW RATE

Test	Fill level (±2.5), percent						
	90	80	70	60	50	35	25
	Equivalent boiloff flow rate, g/s						
Liquid hydrogen (LH_2) baseline	11.9	13.2	12.5	9.1	8.4	7.0	4.9
LH_2 vapor cooling	11.2	11.3	6.4	8.7	8.1	7.3	4.6
Preacoustic LH_2	10.9	11.3	5.9	5.1	4.5	3.1	1.5
Preacoustic LH_2 vapor cooling	7.5	7.5	5.0	5.4	4.7	3.1	1.5
Postacoustic LH_2	-----	9.5	7.1	5.4	4.4	3.6	1.6

5.5 Radio Frequency Mass Gauging Results

Prior to SHIIVER testing with cryogens, a model of the tank interior was created in COMSOL Multiphysics® (COMSOL, Inc.) (Ref. 52) using the computer-aided design (CAD) model of the tank as the reference design to compute the RF mode frequencies of the tank. Shortly after the tank was fabricated, an RF ping test of the tank was conducted using a dipole antenna attached to a short mast in order to measure the RF modes of the tank without any other internal hardware. The measured RF mode frequencies were compared between the model and measurements, and the model was then adjusted by applying small changes to the tank dimension and, to further improve the match, applying a small scaling factor to each orthogonal spatial dimension. This technique of adjusting the RF model to match the measured tank RF spectrum is similar to that used by Moldover et al. for determining the volume of a pressure vessel from microwave measurements (Ref. 53). The capacitance probe and temperature diode rake were then added to the model and the tank spectrum was again measured after the hardware was added. The computed RF modes associated with the temperature rake and capacitance probe did not produce a satisfactory match to the measured data, so only RF modes associated with the tank volume were used in the RFMG algorithm. We believe the wire bundles associated with the temperature diode rake were the source of the discrepancy. The final room temperature tank model was scaled in all three dimensions to account for thermal contraction down to 20 K. The RF model volume of the thermally contracted tank was 30.91 m^3, in good agreement with a value of 30.85 m^3 obtained by thermally contracting the room temperature volumetric measurement of 8,212 gal (31.13 m^3) obtained by the tank manufacturer using water for the measurement.

In order to gauge the mass of fluid in the tank, the RFMG compares the measured tank spectrum to a library of numerical simulations conducted ahead of testing. The RF-fluid simulations are conducted using the COMSOL RF module and utilizes the tank RF model that was created as the base model. The cryogenic fluid is modeled as liquid and vapor dielectric volumes within the tank, separated by a flat interface for 1g tests. Values for the dielectric constant of the liquid and vapor phases are assigned using data from the Reference Fluid Thermodynamic and Transport Properties Database (REFPROP) created by NIST (Ref. 54). RF-fluid simulations are conducted at approximately 1 percent increments in liquid volume, covering the full range 0 to 100 percent (Ref. 55). The simulations were conducted using multiple sets of dielectric data corresponding to different temperatures, which are associated with 101, 138, and 172 kPa saturated vapor pressure conditions (14.7, 20, and 25 psia). The computed RF mode frequencies at the multiple fill levels and various temperatures formed the library of RFMG simulations and served as the lookup table when comparing to measured data. A similar version of the RFMG algorithm is described elsewhere (Ref. 55). The simulations were interpolated to produce a finer resolution on the gauged mass during posttest data analysis, corresponding to 0.1 percent by liquid volume fill-level increments.

As discussed previously, two RFMG loop antennas were installed in the SHIIVER tank, attached to studs welded on the internal sidewall of the tank. The antennas, together with a pair of RF VNAs, were used to measure the RF modes of the tank using a 6,000 point sweep over the frequency range 60 to 125 MHz. Data was collected approximately once every 15 min during boiloff testing and was adjusted to collect data more frequently during some of the fill and drain cycles. The RF spectrum data was analyzed using a custom peak detection algorithm to find the resonant mode frequencies, which appear as drops in the reflected power spectrum. The measured mode frequencies were compared to the database of RF-fluid simulations and a best match between preselected computed modes associated with tank RF modes (and not capacitance probe or diode rake RF modes) and the measured tank spectrum was used to gauge the total mass of fluid in the tank. Figure 225 shows the output of the RFMG from all four SHIIVER tests. As discussed in the following information, the uncertainty of the gauged value is estimated to be within 0.5 percent of full scale.

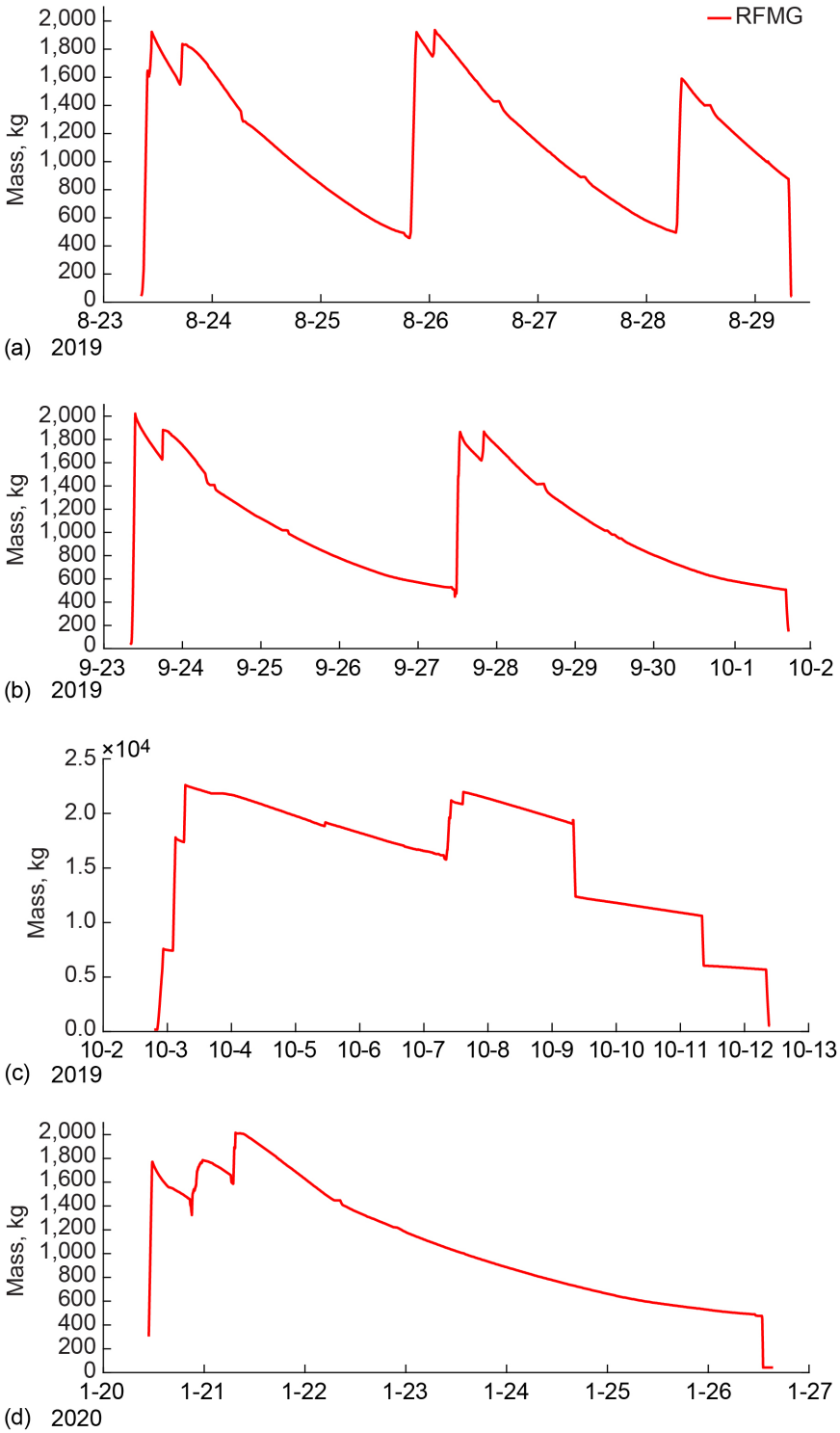

Figure 225.—Radio Frequency Mass Gauge (RFMG) output versus time, reported as total fluid mass (liquid and vapor) in kilogram, from four Structural Heat Intercept, Insulation, and Vibration Evaluation Rig (SHIIVER) tests. (a) Liquid hydrogen (LH_2) baseline. (b) LH_2 Thermal 1. (c) Liquid nitrogen. (d) LH_2 Thermal 2.

As discussed in Section 5.4, the rate of change of total fluid mass versus time was used as an independent estimate of the boiloff rate. The RFMG data was also converted to volumetric fill level versus time data and compared to values inferred from the apparent wet and dry signatures from the diode data and is discussed in more detail here. In order to make the comparison, the measured location of the SD temperature sensors, referenced against a datum line, was entered into the room temperature RF tank model and the volumetric fill-level location of each diode was computed after thermally contracting the tank model. The volumetric fill-level locations of the diodes are shown in Figure 21 and are from the RF model. The RFMG total mass reading was converted to a volumetric percent-fill value by accounting for both liquid and vapor temperatures. The resulting volumetric percent-fill value is calculated as

$$\text{percent fill} = \left(\frac{V_l}{V_{\text{tank}}} \right) 100 \tag{31}$$

where V_{tank} is the model tank volume (30.91 m^3) and V_l is the volume of liquid, calculated from

$$V_l = \frac{m_{\text{fluid}} - \tilde{\rho}_v V_{\text{tank}}}{\rho_l - \tilde{\rho}_v} \tag{32}$$

Here, m_{fluid} is the total mass of the fluid as measured by the RFMG and $\tilde{\rho}_v$ is the average density of the ullage space vapor. Fluid densities are calculated from REFPROP (Ref. 54), using facility pressure and temperature data as inputs. The average ullage temperature is estimated using the average of SD64 and SD83, representing the liquid temperature and upper ullage temperature.

The SD temperature data was used to estimate the liquid level in the tank at times when there was an apparent wet to dry transition, observed as an abrupt increase in temperature at some point in time. However, closer investigation into the SD rake temperature data showed that the apparent wet to dry transitions were not typically associated with the passage of the liquid-vapor interface across the diode location. Figure 226 shows data from SD78 that highlights the problem. Figure 226(a) shows SD78 data during the baseline test, with an apparent wet to dry transition taking place at 12:00 hours on August 26. However, closer examination of the data, as shown in Figure 226(b), shows that the diode temperature exceeds the estimated liquid interface temperature by more than 0.5 K during a short period when the tank pressure rose during valving activity. The liquid interface temperature, $T(P_{sat})$, was estimated by converting the measured tank pressure to a saturated temperature value and is indicated by the blue dashed line. We hypothesize that there is a cold layer of vapor above the evaporating liquid during normal boiloff periods, and when the tank conditions change causing a pressure rise, the convective stream of vapor above the liquid changes, possibly to a mixing convective roll, that causes the temperature of the once cold diode to increase. When normal boiloff continues, the vapor is vented nearly as fast as it boils off, causing the convective stream from the liquid interface to once again cool the diode to temperature values very near the liquid interface temperature value.

A particularly interesting set of data from SD76 and RFMG during the baseline tests show that the apparent diode transitions can be in error by 3.7 percent or more, and the RFMG-gauged value of percent fill is actually within 0.5 percent of full scale of the diode location percent-fill value. Figure 227 presents the data from 09:00 to 18:00 hours on August 28. Initially, we see that the temperature of SD76 is below the $T(P_{sat})$ line, but when the tank is locked up at 12:49, the SD76 temperature increases more than 6 K indicating it is actually in the vapor phase. This transition takes place nearly 3 h before the typical apparent event at 15:38, with a difference in RFMG percent fill between the two events of 3.7 percent of full scale. Approximately 30 min after tank lockup, the temperature of SD76 abruptly drops indicating the expanding liquid volume is rising above the SD76 location engulfing the diode in liquid by 13:41. At 14:04, the tank pressure is slowly vented from 40 to 16.5 psi (the value before tank lockup), and T_{SD76} returns to a value below $T(P_{sat})$. An apparent transition from wet to dry takes place at 15:38, but the earlier data indicates it is already in the vapor phase. At 13:41, when the expanding liquid engulfs the diode, the RFMG indicates a fill level of 64.8 percent, which is within 0.5 percent of the model value of 65.3 percent for SD76 (rounded to 65.5 percent in Figure 21). The data from this event leads us to conclude that the apparent diode transitions can be off by nearly 3 h or a fill-level error of nearly 4 percent full scale. Also, the data indicates the RFMG percent-fill reading agrees with the diode location value to within 0.5 percent when a definitive transition takes place.

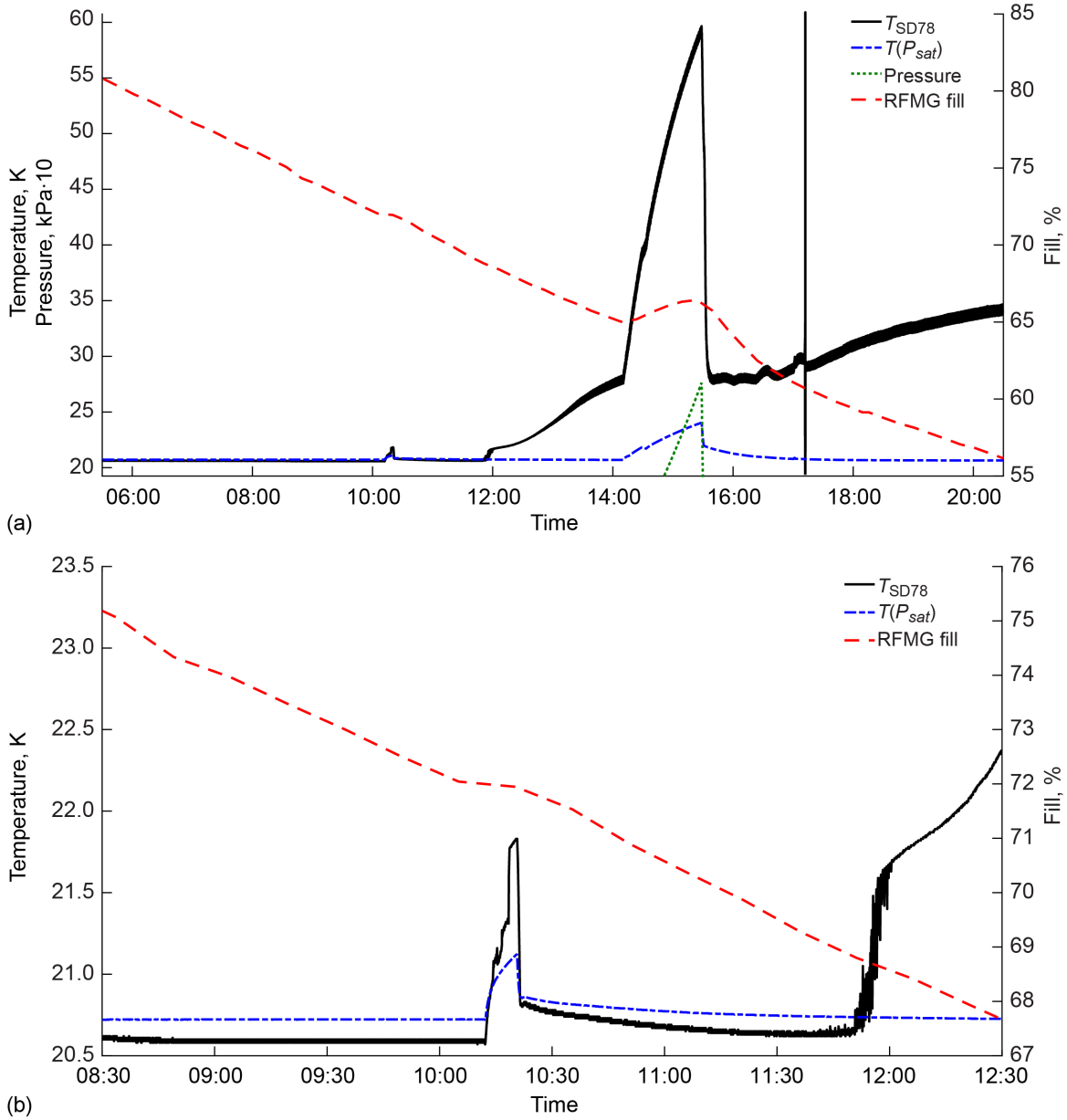

Figure 226.—Structural Heat Intercept, Insulation, and Vibration Evaluation Rig (SHIIVER) baseline liquid hydrogen test (Aug. 26, 2019) temperature data from SD78 (T_{SD78}) (fill level = 75.5 percent) illustrating uncertainty of inferred wet to dry transitions from silicon diode (SD) data. (a) Apparent wet to dry transition takes place just before 12:00, as noted by an abrupt temperature increase. (b) A closer look at SD78 data near 10:15 shows rapid rise in temperature during short period when tank pressure increased due to valving activity, rising well above computed saturated temperature based on tank pressure data, indicated by blue dashed line. Increase of SD78 temperature values over liquid interface temperature $T(P_{sat})$ values indicates SD78 is already in vapor phase at 10:15, well ahead of apparent transition at 12:00. Radio Frequency Mass Gauge (RFMG).

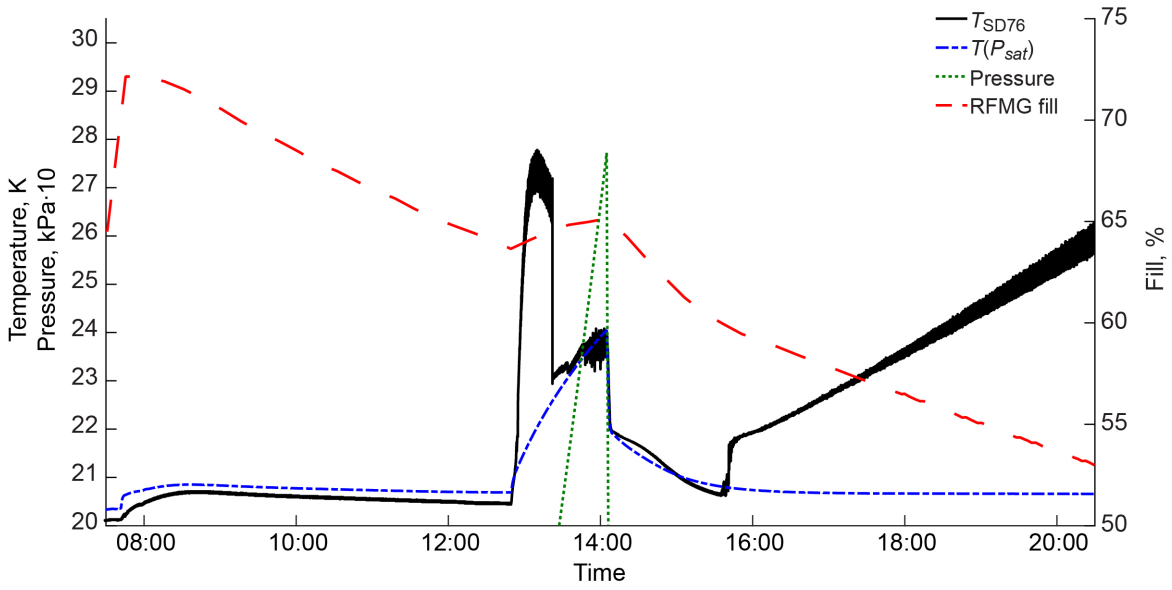

Figure 227.—Radio Frequency Mass Gauge (RFMG) and SD76 data from baseline test on Aug. 28, 2019. Initially, temperature of SD76 (T_{SD76}) is below liquid interface temperature $T(P_{sat})$ line, but when tank fluid is locked up at 12:49, temperature spikes up, indicating it is actually in vapor phase. This transition takes place nearly 3 h before typical apparent event at 15:38, with difference in RFMG percent fill between the two events of 3.7 percent. During tank lockup, temperature of SD76 abruptly drops, indicating expanding liquid volume rising above SD76 location, engulfing diode in liquid.

Understanding that the apparent diode transitions can be in error by nearly 4 percent of the full-scale-fill level for the baseline test, it is nevertheless interesting to plot the RFMG percent-fill output, calculated according to Equation (31), along with the apparent diode transitions for comparison. Figure 228 shows the RFMG volumetric percent-fill output for the baseline and Thermal 1 tests plotted along with the apparent diode transition events, identified as those events where the diode temperature abruptly increases during normal boiloff periods. We note here that the capacitance probe data is referenced against an apparent dry to wet transition of SD81 (90.5 percent location) during the initial fill, as noted in Section 5.4.1, at which time the RFMG indicated a value of 87.7 percent.

Data from the Thermal 2 test is very similar to Thermal 1, and the LN_2 test data lacks clear signatures that might be identified as wet to dry transitions. From the baseline data plot in Figure 228, we see that the apparent SD transitions for SD72 to SD83 consistently produce a 2 to 5 percent of full-scale higher estimated percent fill level at a given time. Below 40 percent fill level, the apparent diode transitions are within 2 percent of full scale of the RFMG value and the agreement between the two becomes better at lower fill levels. Data from Thermal 1 (and Thermal 2) show large errors in apparent diode wet to dry transition events for SD78 to SD83, with nearly simultaneous apparent wet to dry transition events occurring when the RFMG reads 70 percent fill level. The difference between the two tests is the MLI blankets on the domes, which keeps the vapor cold at the high fill levels, leading to much higher errors in estimated fill levels based on apparent wet to dry transitions from the diodes. SD data below the 70-percent fill level is roughly consistent with the baseline test data.

In summary, a close inspection of diode temperature data shows that the apparent wet to dry transition events are in error up to 4 percent of full scale during the baseline test, with much higher errors during the Thermal 1 and Thermal 2 tests. Comparing RFMG data to a more definitive diode dry to wet transition that occurred during a tank lockup period indicates agreement to within 0.5 percent of full scale. From these tests, we thus conclude that the scaling of the RFMG technology to larger tanks is understood and there is no inherent degradation in accuracy due to scaling to larger tank sizes.

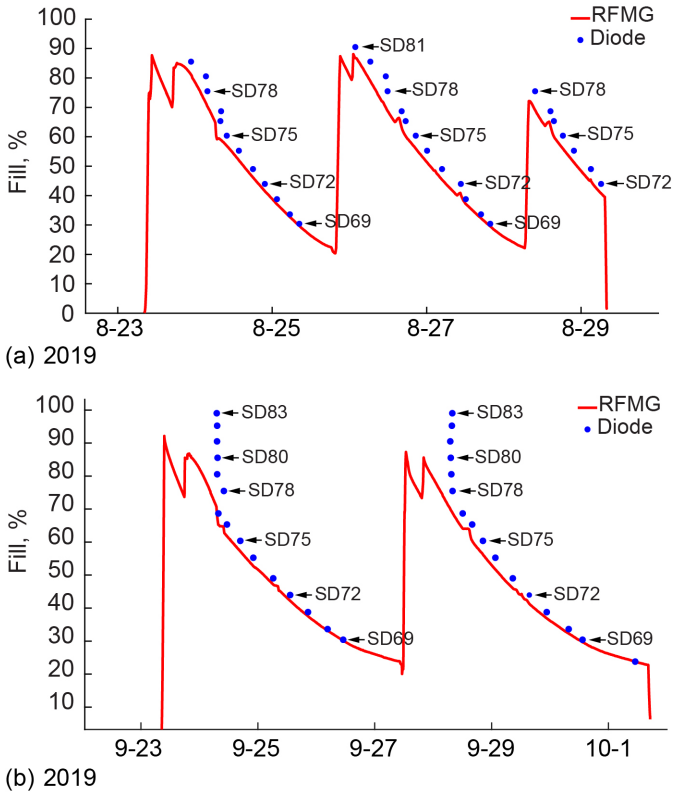

Figure 228.—Radio Frequency Mass Gauge (RFMG) percent-fill output as compared to apparent wet to dry transitions of diode rake sensors for (a) baseline and (b) liquid hydrogen Thermal 1 tests. Uncertainty of wet to dry transitions during baseline tests is estimated to be up to 4 percent of full scale. Silicon diode (SD) data from Thermal 1 shows nearly simultaneous apparent wet to dry transitions for SD78 to SD83, indicating large errors.

5.6 Acoustic Testing

After each test was completed, all data was inspected prior to moving on to the next test. One example of such is shown in Figure 229, for accelerometer VS11Z, on the forward skirt in the ±Z direction. Figure 229(a) shows the full time period of testing, warming up the speakers with 30 s at –9 dB, 30 s at –6 dB, and 30 s at –3 dB (all relative to the targeted OASPL for the specific test) before running the full acoustic spectrum for 130 s as prescribed in the test matrix. Figure 229(b) shows a specific 10 s of acceleration, this section of the data is processed further. Figure 229(c) shows a histogram of the processed data, showing a normal distribution of the data, around 0g, as would be expected.

5.6.1 Structural Assessment

Figure 230 shows an example of the structural signature health check. It is an overlay of the –6 dB pretest to the –6 dB posttest for each accelerometer channel. The amplitudes should be somewhat similar; however, the main metric is to check that the first few (~10) modes (indicated by each peak) have not shifted in frequency by more than 5 percent. All channels passed this check. This helps build the case of no structural damage from the full level and protoqual tests, at least where there is mounted instrumentation.

5.6.2 Assessment of Acoustic Testing

SHIIVER was successfully exposed to both the target full level and protoqual acoustic profiles, within the set tolerances, for the duration required. Based on visual observations, the SHIIVER MLI survived the specified combined acoustic profile with little to no observable damage. A small amount of foreign object debris (FOD) was found to have fallen out of the MLI, with the largest amount coming after the initial –6 dB test and after the +3 dB test. This FOD was limited to very small clippings of netting and reflector coming out of the MLI in addition to small pieces of cryolite that fell out. The FOD from the first –6 dB test was approximately 1 g, and that from all other tests was less than 1 g. Visual observations during the test and of the videos after the test show very little movement within the MLI. While this cannot be fully quantified, it was much less than expected.

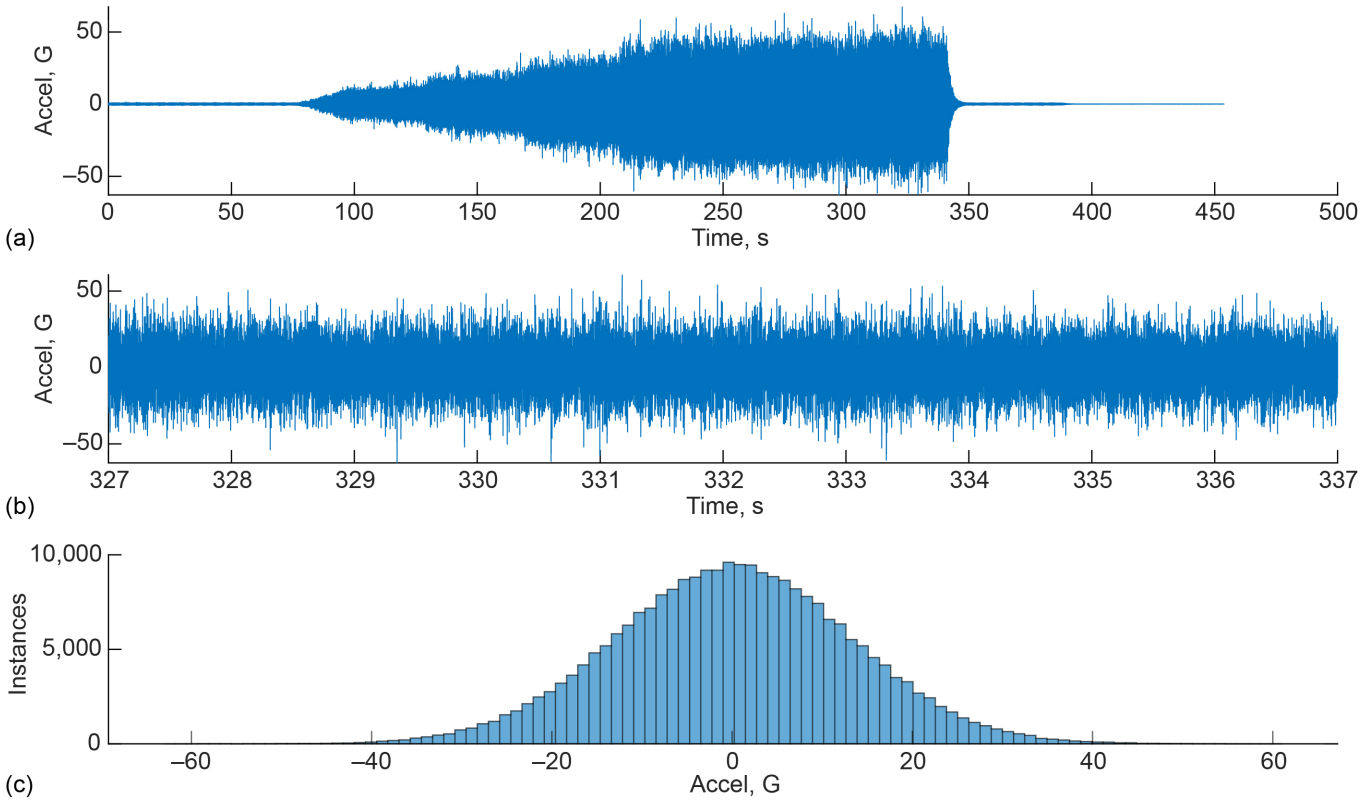

Figure 229.—Sample time history checks of accelerometer VS11Z on forward skirt in ±Z direction. (a) Full time period and threshold of testing. (b) Ten seconds of acceleration from 0 dB section. (c) Processed data histogram from 0 dB section. Root-mean-square is 13.2068 and crest factor is 4.5741.

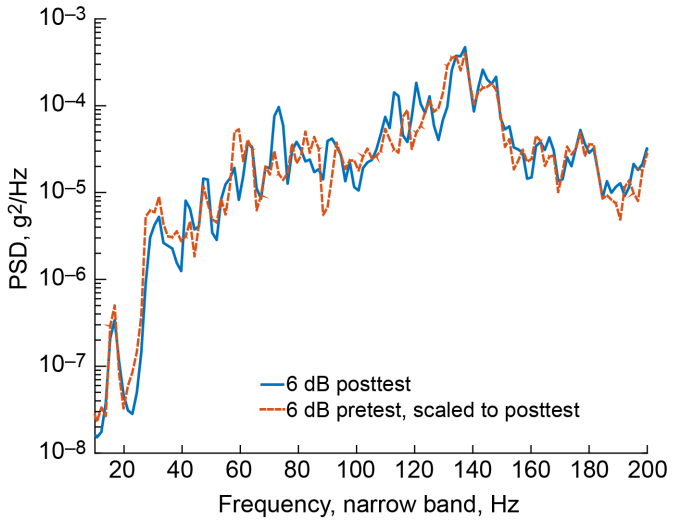

Figure 230.—Sample structural health check from accelerometer channel 1, aft manway cover, VS01X. Power spectral display (PSD).

5.7 Forward Skirt Temperatures

The forward skirt on the SHIIVER test article had two vapor-cooling loops attached to it. Over 50 SDs measuring the temperature as a function of height on the skirt and angle around the skirt. The operation of the SHIIVER system including temperature sensors with the loops both on and off was a key to understanding the performance of the vapor-cooling implementation.

The data verified SHIIVER as a three-dimensional (3D) heat transfer problem, as the temperature along the skirt changed with height along the skirt, angle around the skirt, and time. After accounting for these effects, the benefit of structural vapor cooling and MLI on the tank heat loads for various testing conditions could be quantified using temperature data along the skirt. Furthermore, knowing the locations of the SDs along the skirt helped determine temperature gradients as a function of angle and height for each test. Although there is some uncertainty of the data due to certain testing conditions, overall data trends from each test accurately determined the effects of

structural vapor cooling and MLI on the forward skirt temperature gradients and heat loads.

Figure 231 shows the locations of the temperature instrumentation along the full forward skirt. Figure 232 and Figure 233 show the locations of the temperature instrumentation on each half of the skirt, for clearer visualization of the locations of the sensors. The SDs are numbered serially at each angular station, with the lowest number in each series being closest to the flange; the exact dimensions between each sensor can be found in Section 3.0. Most of the instrumentation functioned nominally for the entirety of testing, which simplified the comparison between tests. The angular stations referenced in the following plots of this section will only be at 180° and 360°. However, data and plots of the rest of the angular station temperature profiles can be found in Appendix B, Appendix D, and Appendix F for the baseline, preacoustic LH_2, and preacoustic LN_2 testing, respectively. The reader is encouraged to review those plots for further investigation into the 3D nature of the temperature gradients on the skirt during the vapor-cooling testing.

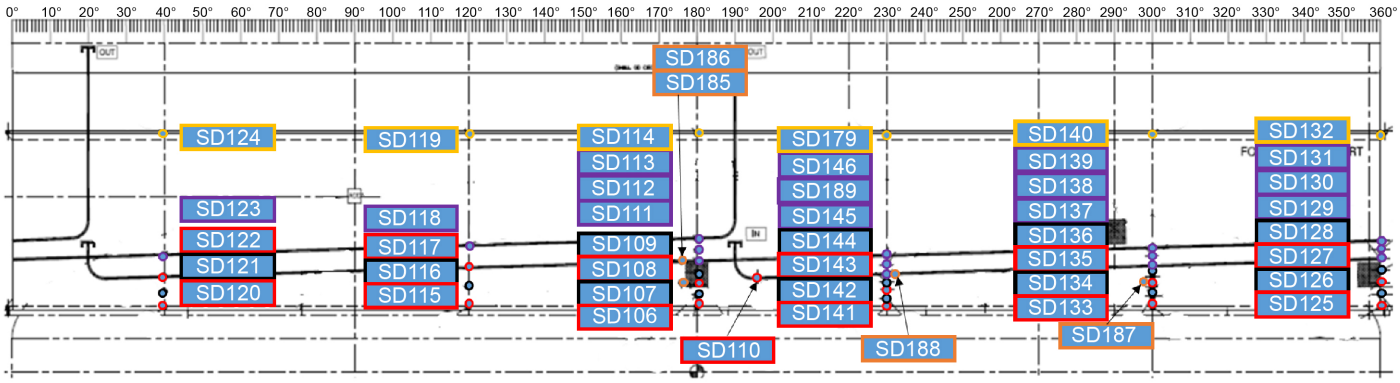

Figure 231.—Vapor-cooled forward skirt temperature silicon diode (SD) instrumentation.

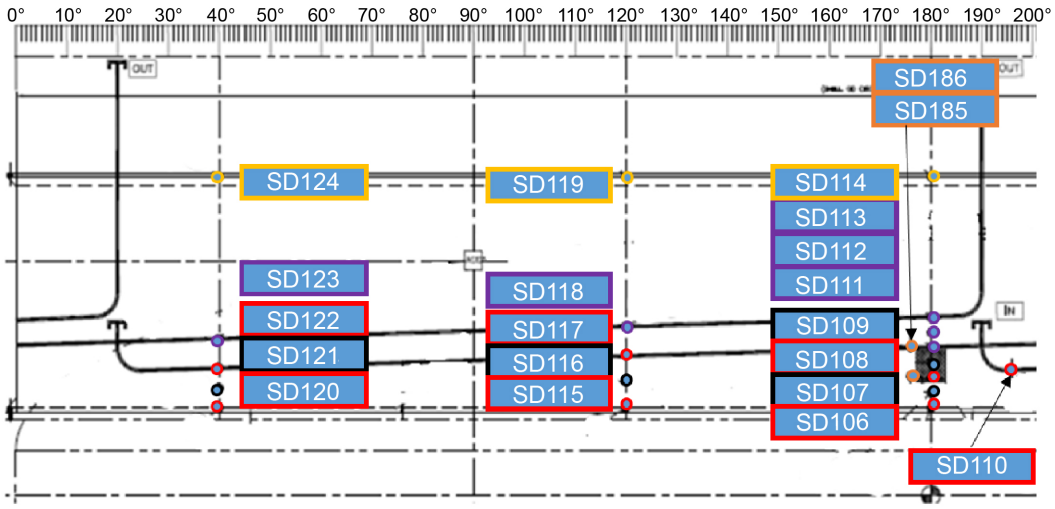

Figure 232.—Placement of silicon diode (SD) temperature measurements on forward skirt and vapor-cooling channels between 0° and 180°. SD185 and SD186 are on outside of skirt, all others are on inside of skirt.

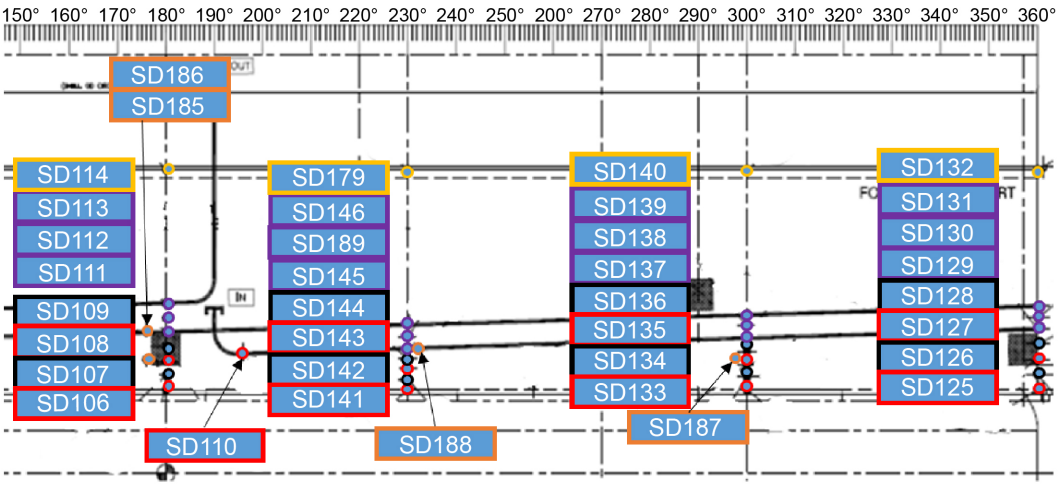

Figure 233.—Placement of silicon diode (SD) temperature measurements on forward skirt and vapor-cooling channels between 180° and 360°. SD185 to SD188 are on outside of skirt, all others are on inside of skirt.

Figure 234 and Figure 235 compare skirt temperatures as a function of height above the flange for both the 180° and 360° stations. Temperatures are plotted for both the boiloff test (yellow) and the vapor-cooling test (blue). The individual series, denoted by the different marker shapes, represent different tank-fill levels at which the measurements were taken. There is a noticeable dip in the skirt temperatures for the vapor-cooling cases around 0.4 m due to the local influence of the vapor-cooling lines, which intersected the diode arrays at this height and angular location. Looking at the region left of the dip, it can be seen that the temperature gradient in the skirt has a substantially smaller slope with vapor cooling when compared to the boiloff temperature gradient. This indicates a decreased temperature gradient entering the forward flange, resulting in a decreased conductive heat load to the tank as a result of the vapor cooling. In fact, in many cases, there are decreases in temperature on both sides of the cooling line indicating that the skirt was picking up more heat than was being conducted into the flange. Another key observation is the general trend to an overall drop in temperature of the forward skirt with increased fill level. However, it can be seen that in the boiloff case the skirt is actually colder at the 75.5-percent fill level than at the 90-percent fill level. This indicates that the thermal capacitance of the skirt was such that it was still in the process of cooling down when the tank was at the 90-percent fill level. One would expect the skirt temperature at steady state to be essentially constant at fill levels in excess of ~70 percent, where the forward tank flange has direct thermal contact with the liquid in the tank. The trends for the boiloff case below ~70 percent, where the flange has gone dry, are consistent with what would be expected where the flange would slowly warm up as the fill level dropped.

The impact of vapor cooling and fill level on the temperature profile in the skirt is shown more clearly in Figure 236 and Figure 237. They show the difference between boiloff and vapor-cooling temperatures along the skirt for 90 and 50 percent fill levels. Once again, note the vapor-cooling lines are about 0.4 m along the skirt so the most benefit (highest temperature difference) occurs at this height. From the figures, it is clear that vapor cooling is much more effective in cooling the skirt when the fill level is higher. This result is consistent with the results obtained during Subscale Laboratory Investigation of Cooling Enhancement (SLICE) testing, which showed that cooling effectiveness was a strong function of boiloff temperature and a weak function of flow rate (Ref. 31). In the case of SHIIVER, the rate of propellant boiloff is highest with the fill level above the forward flange, primarily because heat being conducted from the skirt through the flange contributes directly to boiloff. This is also when the ullage gas flowing into the vapor-cooling channels is the coldest because the least amount of energy is going to sensible heating of the vapor. Once the MLI was installed on the forward dome, little to no temperature variation of the ullage in the forward dome was seen. Once the liquid level drops below the forward flange (~70 percent), much of the heat conducted from the skirt through the flange goes into the ullage, increasing ullage temperature, decreasing boiloff rate, and decreasing the impact of vapor cooling on the boiloff rate. It is noteworthy that this condition does not necessarily translate well to what would be experienced under microgravity conditions as it will be more likely that the walls will be wetted at higher fill levels, increasing the benefit at lower fill levels.

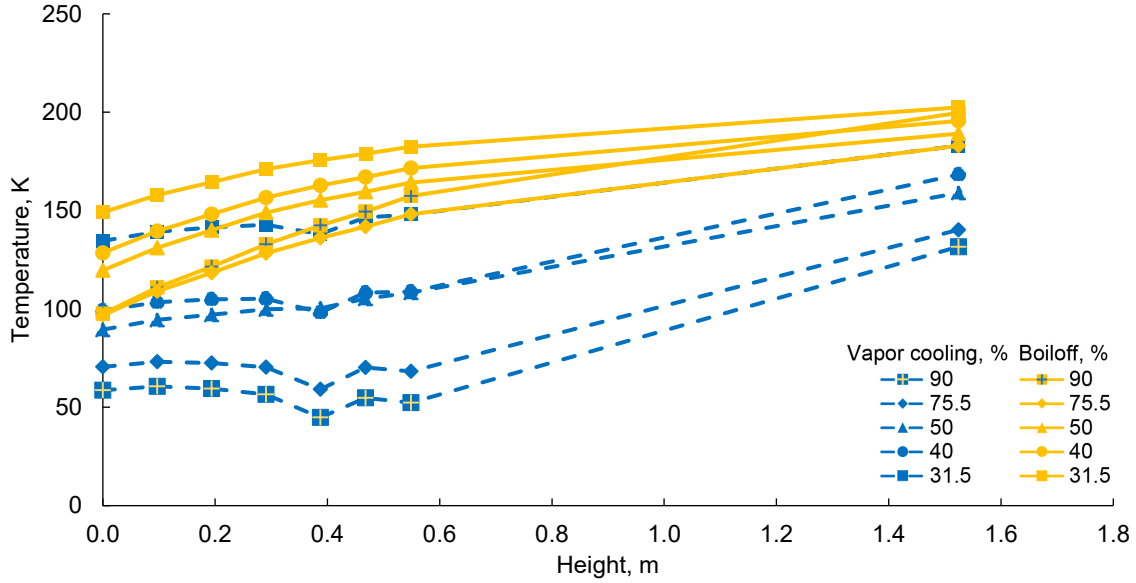

Figure 234.—Baseline temperature versus height at 180° comparing vapor-cooling and boiloff temperatures at every fill level.

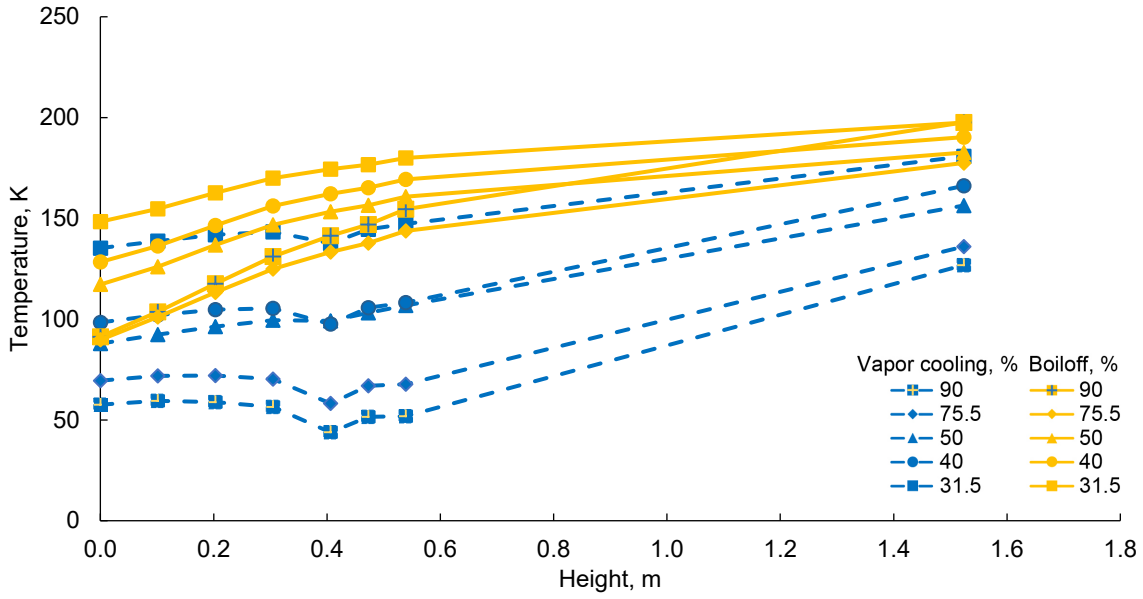

Figure 235.—Baseline temperature versus height at 360° comparing vapor-cooling and boiloff temperatures at every fill level.

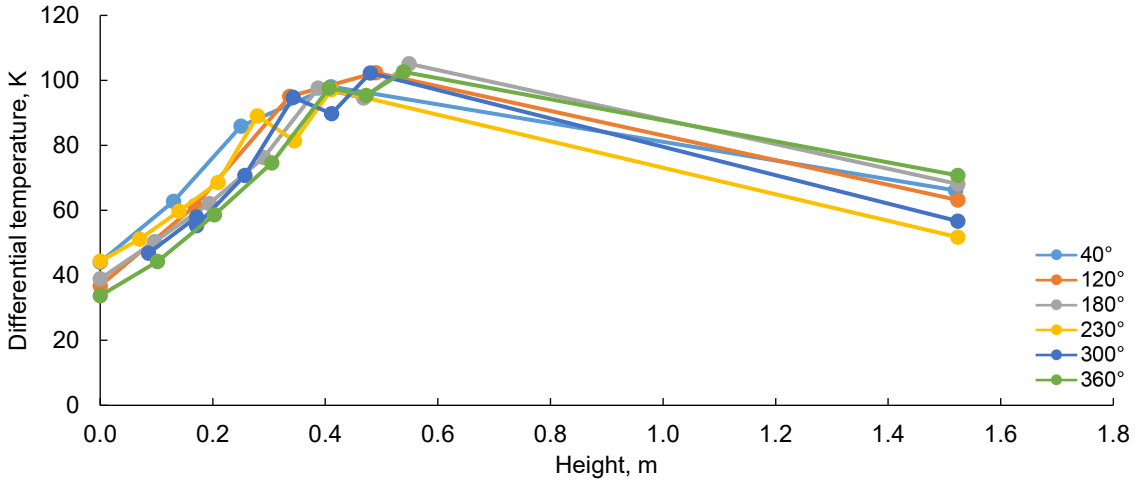

Figure 236.—Baseline difference in boiloff and vapor-cooling temperatures versus height at 90 percent fill.

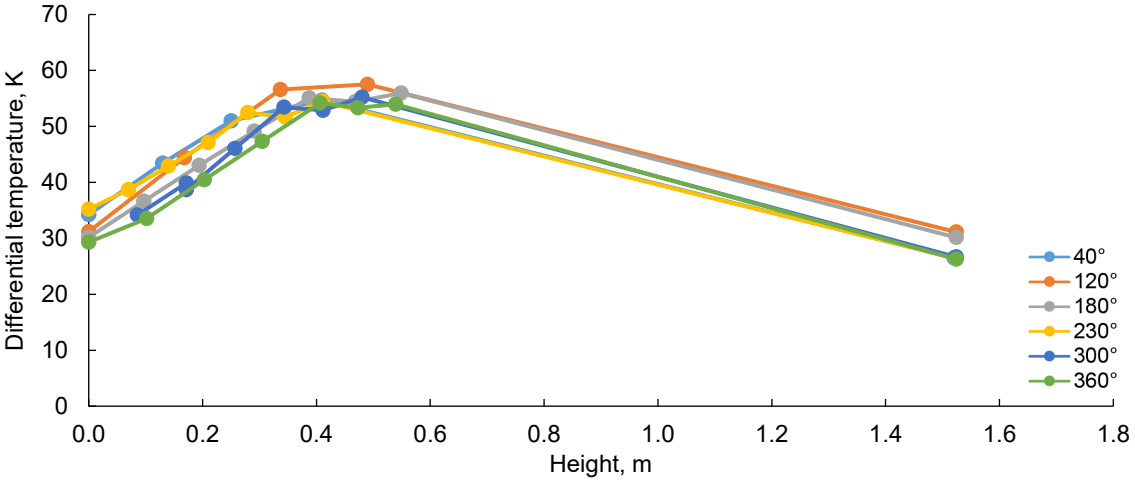

Figure 237.—Baseline difference in boiloff and vapor-cooling temperatures versus height at 50 percent fill.

Figure 234 and Figure 238 show the difference in forward skirt temperatures during the baseline and vapor-cooling tests for the LH_2 baseline and preacoustic test. With MLI, the vapor-cooled temperatures were lower than the baseline above 70 percent fill level, and higher than the baseline below 70 percent. The influences of the forward flange and the boiloff rate are the likely drivers of this outcome as the vapor entering the vapor-cooling circuit was much colder and more uniform as a function of fill level with the MLI on the forward dome. There are two primary modes of heat transfer to the tank: heat conducted into the tank through attached structure (primarily from the skirts and through the flanges) and heat radiated to the tank surface, then conducted through the insulation and tank walls. By drastically reducing the heat being radiated into the forward dome, it drastically affected the vapor temperature into the cooling circuit and the temperatures of the circuit and the skirt as a result. While the flow rate is down by 40+ percent, the colder gas more than makes up for the difference in cooling and the temperatures along the skirt are not a strong function of fill level.

Once the fill level dropped below the forward skirt and the vapor temperature going into the cooling loop began to rise, the effect of cooling the skirt with the MLI in place decreased compared to the baseline and the temperatures on the skirt become warmer than in the baseline testing. At this point, the temperature of the skirt increased much quicker due to the lower heat removal capability and lower flow rate.

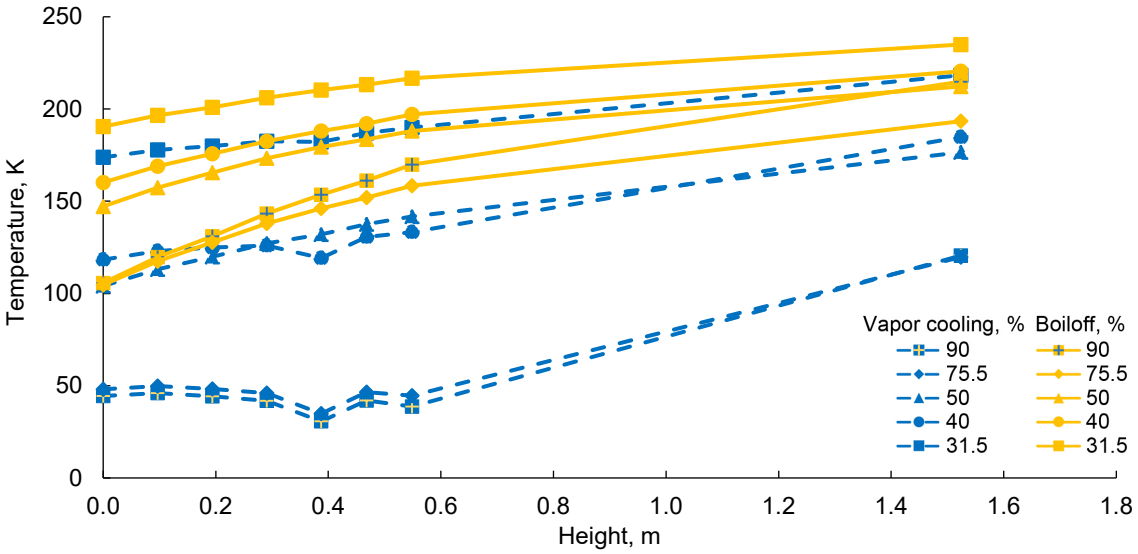

Figure 238.—Thermal 1 hydrogen temperature versus height at 180° comparing vapor-cooling and boiloff temperatures at every fill level.

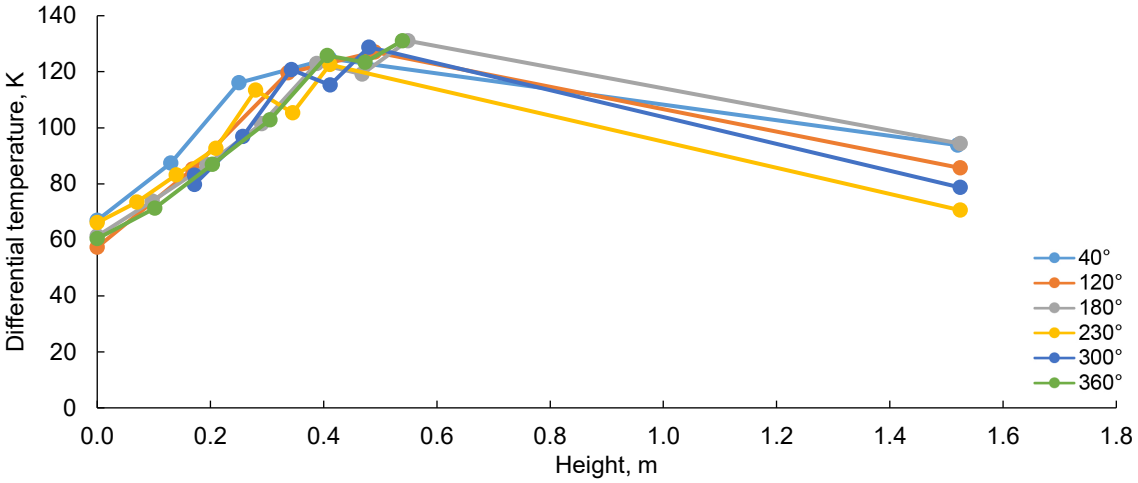

Figure 239.—Preacoustic liquid hydrogen testing difference between boiloff and vapor-cooling test forward skirt temperatures versus height at 90 percent fill.

Figure 236 and Figure 239 show the temperature differences for the baseline and preacoustic LH_2 testing on the forward skirt at approximately 90 percent full. The temperature differences on both tests have nearly the same shape and trends, including the temperature apex at the vapor-cooling-line height around 0.4 m. The temperature differences are about 20 K higher in the preacoustic testing than in the baseline testing. However, as shown in Figure 237 and Figure 240, the behavior at 50 percent fill is quite different between the two tests. While in the baseline testing, the general shape stays the same, but the temperature difference decreases, in the preacoustic test with MLI on the domes, the differential temperature slope is much smaller below the vapor-cooling lines (~<0.4 m). At the flange, there is still about a 20 K difference in the temperature difference between the two tests (i.e., the skirt is colder with the MLI on the domes); however, the cooling lines provide much less of a peak in the temperature difference with the MLI on the domes. This is probably driven by the heat flow in the system, the main heat load into the tank and the ullage is the forward skirt.

Figure 241 shows the temperatures along the skirt at every angle at the 90-percent fill level. The change in cooling change location (evidenced by the valleys in each line) as well as the change in slope of the temperature of the skirt going into the flange can be seen to be a function of the location around the skirt.

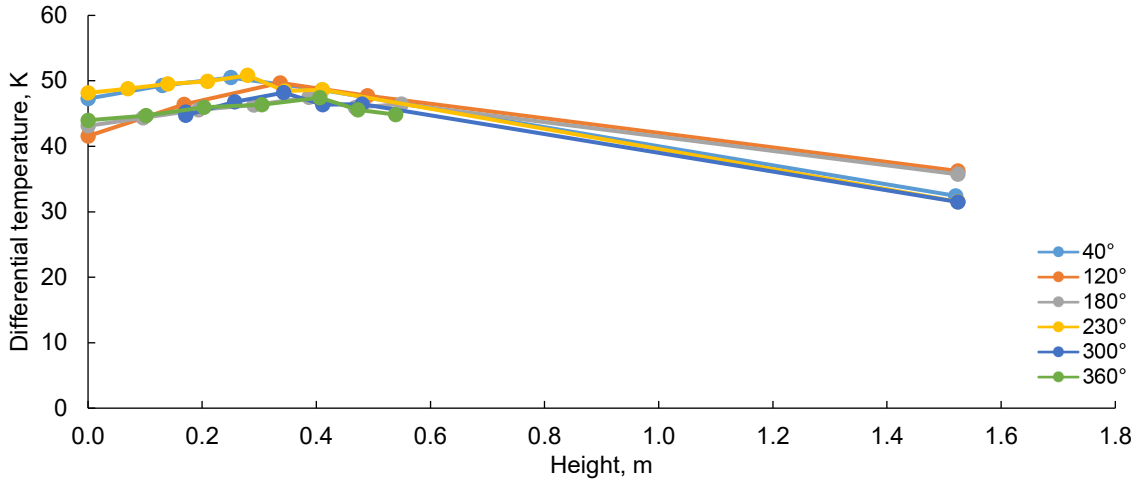

Figure 240.—Preacoustic liquid hydrogen testing difference between boiloff and vapor-cooling test forward skirt temperatures versus height at 50 percent fill.

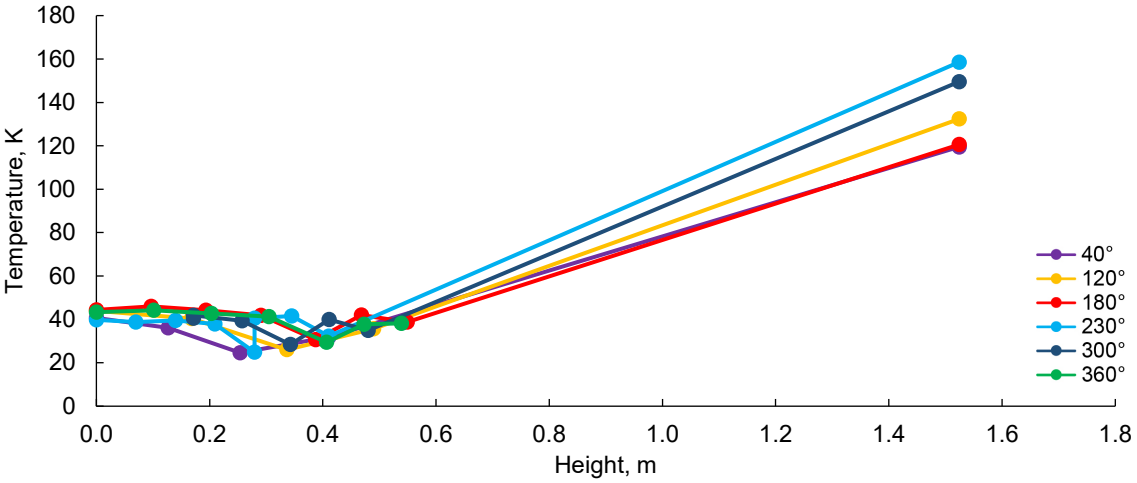

Figure 241.—Forward skirt temperatures at all angles for preacoustic liquid hydrogen vapor-cooling testing at approximately 90 percent fill.

The data from preacoustic LN_2 testing at high fill levels is shown in Figure 242 for the boiloff testing and Figure 243 for vapor-cooling testing, both as a function of angle around the skirt. As seen in Figure 242, there was essentially no variation in the temperature profile around the skirt. In Figure 243, the angular variation is much smaller than in Figure 241 on the LH_2 testing, but at 40° and 230° there are dips associated with the fluid lines where, similar to those in Section 5.8, the cooling dissipated fairly quickly in the LN_2 testing.

Calculated conduction heat loads down the skirt at each of the instrumented locations are shown below in multiple figures. The calculations are based on the lowest two operational temperature sensors and are calculated as a linear heat load (W/m) at the location of the sensors. At 230°, some of the lowest temperature sensors were not reliable and this visibly altered some of the calculations.

Figure 244 shows the calculated heat loads per length for each of the six locations during the LH_2 boiloff testing. In general, other than the 230° location, the heat loads are very similar and show little variation around the circumference of the skirt, as was expected (uniform skirt heat load, constant cross section, and material). Figure 245 shows the same calculations for the preacoustic LH_2 vapor-cooling testing. It is clear that there are angular dependencies in the response with the skirt actually cooling the forward flange around most of the length. This dependency appears to be due to the pitch of the cooling loop and possibly having better contact at the start of the loop.

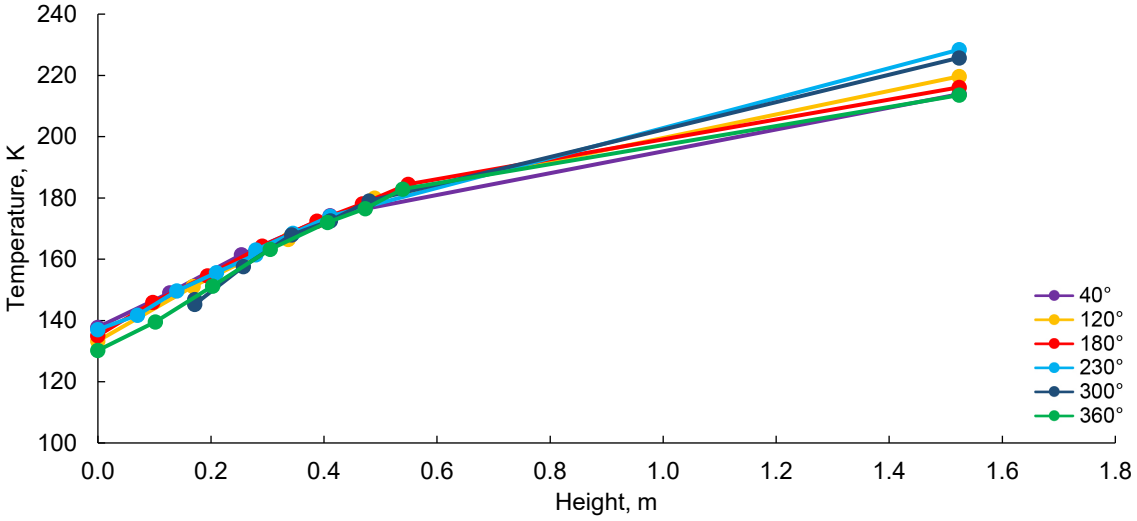

Figure 242.—Forward skirt temperatures at all angles for preacoustic liquid nitrogen boiloff testing at approximately 90 percent fill.

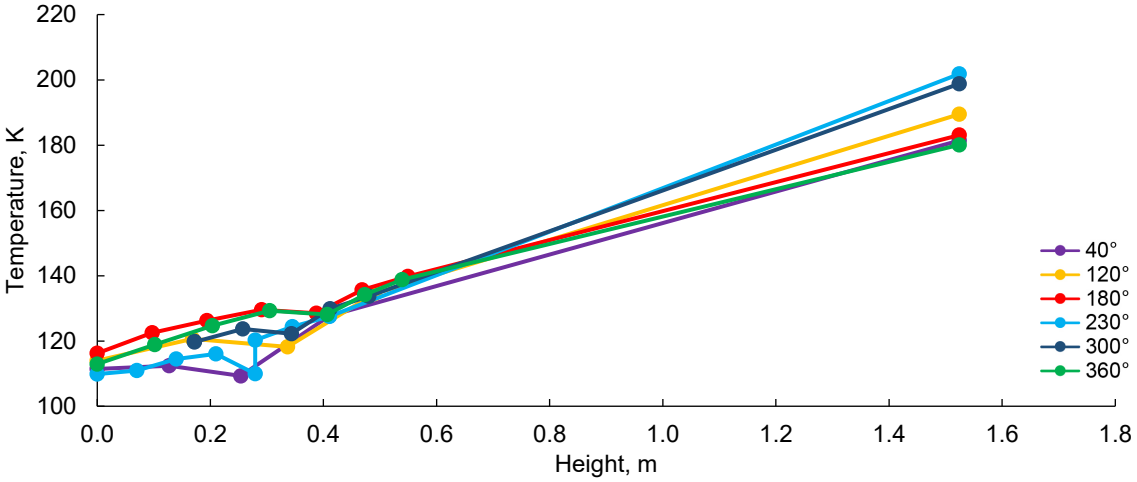

Figure 243.—Forward skirt temperatures at all angles for preacoustic liquid nitrogen vapor-cooling testing at approximately 90 percent fill.

Figure 246 shows the linear heat loads from LN_2 boiloff testing at each of the six locations. Similar to LH_2 testing, the linear heat loads are fairly constant and uniform as would be expected for uniform heat loads. Figure 247 shows the linear heat loads for the LN_2 vapor-cooling test. Similar to what was seen in the hydrogen data, the nitrogen vapor-cooling data is a function of the angle. Unlike the hydrogen case, the heat load does not appear to dip below 0 W. The worst-case reduction of heat load during the nitrogen testing was 50 percent, which was much more than the projected benefits (Ref. 27), suggesting that further consideration be given to oxygen and methane vapor cooling.

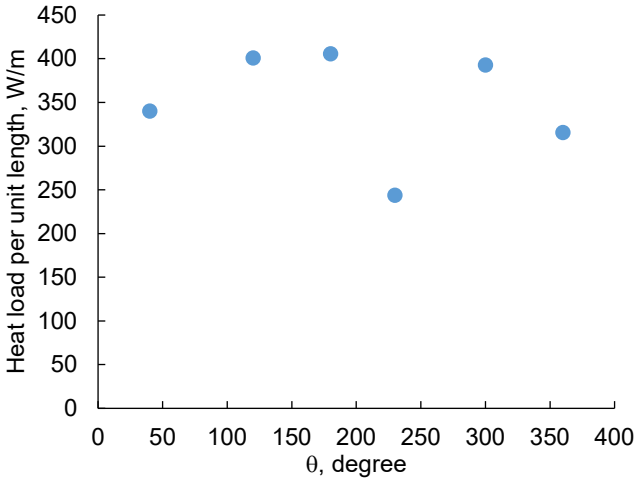

Figure 244.—Calculated linear heat load going into flange via differential temperature during preacoustic liquid hydrogen boiloff testing at ~90 percent fill. Angular location (θ).

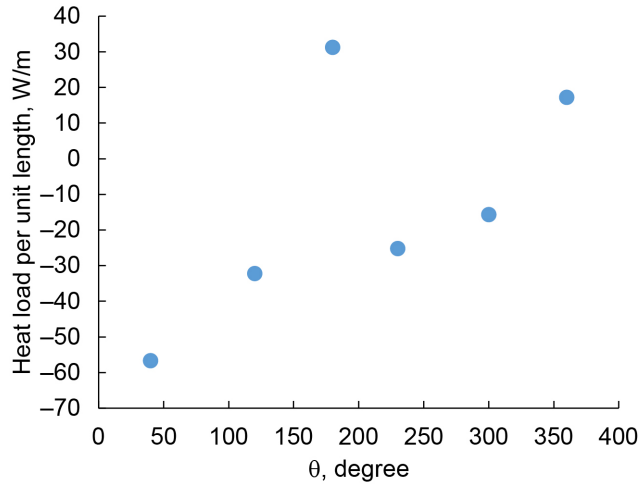

Figure 245.—Calculated linear heat load going into flange via differential temperature during preacoustic liquid hydrogen vapor-cooling testing at ~90 percent fill. Calculated value at 230° is artificially high due to loss of two lowest temperature sensors. Angular location (θ).

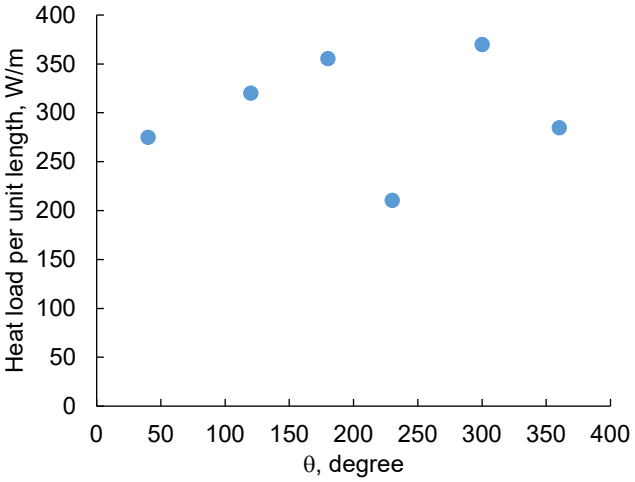

Figure 246.—Calculated linear heat load going into flange via differential temperature during preacoustic liquid nitrogen boiloff testing at high fill level. Angular location (θ).

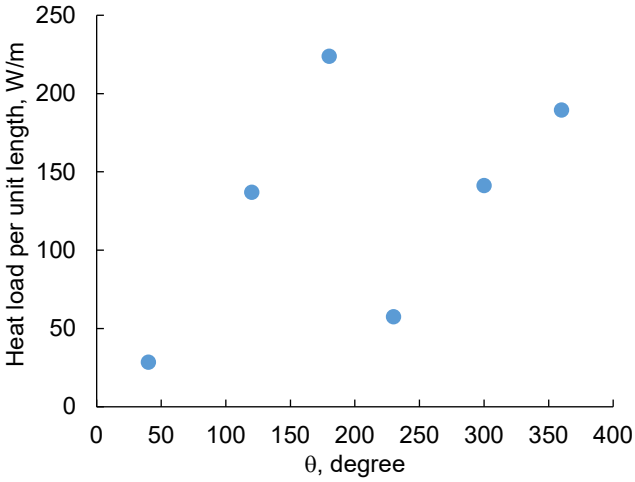

Figure 247.—Calculated linear heat load going into flange via differential temperature during preacoustic liquid nitrogen vapor-cooling testing at ~90 percent fill. Angular location (θ).

5.8 Vapor-Cooling-Line Temperatures and Heat Removal

During vapor-cooling testing, two key parameters were measured on the vapor-cooling system, the mass flow through the tubes and the temperature of the flow and channels. The temperature of the flow gas was measured through probes at the inlet and outlet of each of the two flow channels. Other temperature sensors were placed along the outside of the cooling channels along the length of the tubes. By observing the temperature and flow rate data, the structural cooling of the forward skirt was quantifiable. Although the temperature sensors on the cooling lines worked for most of the test, the vapor-cooling flowmeter only worked well for the preacoustic tests (both LH_2 and LN_2).

Figure 248 shows vapor-cooling-line temperatures as a function of length along the vapor-cooling line and fill-level percentage for the baseline test. No effort was made to try to balance the flow between the two cooling channels, but based on the temperatures in Figure 248, the two flow channels have similar temperatures. This suggests that the flows in the channels were fairly well balanced. As the fill level decreased, the temperature at the inlet increases, but so does the temperature difference across the channels (see Figure 249, the one anomaly is right after the 50-percent pressure rise test). This increase in temperature difference makes up for the decrease in flow rate that is seen during the testing as the fill level drops. However, the flow rate was not directly measured in the baseline testing, as the vapor-cooling flowmeter did not read.

Figure 250 shows the vapor-cooling-line temperatures during the LH_2 preacoustic test. The MLI had an interesting effect on the vapor-cooling-line temperatures during preacoustic test. The data shows the vapor-cooling-line entrance temperatures decreased from the baseline test at fill levels above 70 percent, but the temperatures increased from the baseline test at fill levels below 70 percent. One reason for the increase in temperature below 70 percent could be the reduced boiloff as the fill level decreases. This could be due to the conductivity of the flange. Above ~70 percent full, the flange is wet and has less contact resistance with the fluid and a higher temperature gradient. This conduction is the main driver of heat removal from the forward skirt above 70 percent full. Contrarily, the flange is dry below 70 percent, which limits the conduction between the flange and skirt. Since conduction below 70 percent full is less noticable, the radiation from the MLI on the forward dome is more observable. When the MLI is installed, it reflects radiation from the MLI on the inner skirt back to the skirt. Although this process occurs whether the flange is wet or dry, it is more prominent when the flange is dry because the skirt and tank MLI operates at a higher temperature and reflects more radiation to the skirt due to radiation's nonlinearity with temperature. These two phenomena explain the difference in heat loads between tests under 70 percent. Since the MLI generally reduced the boiloff rate more effectively below 70 percent fill level, there was less cold boiloff vapor present in the vapor-cooling lines, as shown in Figure 251.

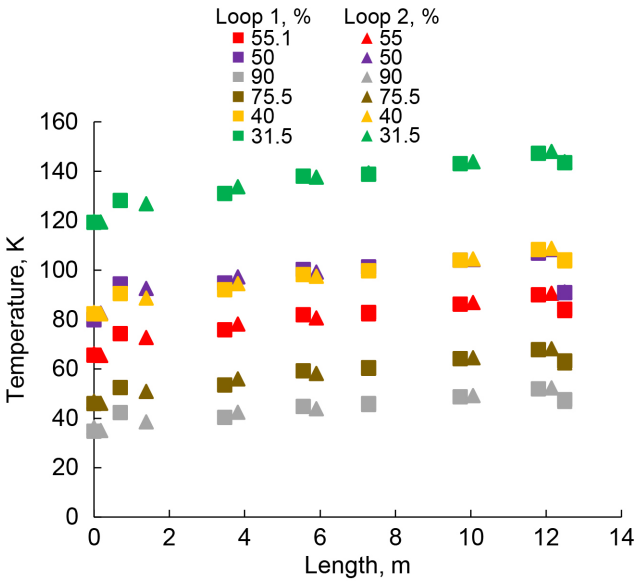

Figure 248.—Baseline vapor-cooling-line temperatures versus length for all fill levels.

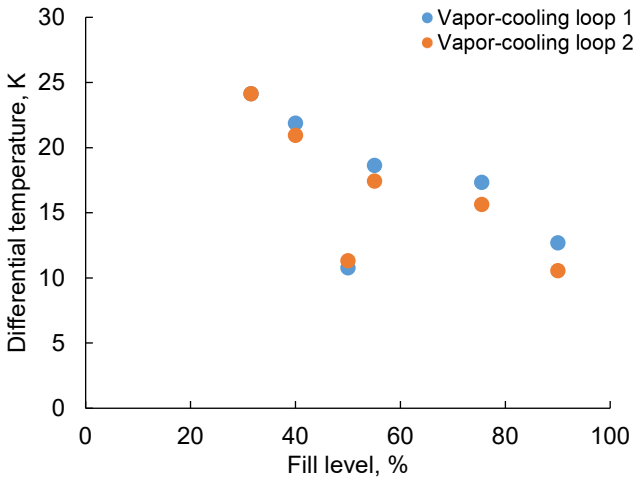

Figure 249.—Temperature difference across vapor-cooling channels as function of fill level.

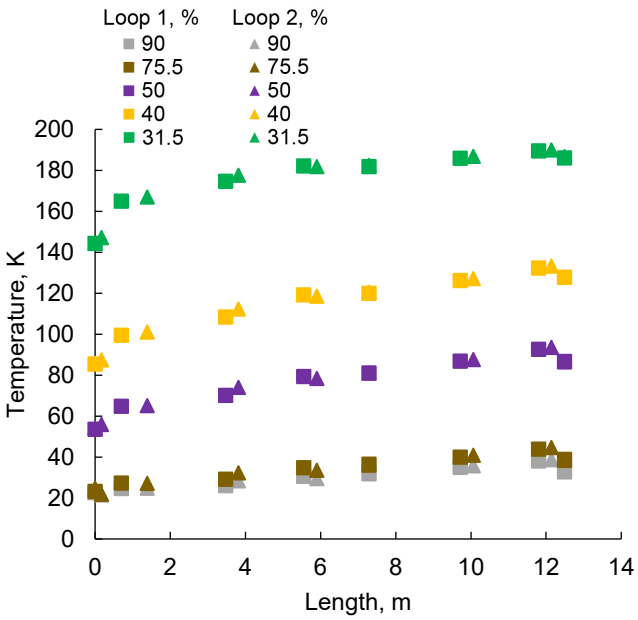

Figure 250.—Liquid hydrogen Thermal 1 vapor-cooling-line temperatures versus length for all fill levels.

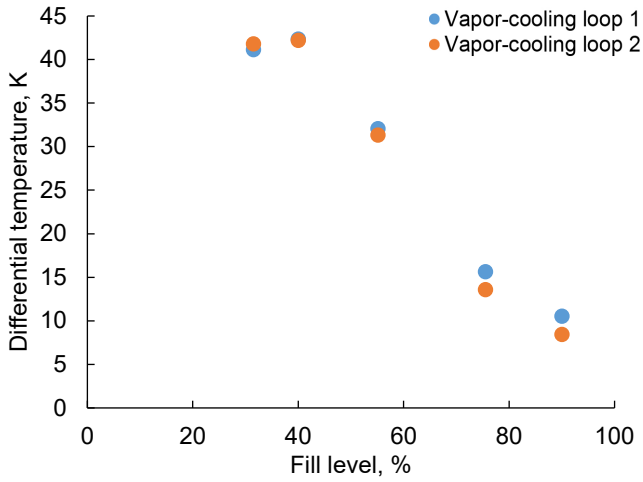

Figure 251.—Differential temperatures across vapor-cooling flow channels as function of fill level.

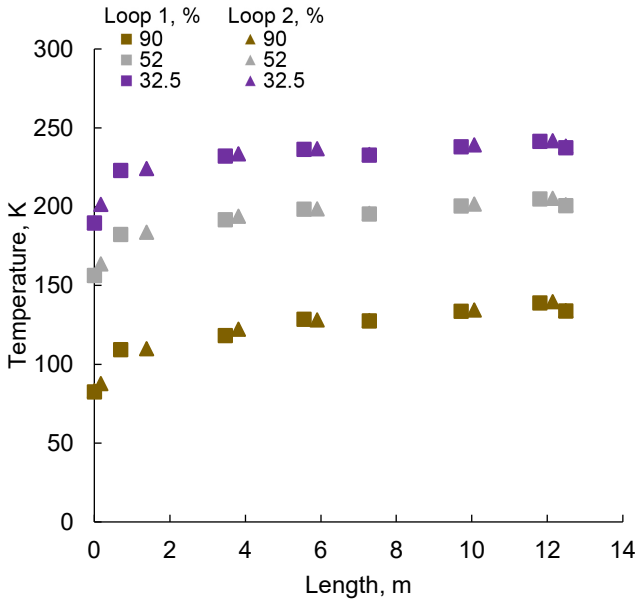

Figure 252.—Liquid nitrogen Thermal 1 vapor-cooling-line temperatures versus length for all fill levels.

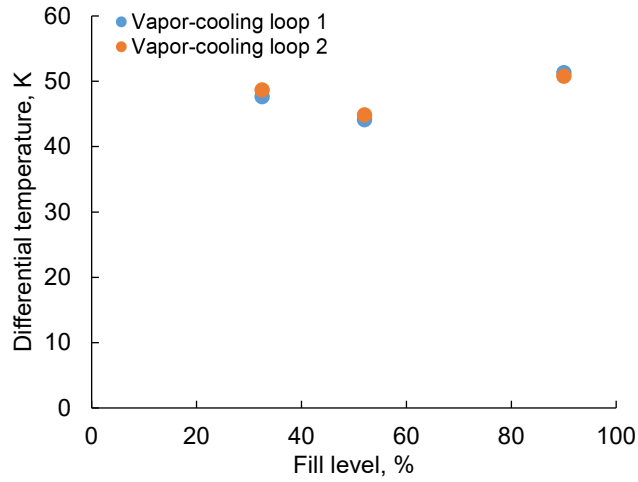

Figure 253.—Differential temperatures across vapor-cooling flow channels as function of fill level.

Figure 252 shows the vapor-cooling-line temperatures from LN_2 preacoustic testing. The shapes of the curves are much different than the LH_2 ones. Most of the cooling is used up within the first meter and then the cooling tapers out as it passes around the skirt. However, due to the change in inlet temperature as a function of fill level, the entrance temperatures into the vapor-cooling circuit do vary with fill level. Figure 253 shows that while the inlet temperature does vary, the change in temperature across the skirts does not really vary with fill level.

When the vapor-cooling flowmeters operated correctly during the preacoustic test, the total heat rejected from the skirt was quantifiable. By performing an energy balance of the vapor-cooling lines, by neglecting radiation, friction, kinetic effects, and potential effects, the heat rejected from the skirt through the vapor-cooling channels is given by the following equation:

$$\dot{Q}_{\text{vapor,intercept}} = \dot{m}\left(h_2 - h_1\right) \tag{33}$$

where $\dot{m}$ is the mass flow rate through the vapor-cooling lines, h_1 and h_2 are the vapor enthalpies at the entrance and exit to the channels, respectively, and $\dot{Q}_{\text{vapor,intercept}}$ is the heat removed from the skirt by the vapor cooling flow. This equation is useful for evaluating heat loads at certain points in the vapor-cooling lines, and since the mass flow rate remains constant throughout the vapor-cooling lines, the temperature gradients (and thus the enthalpies) show the effectiveness of the vapor cooling as a function of position around the skirt. The total heat removed from the skirts as a function of fill level is shown in Figure 254 for the preacoustic LH_2 testing and Figure 255 for the preacoustic LN_2 testing. For the calculations, the flow was assumed to be split evenly between the two flow channels. The hydrogen testing shows a 15 to 20 percent difference in enthalpy change at the higher fill levels, so it is possible there is a bit of flow imbalance (there is no reason for one channel to pick up more heat than the other). It should be noted that there is high uncertainty in the 30-percent-fill-level data point in the LH_2 testing, due to the loss of the vapor-cooling flowmeter. In this case, the flow rate from the change in capacitance was used, which was very noisy. The nitrogen data for the two cooling loops is much closer but does not vary with fill level. It is interesting to note, at high fill levels, the nitrogen is able to remove as much if not more energy from the skirt than hydrogen demonstrated. Also, with the hydrogen test, the heat removal continued to increase with fill level, even as the boiloff did not decrease. This shows that the benefits of vapor cooling a tank are complex even for such a simple test as SHIIVER.

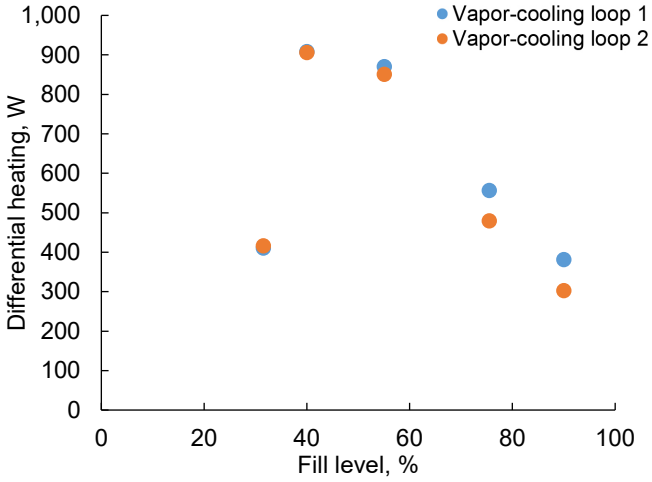

Figure 254.—Differential heating across vapor-cooling channels from preacoustic liquid hydrogen testing.

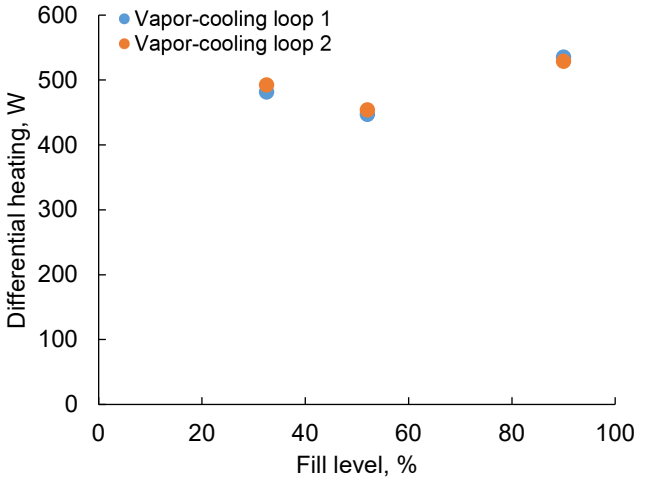

Figure 255.—Differential heating across vapor-cooling channels from preacoustic liquid nitrogen testing.

5.9 Multilayer Insulation

The MLI was installed onto the forward and aft dome of the tank after the baseline test. Typically, it took the MLI about 80 h to come to steady state, which was much longer than it took the tank boiloff to come to steady state. While the data from the MLI layers is not used to calculate heat loads, it can be used to give an indication for compression or other issues within the blankets. Due to the large total heat load into the SHIIVER test article relative to the MLI heat loads, the calculation of MLI heat loads has a large uncertainty (over 100 percent).

5.9.1 Liquid Hydrogen Preacoustic Testing

Of the three stacks of diodes in the forward dome MLI and three stacks of diodes in the aft dome MLI, all the top cross sections and bottom cross sections looked very similar. The diodes were installed on the SOFI surface (not present at all cross sections, but identified as SD31, SD32, SD37, and SD38); the inside of the 1st, 5th, 10th, and 20th layer; and a thermocouple on the outer cover for all of the cross sections. Figure 256 to Figure 258 demonstrate this similarity for the forward dome during hydrogen boiloff testing and Figure 259 to Figure 261 demonstrate this for the aft dome during hydrogen boiloff testing (note that the small gaps in the data are where pressure rise tests were completed). This indicates that large portions of the MLI layers on the dome were essentially isothermal and should yield excellent performance. The aft dome MLI came to steady state (MLI layers changing in temperature less than 0.5 K/h) on the outer layers of the MLI somewhere between 70 and 80 h into the test. The forward dome MLI never really came to a true steady state as the layers warmed up as the top of the tank was warming up. During the testing, it was observed that most of the heat into the forward dome came in through the forward flange and was conducted up by both the stainless steel tank and the hydrogen gas flowing

out of the tank. This was very different than with just SOFI on the tank. As recorded elsewhere in this report, the heat flux through the MLI on the forward dome was actually negative due to the energy flow patterns in the system.

Figure 262 shows the MLI on the forward dome cooled off much quicker with vapor cooling than when it was not used. The MLI achieved quasi-steady state in the 120 to 130 h time frame, after restarting the test at approximately 108 h. It can also be observed that, as the forward dome warmed up, the MLI did not warm as much with vapor cooling versus no vapor cooling. Overall, the vapor cooling on the skirt did not affect the performance of the MLI, but the response of the tank system to the vapor cooling did change how the MLI responded to the warmup.

Figure 263 shows that the MLI on the aft dome was very steady through the whole duration of vapor-cooling testing. Figure 264 shows the profile of the steady-state data averaged over the durations shown in Figure 263. The profile is what one might expect to see from a radiation-dominated blanket system.

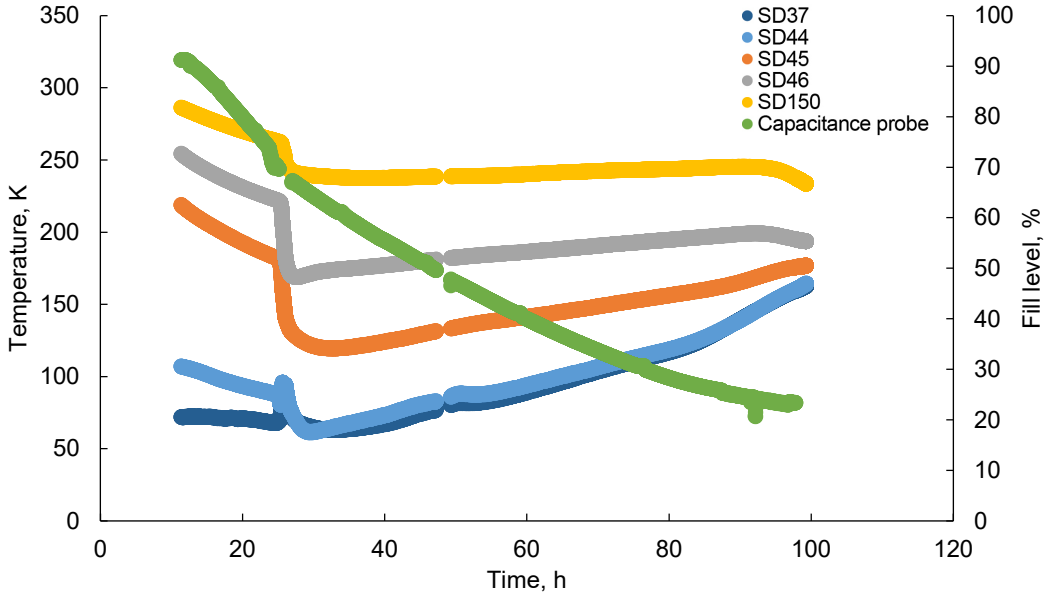

Figure 256.—Forward dome stack 1 during liquid hydrogen preacoustic boiloff testing.

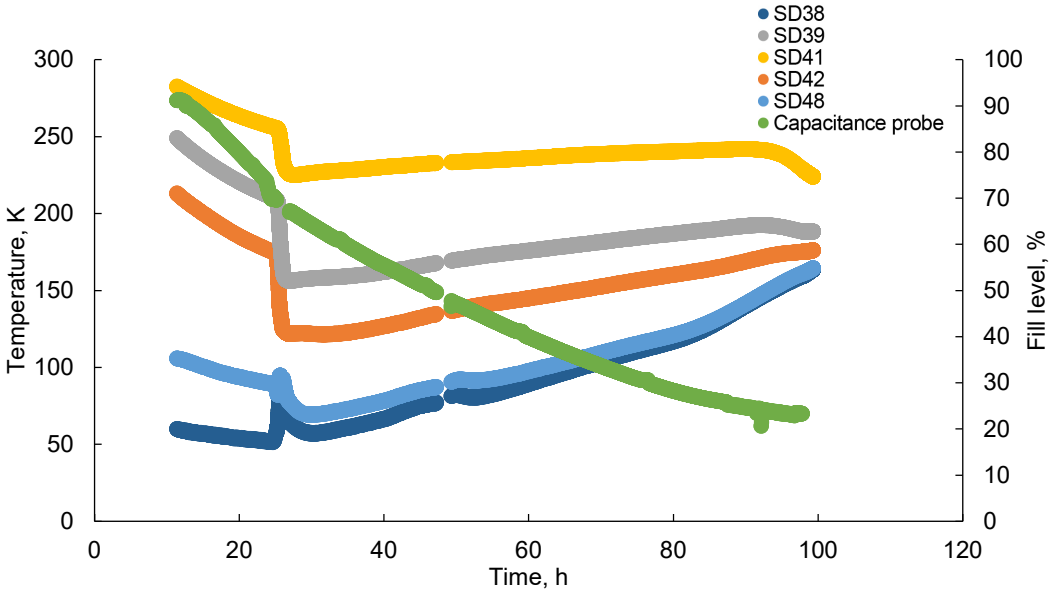

Figure 257.—Forward dome stack 2 during liquid hydrogen preacoustic boiloff testing.

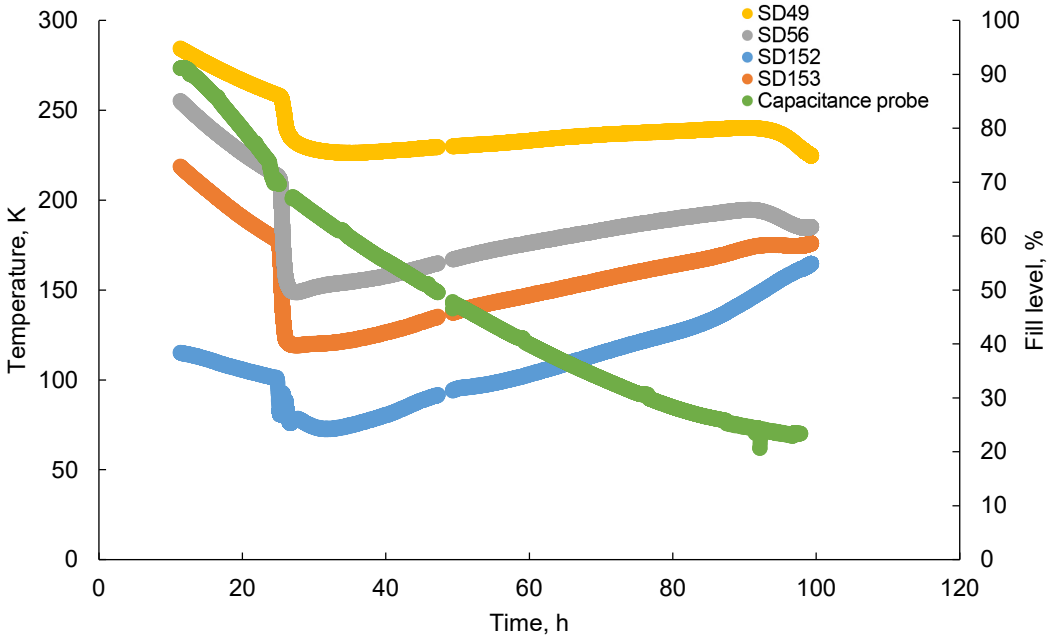

Figure 258.—Forward dome stack 3 during liquid hydrogen preacoustic boiloff testing.

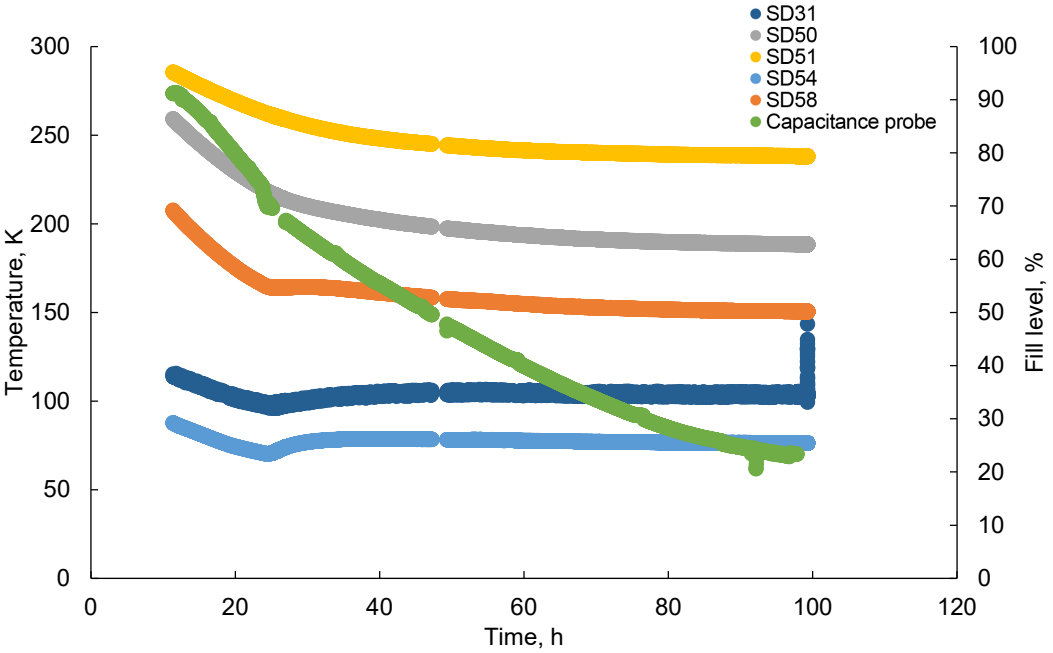

Figure 259.—Aft dome stack 1 during liquid hydrogen preacoustic boiloff testing.

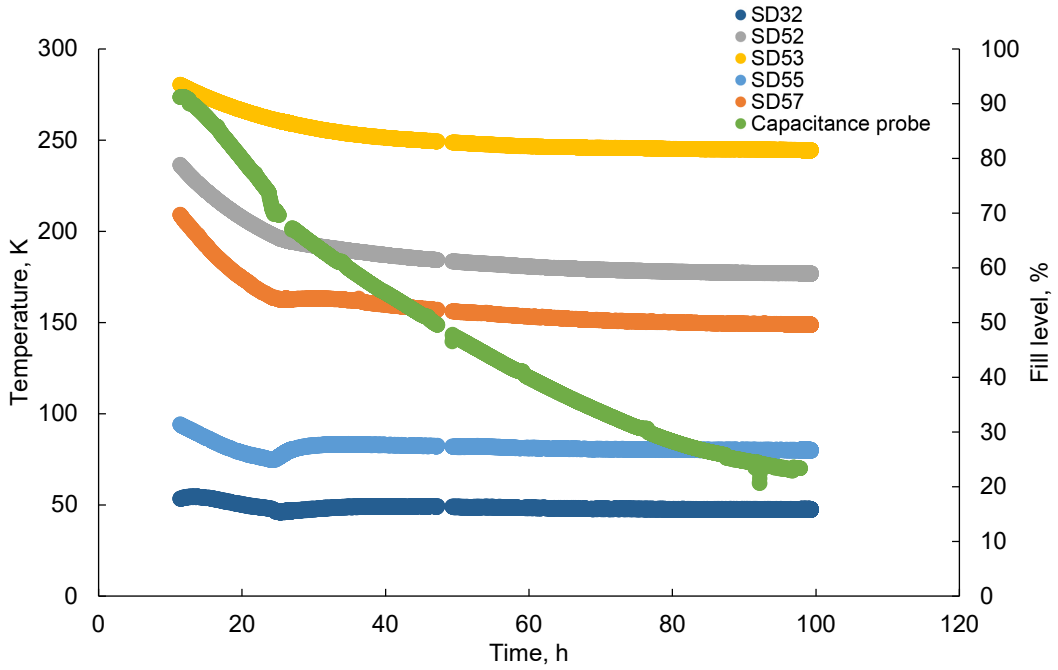

Figure 260.—Aft dome stack 2 during liquid hydrogen preacoustic boiloff testing.

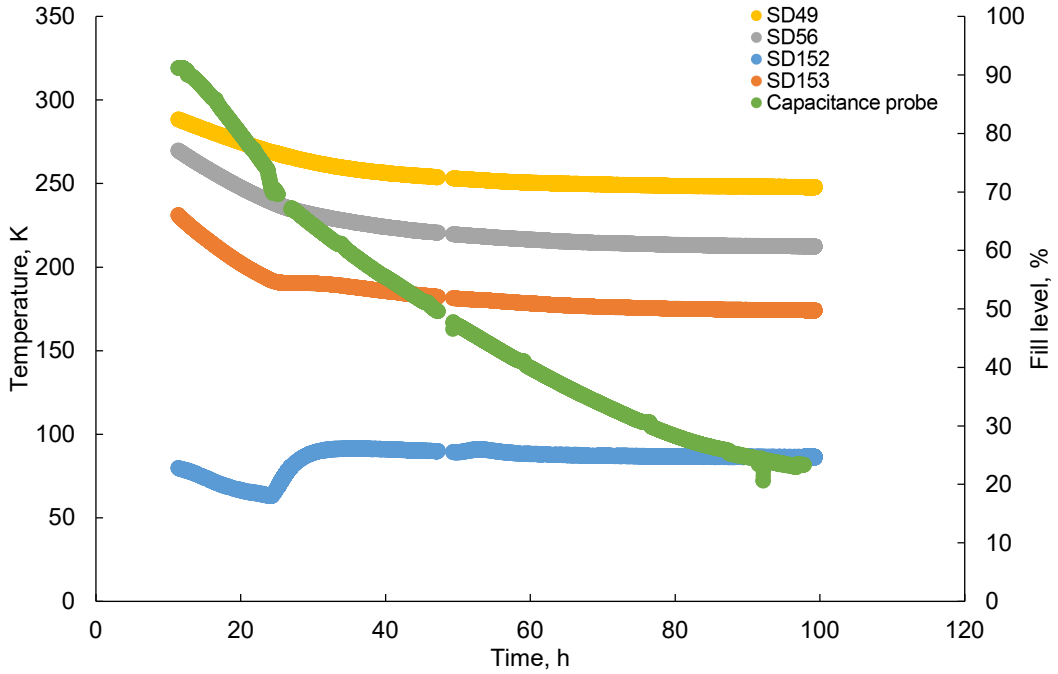

Figure 261.—Aft dome stack 3 during liquid hydrogen preacoustic boiloff testing.

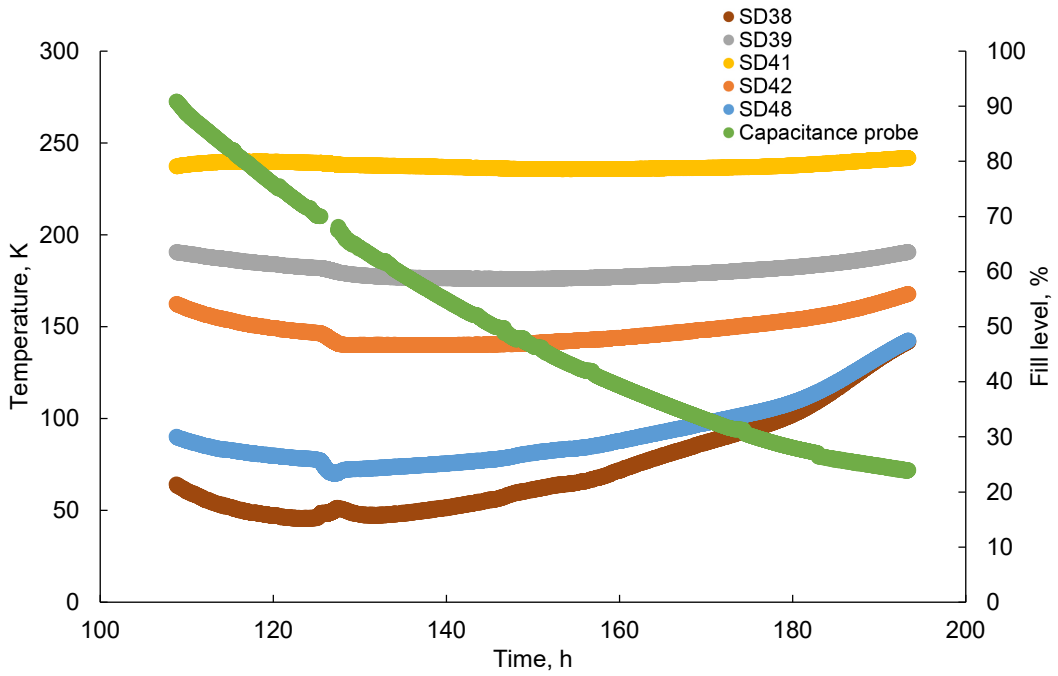

Figure 262.—Forward dome stack 2 during liquid hydrogen preacoustic vapor-cooling testing.

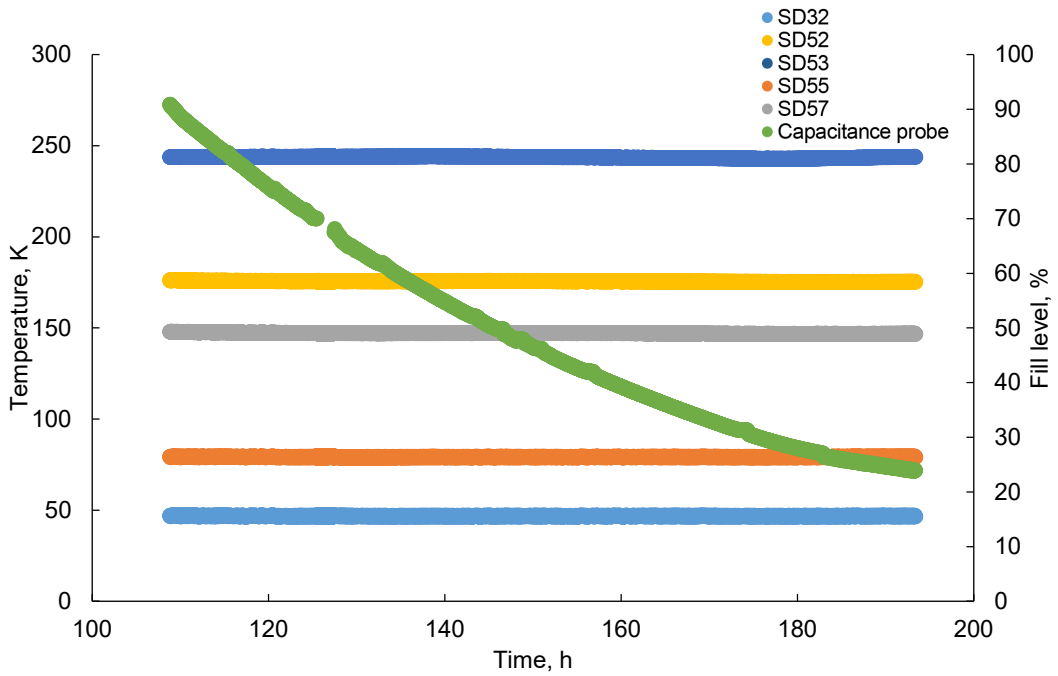

Figure 263.—Aft dome stack 2 during liquid hydrogen preacoustic vapor-cooling testing.

5.9.2 Liquid Nitrogen Preacoustic Testing

The LN_2 testing commenced with little delay after the LH_2 testing. This short turnaround did not allow the bottom of the tank or MLI to warm up and thus steady state was reached in 60 to 70 h on the forward dome as seen in Figure 265, but before 30 h on the aft dome as seen in Figure 266. At approximately 100 h, the liquid-vapor interface crossed the forward flange causing the ullage to begin to stratify, the dome to warm up, and the inner layers of MLI to warm up as seen on SD38 and SD48. Similar to the LH_2 preacoustic test, the different MLI stacks responded essentially identically, so only one plot of each is shown. The temperature profile through the aft dome is shown in Figure 267. The profiles and traces show no unexpected trends or issues within the blanket fabrication.

5.9.3 Postacoustic Liquid Hydrogen Testing

During postacoustic testing, the MLI responded similar to preacoustic testing, never reaching steady state on the forward dome (see Figure 268) and reaching steady state at about 80 h on the aft dome (see Figure 269). The temperature profile through the MLI blanket during postacoustic LH_2 testing is seen in Figure 270.

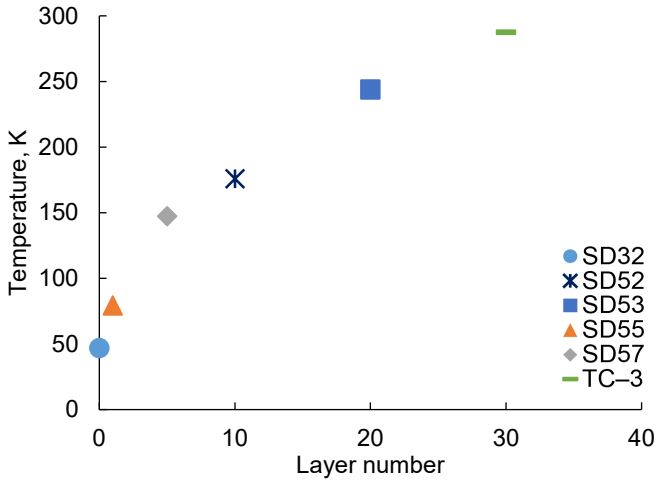

Figure 264.—Multilayer insulation (MLI) temperature profile for aft dome MLI stack 2 during liquid hydrogen vapor-cooling testing.

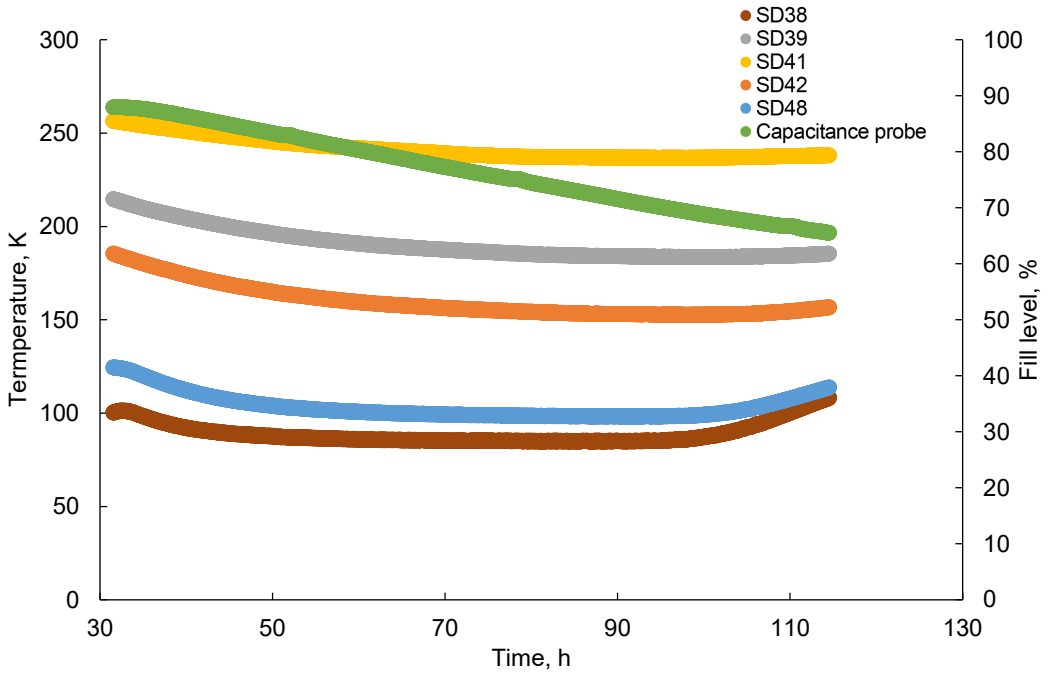

Figure 265.—Forward dome stack 2 liquid nitrogen preacoustic boiloff testing.

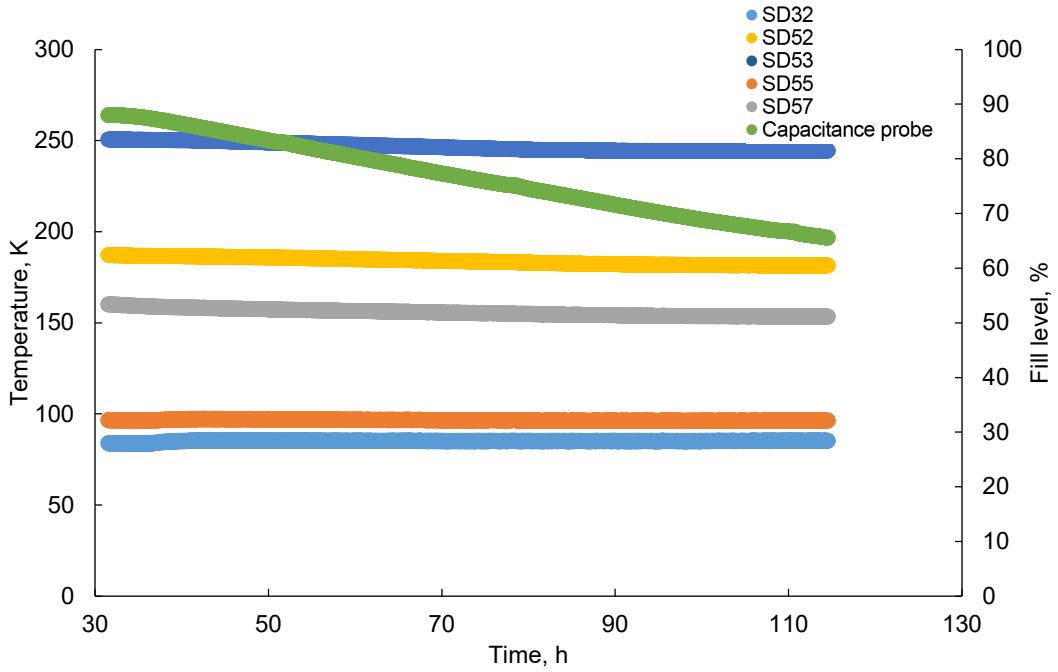

Figure 266.—Aft dome stack 2 liquid nitrogen preacoustic boiloff testing.

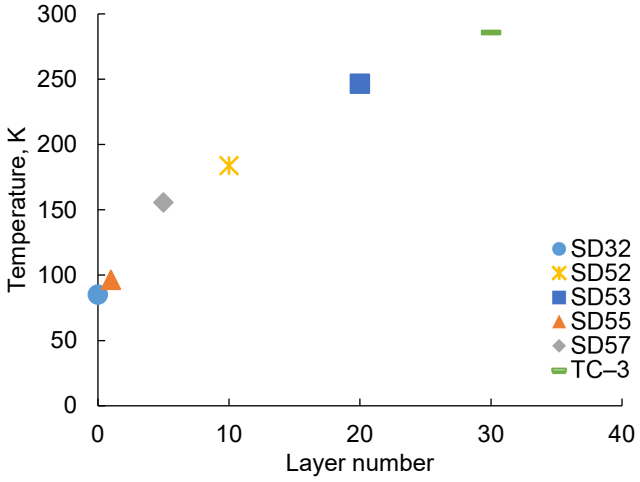

Figure 267.—Liquid nitrogen boiloff testing multilayer insulation profile.

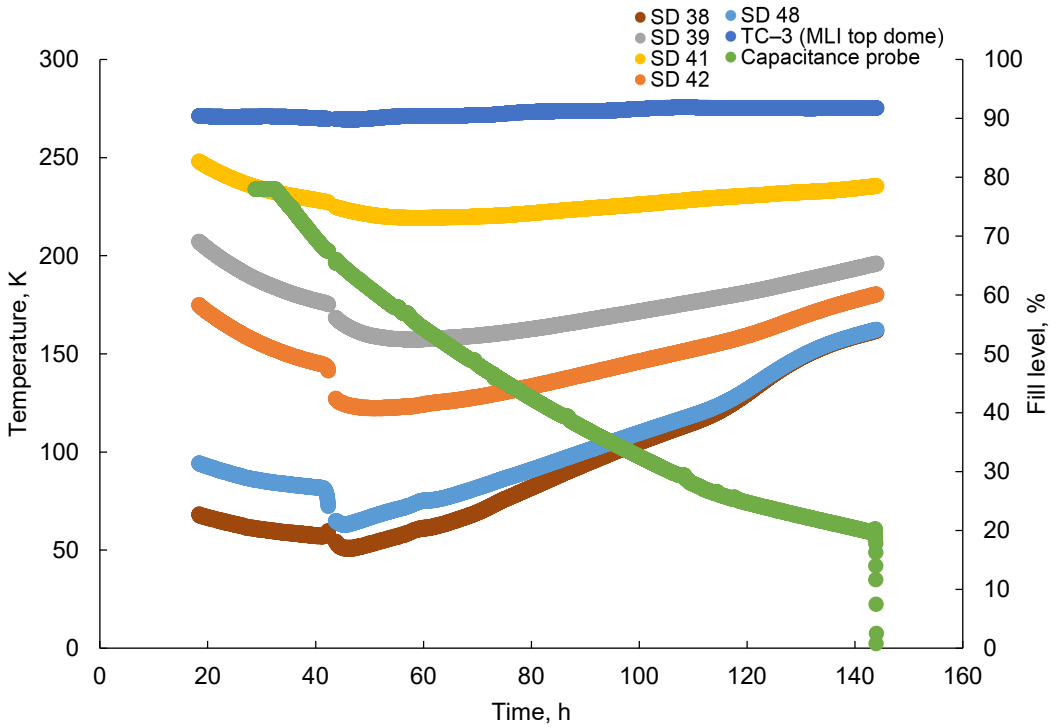

Figure 268.—Forward dome stack 2 during liquid hydrogen postacoustic boiloff testing. Multilayer insulation (MLI).

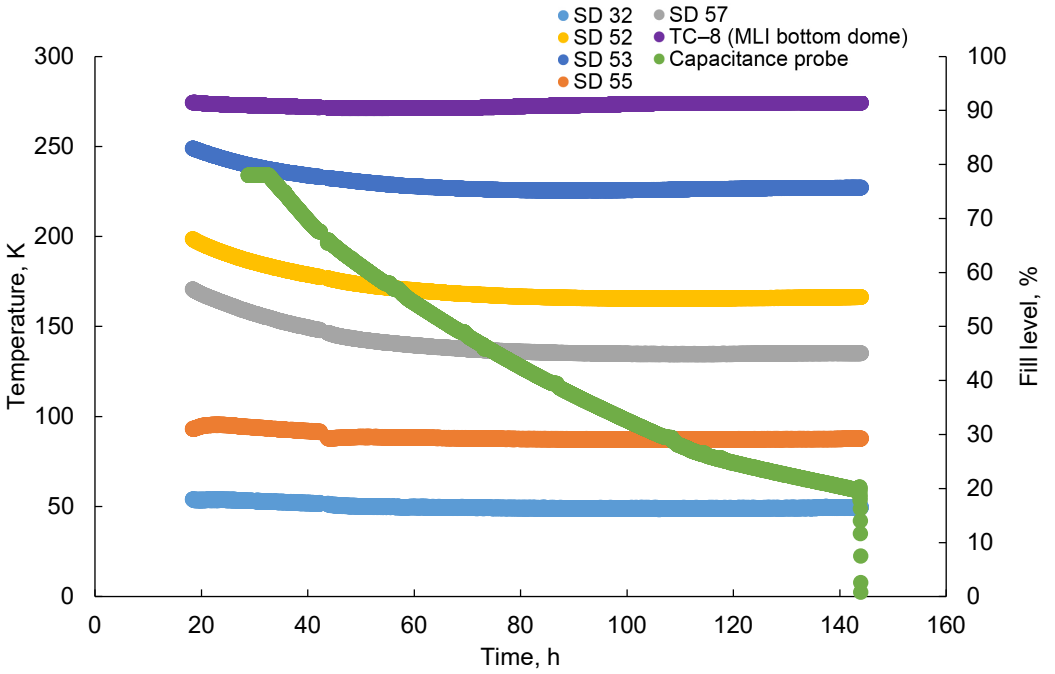

Figure 269.—Aft dome stack 2 during liquid hydrogen postacoustic boiloff testing. Multilayer insulation (MLI).

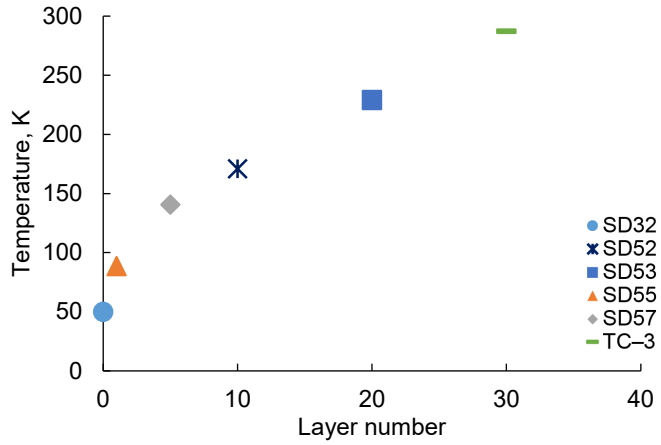

Figure 270.—Postacoustic liquid hydrogen boiloff testing multilayer insulation profile.

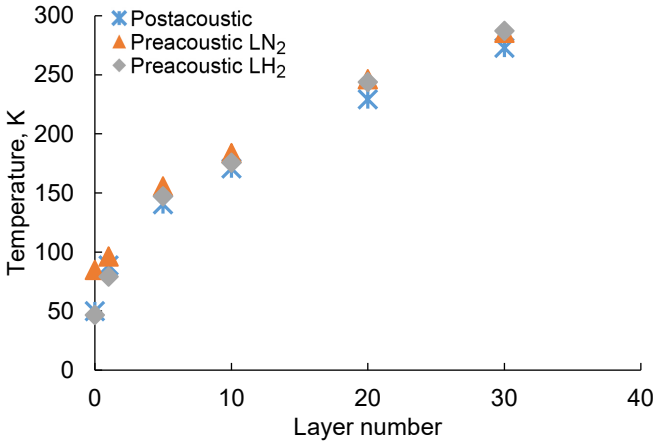

Figure 271.—Aft dome temperature profiles for all three tests. Liquid nitrogen (LN_2). Liquid hydrogen (LH_2).

All three MLI profiles are shown in Figure 271 and tabulated in Table 35. In comparing the preacoustic LH_2 and LN_2 tests, the SOFI external temperatures were very different between tests, but the MLI layer temperatures were actually very similar. The MLI layer 1 temperatures were much closer together and continued to converge together until by the 20th layer they were within 2.7 K of each other. This suggests that the heat flowing through the blankets was very similar for the two tests. Comparing the preacoustic and postacoustic LH_2 temperatures, the first layer was a bit warmer on the postacoustic test while the rest of the layers were progressively cooler in relation. This may indicate a slightly larger heat flow between the MLI and the SOFI. However, as previously noted, that difference was overwhelmed by the environmental effects on the whole test article.

TABLE 35.—MULTILAYER INSULATION (MLI) PROFILE TEMPERATURES FOR AFT DOME

MLI layer	Diode	Postacoustic LH_2[a]	Preacoustic LN_2[b]	Preacoustic LH_2[a]
0	SD32	49.9	85.1	46.8
1	SD55	88.7	96.5	79.3
5	SD57	140.7	155.7	147.2
10	SD52	170.9	183.8	175.7
20	SD53	229.3	246.6	243.9
30	TC–3	273.1	285.8	287.4

[a]Liquid hydrogen (LH_2).
[b]Liquid nitrogen (LN_2).

5.10 Heat Flux Sensors

The 12 heat flux sensors that were on the tank yielded very interesting results. Based on the calibration results (Ref. 56), the heat flux sensors voltage was converted to heat flux $\dot{q}$ using the equation:

$$\dot{q} = \frac{V_{\text{sensor}}}{a} + b \tag{34}$$

where a is the sensor sensitivity provided by the vendor in $\mu V/(W/m^2)$, V_{sensor} is the sensor voltage, and b is a zero heat flux offset in W/m^2. The zero heat flux offset was determined based on the voltage at ambient temperature prior to filling the SHIIVER test article for the preacoustic LH_2 testing between hours 0.75 and 0.85.

Calibration of the heat flux sensors did not yield a low uncertainty with the sensors, but did show that the sensitivities provided by the manufacturer were generally appropriate at both 20 and 77 K. The calibration exercise also gave general confidence that the sensors would work and showed they could be installed upside down or wired backwards (reads out negative voltage). Voltage sign was correctable in the data system.

During testing, in order to keep the heat flux sensors reading within range of the DAQ system, voltage gains were used. Table 36 shows the gains for each heat flux sensor at the start of each test and any time during the test when they were changed. The gain (G) was simply a multiplication factor to yield the measured voltage V_{measured} as:

$$V_{\text{measured}} = GV_{\text{sensor}} \tag{35}$$

Table 37 shows the measured voltage, applied gain, and the calculated zero heat flux voltage for each sensor. It was found that some sensors appeared to be plugged in backwards in reference to their installation. As such, care was taken to convert the negative heat fluxes to positive heat fluxes (referenced to positive heat flux going into the tank) after the zero heat flux was set. The zero heat flux data is shown in Figure 272 and Figure 273. Table 38 shows the vendor provided sensitivities for each of the sensors.

In processing the data for each of the sensors, it was found to be easier to understand how the sensors were behaving by using location grouped plots (such as barrel and domes) as opposed to time grouped plots throughout testing. This is described in the following information:

TABLE 36.—CHANGING OF GAIN ON EACH HEAT FLUX SENSOR (HFS) DURING TESTING

Test	Baseline LH_2[a]					Thermal 1 LH_2[a]		Thermal 1 LN_2[b]		Thermal 2 LH_2[a]	
Date	8/23/2019	8/24/2019	8/25/2019	8/26/2019	8/29/2019	9/23/2019	9/23/2019	10/2/2019	10/12/2019	1/21/2020	1/21/2020
Time, EST	3:15 p.m.	4:10 p.m.	11:59 a.m.	12:49 p.m.	9:00 a.m.	7:57 a.m.	4:20 p.m.	9:00 a.m.	8:00 a.m.	9:00 a.m.	5:41 p.m.
HFS01	128	128	128	128	128	128	256	256	256	128	128
HFS02	128	128	128	128	128	128	256	256	256	128	128
HFS03	128	128	128	128	128	128	256	256	256	128	128
HFS04	128	128	128	128	128	128	1,024	1,024	1,024	128	128
HFS05	128	128	128	128	128	128	512	512	512	128	128
HFS06	128	128	128	128	128	128	512	512	512	128	128
HFS07	128	128	128	128	128	128	512	512	512	128	128
HFS08	128	128	128	128	128	128	512	512	512	128	128
HFS09	128	128	128	128	128	128	128	128	128	128	128
HFS10	2,048	2,048	2,048	2,048	2,048	2,048	128	128	128	2,048	256
HFS11	128	128	128	128	128	128	128	128	128	128	128
HFS12	2,048	128	128	128	128	128	128	128	128	128	128
HFS17	128	1,024	1,024	1,024	1,024	1,024	128	128	128	64	64
HFS18	128	128	64	64	64	64	64	64	64	64	64
HFS19	128	128	128	64	64	64	128	128	128	128	128
HFS20	128	128	128	128	128	128	128	128	128	128	128

[a]Liquid hydrogen (LH_2).

[b]Liquid nitrogen (LN_2).

TABLE 37.—CALCULATION OF ZERO
HEAT FLUX OFFSET VALUES
[Heat flux sensor (HFS).]

Sensor	Measured voltage	Gain	Zero heat flux sensor voltage
Forward dome			
HFS01	0.0021	128	1.68×10^{-5}
HFS02	.0078	128	6.06×10^{-5}
HFS03	.0041	128	3.18×10^{-5}
HFS04	.0076	128	5.90×10^{-5}
Aft dome			
HFS05	–0.0006	128	-4.56×10^{-6}
HFS06	.0026	128	2.06×10^{-5}
HFS07	.0004	128	2.85×10^{-6}
HFS08	.0028	128	2.19×10^{-5}
Tank barrel			
HFS09	0.0424	128	3.31×10^{-4}
HFS10	.5676	2,048	2.77×10^{-4}
HFS11	–.0197	128	-1.54×10^{-4}
HFS12	–.0328	128	-2.56×10^{-4}
Forward skirt			
HFS17	–0.0038	1,024	-3.73×10^{-6}
HFS18	–.0169	64	-2.64×10^{-4}
HFS19	–.0147	64	-2.30×10^{-4}
HFS20	–.0100	128	-7.84×10^{-5}

TABLE 38.—SENSITIVITY OF EACH CAPTEC
ENTREPRISE HEAT FLUX SENSOR (HFS)
[Sensors procured for Structural Heat Intercept, Insulation, and Vibration Evaluation Rig (SHIIVER). Values provide by Captec Entreprise.]

Sensor	Sensitivity, $\mu V/(W/m^2)$	Sensor	Sensitivity, $\mu V/(W/m^2)$
HFS01	361	HFS09	357
HFS02	362	HFS10	358
HFS03	363	HFS11	366
HFS04	346	HFS12	359
HFS05	346	HFS17	356
HFS06	348	HFS18	367
HFS07	353	HFS19	372
HFS08	364	HFS20	335

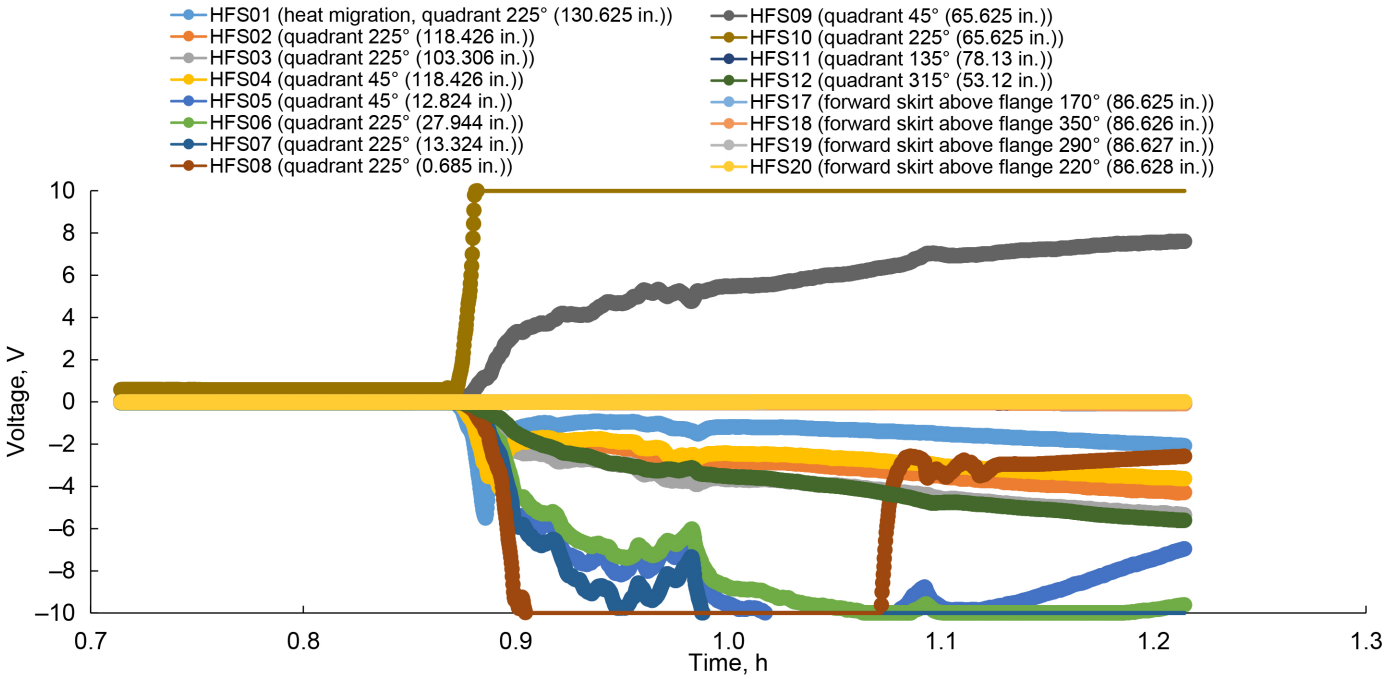

Figure 272.—Heat flux sensor measured voltage data during preacoustic test chilldown, plot shows values over data acquisition input range.

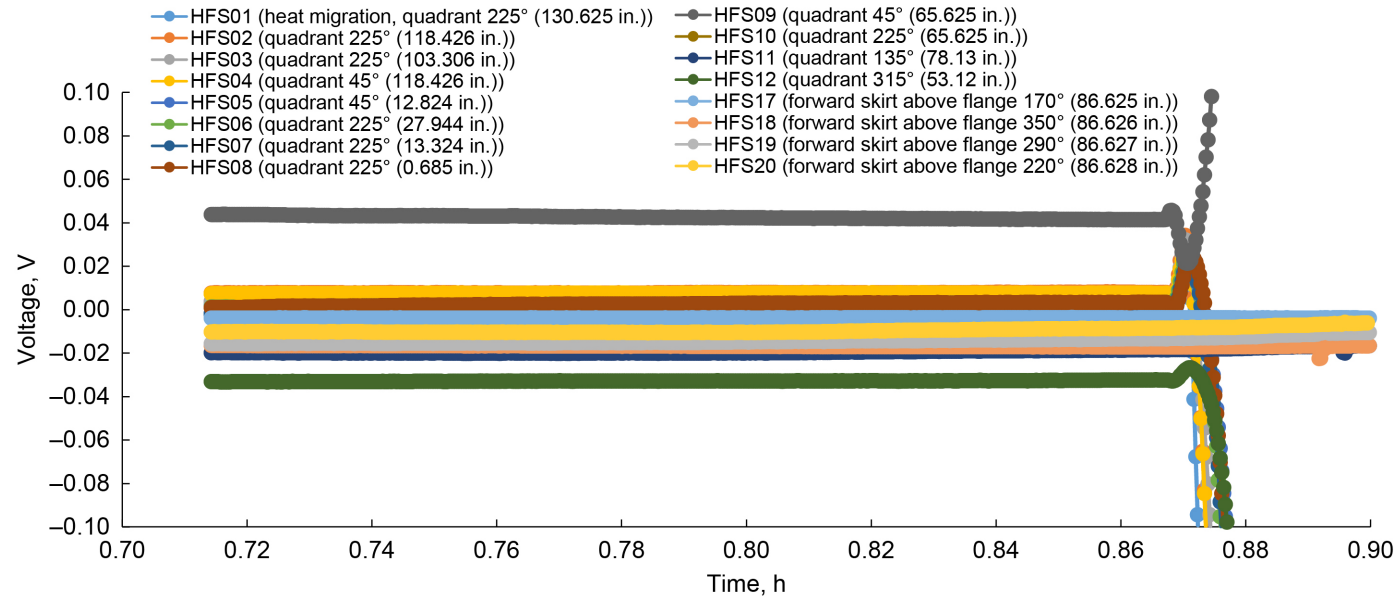

Figure 273.—Heat flux sensor data during preacoustic test chilldown, showing section used for zero-offset calculations.

5.10.1 Barrel Spray-On Foam Insulation Heat Flux Sensors

Four heat flux sensors were placed on the outside of the tank barrel. The sensors HFS09 (45°) and HFS10 (225°) were installed in line with the heaters on the midline (50 percent full) of the tank. Sensor HFS11 was installed centered on 135° and 0.32 m (12.5 in.) above the center line at a fill level of approximately 65 percent full. Sensor HFS12 was installed centered on 315° and 0.34 m (13.5 in.) below the center line at a fill level of approximately 40 percent.

Based on the external temperature of the SOFI (~245 K), the measured SOFI thickness, and the measured thermal conductivities of the Stepan S-180 SOFI (Stepan Company), the expected heat flux for baseline testing would be between 160 to 210 W/m^2 as shown in Table 39, depending on heat flux sensor location. The thermal conductivities used are all measured at a pressure of one atmosphere. Measurements by Fesmire (Ref. 33) and Barrios (Ref. 57) suggest that the performance of SOFI increases with residual gas pressure, which for SHIIVER was in the 10^{-4} to 10^{-6} torr range. It is also suggested that both aging and weathering can negatively affect SOFI thermal conductivity (increase conductivity). The SHIIVER test article was covered once it was shipped from Marshall Space Flight Center with skirts and a tarp to protect it from ultraviolet, however, during storage a small portion of it did start to color. Additionally, from the date of spray to the start of the baseline test was 424 days, so the aging of the SOFI, as indicated by Fesmire, would certainly have taken place. As such, the exact thermal conductivity of the SOFI has uncertainty, but with lack of other data, values from Reference 2 are used to compare the heat flux sensor data.

During the baseline testing, HFS10 never read an appropriate heat flux. After approximately 28 h, the gain was reduced on HFS12 to bring the measured voltage into the range of the DAQ system, such that it read approximately 80 W/m^2 (see Figure 274 and Figure 275). Since the gain was adjusted down, the sensor went from being "off scale high," to being read by the DAQ system still skewing the calculated heat flux, to on scale. During the boiloff testing, HFS09 varied between 20 and 100 W/m^2, seemingly at the lower value when the sensor was wetted and the higher value when the sensor was against dry tank. Sensor HFS11 varied between 140 and 200 W/m^2, with the lower value at higher fill levels and higher value at lower fill levels. These are seemingly on the right order of magnitude as the expected values shown in Table 39, but do not inspire a lot of confidence with respect to accuracy.

TABLE 39.—CALCULATED HEAT FLUXES EXPECTED AT HEAT FLUX SENSOR (HFS) LOCATIONS ON BARREL

Sensor	Mean SOFI[a] thickness, m (in.)	Baseline heat flux, W/m^2 (WBT[b] ~245 K)	Preacoustic heat flux, W/m^2 (WBT[b] ~260 K)	Postacoustic heat flux, W/m^2 (WBT[b] ~240 K)
HFS09	0.020 (0.804)	196	214	190
HFS10	.019 (.752)	210	230	203
HFS11	.021 (.810)	194	213	188
HFS12	.025 (.984)	160	176	155

[a]Spray-on foam insulation (SOFI).

[b]WBT is the warm boundary temperature of the SOFI, an average of SD33, SD34, SD35, and SD36.

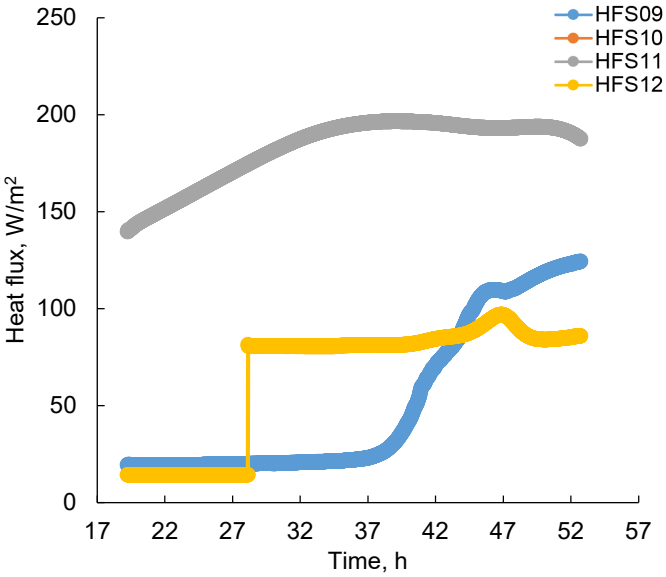

Figure 274.—Barrel heat flux sensors during baseline boiloff testing.

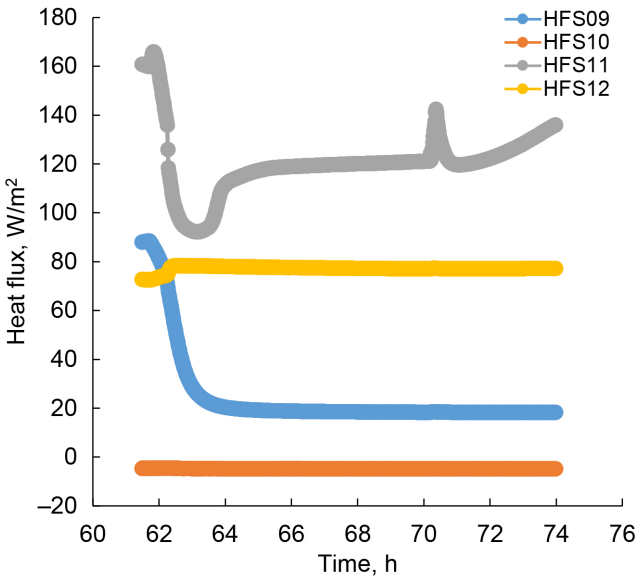

Figure 275.—Barrel heat flux sensor data during baseline vapor-cooling testing at high fill level.

During Thermal 1 testing, similar trends could be seen on the heat flux sensors (see Figure 276), except now, HFS10 began to work after the 50-percent-fill-level pressure rise testing. The heat flux sensors readings are similar for the Thermal 1 and baseline testing. Thermal 2 testing (see Figure 277) also shows similar trends, but lower values due to the lower environmental temperatures. The values in Table 39 are not that much different between the Thermal 2 and baseline tests because the diodes on the SOFI surface were at similar temperatures even though the cold wall temperatures varied more.

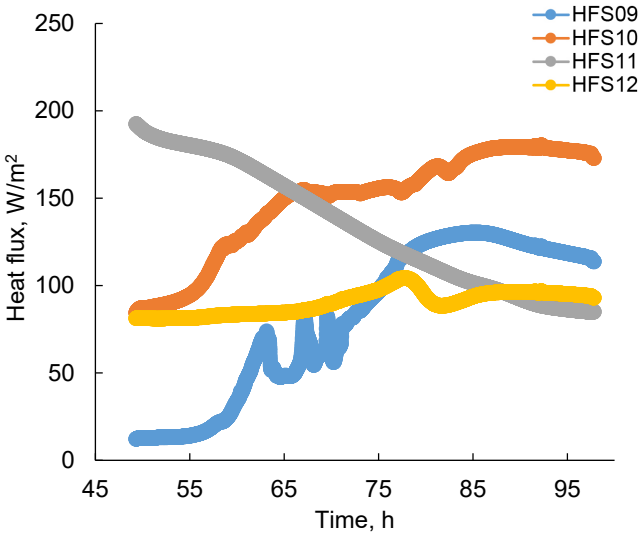

Figure 276.—Thermal 1 test heat flux sensor data during low-fill-level boiloff testing.

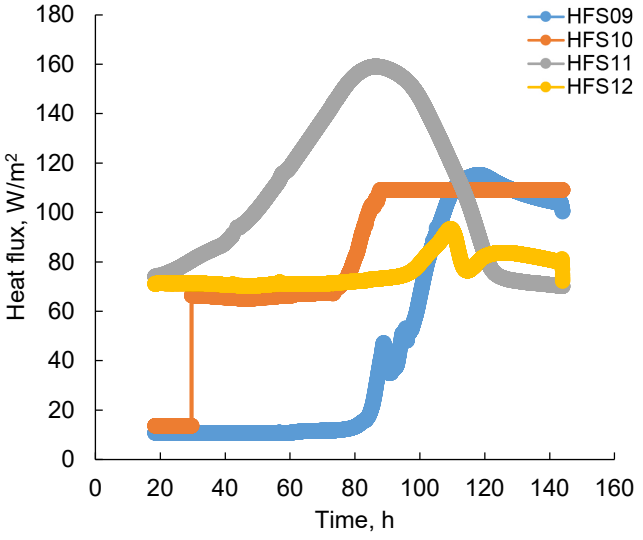

Figure 277.—Heat flux sensors during liquid hydrogen postacoustic testing.

5.10.2 Aft Dome Heat Flux Sensors

Four heat flux sensors were placed on the outside of the aft dome. Sensor HFS08 was centered at 225° and a measured arc length of approximately 0.13 m (5.3 in.) off of the aft manway at a fill level of approximately 1 percent full. Sensors HFS07 (225°) and HFS05 (45°) were both centered at an arc length of 0.94 m (37.1 in.) off of the aft manway at a fill level close to 4 percent full. Sensor HFS06 was centered at 225° and an arc length of 1.51 m (59.5 in.) from the aft manway at a fill level of approximately 14 percent.

Heat fluxes measured on the aft dome were fairly consistent over time as shown in Figure 278 to Figure 281. For the preacoustic and postacoustic tests, it is also consistent with MLI temperatures in the aft dome being relatively flat as shown in Section 5.9. Comparing values between the plots and Table 40, the heat fluxes in the plots for the baseline tests are approximately half that of the calculated SOFI heat fluxes. Once the MLI was installed, the SOFI-derived heat fluxes and measured heat fluxes are different by an order of magnitude. However, the calculations at the low heat fluxes with SOFI are somewhat questionable due to the limited low-temperature SOFI data available. It can also be seen, comparing Figure 280 and Figure 281, that the measured MLI heat flux decreased with the lower environmental temperatures for the postacoustic tests, whereas the calculated SOFI heat flux did not. Taking all of this into account, it is probably safe to say that the MLI heat leak was less than 1 W/m^2 and that there was a decrease in the postacoustic test that is accounted for in the change in environmental temperature. However, reading much more into the data is not possible.

TABLE 40.—CALCULATED HEAT FLUXES EXPECTED AT HEAT FLUX SENSOR (HFS) LOCATIONS ON AFT DOME BASED ON SPRAY-ON FOAM INSULATION (SOFI) TEMPERATURES

[Warm boundary temperature of the SOFI is SD32.]

Sensor	Mean SOFI thickness, m (in.)	Baseline heat flux, W/m^2	Preacoustic heat flux, W/m^2	Postacoustic heat flux, W/m^2
HFS05	0.025 (0.971)	155	12	14
HFS06	.030 (1.168)	129	9.7	11
HFS07	.028 (1.087)	138	10	12
HFS08	.033 (1.285)	117	8.8	11

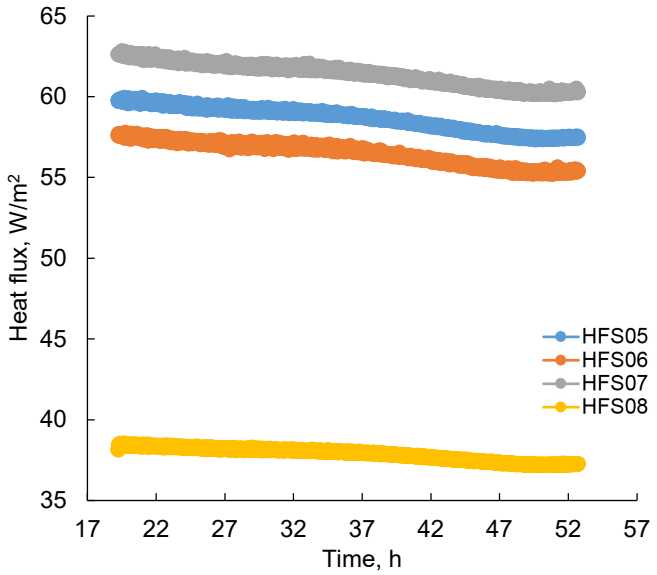

Figure 278.—Heat flux sensors during baseline boiloff, medium and low fill levels.

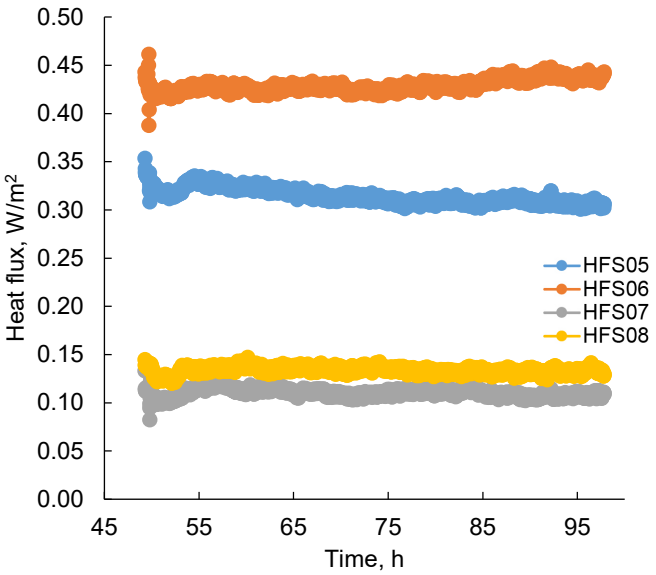

Figure 280.—Heat flux sensor response during preacoustic thermal testing at low fill levels.

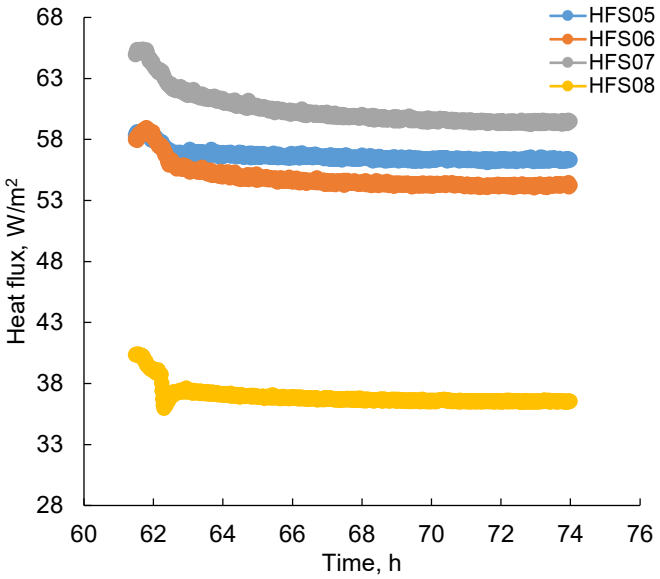

Figure 279.—Heat flux sensors during baseline vapor-cooling test, high fill level.

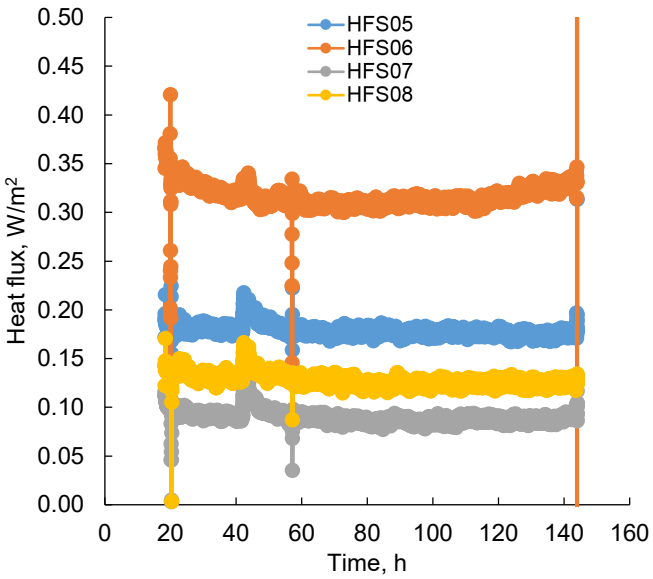

Figure 281.—Aft dome heat flux sensor response during postacoustic thermal boiloff testing.

5.10.3 Forward Dome Sensors

Four heat flux sensors were placed on the outside of the forward dome. Sensor HFS01 was centered at 225° and a measured arc length of approximately 0.13 m (5.3 in.) off of the forward manway at a fill level greater than 99 percent full. Sensors HFS02 (225°) and HFS04 (45°) were both centered at an arc length of 0.94 m (37.1 in.) off of the forward manway at a fill level close to 96 percent full. Sensor HFS03 was centered at 225° and an arc length of 1.51 m (59.5 in.) from the forward manway at a fill level of approximately 86 percent.

During the baseline testing, the heat flux measured on the forward dome was fairly steady after some initial transients in the system (see Figure 282 and Figure 283), however, once the MLI was installed, the heat flux measured on the forward dome is strongly dependent on fill level (see Figure 284). The heat fluxes calculated through the forward dome in Table 41 are generally lower due to the thicker SOFI and trend of the forward dome to warm up as the fill level significantly decreased during tests with MLI. Figure 285 shows the temperature of the tank dome wall and SOFI exterior during preacoustic testing and it is seen that the SOFI is colder than the tank dome, especially towards the end of the testing period. This is calculated numerically in Table 41. Figure 286 shows a similar trend in the postacoustic testing, but with lower absolute values as the measured heat fluxes decrease due to the lower environmental temperatures. The calculations in Table 41 do not show a decrease between the preacoustic and postacoustic tests but are at different times in the test profile so should not be taken as a ratio of heat fluxes between the two tests.

TABLE 41.—CALCULATED HEAT FLUXES EXPECTED AT HEAT FLUX SENSOR (HFS) LOCATIONS ON FORWARD DOME

[Warm boundary temperature of the spray-on foam insulation (SOFI) is SD37.]

Sensor	Mean SOFI thickness, m (in.)	Baseline heat flux, W/m^2	Preacoustic heat flux,[a] W/m^2	Postacoustic heat flux,[b] W/m^2
HFS01	0.028 (1.08)	143	–4.8	0.90
HFS02	.037 (1.47)	105	–3.6	.66
HFS03	.031 (1.24)	125	–4.2	.78
HFS04	.042 (1.65)	94	–3.2	.59

[a]Taken between the hours of 94 and 95.

[b]Taken between the hours of 32 and 35.

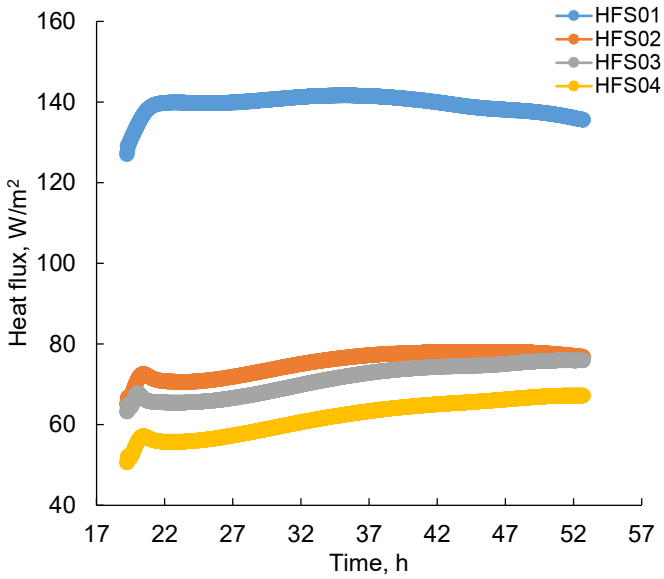

Figure 282.—Forward dome heat flux sensors during baseline boiloff testing medium to low fill level.

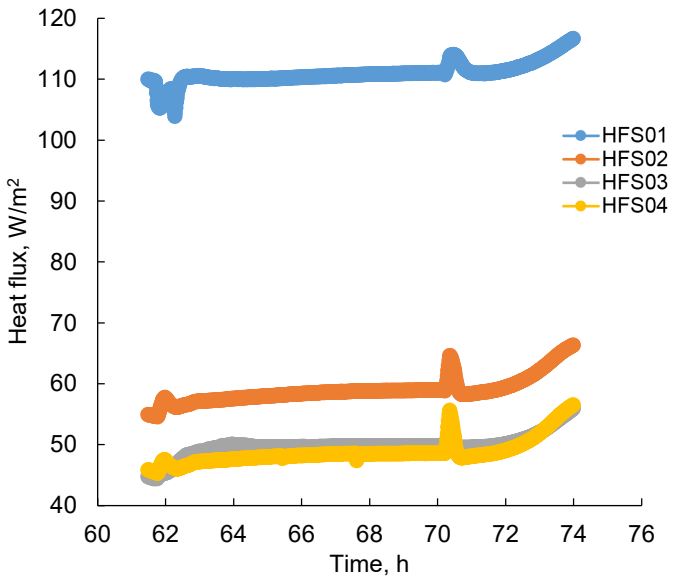

Figure 283.—Heat flux sensors during baseline vapor-cooling testing at high fill levels.

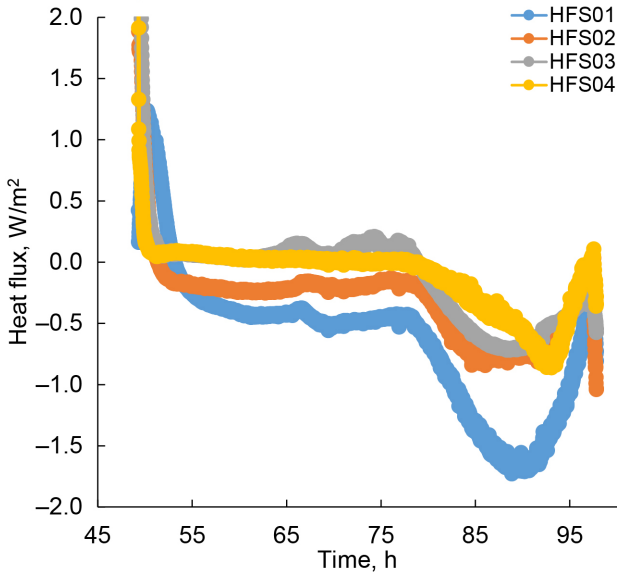

Figure 284.—Heat flux sensors during preacoustic thermal boiloff testing at low fill levels.

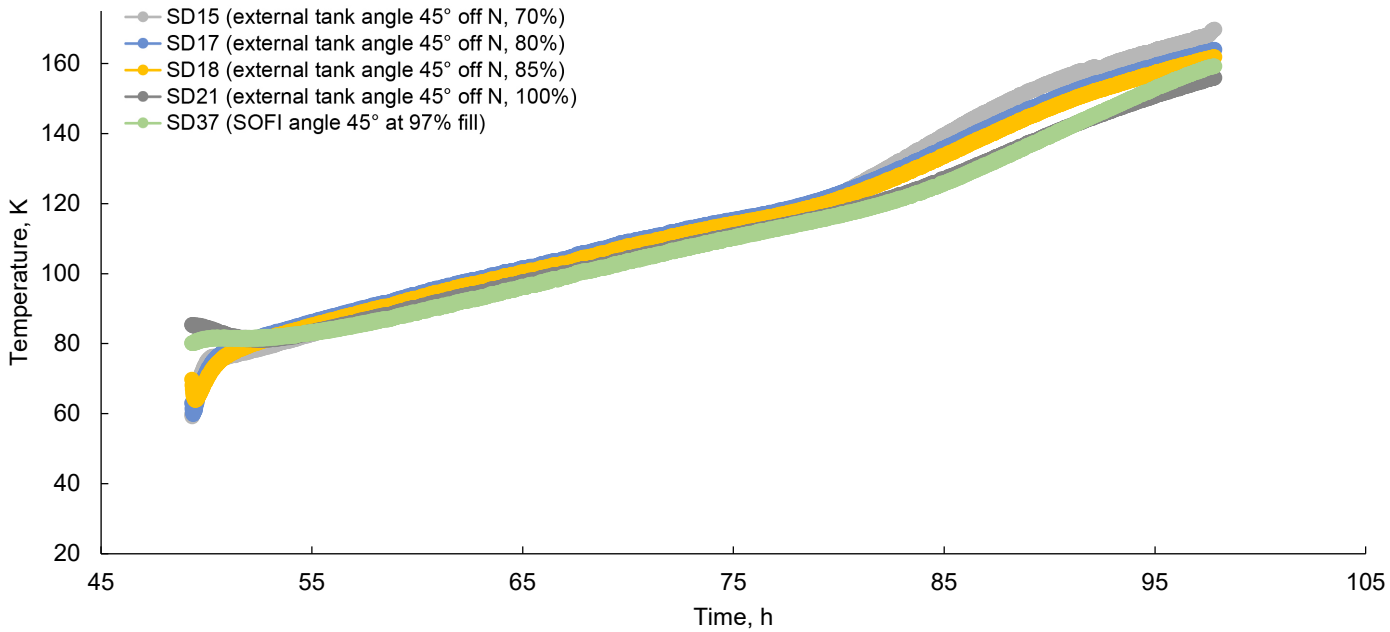

Figure 285.—Forward dome tank wall and spray-on foam insulation (SOFI) temperatures during preacoustic boiloff testing.

5.10.4 Forward Skirt Heat Flux Sensors

Four heat flux sensors were placed on the outside of the forward skirt. Sensor HFS17 was centered at 180° with the bottom of the sensor approximately 0.17 m (6.5 in.) above the forward flange, however, it never gave a good reading during any part of the testing. Sensor HFS18 was placed such that the right side of the sensor was on the 0° line and also 0.17 m above the forward flange. Sensor HFS19 was centered at 290° and 0.53 m (21 in.) above the forward flange. Sensor HFS20 was centered at 220° and 0.46 m (18 in.) above the forward flange.

Based on the locations of the heat flux sensors, it would be expected that HFS18 would have the highest heat flux and HFS19 is slightly higher than HFS20. That is seen to be generally true throughout (see Figure 287 and Figure 288). There are several times when the gains for these heat flux sensors were changed and a dramatic change in output is seen. It is also seen between Figure 289 and Figure 290 that turning on the vapor-cooling loop significantly cooled the skirt and increased the heat flux. Some of the trends in the data, especially the big peak in Figure 291 are not fully understood at this time.

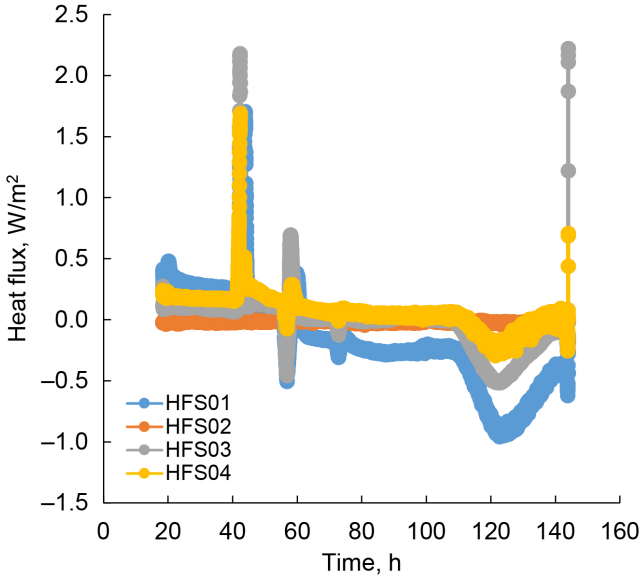

Figure 286.—Heat flux sensors during postacoustic thermal boiloff testing at all fill levels.

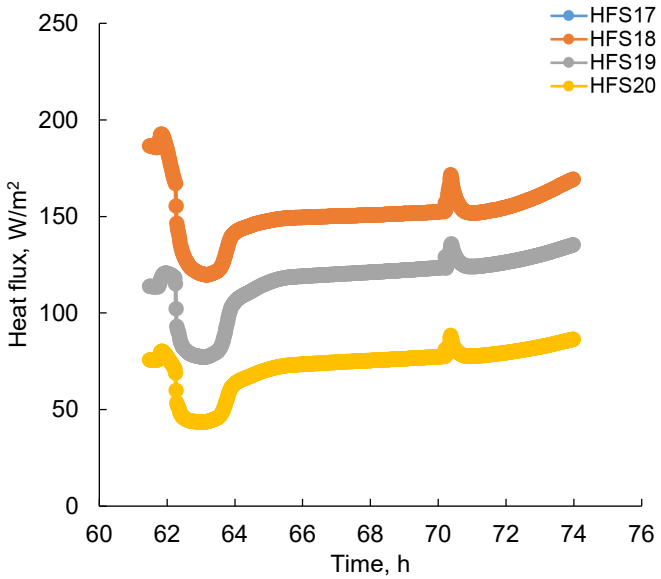

Figure 288.—Forward skirt heat flux sensors during baseline vapor-cooling testing at high fill level.

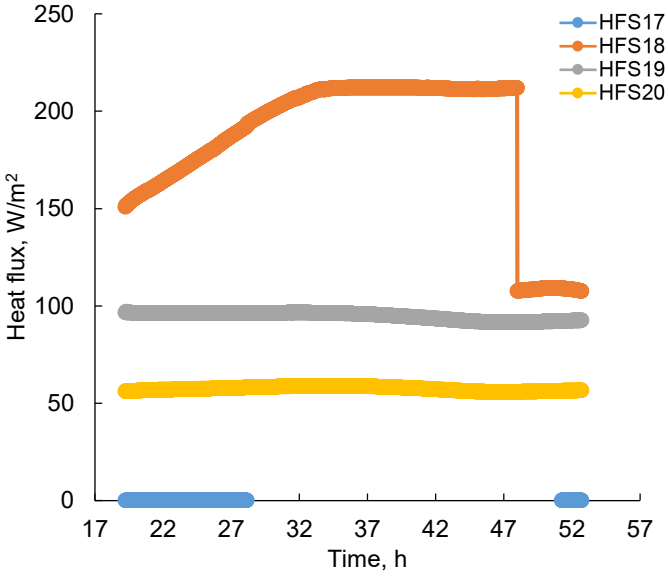

Figure 287.—Forward skirt heat flux sensors during baseline boiloff test at medium to low fill levels.

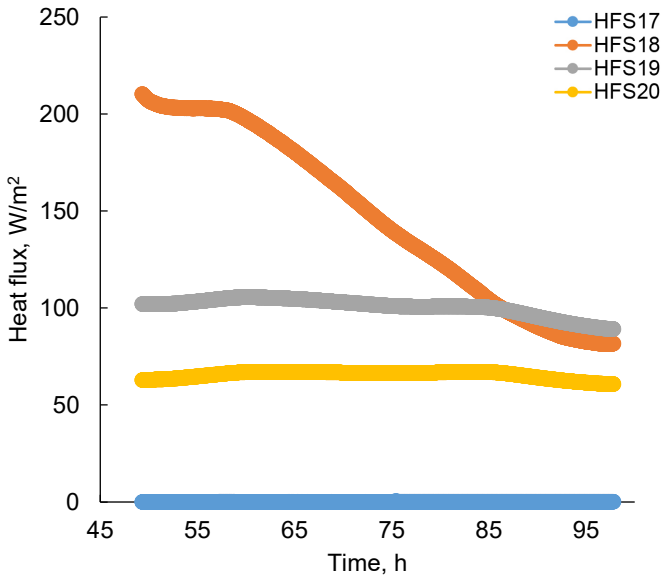

Figure 289.—Forward skirt heat flux sensors during preacoustic boiloff testing at low fill level.

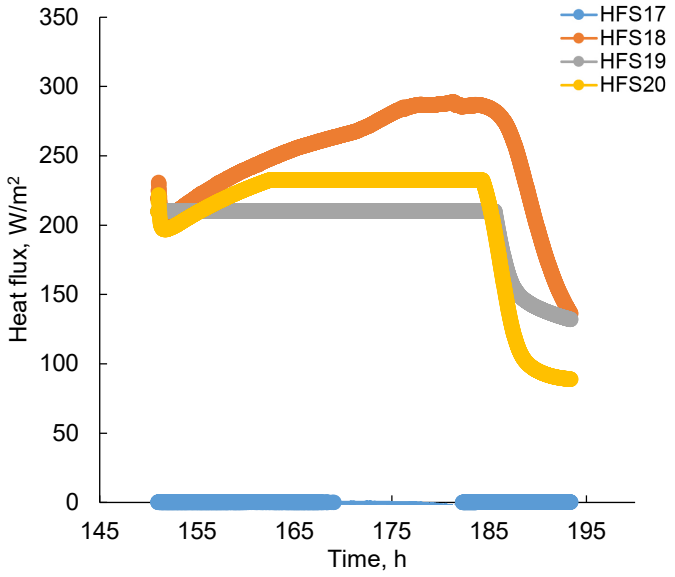

Figure 290.—Forward skirt heat flux sensors during preacoustic testing with vapor cooling at low fill level.

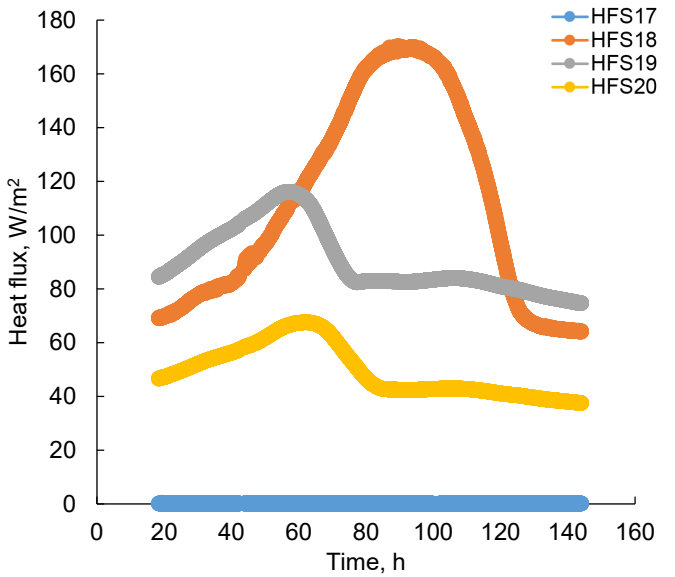

Figure 291.—Forward skirt heat flux sensors during postacoustic boiloff testing at all fill levels.

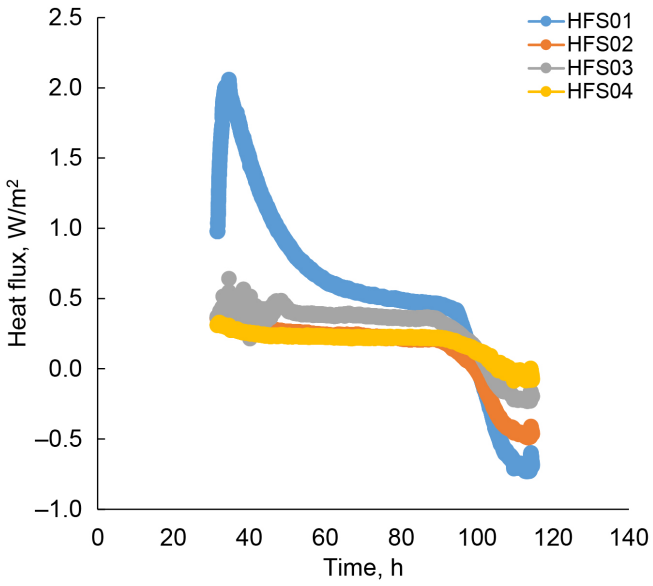

Figure 292.—Forward dome heat flux sensor response during liquid nitrogen boiloff testing.

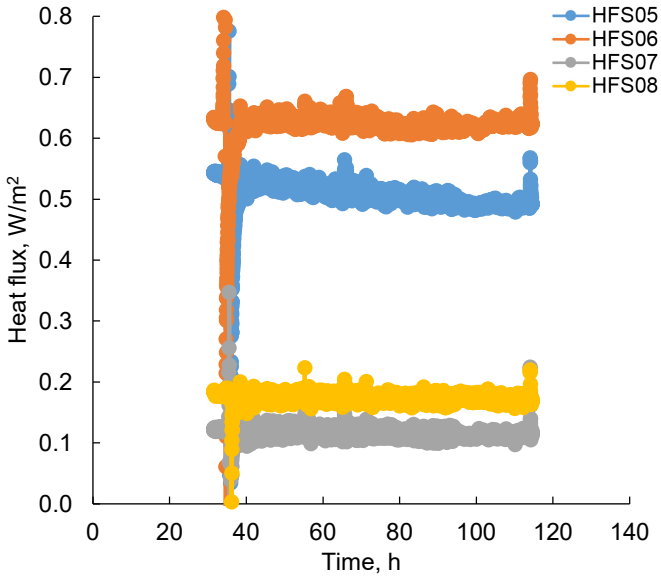

Figure 293.—Aft dome heat flux sensor response during liquid nitrogen boiloff testing.

5.10.5 Liquid Nitrogen Testing

In general, the heat flux sensors had a very similar response during LN_2 testing as during LH_2 testing (see Figure 292 and Figure 293). In the figures, HFS10 does fail just after 60 h. However, as seen in Table 42, the heat flux sensors all read a higher heat flux during nitrogen testing. This is quite interesting as one would expect the opposite to occur due to the larger temperature difference in the MLI blankets during LH_2 testing. However, due to the overwhelming impact of the heat loads through the structural elements and the barrel, the heat flux cannot be verified via boiloff measurements. Similar effects have been noted in the calibration tests with the heat flux sensors (Ref. 56). Standing alone, it could be attributed to possible temperature sensitivity of the sensors zero heat load offset. However, it has also been identified by Black and Glaser (Ref. 58) and Srinivasan (Ref. 59). While each report gave reasons that the observed phenomena could be being masked, Elchert (Ref. 60) showed that temperature dependent spectral emissivity properties could numerically explain the difference.

It is hard to tell based on reviewing the data, but in general, the heat flux sensors on the barrel behaved much better during

postacoustic testing than during preacoustic testing (see Figure 294), but the heat fluxes are of the same range.

6.0 General Summary and Lessons Learned

The SHIIVER testing provided a large amount of data, not all of which has been fully evaluated, especially from the vapor-cooling testing and the forward skirt. A summary on the system-level performance as well as the component-level performances are provided along with lessons learned by the team through the preparation and testing.

6.1 General Summary

Table 43 shows the heat load to the tank at various fill levels, and Table 44 shows the associated heat load reductions for the various test series relative to the baseline test. For the hydrogen tests, the maximum heat load is 7,117 W (baseline test, 90 percent fill level) and the minimum heat load is 2,537 W (postacoustic test, 25 percent fill level). Vapor cooling reduces the baseline heat load by 5 to 19 percent (depending on the fill level). The addition of MLI resulted in heat load reduction of 42 to 58 percent, and the combined effect of MLI and vapor cooling resulted in heat load reduction of 51 to 62 percent.

Table 45 shows the boiloff flow rate at various fill levels, and Table 46 shows the associated boiloff flow rate reduction. Comparing similar tests with and without vapor cooling, it is seen that vapor cooling is effective for fill levels above 70 percent, with reductions in the boiloff flow rate by 6 to 49 percent for baseline tests and 15 to 33 percent for tests with MLI.

TABLE 42.—AVERAGED MEASURED HEAT FLUXES ON AFT DOME DURING STEADY-STATE MULTILAYER INSULATION TESTING
[Heat flux sensor (HFS).]

Sensors	Preacoustic LH_2,[a] W/m^2	Postacoustic LH_2,[a] W/m^2	Preacoustic LN_2,[b] W/m^2
HFS05	0.31	0.18	0.50
HFS06	.43	.32	.62
HFS07	.11	.09	.12
HFS08	.14	.12	.18

[a]Liquid hydrogen (LH_2).
[b]Liquid nitrogen (LN_2).

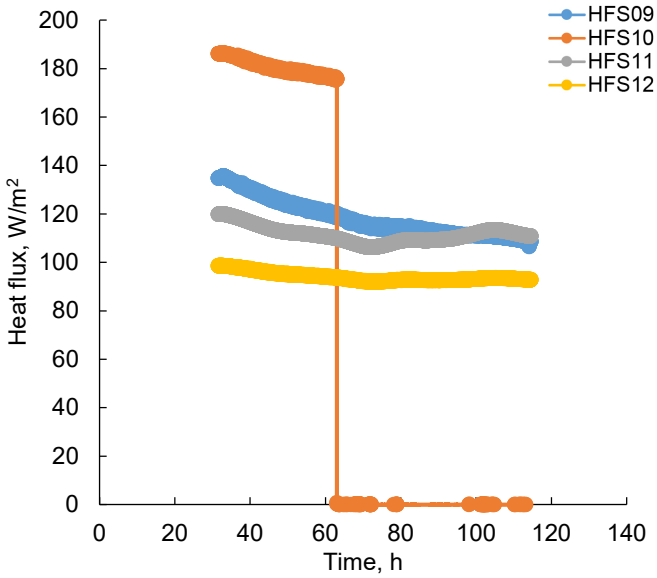

Figure 294.—Heat flux sensor response during liquid nitrogen testing on tank barrel.

TABLE 43.—FILL-LEVEL-AVERAGED TANK HEAT LOADS

Test	Fill level (±2.5), percent						
	90	80	70	60	50	35	25
	Total average tank heat load, W						
Liquid hydrogen (LH_2) baseline	7,117	6,873	6,854	6,708	6,810	6,784	6,489
LH_2 vapor cooling	5,738	5,925	5,847	6,055	6,151	6,317	6,176
Preacoustic LH_2	3,799	3,844	3,882	3,864	3,731	3,402	2,749
Preacoustic LH_2 vapor cooling	2,671	2,669	2,698	2,915	3,070	3,301	2,666
Preacoustic liquid nitrogen (LN_2)	3,640	3,355	3,212	NA	NA	NA	NA
Preacoustic LN_2 vapor cooling	3,281	NA	NA	NA	2,886	NA	1,873
Postacoustic LH_2	NA	3,329	3,316	3,353	3,426	3,296	2,537

TABLE 44.—FILL-LEVEL-AVERAGED TANK HEAT LOAD REDUCTION

Test	Fill level (±2.5), percent						
	90	80	70	60	50	35	25
	Heat load reduction, percent						
Liquid hydrogen (LH_2) vapor cooling from baseline	19	14	15	10	10	7	5
Preacoustic LH_2 from baseline	47	44	43	42	45	50	58
Preacoustic LH_2 vapor cooling from baseline	62	61	61	57	55	51	59
Preacoustic LH_2 vapor cooling from preacoustic LH_2	30	31	30	25	18	3	3
Preacoustic liquid nitrogen (LN_2) vapor cooling from preacoustic LN_2	10	NA	NA	NA	NA	NA	NA
Postacoustic LH_2 from baseline	NA	52	52	50	50	51	61

TABLE 45.—FILL-LEVEL-AVERAGED EQUIVALENT BOILOFF FLOW RATES

Test	Fill level (±2.5), percent						
	90	80	70	60	50	35	25
	Equivalent boiloff flow rate, g/s						
Liquid hydrogen (LH_2) baseline	11.9	13.2	12.5	9.1	8.4	7.0	4.9
LH_2 vapor cooling	11.2	11.3	6.4	8.7	8.1	7.3	4.6
Preacoustic LH_2	10.9	11.3	5.9	5.1	4.5	3.1	1.5
Preacoustic LH_2 vapor cooling	7.5	7.5	5.0	5.4	4.7	3.1	1.5
Preacoustic liquid nitrogen (LN_2)[a]	20.5	21.8	20.4	NA	NA	NA	NA
Preacoustic LN_2 vapor cooling[a]	18.3	18.6	NA	NA	10.7	NA	4.6
Postacoustic LH_2	NA	9.5	7.1	5.4	4.4	3.6	1.6

[a]Actual boiloff rates.

TABLE 46.—FILL-LEVEL-AVERAGED EQUIVALENT BOILOFF FLOW RATE REDUCTION

Test	Fill level (±2.5), percent						
	90	80	70	60	50	35	25
	Equivalent boiloff flow rate reduction, percent						
Liquid hydrogen (LH_2) vapor cooling from baseline	6	14	49	4	3	–3	7
Preacoustic LH_2 from baseline	9	15	53	44	46	55	70
Preacoustic LH_2 vapor cooling from baseline	37	43	60	41	44	56	69
Preacoustic LH_2 vapor cooling from preacoustic LH_2	31	33	15	–5	–4	3	–3
Preacoustic liquid nitrogen (LN_2) vapor cooling from preacoustic LN_2[a]	11	15	NA	NA	NA	NA	NA
Postacoustic LH_2 from baseline	NA	28	43	41	48	49	68

[a]Actual boiloff rate reduction.

6.1.1 Multilayer Insulation System

The tank dome MLI system had a mass of 18.5 kg and the installation was completed in 4 days. The MLI system on the tank domes performed better than expected. Based on the heat flux sensor measurements, the heat load through the MLI was less than 1 W/m^2 compared to the design requirement of 1.1 W/m^2. The presence of MLI in the preacoustic and postacoustic tests enabled reductions in both boiloff and total heat load to the tank, compared with the values in the baseline tests.

It typically took the MLI about 80 h to attain a steady state and represented the longest time scale in the thermal response of the entire system. The forward dome MLI, however, never came to a true steady state because the top of the tank was continually warming up as the tests progressed and the liquid level decreased. Certain peculiarities were observed in the temperature within the tank that are attributed to the MLI. First, when the liquid level is above the forward flange, the tank was very isothermal and there was no distinction between the temperature of the liquid and the ullage (once the liquid level is below the forward flange, heat from the flange directly entered the ullage space, and the ullage temperature rose above that of the liquid). Second, when the liquid level is below the forward flange, most of the heat into the forward dome came in through the forward flange and not through the MLI (this heat was conducted by both the tank wall and by the hydrogen gas flow in the tank, and transported to the upper portion of the forward dome; the heat flux through the MLI on the forward dome was actually negative due to this energy flow pattern).

While originally contemplated during early test planning, tests were not performed with MLI on the barrel section of the tank. It is expected that barrel and skirt MLI systems, if feasible, would be very beneficial to heat load and boiloff reduction. However, such concepts are contingent on further development to demonstrate the technology can survive aerodynamic loads.

6.1.2 Vapor Cooling

From a heat-load-reduction point of view, vapor cooling performed quite well. There is a general confusion about "reduction in heat load" as compared to the amount of heat load removed via the vapor-cooling flow stream. The heat load into the vapor-cooled component is not the same with and without cooling. With a cooling flow activated, the total heat flow to the system is increased, due to a larger or colder section of the skirt (cooled surface) that slightly increases radiation heat transfer as well as shorter conduction paths. Thus, one cannot take the uncooled heat into the system, subtract out the heat being removed by the cooling flow, and use the difference as the new heating into the system.

In baseline testing, vapor cooling reduced the heat load from 5 to 19 percent for fill levels in the range 25 to 90 percent. The corresponding heat load reduction, due to vapor cooling, for the preacoustic LH_2 is 3 to 31 percent when compared with that test's uncooled heat load. For the preacoustic LN_2 test, vapor cooling reduced the heat load by 10 percent at a fill level of 90 percent. In general, vapor cooling has a larger benefit at higher fill levels, where the heat load from the forward skirt enters the liquid in the tank via the flange. When the liquid level is below the flange, there is less benefit from vapor cooling.

Unfortunately, several test anomalies caused increase uncertainty in boiloff flow rate data used to compare vapor-cooling performance. First, the tank pressure was not constant in both the baseline and preacoustic tests without vapor cooling; therefore, an equivalent boiloff flow rate that takes into account the fluid enthalpy increase due to the pressure rise has been used. Second, the flowmeter to measure the vapor-cooling flow rate was not operational during the baseline tests; therefore, the capacitance probe empirical correlation was used. Nevertheless, as with the heat load, the data shows vapor cooling has a substantial benefit at higher fill levels and a negligible benefit when the liquid level is below the forward flange. At a fill level of 80 percent, vapor cooling reduces the uncooled boiloff rate by 14 and 33 percent for the baseline and preacoustic LH_2 tests, respectively. Vapor cooling also has a modest benefit in the case of LN_2, with a heat load reduction of 10 percent and a boiloff reduction of 11 percent at a fill level of 90 percent.

The benefit of vapor cooling on self-pressurization is very clear and equally important. For the baseline and preacoustic tests, the reduction in the rate of pressure rise with vapor cooling is in excess of 50 and 33 percent, respectively.

A cyclical pressurization test with vapor cooling was performed during preacoustic testing, which was intended to simulate the operation of a bang-bang pressure control system such as a TVS. However, it did not produce a significant benefit. At the end of three cycles, the rate of pressurization was rising, appearing to approach that without vapor cooling. Furthermore, vapor cooling was on during 60 percent of each cycle, which is much greater than the 5- to 10-percent durations in a typical bang-bang pressure control system.

The combined effect of vapor cooling and MLI appears to be very beneficial. The two technologies appear complementary to each other, and the reduction in heat loads from the two appear to add up, to a first approximation.

The vapor-cooling system had a total mass of approximately 150 kg. The system, however, was not designed with the objective of optimizing its mass, which needs to be addressed in the future. The spiraling cooling loops also produced 3D temperature distributions in the forward skirt, and future

improvements to distribute the vapor cooling more uniformly would be beneficial.

6.1.3 Radio Frequency Mass Gauging

The RFMG has been successfully demonstrated on a large tank. Deformations of the tank at cryogenic temperatures must be accounted for to match the measured resonance frequencies so as to determine the gauged mass accurately. Other methods of mass gauging (capacitance probe and diode wet to dry transitions) had large uncertainties. Hence, comparisons of measured mass or fill level are qualitative, and quantitative determination of uncertainties is difficult to obtain.

6.1.4 Future Use of Structural Heat Intercept, Insulation, and Vibration Evaluation Rig (SHIIVER) Hardware

The SHIIVER test hardware including several pieces of support hardware for use in the ISPF have been stored in a clamshell building at PBS so that it can be available for future testing. Future tests might compare advanced insulation systems; improve the structural support designs, representative of lower heat load systems that may be needed for long-duration storage of cryogenic propellants in space; and demonstration of fluids components within a large-scale, representative tank.

6.2 Lessons Learned

Multiple lessons were learned during the testing of SHIIVER. Some of these are discussed in detail here.

Communication during assembly, integration, and testing was important and having knowledgeable personnel onsite and other personnel ready to visit if needed helped to ensure that the integration of the test hardware into the facility went as smoothly as possible. Additionally, the SHIIVER team began laying out the integration of the test hardware into the test facility and the processes and order of operations many months ahead of time. This helped to streamline the assembly and integration processes and ensure that all hardware (down to the nuts and bolts) were ready when it was needed and properly organized.

During the hardware manufacturing and instrumentation processes, the principal investigator and researchers made sure to mark instrumentation locations on the test hardware with the technicians who were going to install the instrumentation present. This was very helpful to make sure that the instrumentation was installed in the right spot and additionally that the process and instrumentation diagrams (P&ID) matched the actual installation. There were several instances where the researchers showed up to make the marks and the hardware was built in a way that the instrumentation could not have been installed as shown in the P&ID. This allowed the research team the opportunity to come up with and document a plan in realtime. These documentation changes were then captured in the P&ID prior to finalization. The one time this was not followed, a large amount of rework on the instrumentation that had been installed was required.

The SHIIVER team came into testing with a plan ready to handle the data. Spreadsheets were prepared in advance that helped to reduce data in near realtime. They also helped to reduce the data more uniformly allowing for easier creation of plots and use in calculations. While further calculations were done postexperiment, without this level of organization up front, the data would have taken much longer to evaluate. Furthermore, processes were in place ahead of time to modify the test plan and matrix in near realtime, which was helpful to make necessary adjustments during the test. This was used several times to allow the best use of the test time allocated and maximize usefulness of the data. It also made sure that everyone agreed upon the change processes. When these processes were not used, issues arose. One issue that caused a lot of extra work and about a month of schedule delay was the lack of communication of the operational guidelines for installed heaters prior to their use. Four heaters were originally installed on the forward dome and four more on the aft dome to condition the test tank for a certain series of testing. Initial analysis by the research team had shown that operation of these heaters on the stainless steel tank could cause large hot spots, as the tank did not conduct the heat away from the heaters well. The limits agreed to by the research team to try to prevent the hot spots were not communicated to the operations team. The operations team then, unknowingly, used the heaters outside of those bounds and burned through the SOFI. This required the removal and replacement of sections of the SOFI.

Two observations were made during SHIIVER testing with regards to the SDs as temperature measurements. First, it was observed that the chosen diodes did not behave as expected when used in wet to dry mode. Wet to dry mode is the process where a diode is overpowered via a higher current (0.03 A) than normal (1×10^{-5} A), and then based on the response of the diode at the higher current, it can be determined whether the diode is in liquid or vapor (Ref. 61). Upon attempting this, it was found that the SDs used for SHIIVER did not respond in this manner. Typically, small lightweight or bare diodes are used within the tank for this measurement, however SHIIVER used cylindrical diode containers. Upon evaluation, the SHIIVER diodes have a much lower power to mass ratio and heat flux (85 W/kg and 590 W/m^2) than the bare diodes (1.1 kW/kg and 1.4 kW/m^2) and thus with the higher thermal mass were harder to heat up to achieve the same result. Second, it was observed, during analysis of the test data, that the temperature measurements on the SOFI (and MLI) may have been higher than the actual temperature. This is mainly due to the dissipation of

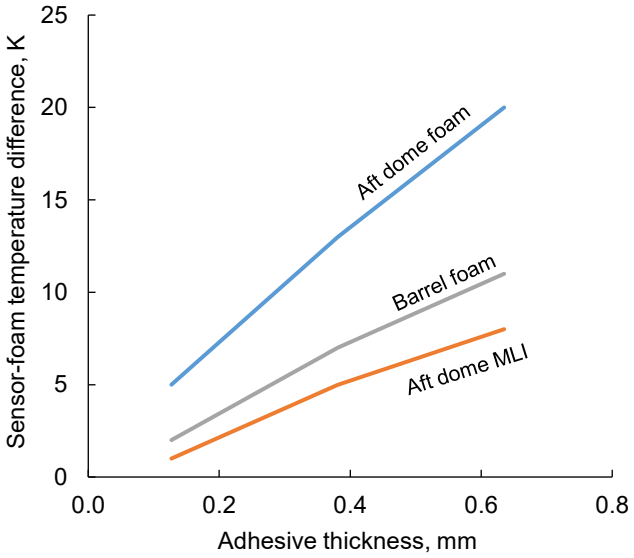

Figure 295.—Sensor temperature difference as function of adhesive thickness. Multilayer insulation (MLI).

heat generated by the sensor. While the SDs generally only generate approximately 10 μW at 20 to 50 K and even 7 μW at 250 K, based on the surface area of the 2.3-mm-diameter by 6.4-mm-long diode, this equates to approximately 2 W/m^2 that has to be dissipated. This is similar magnitude to the heat flux that was measured going through the MLI, therefore, it most certainly increases the temperature locally near the sensor.

The sensors on the SOFI were installed with an adhesive (epoxy), and the difference in measured temperature versus actual temperature, for the three scenarios on the aft dome, is shown in Figure 295. The effect of those sensor differences on calculated heat flux for conduction through the SOFI or radiation to the SOFI (as calculated in Section 5.2) is shown in Figure 296.

Several lessons were learned during the fabrication and installation of the MLI. It was determined by the vendor that installation of the MLI on the domes with the tank in a horizontal orientation would probably be easier than with the tank in the vertical orientation. The hooks in place circumferentially around the interior of the skirts, the scaffolding, and vapor-cooling tubes made it much harder to reach the hooks on the forward skirt. Tying the lacing cord to the hooks prior to installation would have alleviated this. However, it was suggested that the hooks on the skirts made the installation of the MLI easier than with standoffs mounted directly to the tank domes. Additionally, the standoffs on the tank domes would have had to have been worked around during the foam application process, complicating both the spraying and the subsequent trimming.

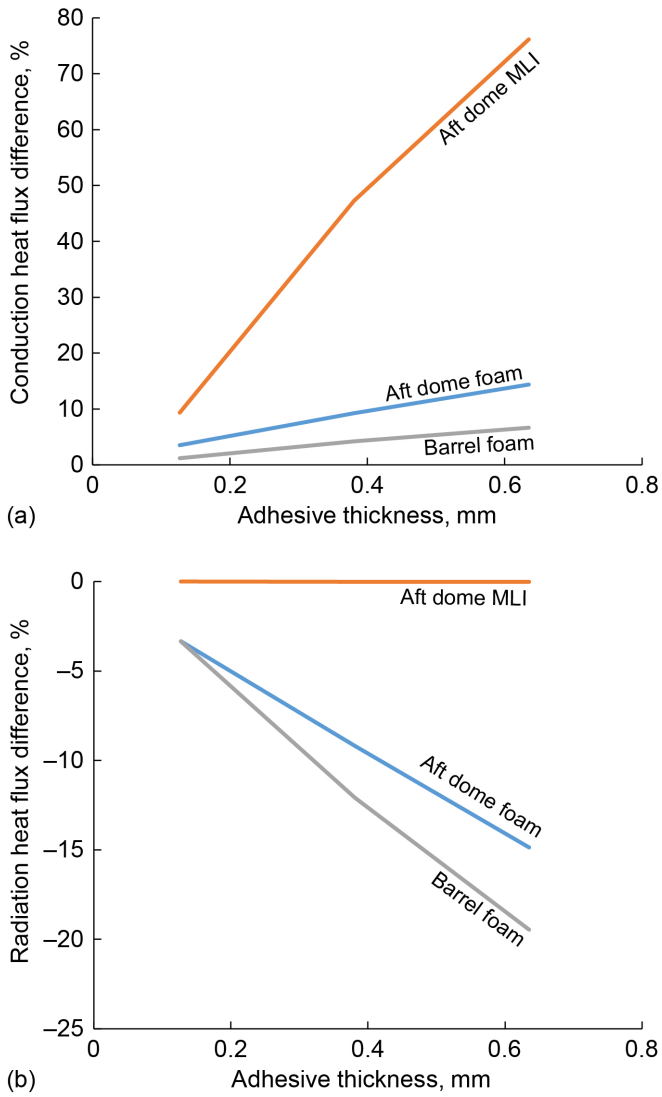

Figure 296.—Differences in calculated conduction and radiation heat flux due to temperature difference in silicon diode. Multilayer insulation (MLI). (a) Conduction heat flux. (b) Radiation heat flux.

The manufacturing of the SHIIVER MLI blankets took approximately 350 h for all the subblankets. Installation and location of diodes took a significant portion of that time (10 to 20 percent). There would probably be improvement for subsequent builds, but that cannot be quantified at this time. If changing the tank size, it would not quadruple the manufacturing time for an 8-m tank, but the labor hours would increase. Simply doubling people does not cut the time for manufacturing in half, there are certain times when multiple people would help speed things up, but there are other times where they do not. A fit check prior to the MLI blanket would probably not be worth the time with the 3D laser image of the tank that was taken before and after SOFI

spray (see Section 2.3.1). This would save time in a manufacturing and integration flow of a flight system and leave them on separate paths.

Installation of the MLI on the domes took 4 days with three to four people but could have been done in 2 days with two separate teams (of three to four people on each team). If possible, the MLI should be installed before piping and other components to make it easier and generate less FOD. Note that this might also lead to more contamination of the outer layer. During the SHIIVER testing, FOD was also generated by a few modifications that had to be made to install the accelerometers for the acoustic test. With the installation of the accelerometers, the MLI was cut and the outer layer was taped (using standard aluminized Kapton® tape (DuPont™)) for reinforcement at the cuts, but no enlarging of the holes or tearing of the blanket was observed. However, the FOD collected during the acoustic test was no more than a few grams. With variable placement of different hardware on multiples of a stage, each MLI blanket might be slightly different, this would have to be investigated. NASA has previously seen this on reduced boiloff (RBO) and vibroacoustic test article (VATA) tanks (Ref. 30) where two tanks made to the same drawing and insulated with SOFI to identical specifications came out slightly different.

Initially, there was a lot of concern on the team about making sure the vapor-cooling lines were in good thermal contact with the skirt. However, subsequent testing showed that within a certain reasonable value, the thermal contact between the cooling element and the skirt is not a dominating restriction in heat flow. The change to the long conduction path or standoff between the skirt and the cooling tube of the "Prototype" reduced its thermal performance as it became the thermal restriction in heat flow. However, the SHIIVER application both reduced the standoff length and doubled it to address these concerns and other manufacturability concerns (Ref. 31). Vapor cooling on the aft skirt would have reduced the boiloff rate much more commensurately with the heat load reduction. In an application on orbit in a surface tension environment where the fluid has a curved liquid-vapor interface and wets the walls more than in a test in 1g, this would promote more benefits from vapor cooling as the flange is more likely to be wetted and the heat load going into the liquid.

During testing, as mentioned in Sections 4.0 and 5.0, pressure control was a challenge and resulted in several lessons learned. The use of redundant measurements using the capacitance probe, RFMG, and diodes provided good corroboration of the boiloff flow rates and allowed the team to understand when the flowmeters were reliable. Furthermore, Coriolis meters need to be installed correctly with appropriate zeroing and calibration of the device. While Coriolis meters have excellent uncertainty values, using them with hydrogen vapor, is pushing their capability, due to the low density of the vapor. Finally, no

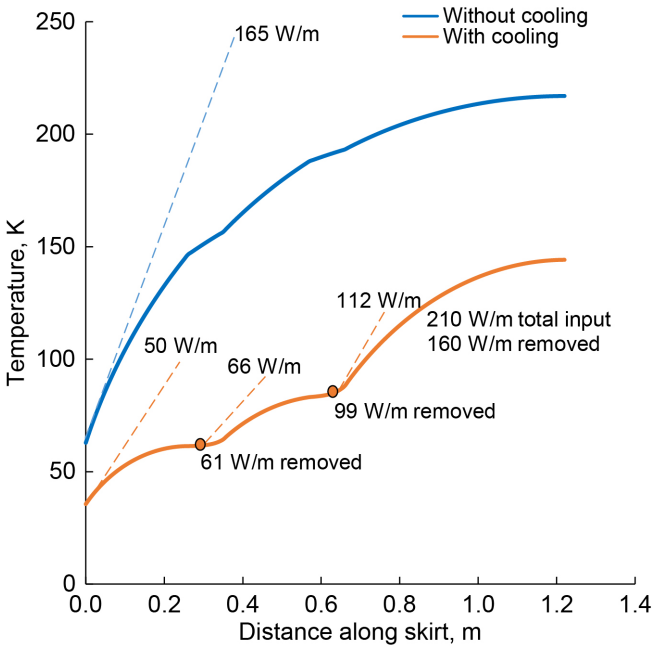

Figure 297.—Thermodynamic balance example of cooling in two locations along skirt.

analysis was done prior to testing to determine the pressure drops in the system with hydrogen gas flow. While this would have been a hard analysis, the assumption was made that the flowmeters' pressure drops were much less than the system, which turned out not to be the case. As a result, the team had no good method to determine when a flowmeter could handle a flow rate and when it could not. On the vapor-cooling side, this resulted in the pressure drop through the system being lower than expected. With no backpressure control system on the vapor-cooling side (it was assumed that it would always be the maximum flow allowable and the main vent would have to be used in parallel to the vapor-cooling lines). The pressure could not be maintained at 20 psia for a more direct comparison. Lastly, make sure that it is clear to the vendor when buying a Coriolis flowmeter, when a fluid that could condense nitrogen gas may be used, as it will change certain steps in the manufacturing process.

During the series of tests, the first test will generally be the roughest and follow-on tests will run smoother based on increasing familiarity of the test team with the test system. For this test series, it was determined to perform the baseline test first, before the MLI was installed. This caused the test with the lowest fidelity and highest uncertainty to be used for comparison with all other testing to determine the benefits of the added technologies. While it is never desired for any test to be less than ideal, it would have been good to at least consider another test as the first test.

As mentioned before, one cannot take the uncooled heat into the system, subtract out the heat being removed by the cooling

flow, and use the difference as the new heating into the system. Figure 297 shows this for a skirt cooled in two locations. For the skirt without cooling, 165 W/m is transferred into the skirt and tank. For the skirt with cooling, a total of 210 W/m is transferred into the skirt, but with the removal of 160 W/m, only 50 W/m makes it into the tank. Thus, the artifact of cooling the skirt increases the total heat load on the skirt but decreases the net heat load into the tank.

As seen in Section 5.2, heat loads are not directly proportional to boiloff rates. As the fill level decreases and the ratio of wetted to dry tank area changes, heat can be picked up in the ullage and transferred directly to the vapor. This causes the vapor temperature to rise and thus usually, the vapor is vented at a temperature that is much warmer than saturation. Thus, while the vapor cooling maintains the same benefit in heat load reduction down to the aft flange, the boiloff reduction tapers off dramatically at the forward flange as the heat from the skirt is transmitted to the vapor. This will again, be affected by the gravitational environment where a surface tension dominated situation may cause much more of the tank wall surface area to be wetted in comparison to the ground testing.

7.0 Conclusions

The Structural Heat Intercept, Insulation, and Vibration Evaluation Rig (SHIIVER) hardware has been successfully built, assembled, and tested under both thermal vacuum and acoustic loading conditions. The hardware is very representative of a realistic stage-like configuration in terms of scale, forward skirt material, and structure-borne heat loads. The assembled hardware incorporates sophisticated technologies including multilayer insulation (MLI), vapor cooling in the forward skirt, and Radio Frequency Mass Gauge (RFMG). The external structures, cooling channels, and the tank were fully instrumented to measure temperatures, pressure, heat flux, liquid level, and vibrations. There were flowmeters to measure boiloff and vapor-cooling flow rates. The instruments performed well, though there were some anomalies identified and workarounds developed throughout the test program.

A series of four thermal vacuum test campaigns were performed that included tests to characterize boiloff flow rates as a function of fill level, with and without vapor cooling, RFMG, and self-pressurization when the tank was locked up. After a liquid hydrogen (LH_2) baseline test (spray-on foam insulation (SOFI) on the tank exterior; MLI on the interior of the forward and aft skirts), MLI was installed on the forward and aft domes. With dome MLI installed, preacoustic tests were completed with both hydrogen and nitrogen liquids. The acoustic test was then performed, which subjected the hardware, with the MLI attached, to acoustic loads representative of launch loads. Finally, postacoustic tests were performed with LH_2 to determine the postdynamics thermal performance of the tank and assess any change in it. Results show that no MLI performance degradation occurred after exposure to the acoustic loading associated with launch.

The SHIIVER hardware has been an extremely valuable test asset to assess the performance of the MLI, vapor-cooling, and RFMG technologies. It likely will be a very useful capability for future use in various projects by the agency and industrial collaborators.

Appendix A.—Acronyms and Symbols List

A.1 Acronyms

3D	three dimensional
AFM	Aerospace Fabrication & Materials, LLC
ASME	American Society of Mechanical Engineers
BAC	broad area cooling
BNC	bayonet nut coupling
CAD	computer-aided design
CPST	Cryogenic Propellant Storage and Transfer
CRES	corrosion resistant steel
DAQ	data acquisition
DCSS	Delta Cryogenic Second Stage
EUS	Exploration Upper Stage
FLS	capacitance probe
FM	flowmeter
FOD	foreign object debris
FSO	full-scale output
GEO	geosynchronous Earth orbit
HFS	heat flux sensor
HR	heater
IG	ion gauge
ISPF	In-Space Propulsion Facility
ITO	indium-tin-oxide
LEO	low Earth orbit
LH_2	liquid hydrogen
LN_2	liquid nitrogen
LS	limit switch
MHTB	Multipurpose Hydrogen Test Bed
MLI	multilayer insulation
MNV	Mars Nuclear Vehicle
NBS	National Bureau of Standards
NC	normally closed
NIST	National Institute of Standards and Technology
NO	normally open
OASPL	overall sound pressure level
OTOB	one-third octave band
OTTA	oxygen thermal test article
P&ID	process and instrumentation diagram
PBS	Plum Brook Station
PET	polyethylene terephthalate
PI	polyimide
PID	proportional–integral–derivative
PRSD	Power Reactant Storage and Distribution
PSD	power spectral display
PT	pressure transducer
r, θ, and z	cylindrical coordinate system
RATF	Reverberant Acoustic Test Facility
RBO	reduced boiloff
REFPROP	Reference Fluid Thermodynamic and Transport Properties Database
RF	radio frequency
RFMG	Radio Frequency Mass Gauge
RGA	residual gas analyzer
SD	silicon diode
SEI	Space Exploration Initiative
SHIIVER	Structural Heat Intercept, Insulation, and Vibration Evaluation Rig
SI	International System of Units
SLICE	Subscale Laboratory Investigation of Cooling Enhancements
SOFI	spray-on foam insulation
TC	thermocouple
TVS	thermodynamic vent system
USB	universal serial bus
VATA	vibroacoustic test article
VC	vapor cooling
VCS	vapor-cooling system
VNA	vector network analyzer
VPN	virtual private network
VS	accelerometer
WBT	warm boundary temperature
θ	angular location

A.2 Symbols

a	sensor sensitivity provided by the vendor, $\mu V/(W/m^2)$
a_0	0.004313685
a_1	0.415495996
a_2	12.64099669
a_3	–18.97029258
a_4	31.00067342
a_5	–30.00629244
a_6	16.42370017
a_7	–5.090779682

a_8	0.836222529
a_9	–0.057180538
a_{10}	0.000122776
a_c	accommodation coefficient at vacuum chamber wall
a_s	accommodation coefficient at SOFI surface
A/L	cross-section area per unit length of the interface, m
A_{MLI}	surface area of MLI, m^2
A_{SOFI}	surface area of SOFI, m^2
b	zero heat flux offset, W/m^2
C_1	integration constant that is to be determined
C_g	empirical constant, 14,600
C_r	empirical constant, 5.39×10^{-10}
C_s	empirical constant, 2.4×10^{-4}
d	wire diameter, m
d_c	diameter of vacuum chamber, m
d_s	diameter of SOFI surface, m
D	diameter of the forward skirt, m
$f(\phi)$	correction factor that depends on the fill level
F_e	energy conversion factor, 1 J/g = 1,000 m^2/s^2
F_g	ion gauge factor
G	gain, multiplication factor to yield measured voltages
h_1 and h_2	vapor enthalpies at the entrance and exit to the vapor-cooling channels, J/g
h	liquid height, m
h_0	gap between the capacitance probe and the bottom of the tank, m
h_L	tank bulk liquid enthalpy, J/g
h_v	tank bulk vapor enthalpy, J/g
h_{vent}	calculated enthalpy of vent gas, J/g
k_{line}	line material thermal conductivity, W/m·K
k_{skirt}	skirt material thermal conductivity, W/m·K
k_{SOFI}	thermal conductivity of SOFI, K
k_{wire}	wire material thermal conductivity, W/m·K
L	active length of the capacitance probe when the maximum calibration command was issued, m
$(L/A)_{eff}$	effective ratio of conduction length of cross-section area, per meter
L_i	length of the forward skirt segment between temperature measurement locations, m
m_{fluid}	total mass of the fluid as measured by the RFMG, kg
m_L	calculated mass of liquid in tank, kg
m_v	calculated mass of vapor, kg
$\dot{m}$	mass flow rate through the vapor-cooling lines, g/s
$\dot{m}_{\text{boiloff}}$	boiloff flow rate, g/s
$\dot{m}_v$	calculated boiloff rate, g/s
$\dot{m}_{v,\text{equivalent}}$	equivalent boiloff rate, g/s
$\dot{m}_{v,\text{measured}}$	measured vent flow rate, g/s
M_{H_2}	hydrogen mass in the tank, kg
M_l	liquid mass of the tank fully filled, kg
M_w	molecular mass of air in the vacuum chamber, g/mol
N_{coaxial}	quantity of coaxial cables at the interface
$N_{\text{heatfluxsensor}}$	quantity of heat flux sensors
N_{heater}	quantity of heaters at the interface
N_s	number of MLI layers
$N_{\text{temperaturesensor}}$	quantity of temperature sensors at the interface
$\overline{N}$	MLI density, layers per centimeter
P	vacuum chamber pressure, Pa or torr
P	pressure
P_{end}	pressure at the end of pressure rise test, kPa
P_{start}	pressure at the start of pressure rise test, kPa
Q or $\dot{Q}$	heat load or heat leak, W
$\dot{Q}_{\text{coaxial}}$	heat load for a single coaxial cable conductor, W
$\dot{Q}_{cond}$	conduction heat load, W
$\dot{Q}_f$	total heat load to the fluid, W
$\dot{Q}_{\text{fin}}$	radiation heat load estimate for an infinite length fin, W
$\dot{Q}_{\text{heater}}$	heat load for a single heater conductor, W
$\dot{Q}_{\text{heatfluxsensor}}$	heat load for a single heat flux sensor conductor, W
$\dot{Q}_{\text{interface}}$	radiation heat load at each interface, W
$\dot{Q}_{rad}$	forward skirt radiation heat load, W
$\dot{Q}_{\text{temperaturesensor}}$	heat load for a single temperature sensor conductor, W

$\dot{Q}_{\text{vapor,intercept}}$	heat removed from the skirt by the vapor cooling flow, W
$\dot{Q}_{\text{wire}}$	radiation heat load estimated for a single lead wire, W
$q_{cond}l_{p\text{chamber}}$	conduction heat flux at measured chamber, W/m^2
$q_{cond}l_{p\text{max-allow}}$	conduction heat flux at maximum allowable chamber pressure, W/m^2
$q_{\text{conduction}}$	conduction heat flux, W/m^2
q_{cover}	cover and manway heat flux, W/m^2
q_{gas}	interstitial gas conduction, W/m^2
$q_{\text{gas}}p_{\text{chamber}}$	interstitial gas conduction heat flux at measured chamber pressure, W/m^2
$q_{\text{gas}}p_{\text{max-allow}}$	interstitial gas conduction heat flux at maximum allowable chamber pressure, W/m^2
q_{MLI}	MLI heat flux, W/m²
$q_{\text{radiation}}$	radiation heat flux, W/m^2
$\dot{q}$	heat flux
R_u	universal gas constant, J/mol·K
S	scale factor that accounts for conversion of units, 50
S_{H_2}	0.46
S_{He}	0.18
t	time, h
t_{end}	time at the end of pressure rise test, h
t_{smooth}	time correlating to $V_{cap,\text{smooth}}$ points
t_{start}	time at the start of pressure rise test, h
T_1 and T_2	measured fluid line temperatures, K
$T(P_{sat})$	liquid interface temperature
T_{chamber}	temperature of the vacuum chamber wall, K
T_{cover}	temperature of the cover, K
T_{flange}	temperature of the flange, K
T_i	temperature of the forward skirt segment, K
$T_{\text{interface}}$	temperature of the wire interface, K
T_{SOFI}	temperatures of SOFI surface, K
T_{subs}	temperature of tank substrate, K
T_{surf}	temperature of vacuum chamber wall, support structure, or MLI surface, K
T_{wall}	temperature of the skirt wall, K
V_{cap}	voltage measured by capacitance probe, V
$V_{cap,\text{smooth}}$	voltage measured by capacitance probe smoothed over 30 points, V
V_l	volume of liquid, m^3
V_{measured}	measured voltage of heat flux sensor, V
V_{sensor}	sensor voltage, V
V_{tank}	volume of tank, m^3
w	fin width (skirt circumference), m
x	active liquid height, $h - h_0$, m
$\Delta(\ )/\Delta t$	time rate of change, per second
Δx	skirt thickness, m
Δx_{SOFI}	local thickness of SOFI at the temperature measurement location, m
ε	heat transfer error
$\varepsilon_{\text{chamber}}$	emissivity of the vacuum chamber wall, 0.9
$\varepsilon_{\text{cover}}$	emissivity of the cover
ε_{env}	emissivity of the environment surface
ε_s	emissivity of foam surface
ε_{SOFI}	emissivity of SOFI
$\varepsilon_{\text{skirt}}$	emissivity of the forward skirt, 0.152
ε_{sksurf}	emissivity of skirt surface
ε_{surf}	emissivity of vacuum chamber wall, support structure, or MLI
ε_{TR}	effective transmission of MLI layers
$\varepsilon_{\text{wire}}$	effective emissivity of the wire insulation and chamber wall
γ	specific heat ratio
ϕ	tank fill level, percent
ϕ_{mass}	tank fill-level mass, $= (\rho_l/\rho_{l_i})\phi_{vol} + (\rho_v/\rho_{l_i})(1 - \phi_{vol})$, percent
ϕ_{ratio}	tank fill-level ratio, percent
ϕ_{vol}	tank fill-level volume, percent
ρ_l	liquid density, kg/m^3
ρ_{l_i}	initial liquid density when the tank was filled, kg/m^3
ρ_{ratio}	ratio of LN_2 to LH_2, kg/m^3
ρ_v	vapor density, kg/m^3
$\tilde{\rho}_v$	average density of the ullage space vapor, kg/m^3
σ	Stefan-Boltzmann constant, 5.6704×10^{-8} W/m²K4

Appendix B.—Skirt Temperatures Baseline Test

All plots (Figure B.1 to Figure B.63) are shown as a function of height along the forward skirt, the height being the distance in the vertical direction from the forward flange (where the forward skirt and tank meet) along the skirt surface. Essentially, these should be considered z-axis (in an r, θ, and z cylindrical coordinate system) profiles at different θ locations, where θ is indicated by an angle, and at different times, where the time is indicated by a fill level.

B.1 Summary Plot for Each Angle Including All Fill Levels for Boiloff and Vapor Cooling

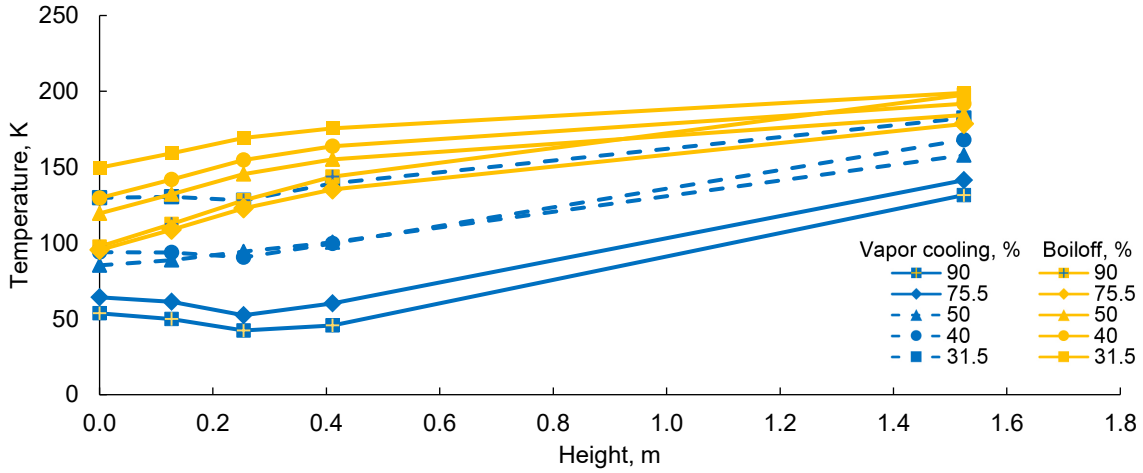

Figure B.1.—Temperature versus height at 40° comparing vapor-cooling and boiloff temperatures at every fill level.

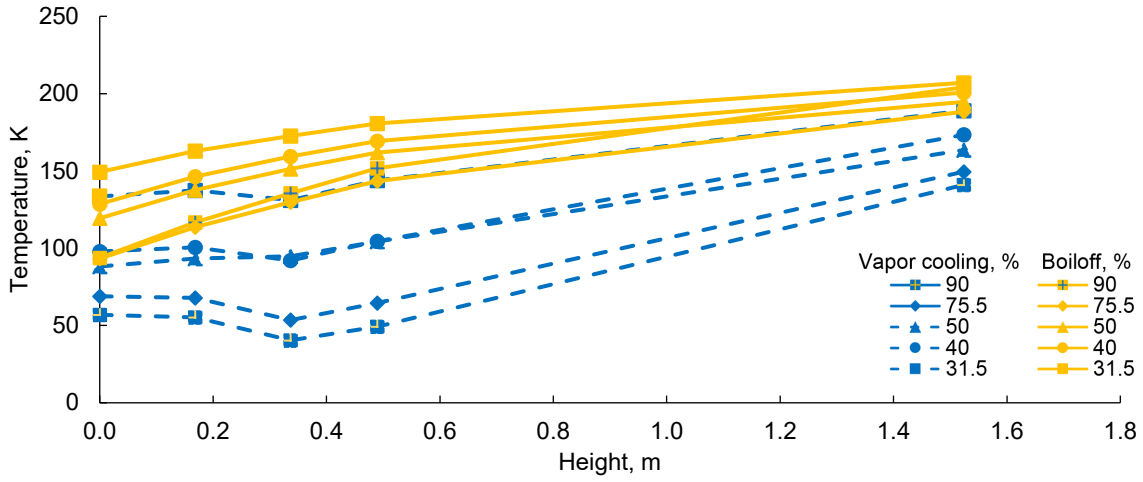

Figure B.2.—Temperature versus height at 120° comparing vapor-cooling and boiloff temperatures at every fill level.

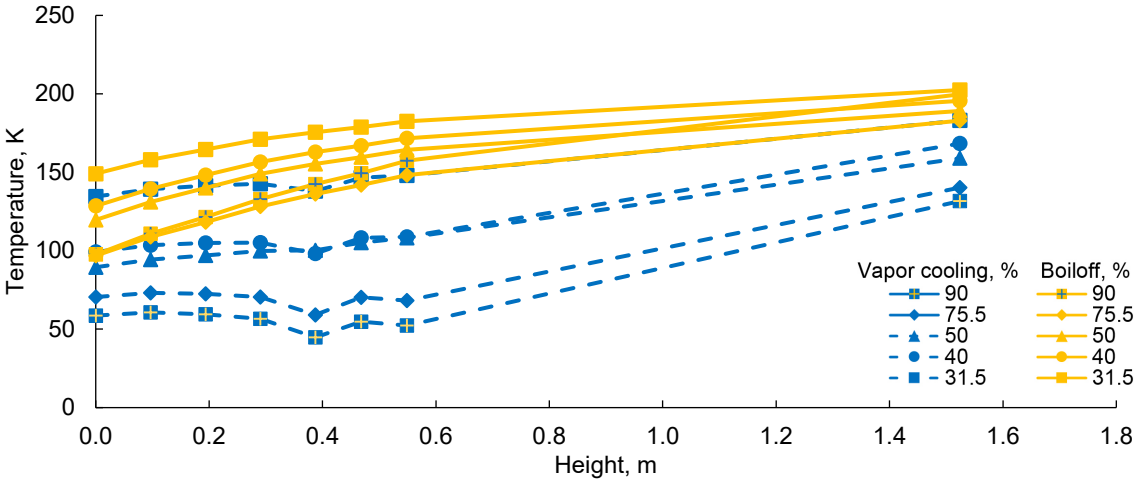

Figure B.3.—Temperature versus height at 180° comparing vapor-cooling and boiloff temperatures at every fill level.

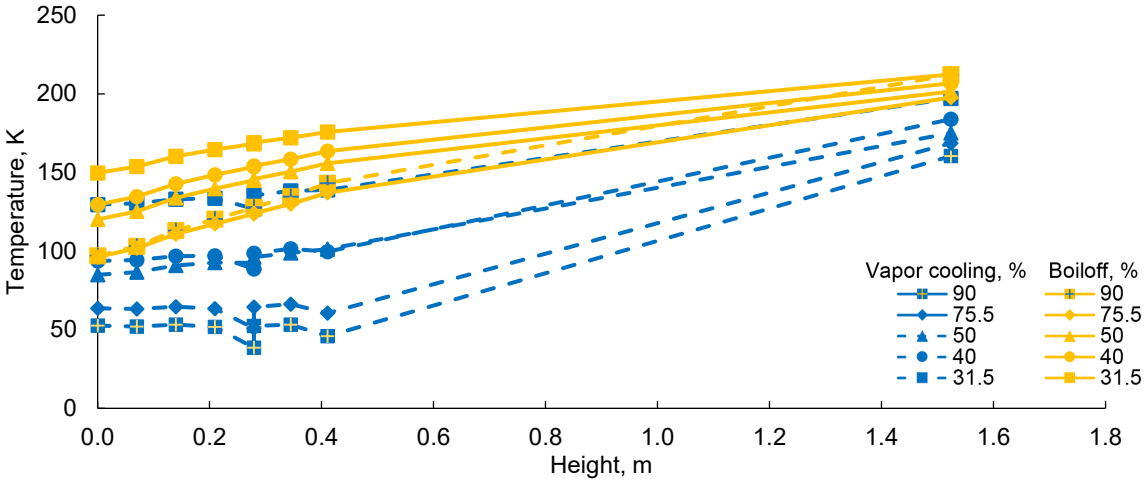

Figure B.4.—Temperature versus height at 230° comparing vapor-cooling and boiloff temperatures at every fill level.

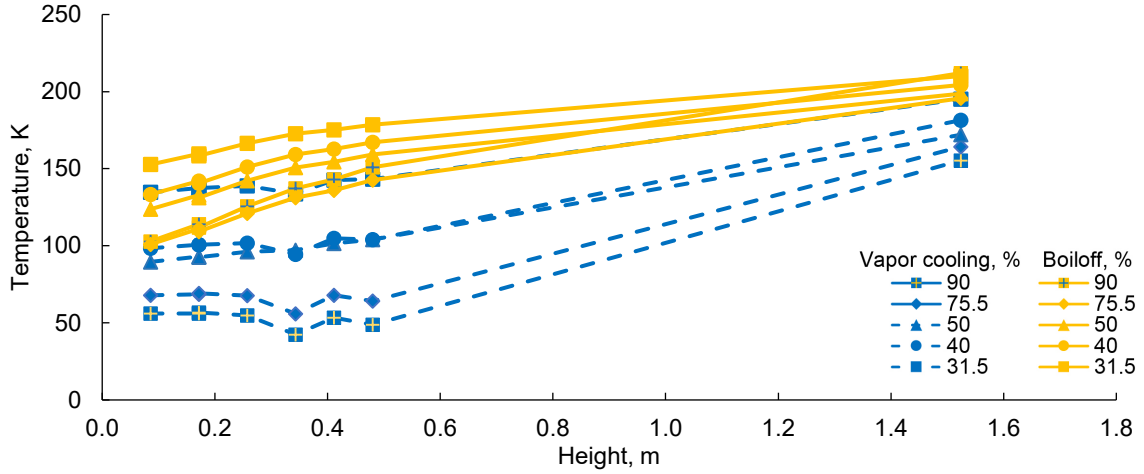

Figure B.5.—Temperature versus height at 300° comparing vapor-cooling and boiloff temperatures at every fill level.

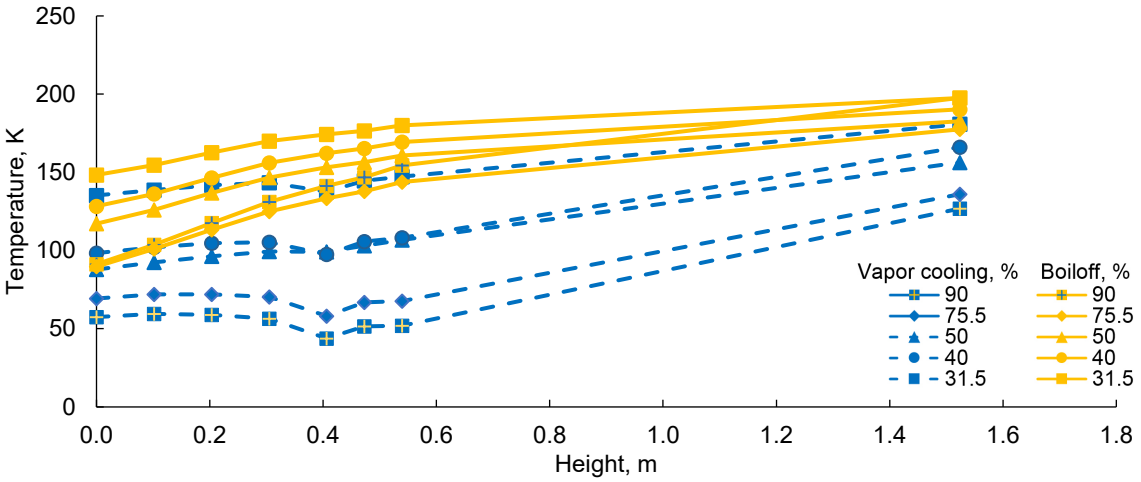

Figure B.6.—Temperature versus height at 360° comparing vapor-cooling and boiloff temperatures at every fill level.

B.2 Summary Plot for Each Angle Including All Fill Levels for Boiloff

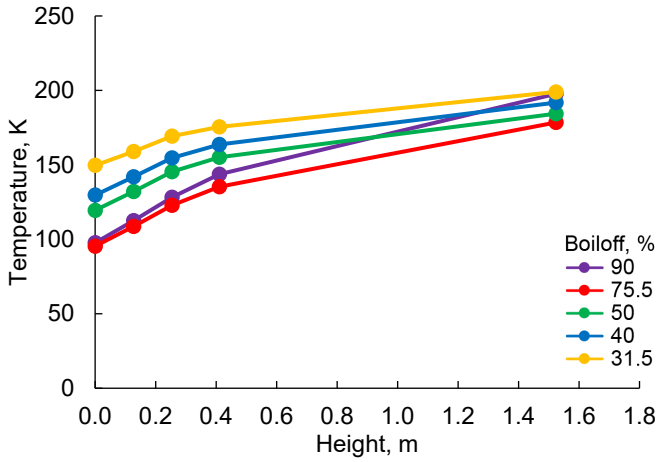

Figure B.7.—Boiloff temperature versus height at 40° for every fill level.

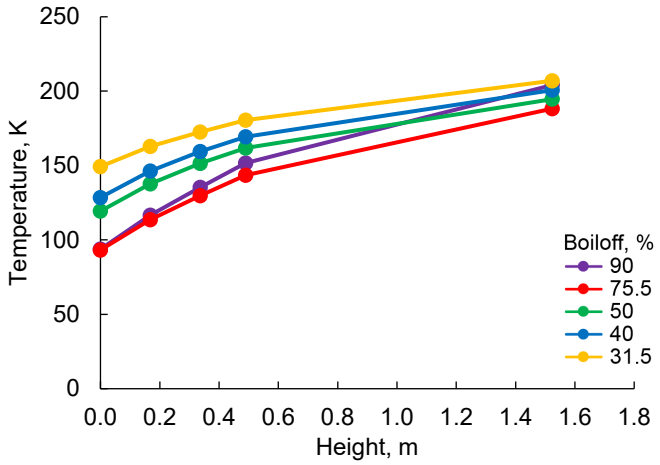

Figure B.8.—Boiloff temperature versus height at 120° for every fill level.

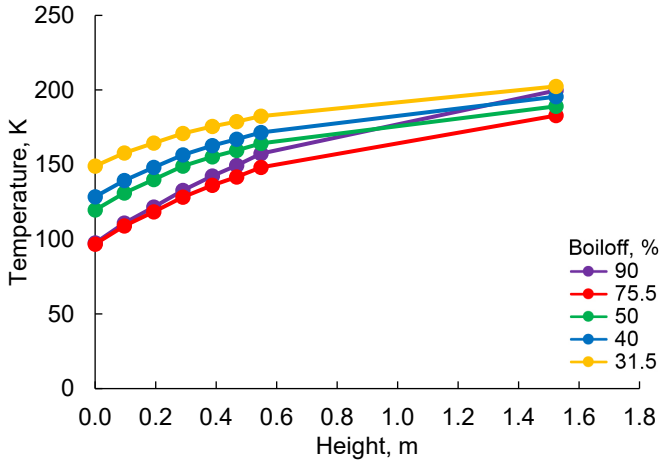

Figure B.9.—Boiloff temperature versus height at 180° for every fill level.

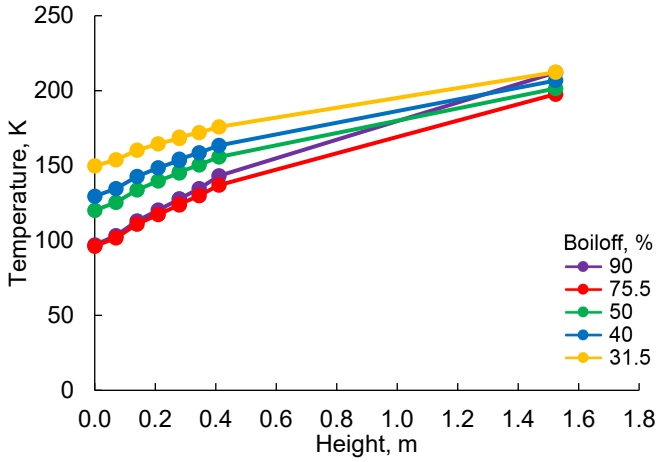

Figure B.10.—Boiloff temperature versus height at 230° for every fill level.

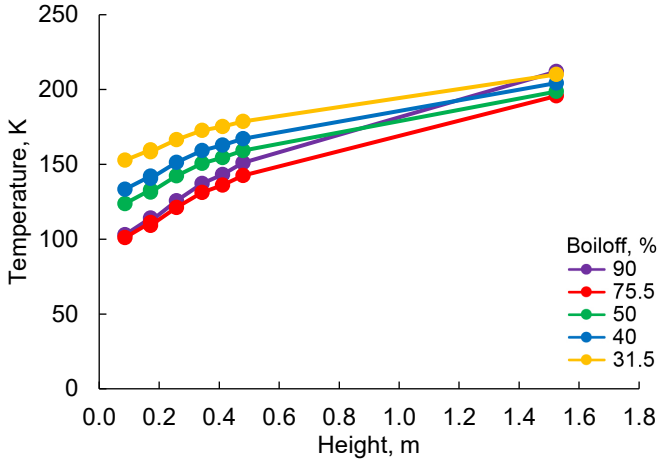

Figure B.11.—Boiloff temperature versus height at 300° for every fill level.

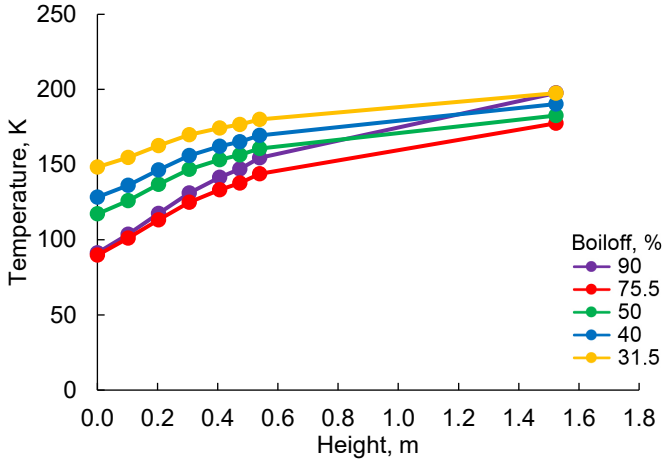

Figure B.12.—Boiloff temperature versus height at 360° for every fill level.

B.3 Summary Plot for Each Angle Including All Fill Levels for Vapor Cooling

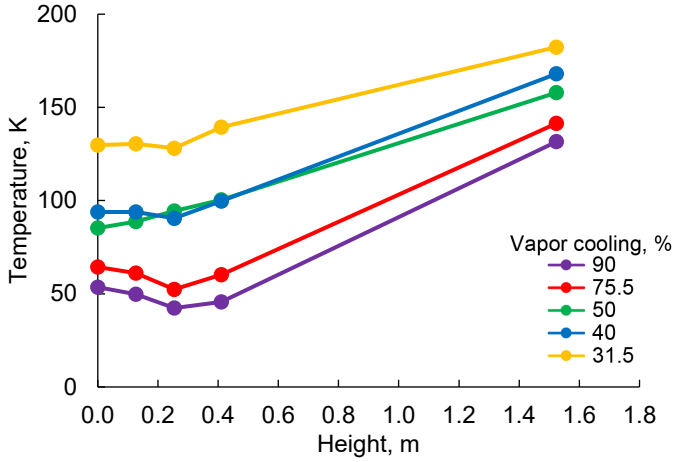

Figure B.13.—Vapor-cooling temperature versus height at 40° for every fill level.

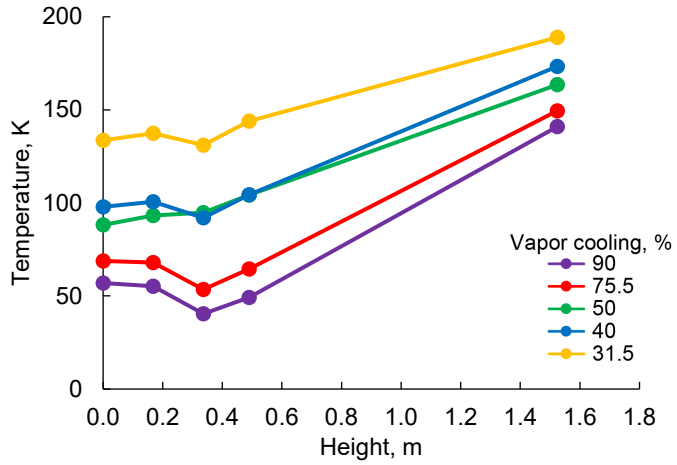

Figure B.14.—Vapor-cooling temperature versus height at 120° for every fill level.

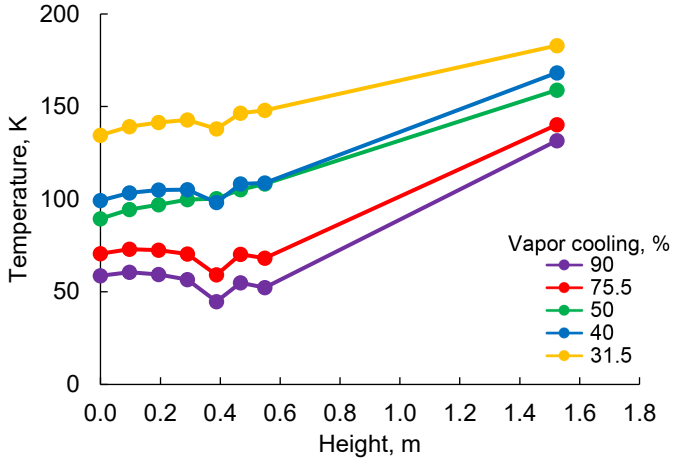

Figure B.15.—Vapor-cooling temperature versus height at 180° for every fill level.

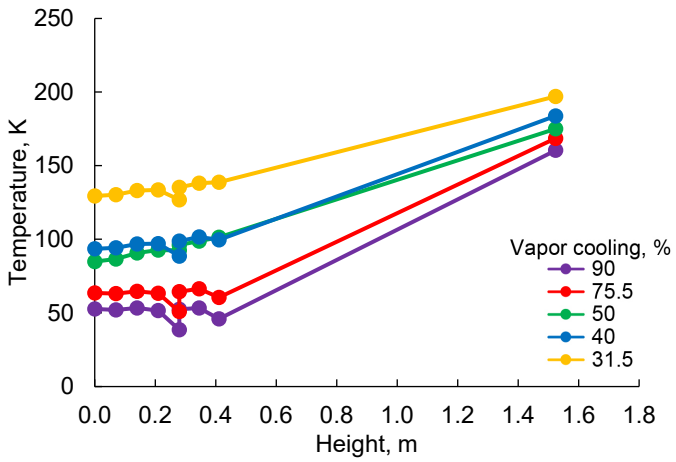

Figure B.16.—Vapor-cooling temperature versus height at 230° for every fill level.

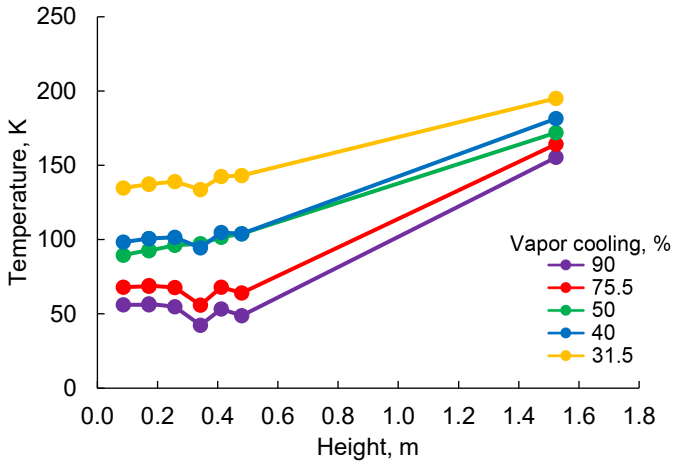

Figure B.17.—Vapor-cooling temperature versus height at 300° for every fill level.

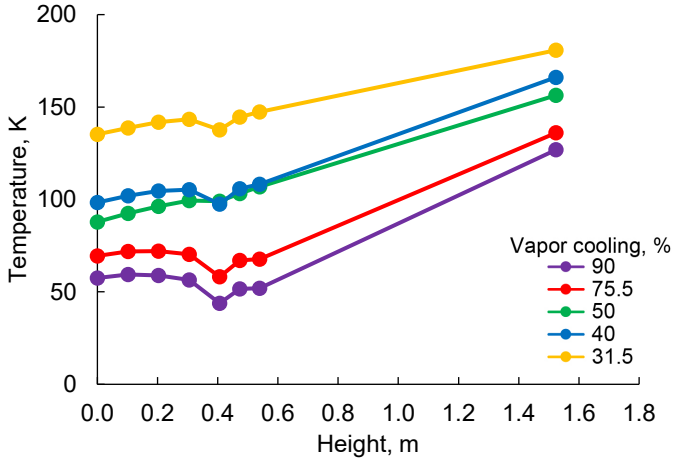

Figure B.18.—Vapor-cooling temperature versus height at 360° for every fill level.

B.4 Temperature Versus Height at Each Fill Level for All Angular Stations

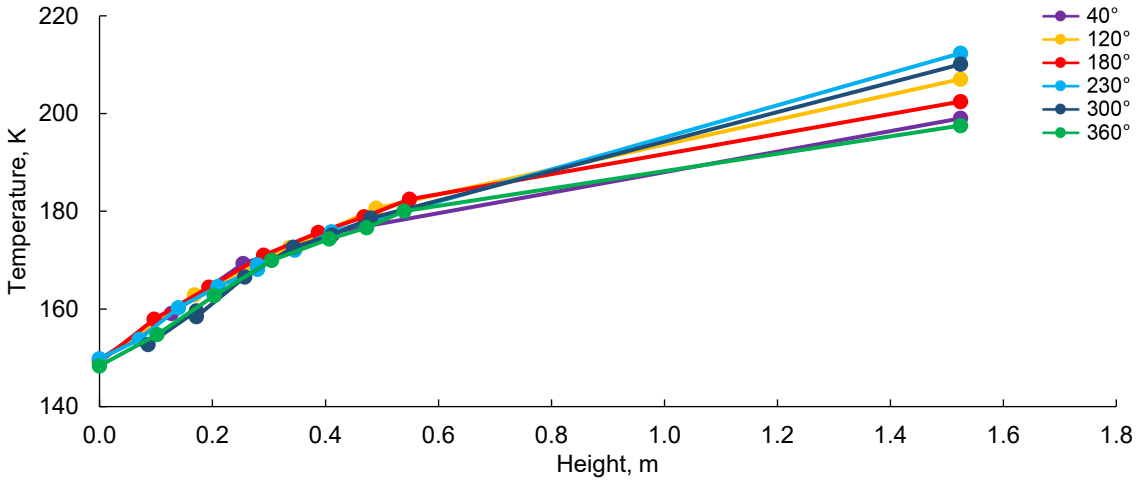

Figure B.19.—Boiloff temperature versus height at 31.5 percent fill level for every angular station.

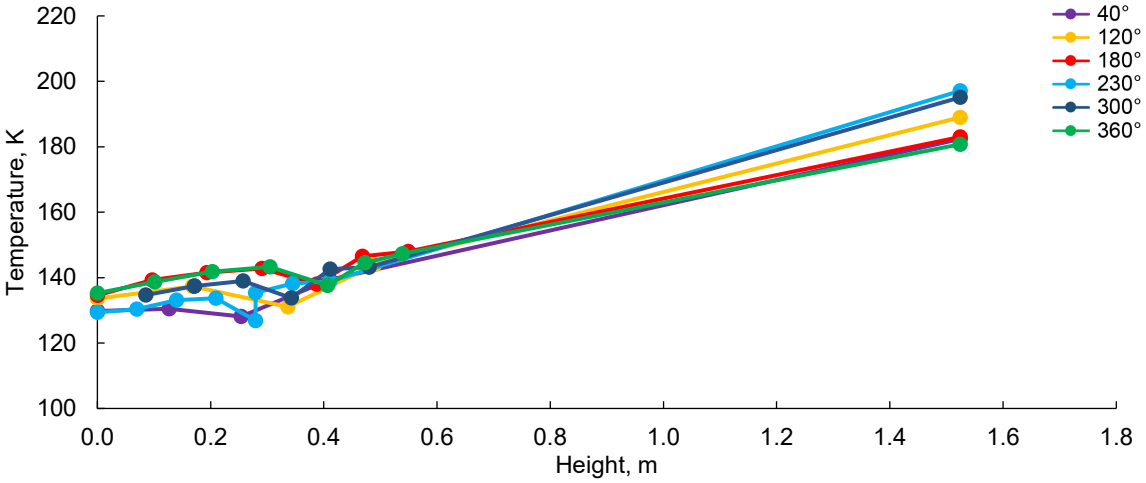

Figure B.20.—Vapor-cooling temperature versus height at 31.5 percent fill level for every angular station.

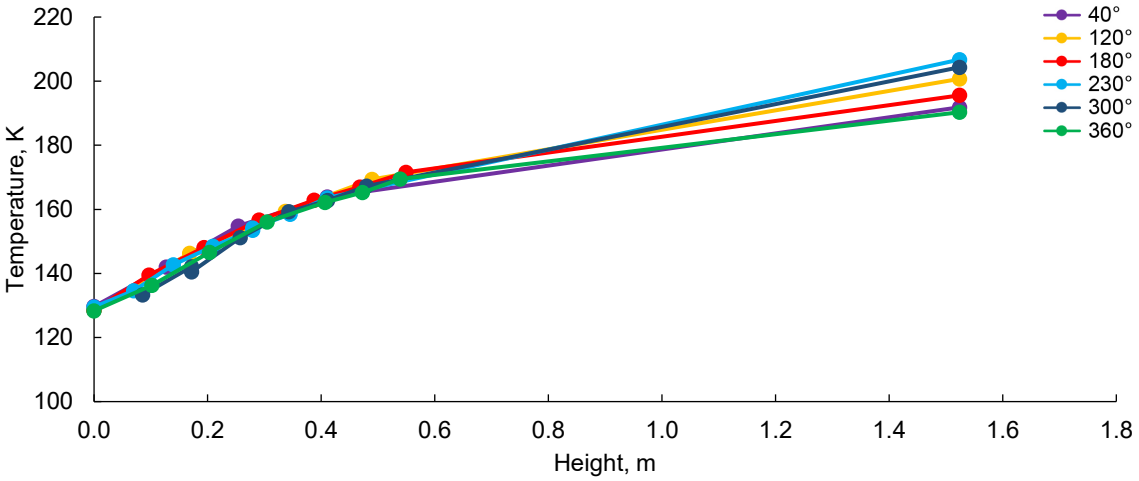

Figure B.21.—Boiloff temperature versus height at 40 percent fill level for every angular station.

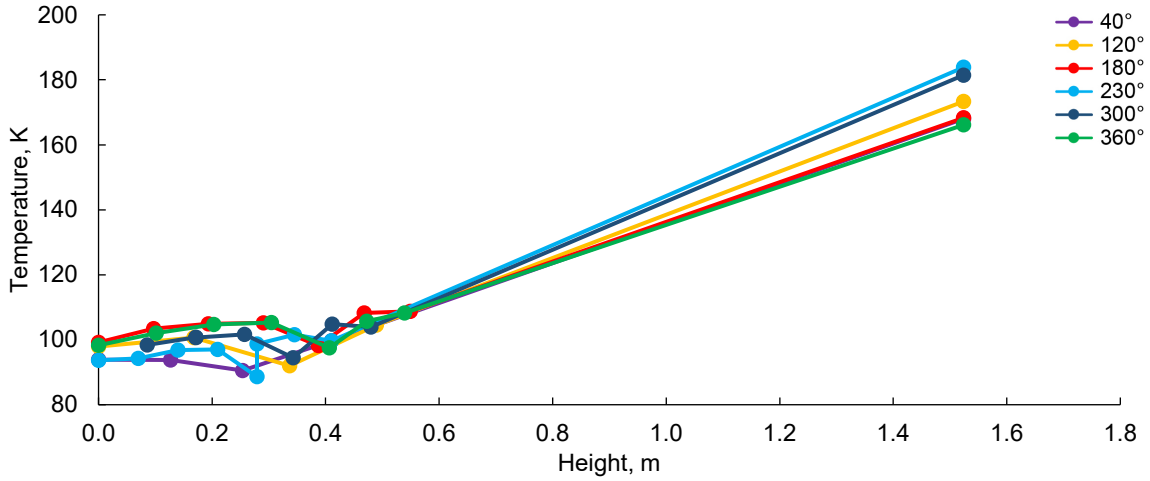

Figure B.22.—Vapor-cooling temperature versus height at 40 percent fill level for every angular station.

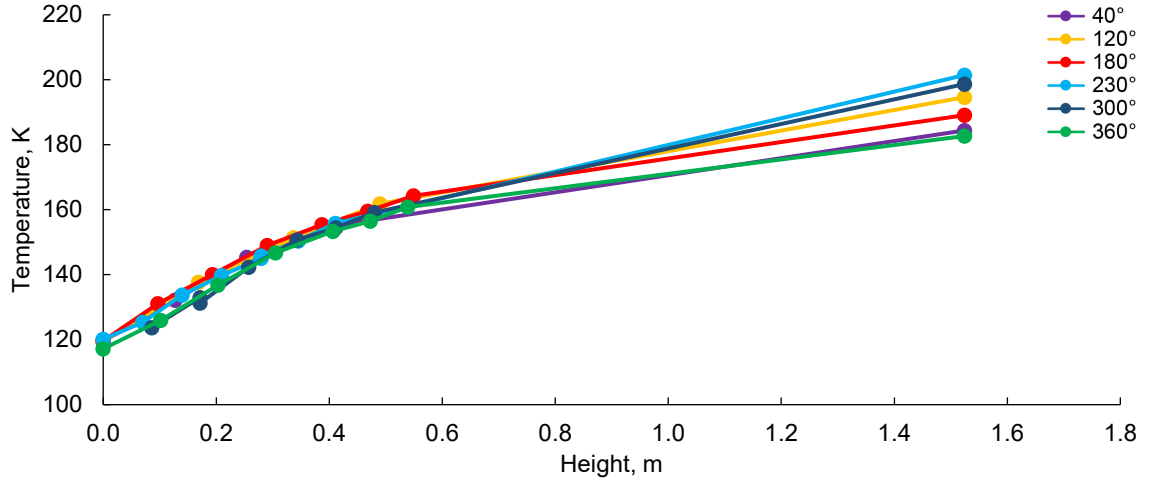

Figure B.23.—Boiloff temperature versus height at 50 percent fill level for every angular station.

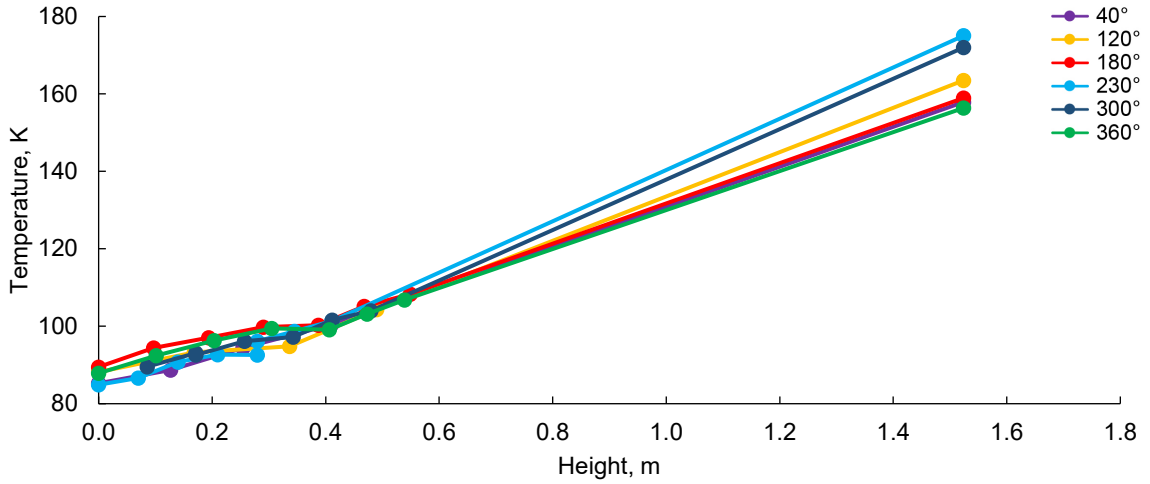

Figure B.24.—Vapor-cooling temperature versus height at 50 percent fill level for every angular station.

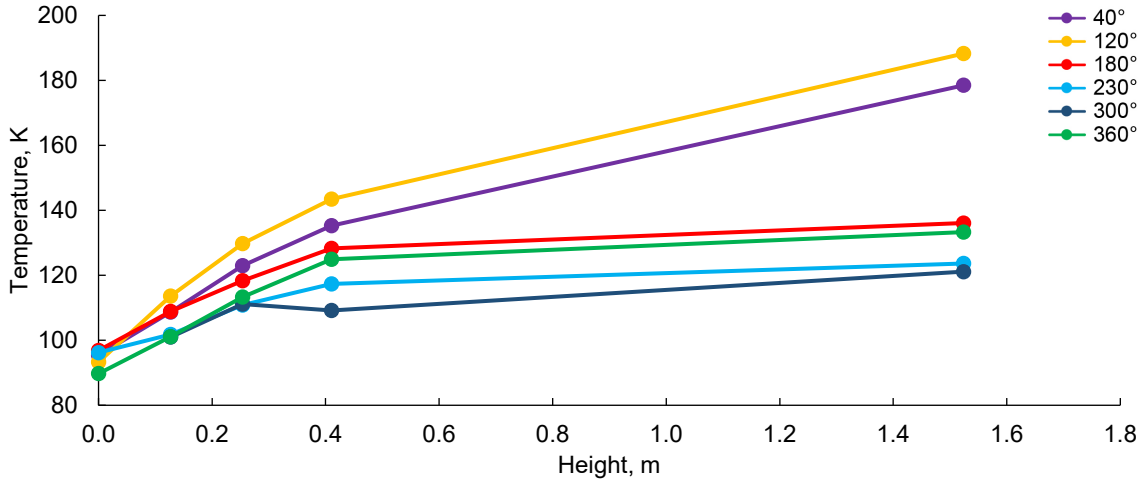

Figure B.25.—Boiloff temperature versus height at 75.5 percent fill level for every angular station.

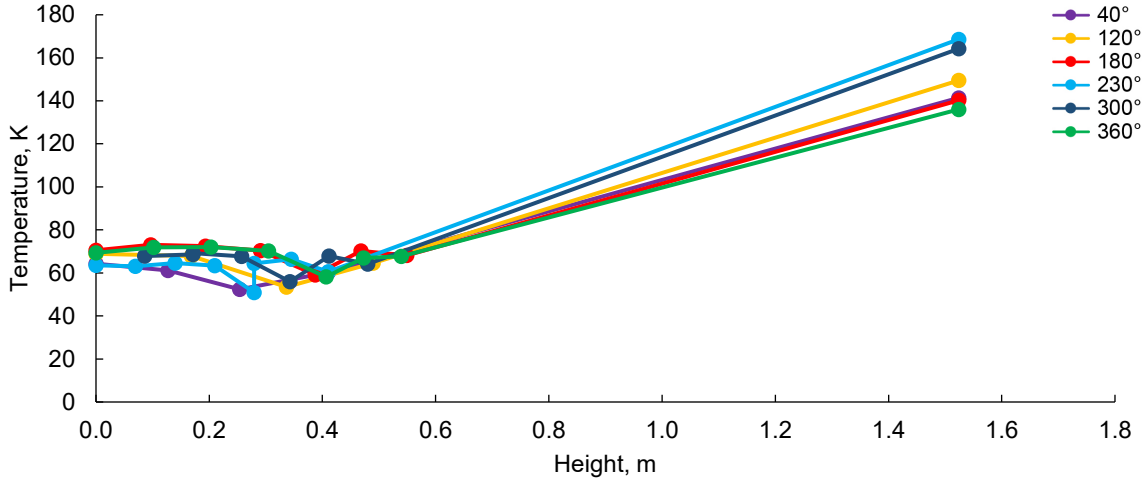

Figure B.26.—Vapor-cooling temperature versus height at 75.5 percent fill level for every angular station.

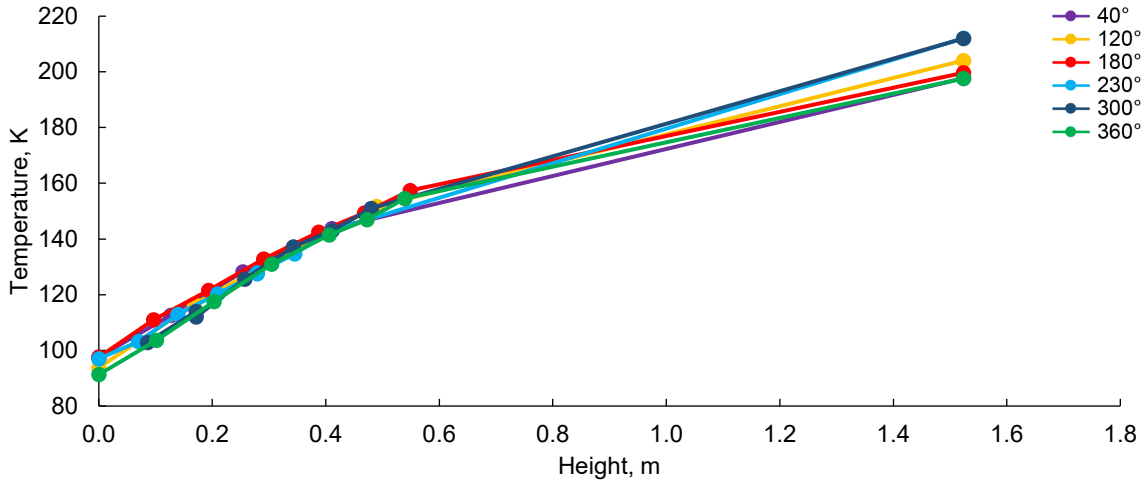

Figure B.27.—Boiloff temperature versus height at 90 percent fill level for every angular station.

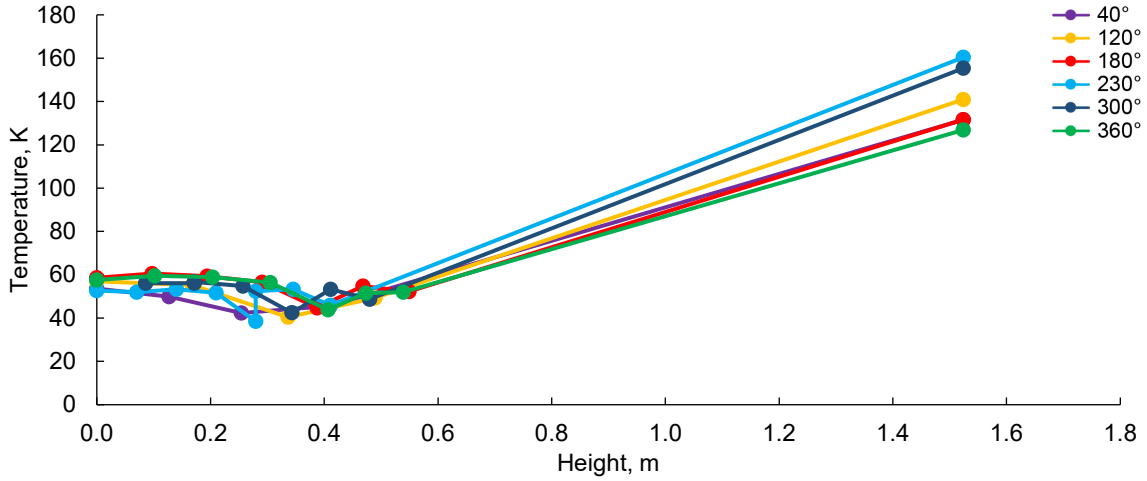

Figure B.28.—Vapor-cooling temperature versus height at 90 percent fill level for every angular station.

B.5 Temperature Versus Height at Each Fill Level and Each Angular Station Comparing Vapor Cooling and Boiloff

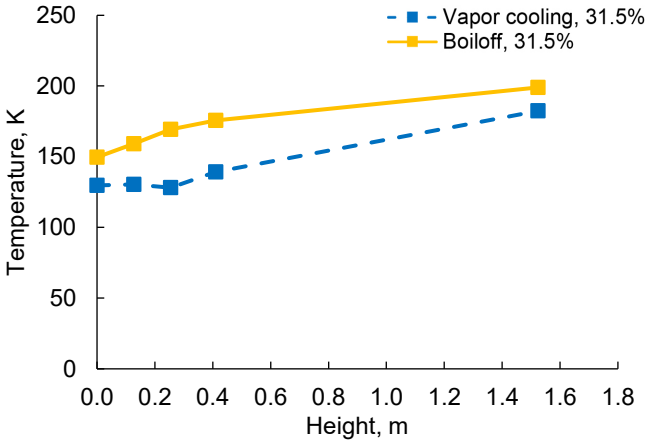

Figure B.29.—Vapor-cooling and boiloff temperature versus height at 31.5 percent fill and 40°.

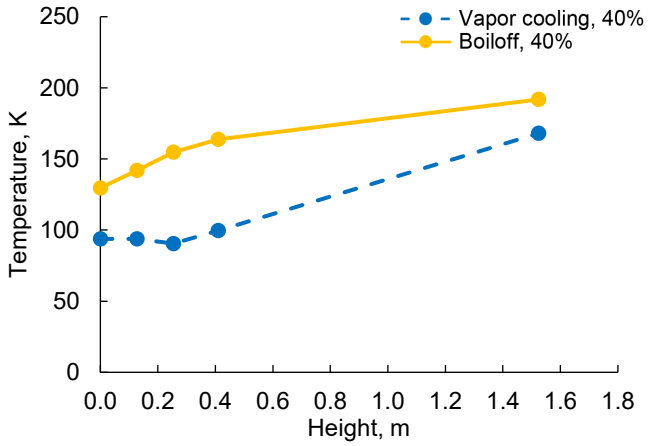

Figure B.30.—Vapor-cooling and boiloff temperature versus height at 40 percent fill and 40°.

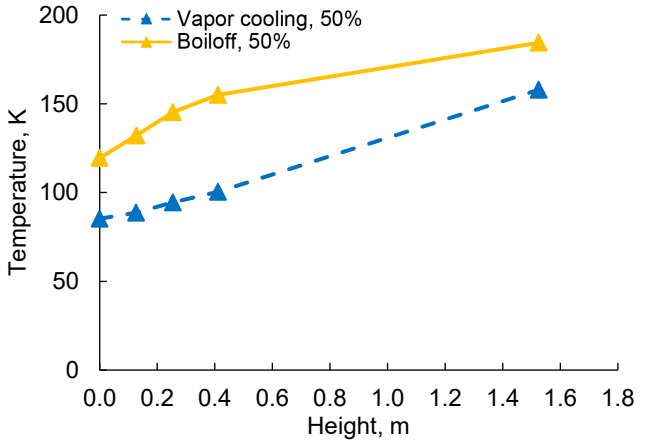

Figure B.31.—Vapor-cooling and boiloff temperature versus height at 50 percent fill and 40°.

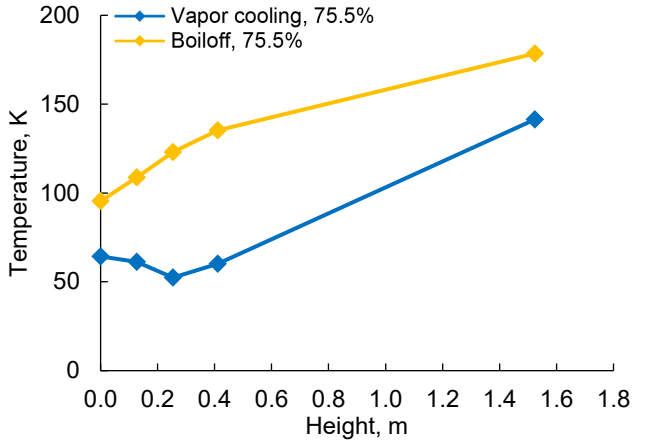

Figure B.32.—Vapor-cooling and boiloff temperature versus height at 75.5 percent fill and 40°.

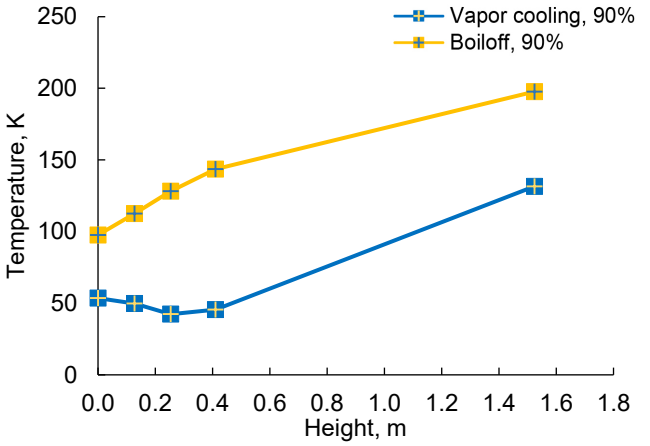

Figure B.33.—Vapor-cooling and boiloff temperature versus height at 90 percent fill and 40°.

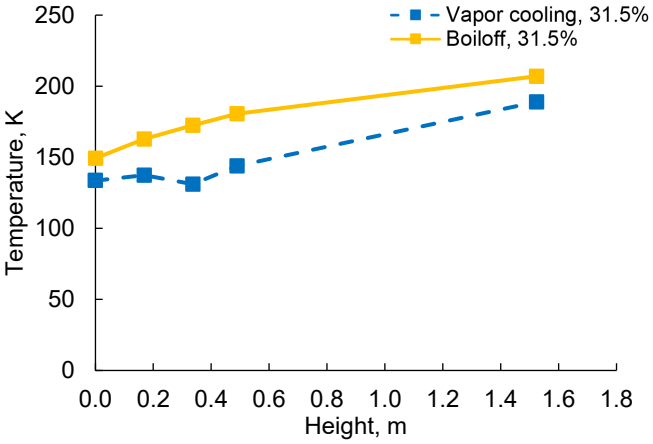

Figure B.34.—Vapor-cooling and boiloff temperature versus height at 31.5 percent fill and 120°.

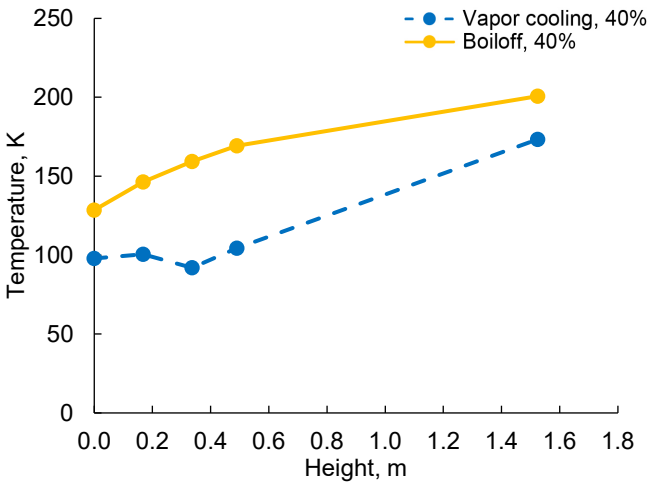

Figure B.35.—Vapor-cooling and boiloff temperature versus height at 40 percent fill and 120°.

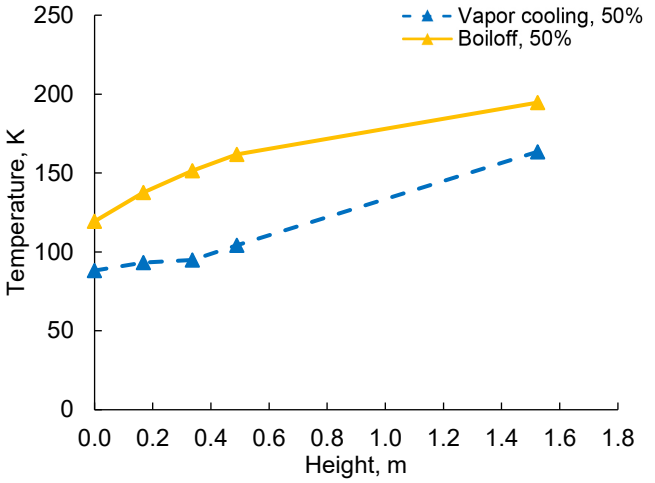

Figure B.36.—Vapor-cooling and boiloff temperature versus height at 50 percent fill and 120°.

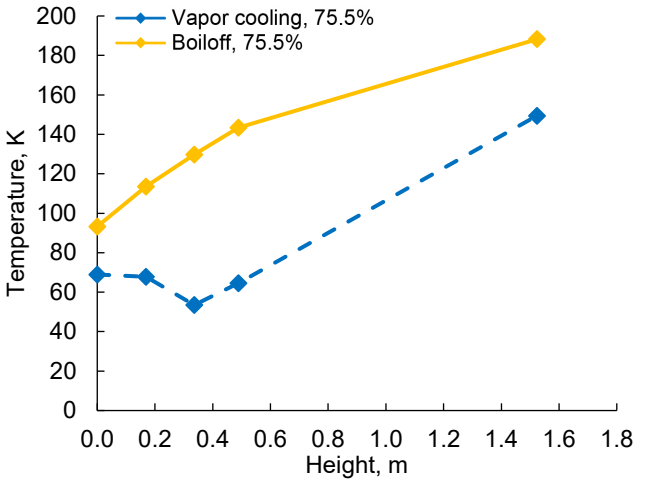

Figure B.37.—Vapor-cooling and boiloff temperature versus height at 75.5 percent fill and 120°.

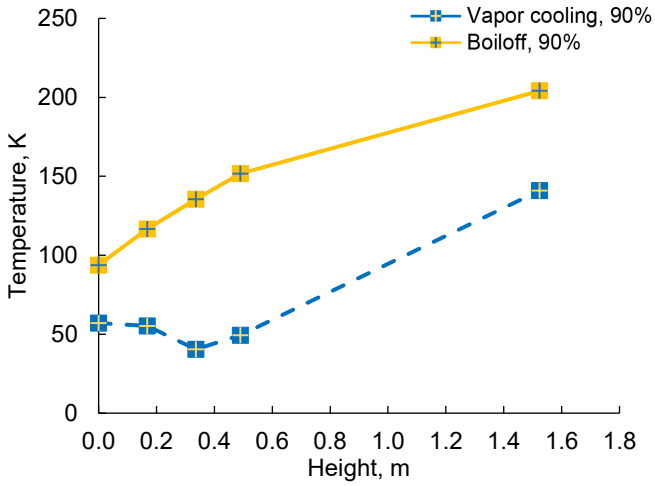

Figure B.38.—Vapor-cooling and boiloff temperature versus height at 90 percent fill and 120°.

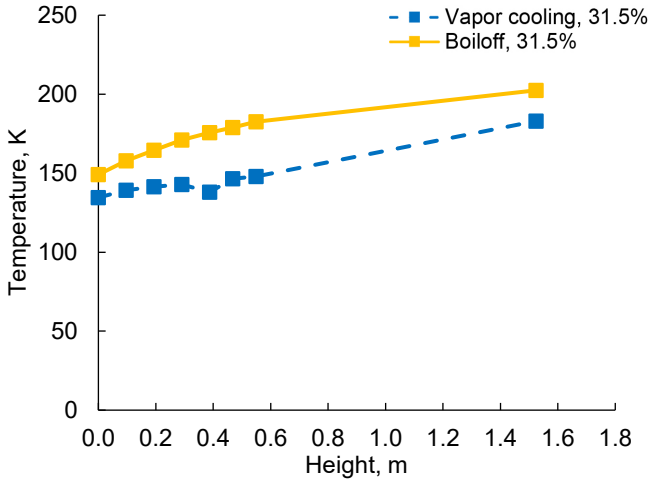

Figure B.39.—Vapor-cooling and boiloff temperature versus height at 31.5 percent fill and 180°.

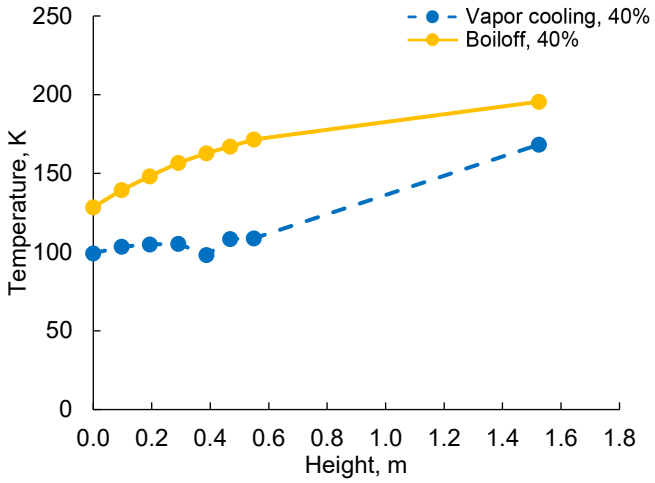

Figure B.40.—Vapor-cooling and boiloff temperature versus height at 40 percent fill and 180°.

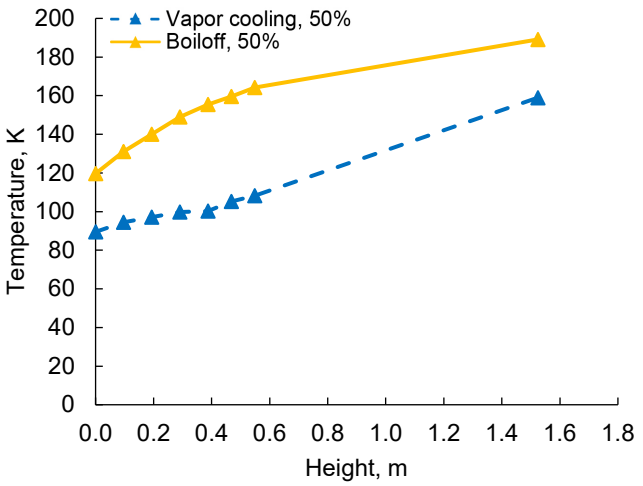

Figure B.41.—Vapor-cooling and boiloff temperature versus height at 50 percent fill and 180°.

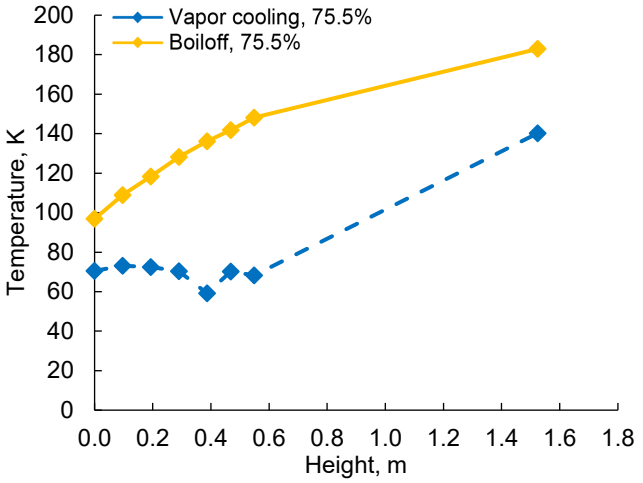

Figure B.42.—Vapor-cooling and boiloff temperature versus height at 75.5 percent fill and 180°.

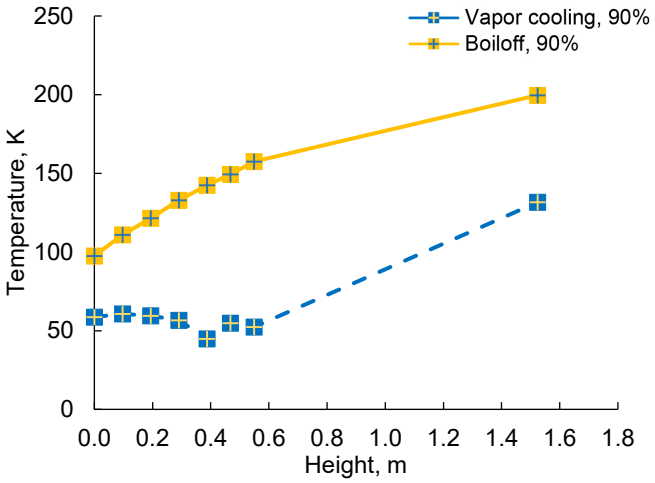

Figure B.43.—Vapor-cooling and boiloff temperature versus height at 90 percent fill and 180°.

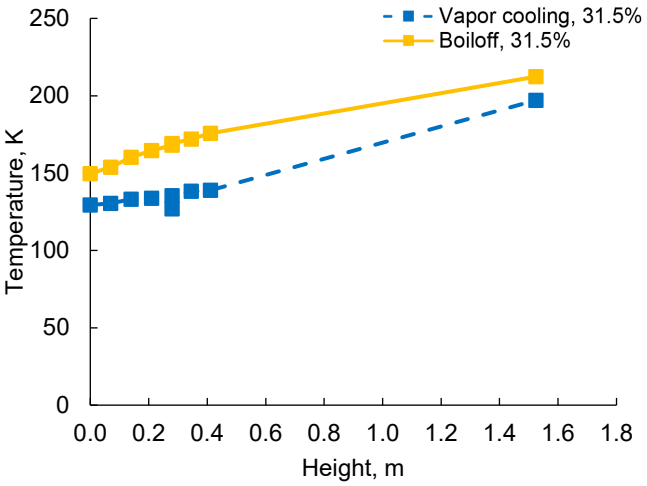

Figure B.44.—Vapor-cooling and boiloff temperature versus height at 31.5 percent fill and 230°.

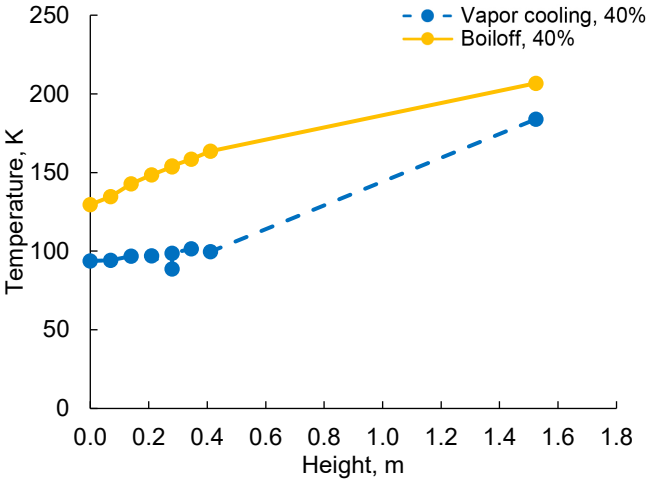

Figure B.45.—Vapor-cooling and boiloff temperature versus height at 40 percent fill and 230°.

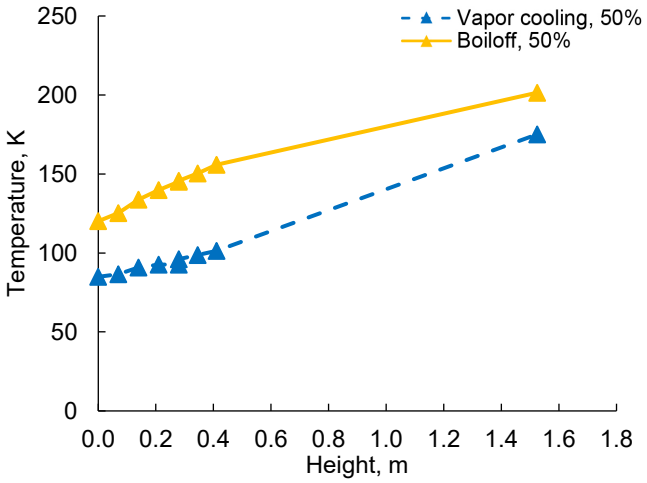

Figure B.46.—Vapor-cooling and boiloff temperature versus height at 50 percent fill and 230°.

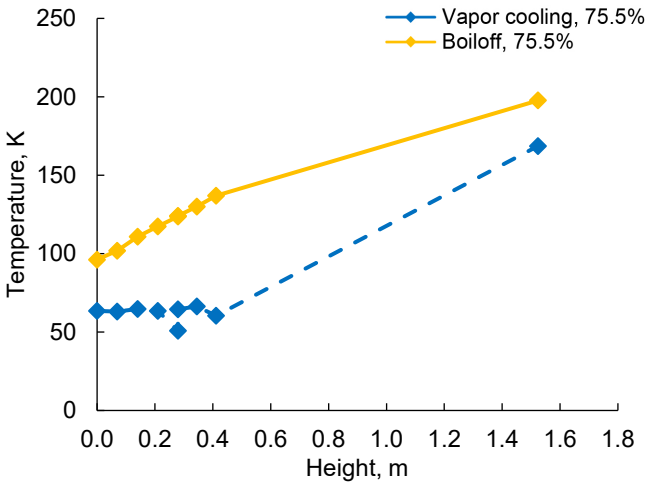

Figure B.47.—Vapor-cooling and boiloff temperature versus height at 75.5 percent fill and 230°.

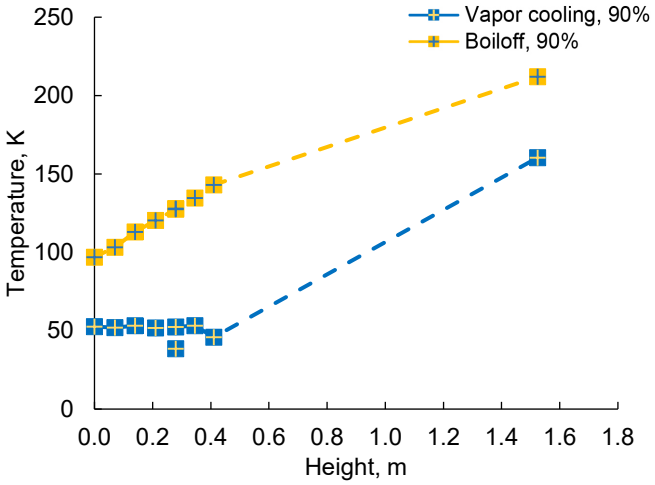

Figure B.48.—Vapor-cooling and boiloff temperature versus height at 90 percent fill and 230°.

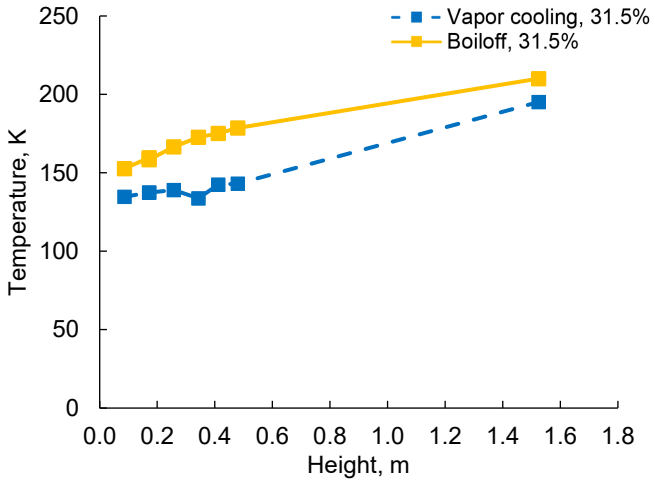

Figure B.49.—Vapor-cooling and boiloff temperature versus height at 31.5 percent fill and 300°.

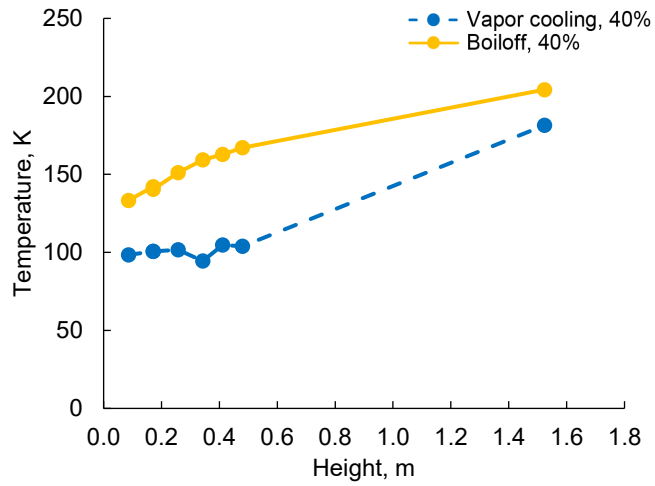

Figure B.50.—Vapor-cooling and boiloff temperature versus height at 40 percent fill and 300°.

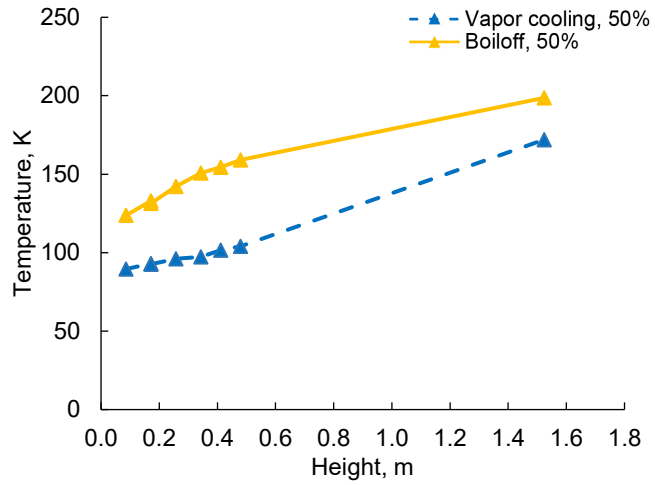

Figure B.51.—Vapor-cooling and boiloff temperature versus height at 50 percent fill and 300°.

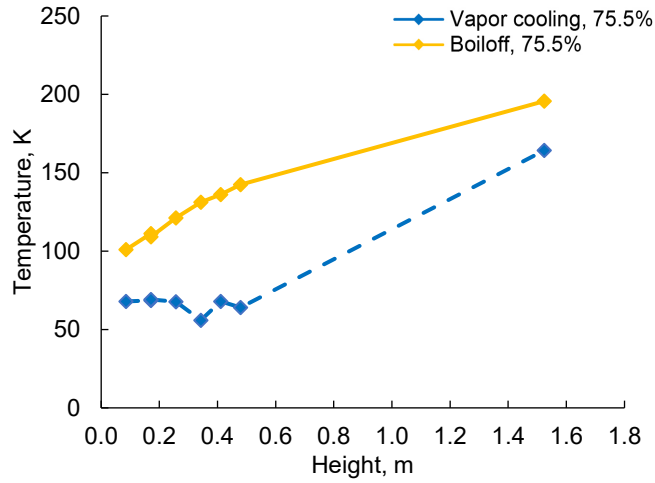

Figure B.52.—Vapor-cooling and boiloff temperature versus height at 75.5 percent fill and 300°.

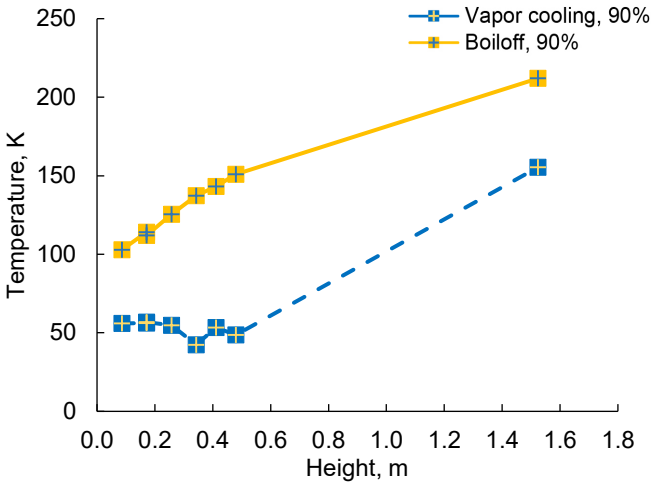

Figure B.53.—Vapor-cooling and boiloff temperature versus height at 90 percent fill and 300°.

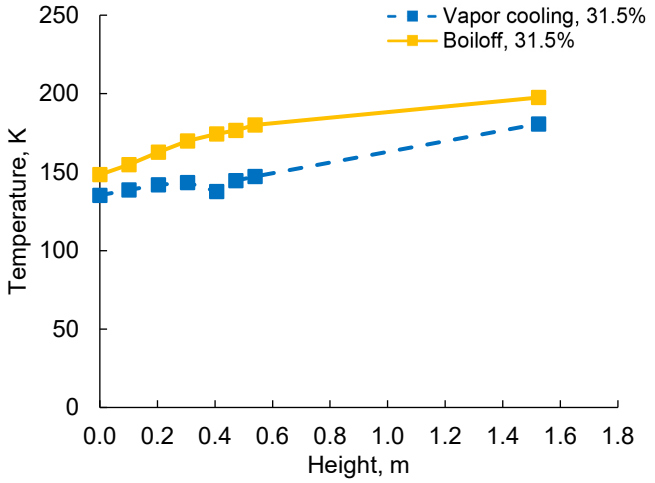

Figure B.54.—Vapor-cooling and boiloff temperature versus height at 31.5 percent fill and 360°.

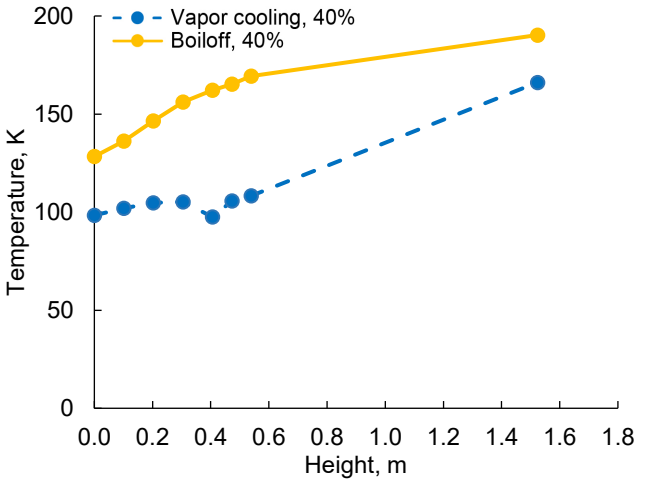

Figure B.55.—Vapor-cooling and boiloff temperature versus height at 40 percent fill and 360°.

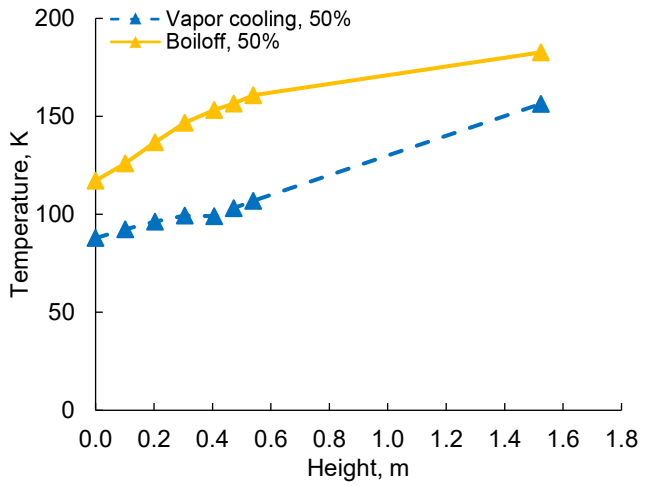

Figure B.56.—Vapor-cooling and boiloff temperature versus height at 50 percent fill and 360°.

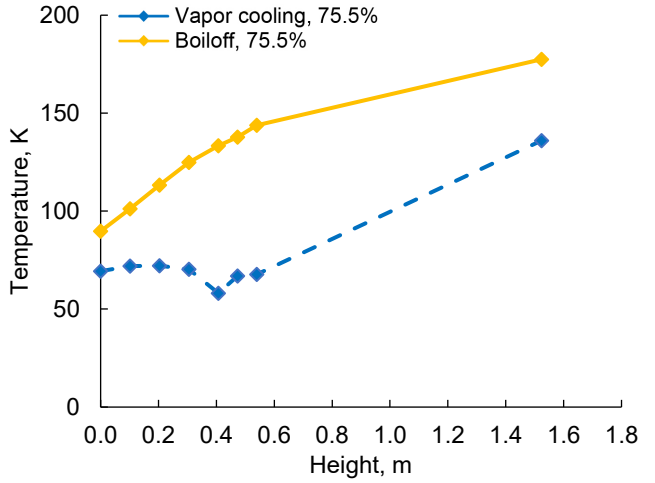

Figure B.57.—Vapor-cooling and boiloff temperature versus height at 75.5 percent fill and 360°.

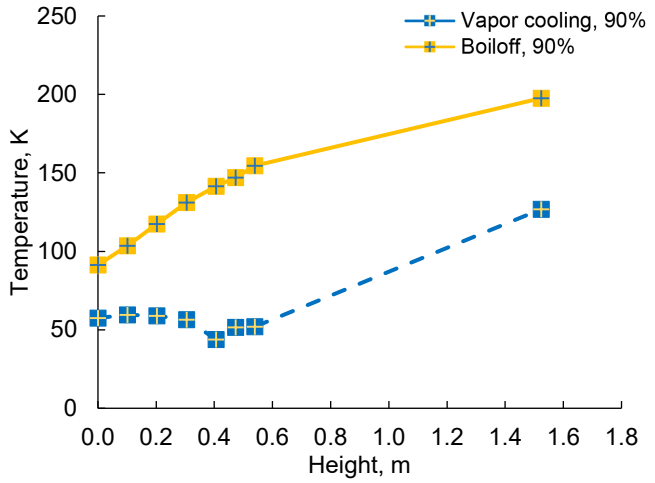

Figure B.58.—Vapor-cooling and boiloff temperature versus height at 90 percent fill and 360°.

B.6 Difference Between Boiloff and Vapor-Cooling Temperatures Versus Height at Each Fill Level for All Angular Stations

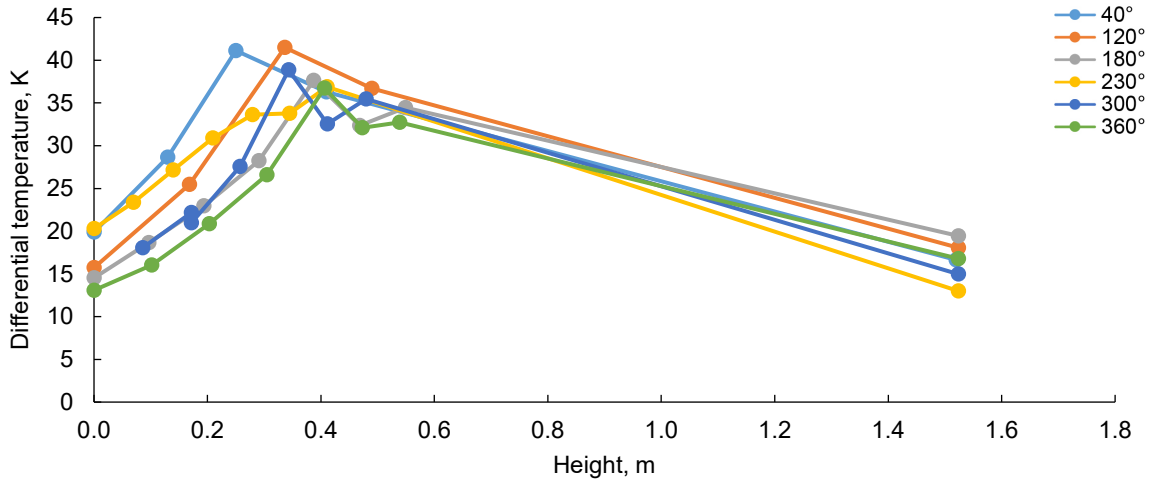

Figure B.59.—Difference between boiloff and vapor-cooling temperatures versus height at 31.5 percent fill.

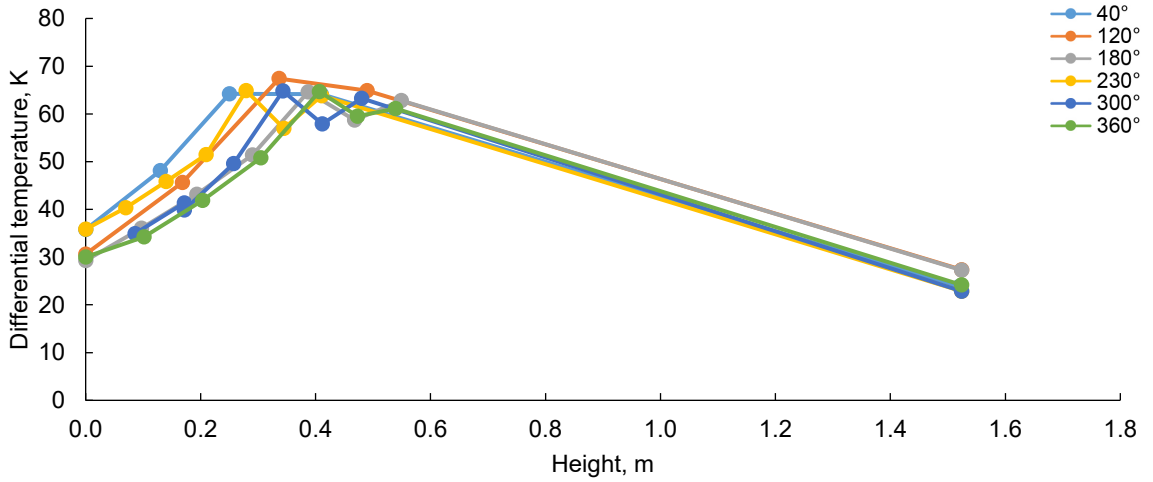

Figure B.60.—Difference between boiloff and vapor-cooling temperatures versus height at 40 percent fill.

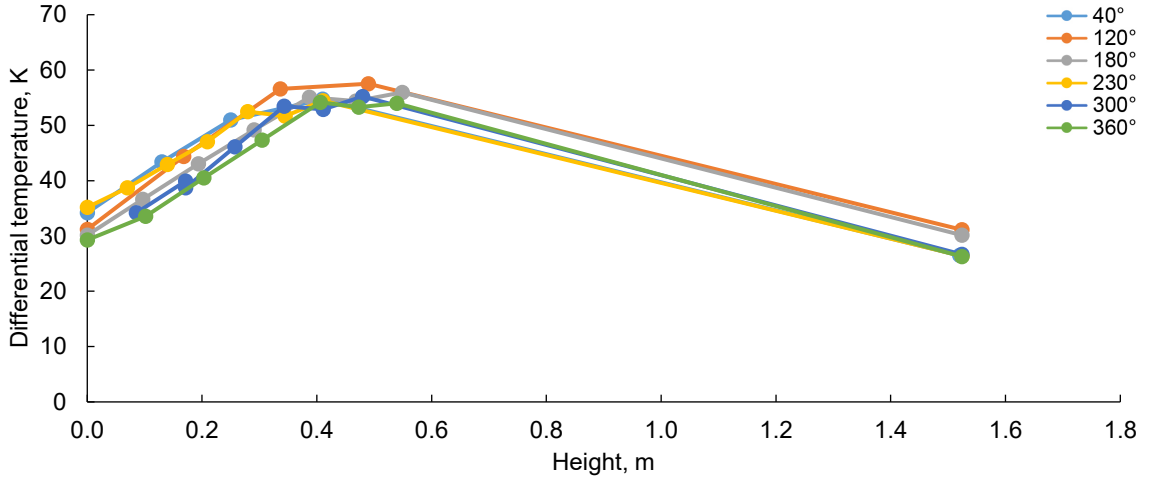

Figure B.61.—Difference between boiloff and vapor-cooling temperatures versus height at 50 percent fill.

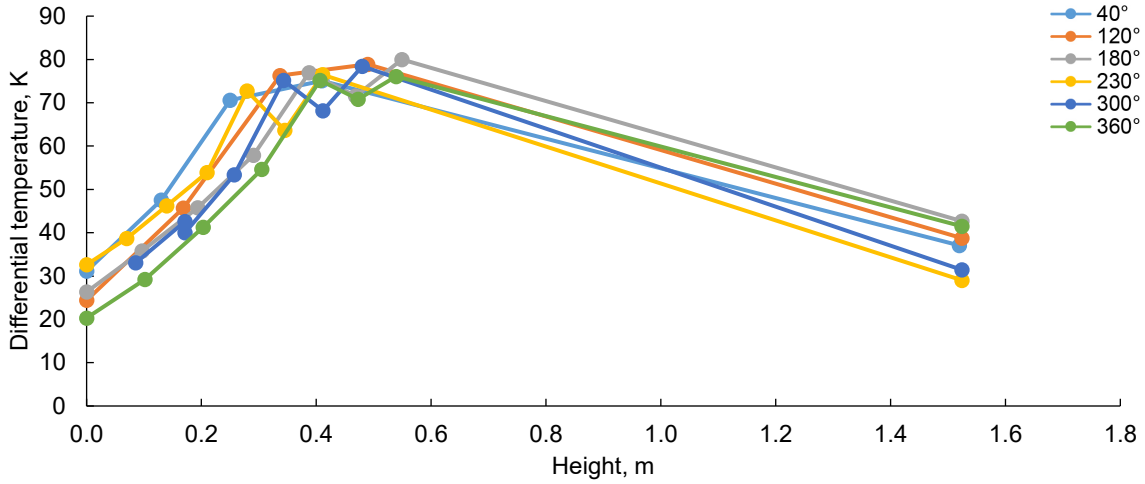

Figure B.62.—Difference between boiloff and vapor-cooling temperatures versus height at 75.5 percent fill.

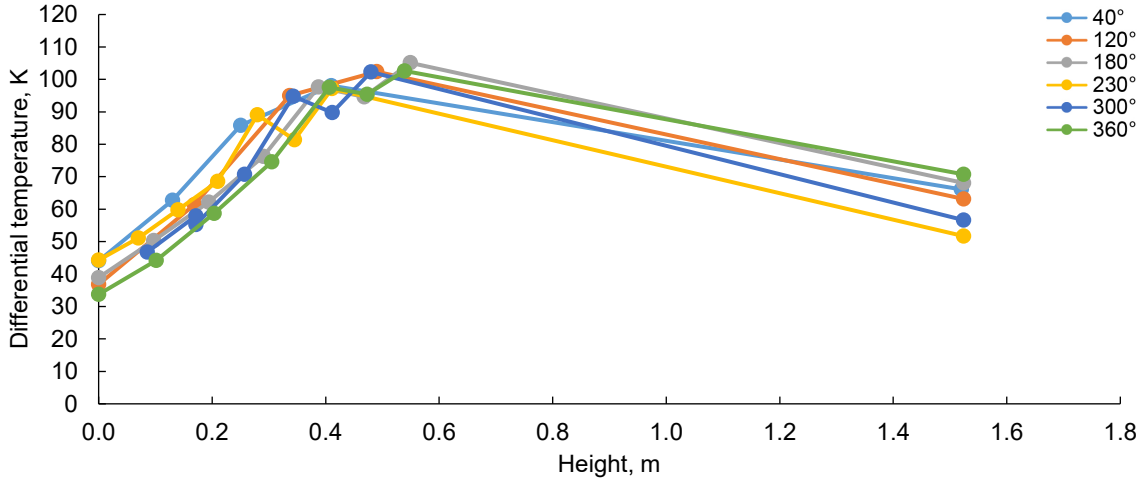

Figure B.63.—Difference between boiloff and vapor-cooling temperatures versus height at 90 percent fill.

Appendix C.—Vapor-Cooling-Line Temperatures Baseline Test

Figure C.1 to Figure C.6 show the various vapor-cooling-line temperatures during the baseline test.

C.1 Summary Plot of Vapor-Cooling-Line Temperatures Versus Vapor-Cooling-Line Length Including All Fill Levels

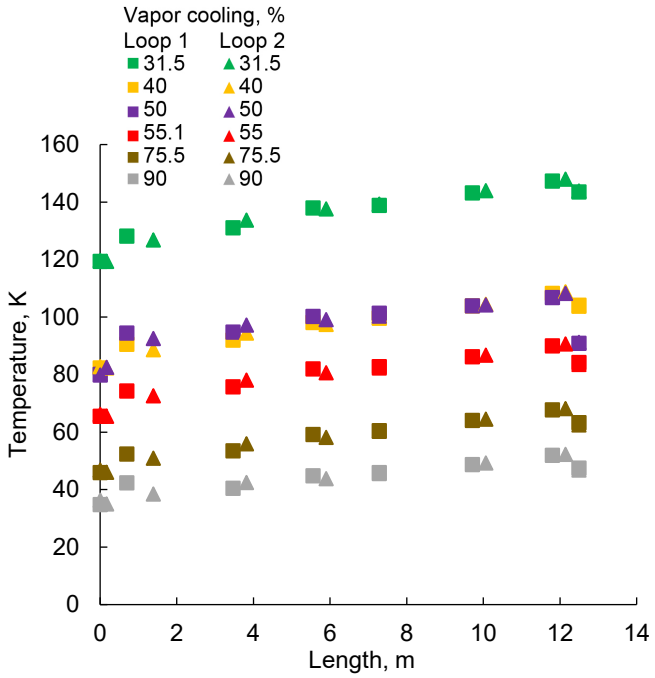

Figure C.1.—Vapor-cooling-line temperatures versus length for all fill levels.

C.2 Plots of Vapor-Cooling-Line Temperatures Versus Length for Each Fill Level

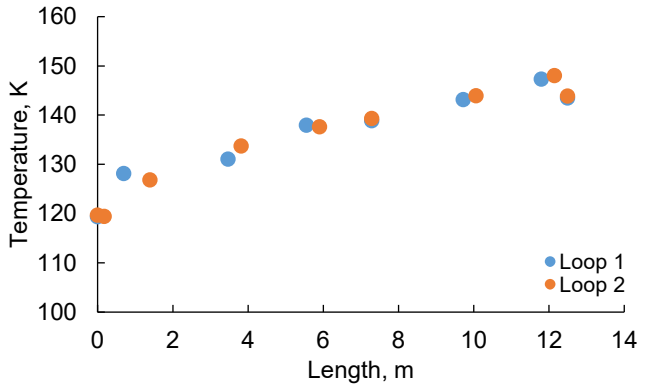

Figure C.2.—Vapor-cooling-line temperatures versus length at 31.5 percent fill.

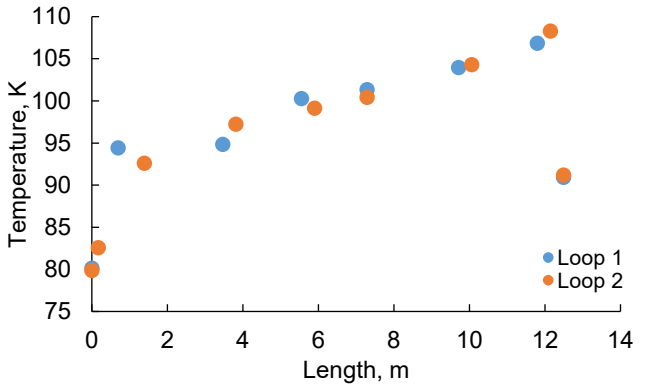

Figure C.4.—Vapor-cooling-line temperatures versus length at 50 percent fill.

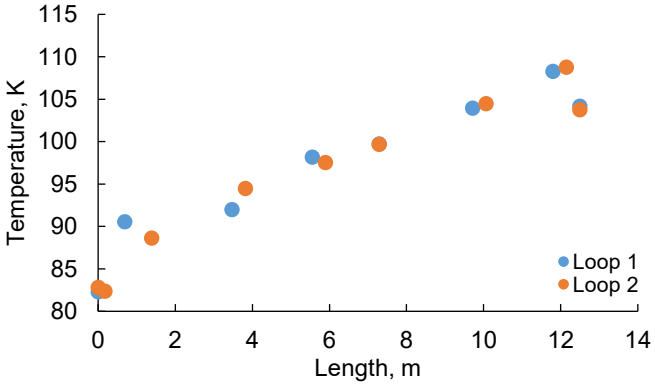

Figure C.3.—Vapor-cooling-line temperatures versus length at 40 percent fill.

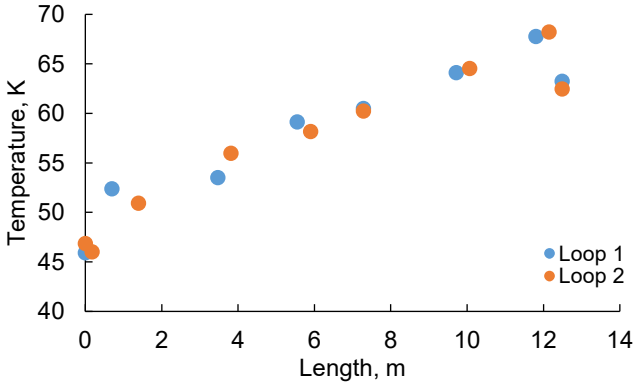

Figure C.5.—Vapor-cooling-line temperatures versus length at 75.5 percent fill.

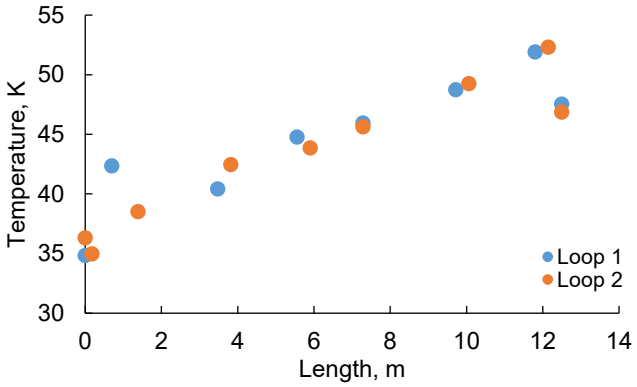

Figure C.6.—Vapor-cooling-line temperatures versus length at 90 percent fill.

Appendix D.—Skirt Temperatures Thermal 1 Test

Figure D.1 to Figure D.63 show the skirt temperatures during the Thermal 1 test.

D.1 Summary Plot for Each Angle Including All Fill Levels for Boiloff and Vapor Cooling

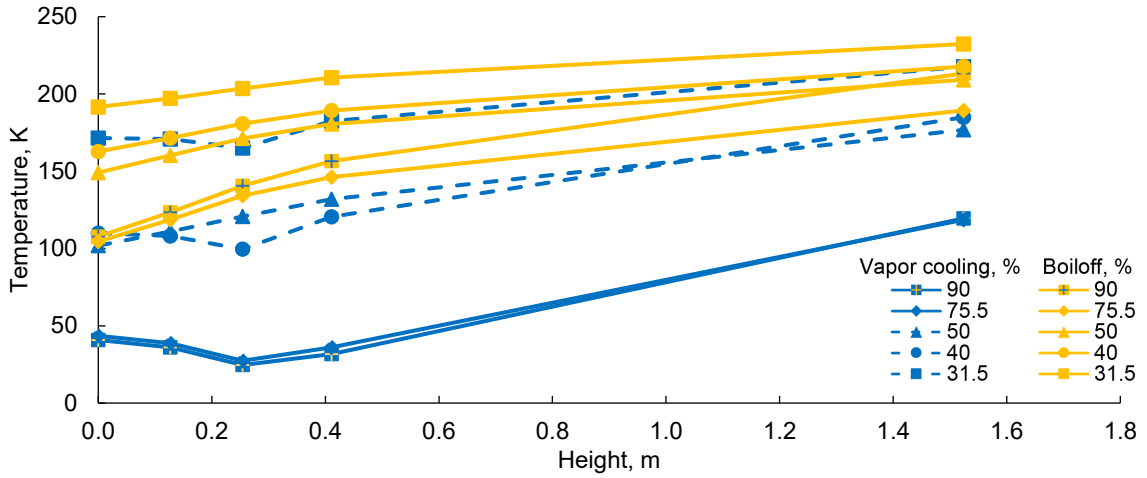

Figure D.1.—Temperature versus height at 40° comparing vapor-cooling and boiloff temperatures at every fill level.

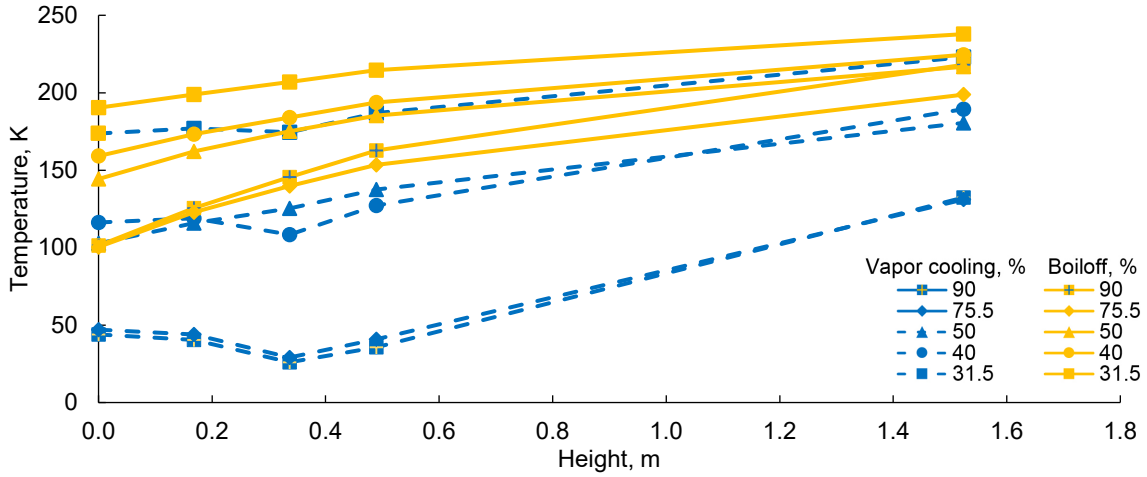

Figure D.2.—Temperature versus height at 120° comparing vapor-cooling and boiloff temperatures at every fill level.

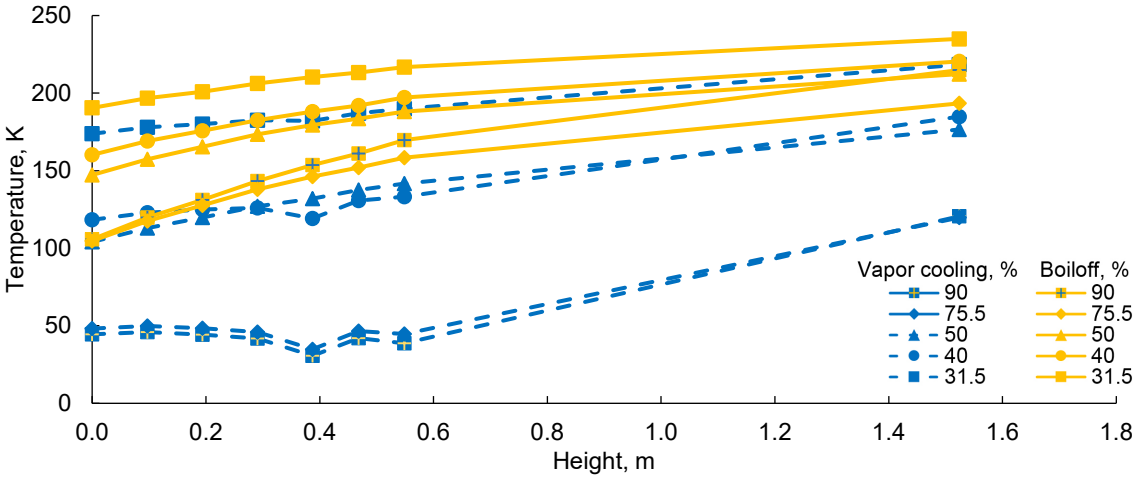

Figure D.3.—Temperature versus height at 180° comparing vapor-cooling and boiloff temperatures at every fill level.

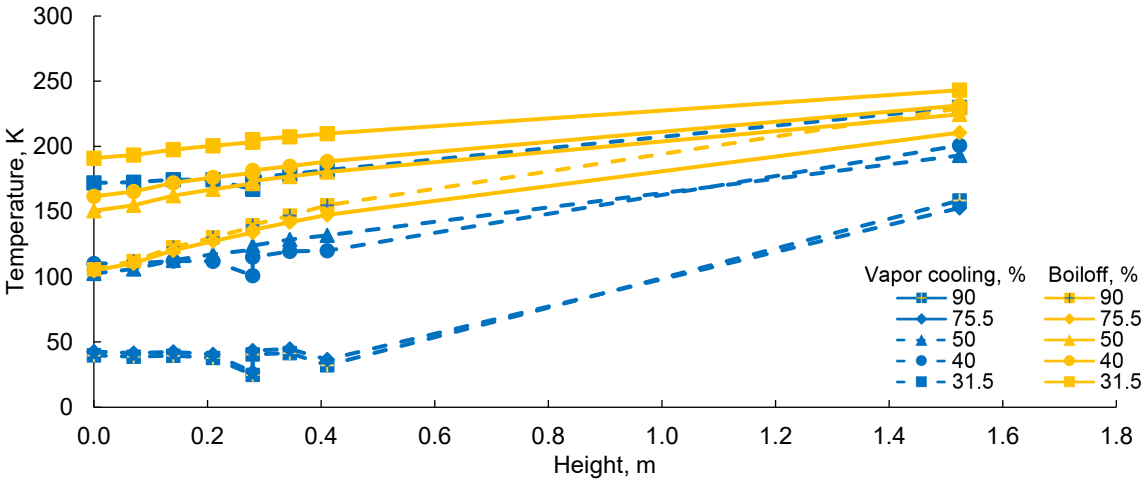

Figure D.4.—Temperature versus height at 230° comparing vapor-cooling and boiloff temperatures at every fill level.

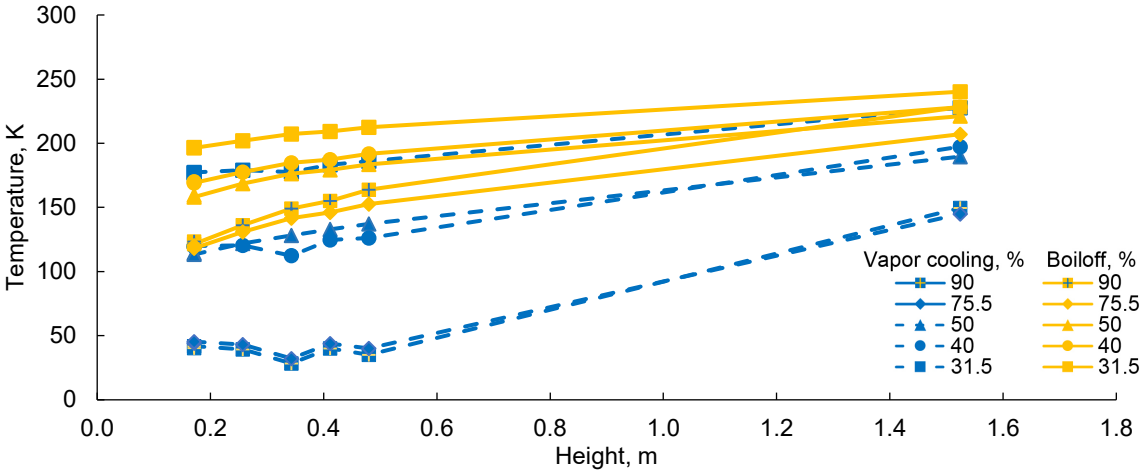

Figure D.5.—Temperature versus height at 300° comparing vapor-cooling and boiloff temperatures at every fill level.

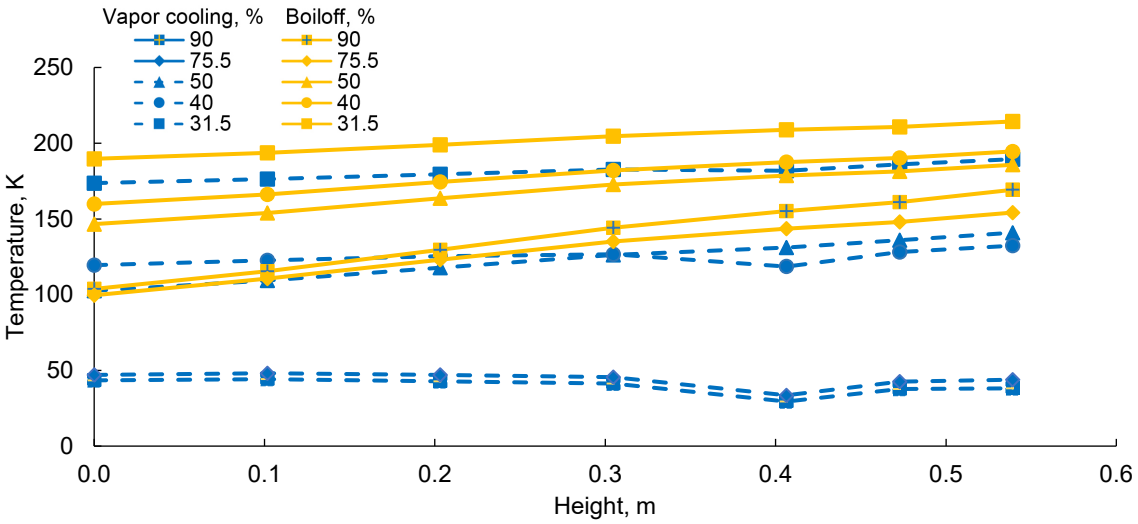

Figure D.6.—Temperature versus height at 360° comparing vapor-cooling and boiloff temperatures at every fill level.

D.2 Summary Plot for Each Angle Including All Fill Levels for Boiloff

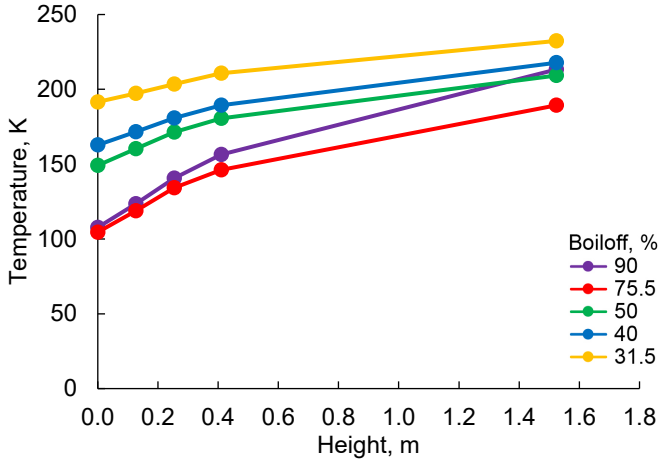

Figure D.7.—Boiloff temperature versus height at 40° for every fill level.

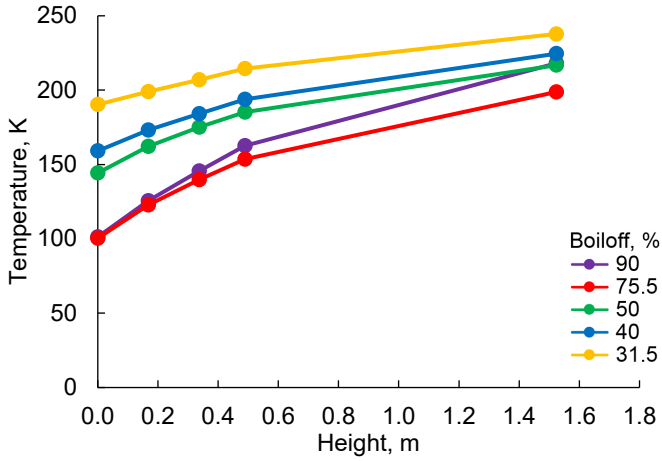

Figure D.8.—Boiloff temperature versus height at 120° for every fill level.

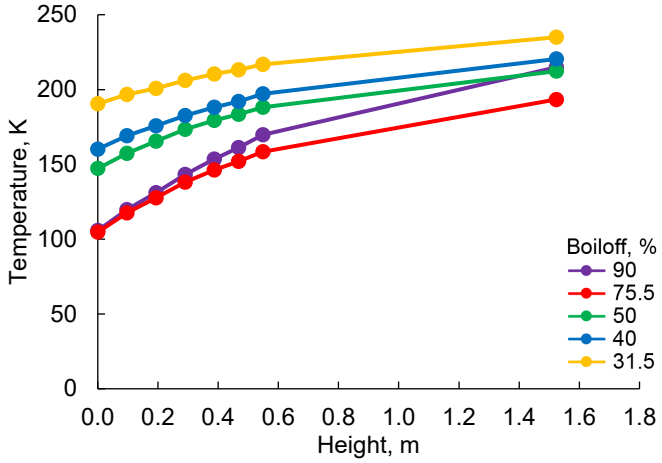

Figure D.9.—Boiloff temperature versus height at 180° for every fill level.

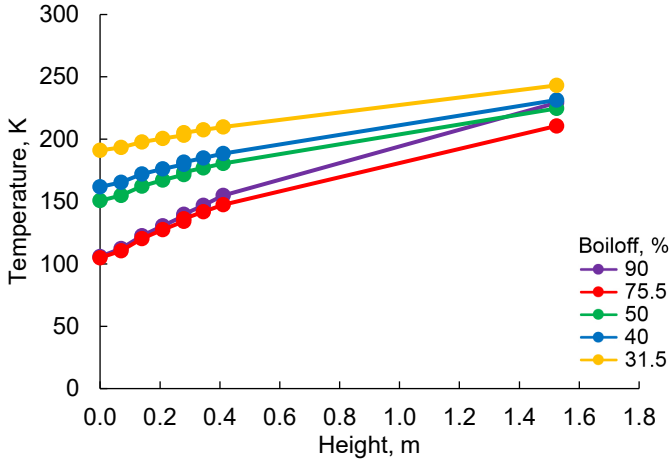

Figure D.10.—Boiloff temperature versus height at 230° for every fill level.

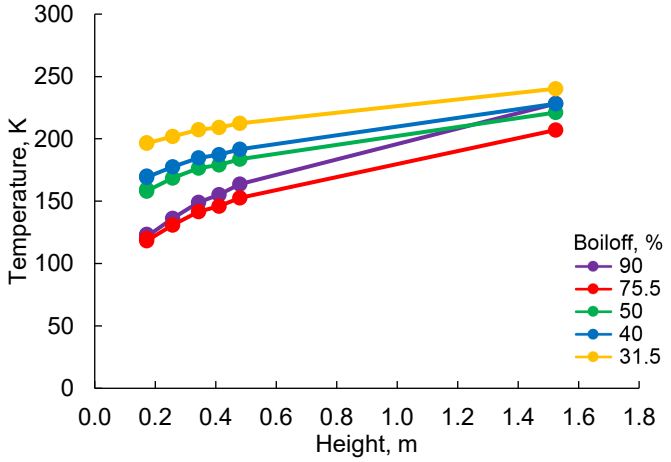

Figure D.11.—Boiloff temperature versus height at 300° for every fill level.

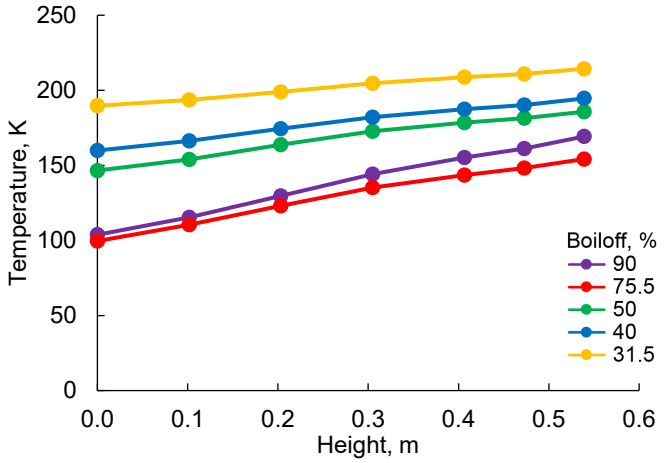

Figure D.12.—Boiloff temperature versus height at 360° for every fill level.

D.3 Summary Plot for Each Angle Including All Fill Levels for Vapor Cooling

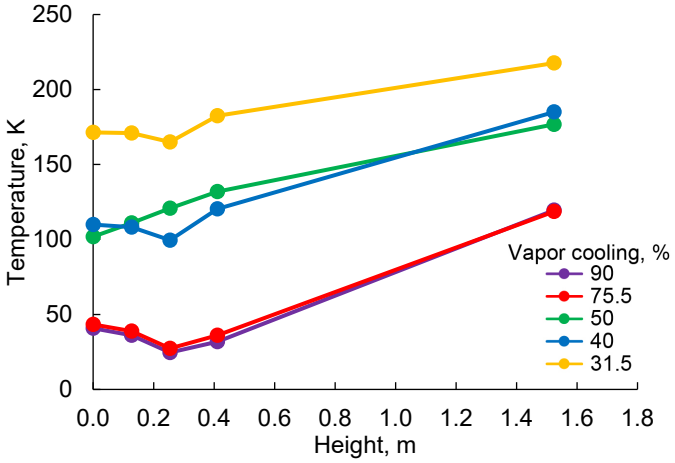

Figure D.13.—Vapor-cooling temperature versus height at 40° for every fill level.

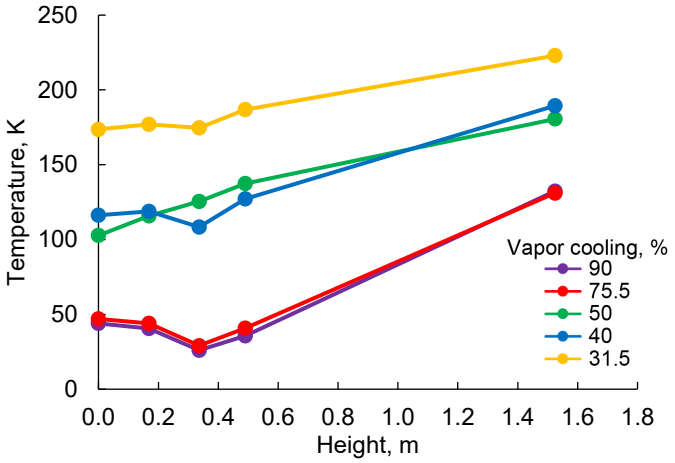

Figure D.14.—Vapor-cooling temperature versus height at 120° for every fill level.

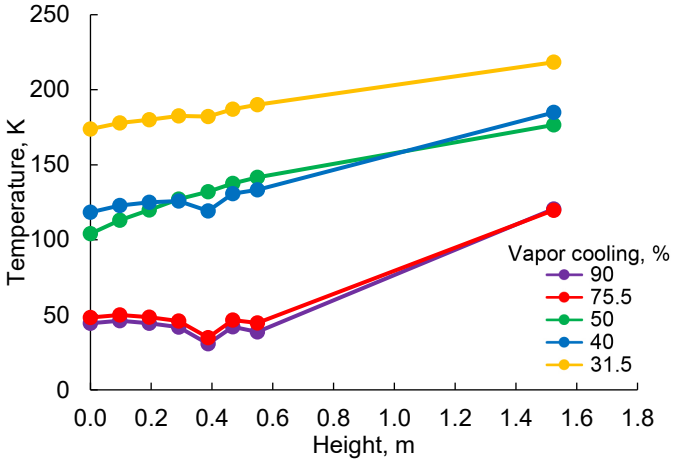

Figure D.15.—Vapor-cooling temperature versus height at 180° for every fill level.

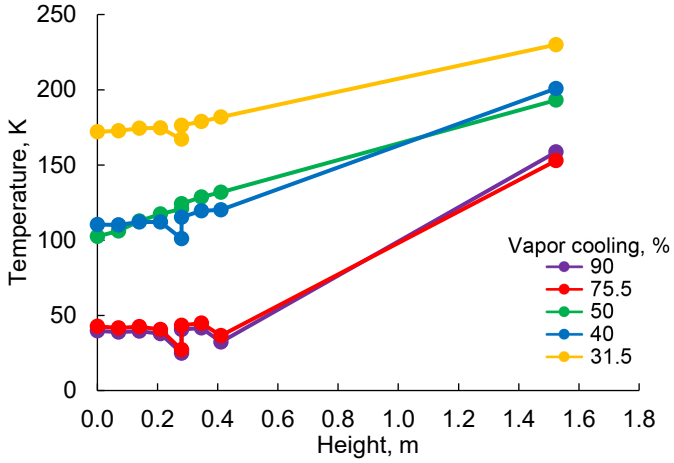

Figure D.16.—Vapor-cooling temperature versus height at 230° for every fill level.

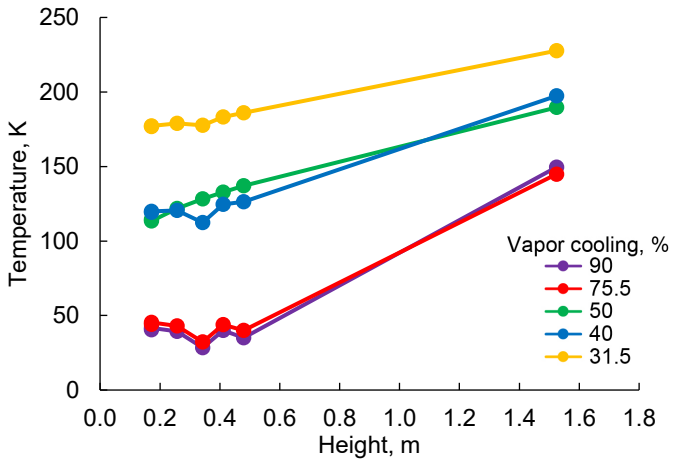

Figure D.17.—Vapor-cooling temperature versus height at 300° for every fill level.

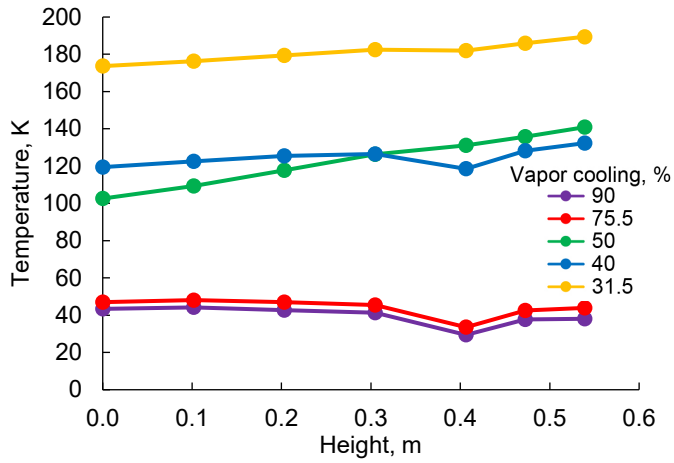

Figure D.18.—Vapor-cooling temperature versus height at 360° for every fill level.

D.4 Temperature Versus Height at Each Fill Level for All Angular Stations

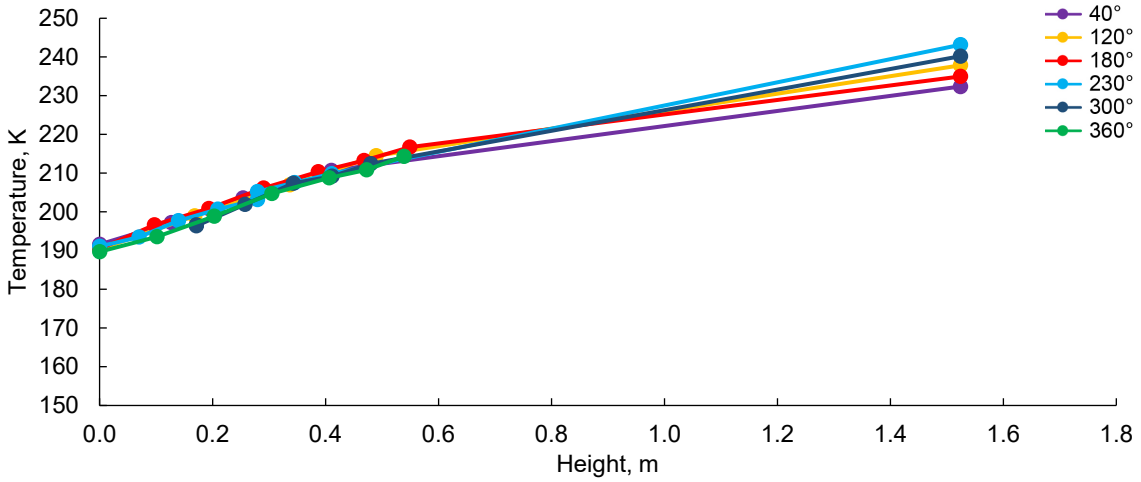

Figure D.19.—Boiloff temperature versus height at 31.5 percent fill level for every angular station.

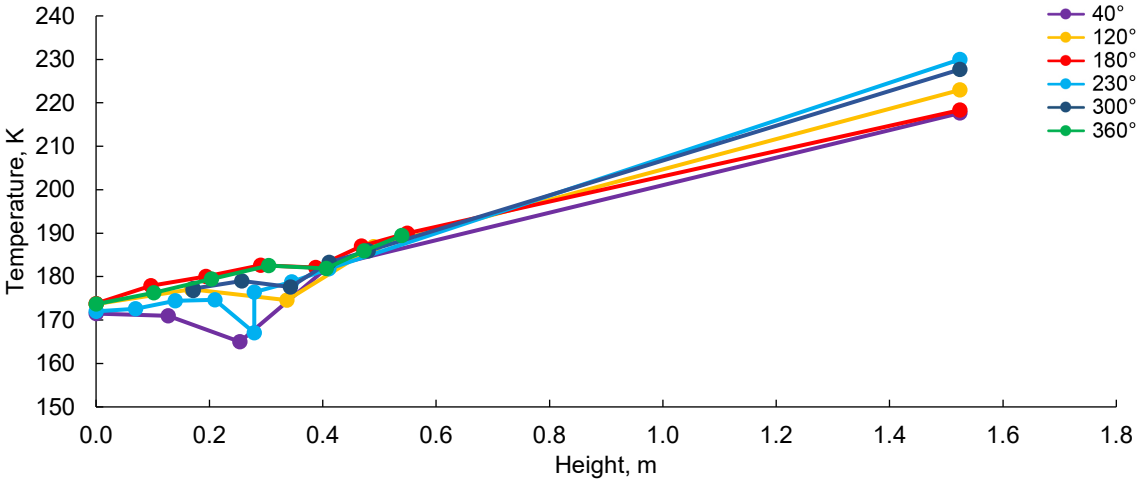

Figure D.20.—Vapor-cooling temperature versus height at 31.5 percent fill level for every angular station.

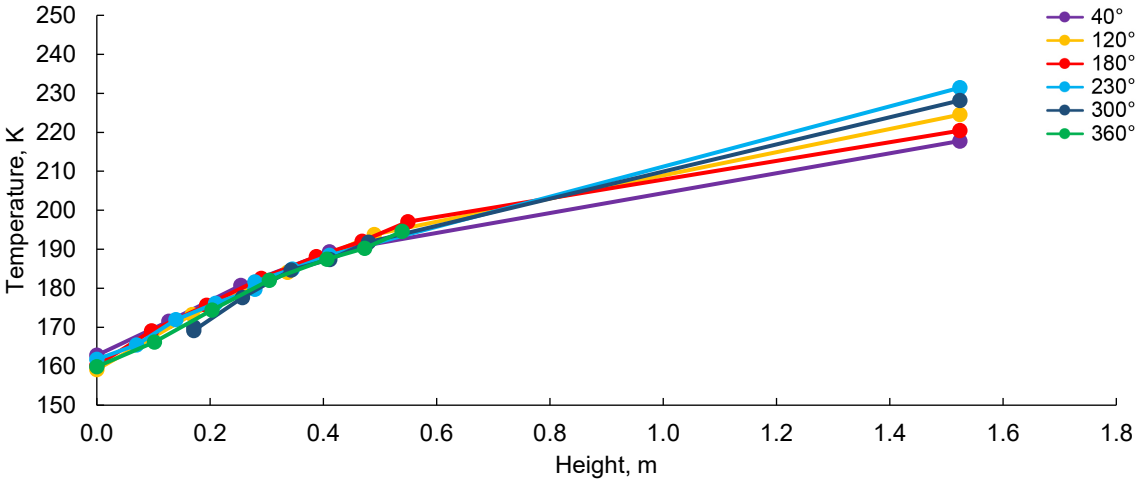

Figure D.21.—Boiloff temperature versus height at 40 percent fill level for every angular station.

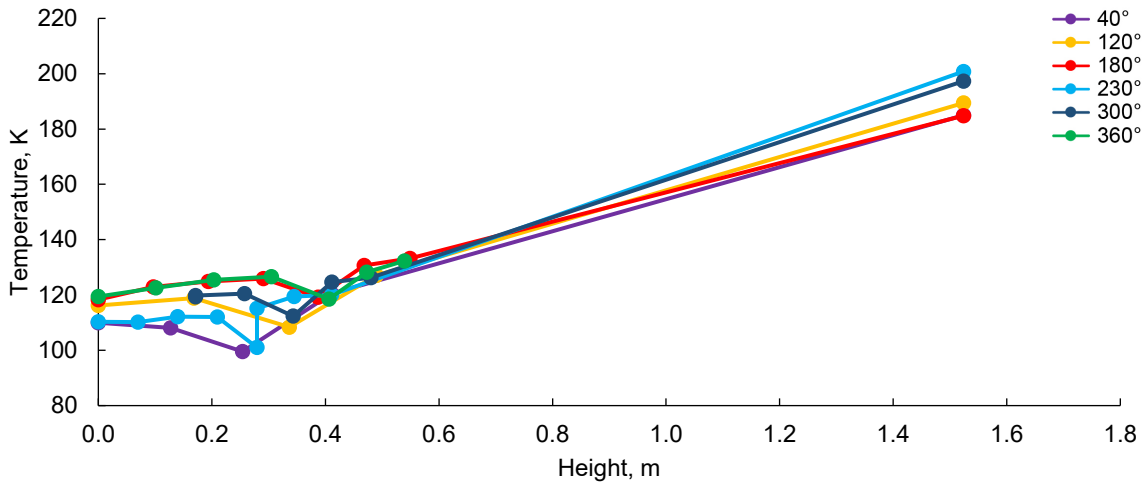

Figure D.22.—Vapor-cooling temperature versus height at 40 percent fill level for every angular station.

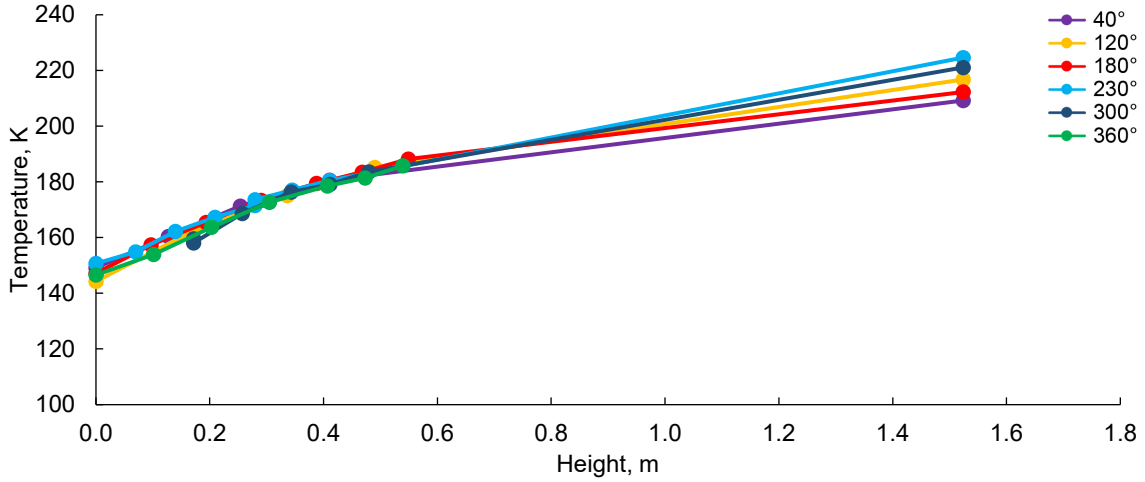

Figure D.23.—Boiloff temperature versus height at 50 percent fill level for every angular station.

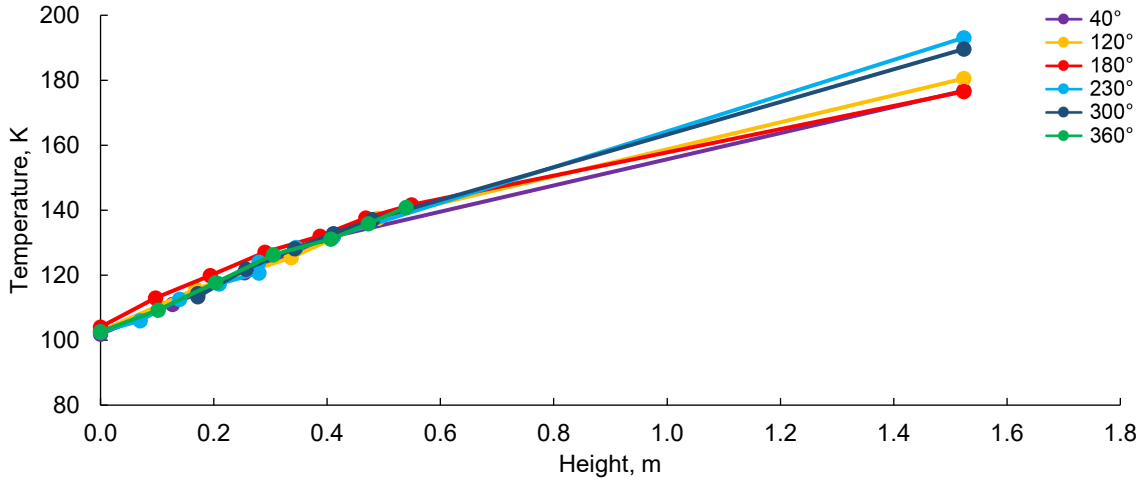

Figure D.24.—Vapor-cooling temperature versus height at 50 percent fill level for every angular station.

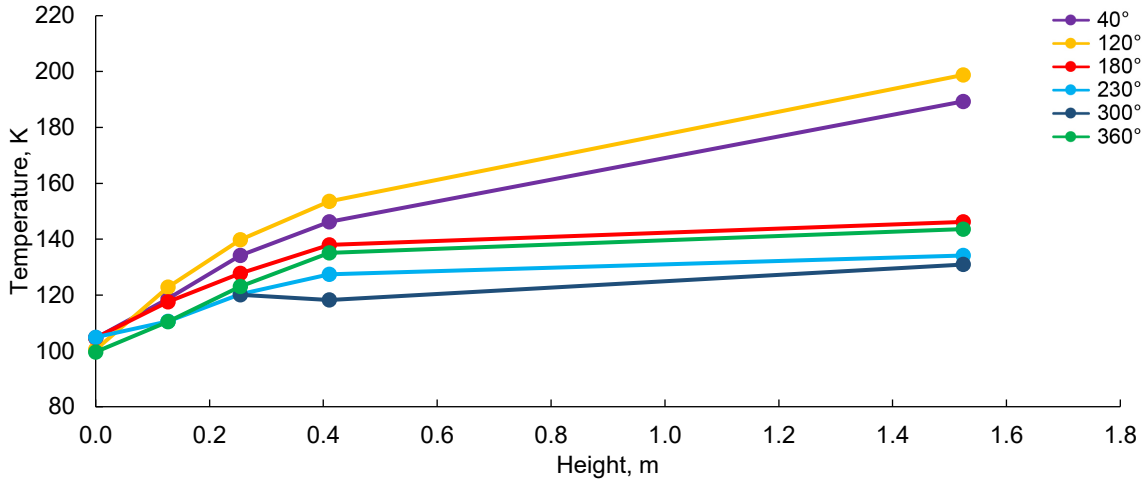

Figure D.25.—Boiloff temperature versus height at 75.5 percent fill level for every angular station.

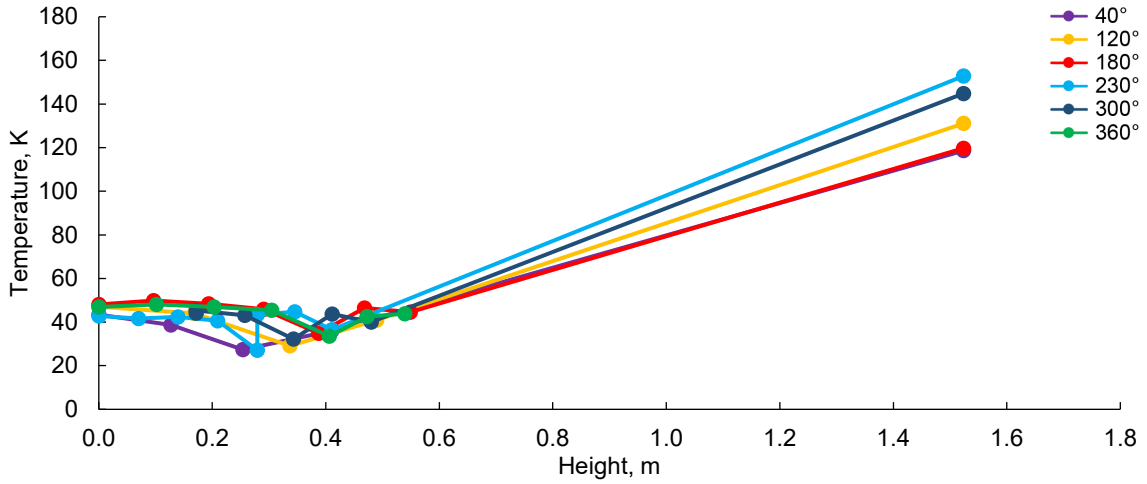

Figure D.26.—Vapor-cooling temperature versus height at 75.5 percent fill level for every angular station.

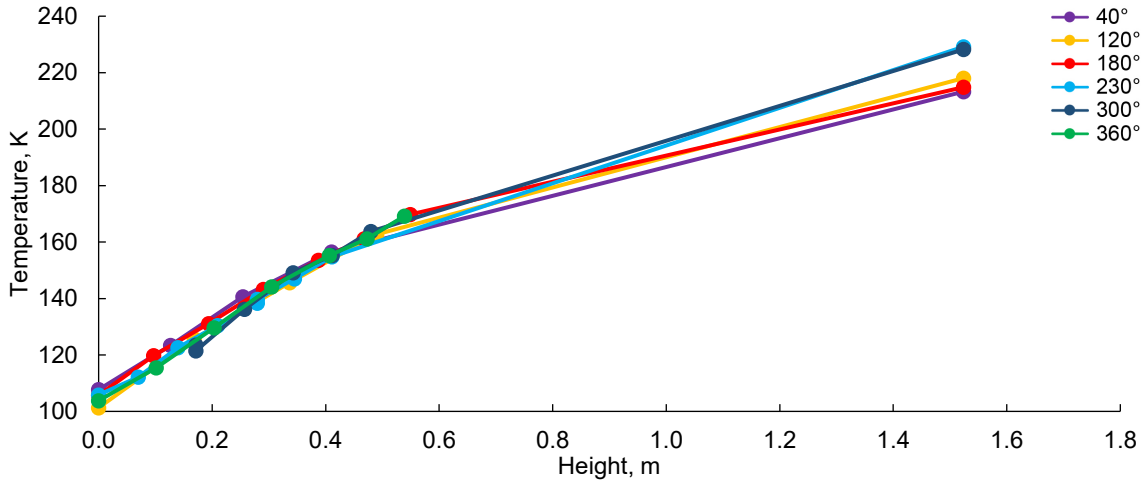

Figure D.27.—Boiloff temperature versus height at 90 percent fill level for every angular station.

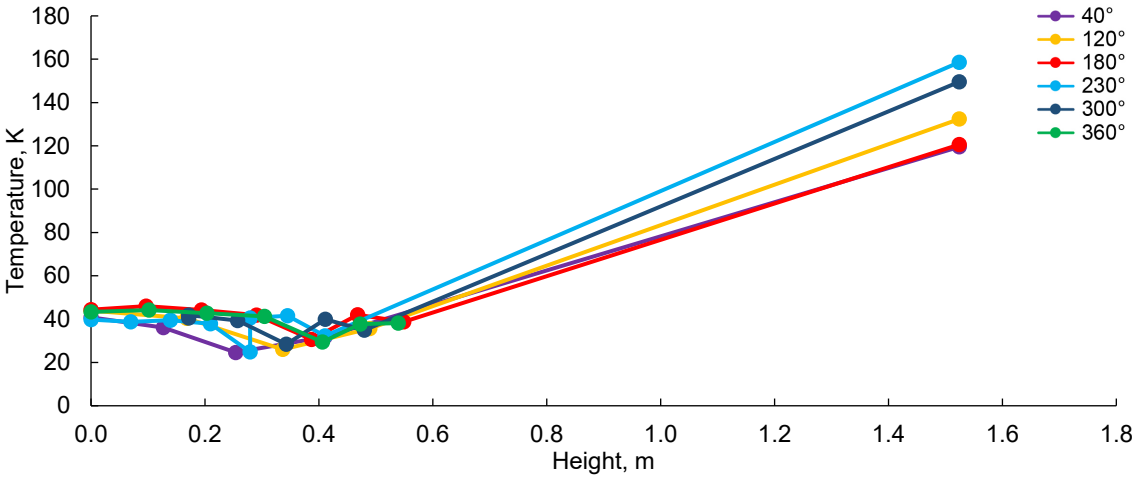

Figure D.28.—Vapor-cooling temperature versus height at 90 percent fill level for every angular station.

D.5 Temperature Versus Height at Each Fill Level and Each Angular Station Comparing Vapor Cooling and Boiloff

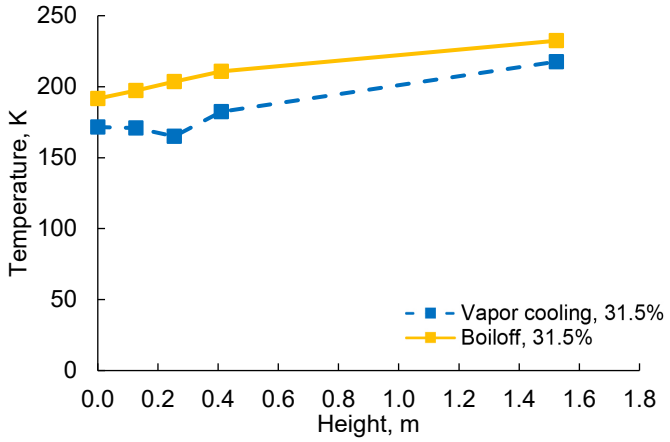

Figure D.29.—Vapor-cooling and boiloff temperature versus height at 31.5 percent fill and 40°.

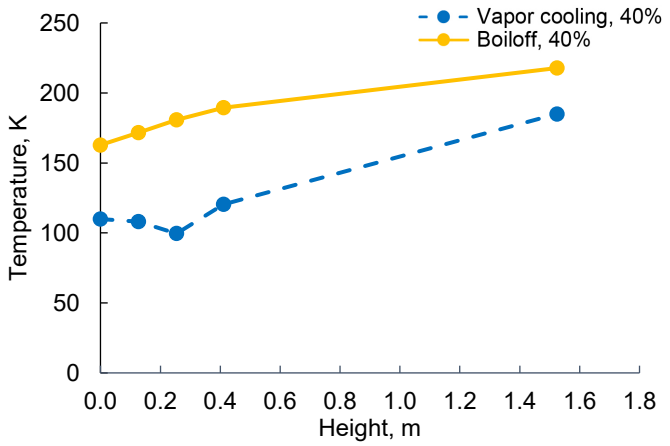

Figure D.30.—Vapor-cooling and boiloff temperature versus height at 40 percent fill and 40°.

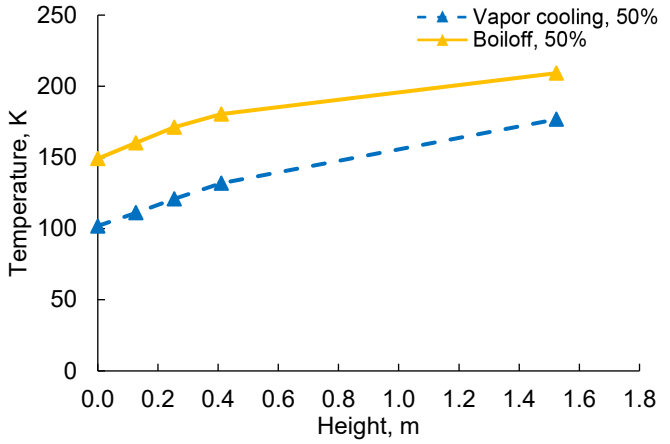

Figure D.31.—Vapor-cooling and boiloff temperature versus height at 50 percent fill and 40°.

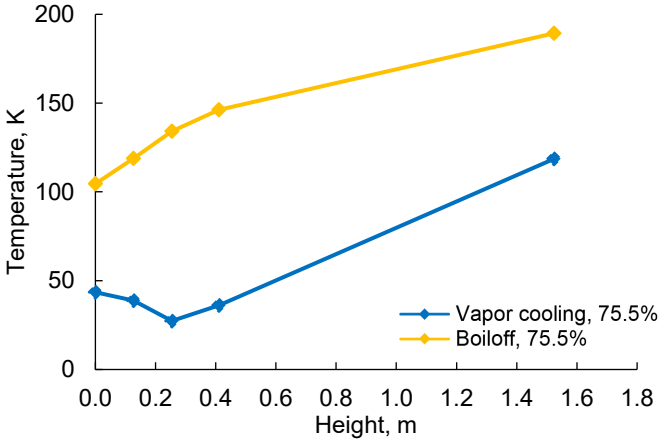

Figure D.32.—Vapor-cooling and boiloff temperature versus height at 75.5 percent fill and 40°.

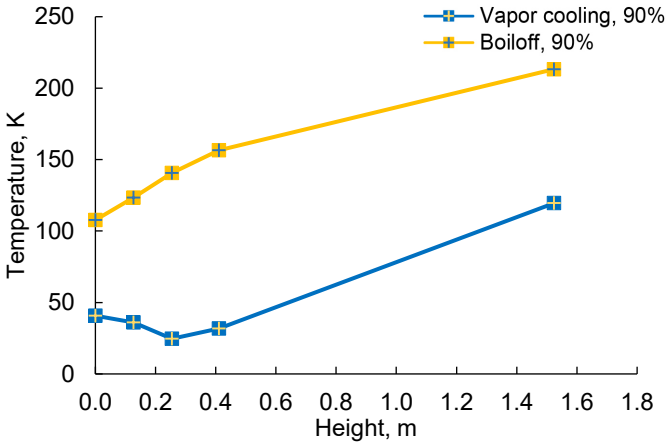

Figure D.33.—Vapor-cooling and boiloff temperature versus height at 90 percent fill and 40°.

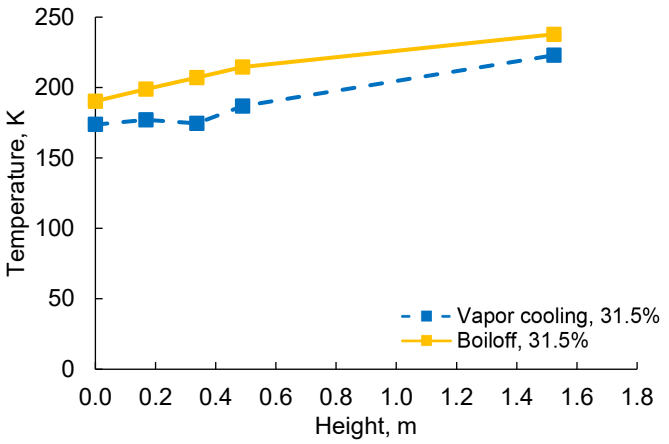

Figure D.34.—Vapor-cooling and boiloff temperature versus height at 31.5 percent fill and 120°.

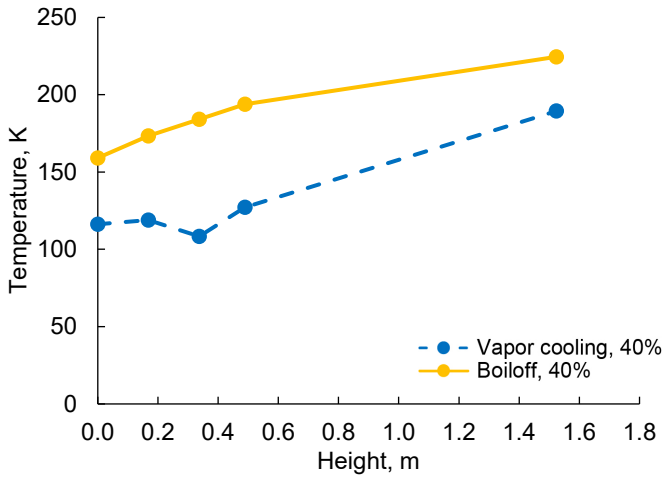

Figure D.35.—Vapor-cooling and boiloff temperature versus height at 40 percent fill and 120°.

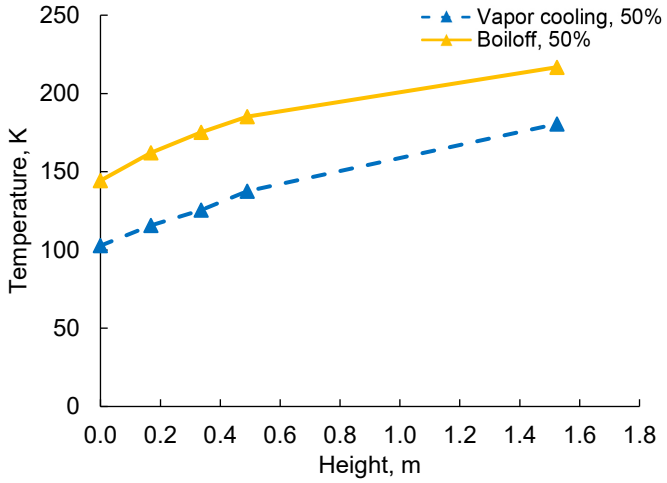

Figure D.36.—Vapor-cooling and boiloff temperature versus height at 50 percent fill and 120°.

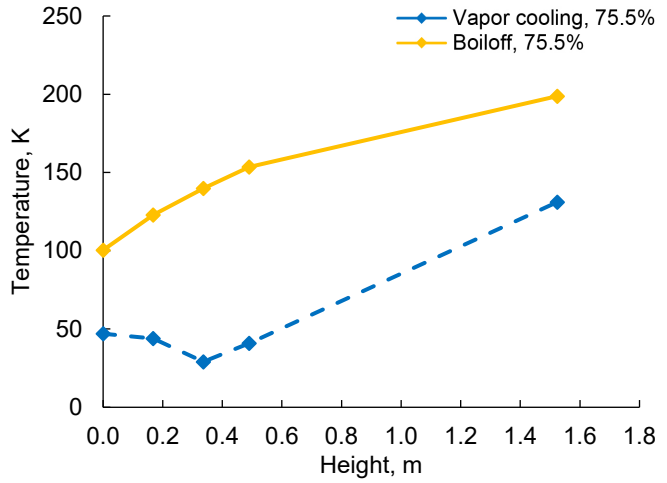

Figure D.37.—Vapor-cooling and boiloff temperature versus height at 75.5 percent fill and 120°.

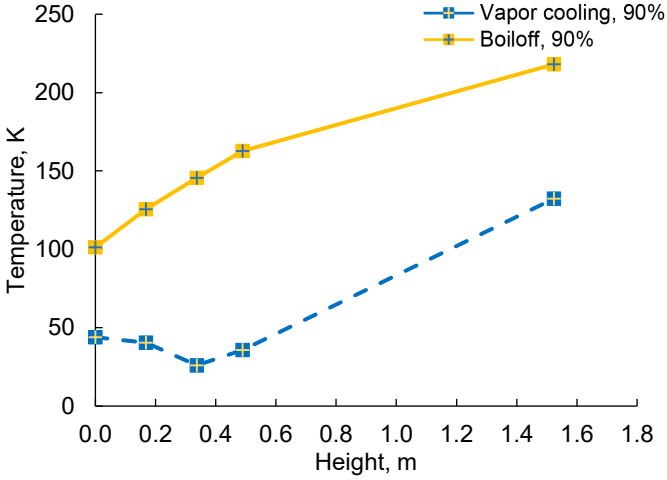

Figure D.38.—Vapor-cooling and boiloff temperature versus height at 90 percent fill and 120°.

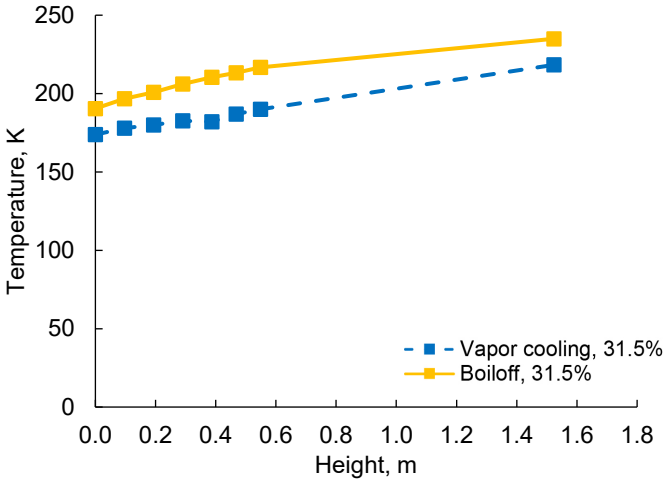

Figure D.39.—Vapor-cooling and boiloff temperature versus height at 31.5 percent fill and 180°.

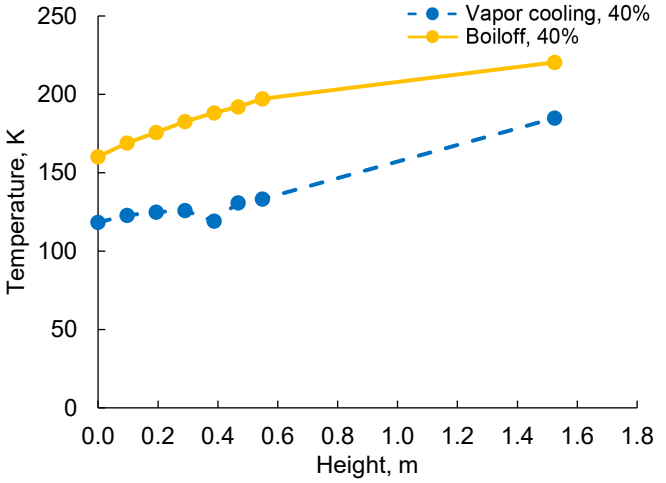

Figure D.40.—Vapor-cooling and boiloff temperature versus height at 40 percent fill and 180°.

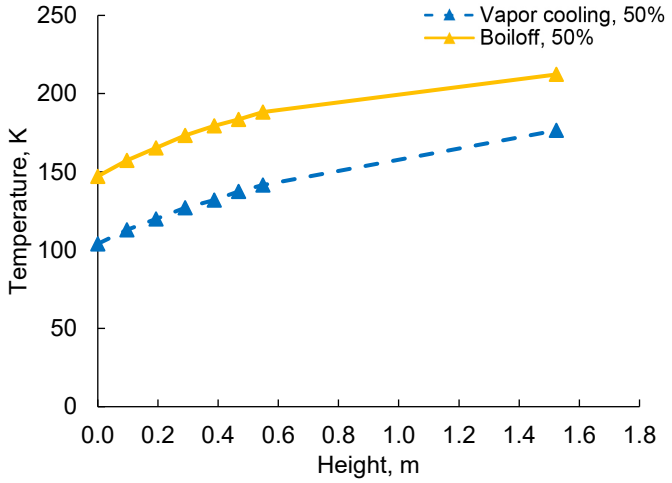

Figure D.41.—Vapor-cooling and boiloff temperature versus height at 50 percent fill and 180°.

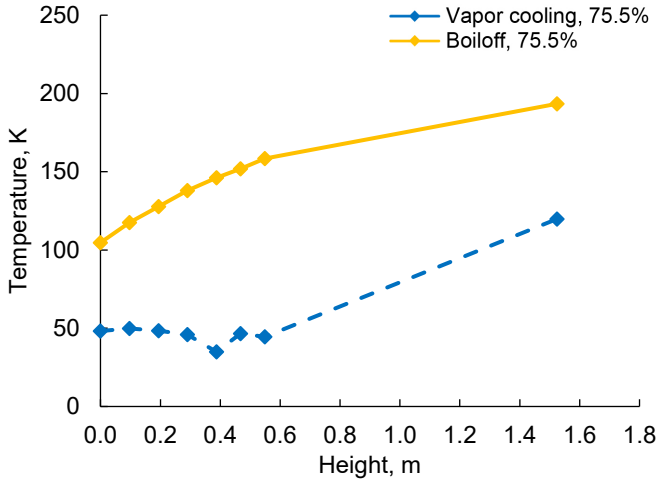

Figure D.42.—Vapor-cooling and boiloff temperature versus height at 75.5 percent fill and 180°.

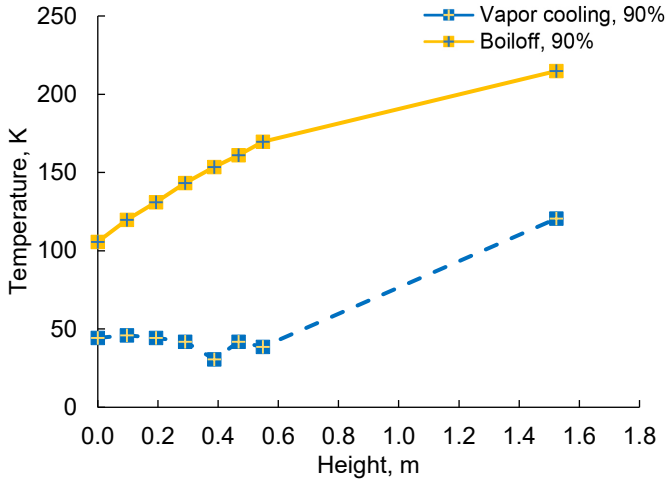

Figure D.43.—Vapor-cooling and boiloff temperature versus height at 90 percent fill and 180°.

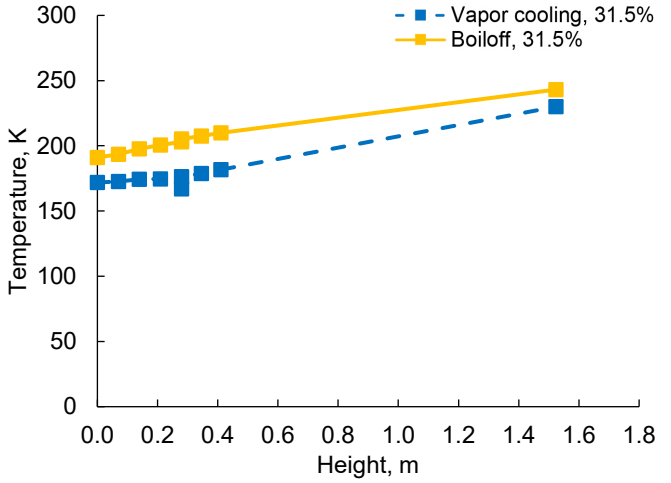

Figure D.44.—Vapor-cooling and boiloff temperature versus height at 31.5 percent fill and 230°.

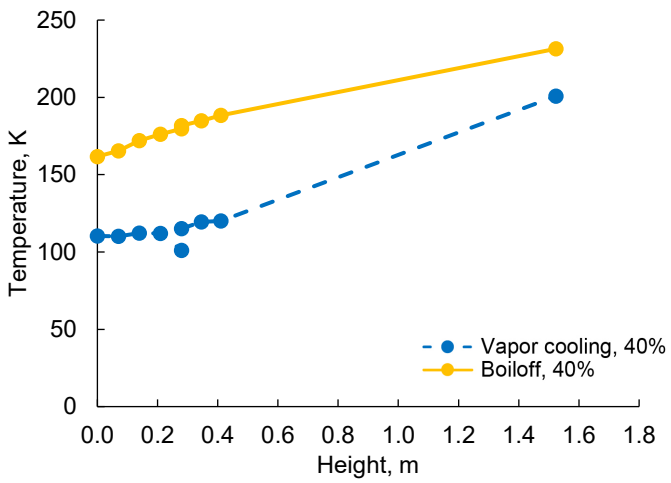

Figure D.45.—Vapor-cooling and boiloff temperature versus height at 40 percent fill and 230°.

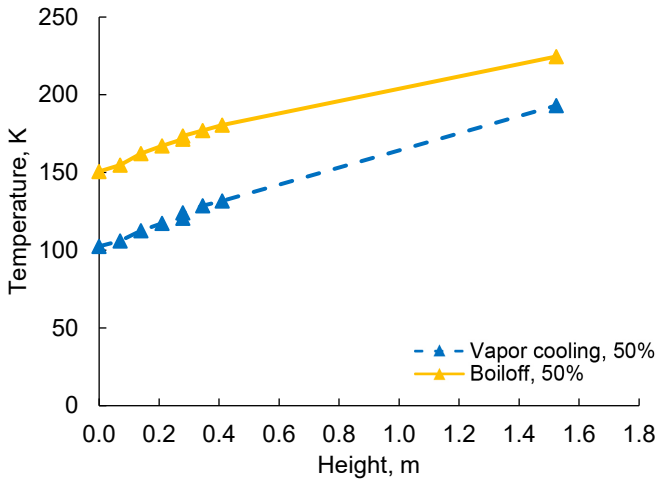

Figure D.46.—Vapor-cooling and boiloff temperature versus height at 50 percent fill and 230°.

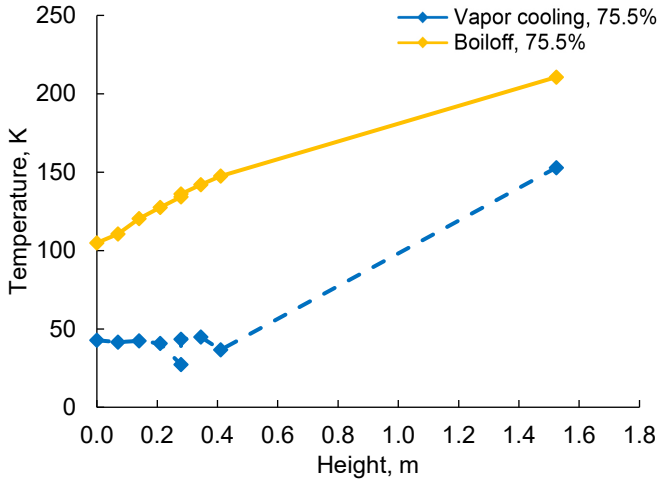

Figure D.47.—Vapor-cooling and boiloff temperature versus height at 75.5 percent fill and 230°.

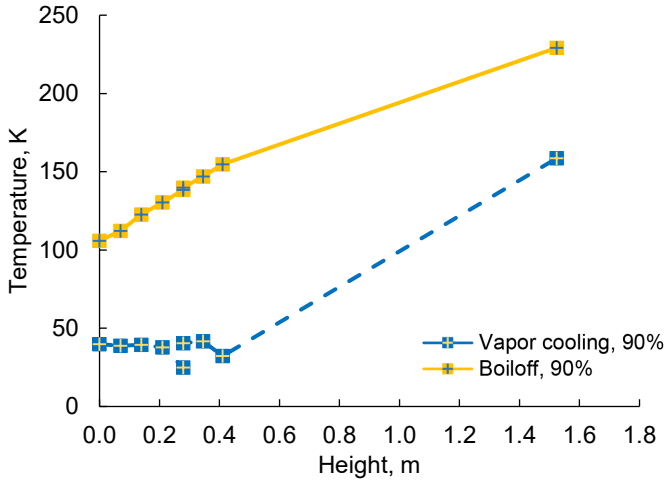

Figure D.48.—Vapor-cooling and boiloff temperature versus height at 90 percent fill and 230°.

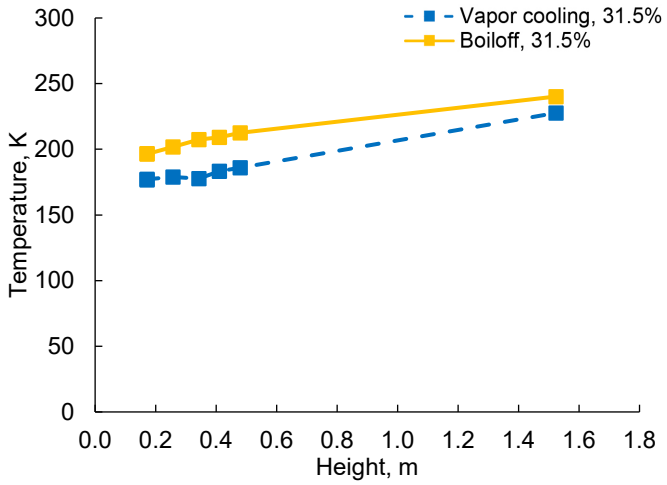

Figure D.49.—Vapor-cooling and boiloff temperature versus height at 31.5 percent fill and 300°.

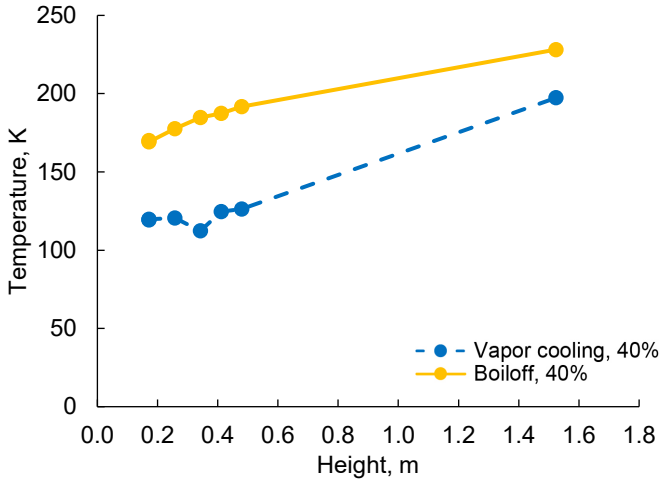

Figure D.50.—Vapor-cooling and boiloff temperature versus height at 40 percent fill and 300°.

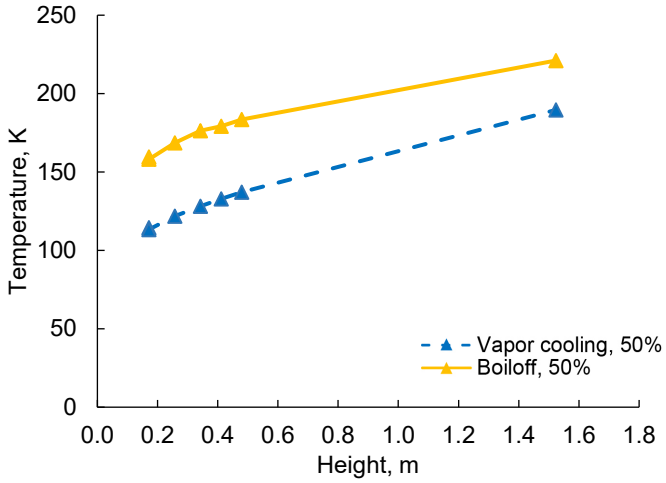

Figure D.51.—Vapor-cooling and boiloff temperature versus height at 50 percent fill and 300°.

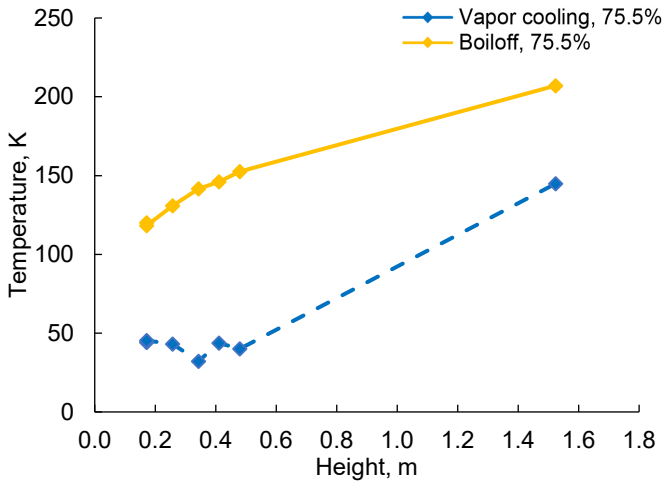

Figure D.52.—Vapor-cooling and boiloff temperature versus height at 75.5 percent fill and 300°.

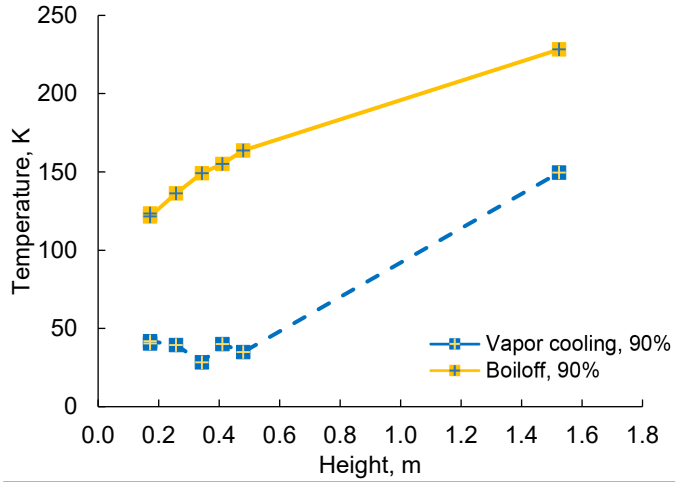

Figure D.53.—Vapor-cooling and boiloff temperature versus height at 90 percent fill and 300°.

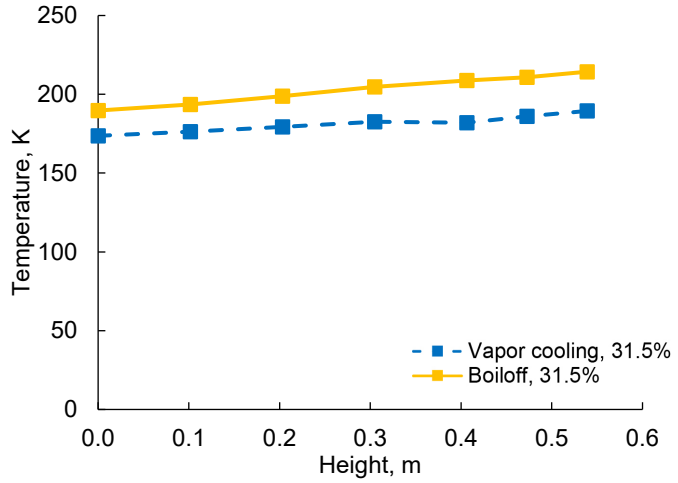

Figure D.54.—Vapor-cooling and boiloff temperature versus height at 31.5 percent fill and 360°.

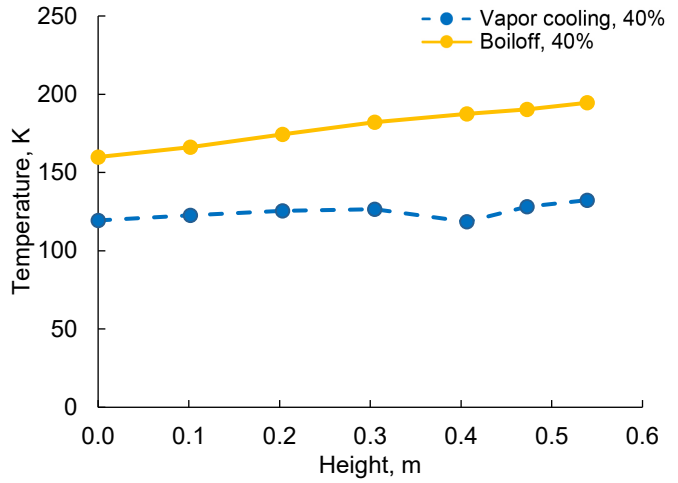

Figure D.55.—Vapor-cooling and boiloff temperature versus height at 40 percent fill and 360°.

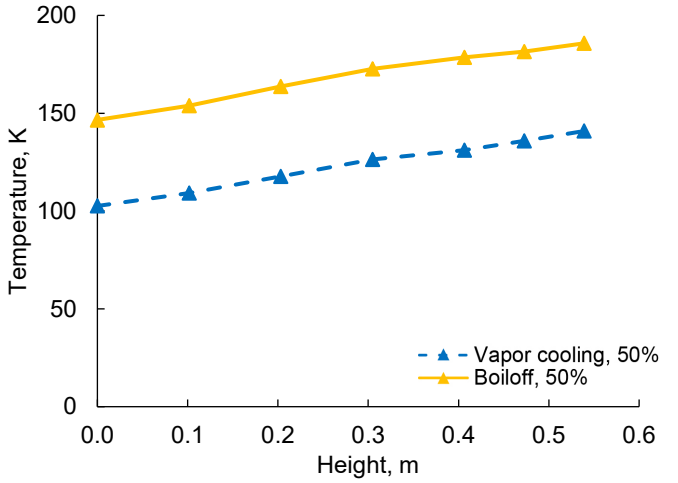

Figure D.56.—Vapor-cooling and boiloff temperature versus height at 50 percent fill and 360°.

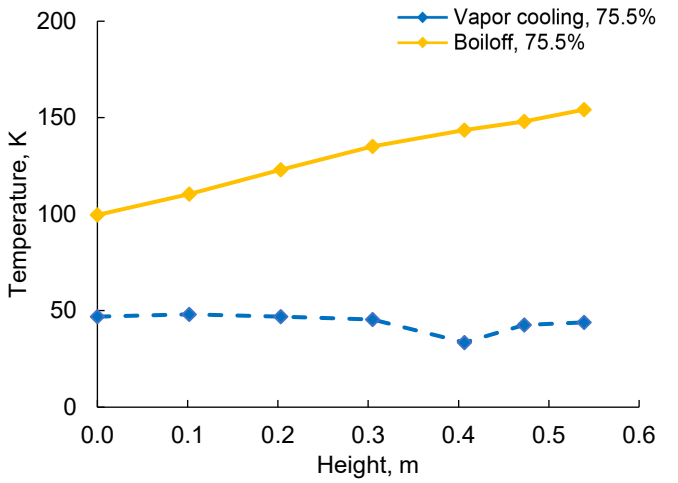

Figure D.57.—Vapor-cooling and boiloff temperature versus height at 75.5 percent fill and 360°.

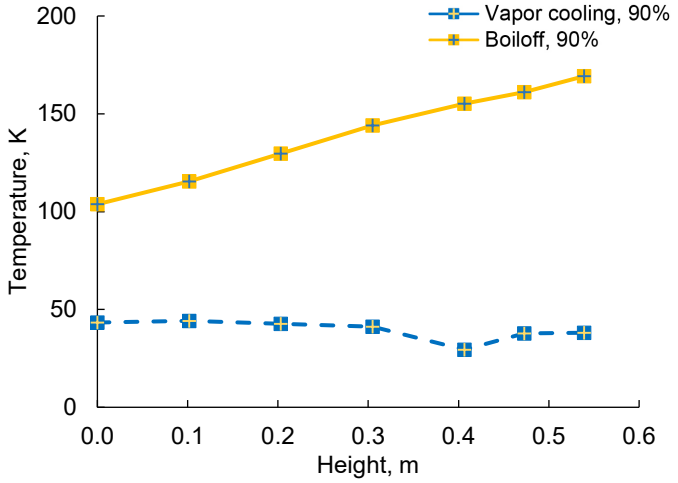

Figure D.58.—Vapor-cooling and boiloff temperature versus height at 90 percent fill and 360°.

D.6 Difference Between Boiloff and Vapor-Cooling Temperatures Versus Height at Each Fill Level for All Angular Stations

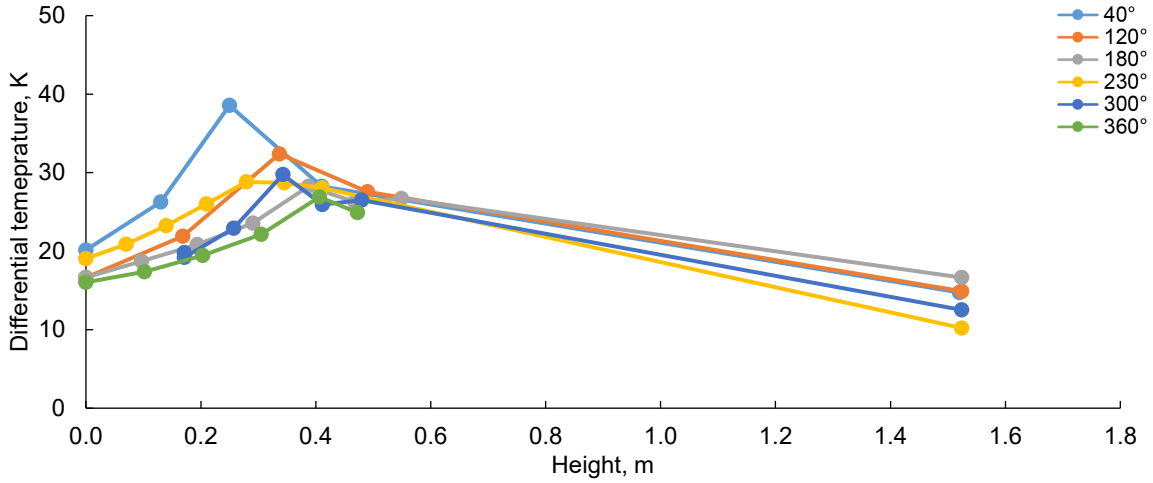

Figure D.59.—Difference between boiloff and vapor-cooling temperatures versus height at 31.5 percent fill.

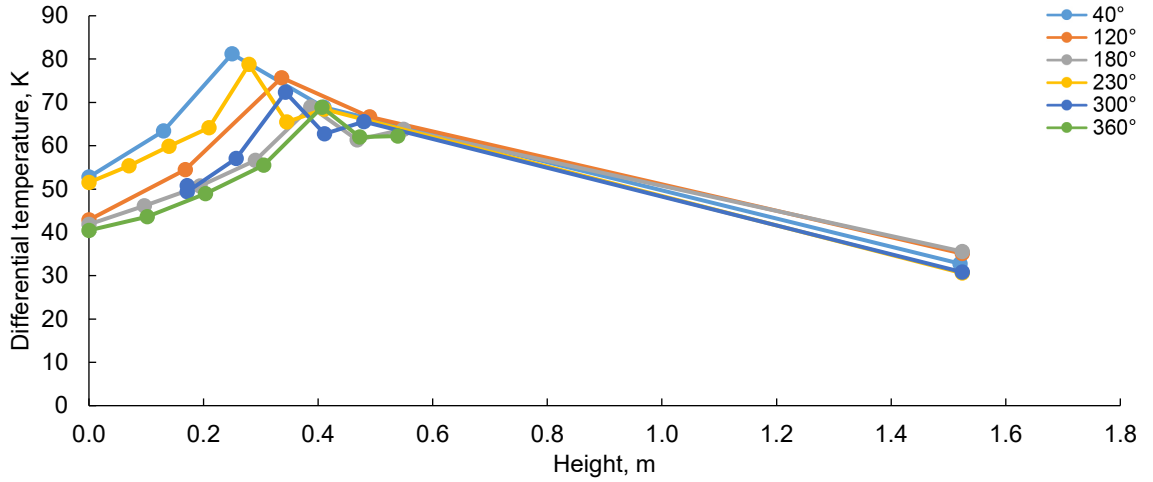

Figure D.60.—Difference between boiloff and vapor-cooling temperatures versus height at 40 percent fill.

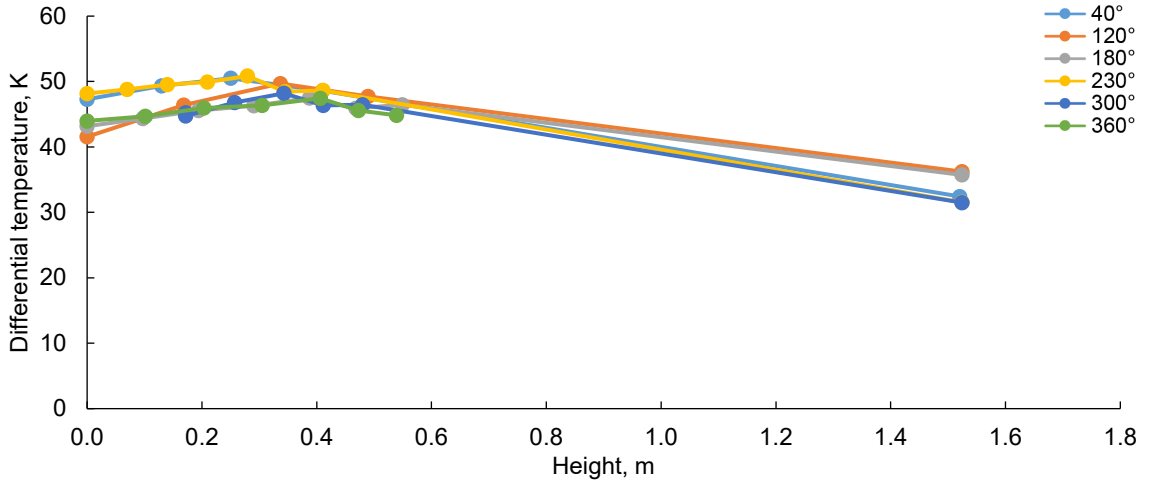

Figure D.61.—Difference between boiloff and vapor-cooling temperatures versus height at 50 percent fill.

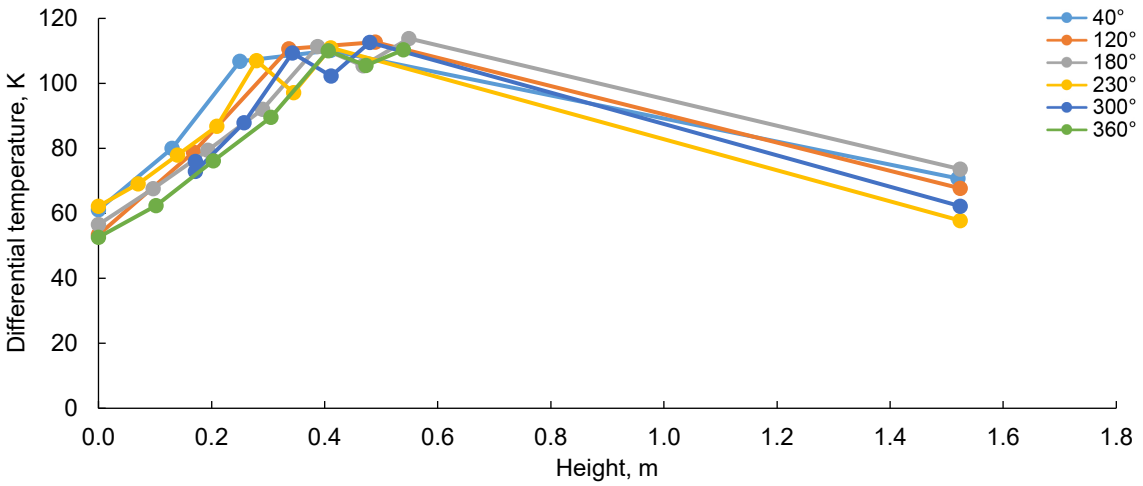

Figure D.62.—Difference between boiloff and vapor-cooling temperatures versus height at 75.5 percent fill.

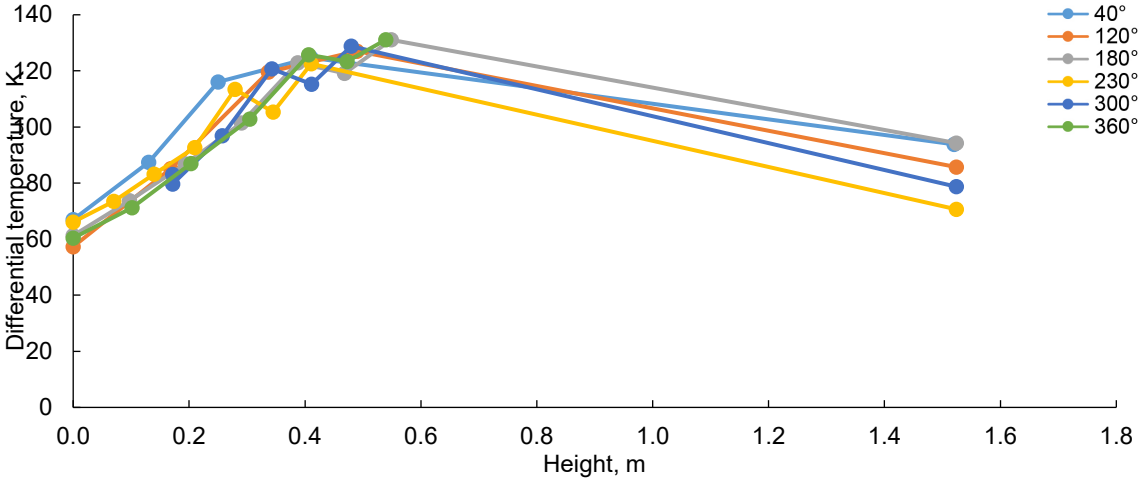

Figure D.63.—Difference between boiloff and vapor-cooling temperatures versus height at 90 percent fill.

Appendix E.—Vapor-Cooling-Line Temperatures Thermal 1 Test

Figure E.1 to Figure E.6 show the vapor-cooling-line temperatures during the Thermal 1 test.

E.1 Summary Plot of Vapor-Cooling-Line Temperatures Versus Vapor-Cooling-Line Length Including All Fill Levels

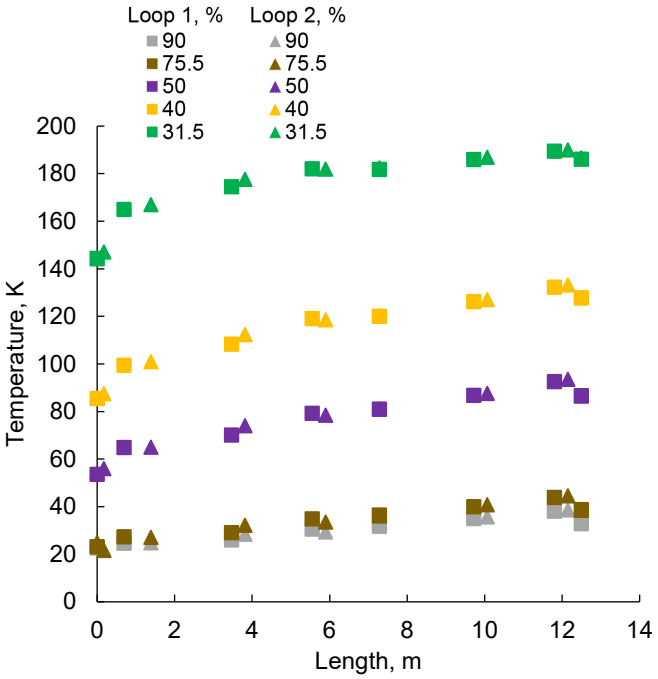

Figure E.1.—Vapor-cooling-line temperatures versus length for all fill levels.

E.2 Plots of Vapor-Cooling-Line Temperatures Versus Length for Each Fill Level

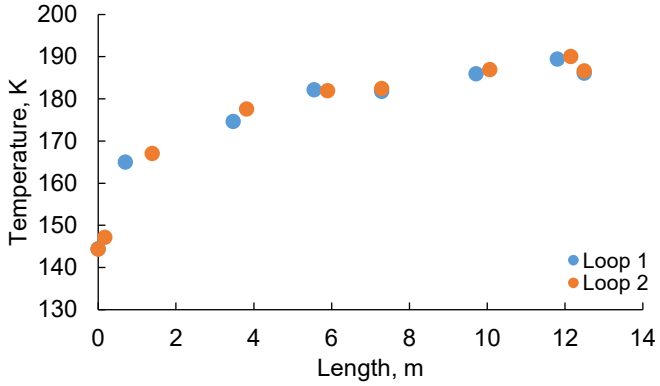

Figure E.2.—Vapor-cooling-line temperatures versus length at 31.5 percent fill.

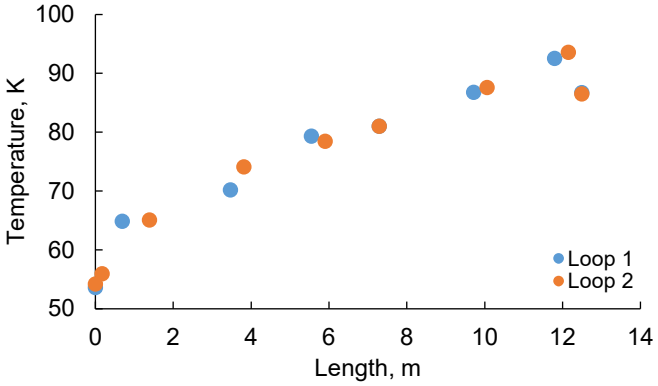

Figure E.4.—Vapor-cooling-line temperatures versus length at 50 percent fill.

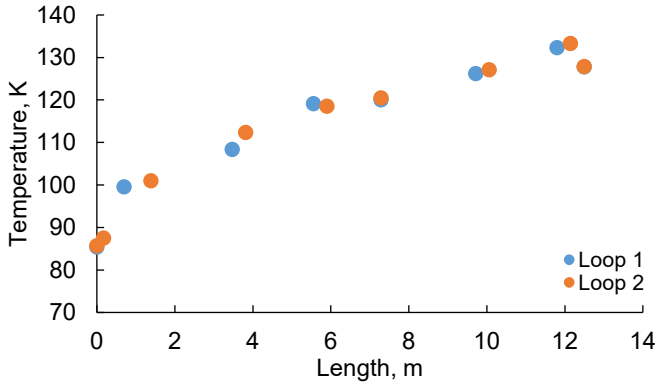

Figure E.3.—Vapor-cooling-line temperatures versus length at 40 percent fill.

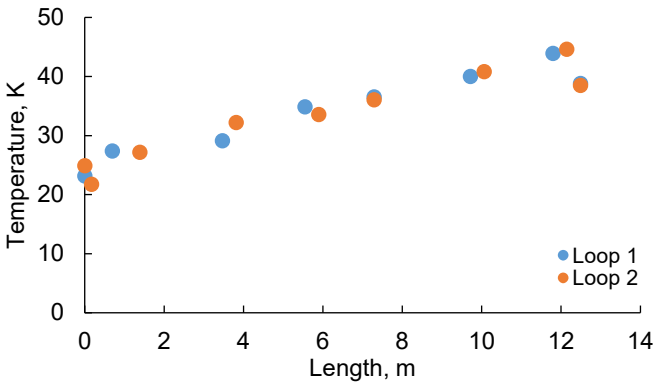

Figure E.5.—Vapor-cooling-line temperatures versus length at 75.5 percent fill.

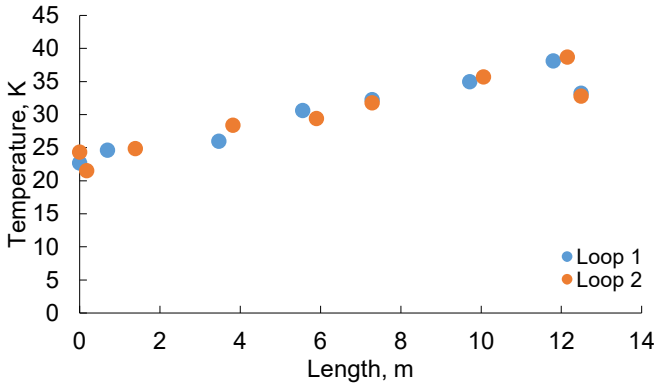

Figure E.6.—Vapor-cooling-line temperatures versus length at 90 percent fill.

Appendix F.—Skirt Temperatures Preacoustic Nitrogen Test

Figure F.1 to Figure F.30 show the skirt temperature data from the preacoustic nitrogen test.

F.1 Summary Plot for Each Angle Including All Fill Levels for Boiloff and Vapor Cooling

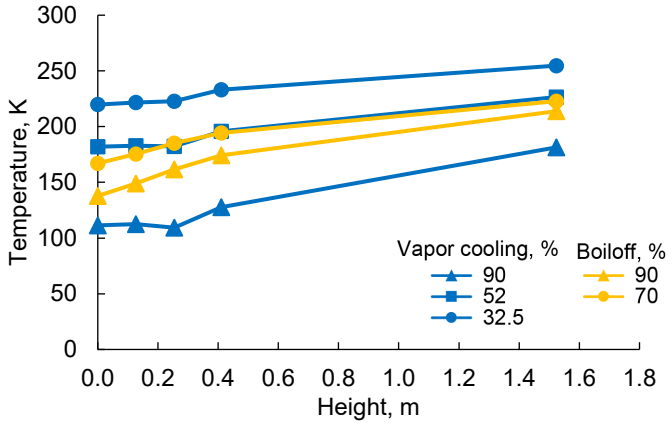

Figure F.1.—Temperature versus height at 40° comparing vapor-cooling and boiloff temperatures at every fill level.

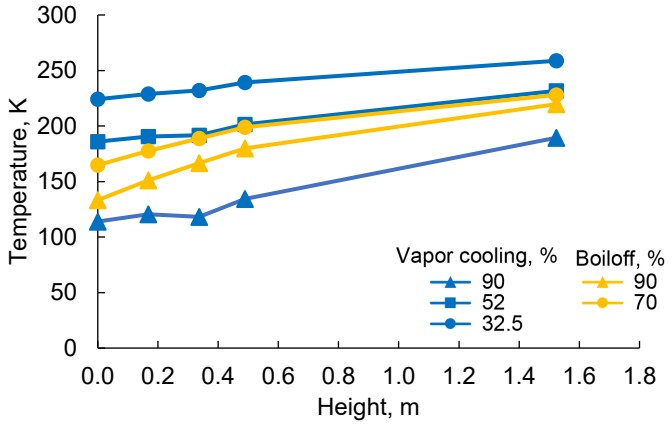

Figure F.2.—Temperature versus height at 120° comparing vapor-cooling and boiloff temperatures at every fill level.

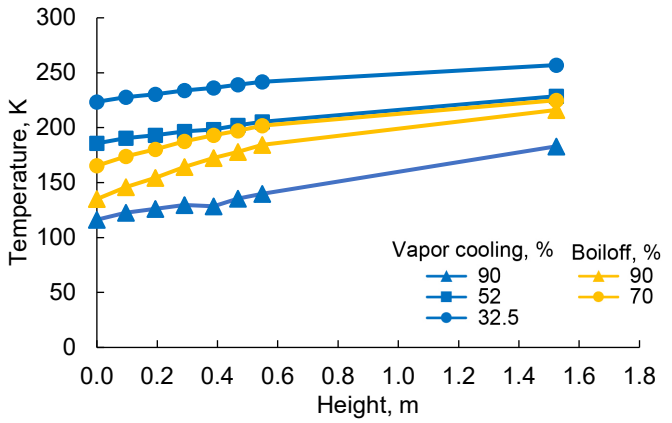

Figure F.3.—Temperature versus height at 180° comparing vapor-cooling and boiloff temperatures at every fill level.

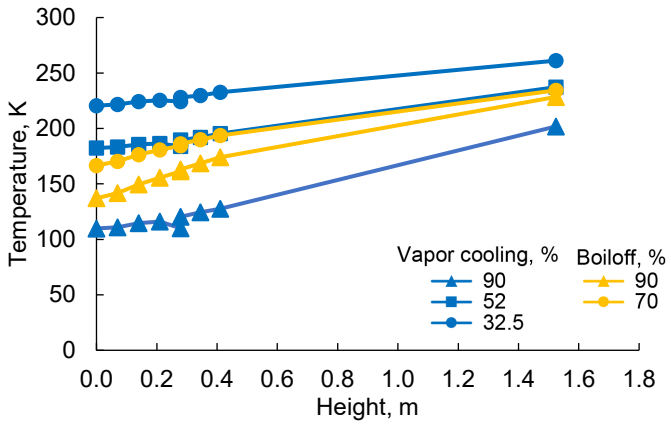

Figure F.4.—Temperature versus height at 230° comparing vapor-cooling and boiloff temperatures at every fill level.

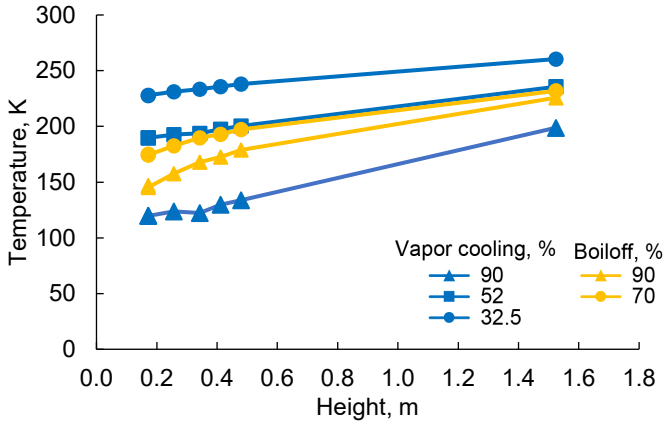

Figure F.5.—Temperature versus height at 300° comparing vapor-cooling and boiloff temperatures at every fill level.

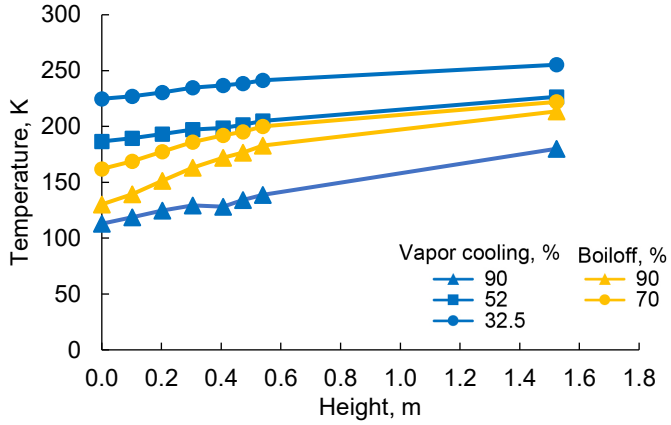

Figure F.6.—Temperature versus height at 360° comparing vapor-cooling and boiloff temperatures at every fill level.

F.2 Summary Plot for Each Angle Including All Fill Levels for Boiloff

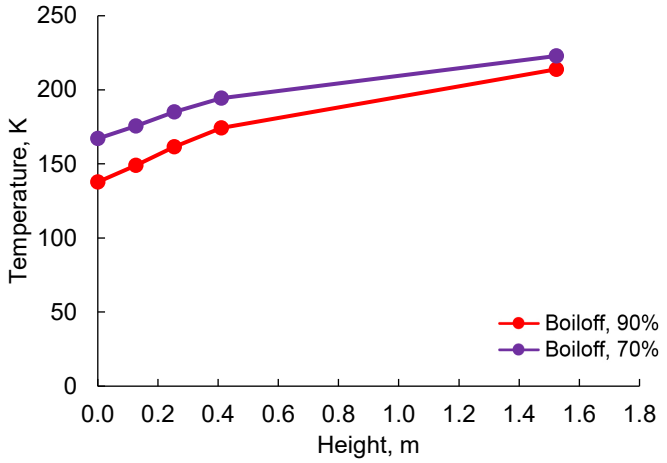

Figure F.7.—Boiloff temperature versus height at 40° for every fill level.

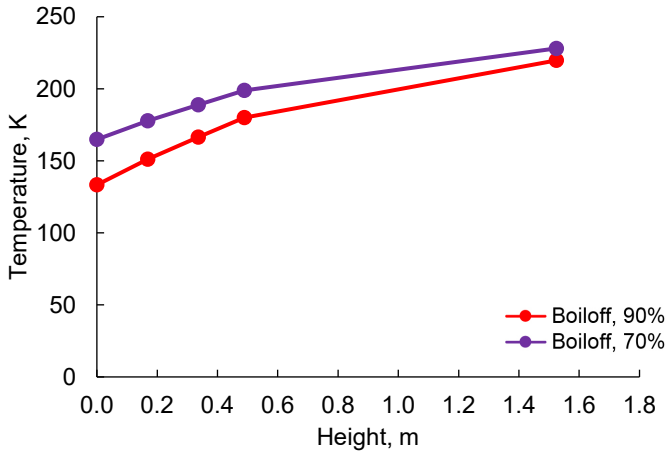

Figure F.8.—Boiloff temperature versus height at 120° for every fill level.

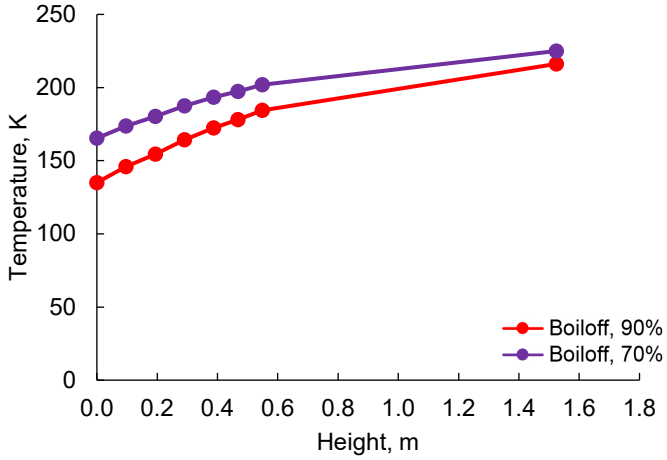

Figure F.9.—Boiloff temperature versus height at 180° for every fill level.

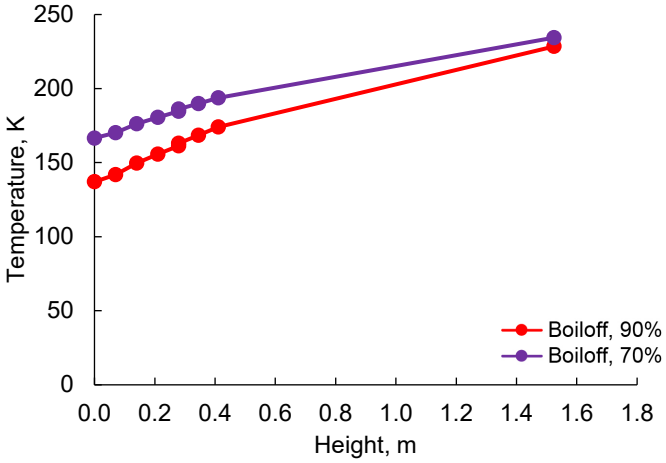

Figure F.10.—Boiloff temperature versus height at 230° for every fill level.

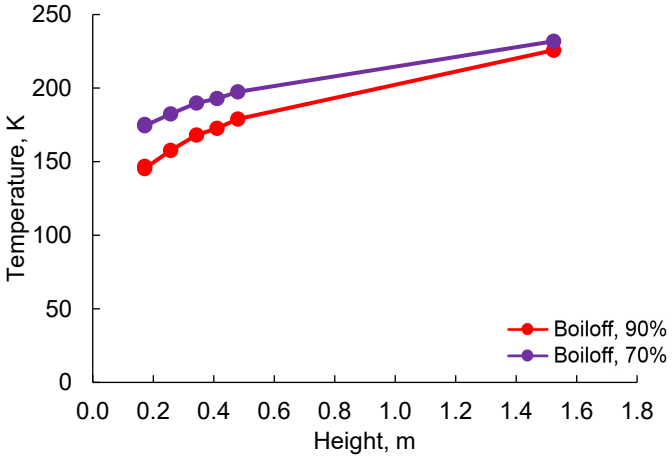

Figure F.11.—Boiloff temperature versus height at 300° for every fill level.

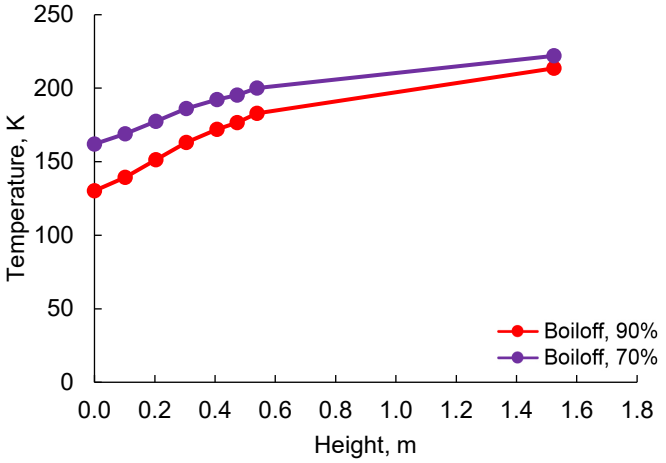

Figure F.12.—Boiloff temperature versus height at 360° for every fill level.

F.3 Summary Plot for Each Angle Including All Fill Levels for Vapor Cooling

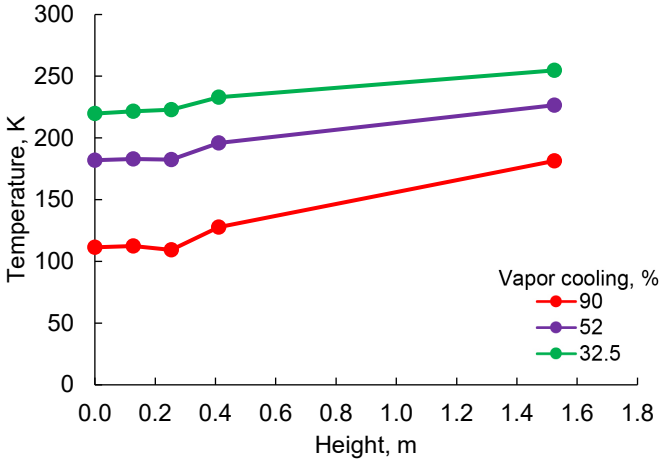

Figure F.13.—Vapor-cooling temperature versus height at 40° for every fill level.

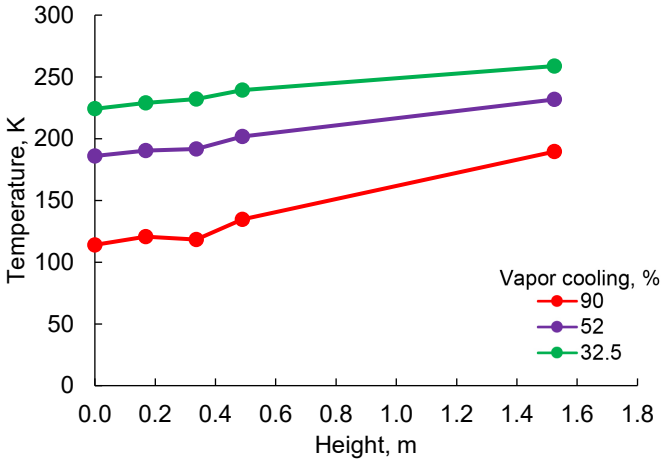

Figure F.14.—Vapor-cooling temperature versus height at 120° for every fill level.

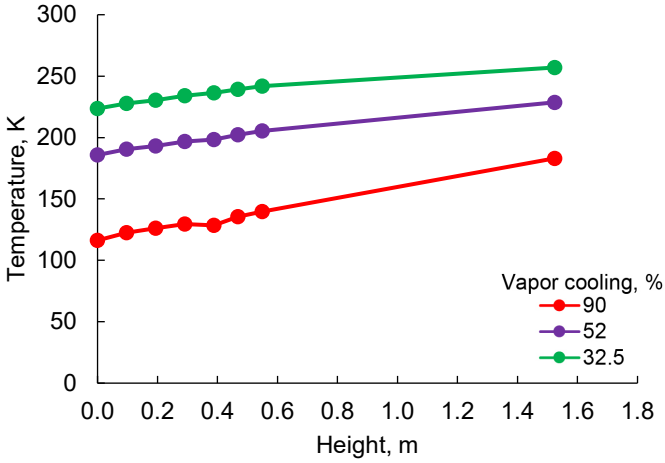

Figure F.15.—Vapor-cooling temperature versus height at 180° for every fill level.

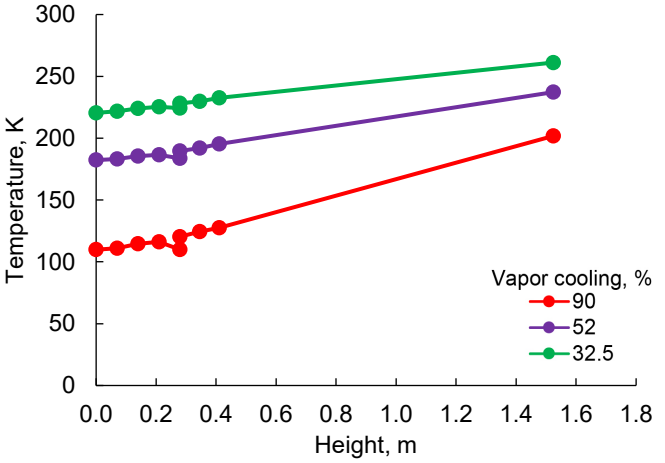

Figure F.16.—Vapor-cooling temperature versus height at 230° for every fill level.

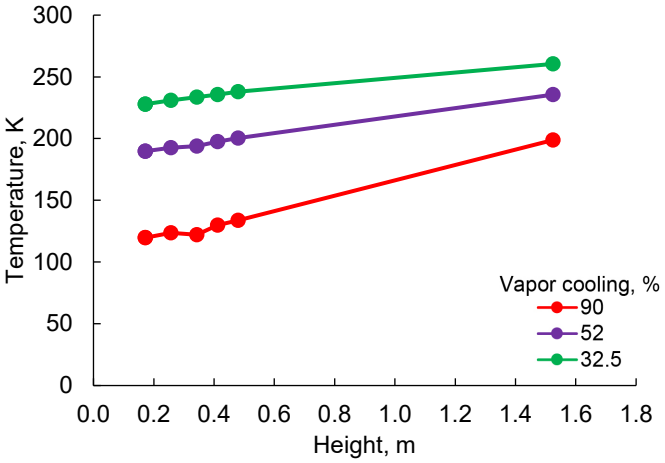

Figure F.17.—Vapor-cooling temperature versus height at 300° for every fill level.

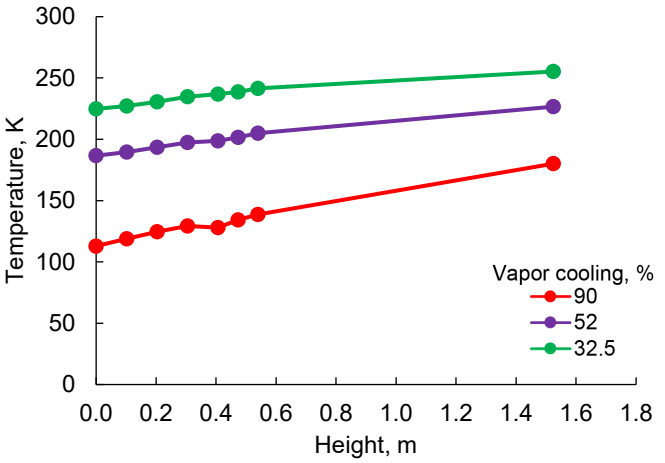

Figure F.18.—Vapor-cooling temperature versus height at 360° for every fill level.

F.4 Temperature Versus Height at Each Fill Level for All Angular Stations

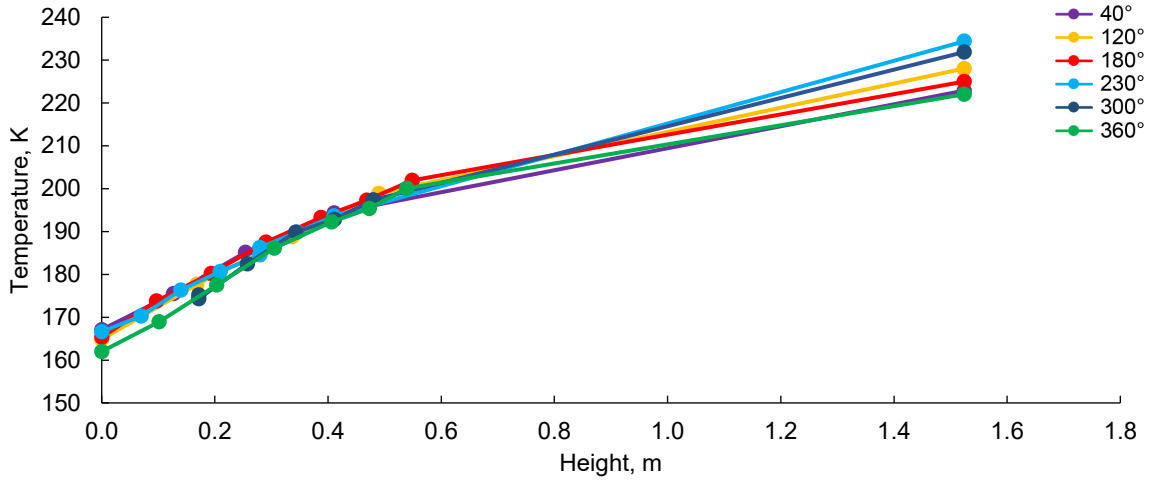

Figure F.19.—Boiloff temperature versus height at 70 percent fill level for every angular station.

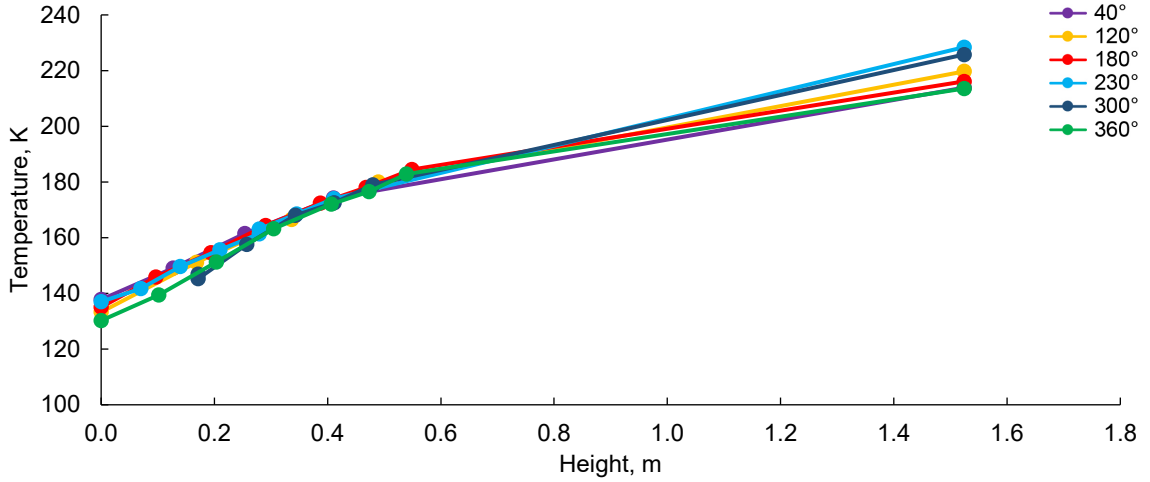

Figure F.20.—Boiloff temperature versus height at 90 percent fill level for every angular station.

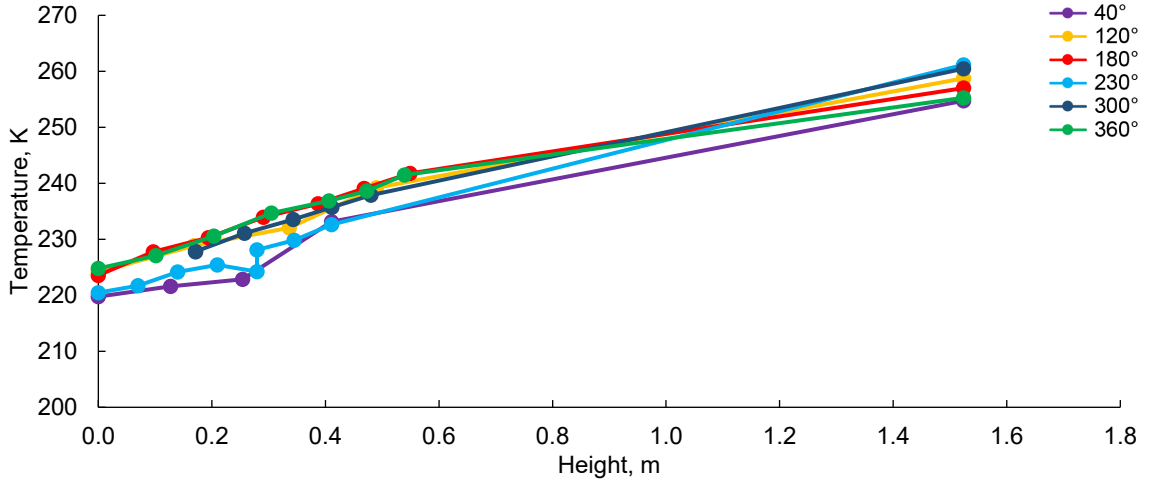

Figure F.21.—Vapor-cooling temperature versus height at 32.5 percent fill level for every angular station.

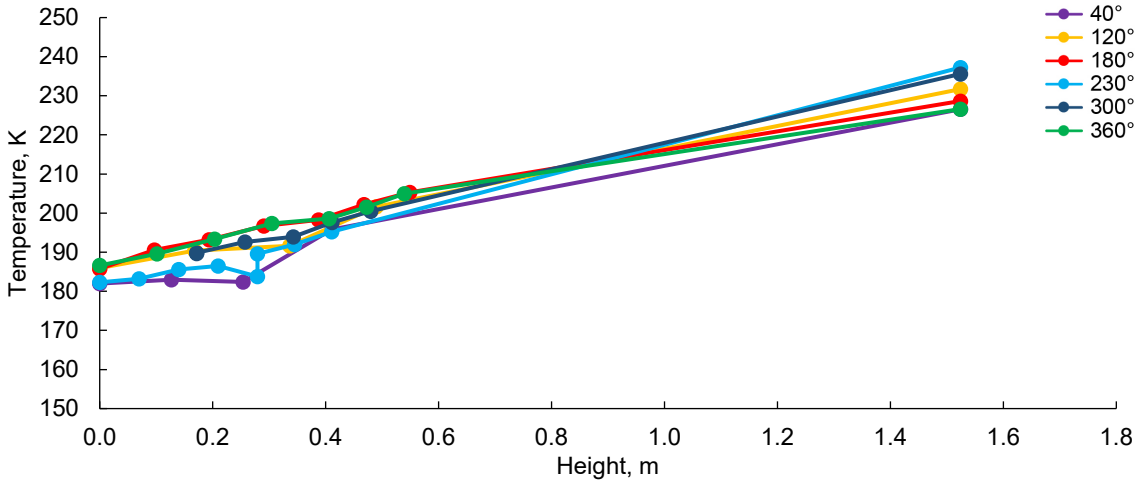

Figure F.22.—Vapor-cooling temperature versus height at 52 percent fill level for every angular station.

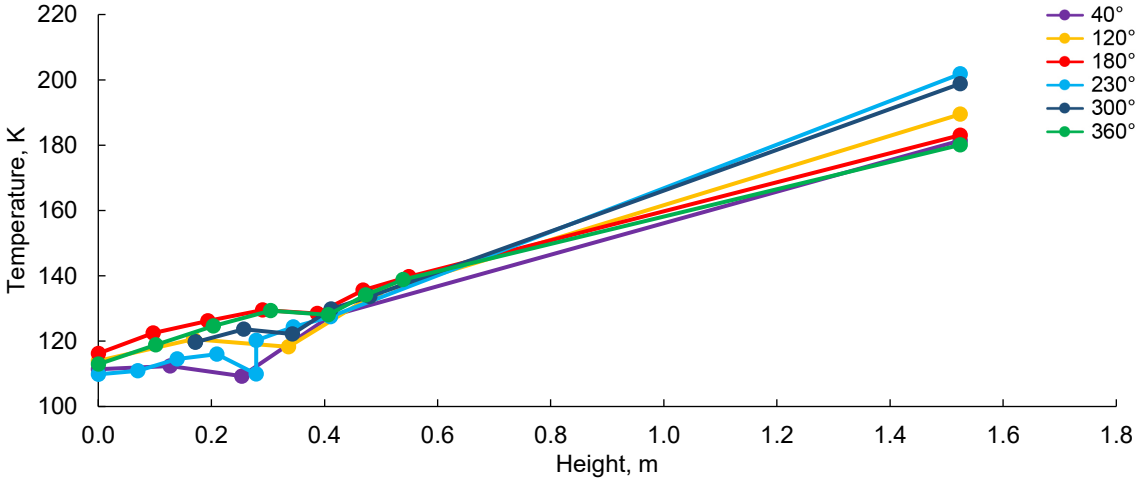

Figure F.23.—Vapor-cooling temperature versus height at 90 percent fill level for every angular station.

F.5 Temperature Versus Height at Each Fill Level and Each Angular Station Comparing Vapor Cooling and Boiloff

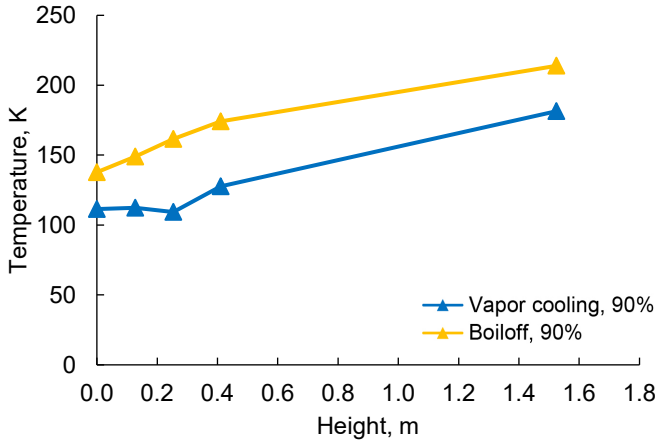

Figure F.24.—Vapor-cooling and boiloff temperature versus height at 90 percent fill and 40°.

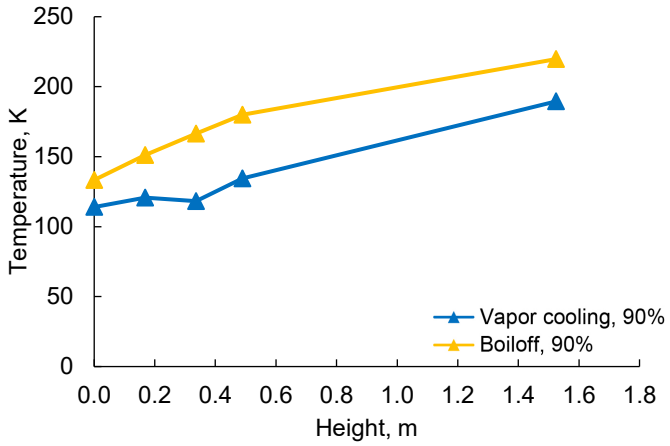

Figure F.25.—Vapor-cooling and boiloff temperature versus height at 90 percent fill and 120°.

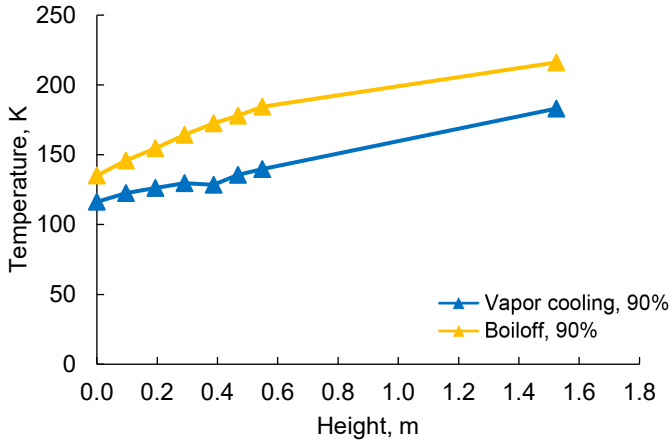

Figure F.26.—Vapor-cooling and boiloff temperature versus height at 90 percent fill and 180°.

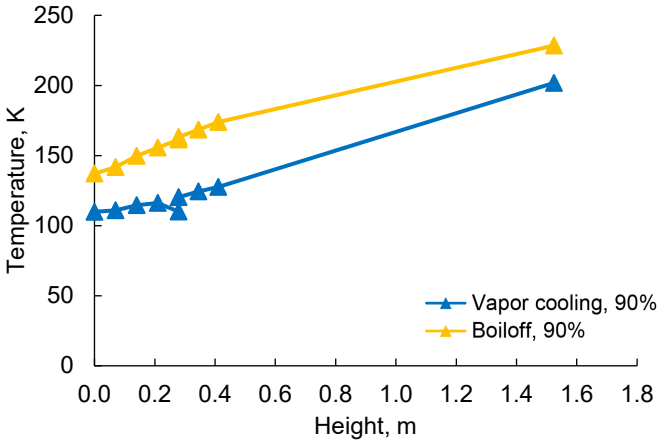

Figure F.27.—Vapor-cooling and boiloff temperature versus height at 90 percent fill and 230°.

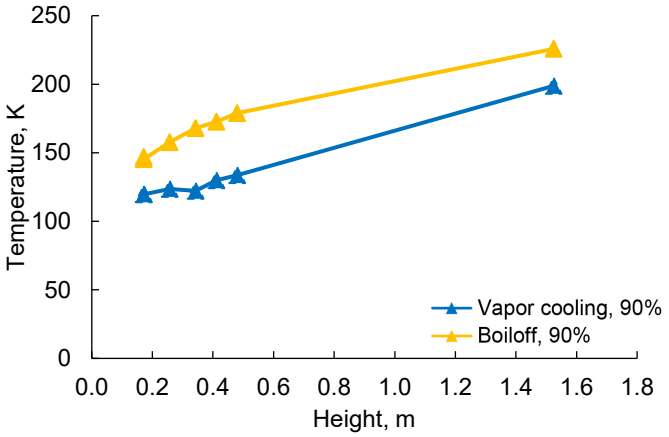

Figure F.28.—Vapor-cooling and boiloff temperature versus height at 90 percent fill and 300°.

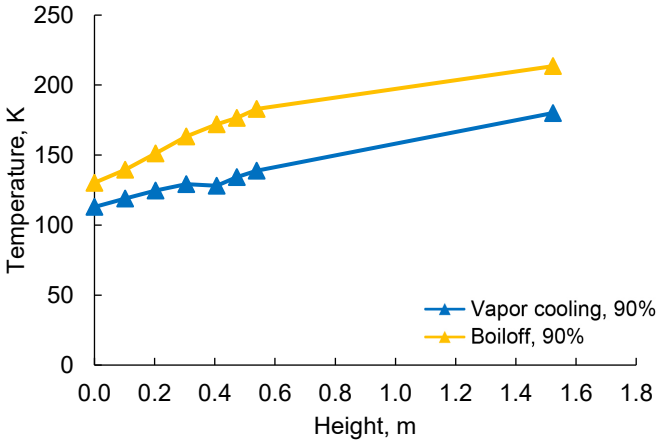

Figure F.29.—Vapor-cooling and boiloff temperature versus height at 90 percent fill and 360°.

F.6 Difference Between Boiloff and Vapor-Cooling Temperatures Versus Height at Every Angular Station

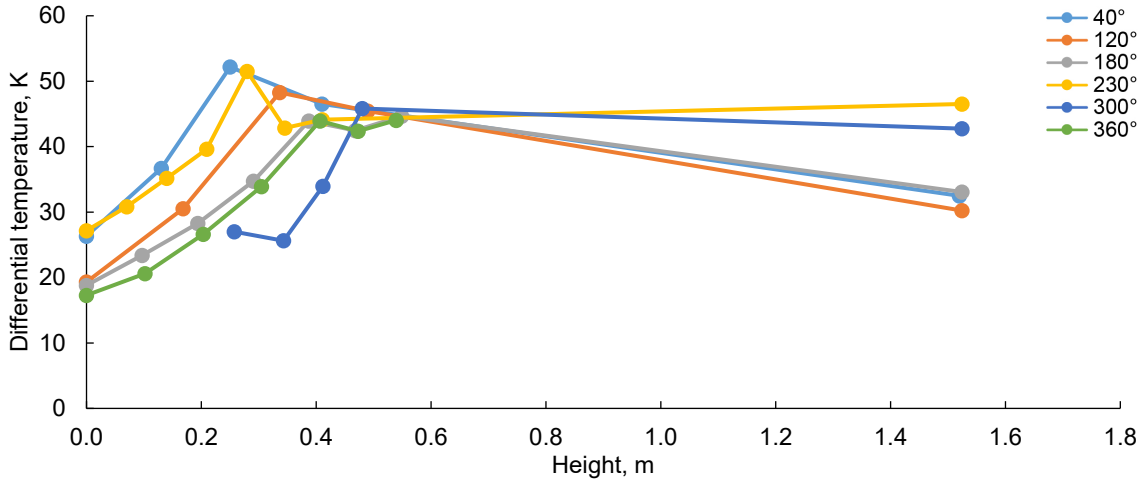

Figure F.30.—Difference between boiloff and vapor-cooling temperatures versus height at 90 percent fill.

Appendix G.—Vapor-Cooling-Line Temperatures Preacoustic Nitrogen Test

Figure G.1 to Figure G.4 capture the vapor-cooling-line temperature data from the preacoustic nitrogen testing.

G.1 Summary Plot of Vapor-Cooling-Line Temperatures Versus Vapor-Cooling-Line Length Including All Fill Levels

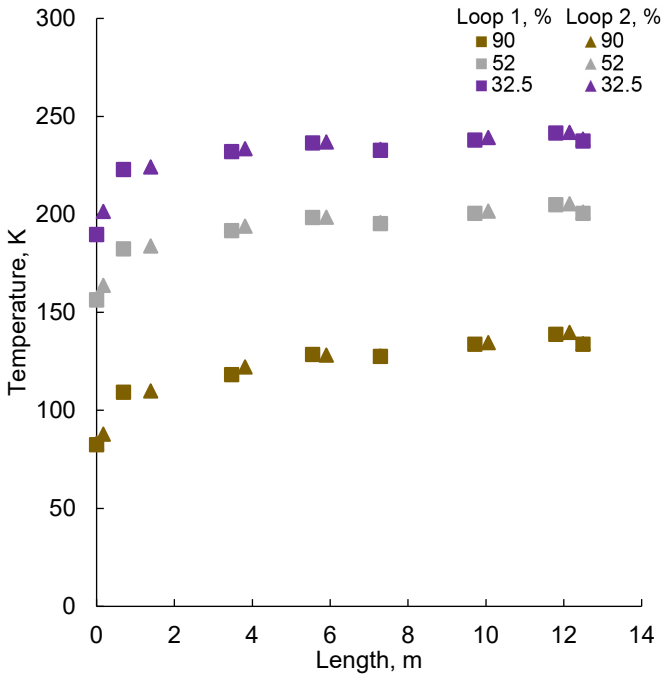

Figure G.1.—Vapor-cooling-line temperatures versus length for all fill levels.

G.2 Plots of Vapor-Cooling-Line Temperatures Versus Length for Each Fill Level

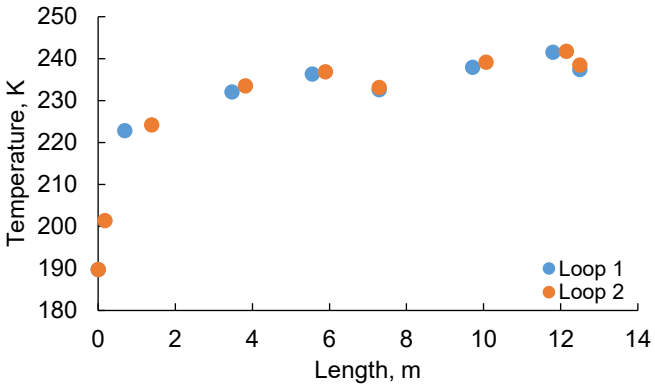

Figure G.2.—Vapor-cooling-line temperatures versus length at 32.5 percent fill.

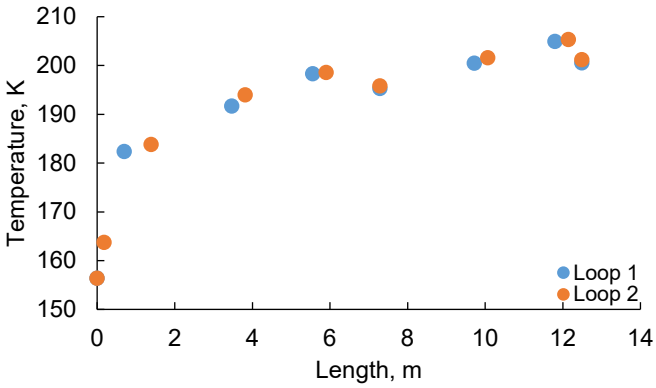

Figure G.3.—Vapor-cooling-line temperatures versus length at 52 percent fill.

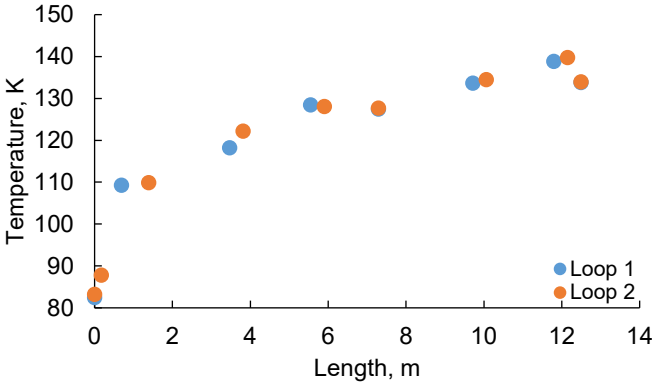

Figure G.4.—Vapor-cooling-line temperatures versus length at 50 percent fill.

Appendix H.—Description of Instrumentation and Locations

Appendix H lists instrumentation used on the Structural Heat Intercept, Insulation, and Vibration Evaluation Rig (SHIIVER) test article in tables that identify the sensors' application, type, serial number, and location. This appendix's intended use is as a lookup guide for the instrumentation employed during testing of SHIIVER hardware. The application of various sensors used to monitor temperatures within the tank and the system, tank pressure, the level of liquid hydrogen in the tank, along with vibrations generated during moving the equipment and testing are all shown here. Table H.1 identifies each sensor type along with their general location. All instrumentation, which includes the Radio Frequency Mass Gauge and associated electronics used on the test article locations, are defined in Table H.2 to Table H.19.

TABLE H.1.—TEST ARTICLE INSTRUMENTATION

Instrument and electronics	Location
Accelerometer	Forward and aft skirts Forward and aft manways
Capacitance probe	Inside tank
Flowmeter	Backpressure control cart
Heater strip	Forward and aft tank domes Tank barrel section
Heat flux sensor	Forward and aft tank domes Tank barrel section Forward skirt above the flange
Microlimit sensor	On fluid valves
Pressure sensor	In-line cooling In-line venting
Radio Frequency Mass Gauge	Inside tank
Silicon diode	Rake inside tank Forward and aft tank domes Tank barrel section Multilayer insulation (MLI) In-line and on-line cooling In-line venting On-line fill and drain On fluid valves On capacitance probe Cabling bundles
Thermocouple	In-line relief MLI

H.1 Accelerometers: Triaxial Vibration Sensor (PCB Piezotronics, Inc., Model 356A33)

TABLE H.2.—ACCELEROMETER (VS) LOCATIONS

Designation	P&ID[a] tag number	Field type	Manufacturer	Model	Description	Location from P&ID[a] except where noted	Connector pin-out|test article (inboard)
VS01	ACC 2265	Data	PCB Piezotronics, Inc.	356A33	Triaxial vibration sensor	Aft manhole (center)	VS01: Sig(X, Y, Z)|BNC 1D-X, R-Y, R-Z
VS02	ACC 2266	Data	PCB Piezotronics, Inc.	356A33	Triaxial vibration sensor	Aft valve	VS02: Sig(X, Y, Z)|BNC R-X, R-Y, R-Z
VS03	ACC 2267	Data	PCB Piezotronics, Inc.	356A33	Triaxial vibration sensor	Aft line free end (on flange flat face)	VS03: Sig(X, Y, Z)|BNC 2D-X, R-Y, R-Z
VS04	ACC 2268	Data	PCB Piezotronics, Inc.	356A33	Triaxial vibration sensor	Aft skirt (centered axially, in-line with VS03)	VS04: Sig(X, Y, Z)|BNC 2D-X, R-Y, R-Z
VS05	ACC 2269	Data	PCB Piezotronics, Inc.	356A33	Triaxial vibration sensor	Forward manhole (near feedline)	VS05: Sig(X, Y, Z) | BNC 2D-X, R-Y, R-Z
VS06	ACC 2270	Data	PCB Piezotronics, Inc.	356A33	Triaxial vibration sensor	Forward valve	VS06: Sig(X, Y, Z) | BNC 2D-X, R-Y, R-Z
VS07	ACC 2277	Data	PCB Piezotronics, Inc.	356A33	Triaxial vibration sensor	Left actuator (when box beam is in rear)	Connectors located at RATF
VS08	ACC 2278	Data	PCB Piezotronics, Inc.	356A33	Triaxial vibration sensor	Right actuator (when box beam is in rear)	Connectors located at RATF
VS09	ACC 2279	Data	PCB Piezotronics, Inc.	356A33	Triaxial vibration sensor	Vapor-cooling line (midspan on the pipe itself)	Connectors located at RATF
VS10	ACC 2280	Data	PCB Piezotronics, Inc.	356A33	Triaxial vibration sensor	Box beam (near connection to the line without the valve)	Connectors located at RATF
VS11	ACC 2281	Data	PCB Piezotronics, Inc.	356A33	Triaxial vibration sensor	Forward skirt 1 (centered axially and at the tangential position of the aft line)	Connectors located at RATF
VS12	ACC 2282	Data	PCB Piezotronics, Inc.	356A33	Triaxial vibration sensor	Forward skirt 2 (centered axially, 90° away from VS03)	Connectors located at RATF

[a]Process and instrumentation diagram (P&ID).

H.2 Capacitance Probe: Liquid Level Measurement Sensor With Associated Electronics

TABLE H.3.—CAPACITANCE PROBE LOCATION

Device	Designation	P&ID[a] tag number	Field type	Manufacturer	Model	Description	Location from P&ID[a] except where noted	Connector pin-out|test article (inboard)
Capacitance probe	FLS01	2274	Data	American Magnetics Inc.	AM-001	Internal liquid level	Instrumentation port forward manway	CP01|BNC RPG-188
Probe oscillator	FL01-a	2274-1	NA	American Magnetics Inc.	AM-002	NA	NA	NA
Probe electronics	FL01-b	2274-2	NA	American Magnetics Inc.	AM-003	NA	NA	NA

[a]Process and instrumentation diagram (P&ID).

H.3 Flowmeters: Gas Flow Measurement Using Micro Motions ELITE Series Coriolis Sensors

TABLE H.4.—FLOWMETER SENSOR (FM) LOCATIONS

Designation	P&ID[a] tag number	Field type	Manufacturer	Model	Description	Location from P&ID[a] except where noted	Connector pin-out|test article (inboard)
FM1	2208	Data	Emerson Electric Co.	CMFS100M	Coriolis	Backpressure control cart	PT01: Ex±|Sig±|Shd(A,B,C,D,E)
FM2	2209	Data	Emerson Electric Co.	CMF100M	Coriolis	Backpressure control cart	PT02: Ex±|Sig±|Shd(F,G,H,I,K)
FM3	2210	Data	Emerson Electric Co.	CMF050M	Coriolis	Backpressure control cart	PT03: Ex±|Sig±|Shd(L,M,N,P,R)
FM4	2211	Data	Emerson Electric Co.	CMF025M	Coriolis	Backpressure control cart	PT04: Ex±|Sig±|Shd(S,T,U,V,W)

[a]Process and instrumentation diagram (P&ID).

H.4 Heaters: Tank Warmup and Liquid Stratification

TABLE H.5.—HEATERS (HR) ON TANK SURFACE

Designation	P&ID[a] tag number	Field type	Manufacturer	Model	Description	Location from P&ID[a] except where noted	Connector pin-out|test article (inboard)
HR01	2271-1	Control	All Flex Heaters	AF-1512756355 HT	Etched foil	Tank dome heater quadrant 45°	HR01: Sig±|Shd(A,B,C)
HR02	2271-2	Control	All Flex Heaters	AF-1512756355 HT	Etched foil	Tank dome heater quadrant 315°	HR02: Sig±|Shd(E,F,G)
HR14	2271-3	Control	All Flex Heaters	AF-1512756355 HT	Etched foil	Tank dome heater quadrant 135°	HR14: Sig±|Shd(J,K,L)
HR15	2271-4	Control	All Flex Heaters	AF-1512756355 HT	Etched foil	Tank dome heater quadrant 225°	HR15: Sig±|Shd(T,U,V)
HR03	2272-1	Control	EGC Components	NTC-60-12-375W	Graphite	Heater barrel section quadrant 200°	HR03: Sig±|Shd(A,B,C)
HR04	2272-2	Control	EGC Components	NTC-60-12-375W	Graphite	Heater barrel section quadrant 157°	HR04: Sig±|Shd(E,F,G)
HR05	2272-3	Control	EGC Components	NTC-60-12-375W	Graphite	Heater barrel section quadrant 113°	HR05: Sig±|Shd(J,K,L)
HR06	2272-4	Control	EGC Components	NTC-60-12-375W	Graphite	Heater barrel section quadrant 70°	HR06: Sig±|Shd(T,U,V)
HR07	2272-5	Control	EGC Components	NTC-60-12-375W	Graphite	Heater barrel section quadrant 20°	HR07: Sig±|Shd(X,Z,a)
HR08	2272-6	Control	EGC Components	NTC-60-12-375W	Graphite	Heater barrel section quadrant 250°	HR08: Sig±|Shd(b,c,d)
HR09	2272-7	Control	EGC Components	NTC-60-12-375W	Graphite	Heater barrel section quadrant 293°	HR09: Sig±|Shd(e.f.g)
HR10	2272-8	Control	EGC Components	NTC-60-12-375W	Graphite	Heater barrel section quadrant 337°	HR10: Sig±|Shd(h,j,k)

[a]Process and instrumentation diagram (P&ID).

H.5 Heat Flux Sensor: Heat Load Measurements Using Captec Entreprise 200- by 200-mm Sensors

TABLE H.6.—HEAT FLUX SENSORS (HFSs) ON TANK SURFACE AND FORWARD SKIRT

Designation	P&ID[a] tag number	Field type	Manufacturer	Model	Description	Location from P&ID[a] except where noted	Connector pin-out|test article (inboard)
HFS01	2261-1	Data	Captec Entreprise	200 by 200 mm	Thermal difference	Tank surface, quadrant 225°	HFS01: Sig±|Shd(A,B,C)
HFS02	2261-2	Data	Captec Entreprise	200 by 200 mm	Thermal difference	Tank surface, quadrant 225°	HFS02: Sig±|Shd(D,E,F)
HFS03	2261-3	Data	Captec Entreprise	200 by 200 mm	Thermal difference	Tank surface, quadrant 225°	HFS03: Sig±|Shd(J,K,L)
HFS04	2261-4	Data	Captec Entreprise	200 by 200 mm	Thermal difference	Tank surface, quadrant 45°	HFS04: Sig±|Shd(M,N,P)
HFS05	2262-4	Data	Captec Entreprise	200 by 200 mm	Thermal difference	Tank surface, quadrant 45°	HFS05: Sig±|Shd(A,B,C)
HFS06	2262-3	Data	Captec Entreprise	200 by 200 mm	Thermal difference	Tank surface, quadrant 225°	HFS06: Sig±|Shd(D,E,F)
HFS07	2262-2	Data	Captec Entreprise	200 by 200 mm	Thermal difference	Tank surface, quadrant 225°	HFS07: Sig±|Shd(J,K,L)
HFS08	2262-1	Data	Captec Entreprise	200 by 200 mm	Thermal difference	Tank surface, quadrant 225°	HFS08: Sig±|Shd(M,N,P)
HFS09	2263-1	Data	Captec Entreprise	200 by 200 mm	Thermal difference	Tank surface, quadrant 45°	HFS09: Sig±|Shd(A,B,C)
HFS10	2263-2	Data	Captec Entreprise	200 by 200 mm	Thermal difference	Tank surface, quadrant 225°	HFS10: Sig±|Shd(D,E,F)
HFS11	2263-3	Data	Captec Entreprise	200 by 200 mm	Thermal difference	Tank surface, quadrant 135°	HFS11: Sig±|Shd(J,K,L)
HFS12	2263-4	Data	Captec Entreprise	200 by 200 mm	Thermal difference	Tank surface, quadrant 315°	HFS12: Sig±|Shd(M,N,P)
HFS17	2264-1	Data	Captec Entreprise	200 by 200 mm	Thermal difference	Forward skirt above flange 180°	HFS17: Sig±|Shd(R,S,T)
HFS18	2264-2	Data	Captec Entreprise	200 by 200 mm	Thermal difference	Forward skirt above flange 357°	HFS18: Sig±|Shd(U,V,W)
HFS19	2264-3	Data	Captec Entreprise	200 by 200 mm	Thermal difference	Forward skirt above flange 290°	HFS19: Sig±|Shd(X,Z,a)
HFS20	2264-4	Data	Captec Entreprise	200 by 200 mm	Thermal difference	Forward skirt above flange 220°	HFS20: Sig±|Shd(b,c,d)

[a]Process and instrumentation diagram (P&ID).

H.6 Limit Switch: Valve Position Limit Control Using Honeywell International, Inc., EX-AR800

TABLE H.7.—VALVE LIMIT SWITCHES (LSs) ON EXTERNAL PIPING

Designation	P&ID[a] tag number	Field type	Manufacturer	Model	Description	Location from P&ID[a] except where noted	Connector pin-out|test article (inboard)
LS01	2221-1	Control	Honeywell International, Inc.	EX-AR800	Valve travel limit	Control drain and fill	LS01: Sig±|Shd(A,B,C)
LS02	2221-2	Control	Honeywell International, Inc.	EX-AR800	Valve travel limit	Control drain and fill	LS02: Sig±|Shd(D,E,F)
LS03	2222-1	Control	Honeywell International, Inc.	EX-AR800	Valve travel limit	Control drain and fill	LS03: Sig±|Shd(J,K,L)
LS04	2222-2	Control	Honeywell International, Inc.	EX-AR800	Valve travel limit	Control drain and fill	LS04: Sig±|Shd(M,N,P)
LS05	2223-1	Control	Honeywell International, Inc.	EX-AR800	Valve travel limit	Control main vent line	LS05: Sig±|Shd(A,B,C)
LS06	2223-2	Control	Honeywell International, Inc.	EX-AR800	Valve travel limit	Control main vent line	LS06: Sig±|Shd(D,E,F)
LS07	2224-1	Control	Honeywell International, Inc.	EX-AR800	Valve travel limit	Control vapor-cooling loop	LS07: Sig±|Shd(J,K,L)
LS08	2224-2	Control	Honeywell International, Inc.	EX-AR800	Valve travel limit	Control vapor-cooling loop	LS08: Sig±|Shd(M,N,P)
LS09	2225-1	Control	Honeywell International, Inc.	EX-AR800	Valve travel limit	Control vapor-cooling loop	LS09: Sig±|Shd(R,S,T)
LS10	2225-2	Control	Honeywell International, Inc.	EX-AR800	Valve travel limit	Control vapor-cooling loop	LS10: Sig±|Shd(U,V,W)

[a]Process and instrumentation diagram (P&ID).

H.7 Pressure Sensor: Tank and System Pressure Measurement Using Stellar Technology GT2250

TABLE H.8.—PRESSURE TRANSMITTERS (PTs) ON INTERCONNECT PANEL 1 TO VENT AND COOLING LOOP PIPING

Designation	P&ID[a] tag number	Field type	Manufacturer	Model	Description	Location from P&ID[a] except where noted	Connector pin-out|test article (inboard)
PT01	2240	Data	Stellar Technology	GT2250	Pressure transducer	Vapor-cooling loop line	PT01: Ex±|Sig±|Shd(A,B,C,D,E)
PT02	2241	Data	Stellar Technology	GT2250	Pressure transducer	Vapor-cooling loop line	PT02: Ex±|Sig±|Shd(F,G,H,J,K)
PT03	2242-1	Control and data	Stellar Technology	GT2250	Pressure transducer	Vent line	PT03: Ex±|Sig±|Shd(L,M,N,P,R)
PT04	2242-2	Control and data	Stellar Technology	GT2250	Pressure transducer	Vent line	PT04: Ex±|Sig±|Shd(S,T,U,V,W)
PT05	2213	Data	Stellar Technology	GT2250	Pressure transducer	Facility piping structure	Connectors located at B2 Facility
PT06	2215	Data	Stellar Technology	GT2250	Pressure transducer	Facility piping structure	Connectors located at B2 Facility
PT07	2219	Data	Stellar Technology	GT2250	Pressure transducer	Facility piping structure	Connectors located at B2 Facility
PT08	2220	Data	Stellar Technology	GT2250	Pressure transducer	Facility piping structure	Connectors located at B2 Facility

[a]Process and instrumentation diagram (P&ID).

H.8 Radio Frequency Mass Gauge: Storage Tank Liquid Level Measurement System

TABLE H.9.—RADIO FREQUENCY ANTENNAS LOCATED ON INTERNAL STORAGE TANK SURFACE

Device[a]	Serial/model number	Location
RFMG Antenna 1	150304MEA900-001	Sidewall, 57 percent fill level
RFMG Antenna 2	150304MEA900-002	Sidewall, 14 percent fill level

[a]Radio Frequency Mass Gauge (RFMG).

H.9 Temperature and Liquid Level Measurement Sensors

TABLE H.10.—SILICON DIODES (SDs) LOCATED ON EXTERNAL STORAGE TANK SURFACES

Designation	P&ID[a] tag number	Field type	Manufacturer	Model	Description	Location from P&ID[a] except where noted	Connector pin-out|test article (inboard)
SD01	2245-1	Data	Scientific Instruments, Inc.	Si410AALP4C	Temperature sensor (SD)	External tank angle 45° off N, 0%	SD01: Ex±|Sig±|Shd(A,B,C,D,E)
SD02	2245-2	Data	Scientific Instruments, Inc.	Si410AALP4C	Temperature sensor (SD)	External tank angle 45° off N, 5%	SD02: Ex±|Sig±|Shd(F,G,H,J,K)
SD03	2245-3	Data	Scientific Instruments, Inc.	Si410AALP4C	Temperature sensor (SD)	External tank angle 45° off N, 10%	SD03: Ex±|Sig±|Shd(L,M,N,P,R)
SD04	2245-4	Data	Scientific Instruments, Inc.	Si410AALP4C	Temperature sensor (SD)	External tank angle 45° off N, 15%	SD04: Ex±|Sig±|Shd(S,T,U,V,W)
SD05	2245-5	Data	Scientific Instruments, Inc.	Si410AALP4C	Temperature sensor (SD)	External tank angle 45° off N, 20%	SD05: Ex±|Sig±|Shd(X,Z,a,b,c)
SD06	2245-6	Data	Scientific Instruments, Inc.	Si410AALP4C	Temperature sensor (SD)	External tank angle 45° off N, 25%	SD06: Ex±|Sig±|Shd(d,e,f,g,h)
SD07	2245-7	Data	Scientific Instruments, Inc.	Si410AALP4C	Temperature sensor (SD)	External tank angle 45° off N, 30%	SD07: Ex±|Sig±|Shd(A,B,C,D,E)
SD08	2245-8	Data	Scientific Instruments, Inc.	Si410AALP4C	Temperature sensor (SD)	External tank angle 45° off N, 35%	SD08: Ex±|Sig±|Shd(F,G,H,J,K)
SD09	2245-9	Data	Scientific Instruments, Inc.	Si410AALP4C	Temperature sensor (SD)	External tank angle 45° off N, 40%	SD09: Ex±|Sig±|Shd(L,M,N,P,R)
SD10	2245-10	Data	Scientific Instruments, Inc.	Si410AALP4C	Temperature sensor (SD)	External tank angle 45° off N, 45%	SD10: Ex±|Sig±|Shd(S,T,U,V,W)
SD11	2245-11	Data	Scientific Instruments, Inc.	Si410AALP4C	Temperature sensor (SD)	External tank angle 45° off N, 50%	SD11: Ex±|Sig±|Shd(X,Z,a,b,c)
SD12	2245-12	Data	Scientific Instruments, Inc.	Si410AALP4C	Temperature sensor (SD)	External tank angle 45° off N, 55%	SD12: Ex±|Sig±|Shd(d,e,f,g,h)
SD13	2245-13	Data	Scientific Instruments, Inc.	Si410AALP4C	Temperature sensor (SD)	External tank angle 45° off N, 60%	SD13: Ex±|Sig±|Shd(A,B,C,D,E)
SD14	2245-14	Data	Scientific Instruments, Inc.	Si410AALP4C	Temperature sensor (SD)	External tank angle 45° off N, 65%	SD14: Ex±|Sig±|Shd(F,G,H,J,K)
SD15	2245-15	Data	Scientific Instruments, Inc.	Si410AALP4C	Temperature sensor (SD)	External tank angle 45° off N, 70%	SD15: Ex±|Sig±|Shd(L,M,N,P,R)
SD16	2245-16	Data	Scientific Instruments, Inc.	Si410AALP4C	Temperature sensor (SD)	External tank angle 45° off N, 75%	SD16: Ex±|Sig±|Shd(A,B,C,D,E)
SD17	2245-17	Data	Scientific Instruments, Inc.	Si410AALP4C	Temperature sensor (SD)	External tank angle 45° off N, 80%	SD17: Ex±|Sig±|Shd(F,G,H,J,K)

TABLE H.10.—(Concluded)

Designation	P&ID[a] tag number	Field type	Manufacturer	Model	Description	Location from P&ID[a] except where noted	Connector pin-out|test article (inboard)
SD18	2245-18	Data	Scientific Instruments, Inc.	Si410AALP4C	Temperature sensor (SD)	External tank angle 45° off N, 85%	SD18: Ex±|Sig±|Shd(L,M,N,P,R)
SD19	2245-19	Data	Scientific Instruments, Inc.	Si410AALP4C	Temperature sensor (SD)	External tank angle 45° off N, 90%	SD19: Ex±|Sig±|Shd(S,T,U,V,W)
SD20	2245-20	Data	Scientific Instruments, Inc.	Si410AALP4C	Temperature sensor (SD)	External tank angle 45° off N, 95%	SD20: Ex±|Sig±|Shd(X,Z,a,b,c)
SD21	2245-21	Data	Scientific Instruments, Inc.	Si410AALP4C	Temperature sensor (SD)	External tank angle 45° off N, 100%	SD21: Ex±|Sig±|Shd(d,e,f,g,h)
SD22	2245-22	Data	Scientific Instruments, Inc.	Si410AALP4C	Temperature sensor (SD)	External tank angle 135° off N, 25%	SD22: Ex±|Sig±|Shd(A,B,C,D,E)
SD23	2245-23	Data	Scientific Instruments, Inc.	Si410AALP4C	Temperature sensor (SD)	External tank angle 225° off N, 25%	SD23: Ex±|Sig±|Shd(F,G,H,J,K)
SD24	2245-24	Data	Scientific Instruments, Inc.	Si410AALP4C	Temperature sensor (SD)	External tank angle 315° off N, 25%	SD24: Ex±|Sig±|Shd(L,M,N,P,R)
SD25	2245-25	Data	Scientific Instruments, Inc.	Si410AALP4C	Temperature sensor (SD)	External tank angle 135° off N, 50%	SD25: Ex±|Sig±|Shd(S,T,U,V,W)
SD26	2245-26	Data	Scientific Instruments, Inc.	Si410AALP4C	Temperature sensor (SD)	External tank angle 225° off N, 50%	SD26: Ex±|Sig±|Shd(X,Z,a,b,c)
SD27	2245-27	Data	Scientific Instruments, Inc.	Si410AALP4C	Temperature sensor (SD)	External tank angle 315° off N, 50%	SD27: Ex±|Sig±|Shd(d,e,f,g,h)
SD28	2245-28	Data	Scientific Instruments, Inc.	Si410AALP4C	Temperature sensor (SD)	External tank angle 135° off N, 75%	SD28: Ex±|Sig±|Shd(A,B,C,D,E)
SD29	2245-29	Data	Scientific Instruments, Inc.	Si410AALP4C	Temperature sensor (SD)	External tank angle 225° off N, 75%	SD29: Ex±|Sig±|Shd(F,G,H,J,K)
SD30	2245-30	Data	Scientific Instruments, Inc.	Si410AALP4C	Temperature sensor (SD)	External tank angle 315° off N, 75%	SD30: Ex±|Sig±|Shd(L,M,N,P,R)

[a]Process and instrumentation diagram (P&ID).

TABLE H.11.—SILICON DIODES (SDs) LOCATED ON FORWARD SKIRT SURFACES

Designation	P&ID[a] tag number	Field type	Manufacturer	Model	Description	Location from P&ID[a] except where noted	Connector pin-out|test article (inboard)
SD106	2255-1	Data	Scientific Instruments, Inc.	Si410AA2P4C	Temperature sensor (SD)	Forward skirt 1, 180° Sta 86.625	SD106: Ex±|Sig±|Shd(A,B,C,D,E)
SD107	2255-2	Data	Scientific Instruments, Inc.	Si410AA2P4C	Temperature sensor (SD)	Forward skirt 2, 180° Sta 86.625 ±3 in.	SD107: Ex±|Sig±|Shd(F,G,H,J,K)
SD108	2255-3	Data	Scientific Instruments, Inc.	Si410AA2P4C	Temperature sensor (SD)	Forward skirt 3, 180° Sta 86.625 ±6 in.	SD108: Ex±|Sig±|Shd(L,M,N,P,R)
SD109	2255-4	Data	Scientific Instruments, Inc.	Si410AA2P4C	Temperature sensor (SD)	Forward skirt 4, 180° Sta 86.625 ±9 in.	SD109: Ex±|Sig±|Shd(S,T,U,V,W)
SD110	2255-5	Data	Scientific Instruments, Inc.	Si410AA2P4C	Temperature sensor (SD)	Forward skirt 5, 180° Sta 86.625 ±12 in.	SD110: Ex±|Sig±|Shd(X,Z,a,b,c)
SD111	2255-6	Data	Scientific Instruments, Inc.	Si410AA2P4C	Temperature sensor (SD)	Forward skirt 6, 180° Sta 111.625	SD111: Ex±|Sig±|Shd(d,e,f,g,h)
SD112	2255-7	Data	Scientific Instruments, Inc.	Si410AA2P4C	Temperature sensor (SD)	Forward skirt 7, 180° Sta 117.625	SD112: Ex±|Sig±|Shd(A,B,C,D,E)
SD113	2255-8	Data	Scientific Instruments, Inc.	Si410AA2P4C	Temperature sensor (SD)	Forward skirt 8, 180° Sta 123.625	SD113: Ex±|Sig±|Shd(F,G,H,J,K)
SD114	2255-9	Data	Scientific Instruments, Inc.	Si410AA2P4C	Temperature sensor (SD)	Forward skirt 9, 180° Sta 86.625 ±60 in.	SD114: Ex±|Sig±|Shd(L,M,N,P,R)
SD115	2255-10	Data	Scientific Instruments, Inc.	Si410AA2P4C	Temperature sensor (SD)	Forward skirt 10, 120° Sta 86.625	SD115: Ex±|Sig±|Shd(S,T,U,V,W)
SD116	2255-11	Data	Scientific Instruments, Inc.	Si410AA2P4C	Temperature sensor (SD)	Forward skirt 11, 120° Sta 86.625 ±8 in.	SD116: Ex±|Sig±|Shd(X,Z,a,b,c)
SD117	2255-12	Data	Scientific Instruments, Inc.	Si410AA2P4C	Temperature sensor (SD)	Forward skirt 12, 120° Sta 86.625 ±16 in.	SD117: Ex±|Sig±|Shd(d,e,f,g,h)
SD118	2255-13	Data	Scientific Instruments, Inc.	Si410AA2P4C	Temperature sensor (SD)	Forward skirt 13, 120° Sta 86.625 ±24 in.	SD118: Ex±|Sig±|Shd(A,B,C,D,E)
SD119	2255-14	Data	Scientific Instruments, Inc.	Si410AA2P4C	Temperature sensor (SD)	Forward skirt 14, 120° Sta 86.625 ±60 in.	SD119: Ex±|Sig±|Shd(F,G,H,J,K)
SD120	2255-15	Data	Scientific Instruments, Inc.	Si410AA2P4C	Temperature sensor (SD)	Forward skirt 15, 40° Sta 86.625	SD120: Ex±|Sig±|Shd(L,M,N,P,R)
SD121	2255-16	Data	Scientific Instruments, Inc.	Si410AA2P4C	Temperature sensor (SD)	Forward skirt 16, 40° Sta 99.625	SD121: Ex±|Sig±|Shd(S,T,U,V,W)
SD122	2255-17	Data	Scientific Instruments, Inc.	Si410AA2P4C	Temperature sensor (SD)	Forward skirt 17, 40° Sta 109.625	SD122: Ex±|Sig±|Shd(X,Z,a,b,c)
SD123	2255-18	Data	Scientific Instruments, Inc.	Si410AA2P4C	Temperature sensor (SD)	Forward skirt 18, 40° Sta 120.625	SD123: Ex±|Sig±|Shd(d,e,f,g,h)
SD124	2255-19	Data	Scientific Instruments, Inc.	Si410AA2P4C	Temperature sensor (SD)	Forward skirt 19, 40° Sta 86.625 ±60 in.	SD124: Ex±|Sig±|Shd(A,B,C,D,E)
SD125	2255-20	Data	Scientific Instruments, Inc.	Si410AA2P4C	Temperature sensor (SD)	Forward skirt 20, 360° Sta 86.625	SD125: Ex±|Sig±|Shd(F,G,H,J,K)
SD126	2255-21	Data	Scientific Instruments, Inc.	Si410AA2P4C	Temperature sensor (SD)	Forward skirt 21, 360° Sta 86.625 ±3 in.	SD126: Ex±|Sig±|Shd(L,M,N,P,R)
SD127	2255-22	Data	Scientific Instruments, Inc.	Si410AA2P4C	Temperature sensor (SD)	Forward skirt 22, 360° Sta 86.625 ±6 in.	SD127: Ex±|Sig±|Shd(S,T,U,V,W)
SD128	2255-23	Data	Scientific Instruments, Inc.	Si410AA2P4C	Temperature sensor (SD)	Forward skirt 23, 360° Sta 86.625 ±9 in.	SD128: Ex±|Sig±|Shd(X,Z,a,b,c)

TABLE H.11.—(Concluded)

Designation	P&ID[a] tag number	Field type	Manufacturer	Model	Description	Location from P&ID[a] except where noted	Connector pin-out|test article (inboard)
SD129	2255-24	Data	Scientific Instruments, Inc.	Si410AA2P4C	Temperature sensor (SD)	Forward skirt 24, 360° Sta 86.625 ±12 in.	SD129: Ex±|Sig±|Shd(d,e,f,g,h)
SD130	2255-25	Data	Scientific Instruments, Inc.	Si410AA2P4C	Temperature sensor (SD)	Forward skirt 25, 360° Sta 86.625 ±16 in.	SD130: Ex±|Sig±|Shd(A,B,C,D,E)
SD131	2255-26	Data	Scientific Instruments, Inc.	Si410AA2P4C	Temperature sensor (SD)	Forward skirt 26, 360° Sta 86.625 ±24 in.	SD131: Ex±|Sig±|Shd(F,G,H,J,K)
SD132	2255-27	Data	Scientific Instruments, Inc.	Si410AA2P4C	Temperature sensor (SD)	Forward skirt 27, 360° Sta 86.625 ±60 in.	SD132: Ex±|Sig±|Shd(L,M,N,P,R)
SD133	2255-28	Data	Scientific Instruments, Inc.	Si410AA2P4C	Temperature sensor (SD)	Forward skirt 28, 300° Sta 86.625	SD133: Ex±|Sig±|Shd(S,T,U,V,W)
SD134	2255-29	Data	Scientific Instruments, Inc.	Si410AA2P4C	Temperature sensor (SD)	Forward skirt 29, 300° Sta 86.625 ±4 in.	SD134: Ex±|Sig±|Shd(X,Z,a,b,c)
SD135	2255-30	Data	Scientific Instruments, Inc.	Si410AA2P4C	Temperature sensor (SD)	Forward skirt 30, 300° Sta 86.625 ±8 in.	SD135: Ex±|Sig±|Shd(d,e,f,g,h)
SD136	2255-31	Data	Scientific Instruments, Inc.	Si410AA2P4C	Temperature sensor (SD)	Forward skirt 31, 300° Sta 86.625 ±12 in.	SD136: Ex±|Sig±|Shd(A,B,C,D,E)
SD137	2255-32	Data	Scientific Instruments, Inc.	Si410AA2P4C	Temperature sensor (SD)	Forward skirt 32, 300° Sta 86.625 ±16 in.	SD137: Ex±|Sig±|Shd(F,G,H,J,K)
SD138	2255-33	Data	Scientific Instruments, Inc.	Si410AA2P4C	Temperature sensor (SD)	Forward skirt 33, 300° Sta 86.625 ±20 in.	SD138: Ex±|Sig±|Shd(L,M,N,P,R)
SD139	2255-34	Data	Scientific Instruments, Inc.	Si410AA2P4C	Temperature sensor (SD)	Forward skirt 34, 300° Sta 86.625 ±28 in.	SD139: Ex±|Sig±|Shd(S,T,U,V,W)
SD140	2255-35	Data	Scientific Instruments, Inc.	Si410AA2P4C	Temperature sensor (SD)	Forward skirt 35, 300° Sta 86.625 ±60 in.	SD140: Ex±|Sig±|Shd(X,Z,a,b,c)
SD141	2255-36	Data	Scientific Instruments, Inc.	Si410AA2P4C	Temperature sensor (SD)	Forward skirt 36, 230° Sta 86.625	SD141: Ex±|Sig±|Shd(d,e,f,g,h)
SD142	2255-37	Data	Scientific Instruments, Inc.	Si410AA2P4C	Temperature sensor (SD)	Forward skirt 37, 230° Sta 86.625 ±6 in.	SD142: Ex±|Sig±|Shd(A,B,C,D,E)
SD143	2255-38	Data	Scientific Instruments, Inc.	Si410AA2P4C	Temperature sensor (SD)	Forward skirt 38, 230° Sta 86.625 ±12 in.	SD143: Ex±|Sig±|Shd(F,G,H,J,K)
SD144	2255-39	Data	Scientific Instruments, Inc.	Si410AA2P4C	Temperature sensor (SD)	Forward skirt 39, 230° Sta 86.625 ±18 in.	SD144: Ex±|Sig±|Shd(L,M,N,P,R)
SD145	2255-40	Data	Scientific Instruments, Inc.	Si410AA2P4C	Temperature sensor (SD)	Forward skirt 40, 230° Sta 86.625 ±42 in.	SD145: Ex±|Sig±|Shd(S,T,U,V,W)
SD146	2255-41	Data	Scientific Instruments, Inc.	Si410AA2P4C	Temperature sensor (SD)	Forward skirt 41, 230° Sta 86.625 ±32 in.	SD146: Ex±|Sig±|Shd(X,Z,a,b,c)
SD179	2255-42	Data	Scientific Instruments, Inc.	Si410AA2P4C	Temperature sensor (SD)	Skirt flange temperature	Forward skirt 42, 230° Sta 86.625 ±60 in.
SD185	2255-43	Data	Scientific Instruments, Inc.	Si410AA2P4C	Temperature sensor (SD)	Exterior forward skirt temperature	Forward skirt 43, 182° Sta 86.625 ±8 in.
SD186	2255-44	Data	Scientific Instruments, Inc.	Si410AA2P4C	Temperature sensor (SD)	Exterior forward skirt temperature	Forward skirt 43, 182° Sta 86.625 ±26 in.
SD187	2255-45	Data	Scientific Instruments, Inc.	Si410AA2P4C	Temperature sensor (SD)	Exterior forward skirt temperature	Forward skirt 43, 302° Sta 86.625 ±10 in.
SD188	2255-46	Data	Scientific Instruments, Inc.	Si410AA2P4C	Temperature sensor (SD)	Exterior forward skirt temperature	Forward skirt 43, 232° Sta 86.625 ±9 in.
SD189	2255-47	Data	Scientific Instruments, Inc.	Si410AA2P4C	Temperature sensor (SD)	Exterior forward skirt temperature	Forward skirt 43, 232° Sta 86.625 ±26 in.

[a]Process and instrumentation diagram (P&ID).

TABLE H.12.—SILICON DIODES (SDs) LOCATED ON AFT SKIRT SURFACE

Designation	P&ID[a] tag number	Field type	Manufacturer	Model	Description	Location from P&ID[a] except where noted	Connector pin-out|test article (inboard)
SD180	2260-1	Data	Scientific Instruments, Inc.	Si410AA2P4C	Temperature sensor (SD)	Aft skirt 1, 180° Sta 44.625 – 6 in.	SD180: Ex±|Sig±|Shd(A,B,C,D,E)
SD181	2260-2	Data	Scientific Instruments, Inc.	Si410AA2P4C	Temperature sensor (SD)	Aft skirt 2, 180° Sta 44.625 – 3 in.	SD181: Ex±|Sig±|Shd(F,G,H,J,K)
SD182	2260-3	Data	Scientific Instruments, Inc.	Si410AA2P4C	Temperature sensor (SD)	Aft skirt 3, 180° Sta 44.625	SD182: Ex±|Sig±|Shd(L,M,N,P,R)
SD183	2260-4	Data	Scientific Instruments, Inc.	Si410AA2P4C	Temperature sensor (SD)	Aft skirt 4, 300° Sta 44.625 – 3 in.	SD183: Ex±|Sig±|Shd(S,T,U,V,W)
SD184	2260-5	Data	Scientific Instruments, Inc.	Si410AA2P4C	Temperature sensor (SD)	Aft skirt 5, 300° Sta 44.625	SD184: Ex±|Sig±|Shd(X,Z,a,b,c)

[a]Process and instrumentation diagram (P&ID).

TABLE H.13.—SILICON DIODES (SDs) LOCATED ON SPRAY-ON FOAM INSULATION SURFACE

Designation	P&ID[a] tag number	Field type	Manufacturer	Model	Description	Location from P&ID[a] except where noted	Connector pin-out|test article (inboard)
SD31	2246-1	Data	Scientific Instruments, Inc.	Si410AALP4C	Temperature sensor (SD)	Angle 225° at 3% fill_13.324 ST	SD31: Ex±|Sig±|Shd(S,T,U,V,W)
SD32	2246-2	Data	Scientific Instruments, Inc.	Si410AALP4C	Temperature sensor (SD)	Angle 45° at 3% fill_12.824 ST	SD32: Ex±|Sig±|Shd(X,Z,a,b,c)
SD33	2246-3	Data	Scientific Instruments, Inc.	Si410AALP4C	Temperature sensor (SD)	Angle 225° at 50% fill	SD33: Ex±|Sig±|Shd(A,B,C,D,E)
SD34	2246-4	Data	Scientific Instruments, Inc.	Si410AALP4C	Temperature sensor (SD)	Angle 135° at 50% fill	SD34: Ex±|Sig±|Shd(F,G,H,J,K)
SD35	2246-5	Data	Scientific Instruments, Inc.	Si410AALP4C	Temperature sensor (SD)	Angle 315° at 50% fill	SD35: Ex±|Sig±|Shd(L,M,N,P,R)
SD36	2246-6	Data	Scientific Instruments, Inc.	Si410AALP4C	Temperature sensor (SD)	Angle 45° at 50% fill	SD36: Ex±|Sig±|Shd(S,T,U,V,W)
SD37	2246-7	Data	Scientific Instruments, Inc.	Si410AALP4C	Temperature sensor (SD)	Angle 45° at 97% fill_118.426 ST	SD37: Ex±|Sig±|Shd(S,T,U,V,W)
SD38	2246-8	Data	Scientific Instruments, Inc.	Si410AALP4C	Temperature sensor (SD)	Angle 225° at 97% fill_117.926 ST	SD38: Ex±|Sig±|Shd(X,Z,a,b,c)

[a]Process and instrumentation diagram (P&ID).

TABLE H.14.—SILICON DIODES (SDS) LOCATED IN MULTILAYER INSULATION BLANKET

Designation	P&ID[a] tag number	Field type	Manufacturer	Model	Description	Location from P&ID[a] except where noted	Connector pin-out|test article (inboard)
SD39	2247-1	Data	Scientific Instruments, Inc.	Si410AALP4C	Temperature sensor (SD)	Top dome, sub 2 layer 11, 2	SD39: Ex±|Sig±|Shd(A,B,C,D,E)
SD40	2247-2	Data	Scientific Instruments, Inc.	Si410AALP4C	Temperature sensor (SD)	Top dome, sub 2 layer 11, 3	SD40: Ex±|Sig±|Shd(F,G,H,J,K)
SD41	2247-3	Data	Scientific Instruments, Inc.	Si410AALP4C	Temperature sensor (SD)	Top dome, sub 2 layer 20, 2	SD41: Ex±|Sig±|Shd(L,M,N,P,R)
SD42	2247-4	Data	Scientific Instruments, Inc.	Si410AALP4C	Temperature sensor (SD)	Top dome, sub 1 layer 5, 2	SD42: Ex±|Sig±|Shd(S,T,U,V,W)
SD43	2247-5	Data	Scientific Instruments, Inc.	Si410AALP4C	Temperature sensor (SD)	Top dome, sub 1 layer 5, 3	SD43: Ex±|Sig±|Shd(X,Z,a,b,c)
SD44	2247-6	Data	Scientific Instruments, Inc.	Si410AALP4C	Temperature sensor (SD)	Top dome, sub 1 layer 0, 1	SD44: Ex±|Sig±|Shd(d,e,f,g,h)
SD45	2247-7	Data	Scientific Instruments, Inc.	Si410AALP4C	Temperature sensor (SD)	Top dome, sub 1 layer 5, 1	SD45: Ex±|Sig±|Shd(A,B,C,D,E)
SD46	2247-8	Data	Scientific Instruments, Inc.	Si410AALP4C	Temperature sensor (SD)	Top dome, sub 2 layer 11, 1	SD46: Ex±|Sig±|Shd(F,G,H,J,K)
SD47	2247-9	Data	Scientific Instruments, Inc.	Si410AALP4C	Temperature sensor (SD)	Top dome, sub 1 layer 0, 3	SD47: Ex±|Sig±|Shd(L,M,N,P,R)
SD48	2247-10	Data	Scientific Instruments, Inc.	Si410AALP4C	Temperature sensor (SD)	Top dome, sub 1 layer 0, 2	SD48: Ex±|Sig±|Shd(S,T,U,V,W)
SD49	2247-11	Data	Scientific Instruments, Inc.	Si410AALP4C	Temperature sensor (SD)	Bottom dome, sub 2 layer 20, 3	SD49: Ex±|Sig±|Shd(A,B,C,D,E)
SD50	2247-12	Data	Scientific Instruments, Inc.	Si410AALP4C	Temperature sensor (SD)	Bottom dome, sub 2 layer 11, 1	SD50: Ex±|Sig±|Shd(F,G,H,J,K)
SD51	2247-13	Data	Scientific Instruments, Inc.	Si410AALP4C	Temperature sensor (SD)	Bottom dome, sub 2 layer 20, 1	SD51: Ex±|Sig±|Shd(L,M,N,P,R)
SD52	2247-14	Data	Scientific Instruments, Inc.	Si410AALP4C	Temperature sensor (SD)	Bottom dome, sub 2 layer 11, 2	SD52: Ex±|Sig±|Shd(S,T,U,V,W)
SD53	2247-15	Data	Scientific Instruments, Inc.	Si410AALP4C	Temperature sensor (SD)	Bottom dome, sub 2 layer 20, 2	SD53: Ex±|Sig±|Shd(X,Z,a,b,c)
SD54	2247-16	Data	Scientific Instruments, Inc.	Si410AALP4C	Temperature sensor (SD)	Bottom dome, sub 1 layer 0, 1	SD54: Ex±|Sig±|Shd(d,e,f,g,h)
SD55	2247-17	Data	Scientific Instruments, Inc.	Si410AALP4C	Temperature sensor (SD)	Bottom dome, sub 1 layer 0, 2	SD55: Ex±|Sig±|Shd(A,B,C,D,E)
SD56	2247-18	Data	Scientific Instruments, Inc.	Si410AALP4C	Temperature sensor (SD)	Bottom dome, sub 2 layer 11, 3	SD56: Ex±|Sig±|Shd(F,G,H,J,K)
SD57	2247-19	Data	Scientific Instruments, Inc.	Si410AALP4C	Temperature sensor (SD)	Bottom dome, sub 1 layer 5, 2	SD57: Ex±|Sig±|Shd(L,M,N,P,R)
SD58	2247-20	Data	Scientific Instruments, Inc.	Si410AALP4C	Temperature sensor (SD)	Bottom dome, sub 1 layer 5, 1	SD58: Ex±|Sig±|Shd(S,T,U,V,W)
SD150	2247-21	Data	Scientific Instruments, Inc.	Si410AALP4C	Temperature sensor (SD)	Top dome, sub 2 layer 20, 1	SD150: Ex±|Sig±|Shd(X,Z,a,b,c)
SD151	2247-22	Data	Scientific Instruments, Inc.	Si410AALP4C	Temperature sensor (SD)	Top dome, sub 2 layer 20, 3	SD151: Ex±|Sig±|Shd(d,e,f,g,h)
SD152	2247-23	Data	Scientific Instruments, Inc.	Si410AALP4C	Temperature sensor (SD)	Bottom dome, sub 1 layer 0, 3	SD152: Ex±|Sig±|Shd(A,B,C,D,E)
SD153	2247-24	Data	Scientific Instruments, Inc.	Si410AALP4C	Temperature sensor (SD)	Bottom dome, sub 1 layer 5, 3	SD153: Ex±|Sig±|Shd(F,G,H,J,K)

[a]Process and instrumentation diagram (P&ID).

TABLE H.15.—SILICON DIODES (SDs) LOCATED ON INSTRUMENT RAKE

Designation	P&ID[a] tag number	Field type	Manufacturer	Model	Description	Location from P&ID[a] except where noted	Connector pin-out|test article (inboard)
SD64	2249-1	Data	Scientific Instruments, Inc.	Si410AALP4C	Temperature sensor (SD)	Internal tank rake 5%	SD64: Ex±|Sig±|Shd(A,B,C,D,E)
SD65	2249-2	Data	Scientific Instruments, Inc.	Si410AALP4C	Temperature sensor (SD)	Internal tank rake 10%	SD65: Ex±|Sig±|Shd(F,G,H,J,K)
SD66	2249-3	Data	Scientific Instruments, Inc.	Si410AALP4C	Temperature sensor (SD)	Internal tank rake 15%	SD66: Ex±|Sig±|Shd(L,M,N,P,R)
SD67	2249-4	Data	Scientific Instruments, Inc.	Si410AALP4C	Temperature sensor (SD)	Internal tank rake 20%	SD67: Ex±|Sig±|Shd(S,T,U,V,W)
SD68	2249-5	Data	Scientific Instruments, Inc.	Si410AALP4C	Temperature sensor (SD)	Internal tank rake 25%	SD68: Ex±|Sig±|Shd(X,Z,a,b,c)
SD69	2249-6	Data	Scientific Instruments, Inc.	Si410AALP4C	Temperature sensor (SD)	Internal tank rake 30%	SD69: Ex±|Sig±|Shd(d,e,f,g,h)
SD70	2249-7	Data	Scientific Instruments, Inc.	Si410AALP4C	Temperature sensor (SD)	Internal tank rake 35%	SD70: Ex±|Sig±|Shd(A,B,C,D,E)
SD71	2249-8	Data	Scientific Instruments, Inc.	Si410AALP4C	Temperature sensor (SD)	Internal tank rake 40%	SD71: Ex±|Sig±|Shd(F,G,H,J,K)
SD72	2249-9	Data	Scientific Instruments, Inc.	Si410AALP4C	Temperature sensor (SD)	Internal tank rake 45%	SD72: Ex±|Sig±|Shd(L,M,N,P,R)
SD73	2249-10	Data	Scientific Instruments, Inc.	Si410AALP4C	Temperature sensor (SD)	Internal tank rake 50%	SD73: Ex±|Sig±|Shd(S,T,U,V,W)
SD74	2247-11	Data	Scientific Instruments, Inc.	Si410AALP4C	Temperature sensor (SD)	Internal tank rake 55%	SD74: Ex±|Sig±|Shd(X,Z,a,b,c)
SD75	2249-12	Data	Scientific Instruments, Inc.	Si410AALP4C	Temperature sensor (SD)	Internal tank rake 60%	SD75: Ex±|Sig±|Shd(d,e,f,g,h)
SD76	2249-13	Data	Scientific Instruments, Inc.	Si410AALP4C	Temperature sensor (SD)	Internal tank rake 65%	SD76: Ex±|Sig±|Shd(A,B,C,D,E)
SD77	2249-14	Data	Scientific Instruments, Inc.	Si410AALP4C	Temperature sensor (SD)	Internal tank rake 70%	SD77: Ex±|Sig±|Shd(F,G,H,J,K)
SD78	2249-15	Data	Scientific Instruments, Inc.	Si410AALP4C	Temperature sensor (SD)	Internal tank rake 75%	SD78: Ex±|Sig±|Shd(L,M,N,P,R)
SD79	2249-16	Data	Scientific Instruments, Inc.	Si410AALP4C	Temperature sensor (SD)	Internal tank rake 80%	SD79: Ex±|Sig±|Shd(S,T,U,V,W)
SD80	2249-17	Data	Scientific Instruments, Inc.	Si410AALP4C	Temperature sensor (SD)	Internal tank rake 85%	SD80: Ex±|Sig±|Shd(X,Z,a,b,c)
SD81	2249-18	Data	Scientific Instruments, Inc.	Si410AALP4C	Temperature sensor (SD)	Internal tank rake 90%	SD81: Ex±|Sig±|Shd(d,e,f,g,h)
SD82	2249-19	Data	Scientific Instruments, Inc.	Si410AALP4C	Temperature sensor (SD)	Internal tank rake 95%	SD82: Ex±|Sig±|Shd(A,B,C,D,E)
SD83	2249-20	Data	Scientific Instruments, Inc.	Si410AALP4C	Temperature sensor (SD)	Internal tank rake 99%	SD83: Ex±|Sig±|Shd(F,G,H,J,K)

[a]Process and instrumentation diagram (P&ID).

TABLE H.16.—CONTROL VALVE BODY TEMPERATURES
[Silicon diode (SD).]

Designation	P&ID[a] tag number	Field type	Manufacturer	Model	Description	Location from P&ID[a] except where noted	Connector pin-out|test article (inboard)
SD59	2248-1	Data	Scientific Instruments, Inc.	Si410AALP4C	Temperature sensor (SD)	On relief valve body	SD59: Ex±|Sig±|Shd(A,B,C,D,E)
SD60	2248-2	Data	Scientific Instruments, Inc.	Si410AALP4C	Temperature sensor (SD)	On local vent valve	SD60: Ex±|Sig±|Shd(F,G,H,J,K)
SD61	2248-3	Data	Scientific Instruments, Inc.	Si410AALP4C	Temperature sensor (SD)	On local vent valve	SD61: Ex±|Sig±|Shd(L,M,N,P,R)
SD62	2248-4	Data	Scientific Instruments, Inc.	Si410AALP4C	Temperature sensor (SD)	On local capacitance probe flange	SD62: Ex±|Sig±|Shd(S,T,U,V,W)
SD63	2248-5	Data	Scientific Instruments, Inc.	Si410AALP4C	Temperature sensor (SD)	On local drain valve	SD63: Ex±|Sig±|Shd(X,Z,a,b,c)

[a]Process and instrumentation diagram (P&ID).

TABLE H.17.—WIRE BUNDLE TEMPERATURES
[Silicon diode (SD).]

Designation	P&ID[a] tag number	Field type	Manufacturer	Model	Description	Location from P&ID[a] except where noted	Connector pin-out|test article (inboard)
SD102	2254-1	Data	Scientific Instruments, Inc.	Si410AALP4C	Temperature sensor (SD)	On wire bundle interconnection panel 1	SD102: Ex±|Sig±|Shd(d,e,f,g,h)
SD103	2254-2	Data	Scientific Instruments, Inc.	Si410AALP4C	Temperature sensor (SD)	On wire bundle interconnection panel 2	SD103: Ex±|Sig±|Shd(X,Z,a,b,c)
SD104	2254-3	Data	Scientific Instruments, Inc.	Si410AALP4C	Temperature sensor (SD)	On wire bundle interconnection panel 2	SD104: Ex±|Sig±|Shd(d,e,f,g,h)
SD105	2254-4	Data	Scientific Instruments, Inc.	Si410AALP4C	Temperature sensor (SD)	On wire bundle interconnection panel 3	SD105: Ex±|Sig±|Shd(d,e,f,g,h)

[a]Process and instrumentation diagram (P&ID).

TABLE H.18.—PIPING AND SUPPORT STRUCTURE TEMPERATURES
[Silicon diode (SD).]

Designation	P&ID[a] tag number	Field type	Manufacturer	Model	Description	Location from P&ID[a] except where noted	Connector pin-out|test article (inboard)
SD158	2256-1	Data	Scientific Instruments, Inc.	Si410AALP4C	Temperature sensor (SD)	Fill and drain line 1	SD158: Ex±|Sig±|Shd(A,B,C,D,E)
SD159	2256-2	Data	Scientific Instruments, Inc.	Si410AALP4C	Temperature sensor (SD)	Fill and drain line 2	SD159: Ex±|Sig±|Shd(F,G,H,J,K)
SD160	2265-3	Data	Scientific Instruments, Inc.	Si410AALP4C	Temperature sensor (SD)	Fill and drain line 3	SD160: Ex±|Sig±|Shd(L,M,N,P,R)
SD161	2257-1	Data	Scientific Instruments, Inc.	Si410AALP4C	Temperature sensor (SD)	Main vent 1	SD161: Ex±|Sig±|Shd(S,T,U,V,W)
SD162	2257-2	Data	Scientific Instruments, Inc.	Si410AALP4C	Temperature sensor (SD)	Main vent 2	SD162: Ex±|Sig±|Shd(X,Z,a,b,c)
SD163	2257-3	Data	Scientific Instruments, Inc.	Si410AALP4C	Temperature sensor (SD)	Main vent 3	SD163: Ex±|Sig±|Shd(d,e,f,g,h)
SD164	2258-1	Data	Scientific Instruments, Inc.	Si410AALP4C	Temperature sensor (SD)	Vapor-cooling tee line 1	SD164: Ex±|Sig±|Shd(A,B,C,D,E)
SD165	2258-2	Data	Scientific Instruments, Inc.	Si410AALP4C	Temperature sensor (SD)	Vapor-cooling tee line 2	SD165: Ex±|Sig±|Shd(F,G,H,J,K)
SD166	2258-3	Data	Scientific Instruments, Inc.	Si410AALP4C	Temperature sensor (SD)	Vapor-cooling tee line 3	SD166: Ex±|Sig±|Shd(L,M,N,P,R)
SD167	2216	Data	Scientific Instruments, Inc.	Si410AALP4C	Temperature sensor (SD)	Backpressure control cart	Connectors located at B2 Facility

[a]Process and instrumentation diagram (P&ID).

TABLE H.19.—THERMOCOUPLES (TC) IN MULTILAYER INSULATION BLANKET AND TANK EXHAUST VENT

Designation	P&ID[a] tag number	Field type	Manufacturer	Model	Description	Location from P&ID[a] except where noted	Connector pin-out|test article (inboard)
TC-1A	2277-1	Control	NASA Glenn Research Center	Type E	Temperature sensor (TC)	Vent line 1	TC-1: Sig±|Shd(A,B,C)
TC-1B	2277-2	Control	NASA Glenn Research Center	Type E	Temperature sensor (TC)	Vent line 2	TC-1: Sig±|Shd(E,F,G)
TC-2	2247-25	Data	NASA Glenn Research Center	Type E	Temperature sensor (TC)	Bottom tank dome, ~12.824 at 45°	TC-2: Sig±|Shd(J,K,L)
TC-3	2247-26	Data	NASA Glenn Research Center	Type E	Temperature sensor (TC)	Bottom tank dome, ~13.324 at 225°	TC-3: Sig±|Shd(T,U,V)
TC-4	2247-27	Data	NASA Glenn Research Center	Type E	Temperature sensor (TC)	Bottom tank dome, ~27.994 at 225°	TC-4: Sig±|Shd(A,B,C)
TC-5	2247-28	Data	NASA Glenn Research Center	Type E	Temperature sensor (TC)	Top tank dome, ~118.426 at 45°	TC-5: Sig±|Shd(E,F,G)
TC_6	2247-29	Data	NASA Glenn Research Center	Type E	Temperature sensor (TC)	Top tank dome, ~117.926 at 225°	TC-6: Sig±|Shd(J,K,L)
TC-7	2247-30	Data	NASA Glenn Research Center	Type E	Temperature sensor (TC)	Top tank dome, ~103.306 at 225°	TC-7: Sig±|Shd(T,U,V)
TC-8	2218	Data	NASA Glenn Research Center	Type E	Temperature sensor (TC)	TC-9 facility hardware	Connectors located at B2 Facility

[a]Process and instrumentation diagram (P&ID).

Appendix I.—Fluid Properties

Table I.1 to Table I.6 contain various properties for parahydrogen and nitrogen.

I.1 Isobaric Properties for Parahydrogen at 20 psia (Ref. 62)

TABLE I.1.—ISOBARIC PROPERTIES FOR PARAHYDROGEN AT 20 psia

Temperature, K	Pressure, psia	Pressure, MPa	Density, kg/m^3	Volume, m^3/kg	Internal energy, kJ/kg	Enthalpy, kJ/kg	Phase
20.00	20.00	0.14	71.17	0.014	–4.24	–2.31	Liquid
21.37	20.00	.14	69.52	.014	9.26	11.24	Liquid
21.37	20.00	.14	1.77	.565	373.09	450.94	Vapor
22.50	20.00	.14	1.65	.605	381.62	465.10	Vapor
25.00	20.00	.14	1.45	.692	399.44	494.81	Vapor
27.50	20.00	.14	1.29	.775	416.50	523.31	Vapor
30.00	20.00	.14	1.17	.856	433.14	551.13	Vapor
32.50	20.00	.14	1.07	.936	449.51	578.52	Vapor
35.00	20.00	.14	.99	1.015	465.73	605.62	Vapor
37.50	20.00	.14	.92	1.093	481.83	632.53	Vapor
40.00	20.00	.14	.85	1.171	497.87	659.29	Vapor
42.50	20.00	.14	.80	1.248	513.86	685.95	Vapor
45.00	20.00	.14	.75	1.325	529.83	712.55	Vapor
47.50	20.00	.14	.71	1.402	545.80	739.11	Vapor
50.00	20.00	.14	.68	1.478	561.79	765.66	Vapor
52.50	20.00	.14	.64	1.555	577.83	792.23	Vapor
55.00	20.00	.14	.61	1.631	593.94	818.86	Vapor
57.50	20.00	.14	.59	1.707	610.15	845.56	Vapor
60.00	20.00	.14	.56	1.783	626.50	872.38	Vapor
62.50	20.00	.14	.54	1.859	643.02	899.37	Vapor
65.00	20.00	.14	.52	1.935	659.75	926.55	Vapor
67.50	20.00	.14	.50	2.011	676.73	953.97	Vapor
70.00	20.00	.14	.48	2.086	694.00	981.67	Vapor
72.50	20.00	.14	.46	2.162	711.60	1009.70	Vapor
75.00	20.00	.14	.45	2.237	729.58	1038.10	Vapor
77.50	20.00	.14	.43	2.313	747.95	1066.90	Vapor
80.00	20.00	.14	.42	2.388	766.77	1096.10	Vapor
82.50	20.00	.14	.41	2.463	786.05	1125.70	Vapor
85.00	20.00	.14	.39	2.539	805.82	1155.90	Vapor
87.50	20.00	.14	.38	2.614	826.10	1186.60	Vapor
90.00	20.00	.14	.37	2.689	846.92	1217.80	Vapor
92.50	20.00	.14	.36	2.765	868.27	1249.50	Vapor
95.00	20.00	.14	.35	2.840	890.17	1281.80	Vapor
97.50	20.00	.14	.34	2.915	912.63	1314.60	Vapor
100.00	20.00	.14	.33	2.990	935.63	1347.90	Vapor

TABLE I.1.—(Continued)

Temperature, K	Pressure, psia	Pressure, MPa	Density, kg/m^3	Volume, m^3/kg	Internal energy, kJ/kg	Enthalpy, kJ/kg	Phase
102.50	20.00	0.14	0.33	3.065	959.17	1381.90	Vapor
105.00	20.00	.14	.32	3.140	983.25	1416.30	Vapor
107.50	20.00	.14	.31	3.215	1007.90	1451.20	Vapor
110.00	20.00	.14	.30	3.291	1033.00	1486.70	Vapor
112.50	20.00	.14	.30	3.366	1058.60	1522.70	Vapor
115.00	20.00	.14	.29	3.441	1084.60	1559.10	Vapor
117.50	20.00	.14	.28	3.516	1111.10	1595.90	Vapor
120.00	20.00	.14	.28	3.591	1138.10	1633.20	Vapor
122.50	20.00	.14	.27	3.666	1165.40	1670.90	Vapor
125.00	20.00	.14	.27	3.741	1193.10	1709.00	Vapor
127.50	20.00	.14	.26	3.816	1221.20	1747.40	Vapor
130.00	20.00	.14	.26	3.891	1249.60	1786.10	Vapor
132.50	20.00	.14	.25	3.966	1278.30	1825.20	Vapor
135.00	20.00	.14	.25	4.041	1307.30	1864.50	Vapor
137.50	20.00	.14	.24	4.116	1336.50	1904.00	Vapor
140.00	20.00	.14	.24	4.191	1366.00	1943.80	Vapor
142.50	20.00	.14	.23	4.266	1395.60	1983.80	Vapor
145.00	20.00	.14	.23	4.340	1425.40	2024.00	Vapor
147.50	20.00	.14	.23	4.415	1455.40	2064.30	Vapor
150.00	20.00	.14	.22	4.490	1485.60	2104.70	Vapor
152.50	20.00	.14	.22	4.565	1515.80	2145.30	Vapor
155.00	20.00	.14	.22	4.640	1546.10	2186.00	Vapor
157.50	20.00	.14	.21	4.715	1576.60	2226.70	Vapor
160.00	20.00	.14	.21	4.790	1607.00	2267.50	Vapor
162.50	20.00	.14	.21	4.865	1637.60	2308.40	Vapor
165.00	20.00	.14	.20	4.940	1668.10	2349.30	Vapor
167.50	20.00	.14	.20	5.015	1698.70	2390.20	Vapor
170.00	20.00	.14	.20	5.089	1729.30	2431.10	Vapor
172.50	20.00	.14	.19	5.164	1759.80	2472.00	Vapor
175.00	20.00	.14	.19	5.239	1790.40	2512.80	Vapor
177.50	20.00	.14	.19	5.314	1820.90	2553.70	Vapor
180.00	20.00	.14	.19	5.389	1851.40	2594.50	Vapor
182.50	20.00	.14	.18	5.464	1881.80	2635.20	Vapor
185.00	20.00	.14	.18	5.539	1912.20	2675.90	Vapor
187.50	20.00	.14	.18	5.614	1942.50	2716.60	Vapor
190.00	20.00	.14	.18	5.688	1972.70	2757.10	Vapor
192.50	20.00	.14	.17	5.763	2002.90	2797.60	Vapor
195.00	20.00	.14	.17	5.838	2033.00	2838.00	Vapor

TABLE I.1.—(Continued)

Temperature, K	Pressure, psia	Pressure, MPa	Density, kg/m^3	Volume, m^3/kg	Internal energy, kJ/kg	Enthalpy, kJ/kg	Phase
197.50	20.00	0.14	0.17	5.913	2063.00	2878.40	Vapor
200.00	20.00	.14	.17	5.988	2092.90	2918.60	Vapor
202.50	20.00	.14	.16	6.063	2122.80	2958.80	Vapor
205.00	20.00	.14	.16	6.137	2152.50	2998.80	Vapor
207.50	20.00	.14	.16	6.212	2182.20	3038.80	Vapor
210.00	20.00	.14	.16	6.287	2211.70	3078.70	Vapor
212.50	20.00	.14	.16	6.362	2241.20	3118.50	Vapor
215.00	20.00	.14	.16	6.437	2270.60	3158.10	Vapor
217.50	20.00	.14	.15	6.512	2299.80	3197.70	Vapor
220.00	20.00	.14	.15	6.586	2329.00	3237.20	Vapor
222.50	20.00	.14	.15	6.661	2358.10	3276.60	Vapor
225.00	20.00	.14	.15	6.736	2387.00	3315.90	Vapor
227.50	20.00	.14	.15	6.811	2415.90	3355.10	Vapor
230.00	20.00	.14	.15	6.886	2444.70	3394.20	Vapor
232.50	20.00	.14	.14	6.961	2473.40	3433.20	Vapor
235.00	20.00	.14	.14	7.035	2502.00	3472.10	Vapor
237.50	20.00	.14	.14	7.110	2530.50	3510.90	Vapor
240.00	20.00	.14	.14	7.185	2558.90	3549.70	Vapor
242.50	20.00	.14	.14	7.260	2587.20	3588.30	Vapor
245.00	20.00	.14	.14	7.335	2615.40	3626.80	Vapor
247.50	20.00	.14	.13	7.409	2643.60	3665.30	Vapor
250.00	20.00	.14	.13	7.484	2671.60	3703.70	Vapor
252.50	20.00	.14	.13	7.559	2699.60	3742.00	Vapor
255.00	20.00	.14	.13	7.634	2727.50	3780.20	Vapor
257.50	20.00	.14	.13	7.709	2755.40	3818.30	Vapor
260.00	20.00	.14	.13	7.783	2783.10	3856.40	Vapor
262.50	20.00	.14	.13	7.858	2810.80	3894.40	Vapor
265.00	20.00	.14	.13	7.933	2838.40	3932.30	Vapor
267.50	20.00	.14	.12	8.008	2865.90	3970.10	Vapor
270.00	20.00	.14	.12	8.083	2893.40	4007.90	Vapor
272.50	20.00	.14	.12	8.157	2920.80	4045.60	Vapor
275.00	20.00	.14	.12	8.232	2948.10	4083.30	Vapor
277.50	20.00	.14	.12	8.307	2975.40	4120.90	Vapor
280.00	20.00	.14	.12	8.382	3002.60	4158.40	Vapor
282.50	20.00	.14	.12	8.457	3029.70	4195.80	Vapor
285.00	20.00	.14	.12	8.531	3056.80	4233.30	Vapor
287.50	20.00	.14	.12	8.606	3083.90	4270.60	Vapor
290.00	20.00	.14	.12	8.681	3110.90	4307.90	Vapor

TABLE I.1.—(Concluded)

Temperature, K	Pressure, psia	Pressure, MPa	Density, kg/m^3	Volume, m^3/kg	Internal energy, kJ/kg	Enthalpy, kJ/kg	Phase
292.50	20.00	0.14	0.11	8.756	3137.80	4345.20	Vapor
295.00	20.00	.14	.11	8.831	3164.70	4382.40	Vapor
297.50	20.00	.14	.11	8.905	3191.60	4419.60	Vapor
300.00	20.00	.14	.11	8.980	3218.40	4456.70	Vapor

I.2 Saturation Properties for Parahydrogen (Ref. 63)

TABLE I.2.—LIQUID SATURATION PROPERTIES FOR PARAHYDROGEN

Temperature, K	Pressure, psia	Pressure, MPa	Density, kg/m^3	Volume, m^3/kg	Internal energy, kJ/kg	Enthalpy, kJ/kg
14.00	1.14	0.01	76.87	0.013	–51.43	–51.32
14.50	1.51	.01	76.44	.013	–47.69	–47.56
15.00	1.95	.01	76.00	.013	–44.10	–43.92
15.50	2.48	.02	75.56	.013	–40.53	–40.30
16.00	3.12	.02	75.12	.013	–36.93	–36.64
16.50	3.88	.03	74.66	.013	–33.25	–32.89
17.00	4.76	.03	74.19	.013	–29.47	–29.03
17.50	5.79	.04	73.71	.014	–25.57	–25.03
18.00	6.97	.05	73.22	.014	–21.55	–20.89
18.50	8.32	.06	72.72	.014	–17.39	–16.60
19.00	9.86	.07	72.20	.014	–13.08	–12.14
19.50	11.59	.08	71.66	.014	–8.64	–7.52
20.00	13.52	.09	71.11	.014	–4.04	–2.73
20.50	15.69	.11	70.54	.014	.70	2.23
21.00	18.09	.12	69.96	.014	5.59	7.38
21.50	20.74	.14	69.35	.014	10.64	12.70
22.00	23.66	.16	68.73	.015	15.85	18.22
22.50	26.86	.19	68.08	.015	21.22	23.94
23.00	30.36	.21	67.41	.015	26.75	29.86
23.50	34.17	.24	66.72	.015	32.46	35.99
24.00	38.30	.26	66.00	.015	38.35	42.35
24.50	42.77	.29	65.25	.015	44.43	48.95
25.00	47.60	.33	64.47	.016	50.70	55.79
25.50	52.80	.36	63.65	.016	57.19	62.91
26.00	58.38	.40	62.80	.016	63.91	70.32
26.50	64.36	.44	61.91	.016	70.87	78.04
27.00	70.76	.49	60.97	.016	78.10	86.10
27.50	77.60	.54	59.97	.017	85.62	94.54
28.00	84.88	.59	58.92	.017	93.47	103.40
28.50	92.64	.64	57.79	.017	101.69	112.75
29.00	100.88	.70	56.58	.018	110.35	122.64
29.50	109.63	.76	55.27	.018	119.50	133.18
30.00	118.91	.82	53.84	.019	129.28	144.51
30.50	128.76	.89	52.24	.019	139.83	156.82
31.00	139.18	.96	50.43	.020	151.42	170.44
31.50	150.24	1.04	48.30	.021	164.50	185.95
32.00	161.98	1.12	45.64	.022	180.08	204.55
32.50	174.47	1.20	41.81	.024	201.09	229.86

TABLE I.3.—VAPOR SATURATION PROPERTIES FOR PARAHYDROGEN

Temperature, K	Pressure, psia	Pressure, MPa	Density, kg/m^3	Volume, m^3/kg	Internal energy, kJ/kg	Enthalpy, kJ/kg
14.00	1.14	0.01	0.14	7.19	341.10	397.84
14.50	1.51	.01	.18	5.64	343.88	402.42
15.00	1.95	.01	.22	4.49	346.56	406.88
15.50	2.48	.02	.28	3.62	349.16	411.20
16.00	3.12	.02	.34	2.96	351.69	415.41
16.50	3.88	.03	.41	2.44	354.15	419.50
17.00	4.76	.03	.49	2.04	356.53	423.45
17.50	5.79	.04	.58	1.71	358.83	427.26
18.00	6.97	.05	.69	1.45	361.04	430.92
18.50	8.32	.06	.81	1.24	363.15	434.42
19.00	9.86	.07	.94	1.07	365.16	437.76
19.50	11.59	.08	1.08	.92	367.06	440.91
20.00	13.52	.09	1.24	.80	368.85	443.88
20.50	15.69	.11	1.42	.70	370.52	446.65
21.00	18.09	.12	1.62	.62	372.06	449.21
21.50	20.74	.14	1.83	.55	373.46	451.55
22.00	23.66	.16	2.07	.48	374.72	453.66
22.50	26.86	.19	2.32	.43	375.82	455.52
23.00	30.36	.21	2.60	.38	376.75	457.13
23.50	34.17	.24	2.91	.34	377.51	458.45
24.00	38.30	.26	3.24	.31	378.08	459.49
24.50	42.77	.29	3.61	.28	378.44	460.21
25.00	47.60	.33	4.00	.25	378.57	460.59
25.50	52.80	.36	4.43	.23	378.47	460.62
26.00	58.38	.40	4.90	.20	378.11	460.25
26.50	64.36	.44	5.41	.18	377.45	459.45
27.00	70.76	.49	5.97	.17	376.48	458.19
27.50	77.60	.54	6.58	.15	375.14	456.40
28.00	84.88	.59	7.26	.14	373.40	454.04
28.50	92.64	.64	8.00	.12	371.20	451.00
29.00	100.88	.70	8.83	.11	368.45	447.20
29.50	109.63	.76	9.76	.10	365.05	442.49
30.00	118.91	.82	10.81	.09	360.86	436.68
30.50	128.76	.89	12.03	.08	355.65	429.46
31.00	139.18	.96	13.46	.07	349.09	420.39
31.50	150.24	1.04	15.21	.07	340.55	408.64
32.00	161.98	1.12	17.50	.06	328.75	392.55
32.50	174.47	1.20	20.99	.05	309.97	367.28

I.3 Isobaric Properties for Nitrogen at 20 psia (Ref. 64)

TABLE I.4.—ISOBARIC PROPERTIES FOR NITROGEN AT 20 psia

Temperature, K	Pressure, psia	Pressure, MPa	Density, kg/m^3	Volume, m^3/kg	Internal energy, kJ/kg	Enthalpy, kJ/kg	Phase
75.00	20.00	0.14	816.82	0.0012	–126.96	–126.79	Liquid
77.50	20.00	.14	805.52	.0012	–121.87	–121.70	Liquid
80.00	20.00	.14	793.94	.0013	–116.75	–116.58	Liquid
80.07	20.00	.14	793.62	.0013	–116.61	–116.44	Liquid
80.07	20.00	.14	6.13	.1631	56.66	79.15	Vapor
82.50	20.00	.14	5.92	.1689	58.63	81.92	Vapor
85.00	20.00	.14	5.72	.1748	60.63	84.74	Vapor
87.50	20.00	.14	5.54	.1807	62.62	87.53	Vapor
90.00	20.00	.14	5.36	.1865	64.59	90.30	Vapor
92.50	20.00	.14	5.20	.1922	66.55	93.06	Vapor
95.00	20.00	.14	5.05	.1980	68.50	95.80	Vapor
97.50	20.00	.14	4.91	.2037	70.44	98.53	Vapor
100.00	20.00	.14	4.78	.2094	72.38	101.25	Vapor
102.50	20.00	.14	4.65	.2150	74.30	103.95	Vapor
105.00	20.00	.14	4.53	.2207	76.22	106.65	Vapor
107.50	20.00	.14	4.42	.2263	78.14	109.34	Vapor
110.00	20.00	.14	4.31	.2319	80.05	112.03	Vapor
112.50	20.00	.14	4.21	.2375	81.96	114.70	Vapor
115.00	20.00	.14	4.11	.2431	83.86	117.38	Vapor
117.50	20.00	.14	4.02	.2487	85.76	120.04	Vapor
120.00	20.00	.14	3.93	.2542	87.65	122.71	Vapor
122.50	20.00	.14	3.85	.2598	89.55	125.37	Vapor
125.00	20.00	.14	3.77	.2653	91.44	128.02	Vapor
127.50	20.00	.14	3.69	.2708	93.33	130.67	Vapor
130.00	20.00	.14	3.62	.2763	95.21	133.32	Vapor
132.50	20.00	.14	3.55	.2819	97.10	135.97	Vapor
135.00	20.00	.14	3.48	.2874	98.98	138.61	Vapor
137.50	20.00	.14	3.41	.2929	100.86	141.25	Vapor
140.00	20.00	.14	3.35	.2984	102.75	143.89	Vapor
142.50	20.00	.14	3.29	.3038	104.62	146.52	Vapor
145.00	20.00	.14	3.23	.3093	106.50	149.16	Vapor
147.50	20.00	.14	3.18	.3148	108.38	151.79	Vapor
150.00	20.00	.14	3.12	.3203	110.26	154.42	Vapor
152.50	20.00	.14	3.07	.3258	112.13	157.05	Vapor
155.00	20.00	.14	3.02	.3312	114.00	159.68	Vapor
157.50	20.00	.14	2.97	.3367	115.88	162.31	Vapor
160.00	20.00	.14	2.92	.3422	117.75	164.93	Vapor
162.50	20.00	.14	2.88	.3476	119.62	167.56	Vapor

TABLE I.4.—(Continued)

Temperature, K	Pressure, psia	Pressure, MPa	Density, kg/m^3	Volume, m^3/kg	Internal energy, kJ/kg	Enthalpy, kJ/kg	Phase
165.00	20.00	.14	2.83	.3531	121.49	170.18	Vapor
167.50	20.00	.14	2.79	.3585	123.36	172.80	Vapor
170.00	20.00	.14	2.75	.3640	125.23	175.42	Vapor
172.50	20.00	.14	2.71	.3694	127.10	178.04	Vapor
175.00	20.00	.14	2.67	.3749	128.97	180.66	Vapor
177.50	20.00	.14	2.63	.3803	130.84	183.28	Vapor
180.00	20.00	.14	2.59	.3857	132.71	185.90	Vapor
182.50	20.00	.14	2.56	.3912	134.57	188.52	Vapor
185.00	20.00	.14	2.52	.3966	136.44	191.13	Vapor
187.50	20.00	.14	2.49	.4021	138.31	193.75	Vapor
190.00	20.00	.14	2.45	.4075	140.17	196.36	Vapor
192.50	20.00	.14	2.42	.4129	142.04	198.98	Vapor
195.00	20.00	.14	2.39	.4184	143.90	201.59	Vapor
197.50	20.00	.14	2.36	.4238	145.77	204.21	Vapor
200.00	20.00	.14	2.33	.4292	147.63	206.82	Vapor
202.50	20.00	.14	2.30	.4346	149.50	209.43	Vapor
205.00	20.00	.14	2.27	.4401	151.36	212.04	Vapor
207.50	20.00	.14	2.24	.4455	153.23	214.65	Vapor
210.00	20.00	.14	2.22	.4509	155.09	217.27	Vapor
212.50	20.00	.14	2.19	.4563	156.95	219.88	Vapor
215.00	20.00	.14	2.17	.4617	158.82	222.49	Vapor
217.50	20.00	.14	2.14	.4672	160.68	225.10	Vapor
220.00	20.00	.14	2.12	.4726	162.54	227.71	Vapor
222.50	20.00	.14	2.09	.4780	164.40	230.32	Vapor
225.00	20.00	.14	2.07	.4834	166.27	232.93	Vapor
227.50	20.00	.14	2.05	.4888	168.13	235.53	Vapor
230.00	20.00	.14	2.02	.4942	169.99	238.14	Vapor
232.50	20.00	.14	2.00	.4997	171.85	240.75	Vapor
235.00	20.00	.14	1.98	.5051	173.71	243.36	Vapor
237.50	20.00	.14	1.96	.5105	175.58	245.97	Vapor
240.00	20.00	.14	1.94	.5159	177.44	248.57	Vapor
242.50	20.00	.14	1.92	.5213	179.30	251.18	Vapor
245.00	20.00	.14	1.90	.5267	181.16	253.79	Vapor
247.50	20.00	.14	1.88	.5321	183.02	256.40	Vapor
250.00	20.00	.14	1.86	.5375	184.88	259.00	Vapor
252.50	20.00	.14	1.84	.5429	186.74	261.61	Vapor
255.00	20.00	.14	1.82	.5483	188.60	264.22	Vapor
257.50	20.00	.14	1.81	.5537	190.47	266.82	Vapor
260.00	20.00	.14	1.79	.5591	192.33	269.43	Vapor

TABLE I.4.—(Concluded)

Temperature, K	Pressure, psia	Pressure, MPa	Density, kg/m^3	Volume, m^3/kg	Internal energy, kJ/kg	Enthalpy, kJ/kg	Phase
262.50	20.00	.14	1.77	.5645	194.19	272.03	Vapor
265.00	20.00	.14	1.75	.5700	196.05	274.64	Vapor
267.50	20.00	.14	1.74	.5754	197.91	277.25	Vapor
270.00	20.00	.14	1.72	.5808	199.77	279.85	Vapor
272.50	20.00	.14	1.71	.5862	201.63	282.46	Vapor
275.00	20.00	.14	1.69	.5916	203.49	285.06	Vapor
277.50	20.00	.14	1.68	.5970	205.35	287.67	Vapor
280.00	20.00	.14	1.66	.6024	207.21	290.27	Vapor
282.50	20.00	.14	1.65	.6078	209.07	292.88	Vapor
285.00	20.00	.14	1.63	.6132	210.93	295.48	Vapor
287.50	20.00	.14	1.62	.6186	212.79	298.09	Vapor
290.00	20.00	.14	1.60	.6240	214.65	300.69	Vapor
292.50	20.00	.14	1.59	.6294	216.51	303.30	Vapor
295.00	20.00	.14	1.58	.6348	218.37	305.90	Vapor
297.50	20.00	.14	1.56	.6402	220.23	308.51	Vapor
300.00	20.00	.14	1.55	.6456	222.09	311.11	Vapor

I.4 Saturation Properties for Nitrogen (Ref. 65)

TABLE I.5.—LIQUID SATURATION PROPERTIES FOR NITROGEN

Temperature, K	Pressure, psia	Pressure, MPa	Density, kg/m^3	Volume, m^3/kg	Internal energy, kJ/kg	Enthalpy, kJ/kg
63.50	1.94	0.013	865.79	0.0012	–150.05	–150.04
64.00	2.12	.015	863.73	.0012	–149.05	–149.03
64.50	2.31	.016	861.67	.0012	–148.05	–148.03
65.00	2.52	.017	859.60	.0012	–147.05	–147.03
65.50	2.75	.019	857.52	.0012	–146.05	–146.03
66.00	2.99	.021	855.44	.0012	–145.05	–145.02
66.50	3.25	.022	853.35	.0012	–144.04	–144.02
67.00	3.52	.024	851.25	.0012	–143.04	–143.01
67.50	3.82	.026	849.14	.0012	–142.04	–142.01
68.00	4.13	.028	847.03	.0012	–141.04	–141.00
68.50	4.46	.031	844.91	.0012	–140.03	–140.00
69.00	4.82	.033	842.79	.0012	–139.03	–138.99
69.50	5.19	.036	840.66	.0012	–138.02	–137.98
70.00	5.59	.039	838.51	.0012	–137.02	–136.97
70.50	6.01	.041	836.37	.0012	–136.01	–135.96
71.00	6.46	.045	834.21	.0012	–135.00	–134.95
71.50	6.93	.048	832.05	.0012	–134.00	–133.94
72.00	7.43	.051	829.88	.0012	–132.99	–132.93
72.50	7.95	.055	827.70	.0012	–131.98	–131.91
73.00	8.51	.059	825.51	.0012	–130.97	–130.90
73.50	9.09	.063	823.31	.0012	–129.96	–129.88
74.00	9.71	.067	821.11	.0012	–128.95	–128.87
74.50	10.35	.071	818.89	.0012	–127.94	–127.85
75.00	11.03	.076	816.67	.0012	–126.92	–126.83
75.50	11.74	.081	814.44	.0012	–125.91	–125.81
76.00	12.49	.086	812.20	.0012	–124.90	–124.79
76.50	13.27	.091	809.95	.0012	–123.88	–123.77
77.00	14.09	.097	807.69	.0012	–122.87	–122.75
77.50	14.95	.103	805.43	.0012	–121.85	–121.72
78.00	15.85	.109	803.15	.0012	–120.83	–120.70
78.50	16.78	.116	800.86	.0012	–119.81	–119.67
79.00	17.76	.122	798.56	.0013	–118.79	–118.64
79.50	18.79	.130	796.26	.0013	–117.77	–117.61
80.00	19.85	.137	793.94	.0013	–116.75	–116.58
80.50	20.96	.145	791.61	.0013	–115.73	–115.54
81.00	22.12	.153	789.27	.0013	–114.70	–114.51

TABLE I.5.—(Continued)

Temperature, K	Pressure, psia	Pressure, MPa	Density, kg/m^3	Volume, m^3/kg	Internal energy, kJ/kg	Enthalpy, kJ/kg
81.50	23.32	0.161	786.92	0.0013	–113.68	–113.47
82.00	24.58	.169	784.56	.0013	–112.65	–112.43
82.50	25.88	.178	782.18	.0013	–111.62	–111.39
83.00	27.24	.188	779.80	.0013	–110.59	–110.35
83.50	28.64	.198	777.40	.0013	–109.56	–109.30
84.00	30.11	.208	774.99	.0013	–108.53	–108.26
84.50	31.62	.218	772.57	.0013	–107.49	–107.21
85.00	33.19	.229	770.13	.0013	–106.46	–106.16
85.50	34.82	.240	767.69	.0013	–105.42	–105.11
86.00	36.51	.252	765.23	.0013	–104.38	–104.05
86.50	38.26	.264	762.75	.0013	–103.34	–102.99
87.00	40.07	.276	760.26	.0013	–102.30	–101.93
87.50	41.94	.289	757.76	.0013	–101.25	–100.87
88.00	43.88	.303	755.24	.0013	–100.21	–99.81
88.50	45.88	.316	752.71	.0013	–99.16	–98.74
89.00	47.94	.331	750.16	.0013	–98.11	–97.67
89.50	50.08	.345	747.60	.0013	–97.06	–96.59
90.00	52.28	.360	745.02	.0013	–96.00	–95.52
90.50	54.55	.376	742.43	.0013	–94.94	–94.44
91.00	56.90	.392	739.82	.0014	–93.89	–93.36
91.50	59.32	.409	737.19	.0014	–92.82	–92.27
92.00	61.81	.426	734.54	.0014	–91.76	–91.18
92.50	64.38	.444	731.88	.0014	–90.70	–90.09
93.00	67.02	.462	729.19	.0014	–89.63	–88.99
93.50	69.74	.481	726.49	.0014	–88.56	–87.89
94.00	72.55	.500	723.77	.0014	–87.48	–86.79
94.50	75.43	.520	721.03	.0014	–86.40	–85.68
95.00	78.40	.541	718.26	.0014	–85.32	–84.57
95.50	81.45	.562	715.48	.0014	–84.24	–83.46
96.00	84.58	.583	712.67	.0014	–83.16	–82.34
96.50	87.80	.605	709.84	.0014	–82.07	–81.21
97.00	91.11	.628	706.99	.0014	–80.97	–80.08
97.50	94.51	.652	704.12	.0014	–79.88	–78.95
98.00	97.99	.676	701.22	.0014	–78.78	–77.81
98.50	101.57	.700	698.29	.0014	–77.67	–76.67
99.00	105.25	.726	695.34	.0014	–76.57	–75.52
99.50	109.01	.752	692.36	.0014	–75.45	–74.37

TABLE I.5.—(Continued)

Temperature, K	Pressure, psia	Pressure, MPa	Density, kg/m^3	Volume, m^3/kg	Internal energy, kJ/kg	Enthalpy, kJ/kg
100.00	112.88	0.778	689.35	0.0015	–74.34	–73.21
100.50	116.84	.806	686.32	.0015	–73.22	–72.04
101.00	120.90	.834	683.25	.0015	–72.09	–70.87
101.50	125.06	.862	680.15	.0015	–70.97	–69.70
102.00	129.32	.892	677.03	.0015	–69.83	–68.51
102.50	133.69	.922	673.86	.0015	–68.69	–67.32
103.00	138.16	.953	670.67	.0015	–67.55	–66.13
103.50	142.74	.984	667.44	.0015	–66.40	–64.92
104.00	147.42	1.016	664.17	.0015	–65.24	–63.71
104.50	152.22	1.050	660.86	.0015	–64.08	–62.49
105.00	157.12	1.083	657.52	.0015	–62.92	–61.27
105.50	162.14	1.118	654.13	.0015	–61.74	–60.03
106.00	167.27	1.153	650.70	.0015	–60.56	–58.79
106.50	172.51	1.189	647.22	.0015	–59.38	–57.54
107.00	177.87	1.226	643.70	.0016	–58.18	–56.28
107.50	183.36	1.264	640.13	.0016	–56.98	–55.00
108.00	188.96	1.303	636.50	.0016	–55.77	–53.72
108.50	194.68	1.342	632.83	.0016	–54.55	–52.43
109.00	200.53	1.383	629.10	.0016	–53.33	–51.13
109.50	206.50	1.424	625.31	.0016	–52.09	–49.81
110.00	212.60	1.466	621.45	.0016	–50.85	–48.49
110.50	218.82	1.509	617.54	.0016	–49.59	–47.15
111.00	225.19	1.553	613.55	.0016	–48.32	–45.79
111.50	231.67	1.597	609.50	.0016	–47.05	–44.43
112.00	238.30	1.643	605.36	.0017	–45.76	–43.04
112.50	245.06	1.690	601.15	.0017	–44.46	–41.65
113.00	251.95	1.737	596.85	.0017	–43.14	–40.23
113.50	258.98	1.786	592.47	.0017	–41.82	–38.80
114.00	266.16	1.835	587.98	.0017	–40.47	–37.35
114.50	273.48	1.886	583.40	.0017	–39.11	–35.88
115.00	280.94	1.937	578.70	.0017	–37.74	–34.39
115.50	288.55	1.990	573.89	.0017	–36.34	–32.88
116.00	296.33	2.043	568.96	.0018	–34.93	–31.34
116.50	304.23	2.098	563.88	.0018	–33.49	–29.77
117.00	312.31	2.153	558.66	.0018	–32.04	–28.18
117.50	320.53	2.210	553.28	.0018	–30.55	–26.56
118.00	328.92	2.268	547.73	.0018	–29.04	–24.90

TABLE I.5.—(Concluded)

Temperature, K	Pressure, psia	Pressure, MPa	Density, kg/m^3	Volume, m^3/kg	Internal energy, kJ/kg	Enthalpy, kJ/kg
118.50	337.47	2.327	541.98	0.0018	–27.50	–23.21
119.00	346.19	2.387	536.02	.0019	–25.93	–21.48
119.50	355.07	2.448	529.82	.0019	–24.32	–19.70
120.00	364.13	2.511	523.36	.0019	–22.67	–17.87
120.50	373.36	2.574	516.59	.0019	–20.97	–15.99
121.00	382.77	2.639	509.48	.0020	–19.22	–14.04
121.50	392.37	2.705	501.96	.0020	–17.40	–12.01
122.00	402.15	2.773	493.97	.0020	–15.52	–9.90
122.50	412.12	2.842	485.41	.0021	–13.54	–7.69
123.00	422.29	2.912	476.14	.0021	–11.46	–5.34
123.50	432.68	2.983	465.99	.0021	–9.24	–2.83
124.00	443.26	3.056	454.65	.0022	–6.83	–0.11
124.50	454.07	3.131	441.64	.0023	–4.17	2.91
125.00	465.12	3.207	426.08	.0023	–1.12	6.40
125.50	476.41	3.285	405.84	.0025	2.65	10.74
126.00	487.98	3.365	372.04	.0027	8.53	17.58

TABLE I.6.—VAPOR SATURATION PROPERTIES FOR NITROGEN

Temperature, K	Pressure, psia	Pressure, MPa	Density, kg/m^3	Volume, m^3/kg	Internal energy, kJ/kg	Enthalpy, kJ/kg
63.50	1.94	0.013	0.72	1.3985	46.45	65.11
64.00	2.12	.015	.78	1.2872	46.79	65.59
64.50	2.31	.016	.84	1.1865	47.14	66.06
65.00	2.52	.017	.91	1.0952	47.47	66.54
65.50	2.75	.019	.99	1.0123	47.81	67.01
66.00	2.99	.021	1.07	.9370	48.15	67.47
66.50	3.25	.022	1.15	.8684	48.48	67.94
67.00	3.52	.024	1.24	.8058	48.82	68.40
67.50	3.82	.026	1.34	.7487	49.15	68.86
68.00	4.13	.028	1.44	.6964	49.48	69.31
68.50	4.46	.031	1.54	.6486	49.80	69.76
69.00	4.82	.033	1.65	.6047	50.13	70.21
69.50	5.19	.036	1.77	.5645	50.45	70.66
70.00	5.59	.039	1.90	.5274	50.77	71.10
70.50	6.01	.041	2.03	.4934	51.09	71.54
71.00	6.46	.045	2.16	.4620	51.40	71.97
71.50	6.93	.048	2.31	.4330	51.72	72.40
72.00	7.43	.051	2.46	.4063	52.03	72.83
72.50	7.95	.055	2.62	.3815	52.34	73.26
73.00	8.51	.059	2.79	.3586	52.64	73.68
73.50	9.09	.063	2.96	.3374	52.94	74.09
74.00	9.71	.067	3.15	.3177	53.25	74.50
74.50	10.35	.071	3.34	.2994	53.54	74.91
75.00	11.03	.076	3.54	.2825	53.84	75.32
75.50	11.74	.081	3.75	.2666	54.13	75.72
76.00	12.49	.086	3.97	.2519	54.42	76.11
76.50	13.27	.091	4.20	.2382	54.71	76.50
77.00	14.09	.097	4.44	.2254	54.99	76.89
77.50	14.95	.103	4.69	.2134	55.27	77.27
78.00	15.85	.109	4.94	.2023	55.55	77.64
78.50	16.78	.116	5.21	.1918	55.82	78.02
79.00	17.76	.122	5.49	.1820	56.09	78.38
79.50	18.79	.130	5.79	.1728	56.36	78.74
80.00	19.85	.137	6.09	.1642	56.62	79.10
80.50	20.96	.145	6.40	.1561	56.88	79.45
81.00	22.12	.153	6.73	.1486	57.14	79.80
81.50	23.32	.161	7.07	.1414	57.39	80.14

TABLE I.6.—(Continued)

Temperature, K	Pressure, psia	Pressure, MPa	Density, kg/m^3	Volume, m^3/kg	Internal energy, kJ/kg	Enthalpy, kJ/kg
82.00	24.58	0.169	7.42	0.1347	57.64	80.47
82.50	25.88	.178	7.79	.1284	57.89	80.80
83.00	27.24	.188	8.17	.1224	58.13	81.12
83.50	28.64	.198	8.56	.1168	58.37	81.44
84.00	30.11	.208	8.97	.1115	58.60	81.75
84.50	31.62	.218	9.39	.1065	58.83	82.05
85.00	33.19	.229	9.82	.1018	59.06	82.35
85.50	34.82	.240	10.28	.0973	59.28	82.64
86.00	36.51	.252	10.74	.0931	59.50	82.93
86.50	38.26	.264	11.22	.0891	59.71	83.21
87.00	40.07	.276	11.72	.0853	59.92	83.48
87.50	41.94	.289	12.24	.0817	60.12	83.75
88.00	43.88	.303	12.77	.0783	60.32	84.01
88.50	45.88	.316	13.32	.0751	60.51	84.26
89.00	47.94	.331	13.89	.0720	60.70	84.50
89.50	50.08	.345	14.47	.0691	60.89	84.74
90.00	52.28	.360	15.08	.0663	61.07	84.97
90.50	54.55	.376	15.70	.0637	61.24	85.19
91.00	56.90	.392	16.35	.0612	61.41	85.41
91.50	59.32	.409	17.01	.0588	61.57	85.61
92.00	61.81	.426	17.70	.0565	61.73	85.81
92.50	64.38	.444	18.40	.0543	61.88	86.00
93.00	67.02	.462	19.13	.0523	62.03	86.19
93.50	69.74	.481	19.88	.0503	62.17	86.36
94.00	72.55	.500	20.65	.0484	62.31	86.52
94.50	75.43	.520	21.45	.0466	62.44	86.68
95.00	78.40	.541	22.27	.0449	62.56	86.83
95.50	81.45	.562	23.12	.0433	62.68	86.97
96.00	84.58	.583	23.99	.0417	62.79	87.10
96.50	87.80	.605	24.89	.0402	62.89	87.22
97.00	91.11	.628	25.81	.0387	62.99	87.33
97.50	94.51	.652	26.76	.0374	63.08	87.42
98.00	97.99	.676	27.74	.0360	63.16	87.51
98.50	101.57	.700	28.75	.0348	63.23	87.59
99.00	105.25	.726	29.79	.0336	63.30	87.66
99.50	109.01	.752	30.86	.0324	63.36	87.72
100.00	112.88	.778	31.96	.0313	63.42	87.77

TABLE I.6.—(Continued)

Temperature, K	Pressure, psia	Pressure, MPa	Density, kg/m^3	Volume, m^3/kg	Internal energy, kJ/kg	Enthalpy, kJ/kg
100.50	116.84	0.806	33.10	0.0302	63.46	87.80
101.00	120.90	.834	34.26	.0292	63.50	87.83
101.50	125.06	.862	35.47	.0282	63.53	87.84
102.00	129.32	.892	36.71	.0272	63.54	87.84
102.50	133.69	.922	37.98	.0263	63.55	87.82
103.00	138.16	.953	39.29	.0254	63.56	87.80
103.50	142.74	.984	40.65	.0246	63.55	87.76
104.00	147.42	1.016	42.04	.0238	63.53	87.71
104.50	152.22	1.050	43.48	.0230	63.50	87.64
105.00	157.12	1.083	44.96	.0222	63.46	87.56
105.50	162.14	1.118	46.48	.0215	63.41	87.46
106.00	167.27	1.153	48.06	.0208	63.35	87.35
106.50	172.51	1.189	49.68	.0201	63.28	87.22
107.00	177.87	1.226	51.35	.0195	63.20	87.08
107.50	183.36	1.264	53.08	.0188	63.10	86.92
108.00	188.96	1.303	54.86	.0182	62.99	86.74
108.50	194.68	1.342	56.70	.0176	62.87	86.54
109.00	200.53	1.383	58.59	.0171	62.73	86.33
109.50	206.50	1.424	60.55	.0165	62.58	86.09
110.00	212.60	1.466	62.58	.0160	62.41	85.84
110.50	218.82	1.509	64.67	.0155	62.23	85.56
111.00	225.19	1.553	66.84	.0150	62.03	85.26
111.50	231.67	1.597	69.08	.0145	61.81	84.94
112.00	238.30	1.643	71.41	.0140	61.58	84.59
112.50	245.06	1.690	73.81	.0135	61.32	84.21
113.00	251.95	1.737	76.31	.0131	61.05	83.81
113.50	258.98	1.786	78.90	.0127	60.75	83.38
114.00	266.16	1.835	81.59	.0123	60.43	82.93
114.50	273.48	1.886	84.38	.0119	60.09	82.44
115.00	280.94	1.937	87.29	.0115	59.72	81.91
115.50	288.55	1.990	90.33	.0111	59.33	81.35
116.00	296.33	2.043	93.49	.0107	58.90	80.75
116.50	304.23	2.098	96.79	.0103	58.44	80.11
117.00	312.31	2.153	100.25	.0100	57.95	79.43
117.50	320.53	2.210	103.87	.0096	57.42	78.70
118.00	328.92	2.268	107.67	.0093	56.86	77.92
118.50	337.47	2.327	111.67	.0090	56.25	77.08

TABLE I.6.—(Concluded)

Temperature, K	Pressure, psia	Pressure, MPa	Density, kg/m^3	Volume, m^3/kg	Internal energy, kJ/kg	Enthalpy, kJ/kg
119.00	346.19	2.387	115.89	0.0086	55.59	76.18
119.50	355.07	2.448	120.35	.0083	54.87	75.22
120.00	364.13	2.511	125.09	.0080	54.10	74.17
120.50	373.36	2.574	130.13	.0077	53.26	73.05
121.00	382.77	2.639	135.53	.0074	52.35	71.82
121.50	392.37	2.705	141.33	.0071	51.35	70.49
122.00	402.15	2.773	147.62	.0068	50.24	69.02
122.50	412.12	2.842	154.48	.0065	49.01	67.40
123.00	422.29	2.912	162.05	.0062	47.63	65.60
123.50	432.68	2.983	170.50	.0059	46.06	63.56
124.00	443.26	3.056	180.13	.0056	44.25	61.21
124.50	454.07	3.131	191.40	.0052	42.09	58.44
125.00	465.12	3.207	205.18	.0049	39.40	55.03
125.50	476.41	3.285	223.55	.0045	35.78	50.48
126.00	487.98	3.365	255.22	.0039	29.47	42.66

Appendix J.—Multilayer Insulation Design, Fabrication, and Installation

The Structural Heat Intercept, Insulation, and Vibration Evaluation Rig (SHIIVER) multilayer insulation (MLI) blanket design, fabrication, and installation was contracted to Aerospace Fabrication & Materials, LLC (AFM) with their subcontractor Lockheed Martin Corporation. In addition, testing time was made available at NASA for both thermal and structural testing where NASA and AFM collaboratively developed testing to support design decisions and aid in determining the predicted heat loads through the blanket.

J.1 Multilayer Insulation Design

The SHIIVER MLI system was designed for an 8.4-m-diameter application and scaled down to the 4-m SHIIVER tank. This includes analysis of seams, structure, penetrations, and materials. A detailed analysis effort was performed on the MLI blankets to ensure that they met the SHIIVER requirements (Ref. 42).

The final design was determined (as shown in Figure J.1) to be nominally 30 reflector layers (areas where two reflective cover sheets are touching, are counted as one layer as opposed to two). The blanket was split into three subblankets, of approximately 10 reflector layers each. While the outer layer on SHIIVER is aluminized polyimide, real applications would use a lower solar absorptivity outer coating. Since the testing used a room temperature outer wall with no solar simulators, this was an acceptable substitute. Other than between subblankets, reflector layers are each separated by two layers of netting. The nominal layer density of the blankets were 18 layers per centimeter, this was achieved in the subscale testing. Nylon tags were used at less than 25 per square meter to minimize their thermal penalty while holding the blankets together. Venting was achieved at the edge seams around the maximum diameter of the blanket.

A single seam from the edge to the center of the blanket was used. This scaled to a seam all the way across the blanket on an 8.4-m-diameter tank (same length to surface area ratio). The seams were designed to be clocked around the tank to prevent them from stacking up on top of each other. Seams were overlapped with fastener (hook and loop) tape attached with pressure sensitive adhesive and with tags every 0.30 to 0.45 m. Further seaming was used on the manway caps to allow for installation around the different penetrations through the blanket. Similarly, on the manway, the seams were staggered to minimize overlap.

Structural analysis on the MLI blanket showed that the maximum loads were driven by the depressurization load within the MLI blankets. Historical MLI data (Refs. 3, 66, and 67) shows that the maximum pressure gradient across the MLI during evacuation would be approximately 15 torr. Over the whole SHIIVER dome, this was a total load of 11.6 kN compared to under 1 kN for a 5g acceleration load on the blanket.

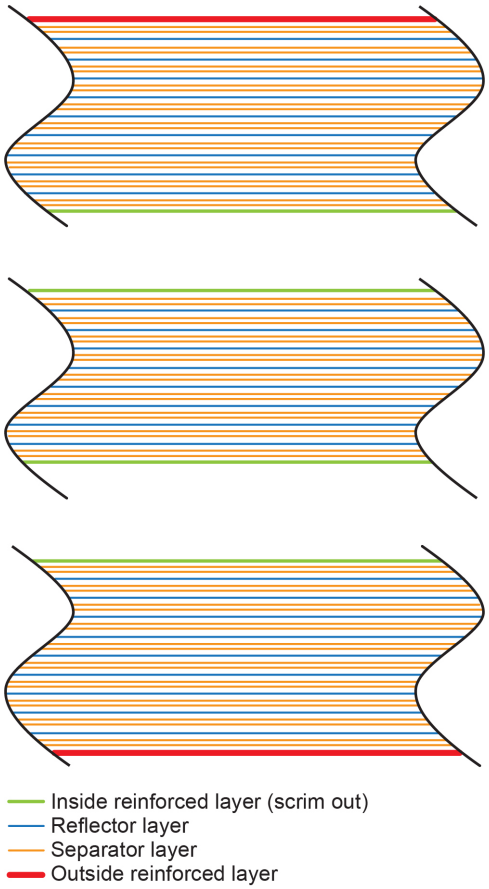

Figure J.1.—Multilayer insulation system cross section.

Originally, it was planned to use multiple Click Bond fasteners (Click Bond, Inc.), anchored only through the inner subblanket to hold the MLI onto the tank. The outer two subblankets were then attached via hook and loop fastener tape to the inner subblanket. However, due to previous experience with MLI attachments providing unanticipated loads onto spray-on foam insulation (SOFI) (Ref. 30), it was decided that the MLI supports had to pass through the SOFI. Since the Click Bond fasteners can only support approximately 180 N, it would have required 66 Click Bond fasteners on the surface of the tank of SHIIVER and four times that on the surface of an 8.4-m tank, leaving no structural margin. After discussions with the SOFI group at Marshall Space Flight Center, it was determined that this would impact the spray process enough to warrant consideration of other options. The option finally settled on was

a structural patch that was tied to a hook on the skirt (see Figure J.2). This meant that none of the load path for the MLI was on the SOFI or on the tank domes. The 44 structural patches were designed to take 376 N each, which entails a safety factor of 1.4 on the 11.6 kN total depressurization load. This would require 195 patches on the 8.4-m-diameter tank. The patches were sewn to the outer subblanket only with 27 total stitches. To help distribute the stress from the depressurization evenly to the patches and tiedowns, lacing was used to add extra stiffness and support on the aft dome (see Figure J.3).

The initial AFM proposal used Dacron® B4A netting (Invista) epoxied onto all of the Kapton® (polyimide) coversheets (DuPont™) that were facing internal to the blanket (i.e., facing other subblankets). This was due to the expectation that the B4A netting would still be able to provide loft and also have flexibility to provide give to stop tears. Based on this original concept and the probability that this was a long lead time material, the material was ordered after preliminary design review for the SHIIVER hardware.

During structural testing and after the material was ordered, it became apparent that the B4A netting was not loose and pliable after being epoxied down and did not provide the ripstop or strength that was desired and needed. As such, the SHIIVER design used a Nomex® (DuPont™) reinforced polyimide instead. However, since the material was already purchased, it was used for SHIIVER. Since SHIIVER did not actually see a rapid depressurization, the function of the coversheets will not be needed. The sling on the bottom of the tank was still made of Nomex® reinforced polyimide. This change does affect the mass of the system slightly.

The total predicted heat flux through both SHIIVER and the 8.4-m-diameter tank is 1.1 W/m^2 as shown in Table J.1 and Table J.2.

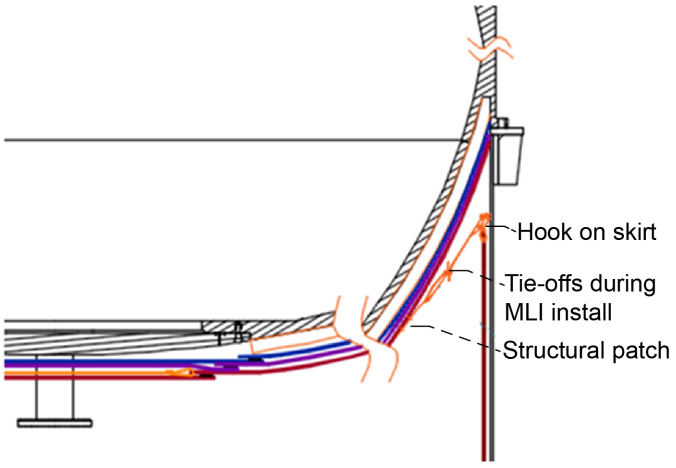

Figure J.2.—Structural Heat Intercept, Insulation, and Vibration Evaluation Rig (SHIIVER) patch and tiedown configuration, shown for aft dome. Multilayer insulation (MLI).

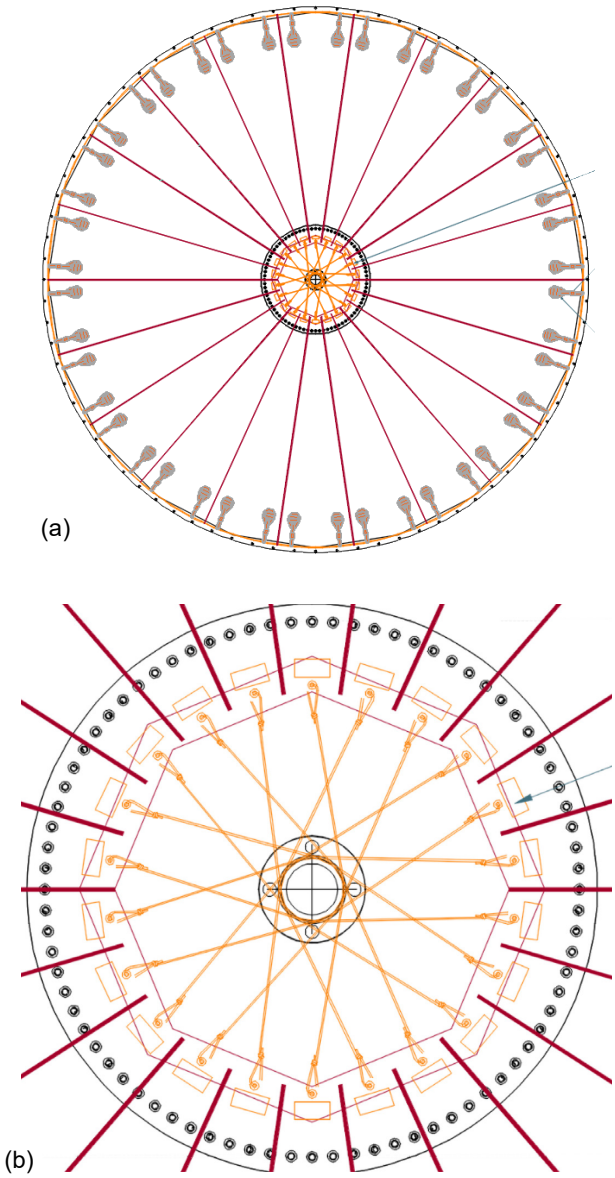

Figure J.3.—Lacing support for aft dome. (a) Full dome. (b) Manway.

TABLE J.1.—PREDICTED SHIIVER[a] MULTILAYER INSULATION THERMAL PERFORMANCE

Item	Q,[b] W	Comment
Basic insulation	17.6	• Based on new Q equation and degradation factor of 1.22 • 1.01 W/m^2 * 17.41 m^2
Simple overlap seam	.6	• Radial from center to outer edge ≤3 m • Manhole cover circumference ≤1 m • 0.147 W/m * 4 m
Structural path	.7	• 44 each at 0.016 W each
Heat leak from structural patch ties	.3	• 44 each at 0.03 W per structural patch
Total	19.2	• Note: 1.5 W/m^2 requirement over 17.41-m^2 dome is 26.1 W
Average heat flux, W/m^2	1.1	• Based on a dome area = 17.41 m^2 (prior to spray-on foam insulation)

[a]Structural Heat Intercept, Insulation, and Vibration Evaluation Rig (SHIIVER).

[b]Heat load or heat leak (Q).

TABLE J.2.—PREDICTED THERMAL PERFORMANCE FOR A SIMILAR BLANKET APPLIED TO A 8.4-m-DIAMETER TANK

Item	Q,[a] W	Comment
Basic insulation	77.8	• Based on new Q equation and degradation factor of 1.22 • 1.01 W/m^2 * 77 m^2
Simple overlap seam	0.9	• Radial from center to outer edge ≤5 m • Manhole cover circumference ≤1 m • 0.147 W/m * 6 m
Structural path	3.1	• 195 each at 0.016 W each
Heat leak from structural patch ties	1.2	• 195 each at 0.03 W per structural patch
Total	82.8	• Note: 1.5 W/m2 requirement over 77-m^2 dome is 116 W
Average heat flux, W/m^2	1.1	• Based on a dome area = 77 m^2 (prior to spray-on foam insulation)

[a]Heat load or heat leak (Q).

TABLE J.3.—TEST MATRIX AS COMPLETED

Test (coupon) number	Description	Number of MLI[a] layers	Number of seams	Number of structural patches
1	Baseline test	50	1	0
2	Reduced layer count	30	1	0
3	Two seams	30	2	0
4	Structural attachments	30	1	4

[a]Multilayer insulation (MLI).

To protect the vapor-cooling lines and inside of the skirt from radiation reflected off the MLI, 10 layer blankets were made for the inside of the skirts. These were designed in the same manner as the subblankets for the domes, with the exception that grommets were placed in 44 locations circumferentially around the blankets for tying off during installation.

J.2 Multilayer Insulation Testing

Structural, thermal, and electrostatic testing was completed on SHIIVER MLI coupons. (Refs. 68 and 69). Structural testing focused on ensuring that the structural patches could hold the required loads (376 N), while thermal testing focused on verifying the thermal design and enabling system-level predictions. Electrostatic testing aimed to understand the fundamental physics that affect the grounding requirements for MLI blankets. All testing was done at the coupon level.

In order to predict MLI performance for the SHIIVER test, some coupon thermal testing was required to assess thermal impact of design decisions. The data from the coupons also informs scaling methodologies that will use the SHIIVER data and extrapolate the SHIIVER results to larger tank sizes. The initial coupon provided a first look at the probable heat load range that can be expected on the SHIIVER test article. Subsequent articles focused on specific design details and their thermal effects on the expected performance. The testing was informed by the preliminary MLI system design. Of the many design details that could have been tested, the effect of the number of layers was thought to be most likely to change the actual design of the MLI system. This was followed by the seam performance and attachment method. All three factors were tested thermally to determine their effect on the thermal performance of the MLI system as shown in Table J.3.

Testing was performed in accordance with ASTM C–1774, using a calorimeter cooled via multiple cryocoolers (as shown in Figure J.4) (Ref. 70). All coupons were fabricated in the same method as the actual SHIIVER blanket, using the same materials and layups including packaging in subblankets of 10 layers each. All seams were staggered at least 0.10 m apart around the circumference. The calorimeter warm boundary temperature was 260 K, which is very similar to what may be expected in the SHIIVER test setup. The 30-layer coupon was found to perform essentially identically to the 50-layer coupon at approximately 0.67 W/m^2. The seam heat load as designed was 147 mW/m and comparable to seam loads measured previously on staggered overlap seams. Analysis was also completed that showed that the two seams in the coupon did not thermally interfere with each other. The stitching on the test coupon with patches only went through the outer subblanket as was done for the actual SHIIVER MLI. The penalty for the patches was approximately 10 mW per patch in close agreement

Figure J.4.—Multilayer insulation test coupons installed on the test calorimeter.

with the measured values. Results are further described by Johnson (Ref. 68).

After initial testing on multiple structural patch concepts was completed at AFM, five coupons were tested structurally via pull testing at –80 °C, representative of the expected temperatures on the outside of a cryogenic fuel tank in Earth orbit. These consisted of a strip of 10 layers of MLI that was wide enough to hold the patch and approximately 0.3 m long. The stitching was the same as when tested in the last calorimeter coupon (coupon 4) test and the grommet only went through the tab (see Figure J.5). Due to a problem in the testing hardware, on three of the five test segments, the highest load that could be applied was 500 N—this was cyclically applied with the coupons surviving up to five cycles at 500 N. The other two coupons failed at 655 N. Both values are much greater than the required strength of 376 N. The typical failure is also shown in Figure J.5, where the grommet pulled out of the patch, tearing it along the top.

Electrostatic testing was performed across three different outer layers of single aluminized polyimide (aluminum facing down), indium-tin-oxide (ITO), and germanium (see Figure J.6). The coupon configuration for the insulation is shown in Figure J.7. The layers of the coupon from the bottom to the top are the test frame, which was made from aluminum 6061, a 1-in.-thick foam substrate (for actual applications this would be a SOFI), the MLI, and a test cover sheet. For each test sample, three Click Bond 9208 insulation fasteners were used to hold the MLI and foam substrate (for actual testing, a polyurethane foam board was used to minimize cost and schedule while retaining general function) in place. The fasteners were epoxied to the aluminum plate and then a spare fastener base was used to retain the MLI.

The arc threshold for the materials was determined to be between –280 and –250 V in all low Earth orbit (LEO) cases. The low temperature testing showed less arcing (once all the sample issues were solved). This suggests that if the spacecraft or coating can be designed to maintain the surface potential in this range, then no arcing should take place.

Most geosynchronous Earth orbit (GEO) orbital environments have current fluxes of approximately 1 nA/cm^2 and most of the energy profile is captured by the 10 keV runs that were done during the low-temperature testing. Testing in that range showed few arcing events.

Figure J.5.—Structural coupon after testing. (a) Coupon in fixture. (b) Damage after testing.

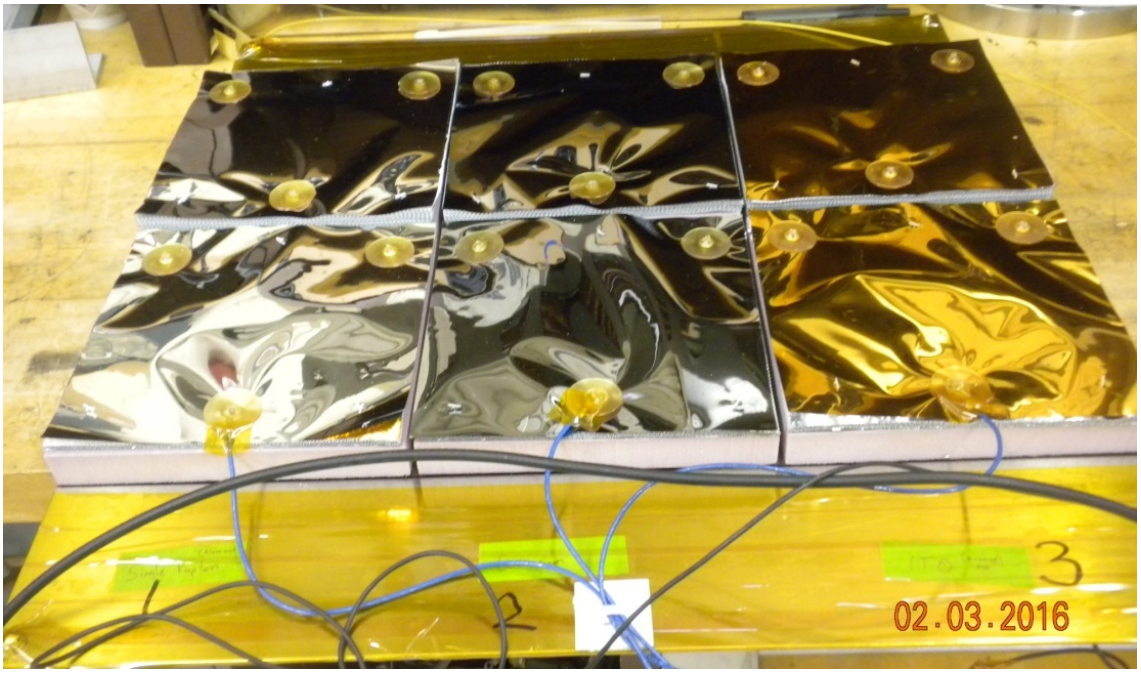

Figure J.6.—Multilayer insulation samples in preparation for electrostatic testing.

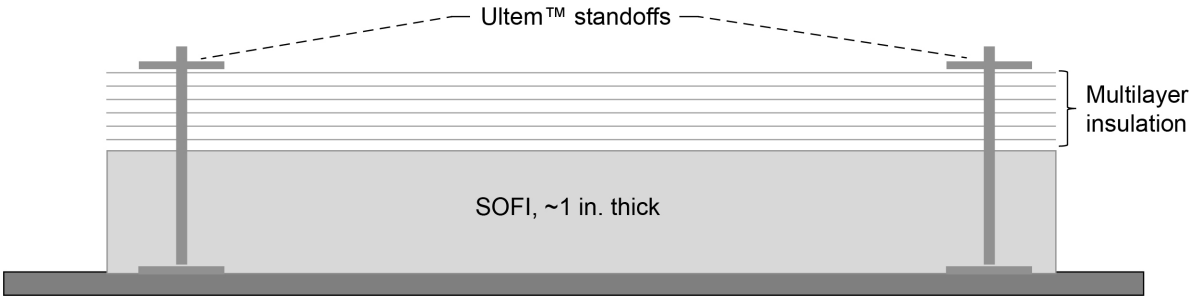

Figure J.7.—General cross section of test specimens. Spray-on foam insulation (SOFI). Ultem™ (SABIC).

While it is expected that further testing of electrostatic coupons would be required for an actual flight installation, the data gathered here suggested that before requirements are levied on a large flight cryogenic MLI system that greatly affects the thermal performance, there should be more discussion.

J.3 Multilayer Insulation Fabrication

MLI fabrication was completed using premade molds based on the size of the SHIIVER test article from 3D imaging or "white light scans" as a basis for fitting the blankets. Two molds were made, one for a SHIIVER tank dome and one for the cylindrical sections.

To form the dome blankets, the individual layers were laid over the mold and taped together to create a single, much wider blanket that conformed to the shape of the mold (see Figure J.8). Due to the size of the SHIIVER domes, access at the center of the dome was achieved through a platform. Once the subblanket was finished, the seam and central manway cover were cut out as well as any other cuts that were required prior to installation (note that holes for structural penetrations were made during installation). Silicon diodes were also installed in the MLI during fabrication with wires coming out of the MLI at the outer circumference.

The second mold was for making the skirt blankets. It was a half cylinder sized to the appropriate diameter for the blanket to be wrapped around it. The cylindrical blankets were made in halves, each going approximately 180° around the inside of the forward or aft skirt. Hook and loop fastener strips were used to attach the half blankets to each other, and grommets were installed to tie the blankets to the skirts (see Figure J.9). The lacing cord was preinstalled on the blankets to ease installation on the skirts.

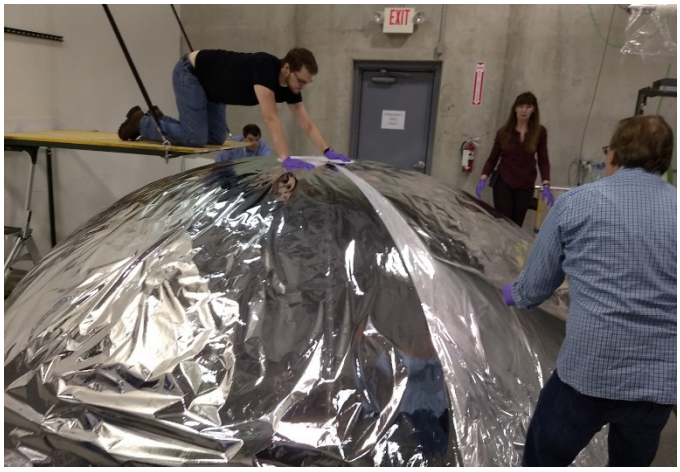

Figure J.8.—Installing multilayer insulation layers on the Structural Heat Intercept, Insulation, and Vibration Evaluation Rig (SHIIVER) dome mold.

Figure J.9.—Multilayer insulation being installed on the inside of the aft skirt.

J.4 Multilayer Insulation Installation

MLI was installed onto the skirts before mating the skirts to the tank and prior to installing the assembly into the vacuum chamber. Fixed tiedown rings were epoxied to the forward and aft skirts, 44 around the aft skirt, 0.25 m from the top and 44 around the forward skirt both on the top and approximately 0.25 m from the bottom (in several locations this interfered with the vapor-cooling channels and the tiedown rings had to be lowered). The MLI was not installed all the way to the extremities where the skirts would meet the tank due to limited room between the skirt and the tank. The blankets were tied between the grommets and the tiedown rings using lacing cord that was preinstalled on the MLI blankets (see Figure J.10 and Figure J.11). On the aft skirt, the MLI was not tied on the bottom because there was no structural reason to do so. Two technicians were able to install the blankets in approximately an hour on each skirt.

Figure J.10.—Multilayer insulation installed on the aft skirt.

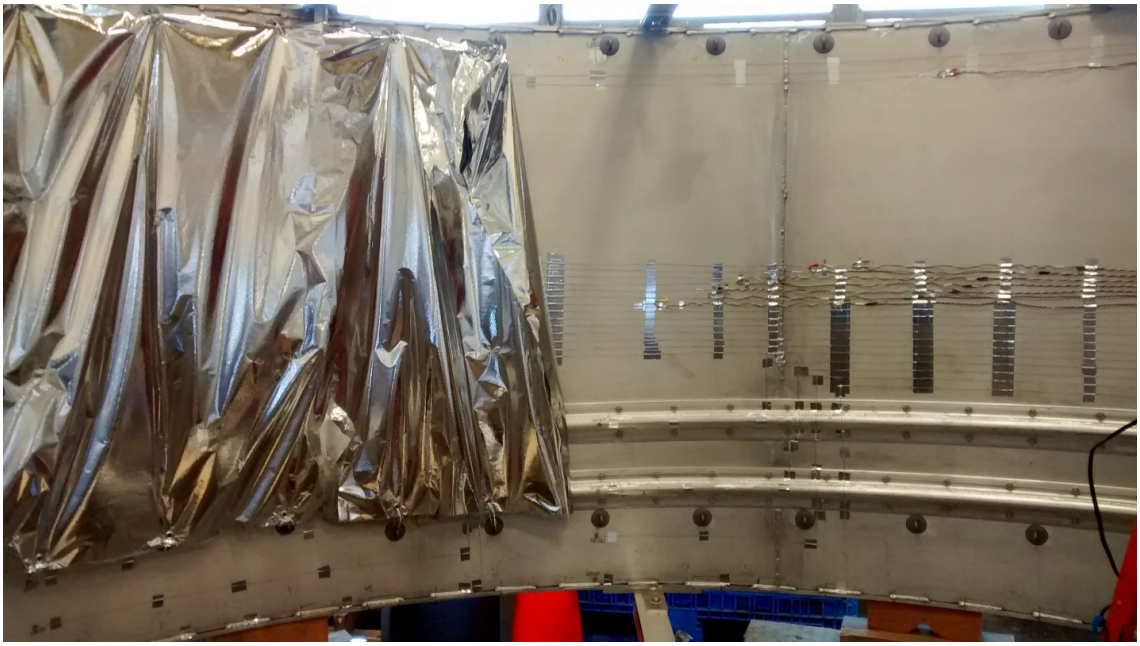

Figure J.11.—Multilayer insulation partially installed on the forward skirt.

Figure J.12.—Installation of the first subblanket on the aft dome. (a) Beginning installation. (b) Installation almost complete.

The dome MLI was installed after the initial baseline test at which point: the skirts had been attached to the tank, the tank was installed in the vacuum chamber, and the piping was installed on the tank. A sling made of ropes tied to the tiedowns on the aft skirt was used to hold the blankets against gravity and to help install the aft dome MLI. The MLI was installed subblanket by subblanket using the sling to hold everything in place and allow positioning of the diodes appropriately aligned with the heat flux sensors and SOFI diodes (see Figure J.12). Holes and slits were cut in the blankets for the MLI to go around the piping standoffs, the slits were repaired after installation (see Figure J.13). The manway cover for the first subblanket was then installed. The second subblanket was installed in much the same way (see Figure J.14). The third subblanket was

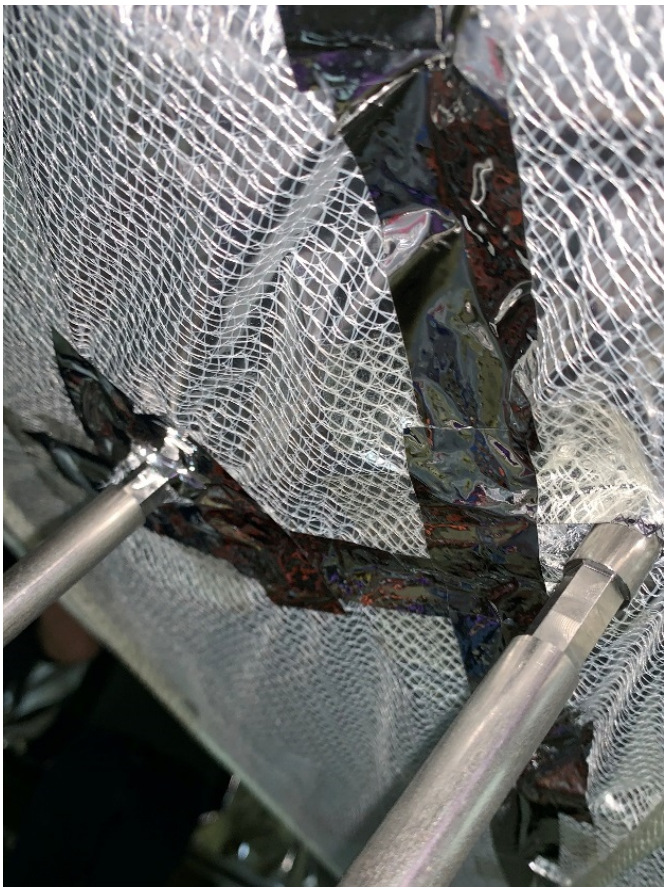

Figure J.13.—Slits in a subblanket for installation around piping standoffs.

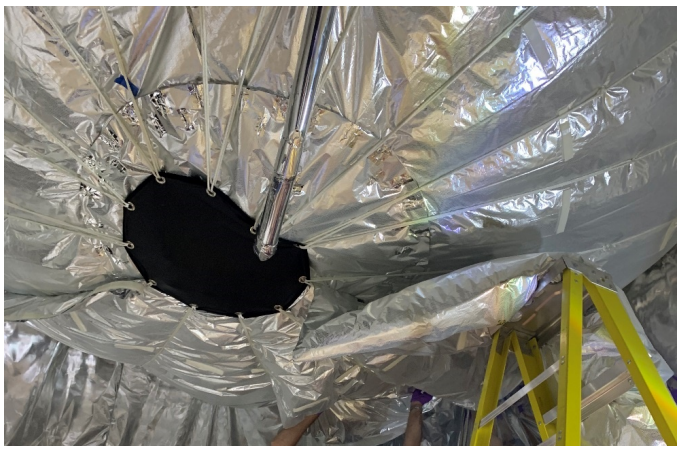

Figure J.14.—Installation of second subblanket on aft dome.

installed by tying the lacing string, preinstalled on the grommets on the structural patches to the same tiedowns on the skirts that the skirt MLI was installed on, working around the circumference (see Figure J.15). Without the vapor-cooling channels interfering with the tiedown locations, all lacing cords were able to be tied in place.

Similarly, on the top dome, while working with gravity, the subblankets were rolled into place around the scaffolding as shown in Figure J.16. It was noticed that the scaffolding and vapor-cooling tubes made it much harder to reach the tiedown rings on the forward skirt than the aft skirt. With those obstacles, only 15 of the 44 tiedowns were used (six between 25° and 65°, five between 115° and 155°, and four between 305° and 355°) as shown in Figure J.17. After the main subblankets were installed, the manway covers were attached as shown in Figure J.18. Once installation was completed, cryolite was placed into the gap between the MLI and the skirt to prevent shorting of the blanket to the skirt.

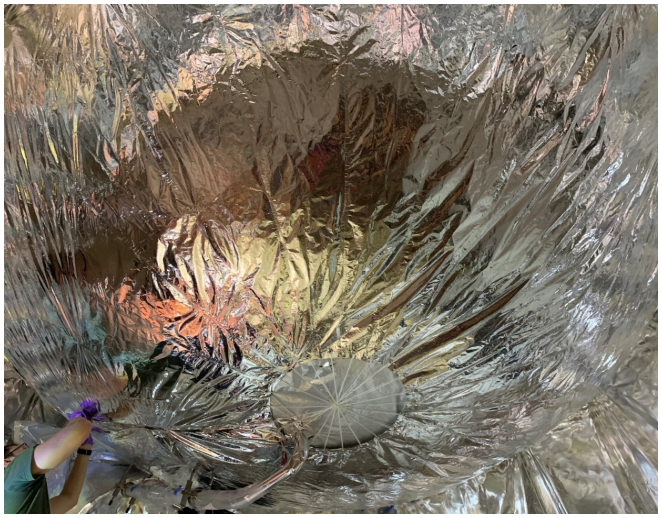

Figure J.15.—Installation of the third subblanket onto the aft dome.

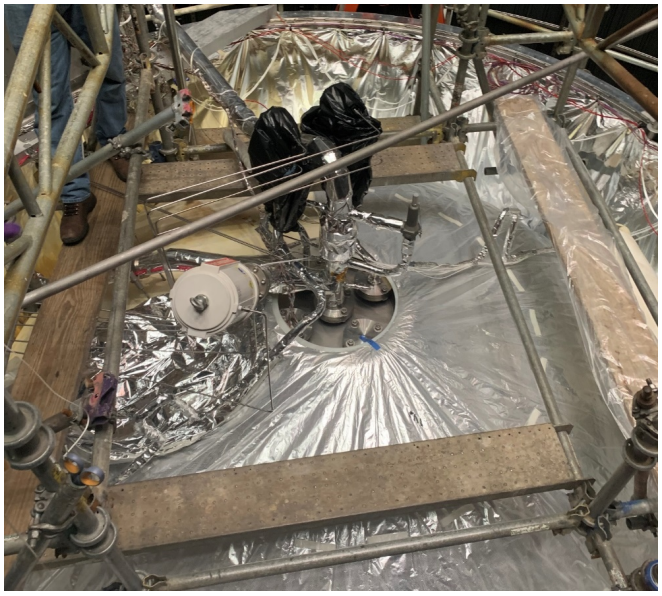

Figure J.16.—Installation of the first subblanket on the forward dome.

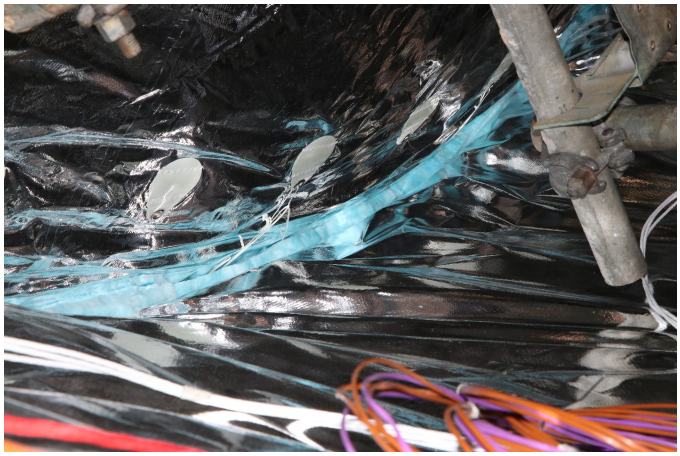

Figure J.17.—Section of multilayer insulation on the forward dome with intermittent tiedowns connected.

Figure J.18.—Attaching manway cover onto the first subblanket on the forward dome.

Four technicians installed the dome MLI in just over four days. However, if eight technicians had been available, both dome MLI could have been done in parallel rather than in series and cut the time in approximately half.

The total installed mass of the MLI on the domes was 37 kg including all hook and loop tape and materials. The mass of the tiedowns was 9.3 kg.

J.5 Multilayer Insulation System Lessons Learned

Several important lessons were learned with this installation. First of all, it may be easiest for future blanket installation on large domes to be done in the horizontal and where the tank can be rotated. The blanket-to-blanket fastener tape between subblankets was unnecessary on the domes and became a nuisance at times. On future builds, it would be ideal to increase blanket length to ensure the blanket reaches further past the tiedown rings (there was about a 0.3-m gap on the outer circumference where the blanket did not fully go down into the Y-joint, see Figure J.19). Cutting slits around standoffs for piping and valves were difficult and, in the future, the MLI should be installed prior to installing piping. Furthermore, those cuts are a foreign object debris (FOD) risk, probably where we got most of the FOD that was generated (see Section 5.6.2 on acoustic testing). It would help to have tied lacing cord to tiedown rings before the skirt was integrated to the dome to be able to reach that lacing cord. AFM would have liked better coordination on location of diodes. Finally, it was noted that the B4A reinforcement on cover materials did little to actually reinforce the base film and stop tear propagation.

Figure J.19.—Closeup image of lacing cord attachment from structural patch to tiedown and gap area above multilayer insulation blankets in Y-joint of the aft dome and skirt.

References

1. DeKruif, Jeffrey S.; and Kutter, Bernard F.: Centaur Upperstage Applicability for Multi-Day Mission Durations With Minor Insulations Modifications. AIAA 2007–5845, 2007.
2. Frederickson, G.O.: Investigation of High-Performance Insulation Application Problems. Final Report, MDC G4727, 1973.
3. Lockheed Missile & Space Company: High-Performance Thermal Protection Systems. Final Report, NASA CR–102624, 1969. https://ntrs.nasa.gov
4. Guill, J.H.: LH_2 Storability in Space Propulsion Vehicles. LMSC–685104, 1968.
5. Lofgren, C.L.; and Gieseking D.E.: Development of Manufacturing Techniques for Application of High Performance Cryogenic Insulation. NASA CR–61557, 1967. https://ntrs.nasa.gov
6. Goodyear Aerospace Corporation: Application of High Performance Insulation to Large Conical Support Structures: Final Summary Report. 1970.
7. Fredrickson, G.O.; Coes, M.C.; and Nowak, F.A.: Ranking and Selection of Insulation Systems for MNV Applications; Special Report No. 1: Investigation of High-Performance Insulation Application Problems. McDonnell Douglas Astronautics Company, 1969.
8. Leonhard, K.E.: Cryogenic Insulation Development: Final Report. NASA CR–123938, 1972. https://ntrs.nasa.gov
9. Hyde, E.H.: Multilayer Insulation Thermal Protection Systems Technology. Cryogenic Research at MSFC: Research Achievements Review, vol. 4, no. 2, 1972, pp. 5–52.
10. Stuckey, J.M.: Multilayer High Performance Insulation Materials. Research Achievements, vol. 4, no. 2, 1972, pp. 93–98.
11. Daniels, D.J., et al.: An Evaluation of Orbital Workshop Passive Thermal Control Surfaces. Presented at a Conference on Environmental Systems, Seattle, WA, 1974.
12. Walburn, A.B.: Design and Development of Pressure and Repressurization System for Reusable Space Shuttle Systems. NASA CR–120701, 1975. https://ntrs.nasa.gov
13. Sumner, Irving E.: Thermal Performance of Gaseous-Helium-Purged Tank-Mounted Multilayer Insulation System During Ground-Hold and Space-Hold Thermal Cycling and Exposure to Water Vapor. NASA TP–1114, 1978. https://ntrs.nasa.gov
14. Chronic, W.L.; Baese, C.L.; and Conder, R.L.: Design Manual Oxygen Thermal Test Article (OTTA). NASA CR–140209, 1973. https://ntrs.nasa.gov
15. Knoll, Richard H.; and DeWitt, Richard L.: Thermal Performance of a Modularized Replaceable Multilayer Insulation System for a Cryogenic Stage. NASA TN D–8282, 1977. https://ntrs.nasa.gov
16. Knoll, Richard H.; MacNeil, Peter N.; and England, James E.: Design, Development, and Test of Shuttle/Centaur G-Prime Cryogenic Tankage Thermal Protection Systems. NASA TM–89825, 1987. https://ntrs.nasa.gov
17. Mohling, R.A., et al.: Multilayer Insulation Thick Blanket Performance Demonstration. AFAL TR–87–037, 1987. Available from the AFAL/TSTR.
18. Mohling, R.A.; Bergeland, M.J.; and Girard, J.D.: Multilayer Insulation Thick Blanket Performance Demonstration. AFAL TR–90–005, 1990.
19. Martin, J.J.; and Hastings, L.J.: Large-Scale Liquid Hydrogen Testing of Variable Density Multilayer Insulation With a Foam Substrate. NASA/TM—2001-211089, 2001. https://ntrs.nasa.gov
20. Cunnington, G.R.: Thermodynamic Optimization of Cryogenic Storage System for Minimum Boiloff. Presented at the AIAA 20th Aerospace Sciences Meeting, Orlando, FL, 1982.
21. Li, Qingfu; Eyssa, Y.M.; and McIntosh, G.E.: Discrete Cooling of Supports and Multi-Layer Insulation in Helium Dewars. Adv. Cryog. Eng., vol. 29, 1984, pp. 785–793.
22. Hopkins, R.A.; and Payne, D.A.: Optimized Support Systems for Spaceborne Dewars. Cryogenics, vol. 27, no. 4, 1987, pp. 209–216.
23. Canavan, E.R.; and Miller, F.K.: Optimized Heat Interception for Cryogen Tank Support. AIP Conf. Proc., vol. 985, 2008.
24. Anderson, John E.; Fester, Dale A.; and Czysz, Paul M.: Evaluation of Long-Term Cryogenic Storage System Requirements. Adv. Cryog. Eng., vol. 35B, 1990, pp. 1725–1731.
25. Flachbart, R.H., et al.: Testing of a Spray-Bar Thermodynamic Vent System in Liquid Nitrogen. AIP Conf. Proc., vol. 823, 2006, pp. 240–247
26. Flachbart, R.H., et al.: Thermodynamic Vent System Performance Testing With Subcooled Liquid Methane and Gaseous Helium Pressurant. Cryogenics, vol. 48, no. 5, 2008, pp. 217–222.
27. Balasubramaniam, R.; and Johnson, Wesley L.: Theoretical Limits of Vapor Cooling Large Cylindrical Structures Using Boil-Off. Cryogenics, vol. 108, article 103051, 2020.
28. Jones, Jason H.: Cryogenic Propellant Storage and Transfer Small-Scale Broad Area Cooling Shield Acoustic Test. ESTSG–FY12–377, 2012.

29. Sterbentz, W.H.; and Baxter, J.W.: Thermal Protection System for a Cryogenic Spacecraft Propulsion Module. NASA CR–54879 (LMSC–A794993), 1966.
30. Johnson, Wesley L., et al.: Tank Applied Testing of Load-Bearing Multilayer Insulation (LB–MILI). AIAA 2014–3581, 2014.
31. Ameen, L.M., et al.: Testing of Hydrogen Vapor Cooling for Large Scale Structural Applications. Presented at the 28th Space Cryogenics Workshop, Southbury, CT, 2019.
32. National Aeronautics and Space Administration: Structural Heat Intercept, Insulation, and Vibration Evaluation Rig (SHIIVER) Vapor Cooled Skirt Engineering Design Report. eCryo–RPT–0119, 2019.
33. Fesmire, J.E., et al.: Spray-On Foam Insulation for Launch Vehicle Cryogenic Tanks. Cryogenics, vol. 52, nos. 4–6, 2012, pp. 251–261.
34. ET–100 Thermal Handheld Emissometer. Surface Optics Corporation. https://surfaceoptics.com/products/reflectometers-emissometers/et100-thermal-hand-held-emissometer/ Accessed March 12, 2020.
35. ASTM E 903–96: Standard Test Method for Solar Absorptance, Reflectance, and Transmittance of Materials Using Integrating Spheres. West Conshohocken, PA, 1996.
36. Kudlac, Maureen T.; Weaver, Harold F.; and Cmar, Mark D.: NASA Plum Brook's B–2 Test Facility: Thermal Vacuum and Propellant Test Facility. NASA/TM—2012-217234, 2012. https://ntrs.nasa.gov
37. Reverberant Acoustic Test Facility (RATF). 2019. https://www1.grc.nasa.gov/facilities/sec/#reverberant-acoustic-test-facility-ratf. Accessed March 4, 2020.
38. Bejan, A.: Advanced Engineering Thermodynamics. John Wiley & Sons, New York, NY, 1988.
39. Guy, Walter W.; and Ellis, Wilbert E.: Vacuum Chamber Heat-Transmission Analysis. NASA TM X–1355, 1967. https://ntrs.nasa.gov
40. Malroy, Eric T.: Free Molecular Heat Transfer Programs for Setup and Dynamic Updating the Conductors in Thermal Desktop. 2007. https://ntrs.nasa.gov/archive/nasa/casi.ntrs.nasa.gov/20070030243.pdf. Accessed Dec. 8, 2020.
41. Summers, R.L.: Empirical Observations on the Sensitivity of Hot Cathode Ionization Type Vacuum Gages. NASA TN–D–5285, 1969. https://ntrs.nasa.gov
42. Frank, D.; Nast, T.; and Mistry, V.: SHIIVER MLI Analysis Report. Lockheed Martin Space Systems Company Advanced Technology Center, Palo Alto, CA, December 2017.
43. Boeing: TPS Material Properties. Design Decision Memorandum DDM–00841, Rev. C, 2017.
44. Finckenor, Miria: Optical Properties of SLS Thermal Control and Thermal Protection System Materials. NASA WR–EM50–2015–0111, 2015.
45. LORD Corporation: Aeroglaze Z306 Flat Black Absorptive Polyurethane, Low Outgassing. Product Information Sheet, 2004.
46. Tuttle, James; Canavan, Edgar; and Jahromi, Amir: Cryogenic Thermal Conductivity Measurements on Candidate Materials for Space Missions. Cryogenics, vol. 88, 2017, pp. 36–43.
47. National Institute of Standards and Technology: Material Properties: 304L Stainless (UNS S30403). https://trc.nist.gov/cryogenics/materials/304LStainless/304LStainless_rev.htm Accessed Dec. 8, 2020.
48. Bejan, Adrian; and Kraus, Allan D.: Heat Transfer Handbook. John Wiley & Sons, Inc., Hoboken, NJ, 2003.
49. Scientific Instruments: Silicone Diode Thermometer Model Si410 Typical Response 020–114. West Palm Beach, FL, Dec. 15, 2005.
50. Van Dresar, Neil T.: Liquid Oxygen Thermodynamic Vent System Testing With Helium Pressurization. NASA/TP—2014-216633, 2014. https://ntrs.nasa.gov
51. Hastings, L.J., et al.: Spray Bar Zero-Gravity Vent System for On-Orbit Liquid Hydrogen Storage. NASA/TM—2003-212926, 2003. https://ntrs.nasa.gov
52. COMSOL Multiphysics: Software Version 5.4, 2018. https://www.comsol.com/release/5.4 Accessed Dec. 9, 2020.
53. Moldover, M., et al.: Microwave Determination of the Volume of a Pressure Vessel. Meas. Sci. Technol., vol. 26, no. 1, 2014.
54. Lemmon, E.; Huber, M.; and McLinden, M.: NIST Standard Reference Database 23: Reference Fluid Thermodynamic and Transport Properties-REFPROP, Version 9.1, 2013. https://www.nist.gov/publications/nist-standard-reference-database-23-reference-fluid-thermodynamic-and-transport Accessed Dec. 9, 2020.
55. Zimmerli, Gregory A., et al.: Radio Frequency Mass Gauge Test Results From Robotic Refueling Mission 3 Operations on International Space Station. NASA/TP-20205000671, 2020. Available from the NASA STI Program.
56. Johnson, W.L.; Balasubramaniam, R.; and Westra, K.: Testing of Heat Flux Sensors at Cryogenic Temperatures. IOP Conf. Ser. Mater. Sci. Eng., vol. 755, no. 012074, 2020.
57. Barrios, M.; and Van Sciver, S.W.: Thermal Conductivity of Rigid Foam Insulations for Aerospace Vehicles. Cryogenics, vols. 55–56, 2013, pp. 12–19.
58. Black I.A.; and Glaser, P.E.: Progress Report on Development of High-Efficiency Insulation. Adv. Cryog. Eng., vol. 6, 1961, pp. 32–41.

59. Srinivasan, J.: A Paradox in Radiation Heat Transfer. Reson., vol. 12, 2007, pp. 85–91.
60. Elchert, J.P.: Cryogenic Multilayer Insulation Theory and an Analysis of Seams Assuming Spherical Blankets Under a Variety of Assumptions. Master's Thesis, Cleveland State University, 2017.
61. Demspey, Paula J.; and Fabik, Richard H.: Using Silicon Diodes for Detecting the Liquid-Vapor Interface in Hydrogen. NASA TM–105541, 1992. https://ntrs.nasa.gov
62. National Institute of Standards and Technology: Isobaric Properties for Parahydrogen. 2018. webbook.nist.gov/cgi/fluid.cgi?P=20&TLow=20&THigh=300&TInc=2.5&Applet=on&Digits=5&ID=B5000001&Action=Load&Type=IsoBar&TUnit=K&PUnit=psia&DUnit=kg%2Fm3&HUnit=kJ%2Fkg&WUnit=m%2Fs&VisUnit=uPa%2As&STUnit=N%2Fm&RefState=DEF Accessed Dec. 3, 2019.
63. National Institute of Standards and Technology: Saturation Properties for Parahydrogen. 2018. webbook.nist.gov/cgi/fluid.cgi?TLow=14&THigh=300&TInc=2.5&Applet=on&Digits=5&ID=B5000001&Action=Load&Type=SatP&TUnit=K&PUnit=psia&DUnit=kg%2Fm3&HUnit=kJ%2Fkg&WUnit=m%2Fs&VisUnit=uPa%2As&STUnit=N%2Fm&RefState=DEF Accessed Dec. 3, 2019.
64. National Institute of Standards and Technology: Isobaric Properties for Nitrogen. 2018. webbook.nist.gov/cgi/fluid.cgi?P=20&TLow=75&THigh=300&TInc=2.5&Applet=on&Digits=5&ID=C7727379&Action=Load&Type=IsoBar&TUnit=K&PUnit=psia&DUnit=kg%2Fm3&HUnit=kJ%2Fkg&WUnit=m%2Fs&VisUnit=uPa%2As&STUnit=N%2Fm&RefState=DEF Accessed Dec. 3, 2019.
65. National Institute of Standards and Technology: Saturation Properties for Nitrogen. 2018. webbook.nist.gov/cgi/fluid.cgi?TLow=63.5&THigh=126&TInc=0.5&Applet=on&Digits=5&ID=C7727379&Action=Load&Type=SatP&TUnit=K&PUnit=psia&DUnit=kg%2Fm3&HUnit=kJ%2Fkg&WUnit=m%2Fs&VisUnit=uPa%2As&STUnit=N%2Fm&RefState=DEF. Accessed Dec. 3, 2019.
66. Nast, T.C.; and Coston, R.M.: Investigation of the Gas Flow Within Multilayer Insulations and Its Effect on Cryogenic Space Vehicle Design. Reprinted from Chemical Engineering Progress Symposium Series, vol. 62, no. 61, 1966.
67. Sumner, Irving E.; and Maloy, Joseph E.: Transient Thermal Performance of Multilayer Insulation Systems During Simulated Ascent Pressure Decay. NASA TN D–6335, 1971. https://ntrs.nasa.gov
68. Johnson, W.L., et al.: Testing of SHIIVER MLI Coupons for Heat Load Predictions. IOP Conf. Ser. Mater. Sci. Eng., vol. 755, no. 1, 2020, p. 02151.
69. Vaynor, B.V.; Galofaro, J.T.; and Johnson, W.L.: Electrostatic Testing of Multilayer Insulation for In-Space Cryogenic Vehicles. IEEE Trans. Plasma Sci., vol. 47, no. 8, 2019, pp. 3810–3815.
70. Chato, David J.; Johnson, Wesley L.; and Van Dresar, Neil T.: Design and Operation of a Calorimeter for Multilayer Insulation Testing. AIAA 2016–4775, 2016.